

Proceedings of the International Conference

Energy & Fluid Mechanics

18. 11. 2026 - 19. 11. 2026

Creative and Cultural Center Linserka

Liberec (Czech Republic)

efmconf.com | efm@efmconf.com

Experimental Fluid Mechanics ● Thermodynamics

Energy ● Energy Systems ● Aeronautics ● Avionics

Sponsor: TechSim Engineering

Steering Committee

Petra Dančová
Jaroslav Pulec

Sciences Committee

Vít Tomáš – Head of the committee
asphericon, s.r.o., Czech Republic

Dančová Petra
Teplárna Liberec, a.s., Czech Republic

Forman Matěj
Keysight, Czech Republic

Koca Kemal
Abdullah Gül University, Turkey

La Mantia Marco
Charles University, Czech Republic

Matas Richard
University of West Bohemia in Pilsen, Czech Republic

Mrázek Petr
Czech Polytechnics Institut Ltd., Czech Republic

Němec Vladimír
Czech Polytechnics Institut Ltd., Czech Republic

Pastuszko Robert
Kielce University of Technology, Poland

Peszynski Kazimierz
Bydgoszcz University of Science and Technology, Poland

Piasecka Magdalena
Kielce University of Technology, Poland

Příhoda Jaromír
professor emeritus at The Czech Academy of Sciences, Czech Republic

Uruba Václav
The Czech Academy of Sciences, Czech Republic

Vinš Václav
The Czech Academy of Sciences, Czech Republic

The texts of the papers in this volume were set individually by the authors. No corrections to the text have been carried out by the publisher. Any options, findings and conclusions or recommendations expressed in this book are those of the individual authors on their own responsibility.

Table of Contents

Contributions

Ondřej Bartoš, Adam Huněk, Jan Hrubý 5
Controlled generation of heterogeneous condensation nuclei from NaCl solutions in a fine aerosol generation unit
Karolina Bębacz, Robert Kaniowski 9
Effect of TiO2 nanoparticles on heat transfer and critical heat flux during pool boiling of water-based nanofluids
Abdelghani Belhanafi, Laouari Adjllout 15
CFD study of eccentric agitator in cylindrical tanks with different bottom geometries
Juraj Čechovič 19
Airfoil polar uncertainty at low Reynolds numbers in the conceptual design of stratospheric aircraft
Tawfiq Chekifi, Reski Khelifi, Mebrouk Adouane, Ahmed Hamada, Khaled Touafek 29
Experimental investigation of a pyramid solar still enhanced with paraffin wax and natural sand for enhanced freshwater
Norbert Dadas, Robert Pastuszko 38
Pool boiling of Novec-649 on surfaces with minichannels partially filled with porous structures
Z. Elkhaldi, F. Bouregba, R. Tayeb, L. Adjlout, O. Imine 42
Hydrodynamic performance of baseline and slotted NACA 4412 hydrofoils under cavitating conditions using transient CFD
Z. Elkhaldi, F. Bouregba, R. Tayeb, L. Adjlout, O. Imine 51
Hydrodynamic performance of baseline and slotted NACA 4412 hydrofoils under cavitating conditions using transient CFD
Baris Gungordu 59
Effect of synthetic jet placement on the near- and post-stall aerodynamics of the NLF(1)-0416 airfoil
Jindřich Hála, Pavel Psota, David Šimurda 67
Multiple flow states in a turbine tip-section cascade with supersonic inlet flow
Jakub Hampejs, Martin Kozelka, Václav Beránek, Martin Libra 75
Mathematical models for forecasting photovoltaic power output
Jiří Haščyn 83
A protocol for synchronized microclimate and air quality monitoring on a Prague metro platform
Michal Hoznedl, Jakub Vlasák, Jindřich Bém, David Hron, Matěj Ranš 87
Measurement of coarse droplets in a steam turbine
Adam Huněk, Ondřej Bartoš 94
Influence of airfoil angle of attack on the size distribution of coarse droplets formed from a liquid film
Michala Jakubcová 100
Machine learning prediction of hourly urban NO2 for air-quality management in decarbonising cities: A random forest approach
Lukáš Jirásek, Ondřej Bartoš, Adam Huněk 110
Experimental investigation of thin liquid films by the laser interferometry
Robert Kaniowski, Robert Pastuszko, Karolina Bębacz, Julia Sacharz, Marta Fryze 116
Analysis of the uncertainty in determining heat flux and heat transfer coefficient during pool boiling
David Koziel 123
Applicability of parallel compressor theory to centrifugal compressors with inlet total pressure distortion
Martin Miczan, Jindřich Bém, Václav Sláma 135
Modernization of valve test rig and validation of measured results
Anna Młynarczykowska, Klaudia Zwolińska-Glądys, Marek Jaszczur 139
Fluid flow mixing efficiency in cylindrical and rectangular stirred tanks: an experimental comparison
Bayode Owolabi, Stepan Nosek, Vladimir Fuka 147
Buoyant flows and pollutant dispersion in three-dimensional street canyons
Robert Pastuszko, Robert Kaniowski, Izabela Cękiel 152
Determination of the temperature effectiveness of cross-flow and glycol run-around heat recovery systems
Magdalena Piasecka, Mirosław Grabowski, Artur Piasecki 158
Effect of mass flow rate on the thermal behaviour of Thermasolv IM6 in a heated rectangular minichannel
Magdalena Piasecka, Artur Piasecki 164
Proposed methodology for electrical and optical diagnostics of gas–liquid flows in pipes and minichannels
Artur Piasecki, Przemysław Kłys, Magdalena Piasecka 170
A modular acquisition and data architecture for wire-mesh sensors in multiphase flow diagnostics
Pavel Procházka, Vladislav Skála, Pavel Antoš 176
Experimental investigation of flow-field topology in a hybrid wind tunnel test section for aeroelastic studies of steam turbine blades
Matěj Ranš, Richard Matas, Michal Hoznedl, Josef Voldřich 184
Numerical simulation of cylindrical rotating cavity noise
Rajkumar Sarma, Monika Součková, Olga Prokopová, Miroslav Čenský, Aleš Blahut, Václav Vinš 192
Comparison of correlations for liquid density of aqueous binary mixtures with selected salts
Jan Sedláček, Richard Matas 200
Experimental validation of the properties of a hybrid low-voltage cable
Huzaifa Amir Syed, Kemal Masera 205
A comparative RANS-EDC study of HEFA (hydroprocessed esters and fatty acids) and Jet A-1 combustion in the Sandia Flame D
František Veselý, Adam Huněk, Ondřej Bartoš, Václav Vinš 211
Experimental evaluation of THF-promoted CO2 hydrate formation for seasonal energy storage and Power-to-X applications
Klaudia Zwolińska-Glądys, Jean Paul Cardona Murillo, Marek Borowski, Marek Jaszczur 216
Influence of electrode geometry on airflow characteristics in a needle-to-cylinder EHD fan: an experimental study

Controlled generation of heterogeneous condensation nuclei from NaCl solutions in a fine aerosol generation unit

Ondřej Bartoš [1*], *Adam* Huněk[1] *and Jan Hrubý*[2]

[1]CTU in Prague, Energy Engineering Department, Technická 4, 166 07 Prague 6, Czechia
[2]Institute of Thermomechanics, Czech Academy of Sciences, Dolejškova 5, 182 00, Praha, Czechia

Abstract. Nucleation experiments in expansion chambers require well-defined populations of heterogeneous condensation nuclei at a known humidity and temperature. This paper describes the Fine Aerosol Generation Unit (FAGU), in which droplets produced by a medical nebulizer are mixed with filtered carrier air and dried in a settling chamber, while the relative humidity and temperature of the outlet gas can be adjusted independently of the aerosol source. The droplet size of the nebulizer was measured by phase Doppler anemometry (PDA); the number-median diameter is approximately 4 µm and the Sauter mean diameter about 8 µm. The unit was tested with pure water and with aqueous sodium chloride solutions of 0.01, 0.1 and 1 wt.%, using a humidity and temperature sensor and a condensation particle counter (CPC) at the outlet. The relative humidity histories of the three NaCl solutions were practically identical, with a maximum of about 55 %. The maximum particle number concentration, however, increased from 1.9×10^5 cm^{-3} for 0.01 wt.% to 3.6×10^5 and 5.7×10^5 cm^{-3} for 0.1 and 1 wt.%. Pure water alone produced 2.0×10^5 cm^{-3} particles, which is attributed to dissolved impurities and sets the lower limit of the method. The results show that the number of nuclei can be tuned through the solution concentration without a visible change of the humidity, which is the capability required for future heterogeneous nucleation experiments.

1 Introduction

Rapid adiabatic expansion accompanied by condensation of the working fluid occurs in steam turbines, compressed air systems and natural gas processing, and it is increasingly relevant for carbon capture, transport, utilization and storage. The formation of droplets is usually classified into unary homogeneous nucleation (pure vapour), binary homogeneous nucleation (mixtures of vapours) and heterogeneous nucleation (in the presence of aerosol particles). Real conditions, however, frequently lead to transitional regimes in which the nucleation pathway cannot be classified unambiguously [1, 2].

To study these regimes in an expansion chamber, the initial state of the gas must be known and controllable. The aerosol should consist of particles of a single substance, ranging from a few nanometres to several hundred nanometres, with an adjustable number concentration, and the relative humidity and temperature of the carrier gas must be set independently of the aerosol source. The most widely used method of generating particles of this size is drying of droplets formed from a sprayed solution [3]. The size of the residual particle is then governed by the droplet size at atomization and by the concentration of the dissolved substance.

In our previous paper [4] we introduced the Fine Aerosol Generation Unit (FAGU) and tested it with a nozzle, a nebulizer and surface evaporation. This paper concentrates on the nebulizer, which proved to be the most suitable atomizer. We present a new schematic of the unit, the droplet size distribution of the nebulizer measured by PDA, and new measurements with aqueous sodium chloride (NaCl) solutions of three concentrations. The question addressed is whether the number of generated nuclei can be changed by the concentration of the solution without affecting the humidity of the outlet gas.

2 Experimental setup

2.1 Fine aerosol generation unit

The FAGU regulates the concentration of aerosol particles while independently controlling the humidity of the carrier gas [3]. The complete setup is shown in Fig. 1 and its schematic in Fig. 2. The carrier air is supplied by an oil-free compressor and passes through a filtration system ending with a HEPA filter rated for the used flow rate. The flow rate is adjustable in the range of 0 to 50 L/min and is regulated by a mass flow meter. The solution is atomized at the top of the unit, where the droplets are mixed with the stream of clean air. The aerosol-laden stream then passes through a settling chamber, which provides sufficient time for the evaporation of the excess moisture. The resulting mixture of residual particles, carrier gas and water vapour proceeds to the outlet, where a combined

* Corresponding author: ondrej.bartos@cvut.cz

humidity and temperature sensor monitors the outlet conditions. Before leaving the device, the flow passes an isokinetic intake that directs a part of the aerosol stream to a condensation particle counter (CPC, TSI Model 3756). The same intake is intended as the future connection point of the expansion chamber.



Fig. 1. The experimental setup with FAGU

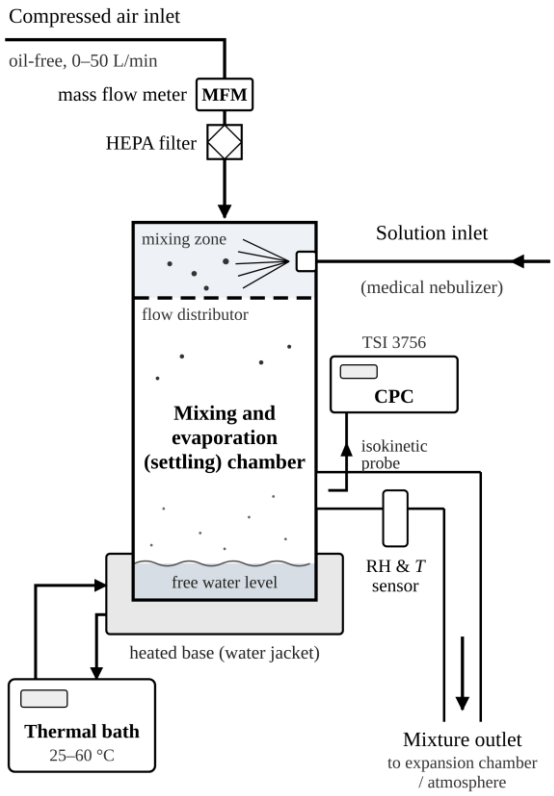


Fig. 2. The schematic of the experiment: the carrier air is filtered and metered before it enters the mixing zone, where the solution is atomized by the nebulizer; droplets evaporate in the settling chamber and the aerosol leaves through the outlet with the isokinetic CPC sampling probe and the humidity and temperature sensor. The base of the chamber is heated by a thermal bath.

If required, the outlet humidity can be adjusted independently of the aerosol source, either by changing the free water level at the bottom of the device or by heating the base of the device by the thermal bath to enhance the evaporation. The process is almost isobaric with a direct connection to the atmosphere. The correct function of the device is assumed when the outlet gas is not saturated and the relative humidity stays below 100 %, because any unbound liquid in the outlet gas would significantly distort the measurement.

2.2 Nebulizer and droplet size

Several atomizers were tested during the development of the unit [4]. The single-phase Schlick 220 nozzle (Sauter mean diameter D_{32} = 30 µm) is sensitive to clogging and produces droplets that are too large to give nuclei of several nanometres without strict limits on the purity of the sprayed water. Two-phase nozzles atomize the liquid better, but they complicate the mass balance of the supplied air. A medical nebulizer, which produces a fine aerosol with a small liquid flow, was therefore selected. It is driven by a volumetric displacement pump, and the air it consumes is led through a HEPA filter so that the interior of the FAGU is not contaminated.

The droplet size distribution of the nebulizer was measured by phase Doppler anemometry (PDA) [5]. The cumulative number distribution is shown in Fig. 3. The number-median diameter is approximately 4 µm and 80 % of the droplets lie between about 1.8 and 7.2 µm. The mean diameters of the distribution are D_{10} = 5.2 µm and D_{32} = 8.4 µm.

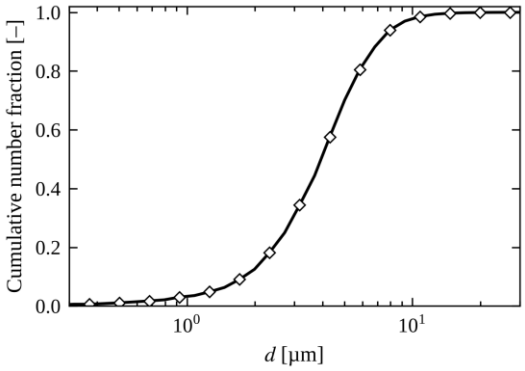


Fig. 3. The cumulative number distribution of the droplets produced by the nebulizer, measured by PDA.

When a droplet of diameter d_d containing the solute at mass fraction c dries completely, it leaves a compact residual particle of volume-equivalent diameter

$$d_p = d_d \left(\frac{c\rho_{sol}}{\rho_s}\right)^{1/3} \quad (1)$$

where ρ_{sol} is the density of the solution and ρ_s the density of the dry particle (2165 kg/m^3 for NaCl). For d_d = 4 µm, Eq. (1) gives $d_p \approx$ 0.14, 0.31 and 0.67 µm for 0.01, 0.1 and 1 wt.% NaCl, respectively. The solution concentration thus changes the size of the nuclei by a factor of 4.6 over the studied range.

2.3 Solutions and measurement procedure

Aqueous NaCl solutions of 0.01, 0.1 and 1 wt.% were prepared by dissolving the salt in water. NaCl was chosen because it is a standard reference material in aerosol science and forms stable residual particles. The operating settings of the FAGU were kept as close as possible for all runs. Each run started with the unit flushed by clean air 12 L/min, followed by a period of background measurement, the start of the nebulizer, its switch-off and a flush-out period. The particle number concentration N was recorded by the CPC every second and the relative humidity (RH) and temperature of the outlet gas by the sensor every 15 s. The outlet temperature stayed between 18 and 20 °C. To compare the runs, the time axis of each run is shifted so that $t = 0$ corresponds to the onset of the CPC signal.

3 Results

3.1 Operation with pure water

The previous tests [4] showed that without any liquid the CPC detects almost no particles at the outlet, whereas the concentration in the laboratory air is of the order of 5000 cm^{-3}, so the flow path is well separated from the surroundings. The bath temperature was set to 40 °C to avoid any undesirable condensation on the FAGU walls. Free water level at the bottom was not in the case of this paper used, all the humidity comes from the nebulizer.

The pure-water run, which was recorded in a separate experimental session, reached a higher maximum RH (67.8 %) and decayed more slowly. Unlike the NaCl runs, the nebulizer was operated for 5 min instead of 3 min, which resulted in a larger amount of water introduced into the system. Since the three NaCl solutions exhibit nearly identical humidity histories despite a hundred-fold change in concentration, the observed difference between pure water and the NaCl runs is attributed primarily to the different duration of nebulization rather than to the presence of dissolved salt.

3.2 Influence of the NaCl concentration

The comparison of pure water and the three NaCl solutions is shown in Fig. 4 and summarised in Table 1. For all NaCl solutions, the nebulizer was operated for 3 min. The relative humidity histories of the three NaCl solutions are practically identical (Fig. 4a): the humidity rises from 11–12.5 % to a maximum of 54.8–56.1 % about 3.5 min after the onset and then decreases. The maxima differ by only 1.3 percentage points although the solution concentration differs by a factor of 100. The pure-water run, which was recorded in a separate session, reached a higher maximum (67.8 %) and decayed more slowly. As the three salt solutions show no systematic dependence on concentration, this difference is probably caused by different operating conditions of that run and not by the dissolved salt.

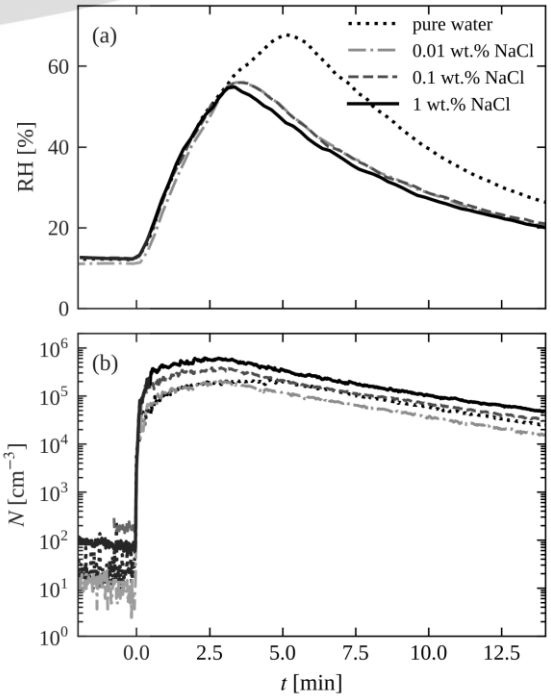


Fig. 4. The relative humidity (a) and the particle number concentration (b) for pure water and NaCl solutions. The time $t = 0$ corresponds to the onset of the CPC signal.

The particle concentration, in contrast, depends strongly on the solution (Fig. 4b). In all runs the concentration jumps within seconds after the nebulizer start, reaches its maximum about 3 min later and decays with practically the same time constant of 4.4 to 4.7 min, which indicates identical flush-out conditions. The maximum concentration is 1.9×10^5 cm^{-3} for 0.01 wt.% NaCl, which is indistinguishable from pure water (2.0×10^5 cm^{-3}), and it increases to 3.6×10^5 cm^{-3} for 0.1 wt.% and 5.7×10^5 cm^{-3} for 1 wt.% (Fig. 5). The background before the nebulizer start was 13–170 cm^{-3} and is negligible compared to these values.

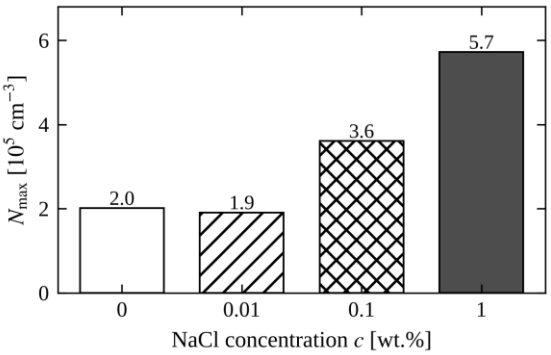


Fig. 5. The maximum particle number concentration (30 s average) as a function of the NaCl mass fraction; 0 denotes pure water.

The increase of the concentration is far from proportional to the amount of dissolved salt: a hundred-fold increase of c from 0.01 to 1 wt.% raises Nmax by a factor of only 3.0. This is expected, because every droplet leaves one residual particle and the number of particles is therefore determined mainly by the number of droplets, while the solute mass determines the size of the residue according to Eq. (1). The growth of the CPC

signal with the concentration is attributed to the smallest droplets, whose residues are too small to be detected at low concentrations and are shifted above the detection limit of the CPC when the concentration increases. For pure water and for 0.01 wt.% NaCl the residue is dominated by the impurities of the water, which explains why the two runs give the same concentration. The increase of CPC signal with increasing concentration is consistent with the estimated increase of the residual particle diameter from 0.14 µm to 0.67 µm.

Table 1. Summary of the nebulizer runs. RH_{max} is the maximum relative humidity, N_{max} the maximum 30 s average particle concentration and τ the time constant of the concentration decay.

c [wt.%]	RH_{max} [%]	N_{max} [10^5 cm^{-3}]	N_{max} ratio to pure water	τ [min]
0 (water)	67.8	2.01	1.00	4.4
0.01	56.1	1.91	0.95	4.6
0.1	56.0	3.60	1.79	4.6
1	54.8	5.72	2.85	4.7

4 Discussion

The measurements show that the FAGU with a nebulizer behaves as a source of nuclei with two practically independent controls. The humidity of the outlet gas is determined by the carrier air, the evaporation inside the unit and the heating of the base, and it did not change visibly when the NaCl concentration was increased a hundred times. The number and size of the nuclei, on the other hand, change with the concentration of the solution. The ability to vary particle concentration while maintaining similar humidity conditions is important for future expansion chamber experiments because it allows separation of thermodynamic and aerosol effects on nucleation. This separation is the main requirement for the planned heterogeneous nucleation experiments in the expansion chamber, where both the thermodynamic state and the number of nuclei influence the observed nucleation. The comparison between pure water and NaCl solutions should be interpreted with respect to the different nebulization times used in the experiments (5 min for pure water and 3 min for NaCl solutions), which explains the higher humidity peak observed in the pure-water run. Nevertheless, the nearly identical humidity histories obtained for all three NaCl concentrations demonstrate that the dissolved salt itself has only a negligible influence on the humidity evolution inside the FAGU.

Two limitations have to be mentioned. First, the water used for the solutions sets the lower limit of the concentration of nuclei: with pure water the unit produces about 2×10^5 cm^{-3} particles, so lower concentrations can only be reached with purer water or by dilution of the aerosol with additional clean air. Second, the CPC counts the particles but does not give their size. The residual sizes estimated from Eq. (1) and the PDA distribution should therefore be verified by a measurement with a differential mobility analyser. At concentrations above 10^5 cm^{-3} the CPC operates close to its upper range, and the highest values should be considered with respect to the coincidence correction of the instrument.

5 Conclusions

The Fine Aerosol Generation Unit with a medical nebulizer was tested with pure water and with NaCl solutions of 0.01, 0.1 and 1 wt.%. The droplet size of the nebulizer measured by PDA has a number-median diameter of approximately 4 µm and a Sauter mean diameter of about 8 µm. The relative humidity of the outlet gas was practically identical for all NaCl solutions, whereas the maximum particle concentration increased from 1.9×105 to 3.6×105 and 5.7×105 cm−3. Pure water gave 2.0×105 cm−3, which corresponds to the impurities of the water and defines the lower limit of the method.

The number of heterogeneous nuclei can thus be controlled by the concentration of the atomized solution while maintaining nearly identical humidity conditions The next steps are the verification of the size of the residual particles, the extension to lower concentrations and the connection of the unit to the expansion chamber.

We gratefully acknowledge the support of the Czech Science Foundation (Grant Agency of the Czech Republic), Grant No. 26-21364S.

References

1. M.J. Moore, C.H. Sieverding, Two-phase steam flow in turbines and separators: theory, instrumentation, engineering (Hemisphere Publishing, Washington, 1976)
2. M. Kolovratník, J. Hrubý, V. Ždímal, O. Bartoš, I. Jiříček et al., Nanoparticles found in superheated steam – a quantitative analysis of possible heterogeneous condensation nuclei. Proc. Inst. Mech. Eng. A J. Power Energy **228**, 186–193 (2014)
3. W.C. Hinds, Aerosol technology, 2nd edn. (John Wiley and Sons, New York, 1999)
4. O. Bartoš, A. Huněk, J. Hrubý, A study of the droplet nucleation in dependence on the gas mixture origin. EPJ Web Conf. **358**, 01001 (2026). https://doi.org/10.1051/epjconf/202635801001
5. A. Huněk, O. Bartoš, Photogrammetric image processing and comparison of experimental result with laser diffraction and the PDA method. Acta Polytech. (2025)

Effect of TiO_2 nanoparticles on heat transfer and critical heat flux during pool boiling of water-based nanofluids

Karolina Bębacz [1,2], *Robert Kaniowski*[1,2*]

[1]Kielce University of Technology, Faculty of Mechatronics and Mechanical Engineering, Al. 1000-lecia P. P. 7, PL-25-314 Kielce, Poland
[2]Central Office of Measures, Elektoralna 2, PL-00-139 Warsaw, Poland

Abstract. Boiling is an effective method of heat removal, enabling high heat fluxes at relatively low temperature differences. This study investigates the effect of titanium dioxide (TiO_2) nanoparticles on pool boiling of water-based nanofluids at concentrations ranging from 0.01 to 1 wt.% under atmospheric pressure. Experiments were performed using copper surface with a roughness of Ra = 0.143 μm. The influence of TiO_2 nanoparticles on heat flux, heat transfer coefficient, and critical heat flux was analyzed under nucleate boiling conditions. The results indicate that the addition of TiO_2 nanoparticles modifies the boiling process and can enhance the critical heat flux. The highest critical heat flux was obtained for a TiO_2 concentration of 0.1 wt.%, resulting in a 64% increase compared with base fluid. The findings highlight the potential of TiO_2/water nanofluids for high-heat-flux cooling applications, including thermal management of electronic systems and power engineering.

1 Introduction

The continuous development of electronic devices poses new challenges related to efficient heat dissipation. Effective cooling is essential for maintaining component temperatures within the required operating range, thereby preventing overheating and associated failures. However, conventional cooling methods may prove insufficient for devices generating high heat fluxes. Consequently, high-intensity heat transfer techniques, such as boiling, are employed [1-3].

An important aspect of cooling system design is the appropriate selection of the heat transfer surface. The surface should be characterized by high thermal conductivity to facilitate efficient heat transfer to the liquid. Copper is one of the most commonly used materials for this purpose, with a thermal conductivity of approximately 380 W m^{-1} K^{-1}. To enhance heat transfer, considerable research has focused on modifying heated surfaces to increase the effective heat transfer area. Various surface modifications have been investigated, including microchannels and minichannels [2, 4–7], fins [8–10], cavities [11], and other surface structures [12], which increase the contact area between the liquid and the heated surface. Another research direction aimed at enhancing heat transfer involves modifying the operating conditions, including changing the system pressure [13]. The selection of an appropriate coolant is equally important and should primarily account for the operating temperature range of the system. When boiling is required at relatively low temperatures, low-boiling-point liquids, such as ethanol, FC-72, and Novec fluids, can be used [14]. These fluids enable boiling at lower temperatures; however, compared with water, they may exhibit a lower capacity for dissipating high heat fluxes. Owing to its favorable thermophysical properties, particularly its high specific heat capacity and latent heat of vaporization, water is widely used in heat transfer applications.

In recent years, considerable research attention has been devoted to the application of nanofluids in boiling heat transfer and their influence on heat transfer performance. Nanofluids exhibit physicochemical and thermal properties that differ from those of the base fluid. They may exhibit enhanced thermal conductivity and modify the characteristics of the heated surface, including its wettability, as reflected by changes in the contact angle [15]. These properties affect the mechanisms of nucleate boiling and can alter boiling performance, including the critical heat flux (*CHF*) [16].

In recent years, considerable research attention has been devoted to the application of nanofluids in boiling heat transfer and their influence on heat transfer performance. Nanofluids exhibit physicochemical and thermal properties that differ from those of the base fluid. They may exhibit enhanced thermal conductivity and modify the characteristics of the heated surface, including its wettability, as reflected by changes in the contact angle [15]. These properties affect the mechanisms of nucleate boiling and can alter boiling performance, including the critical heat flux (*CHF*) [16].

Among the nanoparticles investigated for boiling heat transfer enhancement, metallic nanoparticles, such as gold, silver, and copper, have attracted particular interest because of their high thermal conductivity, which may contribute to heat transfer enhancement. However, owing to the relatively high cost of these

* Corresponding author: kaniowski@tu.kielce.pl

materials, other more readily available nanoparticles, such as titanium dioxide (TiO_2), silicon dioxide (SiO_2), copper (Cu) and aluminum oxide (Al_2O_3), are also being investigated [17-19].

The aim of this study was to experimentally investigate the effect of a titanium dioxide (TiO_2)-based aqueous nanofluid on heat transfer during pool boiling. The influence of TiO_2 nanoparticle concentration on two key boiling parameters was examined: the heat transfer coefficient (*HTC*) and the critical heat flux (*CHF*).

2 Materials and Methods

2.1 Preparation of nanofluids

Titanium(IV) oxide (TiO_2) nanoparticles were selected for the experimental investigation. Under typical experimental conditions, this compound does not react with the base fluid or the material of the heat transfer surface. TiO_2 exhibits high thermal stability, making it a suitable additive for base fluids used in boiling heat transfer studies. In water, TiO_2 forms colloidal suspensions, while its ability to disperse in both polar and nonpolar liquids [19] facilitates the preparation of nanofluids with a relatively uniform particle distribution.

A two-step method was employed to prepare TiO_2 nanofluids using deionized water as the base fluid. This method involves directly introducing nanoparticles into the base fluid, followed by dispersion to obtain a homogeneous suspension. It is widely used in laboratory studies owing to its simplicity and the ability to prepare suspensions with specified nanoparticle concentrations.

The TiO_2 nanopowder used in this study was anatase supplied by POL-AURA, with a declared purity of 99.5%. The average particle size was approximately 20 nm, while the specific surface area exceeded 120 $m^2\ g^{-1}$. Deionized water with an electrical conductivity of 0.003 $mS\ cm^{-1}$ was used to prepare the nanofluids.

Three TiO_2 nanofluid concentrations were prepared for the boiling experiments: 0.01 wt.%, 0.1 wt.%, and 1 wt.%. The appropriate amounts of nanopowder were weighed using a laboratory balance and subsequently added to a pre-weighed quantity of deionized water. The nanoparticles were then dispersed in the base fluid using a mechanical stirrer manufactured by Steinberg Systems (Fig. 1). The samples were stirred for approximately 30 min at a rotational speed of approximately 400 rpm and subsequently subjected to ultrasonic treatment in a bath manufactured by CNCTech (Fig. 2). Sonication was performed for approximately 3 h at an operating frequency of 50 kHz and a power of 120 W. The combination of mechanical stirring and ultrasonication was intended to achieve the most uniform nanoparticle dispersion possible in the base fluid and to limit particle agglomeration.

The prepared suspensions exhibited a milky-white appearance, which prevented direct optical observation of bubble nucleation, growth, and departure during boiling. The nanofluid samples were prepared immediately before the boiling experiments.



Fig. 1. Mixing of the nanofluid using a mechanical stirrer.



Fig. 2. Sonication of nanofluid samples in an ultrasonic bath.

2.2 Experimental setup

The pool boiling experiments were conducted using the experimental setup shown in Fig. 3. During the experiments, the power supplied to the electric heater positioned along the axis of the copper cylinder (Fig. 4a) was regulated using a variable autotransformer.

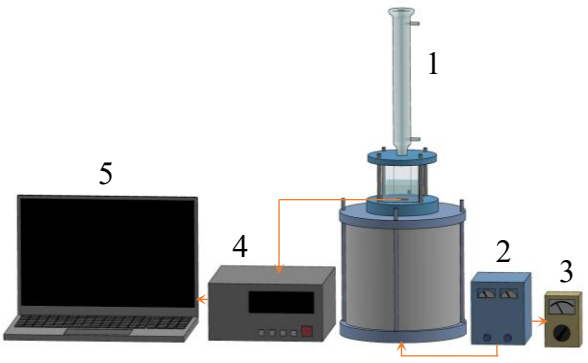


Fig. 3. Schematic diagram of the experimental setup. 1 – main module, 2 – autotransformer, 3 – wattmeter, 4 – data logger, 5 – computer.

The heat flux generated by the electric heater was conducted through the copper cylinder. Thermal insulation applied to the lateral surface of the cylinder minimized heat losses, directing the heat flux upward toward the heat spreader (Fig. 4b). The heat spreader was made of copper and had dimensions of 27 × 27 mm. Its surface was smooth, with an average surface roughness of Ra = 0.143 μm. The heat spreader was soldered to the copper cylinder using tin solder.

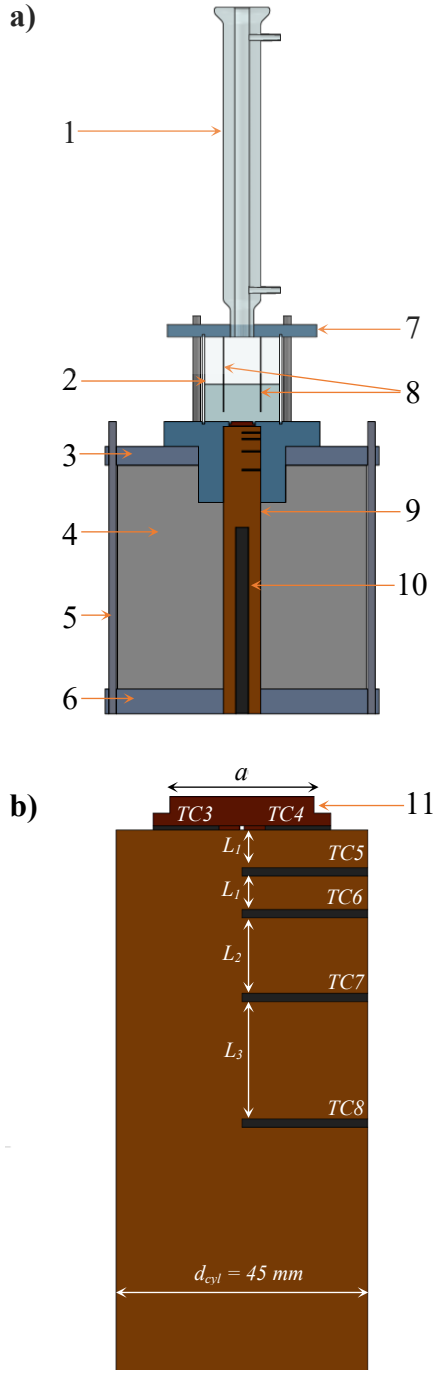


Fig. 4. (a) Cross-section of the main module: 1 – condenser, 2 – glass vessel, 3 – Teflon lid, 4 – insulation, 5 – threaded rode, 6 – Teflon base, 7 – top flange, 8 – thermocouples *TC1* and *TC2*, 9 – copper block, 10 – cartridge heater; (b) Arrangement of thermocouples in a copper cylinder: 11 – test surface, *TC3*, *TC4* – thermocouples under the test surface, *TC5–TC8* – thermocouples in the copper cylinder.

The heat flux conducted through the heat spreader was subsequently transferred to the liquid contained in a glass vessel, causing it to boil. Approximately 200 mL of liquid was used during each measurement. A reflux condenser was attached to the upper part of the glass vessel to condense the vapor and maintain atmospheric pressure within the system.

The boiling experiments were first conducted using the base fluid, followed by the prepared nanofluids immediately after sonication. The measurements were initiated with the lowest nanoparticle concentration. After each experiment, the test setup was thoroughly cleaned using deionized water and lint-free swabs, with particular attention paid to the heat transfer surface.

During the experiments, the temperatures of the liquid (*TC1, TC2*), the material beneath the heat spreader surface (*TC3, TC4*), and the central axis of the copper cylinder (*TC5–TC8*) were measured using K-type thermocouples with a diameter of 0.5 mm. The distances between thermocouples *TC3–TC8* were L_1 = 5 mm, L_2 = 10 mm, and L_3 = 15 mm, respectively. Temperature measurements were recorded approximately 10 min after each adjustment of the autotransformer setting, once the system had reached a steady state. The acquired data were transferred to a data acquisition system, enabling the determination of the parameters characterizing the boiling process, as defined by Eqs. (1)–(3):

$$HTC = \frac{q}{\Delta T} \tag{1}$$

$$q = \lambda_{Cu} \frac{T_{TC8} - T_{TC5}}{\delta_{TC8-TC5}} \frac{\pi d_{cyl}^2}{4a^2} \tag{2}$$

$$\Delta T = \frac{T_{TC3} + T_{TC4}}{2} - q\frac{\delta_s}{\lambda_{Cu}} - \frac{T_{TC1} + T_{TC2}}{2} \tag{3}$$

The experiments were continued until the boiling crisis was reached, which was identified by a rapid increase in the temperature beneath the heat spreader surface.

3 Results

The boiling curves obtained from the experiments are presented in Figs. 5 and 6. The results obtained for TiO_2 nanofluids at different concentrations were compared with those for the base fluid, i.e., deionized water.

The use of TiO_2 nanofluids resulted in a lower heat transfer coefficient (*HTC*) compared with deionized water. One of the factors that may have contributed to this reduction is the deposition of nanoparticles on the heated surface during the boiling process. Visual inspection and scanning electron microscopy (SEM) observations revealed the presence of a thin deposit layer with a thickness on the order of a few micrometers. Given the small thickness of this layer, it cannot be conclusively established that the associated increase in thermal resistance was the dominant cause of the reduction in the heat transfer coefficient. Nanoparticle deposition may also have modified the properties of the heated surface, including its wettability and the conditions governing vapor bubble nucleation and growth. These changes may have affected nucleate boiling behavior and, consequently, heat transfer

performance. However, further investigations are required to identify the dominant mechanism responsible for the observed reduction in *HTC*.

At the same time, the use of TiO_2/water nanofluids resulted in a substantial increase in the critical heat flux (*CHF*). At a nanoparticle concentration of 0.1 wt.%, the *CHF* was 64% higher than that obtained with the base fluid. This increase may be associated with potential changes in the properties of the heated surface, particularly its wettability, resulting from TiO_2 nanoparticle deposition. Improved wettability could facilitate surface rewetting by the liquid following vapor bubble departure, thereby delaying the onset of boiling crisis and allowing higher *CHF* values to be achieved. Furthermore, the presence of nanoparticles may affect selected physicochemical properties of the fluid, such as surface tension and, to a lesser extent, density and viscosity. These changes may influence the dynamics of bubble nucleation, growth, and departure, consequently affecting the boiling process and the critical heat flux.

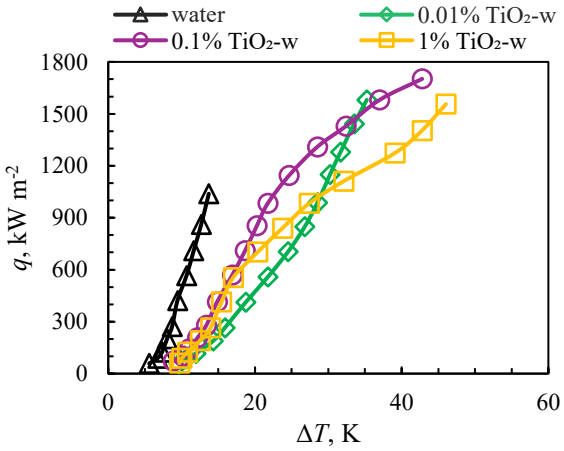


Fig. 5. Pool boiling curves: q vs. ΔT.

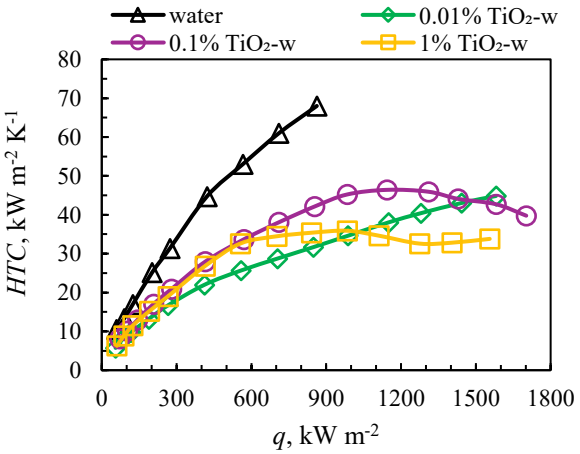


Fig. 6. Pool boiling curves: *HTC* vs. q.

The estimated relative uncertainties varied with the heat flux. At a low heat flux of 60 kW m^{-2}, the uncertainties in heat flux and heat transfer coefficient were ±33% and ±40%, respectively. At a high heat flux of 1702.3 kW m^{-2}, these uncertainties decreased to ±2.6% and ±2.9%, respectively.

A comparison of the critical heat flux (*CHF*) and the maximum heat transfer coefficient (HTC_{max}) obtained for all investigated nanofluid concentrations and deionized water (Fig. 7) enabled the identification of the most favorable nanoparticle concentration for the boiling experiments. The addition of TiO_2 nanoparticles to water resulted in an increase in *CHF*, accompanied by a decrease in *HTC*. The most favorable balance between these two parameters was obtained at a TiO_2 concentration of 0.1 wt.%, for which the *CHF* reached 1702.3 kW m^{-2} and the maximum heat transfer coefficient was 46.3 kW m^{-2} K^{-1}. This concentration was therefore considered optimal among the investigated nanofluids, taking into account the simultaneous enhancement of resistance to boiling crisis and the retention of a relatively high heat transfer performance.

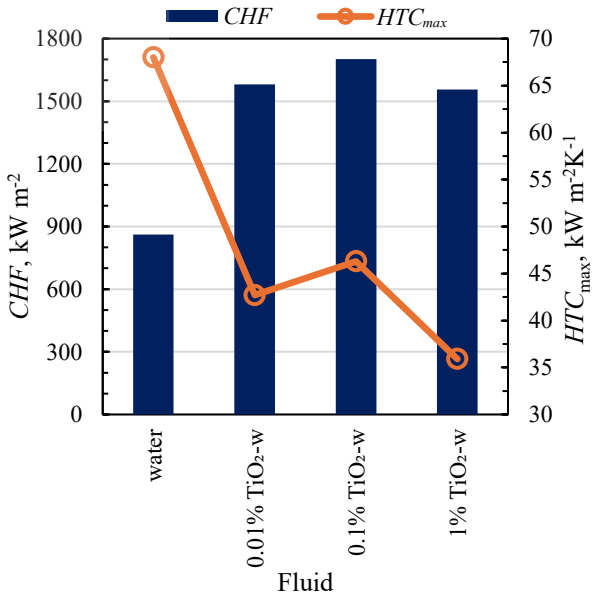


Fig. 7. Effect of TiO_2 nanoparticles concentration on *CHF* and HTC_{max} for optimal concentration selection.

4 Conclusions

The addition of TiO_2 nanoparticles to water affected nucleate pool boiling, resulting in a decrease in the heat transfer coefficient (*HTC*) and an increase in the critical heat flux (*CHF*) compared with deionized water. The most favorable balance between these parameters was obtained at a nanoparticle concentration of 0.1 wt.%, for which the *CHF* reached 1702.3 kW m^{-2}, representing a 64% increase relative to the base fluid, while the maximum heat transfer coefficient (HTC_{max}) was 46.3 kW m^{-2} K^{-1}. This concentration was considered the most favorable among those investigated.

The increase in *CHF* indicates the potential of TiO_2/water nanofluids for boiling heat transfer applications involving high heat fluxes. However, the simultaneous decrease in *HTC* should be considered when evaluating their cooling performance. Therefore, the observed increase in *CHF* alone does not establish an overall improvement in cooling effectiveness.

The increase in *CHF* indicates the potential of TiO_2/water nanofluids for boiling heat transfer applications involving high heat fluxes. However, the simultaneous decrease in *HTC* should be considered when evaluating their cooling performance. Therefore, the observed increase in *CHF* alone does not establish an overall improvement in cooling effectiveness.

Visual inspection and scanning electron microscopy (SEM) revealed a thin TiO_2 deposit layer, with a thickness on the order of a few micrometers, on the heated surface after the experiments. Its potential effects on surface wettability and boiling behavior require further investigation. Future work should include contact angle measurements, assessment of nanofluid stability, and repeatability tests to clarify the mechanisms governing the observed changes in *HTC* and *CHF*.

Nomenclature

a	– width of specimen, mm
CHF	– critical heat flux, W m^{-2}
d	– diameter, mm
HTC	– heat-transfer coefficient, W $m^{-2}K^{-1}$
L	– length, mm,
q	– heat flux, kW m^{-2}
Ra	– roughness, μm
T	– temperature, K,
TC1…TC8	– thermocouple number
w	– water

Greek symbols

δ	– thickness, mm,
λ	– thermal conductivity, W $m^{-1}K^{-1}$
ΔT	– difference of temperature, K,

Subscripts

Cu	– copper
cyl	– cylinder
s	– specimen

References

1. K. Bębacz, R. Kaniowski, Experimental Investigation of Nucleate Pool Boiling Characteristics Using SiO_2 Nanofluids. Energies **19**, 3460 (2026). https://doi.org/10.3390/en19153460
2. R. Kaniowski, K. Bębacz, Enhanced Pool Boiling Heat Transfer of FC-72 and Ethanol on Inclined Microchannel Surfaces. Energies **19**, 3478 (2026). https://doi.org/10.3390/en19153478
3. Y. Sun, Y. Tang, S. Zhang, W. Yuan, H. Tang, A Review on Fabrication and Pool Boiling Enhancement of Three-Dimensional Complex Structures. Renew. Sustain. Energy Rev. **162**, 112437 (2022). DOI: 10.1016/j.rser.2022.112437
4. B. Maciejewska, M. Piasecka, N. Dadas, K. Strąk, Fluid flow and heat transfer characteristics in minichannels - CFD calculations in simcenter STAR-CCM+. Heat Mass Transf. **61**, 22 (2025). https://doi.org/10.1007/s00231-025-03539-7
5. M. Piasecka, A. Piasecki, N. Dadas, An Experimental Investigation and Numerical Simulation of Photovoltaic Cells with Enhanced Surfaces Using the Simcenter STAR-CCM+ Software. Energies **16**, 8047 (2023). https://doi.org/10.3390/en16248047
6. R. Kaniowski, Pool boiling of Novec-649 on Inclined Microchannel. Energies **16**, 2476 (2023). https://doi.org/10.3390/en16052476
7. M. Sikora, T. Bohdal, K. Tandecka, W. Kacalak, T.G. Mathia, The Effect of Channel Surface Roughness on Two–Phase Flow Patterns: A Review. Energies **17**, 5483 (2024) https://doi.org/10.3390/en17215483
8. R. Pastuszko, R. Kaniowski, Boiling visualization on vertical fins with tunnel-pore structures. EPJ Web Conf. **25**, 02019 (2012). https://doi.org/10.1051/epjconf/20122502019
9. T. Li, J. Du, B. Zhao, J. Wang, D. Zheng, Effect of Various Micro-Fin Surfaces on Pool Boiling Heat Transfer. Appl. Therm. Eng. **274**, 126691 (2025). https://doi.org/10.1016/j.applthermaleng.2025.126691
10. A.I. Garivalis, B. Liu, J. Wei, P. Di Marco, Enhancing Pool Boiling in Microgravity Using Micro-Fins and an Electrostatic Field under Different Liquid Subcooling. Exp. Therm. Fluid Sci. **155**, 111179 (2024). https://doi.org/10.1016/j.expthermflusci.2024.111179
11. Z. Wang, Han, J. Liu, S. Liang, J. Nie, Z. Feng, X. Li, Experimental Investigation on Pool Boiling Heat Transfer Enhancement with a Composite Structure of Coiled Wires and Cavities. Int. Commun. Heat Mass Transf. **172**, 110557 (2026). https://doi.org/10.1016/j.icheatmasstransfer.2026.110557
12. K. Dutkowski, M. Kruzel, K. Rokosz, Review of the State-of-the-Art Uses of Minimal Surfaces in Heat Transfer. Energies **15**, 7994 (2025). https://doi.org/10.3390/en15217994
13. D. Kaczmarek-Piastka, T. Halon, B. Zajaczkowski, Experimental study of pool boiling on tube bundles at 3 to 5 kPa. Int. J. Heat Mass Transf. **256**, 127878 (2026). https://doi.org/10.1016/j.ijheatmasstransfer.2025.127878
14. R. Kaniowski, S. Wciślik, Thermal Performance Enhancement in Pool Boiling on Copper Surfaces: Contact Angle and Surface Tension Analysis. Energies **18**, 4471 (2025). https://doi.org/10.3390/en18174471
15. S. Wciślik, S. Mukherjee, Evaluation of Three Methods of Static Contact Angle Measurements for TiO_2 Nanofluid Droplets during Evaporation. Phys. Fluids **34**, 062006 (2022). https://doi.org/10.1063/5.0096644

16. T. Wen, J. Luo, K. Jiao, L. Lu, Experimental study on the pool boiling performance of a highly self-dispersion TiO_2 nanofluid on copper surface. Int. J. Therm. Sci. **184**, 107999 (2023). https://doi.org/10.1016/j.ijthermalsci.2022.107999
17. A. Hadžić, M. Može, K. Arhar, M. Zupančič, I. Golobič, Effect of Nanoparticle Size and Concentration on Pool Boiling Heat Transfer with TiO_2 Nanofluids on Laser-Textured Copper Surfaces. Nanomaterials **12**, 2611 (2022). https://doi.org/10.3390/nano12152611
18. J. Cieslinski, T. Kaczmarczyk, Pool Boiling of Water–Al_2O_3 and Water–Cu Nanofluids Outside Porous Coated Tubes. Heat Transf. Eng. **36**, 553-563 (2015). https://doi.org/10.1080/01457632.2014.939046
19. L. Yang, Y. Hu, Toward TiO_2 Nanofluids-Part 1: Preparation and Properties. Nanoscale Res. Lett. **12**, 417 (2017). http://dx.doi.org/10.1016/j.ijheatmasstransfer.2016.11.086

CFD study of eccentric agitator in cylindrical tanks with different bottom geometries

Abdelghani Belhanafi[1*], *Laouari* Adjllout[2]

[1,2]University of Sciences and Technology of Oran MB-USTO , Department of mechanical engineering, El Mnaouer, BP1505, Bir El Djir 31000, Oran, Algeria

Abstract. This paper presents a numerical analysis investigation of the influence of the tank bottom shape on the hydrodynamic structure of a cylindrical stirred vessel equipped with an eccentric agitator. The turbulent flow generated in stirred tanks is numerically predicted by solving the Navier-Stokes equation using the k-ε turbulent model. The influence of several parameters on the mixing efficiency has been investigated, namely: three different tank bottom shapes and a six pitched blade (6PBT) turbine operating in the down pumping direction. The numerical results were obtained using the CFD code ANSYS Fluent with the Multi-Reference Frame (MRF) approach. Finally, it was found that strong flow instabilities are induced by the vortices formed within the two fluid recirculation loops between the impeller and the tank walls. The characteristic frequency of these instabilities decreases with increasing impeller eccentricity and depends on the bottom geometry of the tank.

1 Introduction

Mechanical agitation is a process used for mixing miscible fluids, has a wide field of application, like in the preparations of industrial, chemical, and pharmaceutical products; the stirring techniques are parameters to be taken into account when the implementation of these mixtures.

Many researchers have focused on the design of bottom tanks and eccentric impeller. Hao et al. [1] who studied the influence of bottom shape on hydrodynamics and particle suspension in a DTB crystallizer. The effect of eccentrically located position of impeller on mixing time was investigated by Koji et al. [2] in agitated vessels of different bottom shapes. They concluded that the bottom shapes do not affect the mixing time but give a significant influence on power consumption. Ameur et al. [3] numerically investigated on the 3D hydrodynamics flow generated in cylindrical tank stirred by multiple eccentric impellers for viscoplastic fluids. For this systems he conclude, the agitators should be placed equally spaced at middle height, near the vessel base and free surface of liquid in order to ensure mixing in the whole vessel volume and to reduce the power consumption. For the hydrodynamics of an unbaffled cylindrical stirred vessel equipped with a six-blade disc Rushton turbine Montante et al. [4] is investigated on the effect of the shaft position (eccentricity) by numerical and experimental technique. Luan et al. [5] work on the mixing performance of pseudoplastic fluid in a flat-bottomed cylindrical tank by a novel stirrer composed of perturbed six-bladed turbine with different shaft eccentricity e=0, e=0.2 and e=0.3 respectively. They found when the eccentricity increase the mixing rate and mixing efficiency are affected. LDV method was used by Aubin et al. [6] to measure one phase turbulent flow regime in a baffle-bottomed tank with two different mobile PBT6 agitation and axial MTT6 operational in two high-beats pumping modes. By changing the pumping direction in the low mode, they observed the formation of two loops of circulation, a lower and upper second turbine with a good high pumping achieved a value of 22.5% (PBT) and 13.7% (MTT).

The objective of this study is to investigate the combined effects of tank bottom geometry, ranging from dished to flat-bottom configurations and impeller eccentricity on the hydrodynamic behavior of a stirred vessel.

2 Stirred tank configurations

As presented in Fig. 1, four geometrically scaled vessels are chosen with different tank heights: equal to H_1=0.190 m named case1, H_2=0.171 m named case 2 and H_3=0.152 m named case 3. The first system configuration is similar to Aubin et al. [6]. In these conditions, the tank height is equal to the diameter H=T for each tested geometry, and completely filled with water. In each case, a six pitched blade turbine PBT45° with diameter $D_1=H_1/2$, $D_2=H_2/2$ and $D_3=H_3/2$, located

*Corresponding author:abdelghani.belhanafi@univ-usto.dz

respectively at an off-bottom clearance $C_1=H_1/3$, $C_2=H_2/3$ and $C_3=H_3/3$. Table 1 presents the values for these cases.

The simulations were performed with an impeller rotational speed of N=240 rpm, corresponding to an impeller Reynolds number of Re=42000. The impeller was positioned at an off-axis location with an eccentricity of E/T=0.2 relative to the vessel axis.

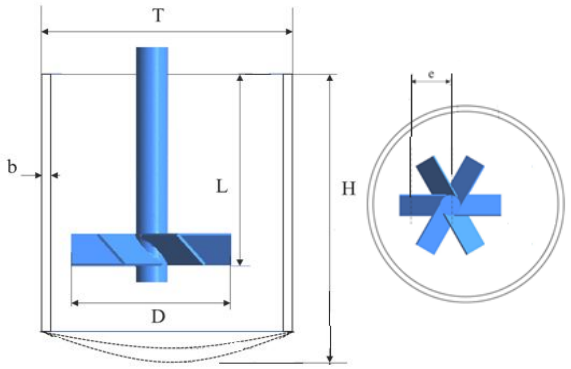


Fig. 1. Mixing vessel dimensions.

Table 1: Geometrical configuration parameters.

Tank height (m)	Impeller diameter (m)	Clearance (m)	Vessel type
H_1=0.190	D_1=0.085	C_1=0.063	Dished bottom (First)
H_2=0.171	D_2=0.088	C_2=0.059	Dished bottom (Second)
H_3=0.152	D_3=0.076	C_3=0.050	Flat bottom (Fourth)

3 Equations and mathematics

The flow in a stirred vessel can be solved by the Navier-Stokes equations. The equations are written in their averaged form RANS (Reynolds Averaged Navier Stokes) used in the case of a turbulent flow, due to the time of the turbulence scales.

The continuity equation is written as follows:

$$\frac{\partial \rho}{\partial t} + \nabla.(\rho \vec{u}) = 0 \qquad (1)$$

Where (ρ) is the density, (t) is the time,($\vec{u}$) is the velocity vector.

For the turbulent Modeling, we have used the standard (k-ε) model based on the following two equations:

$$\frac{\partial \rho k}{\partial t} + \nabla.(\rho \vec{u} k) = \nabla.\left(\left[\mu + \frac{\mu_t}{\sigma k}\right]\nabla k\right) = P - \rho\varepsilon \qquad (2)$$

$$\frac{\partial \rho \varepsilon}{\partial t} + \nabla.(\rho \vec{u} \varepsilon) = \nabla.\left(\left[\mu + \frac{\mu_t}{\sigma \varepsilon}\right]\nabla \varepsilon\right) = C_1 \frac{\varepsilon}{k} P - C_2 \frac{\varepsilon^2}{k} \qquad (3)$$

These equations represent the conservation of the turbulent kinetic energy (k) and the dissipation rate of the turbulent kinetic energy (ε) respectively.

Equations (2) and (3) are based on exact equations and reveal required constants to model the turbulence. The "standard" constant values are:

$C_\mu = 0.09, C_1 = 1.44, C_2 = 1.92, \sigma_k = 1.0, \sigma_\varepsilon = 1.3.$

4 Numerical results

4.1 Comparison with experimental result

Figure 2 shows the radial profile of dimensionless turbulent kinetic energy in axial position z/H=0.057 at up-pumping in the stirred vessel equipped with a six-pitched blade turbine (PBT6). The Comparison between the numerical results and the experimental results found by Aubin et al. [6] shows good agreement, which proves the validity of the adopted numerical method.

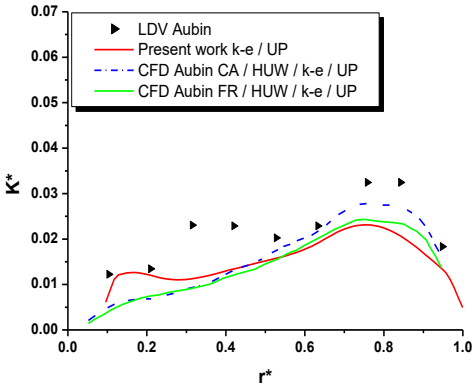


Fig. 2. Radial profiles of dimensionless turbulent kinetic energy.

4.2 Results and discussion

4.2.1 Turbulent viscosity

The vertical presentation planes of turbulent viscosity distribution illustrated in figure 3 for three geometries at the central part of the vessel. In the first configuration (dished-bottom tank), the turbulent viscosity increases throughout the entire tank volume, indicating effective turbulence distribution (fig 3a). But in the second configuration (fig 3b). the turbulent viscosity is mainly concentrated along the tank walls, while lower values are observed in the central region. In the third configuration, reducing the dished-bottom height combined with impeller eccentricity creates a dead zone (fig 3c). This weakens the local flow and decreases mixing efficiency.

a-case 1 b-case 2

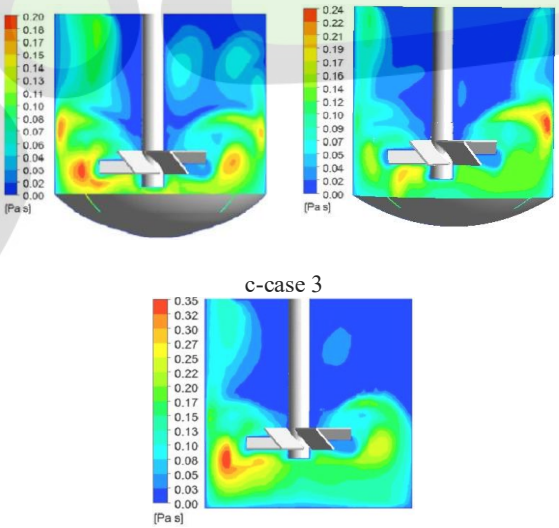


Fig. 3. Turbulent viscosity contours in r-z plane.

4.2.2 Tangential velocity

Figure 4 illustrates the tangential velocity distribution in horizontal plans for three different cases. However, in all configurations, the tangential velocity remains very low near the tank wall due to the presence of the four baffles. This indicates the existence of stagnant fluid regions in these areas. Contrary, the down-pumping action of the eccentric impellers, combined with the bottom shape of stirred vessel, enhances the tangential velocity.

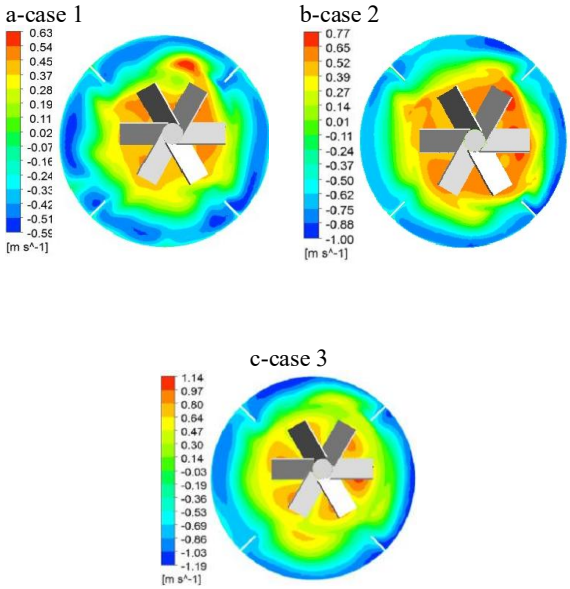


Fig. 4. Tangential velocity distribution at z=40 mm.

4.2.3 Flow patterns

Figure 5 illustrates the flow field in the *r–z* plane containing the blade for the three tank configurations. As the impeller approaches the tank wall, a significantly larger secondary recirculation loop of the flow is develops. In the first configuration, corresponding to the tank with a dished bottom, a third, highly intense recirculation loop is observed above the impeller (fig. 5a). In contrast, this recirculation loop is much weaker in the other two configurations cases 2 and 3 (fig. 5b and 5c). These results indicate that the combined effect of the vessel base and the eccentric positioning of the impeller promotes the formation of a secondary recirculation loop above the impeller, thereby modifying the overall flow structure.

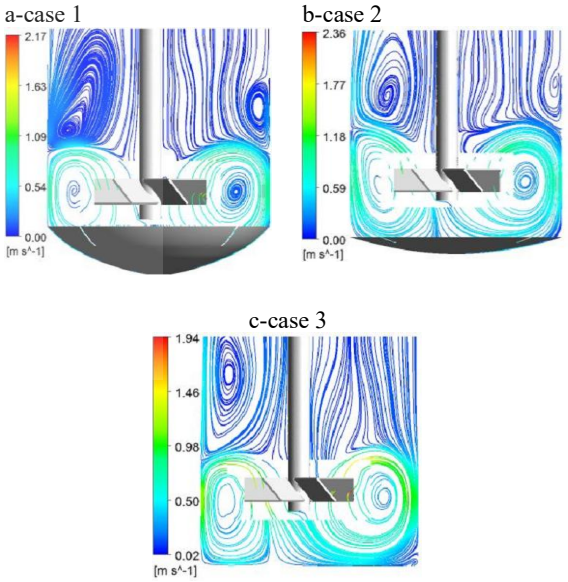


Fig. 5. Flow patterns in vertical plane.

6 Conclusion

This study investigated the influence of two geometric parameters the impeller eccentricity and the tank-bottom geometry on the mixing performance in stirred tanks. Overall, the results showed that, for cases 1 and 2, the combined effect of the dished-bottomed of the tanks and the eccentric impeller position enhanced the distribution of turbulent viscosity throughout almost the entire tank volume. In contrast, for the flat-bottom configuration case 3, the turbulent viscosity remained mainly concentrated below the turbine. Moreover, the eccentric positioning of the impeller significantly enlarged the region of high tangential velocity and increased its maximum values. This flow enhancement effectively reduced, and in some regions eliminated, the dead zones near the bottom of all three tank configurations, leading to improved overall mixing performance.

References

1. P. Hao, J. Li, Y. Jin, B. Yang and X. Li, “Numerical investigation of the effect of bottom shape on the flow field and particle suspension in a DTB crystallizer,” International Journal of Chemical Engineering 11, pp 6862152, (2016). doi.org/10.1155/2016/6862152.

2. T,Koji and D. T. Y. Shigihara, “Laminar mixing in eccentric stirred tank with different bottom,”Journal of chemical engineering of Japan 44, pp931-935, (2012).
doi.org/10.2478/AUSEME-2023-0007
3. Ameur. H, 3D hydrodynamics involving multiple eccentric impellers in unbaffled cylindrical tank, Chinese Journal of Chemical Engineering, 24 572-580 (2016). doi.org/10.1016/j.cjche.2015.12.010
4. Montante. G, FBekker. A, Paglianti. A, Magelli. F, Effect of the shaft eccentricity on the hydrodynamics of unbaffled stirred tanks, Chemical. Engineering. Science. 61 2807–2814 (2006). doi.org/10.1016/j.ces.2005.09.021.
5. luan. D, Zhang. S, Wei. X, Duan. Z, 3Effect of the 6PBT stirrer eccentricity and off-bottom clearance on mixing of pseudoplastic fluid in a stirred tank, Results in Physics, 7 1079-1085 (2017). doi.org/10.1016/J.RINP.2017.02.034.
6. J. Aubin, D. F. Fletcher, C. Xuereb, “Modeling turbulent flow in stirred tanks with CFD: the influence of the modeling approach, turbulence model and numerical scheme,” Experimental Thermal and Fluid Science 28, pp 431-445, (2004).
doi.org/10.1016/j.expthermflusci.2003.04.001.

Airfoil polar uncertainty at low Reynolds numbers in the conceptual design of stratospheric aircraft

Juraj Čechovič[1,2,*]

[1]TechSim Engineering s.r.o., Budějovická 1550/15a, 140 00 Prague, Czech Republic
[2]Institute of Aerospace Engineering, Faculty of Mechanical Engineering, Brno University of Technology, Technická 2896/2, 616 69 Brno, Czech Republic

Abstract. Stratospheric unmanned aerial vehicles (UAVs) are developing fast, from large solar platforms to small balloon-launched aircraft for flexible deployment. Low air density in the stratosphere places their wings at low Reynolds numbers, where the formation of laminar separation bubbles controls airfoil performance. Conceptual design relies on low-fidelity polars, typically from XFOIL, and usually treats them as exact, although their errors are largest here. This paper shows that the polar uncertainty is one of the key factors in the conceptual design of such aircraft. The uncertainty, calibrated with wind-tunnel data, was carried through the endurance optimisation of a 10 kg balloon-launched UAV, used as a case study, with a vortex-lattice method and strip theory. A Sobol sensitivity analysis compared it with the uncertainty in airframe mass and parasitic drag. Uncertainty in transition and profile drag alone changed the predicted endurance by up to 10 %, whereas the uncertainty in maximum lift had only a minor effect. This spread was larger than the difference between competing design strategies, so low-fidelity optimisation cannot reliably rank them. The effect grew at lower Reynolds numbers. Higher-fidelity effort, for example large-eddy simulation, should therefore target transition and profile drag.

1 Introduction

Many services depend on satellites today: navigation, timing, and communication in remote areas. The number of satellites grows fast, mainly through large constellations in low Earth orbit (LEO). The number of active satellites grew from about 3300 at the end of 2020 to more than 14 000 at the end of 2025, and a single constellation, Starlink, made up 66 % of them [1]. Many users therefore depend on a few large LEO systems. The crowded orbit also brings a risk of collisions: a debris object of only 5 mm can disable a satellite [2].

High-altitude platforms in the stratosphere offer a complement to satellites. At an altitude of about 20 km, they fly above commercial air traffic and in weak winds, and they can provide long-term services as satellites do, with communication as one of the main applications [3]. If satellite services are disrupted, such platforms could serve as a regional backup for communication. Several fixed-wing platforms have already flown in the stratosphere [4]. The Airbus Zephyr has a span of 25 m and a mass of 75 kg, and the BAE Systems PHASA-35 a span of 35 m and a mass of 150 kg. The Kea Atmos demonstrator has a span of 12.5 m, and its successor is planned with about 30 m. The SoftBank Sunglider spans 78 m.

All these aircraft have spans of 12–78 m, and those with published masses weigh 75 kg or more. Such large and light structures are difficult to handle on the ground and to bring to altitude. This paper therefore considers a much smaller aircraft: a balloon-launched unmanned aerial vehicle (UAV) with a maximum take-off mass of 10 kg and a span below 3 m. Its span places it in a lower ground-risk class of the EASA specific category [5]. Balloon-launched aircraft have already been flown, for example the HiDRON glider for atmospheric measurements [6], and launch from a balloon has been studied for larger near-space UAVs [7]. The aircraft considered here is battery powered and flies for a few hours. It is not a replacement for a long-endurance platform, but a relay that can be deployed quickly when it is needed.

A small span, however, brings an aerodynamic problem. The chord is small and the air density at 20 km is only about 0.088 kg m^{-3}, so the wing operates at chord Reynolds numbers of about 50 000–200 000. In this range, the laminar separation bubble is the main driver of the airfoil characteristics. It controls the drag, the maximum lift and the hysteresis of the polar, and it can burst at low Reynolds numbers [8, 9]. The common prediction methods have difficulties here. Fully turbulent RANS simulations cannot capture the bubble, and RANS with a transition model works well only for some airfoils, Reynolds numbers and angles of attack [10, 11]. The panel method XFOIL [12] is fast and widely used, but its transition prediction depends on the parameter N_{crit}, which describes the disturbance level and is not known in free flight. Large-eddy simulation resolves the bubble [13], but its cost is far too high for a design loop.

*Corresponding author: juraj.cechovic@gmail.com

Conceptual design studies of solar-powered aircraft nevertheless use XFOIL polars as deterministic inputs [14], although a design study of a HALE aircraft found that XFOIL predicts a lower drag and a higher maximum lift than tunnel tests [15]. The uncertainty of airfoil predictions has been studied at airfoil level [16, 17], but at $Re \approx 5 \times 10^5$. How much this uncertainty changes the predicted endurance of a small stratospheric UAV, and whether it can change the choice between design options, has not been quantified in these studies. This paper addresses this question. The polar uncertainty is calibrated with wind-tunnel data and carried through the endurance optimisation of a 10 kg balloon-launched UAV, which serves as a case study. The model combines a vortex-lattice method with strip theory. A Sobol sensitivity analysis compares the polar uncertainty with the uncertainty in airframe mass and parasitic drag.

2 Methods

2.1 Mission and design problem

The aircraft is released from a stratospheric balloon at an altitude of 20 km. It then flies at this altitude on battery power until the usable energy is spent. Climb and descent are not modelled. Table 1 lists the fixed inputs, including the payload, the battery data and the International Standard Atmosphere. The maximum take-off mass (MTOW) is limited to 10 kg and the span to 2.95 m (Sect. 1).

The aircraft has a conventional layout. A straight-tapered wing with an unswept quarter-chord line and the E387 airfoil is mounted above a capsule fuselage. The E387 was chosen because detailed low-Reynolds-number wind-tunnel data exist for it [9], so the polar uncertainty can be calibrated (Sect. 2.2). A tail boom carries the horizontal and vertical tails with the NACA 0008 airfoil. The tails are sized by fixed volume coefficients [18] and a tail arm proportional to the mean aerodynamic chord $\bar{c}$ (Table 1). Propeller–wing interaction is not modelled. Section 3.5 discusses this assumption.

Seven design variables describe the aircraft: span, root chord, taper ratio, tip twist, wing incidence, centre-of-gravity position (aft of the leading edge of $\bar{c}$) and battery mass (Table 3). The objective is the maximum endurance E in level flight at constant mass:

$$E = \frac{f_u\, e_b\, m_b}{P_{\mathrm{el}}}, \qquad P_{\mathrm{el}} = \frac{\tfrac{1}{2}\rho V^3 S\, C_D}{\eta} + P_{\mathrm{eq}}, \tag{1}$$

where f_u is the usable fraction of the battery energy, e_b the specific energy of the battery, m_b the battery mass, P_{el} the electrical power, η the efficiency of the propulsion chain, P_{eq} the power of avionics and payload, ρ the air density, S the wing area and C_D the drag coefficient. The flight speed follows from lift equal to weight, $V = \sqrt{2mg/(\rho S\, C_L)}$. The endurance is evaluated at the admissible operating point with the lowest electrical power (Sect. 2.4).

Besides the limits on MTOW, span and static margin (Table 1), the lift coefficient may not exceed $0.8\, C_{L,\max}$, and the Mach number may not exceed 0.3. In addition, every wing strip must operate above a minimum Reynolds number $Re_{\min}$. Two design strategies are compared: $Re_{\min} = 60\,000$ and $Re_{\min} = 100\,000$ (60k and 100k in the figures). The span limit of 2.95 m is the main case. A hypothetical span limit of 5 m serves as a variant with a larger wing, slower flight and lower Reynolds numbers. The two strategies and the two span limits give four studies.

Table 1. Mission and fixed model inputs.

Quantity	Value
Altitude (ISA), release and loiter	20 km
Air density ρ	0.0879 kg m^{-3}
Kinematic viscosity ν	1.616×10^{-4} m^2 s^{-1}
Speed of sound a	295.1 m s^{-1}
Payload mass	1.0 kg
Avionics and payload power P_{eq}	50 W
Battery specific energy e_b	280 Wh kg^{-1}
Usable energy fraction f_u	0.85
Propulsion chain efficiency η	0.60
Maximum take-off mass	10 kg
Span limit (regulatory)	2.95 m (variant 5 m)
Wing / tail airfoils	E387 / NACA 0008
Tail volumes V_H / V_V, tail arm	0.5 / 0.025, 4.5 $\bar{c}$
Static margin, C_L margin	$\geq 5\,\%\,\bar{c}$, $C_L \leq 0.8\, C_{L,\max}$

2.2 Airfoil polars and their validation

The section polars come from XFOIL 6.99 [12]. XFOIL couples a panel method with an integral boundary-layer method and predicts transition with the e^N method using the critical amplification factor N_{crit}. A polar database was computed for the E387 wing airfoil and the NACA 0008 tail airfoil. It covers 15 Reynolds numbers between 20 000 and 300 000 and the range $N_{\mathrm{crit}} = 5$–12 in steps of 0.5. Points that do not converge are excluded, and the database is never extrapolated.

The strip theory (Sect. 2.3) needs the section drag as a function of the section lift. For each grid node, the attached branch of the polar, up to maximum lift, gives $c_d(c_l)$. Between the grid nodes, c_d is interpolated linearly in c_l and bilinearly in Re and N_{crit}. A query outside the database is flagged, and the corresponding flight condition is not admissible.

The database was validated against the wind-tunnel data of NASA TM-4062 [9], measured in the Langley Low-Turbulence Pressure Tunnel (LTPT) and in the Stuttgart and Delft tunnels (Fig. 1). The drag is compared at equal lift coefficient, because the strip theory uses the polar in this way. At $Re = 100\,000$, XFOIL agrees best with the LTPT data for $N_{\mathrm{crit}} = 10$. At $Re = 200\,000$, the agreement is almost the same for all $N_{\mathrm{crit}} = 9$–12. For $N_{\mathrm{crit}} = 9$–10, the measured and the computed drag typically differ by 10–15 %. At $N_{\mathrm{crit}} = 9$, the measured drag in the operating range of c_l is on average 1.10 times the XFOIL value. The measured maximum lift is 0.91–0.93 times the XFOIL value. These ratios define the nominal correction factors $k_{C_D} = 1.10$ and $k_{C_{L,\max}} = 0.92$ (Sect. 2.5). Morgado et al. [10] report the same trend for the E387: XFOIL predicts the low-drag range well but gives a slightly higher maximum lift than the experiment.

At $Re = 60\,000$, the LTPT data show a second branch with high drag: $c_d = 0.06$–0.08 at $c_l = 0.60$–0.71 and $\alpha = 5.5$–$7°$. On this branch, the laminar separation bubble bursts [8]. XFOIL does not reproduce this branch for any N_{crit} (Fig. 1b). In Sect. 3.4, a wing strip is counted as inside this burst band when $c_l = 0.55$–0.75 (the measured range widened by 0.05) and $Re < 100\,000$ (no burst was measured at $Re = 100\,000$). In addition, XFOIL has its own regime boundary. Below a critical Reynolds number, the separated flow does not reattach, and $c_{l,\max}$ falls below 1. This critical Reynolds number rises with N_{crit}, from about 30 000–40 000 at $N_{\mathrm{crit}} = 9.5$–10 to 40 000–50 000 at $N_{\mathrm{crit}} = 11$. For this reason, the minimum strip Reynolds number $Re_{\min}$ is a design constraint (Sect. 2.1). The database also has a gap: at $Re = 60\,000$ and $N_{\mathrm{crit}} = 11$, XFOIL did not converge above $\alpha = 2.5°$, so this grid node gives no drag for $c_l > 0.36$. The gap affects only the 60 000 design with the 5 m span at $N_{\mathrm{crit}} > 10.5$ (Sect. 3.4).

2.3 Extended vortex-lattice method

The aerodynamic model combines an inviscid vortex-lattice method with viscous strip theory. The inviscid part is the horseshoe vortex-lattice method [19] of AeroSandbox [20]. Each half of the wing has 32 spanwise and 8 chordwise panels, and each half of the horizontal tail has 12×8 panels, with uniform spanwise spacing. The induced drag is computed in the Trefftz plane, because the near-field drag of the vortex-lattice solution did not converge with mesh refinement on these wings. It was verified on elliptic wings ($e = 1.01$, theory 1) and in a mesh study: with three times more spanwise and twice as many chordwise panels, $C_{D,i}$ at the operating lift coefficients ($C_L \approx 0.9$) changed by less than 2 %.

The vortex-lattice method is linear. The trailing vortices are fixed along the body axis, so the influence matrix does not depend on the angle of attack, and the boundary condition is linear in the freestream velocity. Any freestream direction in the symmetry plane is a combination of two unit vectors: one along the body axis ($\alpha = 0°$) and one normal to it ($\alpha = 90°$). Because the problem is linear, the circulation is the same combination of the two solutions Γ_x and Γ_z, $\Gamma(\alpha) = \cos\alpha\,\Gamma_x + \sin\alpha\,\Gamma_z$. Two solutions are therefore enough for all angles of attack, and the linear system is solved only twice per design instead of once per angle. This simplification was checked against the AeroSandbox solver at $\alpha = -3°$ to $13°$: lift, drag and pitching moment agreed to better than 10^{-9} (relative difference).

The aircraft is trimmed with the incidence of the horizontal tail, which gives $C_m = 0$ at each angle of attack. This gives the trimmed lift coefficient $C_L(\alpha)$, the induced drag coefficient $C_{D,i}(\alpha)$, the strip lift coefficients $c_l(\alpha)$ and the stick-fixed static margin on a 0.1° grid.

The profile drag follows from strip theory. Each wing and tail strip j, with area S_j and chord c_j, has its own lift coefficient $c_{l,j}$ and Reynolds number $Re_j = Vc_j/\nu$, where ν is the kinematic viscosity at flight altitude. The profile drag coefficient is

$$C_{D,p} = \frac{k_{C_D}}{S} \sum_j c_d\big(c_{l,j}, Re_j, N_{\mathrm{crit}}\big)\, S_j, \tag{2}$$

where c_d is interpolated in the polar database (Sect. 2.2) and k_{C_D} is the drag correction factor. Wing stall is defined by the first strip that stalls: $C_{L,\max}$ is the trimmed lift coefficient at which any wing strip first reaches $k_{C_{L,\max}}\, c_{l,\max}(Re_j, N_{\mathrm{crit}})$.

2.4 Endurance optimisation

Besides the profile drag of the lifting surfaces, the drag model contains three parasitic terms. The capsule and the boom have skin-friction drag with a form factor [18]. The skin friction is laminar or turbulent, depending on the body Reynolds number. A crossflow term adds the drag of the fuselage at angle of attack [21]. The five junctions (two at the wing root, two at the horizontal-tail root and one at the vertical-tail root) have interference drag from Hoerner's relation for a wing that joins a wall [22]. Excrescences such as antennas, gaps and hatches are modelled as a fixed drag area of $0.006\,\mathrm{m}^2$. The junction and excrescence drag are both multiplied by the uncertain factor k_{par}. The vertical tail is not part of the vortex-lattice model and adds its profile drag at zero lift.

The wing is a built-up carbon structure. The unidirectional carbon spar caps are sized by the root bending moment at an ultimate load factor of 6. The spanwise load follows the Schrenk approximation [23], the average of a load proportional to the local chord and an elliptic load. This simple approximation is common in conceptual design, because it needs only the planform. The caps must meet a strength limit and a stiffness limit. The shear web, the skin and the ribs have a fixed lay-up. The masses of the tails, the fuselage and the boom follow from their areas and lengths. The propulsion mass follows from the peak shaft power in the speed band from the stall-margin speed to $1.8\,V_{\mathrm{stall}}$. The airframe mass is multiplied by the uncertain factor k_m. The mass, the flight speed, the drag and the motor power depend on each other, so the MTOW is found iteratively: the mass is updated until it no longer changes.

For every trimmed angle of attack, the flight speed follows from lift equal to weight and the electrical power from Eq. (1). A flight condition is admissible when it is trimmed and below stall, and when every strip operates inside its polar database. It must also meet the limits on C_L, Mach number and $Re_{\min}$ (Sect. 2.1). The operating point is the admissible flight condition with the lowest electrical power. When a constraint cuts the power curve, the operating point lies on the constraint boundary. The aircraft must also be trimmable over the whole speed band used for the motor sizing.

The design variables are optimised by differential evolution [24] in its SciPy implementation, with 105 members and 100 generations. Each study is run with two random seeds, which gives eight runs in total. Constraints are handled by the feasibility rule of Deb [25]: a feasible design

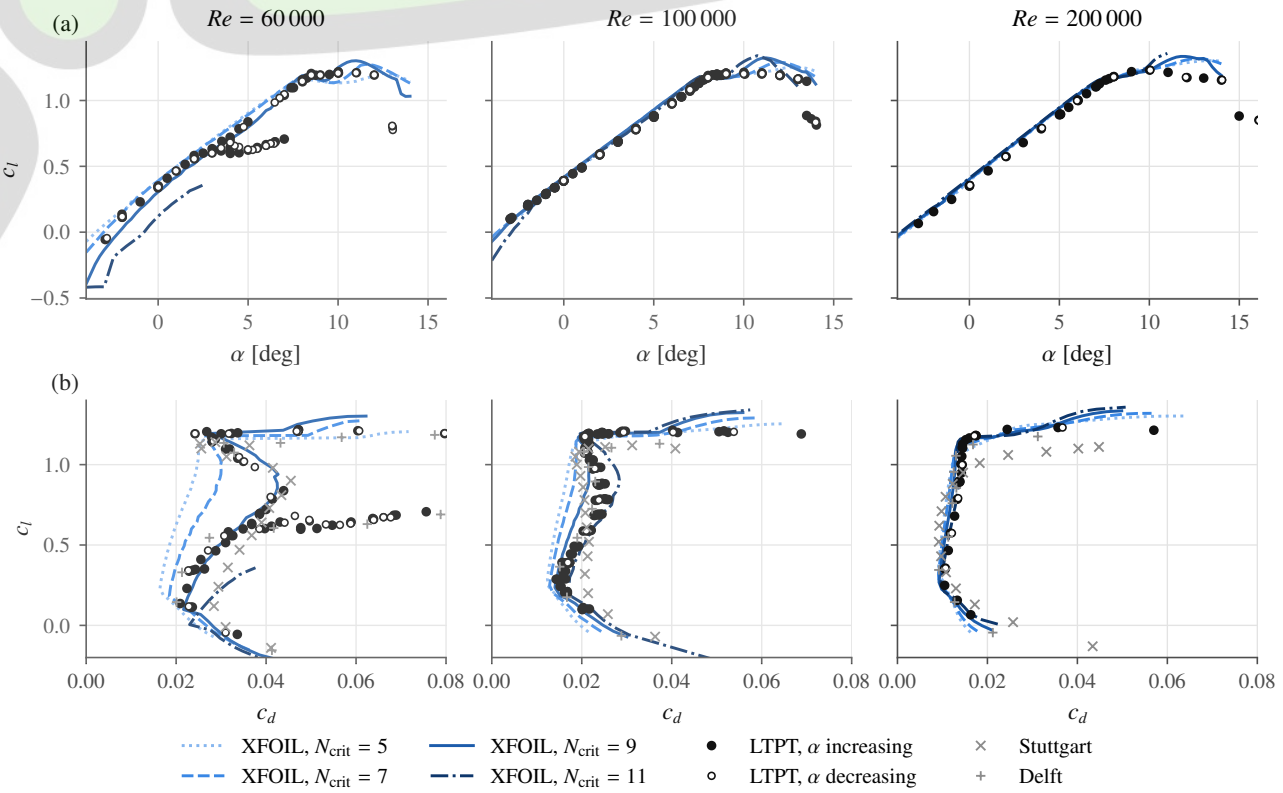


Figure 1. E387: XFOIL (lines) and NASA TM-4062 data [9] (symbols; LTPT filled/open = increasing/decreasing α). (a) Lift; (b) drag.

always ranks above an infeasible one, and infeasible designs are ranked by their total constraint violation. The optimisation uses the nominal values of the uncertain inputs (Table 2).

2.5 Uncertain inputs and global sensitivity analysis

Five uncertain inputs are considered (Table 2). They are independent and uniformly distributed. Two inputs describe the airfoil polar (N_{crit}, k_{C_D}), one the stall ($k_{C_{L,\max}}$), one the airframe mass (k_m) and one the parasitic drag (k_{par}).

N_{crit} represents the unknown disturbance level in free flight. Its range of 7–11 is centred on the value of 9 calibrated against the LTPT data. Mack's correlation [26], $N_{\mathrm{crit}} = -8.43 - 2.4 \ln Tu$, links N_{crit} to the free-stream turbulence intensity Tu (as a fraction). Calmer air gives a higher N_{crit}. The range 7–11 corresponds to $Tu \approx 0.16$–$0.03\,\%$. The correlation, however, was derived for $Tu > 0.1\,\%$; below this level, Mack notes that other disturbances, such as sound, control transition. N_{crit} is therefore treated here as a total disturbance level, not as a turbulence level alone.

k_{C_D} and $k_{C_{L,\max}}$ represent the model-form error of XFOIL beyond the effect of N_{crit}. Their ranges are bounded by the experiment (Sect. 2.2). No E387 data exist below $Re = 60\,000$, so the factors are extrapolated there. The ranges of k_m (±15 %) and k_{par} (±50 %) are estimates without data. Section 3.3 shows how much wider these two ranges would need to be for their variance share to equal that of the polar inputs.

Table 2. Uncertain inputs (uniform distributions).

Input	Range	Nominal	Basis
N_{crit}	7–11	9	LTPT calibration; free-flight turbulence unknown
k_{C_D}	0.95–1.3	1.1	$c_{d,\mathrm{exp}}/c_{d,\mathrm{XFOIL}}$ at equal c_l [9]
$k_{C_{L,\max}}$	0.84–0.94	0.92	$c_{l,\max}$ of three tunnels vs XFOIL [9]
k_m	0.85–1.15	1	airframe mass model, ±15 %
k_{par}	0.5–1.5	1	interference and excrescence, ±50 %

Sobol indices [27] show how much of the variance of the endurance each input causes. The first-order index $S_{1,i}$ is the share of the variance caused by the input X_i alone. The total index $S_{T,i}$ also includes the interactions of X_i with the other inputs. With the output $Y = E$,

$$S_{1,i} = \frac{\mathrm{Var}[\mathbb{E}(Y \mid X_i)]}{\mathrm{Var}(Y)}, \qquad S_{T,i} = \frac{\mathbb{E}[\mathrm{Var}(Y \mid \mathbf{X}_{\sim i})]}{\mathrm{Var}(Y)}, \quad (3)$$

where Var is the variance, $\mathbb{E}$ the expected value and $\mathbf{X}_{\sim i}$ all inputs except X_i. The indices are estimated with the sampling scheme and estimators of Saltelli et al. [28] in SALib. With $N = 4096$ base samples and $k = 5$ inputs, each design needs $N(k+2) = 28\,672$ evaluations. The 95 %

confidence intervals come from 1000 bootstrap resamples; with $N = 1024$ and 2048, S_T changed by at most 0.0016.

Each optimal design is fixed in this analysis. For every sample, the viscous drag, $C_{L,\max}$, the mass loop and the operating point are recomputed, so the aircraft flies at its own best speed. The result therefore measures the robustness of the predicted endurance, not the robustness of the design itself. An MTOW above 10 kg ($k_m > 1$) is accepted, because it is the mass of the aircraft as built. All eight optima were evaluated with the same samples, so the designs can be compared sample by sample. No sample failed.

One-at-a-time sweeps complement the Sobol indices. Each input varies over its range in 21 steps, while the other inputs stay at their nominal values. The Sobol indices give the shares of the variance; the sweeps show the effect of each input in minutes and the shape of the response, for example a sudden change of the active constraint.

3 Results and discussion

3.1 Optimal designs

Figure 2 shows the four optimal designs, and Table 3 lists their design variables and properties. For every study, the two seeds gave the same design, and their endurance agrees within 0.011 % (0.02 min). All runs were within 0.1 % of their final endurance by generation 36–59 and within 0.01 % by generation 60–94.

At the regulatory span of 2.95 m, the span limit is active. The 60 000 strategy reached $E = 158.8$ min and the 100 000 strategy 157.7 min, so the two strategies differ by only 1.1 min. All four optima reach the MTOW limit of 10 kg, and the battery makes up 50–64 % of the MTOW. In all optima, the operating point lies on the stall margin, $C_L = 0.8\,C_{L,\max}$, with $C_L = 0.84$–0.93. The static margin of 0.12–0.13 $\bar{c}$ is above its limit.

The $Re_{\min}$ constraint is active in both 100 000 studies and in the 60 000 study with the 5 m span. At 2.95 m, the lowest strip Reynolds number of the 60 000 design is 76 000, so its constraint is not active. The 60 000 strategy gives a more tapered wing, with a taper ratio of 0.47 instead of 0.66 at 2.95 m and 0.43 instead of 0.83 at 5 m. Its tip strips therefore operate at lower Reynolds numbers.

With the 5 m span limit, the span reached 4.99 m (60 000) and 4.66 m (100 000). These designs fly at 31–32 m s^{-1} instead of 43 m s^{-1}, and their mean-chord Reynolds number falls from 118 000–124 000 to 98 000–110 000. Their endurance is 198 and 189 min. The wing incidence of all optima is 5.4–6.0°, close to its upper bound of 6°. This bound, however, hardly limits the designs: when the incidence changes from 3° to 6°, E changes by at most 0.3 %.

3.2 Power and drag at the operating point

Figure 3 shows the electrical power versus the flight speed. The unconstrained power minimum lies at a lower speed than the stall margin allows: at 39 m s^{-1} instead of 43 m s^{-1} for the 2.95 m designs, and at 28–29 m s^{-1} instead of 31–32 m s^{-1} for the 5 m designs. The reason is the E387 polar. Its best power factor $c_l^{3/2}/c_d$ occurs at $c_l \approx 1.15$–1.19, which is above $0.8\,c_{l,\max}$. The operating point therefore lies on the stall margin. The unconstrained minimum would need 1.4–6.2 % less power. The 5 m variant needs about 35 % less power than the 2.95 m designs (366–378 W instead of 570–575 W).

Figure 4 shows the drag at the operating point. The profile drag of the wing and the tails is 32–33 % of the total drag at 2.95 m and 44–47 % at 5 m. This is the part of the drag that N_{crit} and k_{C_D} control. The induced drag is 59–60 % at 2.95 m and 48–51 % at 5 m. The bodies, the junctions and the excrescences together add 5–8 %.

3.3 Sensitivity of the endurance

Figure 5 gives the Sobol indices of the endurance. The indices of the two seeds differ by at most 0.011.

The one-at-a-time sweeps (Fig. 7) show the size of each effect in minutes. For the 2.95 m designs, N_{crit} changes E by 15.1 and 11.9 min over its range (60 000 and 100 000 strategy), and k_{C_D} by 15.7 and 15.2 min. This is up to 10 % of the endurance. $k_{C_{L,\max}}$ changes E by only 1.9 and 1.8 min. For comparison, k_m changes E by 14.3 and 14.4 min and k_{par} by 10.7 and 10.3 min. The airfoil polar is therefore one of the main sources of uncertainty, but not the only one.

The Sobol indices show which inputs cause the spread of E. Together, N_{crit} and k_{C_D} explain 54–61 % of the variance of E at 2.95 m and 59–78 % at 5 m. For each input, the first-order and the total index are almost equal. Each input therefore acts on its own, and the interactions between the inputs are negligible.

The maximum-lift factor $k_{C_{L,\max}}$ has almost no effect ($S_T \leq 0.007$). A lower $C_{L,\max}$ lowers the allowed lift coefficient ($0.8\,C_{L,\max}$), so the aircraft must fly faster. Near the operating point, however, the power curve is flat (Fig. 3), so the higher speed costs little power.

The variance shares depend on the assumed ranges of k_m and k_{par}, which are only estimates (Sect. 2.5). If these two ranges were 8–25 % wider, the mass and the parasitic drag would explain as much variance as the polar at 2.95 m. The shares alone therefore do not prove that the polar dominates. A measure that does not depend on these ranges is the standard deviation of E caused by the polar inputs alone. It is 4.1 % and 3.6 % of E (about 6 min) for the two 2.95 m designs. With all inputs, the coefficient of variation of E is 4.9–8.1 % (Fig. 6a). At 2.95 m, 90 % of the samples lie between 143 and 170 min.

Because all designs were evaluated with the same input samples, the two strategies can be compared sample by sample (Fig. 6b). At 2.95 m, the 60 000 design is better by 0.9 min on average. The 100 000 design, however, is better in 21 % of all samples, mostly in calm air: among the samples with $N_{\text{crit}} > 10$, it is better in 79 %. Which strategy is better therefore depends on the disturbance level, and this level is poorly known. The difference between the strategies (about 1 min) is also much smaller than the spread caused by the polar (about 6 min).

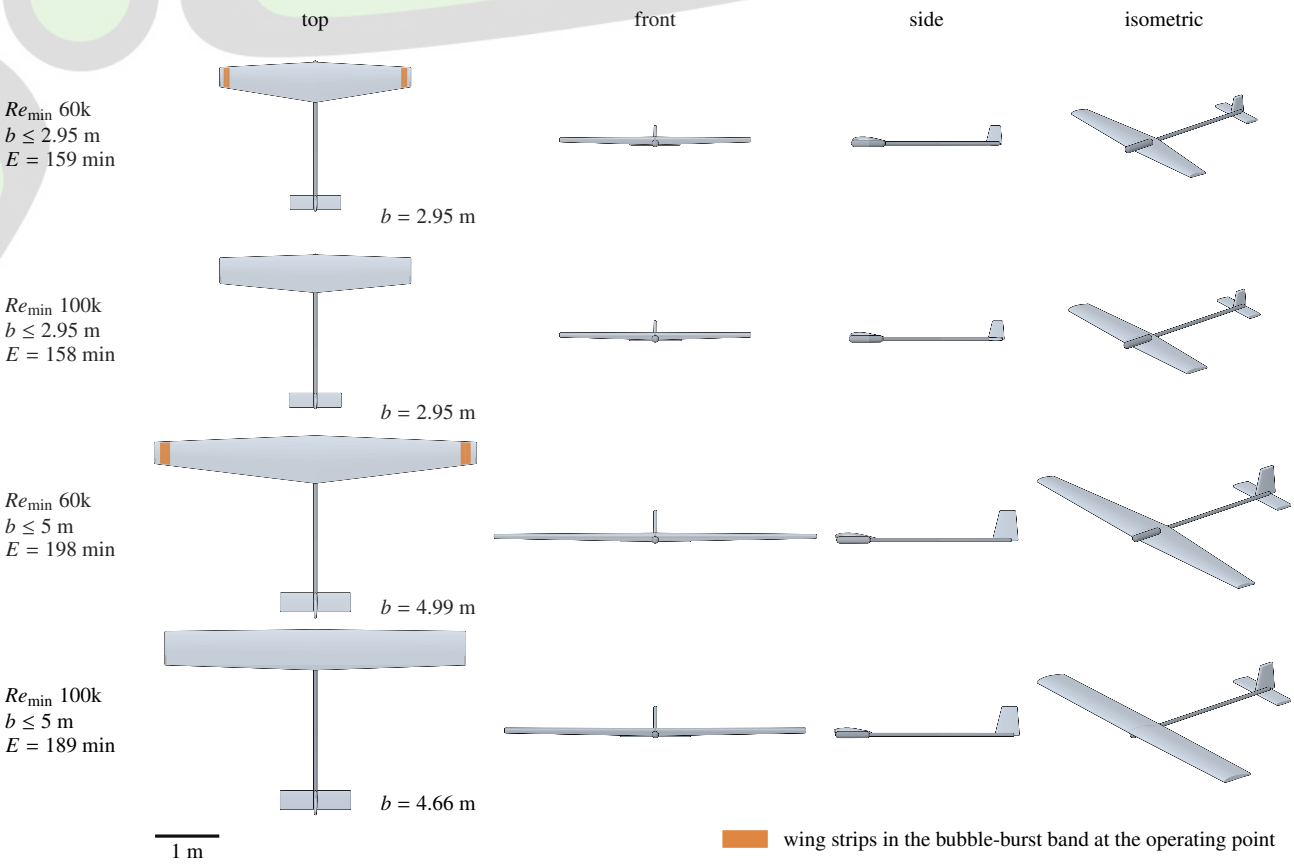


Figure 2. Optimal designs of the four studies (seed 1) at the same scale. Orange: wing strips inside the measured bubble-burst band (Fig. 1b) at the operating point.

Table 3. Design variables and properties of the optima (seed 1, nominal inputs).

		Re_{min} / span limit [m]			
Quantity	Bounds	60k / 2.95	100k / 2.95	60k / 5	100k / 5
Span b [m]	2.00–2.95 (5)	2.95	2.95	4.99	4.66
Root chord c_r [m]	0.2–0.8	0.603	0.568	0.722	0.609
Taper ratio λ	0.3–1.0	0.47	0.66	0.43	0.83
Tip twist [deg]	−5 to 0	−1.53	−3.29	−1.69	−3.82
Wing incidence [deg]	−2 to 6	5.99	5.90	5.43	5.89
CG position [$\bar{c}$]	0.05–0.50	0.347	0.355	0.348	0.375
Battery mass [kg]	0.5–7.0	6.40	6.30	5.08	5.00
Wing area S [m^2]		1.304	1.393	2.582	2.590
Aspect ratio		6.7	6.2	9.7	8.4
MTOW [kg]		10.00	10.00	10.00	10.00
Airframe + propulsion mass [kg]		2.60	2.70	3.92	4.00
Flight speed V [m s^{-1}]		43.1	42.6	30.6	32.1
Lift coefficient C_L		0.921	0.883	0.925	0.838
C_L/C_D		13.4	13.4	15.8	16.0
Electrical power P_{el} [W]		575	570	366	378
Min. wing-strip Re [10^3]		76	100	60	100
Static margin [$\bar{c}$]		0.117	0.129	0.120	0.128
Active constraints[a]		SM	SM, Re	SM, Re	SM, Re
Endurance E [min]		**158.8**	**157.7**	**198.2**	**188.8**

[a] SM: $C_L \leq 0.8\,C_{L,max}$; Re: minimum wing-strip Reynolds number $\geq Re_{min}$.

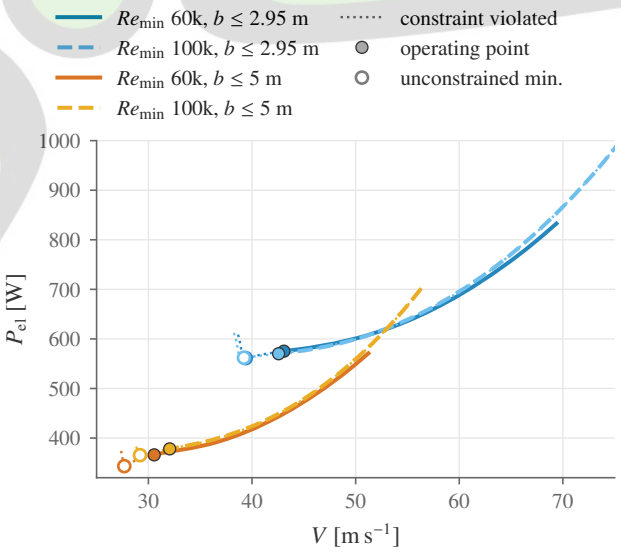


Figure 3. Electrical power in level flight versus speed (nominal inputs). Dotted: a constraint is violated. Filled circles: operating point; open circles: unconstrained minimum.

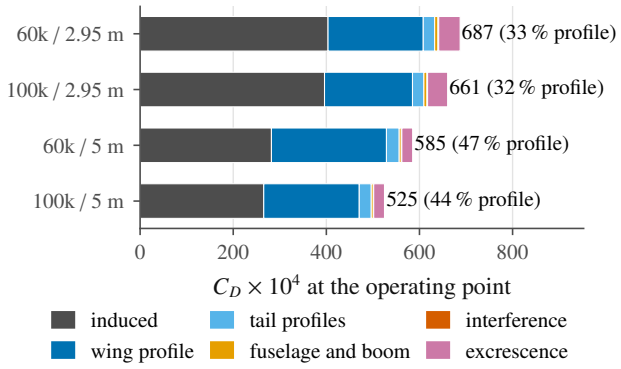


Figure 4. Drag at the operating point (nominal inputs) in drag counts ($C_D \times 10^4$), with the total and the share of profile drag.

The effect of the polar grows as the Reynolds number falls. The standard deviation of E caused by the polar rises from 3.6 to 4.1, 5.0 and 7.2 % as the mean-chord Reynolds number falls from 124 000 to 118 000, 110 000 and 98 000. The last value is raised by the gap in the XFOIL database (Sect. 3.4), but the other three values show the same trend. One reason is that the profile drag forms a larger part of the total drag at 5 m (44–47 % instead of 32–33 %, Sect. 3.2). For the 60 000 design with the 5 m span, N_{crit} alone changes E by 42 min, partly because of this gap.

3.4 Role of the laminar separation bubble

The 60 000 designs operate partly inside the burst band measured for the E387 (Fig. 1b). At nominal inputs, this applies to 4.3 % (2.95 m) and 4.1 % (5 m) of the wing area, on the outboard strips (Fig. 2). Under input uncertainty, this share is 5.3 % and 6.6 % on average and reaches 8.8 % and 22 %; the two 5 m values are raised by the database

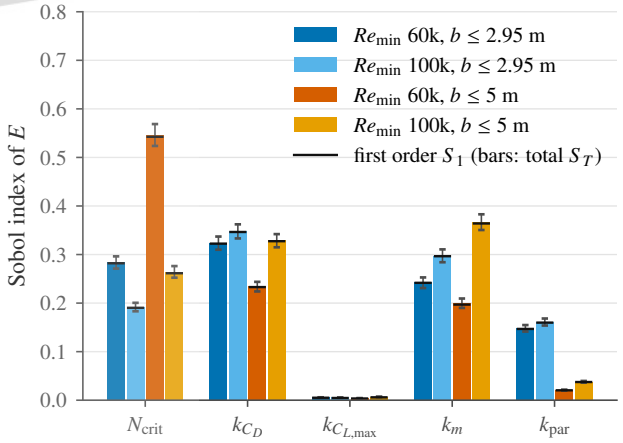


Figure 5. Total (bars, 95 % CI) and first-order (ticks) Sobol indices of the endurance (seed 1, $N = 4096$).

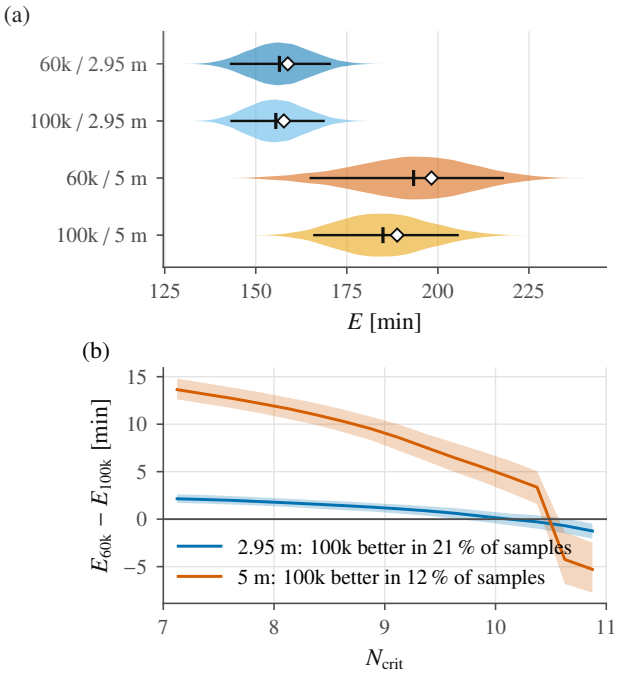


Figure 6. (a) Endurance under input uncertainty: distribution, 5–95 % range (bar), median (tick) and nominal value (diamond). (b) Endurance difference between the strategies (60k minus 100k) for the same samples versus N_{crit}: median and 5–95 % band. Below zero, the 100k strategy is better.

gap (see below). The 100 000 designs have no strip in the burst band in any sample.

At 2.95 m, the burst-band share is driven by $k_{C_{L,\max}}$ ($S_T = 0.93$). Through the stall margin, $C_{L,\max}$ sets the operating lift coefficient and thus the strip c_l. An input with almost no effect on E therefore controls how much of the wing relies on the least reliable part of the polar. At 5 m, the share is driven by N_{crit} ($S_T = 0.97$), but this comes from the gap in the XFOIL database (Sect. 2.2). For $N_{\text{crit}} > 10.5$, the 60 000 design with the 5 m span uses the grid node at $Re = 60\,000$ and $N_{\text{crit}} = 11$. To stay inside the database, it must fly faster, until all wing strips oper-

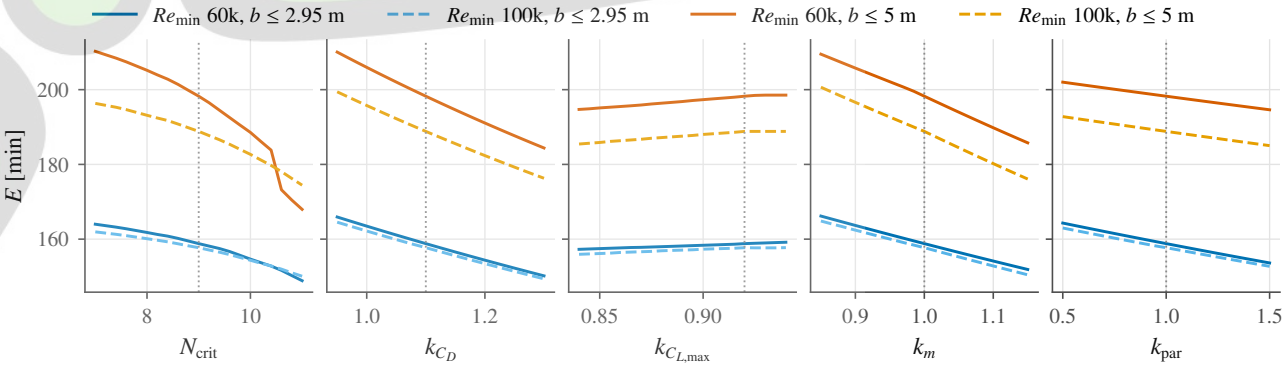


Figure 7. Endurance of the four optima when one uncertain input varies over its full range and the other inputs stay at their nominal values (dotted lines).

ate above $Re = 70\,000$, and no constraint is then active. This applies to 12.5 % of the samples. In these samples, the endurance drops steeply (Fig. 7), the burst-band share rises up to 22 %, and the difference between the two strategies changes sign (Fig. 6b). These effects come from the gap, not from the flow physics, but they show how a single non-converged XFOIL point can change the result at low Reynolds numbers.

Designing for a lower strip Reynolds number thus moves part of the wing towards the regime that XFOIL does not capture. At the regulatory span, the gain of this strategy (1.1 min) is far below the effect of the polar uncertainty.

3.5 Limits of the low-fidelity model

Strip theory uses two-dimensional polars. On a finite wing, however, the separation bubble is three-dimensional and can burst locally without an immediate loss of lift over the whole span [29]. The uniform factors k_{C_D} and $k_{C_{L,\max}}$ cannot represent this behaviour. The factors are also constant in c_l and Re, they are extrapolated below $Re = 60\,000$, and XFOIL does not predict the bubble burst (Sect. 2.2). In addition, XFOIL underestimates the drag of a high-lift airfoil at high angles of attack, and it gives a slightly high $c_{l,\max}$ for the E387 [10].

N_{crit} is treated as a total disturbance level, which has several sources in free flight. The atmospheric turbulence in the lower stratosphere is mostly weak, and its fluctuations are dominated by long waves [6]. A tractor propeller adds a further source. This is the intended layout, because a propeller at the nose of the capsule helps to reach the required position of the centre of gravity. Behind the propeller, the boundary layer cycles between laminar and turbulent at the blade-passage frequency [30]. Transition moves forward and the separation bubble is washed out [31], also at $Re = 10^4$–10^5 [32]. Vibration and surface quality add further disturbances. The model, however, uses one N_{crit} for the whole span, also for the part of the wing in the slipstream.

The tails are sized by fixed rules (V_H, V_V and a tail arm of 4.5 $\bar{c}$) and are not optimised. The horizontal tail operates at $Re = 51\,000$–$53\,000$, while the $Re_{\min}$ constraint covers only the wing. The ranges of k_m and k_{par} are estimates (Sect. 3.3). The sensitivity analysis keeps each design fixed; a re-optimisation for every sample, that is, a robust design, is left for future work. A large-eddy simulation of a spanwise wing strip at the operating Reynolds number [13] could calibrate the transition and the profile drag against resolved bubble physics.

4 Conclusions

The uncertainty of low-Reynolds-number airfoil polars was carried through the endurance optimisation of a 10 kg balloon-launched UAV. The model combines a vortex-lattice method with strip theory, and a Sobol sensitivity analysis compared the polar uncertainty with the uncertainty in airframe mass and parasitic drag. The main findings are:

1. At the regulatory span of 2.95 m, the transition parameter N_{crit} and the profile-drag factor k_{C_D} each changed the endurance by 12–16 min, that is, by up to 10 % of about 158 min. The airframe mass (14 min) and the parasitic drag (10–11 min) have effects of similar size. The airfoil polar is therefore one of the key uncertainties, but not the only one.

2. The uncertainty in maximum lift changed the endurance by only about 2 min, because the operating point lies on the stall margin, where the power curve is flat.

3. The two design strategies, with a minimum strip Reynolds number of 60 000 or 100 000, differ by only 1.1 min. This is much less than the spread caused by the polar. The 100 000 design was better in 21 % of all samples, mostly in calm air: among the samples with $N_{\text{crit}} > 10$, it was better in 79 %. A low-fidelity optimisation therefore cannot rank these strategies reliably.

4. The effect of the polar grows at lower Reynolds numbers. Its standard deviation rose from 3.6 to 5.0 % of the endurance as the mean-chord Reynolds number fell from 124 000 to 110 000, and to 7.2 %

at 98 000, where a gap in the XFOIL database adds to it.

5. Designing for a lower strip Reynolds number moves part of the wing into the measured burst band of the laminar separation bubble, where XFOIL is known to fail. Under input uncertainty, this share reached 8.8 % of the wing area at 2.95 m and 22 % at 5 m, where the gap in the database raises it.

These results hold for fixed designs and for the assumed input ranges; the ranges of airframe mass and parasitic drag are estimates. Higher-fidelity effort, for example large-eddy simulation of a spanwise wing strip, should therefore target transition and profile drag. A robust design, re-optimised under uncertainty, is the next step.

The author thanks the specialist supervisor, Ing. Robert Popela, Ph.D., for guidance and the supervisor, doc. Ing. Jaroslav Juračka, Ph.D., for supervision, both from the Institute of Aerospace Engineering, Brno University of Technology. The optimisation and sensitivity analyses were computed on resources provided by TechSim Engineering s.r.o. Generative AI (Claude, Anthropic) was used to assist with the coding of the design and analysis algorithms, the document structure and language editing. The author reviewed and edited all code and text and takes full responsibility for the content.

This research received no external funding.

References

[1] J. McDowell, Space activities in 2025, Rev. 1.4 (2026), published 4 February 2026, https://planet4589.org/space/papers/space25.pdf

[2] ECHO Consortium, European Higher Airspace Operations (HAO) Concept of Operations, SESAR Joint Undertaking, Brussels (2022), deliverable D4.3, Edition 1.0, Grant 890417 (H2020-SESAR-2020)

[3] J. Gonzalo, D. López, D. Domínguez, A. García, A. Escapa, On the capabilities and limitations of high altitude pseudo-satellites, Prog. Aerosp. Sci. **98**, 37 (2018). https://doi.org/10.1016/j.paerosci.2018.03.006

[4] EUROCAE, Update of Higher Airspace Demand Analysis and Market Developments, D-3 – Final Report, European Union Aviation Safety Agency, Cologne (2025), EASA.2021.FC.14, Special Contract No. 004

[5] European Union Aviation Safety Agency, Easy Access Rules for Unmanned Aircraft Systems (Regulations (EU) 2019/947 and 2019/945), EASA, Cologne (2024), published July 2024

[6] A.N. Haghighi, R.D. Nolin, G.D. Pundsack, N. Craine, A. Stratsilatau, S.C.C. Bailey, High-altitude balloon-launched uncrewed aircraft system measurements of atmospheric turbulence and qualitative comparison with infrasound microphone response, Atmos. Meas. Tech. **17**, 4863 (2024). https://doi.org/10.5194/amt-17-4863-2024

[7] Y. Hu, Y. Hu, X. Ding, G. Zeng, J. Guo, An adaptive launch control for balloon-borne UAVs with large wingspans, Appl. Sci. **12**, 10992 (2022). https://doi.org/10.3390/app122110992

[8] P.B.S. Lissaman, Low-Reynolds-number airfoils, Annu. Rev. Fluid Mech. **15**, 223 (1983). https://doi.org/10.1146/annurev.fl.15.010183.001255

[9] R.J. McGhee, B.S. Walker, B.F. Millard, Experimental Results for the Eppler 387 Airfoil at Low Reynolds Numbers in the Langley Low-Turbulence Pressure Tunnel, NASA Langley Research Center, Hampton, VA (1988), NASA Technical Memorandum TM-4062

[10] J. Morgado, R. Vizinho, M.A.R. Silvestre, J.C. Páscoa, XFOIL vs CFD performance predictions for high lift low Reynolds number airfoils, Aerosp. Sci. Technol. **52**, 207 (2016). https://doi.org/10.1016/j.ast.2016.02.031

[11] Y. Liu, P. Li, K. Jiang, Comparative assessment of transitional turbulence models for airfoil aerodynamics in the low Reynolds number range, J. Wind Eng. Ind. Aerodyn. **217**, 104726 (2021). https://doi.org/10.1016/j.jweia.2021.104726

[12] M. Drela, XFOIL: An Analysis and Design System for Low Reynolds Number Airfoils, in *Low Reynolds Number Aerodynamics*, edited by T.J. Mueller (Springer, Berlin, Heidelberg, 1989), Vol. 54 of *Lecture Notes in Engineering*, pp. 1–12

[13] A. Uranga, P.O. Persson, M. Drela, J. Peraire, Implicit large eddy simulation of transition to turbulence at low Reynolds numbers using a discontinuous Galerkin method, Int. J. Numer. Methods Eng. **87**, 232 (2011). https://doi.org/10.1002/nme.3036

[14] V. Cipolla, A. Dine, A. Viti, V. Binante, MDAO and aeroelastic analyses of small solar-powered UAVs with box-wing and tandem-wing architectures, Aerospace **10**, 105 (2023). https://doi.org/10.3390/aerospace10020105

[15] P. Chmielewski, W. Wróblewski, Selected issues of designing and testing of a HALE-class unmanned aircraft, J. Mar. Eng. Technol. **16**, 365 (2017). https://doi.org/10.1080/20464177.2017.1376371

[16] H. Zhao, Z. Gao, Uncertainty-based design optimization of NLF airfoil for high altitude long endurance unmanned air vehicles, Eng. Comput. **36**, 971 (2019). https://doi.org/10.1108/EC-05-2018-0215

[17] A.S. Lay, J.R. Weinmeister, D.P. Sanjaya, The Fluid Dynamics Uncertainty Quantification Challenge Problem: XFOIL vs. MFOIL, in *AIAA AVIATION Forum and ASCEND 2025* (2025), AIAA Paper 2025-3872

[18] D.P. Raymer, Aircraft Design: A Conceptual Approach, AIAA Education Series, 2nd edn. (American Institute of Aeronautics and Astronautics, Washington, DC, 1992)

[19] J. Katz, A. Plotkin, Low-Speed Aerodynamics, Number 13 in Cambridge Aerospace Series, 2nd edn. (Cambridge University Press, Cambridge, 2001)

[20] P.D. Sharpe, AeroSandbox: A Differentiable Framework for Aircraft Design Optimization, Massachusetts Institute of Technology, Cambridge, MA (2021), S.M. thesis

[21] L.H. Jorgensen, Prediction of Static Aerodynamic Characteristics for Slender Bodies Alone and with Lifting Surfaces to Very High Angles of Attack, NASA Ames Research Center, Moffett Field, CA (1977), NASA Technical Report TR R-474

[22] S.F. Hoerner, Fluid-Dynamic Drag (Published by the author, Midland Park, NJ, 1965)

[23] O. Schrenk, A Simple Approximation Method for Obtaining the Spanwise Lift Distribution, National Advisory Committee for Aeronautics, Washington, DC (1940), NACA Technical Memorandum 948

[24] R. Storn, K. Price, Differential evolution – a simple and efficient heuristic for global optimization over continuous spaces, J. Glob. Optim. **11**, 341 (1997). https://doi.org/10.1023/A:1008202821328

[25] K. Deb, An efficient constraint handling method for genetic algorithms, Comput. Methods Appl. Mech. Eng. **186**, 311 (2000). https://doi.org/10.1016/S0045-7825(99)00389-8

[26] L.M. Mack, Transition and Laminar Instability, Jet Propulsion Laboratory, California Institute of Technology, Pasadena, CA (1977), JPL Publication 77-15, NASA CR-153203

[27] I.M. Sobol', Global sensitivity indices for nonlinear mathematical models and their Monte Carlo estimates, Math. Comput. Simul. **55**, 271 (2001). https://doi.org/10.1016/S0378-4754(00)00270-6

[28] A. Saltelli, P. Annoni, I. Azzini, F. Campolongo, M. Ratto, S. Tarantola, Variance based sensitivity analysis of model output. Design and estimator for the total sensitivity index, Comput. Phys. Commun. **181**, 259 (2010). https://doi.org/10.1016/j.cpc.2009.09.018

[29] C.E. Toppings, S. Yarusevych, Laminar separation bubble formation and bursting on a finite wing, J. Fluid Mech. **986**, A26 (2024). https://doi.org/10.1017/jfm.2024.321

[30] S.J. Miley, R.M. Howard, B.J. Holmes, Wing Laminar Boundary Layer in the Presence of a Propeller Slipstream, in *Proceedings of the 15th Congress of the International Council of the Aeronautical Sciences (ICAS)* (1986), ICAS-86-1.10.2, pp. 1413–1420

[31] H. Aminaei, A.R. Mostofizadeh, M. Dehghan Manshadi, Experimental and numerical study of wing boundary layer behavior in propeller flowfield, J. Vis. **22**, 489 (2019). https://doi.org/10.1007/s12650-019-00553-w

[32] F. Makino, H. Nagai, Propeller slipstream interference with wing aerodynamic characteristics of Mars airplane at low Reynolds number, Trans. Jpn. Soc. Aeronaut. Space Sci. Aerosp. Technol. Jpn. **12**, Tk_13 (2014). https://doi.org/10.2322/tastj.12.tk_13

Pool boiling of Novec-649 on surfaces with minichannels partially filled with porous structures

Norbert Dadas[1,2*], *Robert* Pastuszko[1,2]
[1]Kielce University of Technology, Faculty of Mechatronics and Mechanical Engineering, al. 1000-lecia Państwa Polskiego 7, 25-314 Kielce, Poland
[2]Central Office of Measures, ul. Elektoralna 2, 00-139 Warsaw, *e-mail: ndadas@tu.kielce.pl

Abstract. The influence of porous copper structures integrated into minichannels with a height of 5 mm and a width of 1 mm on heat transfer during pool boiling of Novec 649 was investigated. The experimental results were compared with those obtained for a plain reference surface and minichannels without porous structures. The results revealed variations in the heat transfer coefficient depending on the surface configuration and the applied heat flux. Although minichannels without porous structures exhibited the highest heat transfer coefficients, some configurations incorporating porous structures sustained higher wall superheats. All modified minichannel surfaces outperformed the plain reference surface over the investigated operating range. These findings demonstrate that surface modifications do not necessarily enhance heat transfer in minichannels, as their effectiveness depends on the configuration of the porous structures.

1 Introduction

Nucleate pool boiling removes high heat fluxes through phase change. Its effectiveness depends on the properties of the working-fluid and surface characteristics, including geometry, roughness, and the routes for liquid replenishment and vapour escape [1].

The open minichannels increase the wetted area and create confined spaces in which bubbles grow and move toward the channel outlets. The addition of copper mesh or foam introduces additional cavities and potential nucleation sites. However, increasing the amount of porous material can also obstruct the removal of vapour. Consequently, enhancement relative to a plain surface does not establish that porous filling is preferable to an otherwise identical unfilled minichannel surface.

Pastuszko and Kaniowski [2] visualized water boiling in interconnected horizontal and vertical subsurface tunnels covered with perforated copper foil. Changes in pore activation with superheat linked surface geometry to bubble generation and vapour transport. For Novec-649, Kaniowski [3] compared straight and inclined copper microchannels; straight channels reached the highest reported performance, with a heat transfer coefficient of 19.4 kW m^{-2} K^{-1} and a critical heat flux (CHF) of 262 kW m^{-2}. These studies motivate examining how porous inserts alter the flow paths within minichannels.

Previous experiments with Novec-649 on foam-filled minichannels showed improved heat transfer at low heat flux and a declining benefit as heat flux increased [4]. Novec-649 has a low atmospheric boiling temperature and relatively low surface tension and latent heat of vaporisation. These properties make the balance between nucleation, liquid supply, and vapour transport especially relevant. The present comparison includes both copper mesh and foam, complete and partial filling, and two reference surfaces. Thermal performance is evaluated from the boiling curves and the maximum coefficients attained within the measured ranges.

2 Experimental setup

The experimental rig comprised an electrically heated copper cylinder, a glass boiling vessel, a condenser, data acquisition equipment, and an optical recording system (Fig. 1). An autotransformer regulated power to a cartridge heater over a range up to 2000 W. A wattmeter monitored the electrical input. The condenser was cooled using mains water, while the condensate was returned to the vessel. All measurements were conducted at atmospheric pressure. The type K thermocouples T5–T8 were positioned on the cylinder axis at distances of 5, 10, 20 and 35 mm below its upper face. The thermocouples T3 and T4 were placed in grooves beneath the specimen, while T1 and T2 measured the liquid temperature. The cylinder and specimen were joined with a thin solder layer containing 99% tin and 1% copper. Promasil, refractory felt and PTFE limited heat losses. A digital camera operated in HFR mode, with a KL 2500 LED illuminator, was used to observe the boiling.

The minichannels were milled in copper to a depth of 5 mm and a width of 1 mm, with a pitch of 2 mm. The square specimen base used for heat flux calculation had a side length of 27 mm; the cylinder diameter

was 45 mm. The plain reference had a roughness Ra ≈ 0.125 µm. Porous inserts were placed in the channels without soldering or bonding to the fins. The foam had a pore density of 100 PPI and a porosity of 98%.

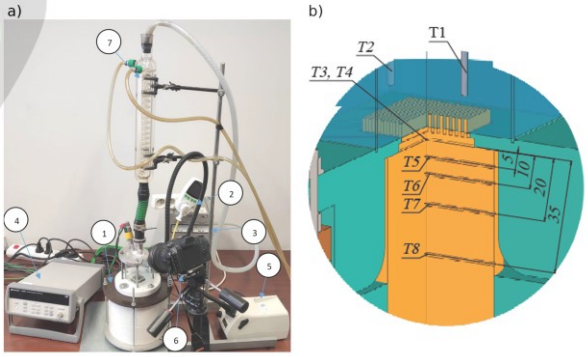


Fig. 1. a) Experimental rig: 1) main module, 2) wattmeter, 3) autotransformer, 4) data acquisition, 5) illuminator, 6) camera, 7) condenser; b) thermocouples in the heating rod.

Table 1. Geometry of the minichannel surfaces included in the Novec-649 curves. Dimensions are in mm.

Specimen	a	l_p	p_p	δ_p
MC	–	–	–	–
MCC-M	0.7	27	–	1
MCC-F	0.25	27	–	1
MCC-M-3-0.5-2	0.3	2	3	0.5
MCC-M-7.6-0.5-2	0.5	3.8	7.6	0.5
MCC-F-3.6-0.3-3	0.25	1.5	3.6	0.3
MCC-F-3.5-0.5-2	0.25	2	3.5	0.5
MCC-F-4.2-0.5-2	0.25	2	4.2	0.5

MC denotes unfilled minichannels; MCC-M and MCC-F denote complete filling with mesh and foam. For partial filling, the suffix gives insert pitch p_p, thickness δ_p and the number n of elements across the channel width. The pore or mesh opening is a and the insert length is l_p. Thus, MCC-M-3-0.5-2 has mesh inserts of 2 mm long separated by 1 mm gaps. Example insert arrangements are shown in Fig. 2.

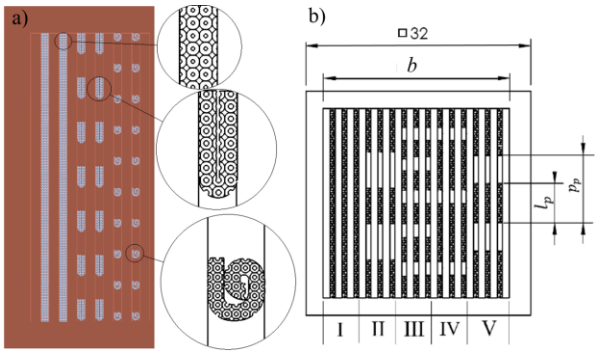


Fig. 2. a) Examples of mesh or foam arrangements between fins; b) plan view of insert arrangement variants. Symbols are defined in Table 1.

Approximately 150 cm³ of liquid was introduced into the vessel. The fluid was initially boiled for about 20 min to remove dissolved gases. The heat flux was then reduced to approximately 5–10 kW m⁻² for the initial Novec-649 measurements. Steady conditions required approximately 15 to 30 min initially and 10 to 15 min after subsequent power changes. Data were collected with increasing heat input. Measurements were stopped when rapid superheat growth indicated deterioration toward the boiling crisis, to protect the solder joint.

3 Data reduction and uncertainty

Heat flux was calculated using one-dimensional conduction through the cylinder, with an area correction from its circular cross-section to the square specimen base:

$$q = \lambda_{Cu} \frac{T_8 - T_5}{L} \frac{\pi d_{cyl}^2}{4b^2} \quad (1)$$

where L = 30 mm is the T5–T8 spacing. The geometric area ratio is approximately 2.18. Near-linear axial temperature distributions supported the one-dimensional reduction. Heat flux was referred to the projected base area rather than the total wetted area of the fins and inserts.

The mean temperature beneath the specimen was corrected for conduction through the copper base and the solder layer to obtain the heating surface temperature:

$$T_w = \frac{T_3 + T_4}{2} - q\left(\frac{l_{bs}}{\lambda_{Cu}} + \frac{l_{Sn}}{\lambda_{Sn}}\right) \quad (2)$$

The wall superheat and the heat transfer coefficient were then determined from the mean liquid temperature and the corrected surface temperature:

$$\Delta T = T_w - \frac{T_1 + T_2}{2}, \quad \alpha = \frac{q}{\Delta T} \quad (3)$$

The thermocouples were checked with a dry-block calibrator at 49–250 °C using a reference Pt100 sensor. Temperature differences did not exceed ±0.2 K. The uncertainty assessment used sensitivity coefficients for the measured quantities, consistent with first-order propagation methods [5]. The relative standard uncertainty in heat flux was highest at the smallest measured fluxes and remained below 15%; the reported relative uncertainty in the heat transfer coefficient for Novec-649 was below 8%.

As a check on the experimental setup, the boiling measurements on plain copper were compared with published correlations (Fig. 3). The Rohsenow correlation [6] overpredicted the heat transfer coefficient in all measured heat fluxes with $C_{sf} = 0.0128$. With $C_{sf} = 0.022$, fitted to the reference data, the relative deviations ranged from −22% to +32%. At 126.1 kW m⁻², the Cooper [7] and Ribatski–Jabardo [8] predictions were 10% below and 5% above the measured coefficient of 4.25 kW m⁻² K⁻¹, respectively.

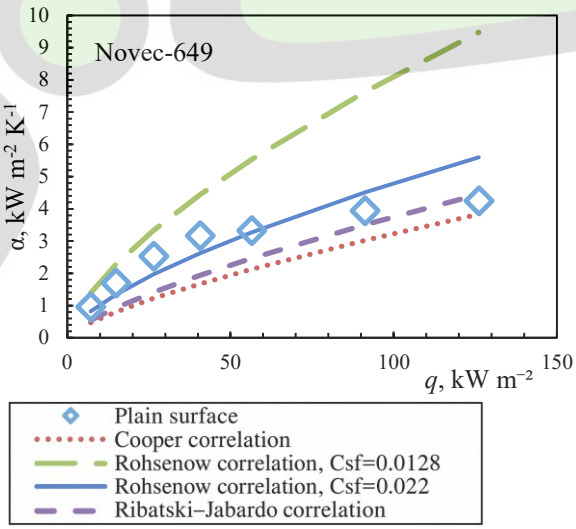


Fig. 3. Plain-surface Novec-649 coefficients compared with the evaluated literature correlations.
Csf is the surface–fluid coefficient.

4 Results

Figure 4 compares the heat transfer coefficient as a function of heat flux. Unfilled minichannels reached the highest coefficient, 25.4 kW m⁻² K⁻¹, at a heat flux of 382.5 kW m⁻². The plain surface reached only 4.2 kW m⁻² K⁻¹ within its measured range. All minichannel configurations provided coefficients higher than those of the plain surface at comparable heat fluxes, but the addition of porous material did not improve the peak coefficient relative to MC.

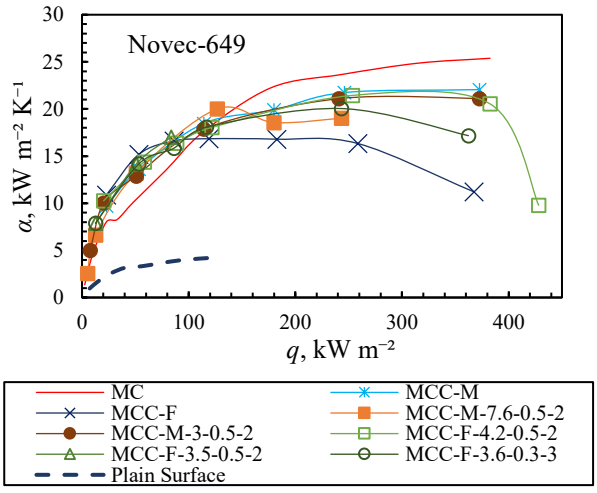


Fig. 4. Heat transfer coefficient versus heat flux for pool boiling of Novec-649 at atmospheric pressure.

The MCC-M completely mesh-filled surface reached 22.1 kW m⁻² K⁻¹. Among the partially filled surfaces, MCC-M-3-0.5-2 and MCC-F-4.2-0.5-2 reached approximately 21.1 and 21.4 kWm⁻²K⁻¹, respectively. The former value was approximately five times the highest plain-surface coefficient, but about 17% below MC. Thus, the porous structures offered a clear advantage relative to the plain surface, while retaining a penalty relative to the unfilled minichannels.

The influence of arrangement is apparent from the mesh specimens: the MCC-M-7.6-0.5-2 with a larger-pitch reached approximately 20.0 kW m⁻² K⁻¹, while MCC-M-3-0.5-2 reached approximately 21.1 kW m⁻² K⁻¹. Foam configurations exhibited distinct peaks followed by deterioration as superheat increased. Consequently, the highest recorded heat flux and the highest heat transfer coefficient should be considered separately.

Figure 5 shows that MCC-F-4.2-0.5-2 reached a recorded heat flux of 428.1 kW m⁻² at a superheat of 43.7 K, with a coefficient of only 9.8 kW m⁻² K⁻¹. At 382.5 kW m⁻², its coefficient was 20.5 kW m⁻² K⁻¹, compared with 25.4 kW m⁻² K⁻¹ for MC.

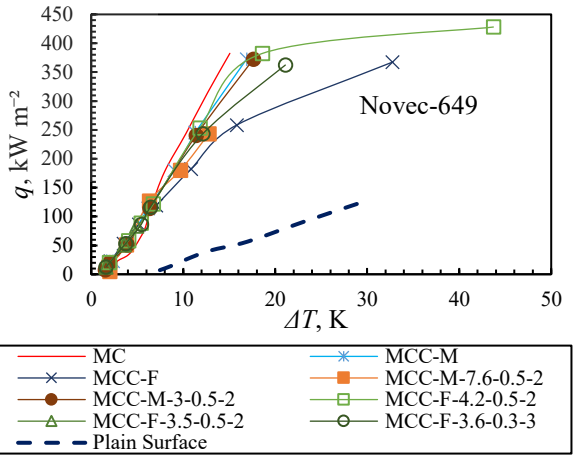


Fig. 5. Recorded heat flux versus wall superheat for Novec-649.

Table 2. The maximum recorded heat transfer coefficient α_{max} and the corresponding heat flux $q_{(\alpha_{max})}$.

Specimen	$q_{(\alpha_{max})}$ kW m⁻²	α_{max} kW m⁻² K⁻¹
MC	382.5	25.4
MCC-M	372.4	22.1
MCC-F	182.4	16.8
MCC-M-3-0.5-2	372.4	21.1
MCC-M-7.6-0.5-2	126.7	20.0
MCC-F-3.6-0.3-3	243.2	20.0
MCC-F-3.5-0.5-2	83.6	17.0
MCC-F-4.2-0.5-2	253.3	21.4
Plain Surface	126.1	4.2

For complete foam filling, the coefficient peaked at approximately 16.8 kW m⁻² K⁻¹ and fell to 11.2 kW m⁻² K⁻¹ at the last recorded point. Partial filling with MCC-F-3.6-0.3-3 gave a peak near 20.0 kW m⁻² K⁻¹, followed by a reduction at the largest recorded flux.

The minichannel surfaces initiated boiling at lower superheat than the plain reference; the reported reduction was approximately 7 K. This benefit at boiling onset is compatible with the presence of additional cavities and an extended surface. It does not imply that the same geometry remains favourable at high heat flux, where vapour removal can become the limiting process.

For the specimen MCC-M-3-0.5-2, the coefficient was 21.1 kW m^{-2} K^{-1} at both 240.7 and 372.4 kW m^{-2}. The spacing of the insert therefore influences both the size of the confined region and the paths available for liquid and vapour. For MCC-M-3-0.5-2, 1 mm gaps separate successive mesh elements; for MCC-F-4.2-0.5-2, the gaps are 2.2 mm. The recorded curves show that neither an additional porous area nor a larger free gap guarantees a higher coefficient than MC.

5 Conclusions

Machining minichannels on the copper surface reduced the wall superheat required to initiate the pool boiling of Novec-649 by approximately 7 K relative to plain copper. All minichannel geometries also gave higher coefficients than plain copper at comparable heat fluxes after the boiling had developed. The benefit of adding an insert was smaller and depended on the operating point: no filled surface exceeded the largest coefficient measured on unfilled minichannels, 25.4 kW m^{-2} K^{-1} at 382.5 kW m^{-2}.

For foam, the specimen with 2.2 mm gaps had a peak coefficient of 21.4 kW m^{-2} K^{-1}, compared to 16.8 kW m^{-2} K^{-1} for complete filling. The best partially meshfilled specimen, with 1 mm gaps, reached 21.1 kW m^{-2} K^{-1}, while complete mesh filling reached 22.1 kW m^{-2} K^{-1}.

The open spaces between foam inserts provide a route for growing bubbles to reach the channel outlets, as previously observed for Novec-649 [4]. The porous material may also draw liquid towards the heated surface by capillary action.

The experiments showed that an appropriate choice the type of the porous insert (copper foam or copper mesh) and the filling fraction of the minichannel can significantly increase the critical (maximum) heat flux. The greatest heat transfer enhancement during boiling was observed when the inserts occupied approximately 30% of the minichannel volume for Novec-649.

Foam-filled channels exhibited pronounced deterioration at high superheat. The results show that an effective surface design for Novec-649 requires access for liquid replenishment and vapour escape in addition to a large wetted area. Further work should examine insert spacing and filling during pool boiling.

This research was funded in whole or in part by the National Science Centre, Poland, grant no. 2025/57/N/ST8/00762. For the purpose of Open Access, the author has applied a CC-BY public copyright licence to any Author Accepted Manuscript (AAM) version arising from this submission.

6 Nomenclature

a	Pore or mesh opening, mm
b	Specimen base side length, mm
d_{cyl}	Heating cylinder diameter, mm
L_{T5-T8}	thermocouple spacing, mm
l_p	Porous insert length, mm
p_p	Porous insert pitch, mm
δ_p	Porous element thickness, mm
n	Elements across the channel width
q	Heat flux, W m^{-2}
T_w	Heating surface temperature, K
α	Heat transfer coefficient, W m^{-2} K^{-1}
ΔT	Wall superheat, K
λ	Thermal conductivity, W m^{-1} K^{-1}
l_{bs}	Conduction distance through copper, m
l_{Sn}	Conduction distance through solder, m
C_{sf}	Surface–fluid coefficient

7 References

1. I.L. Pioro, W. Rohsenow, S.S. Doerffer, Nucleate pool-boiling heat transfer. I: Review of parametric effects of boiling surface. Int. J. Heat Mass Transf. 47, 5033–5044 (2004). https://doi.org/10.1016/j.ijheatmasstransfer.2004.06.019
2. R. Pastuszko, R. Kaniowski, Boiling visualization on vertical fins with tunnel-pore structures. EPJ Web Conf. 25, 02019 (2012). https://doi.org/10.1051/epjconf/20122502019
3. R. Kaniowski, Pool boiling of Novec-649 on inclined microchannel. Energies 16, 2476 (2023). https://doi.org/10.3390/en16052476
4. R. Pastuszko, N. Dadas, R. Kaniowski, Pool boiling of Novec-649 on minichannels filled with copper foam. EPJ Web Conf. 264, 01028 (2022). https://doi.org/10.1051/epjconf/202226401028
5. JCGM, Evaluation of measurement data—Guide to the expression of uncertainty in measurement. JCGM 100:2008 (2008). https://doi.org/10.59161/JCGM100-2008E
6. W.M. Rohsenow, A method of correlating heat transfer data for surface boiling of liquids. Technical Report No. 5, MIT Heat Transfer Laboratory, Cambridge, MA (1951).
7. M.G. Cooper, Heat flow rates in saturated nucleate pool boiling—A wide-ranging examination using reduced properties. Adv. Heat Transf. 16, 157–239 (1984). https://doi.org/10.1016/S0065-2717(08)70205-3
8. G. Ribatski, J.M. Saiz Jabardo, Experimental study of nucleate boiling of halocarbon refrigerants on cylindrical surfaces. Int. J. Heat Mass Transf. 46, 4439–4451 (2003). https://doi.org/10.1016/S0017-9310(03)00252-7

Hydrodynamic performance of baseline and slotted NACA 4412 hydrofoils under cavitating conditions using transient CFD simulation

Z.Elkhaldi[1], F. Bouregba[1], R. Tayeb[1], L. Adjlout[1], and O.Imine[2]

[1]Naval Aero-Hydrodynamic Laboratory, Marine Engineering Department, University of Sciences and Technology of Oran Mohamed Boudiaf, USTO-MB, Oran, Algeria

[2]Aeronautics and Propulsion Systems Laboratory, Department of Aeronautical Engineering, University of Science and Technology of Oran Mohamed Boudiaf, USTO-MB, Oran, Algeria

Abstract. Hydrofoils are increasingly employed in modern marine and renewable energy applications, including high speed vessels, underwater vehicles, and marine current energy systems, where hydrodynamic efficiency and cavitation control remain critical engineering challenges. In this context, the present study numerically investigates the transient cavitating flow around a NACA 4412 hydrofoil using ANSYS CFX. A pseudo-three-dimensional computational model having a span thickness of 0.5 mm was used to analyze the hydrodynamic and cavitation characteristics at an angle of attack of 8° and a cavitation number of $\sigma = 0.8$. The simulations were performed using the $k_{\omega}\ SST$ turbulence model coupled with the Rayleigh–Plesset cavitation model, at a Reynolds number of 7×10^5. The numerical investigation focuses on evaluating the lift coefficient, drag coefficient, lift-to-drag ratio, pressure distribution, and vapor volume fraction. A comparative study between a conventional NACA 4412 hydrofoil (baseline configuration) and a slotted configuration was carried out to assess the influence of slot implementation on cavitation behavior and hydrodynamic performance. The obtained results indicate that the slotted hydrofoil provides improved performance under cavitating conditions. Compared with the baseline configuration, the slotted hydrofoil increased the lift coefficient while reducing the drag coefficient, leading to an improvement in the lift-to-drag ratio. Pressure and vapor volume fraction distributions revealed noticeable modifications in cavitation development associated with the slot geometry. These findings demonstrate the potential of slotted hydrofoil configurations for cavitation mitigation and hydrodynamic performance enhancement in marine applications.

1 Introduction

Hydrofoils have attracted considerable attention in marine engineering applications, including high-speed vessels, underwater vehicles, marine current turbines, and renewable energy systems. Their capability to generate significant lift while reducing hydrodynamic resistance makes them particularly attractive for improving propulsion efficiency and operational performance. However, under severe operating conditions, the local pressure on the suction side of a hydrofoil may fall below the vapor pressure of water, leading to cavitation inception. Cavitation is generally associated with several detrimental effects, such as lift degradation, drag increase, noise generation, vibration, surface erosion, and structural damage, thereby limiting the overall performance and durability of marine systems.

Over the past decades, extensive research efforts have been devoted to understanding and predicting cavitating flows around hydrofoils through both experimental and numerical approaches. The rapid development of Computational Fluid Dynamics (CFD) has significantly enhanced the capability to simulate complex cavitation phenomena. In particular, cavitation models derived from the Rayleigh–Plesset equation have been widely employed for predicting unsteady cavitating flows around hydrofoils and marine propellers. Among the most widely adopted cavitation formulations are the models proposed by Singhal et al. [1], Zwart et al. [2], and Schnerr and Sauer [3]. When coupled with advanced turbulence models, especially the SST k–ω model proposed by Menter [4], these approaches have demonstrated satisfactory capabilities for capturing cavity inception, growth, shedding, and collapse mechanisms.

Several researchers have investigated transient cavitating flows around conventional hydrofoils. Kermeen [5] performed pioneering experimental investigations on NACA hydrofoils operating under cavitating conditions, providing valuable benchmark data for the validation of numerical simulations. Later, Ji et al. [6] employed Large Eddy Simulation (LES) to study the unsteady cavitation dynamics around hydrofoils and successfully reproduced the cavity growth and shedding processes. Furthermore, Coutier-Delgosha et al. [7] demonstrated that the prediction accuracy of cavitating flows strongly depends on the selected turbulence model, highlighting the necessity of adopting appropriate turbulence closures for unsteady

cavitation simulations. Arndt [8] provided a comprehensive review of cavitation phenomena in hydraulic machinery and emphasized the complex interactions between cavitation, turbulence, and hydrodynamic performance. Franc and Michel [9] further established the theoretical foundations of cavitation dynamics and provided extensive experimental observations regarding cavity inception and development.

Besides improving numerical methodologies, considerable attention has been devoted to passive flow-control techniques aimed at mitigating cavitation and enhancing hydrodynamic performance. Various geometrical modifications, including leading-edge tubercles, dimples, grooves, and multi-element configurations, have shown promising capabilities for delaying flow separation, reducing cavity extent, and improving hydrodynamic efficiency. Young [10] demonstrated that fluid–structure interaction effects may significantly influence the hydrodynamic behavior and cavitation characteristics of marine lifting surfaces. Among passive control techniques, slotted hydrofoils have recently emerged as an effective solution because the fluid jet passing through the slot can re-energize the boundary layer, promote flow reattachment, and consequently improve the overall hydrodynamic performance.

Prabhakar et al. [11] numerically investigated the cavitating flow around a modified NACA 4412 hydrofoil incorporating a slot and reported improvements in lift characteristics together with a reduction in drag. More recently, Biswas and Harish [12] demonstrated that triangular-slot configurations significantly modify cavity development and reduce wake intensity under cavitating conditions. Similar conclusions were reported by several recent numerical studies devoted to passive flow control in hydrofoils and marine lifting surfaces, confirming the potential of slot-based configurations for enhancing hydrodynamic efficiency under cavitating conditions [13,14]. Nevertheless, detailed investigations concerning the transient cavitation characteristics and pressure redistribution mechanisms induced by a triangular slot under severe cavitation conditions remain limited.

Therefore, the present study aims to numerically investigate the transient cavitating flow around conventional and triangular-slotted NACA 4412 hydrofoils using ANSYS CFX. The simulations are performed using the SST k–ω turbulence model coupled with the Rayleigh–Plesset cavitation model. Particular attention is devoted to evaluating the influence of slot implementation on hydrodynamic coefficients, pressure distribution, vapor volume fraction, and cavitation characteristics under intense cavitating conditions. The findings are expected to provide further insight into the effectiveness of passive flow-control strategies for improving hydrofoil performance in marine applications.

The remainder of this paper is organized as follows. Section 2 presents the governing equations and numerical methodology. Section 3 describes the computational domain, mesh generation, and validation procedure. Section 4 discusses the numerical results and hydrodynamic performance analysis. Finally, the main conclusions and future research perspectives are summarized in Section 5.

Unlike previous studies that mainly investigated conventional slots or hemispherical dimples, the present work proposes a triangular surface slot and performs a transient cavitating CFD analysis focusing on cavity evolution, pressure redistribution, and hydrodynamic performance under severe cavitation.

Table 1. Nomenclature.

σ	Cavitation number
α	Angle of attack,
U	Free Stream Velocity, m/s
P_l	Density of Liquid, Kg/m^3
p_v	Vapor pressure of liquid,
p_1	Static Pressure at cavitation number 1,
c	Chord length of hydrofoil,m
Re	Reynolds number based on chord length
A	Area of hydrofoil, m^2
C_L	Lift coefficient
C_D	Drag coefficient
C_p	Pressure coefficient
μ	Molecular viscosity, Pa.s

2 Numerical setup

2.1 Governing Mathematical Equations

All CFD simulations are ultimately grounded in three fundamental conservation laws expressed as partial differential equations (PDEs). These are listed below for an incompressible, Newtonian fluid in the most general form used in engineering solvers

2.1.1 Conservation of Mass (Continuity Equation)

The continuity equation enforces the principle that mass cannot be created or destroyed within the control volume:

$$\partial\rho/\partial t + \nabla\cdot(\rho v) = 0 \quad (1)$$

2.1.2 Conservation of Momentum (Navier-Stokes Equations)

The Navier-Stokes equations describe the evolution of the momentum field and are the centrepiece of every viscous flow simulation:

$$\partial(\rho v)/\partial t + \nabla\cdot(\rho v v) = -\nabla p + \nabla\cdot[\mu(\nabla v + \nabla v^T)] + \rho g + F \quad (2)$$

2.2 Turbulence Modeling

The Shear-Stress Transport (SST) k-ω model is the industry-recommended choice for flows involving boundary-layer separation, adverse pressure gradients, and cavitation. It achieves this by blending the k-ω formulation in the near-wall region with the k-ε formulation in the free stream, avoiding the free-stream sensitivity of pure k-ω models.

Two transport equations are solved one for turbulent kinetic energy k and one for specific dissipation rate ω. The model is validated across a wide range of hydrofoil and turbomachinery applications and was selected in the NACA 4412 cavitation study precisely because of its proven accuracy in capturing boundary-layer dynamics and cavitation-induced flow separation.

2.3 Multi phase Flow and Cavitation Modeling

2.3.1 Homogeneous Mixture Model

In the homogeneous mixture model, liquid and vapor phases are treated as sharing the same velocity and pressure field. The mixture density is computed from the vapor volume fraction α:

$$\rho_m = \alpha \cdot \rho_v + (1-\alpha) \cdot \rho_L \quad (3)$$

This model is widely used for sheet and cloud cavitation simulations because it is computationally inexpensive while capturing the key physics of vapor generation and collapse.

2.3.2 Rayleigh-Plesset equation

The Rayleigh-Plesset equation is a fundamental second-order ordinary differential equation in fluid mechanics governing the dynamic behavior of a spherical bubble inside an infinite body of incompressible liquid. Derived initially by Lord Rayleigh in 1917 for an empty collapsing cavity, and extended by Milton S. Plesset in 1949 to include viscous damping and surface tension, it serves as the cornerstone for modelling hydrodynamic cavitation, acoustic cavitation, and bubble dynamics.

Mathematical Formulation:

$$R.\frac{dR^2}{dt^2} + \frac{3}{2}.\left(\frac{dR}{dt}\right)^2 = \frac{1}{\rho_e}.\left[\left(P_v - P_\infty(t)\right) + (P_\infty - P_v).\left(\frac{R_0}{R}\right)^3 k - \frac{2\gamma}{R} - \frac{4\mu_e}{R}.\frac{dR}{dt}\right] \quad (4)$$

The Rayleigh–Plesset cavitation model was employed because it accurately describes bubble growth and collapse dynamics while remaining computationally efficient for transient engineering simulations.

3 Computational Domain and Meshing

This study presents the hydrodynamic performance and cavitation phenomena of the baseline and modified (triangular-slot) NACA 4412 hydrofoil, simulated using a CFX solver. The lift coefficient (C_L), drag coefficient (C_D), and lift-to-drag ratio (L/D) constitute the hydrodynamic performance evaluation parameters. The study was conducted at an angle of attack of 8° and a cavitation number σ = 0.8, with a Reynolds number of approximately Re = 7×10^5.

Normalized NACA 4412 coordinates were sourced from a verified database and imported into the ANSYS geometry editor. The profile was scaled by a factor of 0.1 to establish the required chord length of $c = X_{web} \times$ Scale Factor $= 1.0 \times 0.1 = 0.1$ m.

Spanwise thickness of 0.5 mm was selected to achieve a pseudo-three-dimensional configuration while minimizing computational cost. Previous studies have shown that such a thin span is sufficient to reproduce two-dimensional hydrodynamic behavior when symmetry conditions are applied and spanwise flow effects are negligible.

Boundaries were defined within the geometry interface, labeling the outer limits as Inlet, Outlet, and Symmetry, and the profile edges as Hydrofoil.

The computational domain is a rectangular channel of 3.2 m × 1.5 m. The hydrofoil leading edge is placed 1.2 m downstream from the inlet (12 chord lengths), and the outlet is located 2.0 m downstream of the trailing edge (20 chord lengths). The upper and lower boundaries are treated as no-slip walls, replicating a confined water tunnel environment. This domain sizing ensures that inlet disturbances do not affect the near-foil flow field and that the wake is fully developed before reaching the outlet boundary.

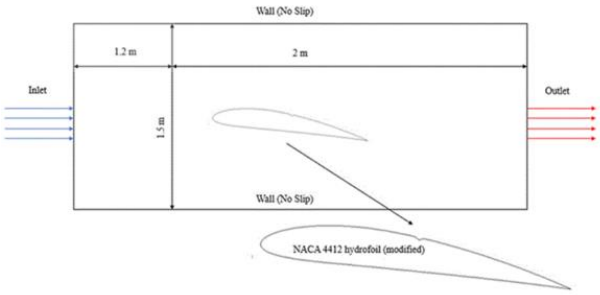


Fig. 1. Computational Domain and Boundary Conditions.

4 Grid Independence and Validation

A structured hexahedral mesh was generated for both the baseline and modified configurations. The choice of hexahedral elements over 500 000 cells is motivated by their superior accuracy in resolving boundary layer velocity gradients and their reduced numerical diffusion in convection-dominated flow regions a critical advantage when tracking the sharp liquid–vapor interface in cavitating flows.

The near-wall mesh was designed to maintain y+ values between 5 and 25, ensuring an adequate resolution of the boundary layer required by the SST turbulence model.

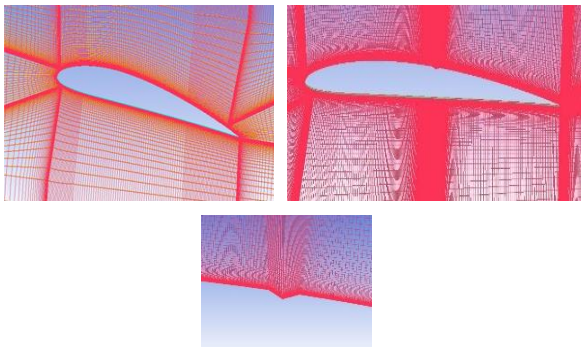


Fig. 2. Meshing around NACA 4412 baseline and slotted hydrofoil at α = 8º.

To ensure solution independence from mesh resolution, a mesh sensitivity study was carried out using three successive refinement levels, as summarised in Table below:

Table 2. Time averaged lift coefficient vs Number of cells, NACA4412 hydrofoil without slot at $\alpha = 8^{o}$ and $\sigma = 1$.

Case	Cells Number	Lift Coefficient(Cl) for NACA4412 (Base)
M_0	37 000	1.02
M_1	200 000	0.99773
M_2	500 000	0.97586
M_3	800 000	0.97423

A mesh independence study was performed at the operating condition of interest by testing three successive grid refinement levels. The variation in time-averaged lift coefficient between the medium and fine grids was found to be below 1%, confirming that the retained mesh hexahedral cells provides spatially converged results. The structured hexahedral topology further ensures favourable aspect ratio and orthogonal quality metrics throughout the domain, which is essential for the accurate resolution of the thin sheet cavity that forms on the suction surface at low cavitation numbers.

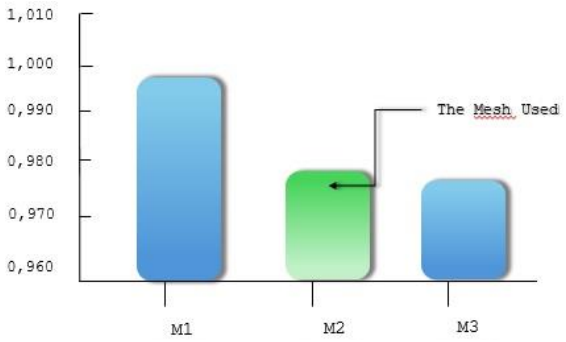


Fig. 3. Variation of Cl with number of cells for NACA4412 hydrofoil without slot at $\alpha = 8^{o}$, $\sigma = 1$.

The dependency of the solution on the time step size has been examined using three different time step sizes 10^{-2}, 5.10^{-3}, 1.10^{-3} and 10^{-4}. The time step independent solution has been found for step size 10^{-3}.

NACA4412 hydrofoil simulation has been compared with the experimental work by Kermeen (1956) at Re = 7×10^5 and 8^{o} angle of attack, to validate the numerical setup. A qualitative comparison of vapor fraction contour at cavitation number equal $\sigma = 1.87$ shown in Fig. 4.

Validation which is performed by obtaining the variation of time averaged lift coefficient versus angle of attack is shown in Fig. 5.

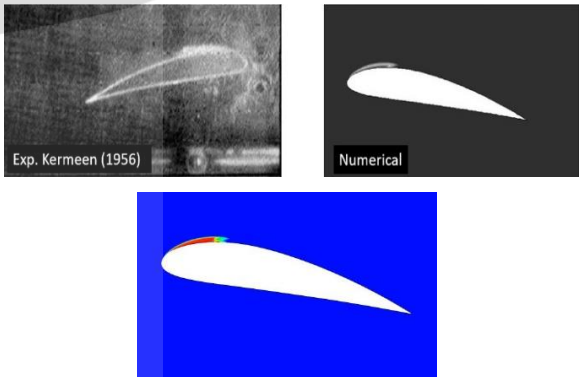


Fig. 4. Comparison of vapor volume fraction of present computational work and experimental work of (Kermeen, 1956) at $\sigma = 1.87$ and $\alpha = 8^{o}$

In the beginning, with the increase in angle of attack, lift is observed to be increased. Later, due to decrease in pressure in suction side of hydrofoil, the difference of pressure between the pressure side and suction side increases on the hydrofoil and reaches to maximum value.

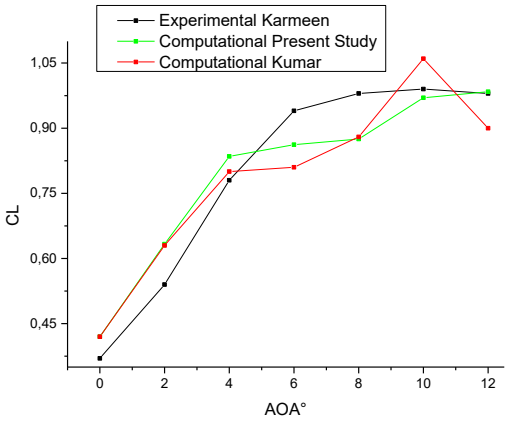


Fig. 5. Comparison of time averaged lift coefficient of present computational work with experimental work of Kermeen and Kumar [11]. Computational study at $\sigma = 1$.

5 Results and Discussion

All simulations were performed using a CFD solver implementing the finite volume method (FVM) for the numerical discretisation of the governing fluid flow equations. A pressure-based, transient solver was selected, consistent with the unsteady nature of cavitating two-phase flow. The inlet velocity was adjusted to obtain Re = 7×10^5, and the outlet pressure was derived from the cavitation number. No-slip boundary conditions were applied on all solid walls including the hydrofoil surface.

The cavitation number $\sigma = 0.8$ was selected because it represents a severe cavitating condition characterized by a stable attached sheet cavity, allowing a clear assessment of the influence of the triangular slot on cavity development and hydrodynamic performance.

An angle of attack of 8° was selected because it provides relatively high lift while maintaining an attached cavitating flow, making it suitable for

evaluating the effectiveness of passive flow-control techniques.

The triangular slot was positioned at mid-chord (x/c = 0.5), where the adverse pressure gradient becomes significant and the boundary layer starts losing momentum. This location allows the injected flow to effectively re-energize the boundary layer and delay flow separation.

Turbulence was modelled using the SST model, which combines the accuracy of the standard k–ω formulation in the near-wall region with the free-stream robustness of the k–ε model. This model is particularly well-suited to hydrofoil flows with adverse pressure gradients and cavitation dynamics, as it accurately captures boundary layer separation and the unsteady shedding of cavity structures. The Production Limiter was activated to prevent over-production of turbulent kinetic energy in stagnation zones.

The liquid–vapor phase change is governed by the Rayleigh–Plesset equation, which describes the inertia-driven growth and collapse of a spherical bubble in a surrounding liquid under a time-varying pressure field.

A time step of $\Delta t = 10^{-3}$ s was used. Time-averaged coefficients were computed over the last 500 time steps of the established pseudo-periodic regime after reaching a statistically periodic state.

5.1 Effect of Cavitation on Velocity Contours

Figure 6 presents the velocity contours obtained for the baseline and modified hydrofoils. At this low cavitation number, vapor formation is strongly promoted on the suction side of both hydrofoils, as the local static pressure falls well below the vapor pressure P_v = 3530 Pa over an extended region of the suction surface.

On the baseline hydrofoil, the velocity field reveals a high-speed region that hugs the suction surface, driven by the displacement effect of the thick attached vapor cavity. This cavity forces the outer flow to travel over a larger effective body, locally accelerating the fluid above the vapor–liquid interface. Downstream of the cavity closure, a broad low-velocity recirculation zone is visible in the near-wake region, reflecting the abrupt flow detachment as the sheet cavity collapses and the re-entrant jet penetrates upstream.

On the modified hydrofoil, the velocity field upstream of the triangular slot closely resembles that of the baseline. However, at the slot location (x/c = 0.5), a localized velocity perturbation is clearly visible: fluid from the high-pressure side is accelerated through the narrow triangular gap and injected as a jet onto the suction surface. This controlled injection energizes the near-wall flow, reduces the extent of the recirculation zone that would otherwise develop at that chord station. Downstream of the slot, the wake region of the modified profile is comparatively narrower and less intense than that of the baseline hydrofoil, indicating that the slot suggesting a reduction in the separated flow region.

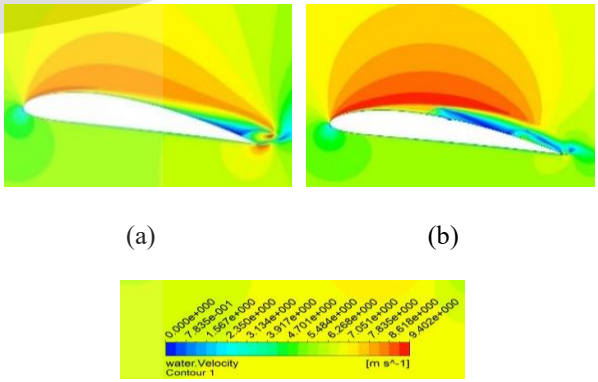


Fig. 6. Velocity contour for base and modified hydrofoil at σ = 0.8 and α = 8º

5.2 Temporal Evolution of Cavitation

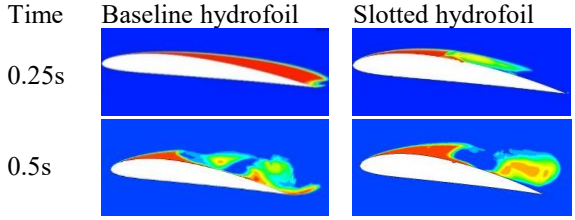
The evolution of the cavitation cavity over time for both hydrofoils is presented in the sequence of Figure 7 below. The vapor volume fraction contours are shown at successive simulation times ranging from 0.25 s to 3 s, providing a detailed view of the transient cavitation dynamics as the flow progresses from the initial state toward a statistically stationary regime.

The vapor volume fraction contours provide a direct visualization of the cavitation development around the hydrofoils. For the baseline hydrofoil, a larger vapor region is observed near the leading edge and extends downstream along the suction surface, indicating the development of an attached sheet cavity.

For the slotted hydrofoil, the vapor region becomes shorter and less intense compared with the baseline configuration. The triangular slot disrupts the continuity of the attached cavity and modifies the local pressure distribution, leading to a reduction in cavity growth.

The reduction in vapor volume fraction explains the slight improvement in hydrodynamic performance, as the smaller cavity region reduces the disturbance of the pressure distribution and improves the effective lifting surface.

For the baseline hydrofoil, the vapor cavity begins to form near the leading edge at the earliest time step (0.25 s) and progressively extends toward mid-chord and beyond as the simulation advances. Between t = 0.5 s and t = 1 s, the cavity reaches a quasi-steady attached sheet form that persists with minor oscillations at its trailing boundary. This relative stability is characteristic of the low cavitation number regime (σ = 0.8), where the high rate of vapor production sustains the cavity against the condensing action of the re-entrant jet. At later times (t = 1.5 s to 3 s), the cavity length changes only gradually, indicating a slowly evolving unsteady cycle rather than the rapid periodic shedding associated with cloud cavitation at higher σ values.



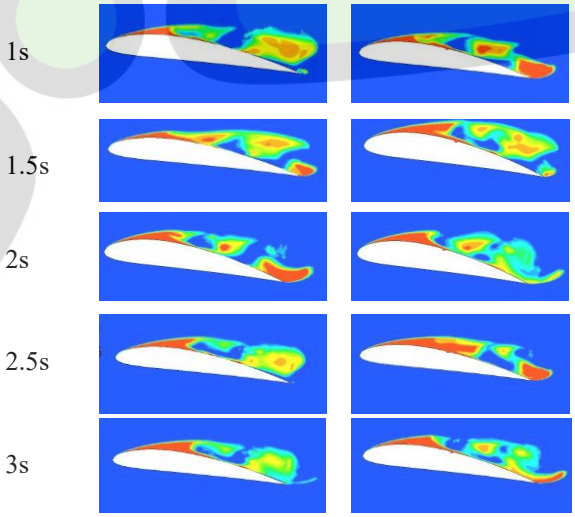
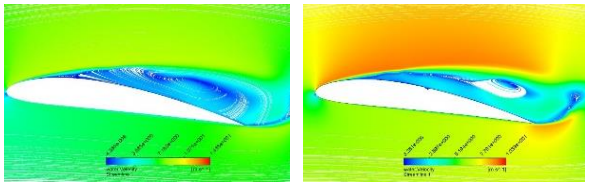


Fig. 7. Vapor volume fraction for base and modified hydrofoil at σ = 0.8 and α = 8º

For the modified hydrofoil, the initial cavity growth pattern (t = 0.25 s) is broadly similar to the baseline. However, from t = 0.5 s onward, the influence of the triangular slot becomes increasingly apparent: the slot location at x/c = 0.5 acts as a persistent perturbation point that interrupts the spatial continuity of the growing cavity. The downstream portion of the cavity undergoes more frequent and more pronounced thickness variations compared to the base case, reflecting the slot's role in modifying the local condensation–evaporation process. By t = 3 s, while the base hydrofoil maintains a smooth, spatially coherent attached sheet, the modified profile sustains a fragmented, dynamically active cavity structure in which the upstream and downstream portions cycle semi-independently. This increased unsteadiness induced by the slot at σ = 0.8 has direct implications for pressure fluctuation levels and structural loading on the hydrofoil surface.

5.3 Streamline Contours

The streamline patterns around both hydrofoils are presented in Figure 8. These flow visualisations reveal the global and local topology of the near-body and wake flow, and are particularly informative for identifying recirculation zones, vortex structures, and the effect of the triangular slot on flow organisation.



(a) (b)

Fig. 8. Streamline contours: a) baseline hydrofoil and b) modified hydrofoil

The velocity streamlines presented in Figure 8 reveal a strong acceleration region near the leading edge, corresponding to the low-pressure zone observed in the pressure contours.

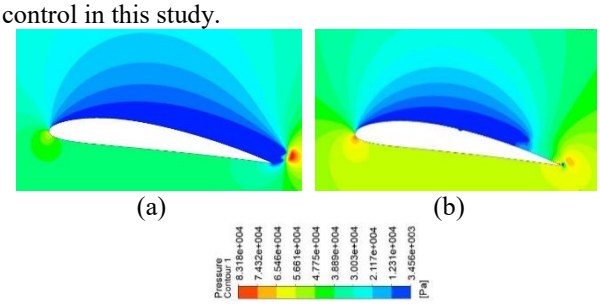
In the case of the slotted hydrofoil, the triangular slot generates a local recirculation zone inside the cavity region. This recirculation enhances momentum exchange between the high-momentum outer flow and the low-momentum boundary layer, which helps to delay flow separation.

For the baseline hydrofoil, the streamlines on the suction side curve smoothly over the attached vapor cavity and then diverge broadly in the near-wake region, where a large and elongated recirculation zone is visible behind the trailing edge. The streamlines within this zone are tightly wound, indicating elevated vorticity and significant turbulent kinetic energy dissipation. This vortex structure extends from the mid-chord region to well downstream of the trailing edge, producing a wide, energetically costly wake. The presence of this large vortex is consistent with the strong pressure drag component expected at σ = 0.8, where the thick cavity significantly displaces the outer flow.

For the modified hydrofoil, the streamlines upstream of the slot (x/c < 0.5) closely resemble those of the baseline, confirming that the slot does not disturb the upstream flow organisation. At the slot location, however, the streamlines exhibit a clear bifurcation: a portion of the flow from the pressure side is drawn through the slot opening and re-injected at the suction surface, producing a compact jet-reattachment signature that is visible as a streamline convergence zone immediately downstream of the slot. This jet prevents the large-scale separation that would otherwise develop naturally from the cavity closure and propagate toward the trailing edge.

5.4 Pressure Contours

Figure 9 illustrates the static pressure distribution over both hydrofoil. The pressure field is the primary driver of both the hydrodynamic loading and the cavitation dynamics, and its modification by the triangular slot constitutes the central mechanism of passive flow control in this study.



(a) (b)

Fig. 9. Pressure distribution contours: a) baseline hydrofoil and b) modified hydrofoil

Figure 9 illustrates the pressure distribution around the baseline and slotted hydrofoils under cavitating conditions. As expected, a low-pressure region develops near the leading edge on the suction side due to the acceleration of the flow over the hydrofoil surface. When the local pressure decreases below the vapor pressure, vapor formation occurs and a cavitation region is initiated.

For the slotted hydrofoil, the triangular slot modifies the local pressure field by redistributing the pressure along the suction surface. The slot introduces a local disturbance that enhances momentum exchange

between the external flow and the near-wall region, resulting in a smoother pressure recovery downstream of the slot.

This modified pressure distribution contributes to reducing the extension of the low-pressure region, which limits the growth of the attached cavity compared with the baseline hydrofoil.

On the baseline hydrofoil, a large and continuous low-pressure region (below the vapor pressure Pv) occupies the suction surface, extending from the leading edge to well past mid-chord. This extended pressure trough is the direct consequence of the high lift generated at 8° angle of attack combined with the low cavitation number: the favourable pressure gradient on the suction surface accelerates the flow strongly, producing a persistent low-pressure zone that sustains the attached vapor cavity. The pressure recovers gradually toward the trailing edge as the cavity closes and the flow partially reattaches, but the recovery is gradual and the associated wake remains energetically costly.

On the modified hydrofoil, the triangular slot introduces a localized pressure perturbation at x/c = 0.5. High-pressure fluid from the pressure side is channelled through the slot and injected into the low-pressure suction region, locally raising the surface pressure immediately downstream of the slot. This injection fragments the otherwise continuous low-pressure trough into two distinct sub-regions: one upstream of the slot, whose intensity is broadly comparable to the baseline, and one downstream of the slot, which is visibly attenuated. The consequence of this pressure redistribution is a reduction in the spatial coherence and intensity of the vapor cavity, as is confirmed by the vapor volume fraction contours discussed in the following section. The pressure field also shows a less abrupt recovery gradient near the trailing edge on the modified profile, indicating a smoother flow reattachment that reduces the pressure drag contribution.

5.5 Global Performance Analysis (C_L, C_D, and Efficiency).

Table 3. Comparison of Hydrodynamic Coefficients and Performance Gains.

Parameter	Baseline Profile		Slotted Profile	
	C_L	C_D	C_L	C_D
Coefficient value	0.8708	0.1518	0.8735	0.1507
Lift-to-drag ratio (C_L/C_D)	5.736		5.796	
Performance Gains : Slotted vs Baseline				
Lift gain (ΔC_L)	+0.31 % (0.8708 → 0.8735)			
Drag reduction (ΔC_D)	−0.72 % (0.1518 → 0.1507)			
L/D ratio improvement (C_L/C_D)	+1.05 % (5.736 → 5.796)			

The analysis of this data highlights a measurable improvement in the overall performance of the hydrofoil after modification:

Increase in Lift: The C_L coefficient increases from 0.8708 to 0.8735, representing a gain of 0.31%. This phenomenon is explained by the re-energization of the boundary layer on the suction side (extrados), which maintains a stronger circulation around the profile.

Reduction in Drag: The C_D coefficient undergoes a significant drop, decreasing from 0.1518 to 0.1507 (a reduction of 0.72%). The fluid injection through the slot suppresses or delays flow separation, drastically reducing the pressure drag associated with a turbulent wake.

Optimization of Hydrodynamic Efficiency: As a direct consequence of these two variations, the overall lift-to-drag ratio (C_L/C_D) increases by 1.05 %, rising from 5.736 to 5.796. This improvement confirms that the slotted configuration delivers much higher hydrodynamic efficiency.

5.6 Validation of Numerical Results Against Kermeen Experimental Data and CFD Literature (AoA = 8°, σ = 0.8)

Table 4. Validation of the present numerical results against the experimental data of Kermeen [5] and the numerical results of Kumar et al[11]. at AoA = 8° and σ = 0.8..

α=8	σ = 0,8	Kermeen experiment		Kumar et al.		Present study	
		C_L	C_D	C_L	C_D	C_L	C_D
		0.85	0.091	0.78	0.13	0.87	0.15

The predicted lift coefficient agrees well with the experimental measurements of Kermeen, with a maximum relative error of only 2.35 %, confirming the reliability of the present numerical methodology.

Although the increase in lift coefficient is relatively small, the triangular slot significantly modifies the local flow structure by reducing the cavity extent, promoting smoother pressure recovery, and reducing wake intensity. These changes improve the overall hydrodynamic behaviour even when the variation in the global coefficients remains limited.

Unlike the hemispherical dimple proposed by Kumar et al [11]., the present study employs a triangular surface slot, providing a different geometric approach to passive flow control while pursuing the same objective of modifying the boundary layer and cavitation behavior.

The difference between the present results and those of Kumar et al. (11.54%) may be attributed to differences in the numerical setup, mesh resolution, cavitation model, turbulence treatment, and computational domain.

5.7 Analysis of the Pressure Coefficient (Cp) Distribution

Figure 10 presents the pressure coefficient (Cp) distribution along the non-dimensional chord (x/c) for both the baseline and the slotted NACA 4412 hydrofoils under cavitating conditions.

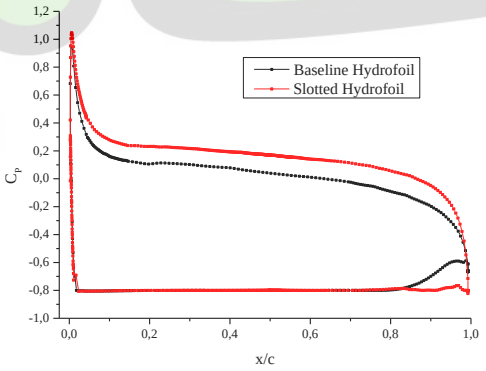


Fig. 10. Pressure coefficient distribution.

The upper curves correspond to the pressure side, whereas the lower curves represent the suction side.

On the pressure side, both hydrofoils exhibit a high positive pressure coefficient near the leading edge, followed by a rapid pressure decrease over the first portion of the chord as the flow accelerates around the hydrofoil. Downstream, the pressure recovery becomes gradual toward the trailing edge. Compared with the baseline hydrofoil, the slotted configuration maintains slightly higher pressure coefficient values over most of the pressure side, indicating that the slot modifies the pressure redistribution without introducing abrupt pressure variations.

On the suction side, both hydrofoils experience a strong pressure drop immediately downstream of the leading edge, where the local pressure reaches values close to the vapor pressure, promoting cavitation inception. For the baseline hydrofoil, the pressure coefficient gradually recovers near the trailing edge, suggesting the development of a stronger adverse pressure gradient associated with the cavity closure and wake formation.

In contrast, the slotted hydrofoil exhibits a more uniform pressure distribution over most of the suction surface, while the pressure recovery near the trailing edge becomes smoother. This behaviour indicates that the triangular slot modifies the local pressure field and alleviates the adverse pressure gradient responsible for the development of large separated flow regions. Consequently, the pressure difference between the pressure and suction sides is maintained over a larger portion of the chord, which is consistent with the slight increase in lift coefficient and the reduction in drag obtained for the slotted hydrofoil.

Overall, the pressure coefficient distribution confirms that the triangular slot acts as an effective passive flow-control device by redistributing the surface pressure, moderating the pressure recovery near the trailing edge, and contributing to a more stable hydrodynamic behaviour under cavitating conditions.

6 Conclusions

This study investigated the effect of a triangular slot introduced on the suction side of a NACA 4412 hydrofoil at mid-chord (x/c = 0.5) as a passive flow-control strategy. Transient CFD simulations were carried out in ANSYS CFX using the SST k–ω turbulence model and the Rayleigh–Plesset cavitation model, at Re ≈ 7 ×10^5, AoA = 8°, and σ = 0.8.

The results showed that the slot acts through two complementary mechanisms: it injects a high-momentum jet onto the suction surface that re-energizes the boundary layer, and it splits the attached vapor cavity into two less intense sub-regions, reducing the total cavitation extent and narrowing the downstream wake.

In terms of global performance, the slotted hydrofoil achieved a lift gain of 0.31 %, a drag reduction of 0.72 %, and an improvement of 1.05 % in the lift-to-drag ratio, confirming the effectiveness of this passive solution under intense cavitation conditions.

The present results demonstrate that the proposed triangular-slot configuration represents a promising passive flow-control technique for mitigating cavitation while preserving the hydrodynamic efficiency of marine lifting surfaces.

The present investigation is limited to a single cavitation number, one angle of attack, and a pseudo-three-dimensional numerical model. Future studies should extend the analysis to different operating conditions and fully three-dimensional simulations.

The proposed passive flow-control strategy may contribute to reducing cavitation-induced erosion, vibration, and efficiency losses in marine propellers, hydrofoils, tidal turbines, and high-speed marine vehicles. Future work could extend this study to a wider range of cavitation numbers and slot geometries, incorporate three-dimensional simulations to capture spanwise effects, and validate the findings experimentally using PIV or LDV measurements.

References

1. A.K. Singhal, M.M. Athavale, H. Li, Y. Jiang, Mathematical basis and validation of the full cavitation model. J. Fluids Eng. 124, 617-624 (2002). https://doi.org/10.1115/1.1486223
2. P.J. Zwart, A.G. Gerber, T. Belamri, A two-phase flow model for predicting cavitation dynamics, in Proceedings of the Fifth International Conference on Multiphase Flow, Yokohama, Japan (2004)
3. G.H. Schnerr, J. Sauer, Physical and numerical modeling of unsteady cavitation dynamics, in Proceedings of the Fourth International Conference on Multiphase Flow, New Orleans, USA (2001)
4. F.R. Menter, Two-equation eddy-viscosity turbulence models for engineering applications. AIAA J. 32, 1598-1605 (1994). https://doi.org/10.2514/3.12149
5. R.W. Kermeen, Water tunnel tests of NACA 4412 and Walchner profile 7 hydrofoils in noncavitating and cavitating flows. California Institute of Technology Report 47-5 (1956)
6. B. Ji, X.W. Luo, R.E.A. Arndt, X.X. Peng, Large eddy simulation and theoretical investigations of the transient cavitating vortical flow structure around a NACA66 hydrofoil. Int. J. Multiphase

Flow 51, 33-43 (2013). https://doi.org/10.1016/j.ijmultiphaseflow.2012.11.004

7. O. Coutier-Delgosha, R. Fortes-Patella, J.L. Reboud, Evaluation of the turbulence model influence on the numerical simulations of unsteady cavitation. J. Fluids Eng. 125, 38-45 (2003). https://doi.org/10.1115/1.1524584
8. R.E.A. Arndt, Cavitation in fluid machinery and hydraulic structures. Annu. Rev. Fluid Mech. 34, 143-175 (2002). https://doi.org/10.1146/annurev.fluid.34.082301.114920
9. J.P. Franc, J.M. Michel, Fundamentals of Cavitation (Kluwer Academic Publishers, Dordrecht, 2004)
10. Y.L. Young, Fluid-structure interaction analysis of flexible composite marine propellers. J. Fluids Struct. 24, 799-818 (2008). https://doi.org/10.1016/j.jfluidstructs.2007.10.010
11. K. Prabhakar, S. Srijna, R.S. Rajesh, Assessment of unsteady cavitating flow around modified NACA4412 hydrofoil. Ocean Eng. 266, 113039 (2022). https://doi.org/10.1016/j.oceaneng.2022.113039
12. S. Biswas, R. Harish, Effect of unsteady cavitation on hydrodynamic performance of NACA 4412 hydrofoil with novel triangular slot. Heliyon 11, e42266 (2025). https://doi.org/10.1016/j.heliyon.2025.e42266
13. T. Kinsey, G. Dumas, Parametric study of an oscillating hydrofoil in a power-extraction regime. Renew. Energy 36, 131-142 (2011). https://doi.org/10.1016/j.renene.2010.06.011
14. B. Huang, Y.L. Young, Z. Liu, Numerical investigation of ventilated and cavitating hydrofoil performance characteristics. Ocean Eng. 187, 106175 (2019). https://doi.org/10.1016/j.oceaneng.2019.106175
15. C.E. Brennen, Cavitation and Bubble Dynamics (Oxford University Press, New York, 1995)
16. J.P. Franc, J.M. Michel, Attached cavitation and the boundary layer: experimental investigation and numerical treatment. J. Fluid Mech. 154, 63-90 (1985). https://doi.org/10.1017/S0022112085001453
17. Y.L. Young, M.R. Motley, T.J. Barber, Modeling and simulation of surface-piercing hydrofoils. Annu. Rev. Fluid Mech. 49, 339-362 (2017). https://doi.org/10.1146/annurev-fluid-010816-060238
18. P.R. Spalart, W.H. Jou, M. Strelets, S.R. Allmaras, Comments on the feasibility of LES for wings and on a hybrid RANS/LES approach, in Advances in DNS/LES, First AFOSR International Conference on DNS/LES, Ruston, Louisiana, USA (1997)
19. J. Katz, A. Plotkin, Low-Speed Aerodynamics (Cambridge University Press, Cambridge, 2001)

Hydrodynamic performance of baseline and slotted NACA 4412 hydrofoils under cavitating conditions using transient CFD simulation

Z. Elkhaldi[1], F. Bouregba[1], R. Tayeb[1], L. Adjlout[1], and O. Imine[2]

[1]Naval Aero-Hydrodynamic Laboratory, Marine Engineering Department, University of Sciences and Technology of Oran Mohamed Boudiaf, USTO-MB, Oran, Algeria
[2]Aeronautics and Propulsion Systems Laboratory, Department of Aeronautical Engineering, University of Science and Technology of Oran Mohamed Boudiaf, USTO-MB, Oran, Algeria

Abstract. Hydrofoils are widely used in marine applications, where hydrodynamic performance and cavitation control are important engineering challenges. The present study numerically investigates transient cavitating flow around a baseline NACA 4412 hydrofoil and a modified configuration featuring a triangular groove on the suction surface. Simulations were performed using ANSYS CFX with the SST k–ω turbulence model and the Rayleigh–Plesset cavitation model. A pseudo-three-dimensional computational domain with a spanwise thickness of 0.5 mm was considered at an angle of attack of 8°, a cavitation number of 0.8, and a Reynolds number of approximately 7×10^5. The analysis focuses on the lift and drag coefficients, lift-to-drag ratio, pressure coefficient distribution, and vapor volume fraction. Compared with the baseline configuration, the modified hydrofoil exhibits a 0.31% increase in lift coefficient and a 0.72% reduction in drag coefficient, resulting in a 1.04% improvement in the lift-to-drag ratio. The pressure coefficient and vapor volume fraction distributions also reveal changes in the flow and cavitation patterns associated with the groove. These findings indicate a modest improvement in hydrodynamic performance under the investigated operating condition. Further simulations and experimental investigations are required to assess the influence of groove geometry and operating conditions on cavitation behavior.

1 Introduction

Hydrofoils have attracted considerable attention in marine engineering applications, including high-speed vessels, underwater vehicles, marine current turbines, and renewable energy systems. Oscillating hydrofoils have also been investigated for energy extraction from water currents [1]. Their capability to generate significant lift while reducing hydrodynamic resistance makes them particularly attractive for improving propulsion efficiency and operational performance. However, under severe operating conditions, the local pressure on the suction side of a hydrofoil may fall below the vapor pressure of water, leading to cavitation inception. Cavitation is generally associated with several detrimental effects, such as lift degradation, drag increase, noise generation, vibration, surface erosion, and structural damage [2], thereby limiting the overall performance and durability of marine systems. The development of attached cavitation is closely linked to boundary-layer behavior and the local flow field near the hydrofoil surface [3].

Over the past decades, extensive research efforts have been devoted to understanding and predicting cavitating flows around hydrofoils through both experimental and numerical approaches. The rapid development of Computational Fluid Dynamics (CFD) has significantly enhanced the capability to simulate complex cavitation phenomena. In particular, cavitation models derived from the Rayleigh–Plesset equation have been widely employed for predicting unsteady cavitating flows around hydrofoils and marine propellers. Among the most widely adopted cavitation formulations are the models proposed by Singhal et al. [4], Zwart et al. [5], and Schnerr and Sauer [6]. When coupled with advanced turbulence models, especially the SST k–ω model proposed by Menter [7], these approaches have demonstrated satisfactory capabilities for capturing cavity inception, growth, shedding, and collapse mechanisms.

Several researchers have investigated transient cavitating flows around conventional hydrofoils. Kermeen [8] performed pioneering experimental investigations on NACA hydrofoils operating under cavitating conditions, providing valuable benchmark data for the validation of numerical simulations. Later, Ji et al. [9] employed Large Eddy Simulation (LES) to study the unsteady cavitation dynamics around hydrofoils and successfully reproduced the cavity growth and shedding processes. Furthermore, Coutier-Delgosha et al. [10] demonstrated that the prediction accuracy of cavitating flows strongly depends on the selected turbulence model, highlighting the necessity of adopting appropriate turbulence closures for unsteady cavitation simulations. Arndt [11] provided a comprehensive review of cavitation phenomena in hydraulic machinery and emphasized the complex interactions between cavitation, turbulence, and

hydrodynamic performance. Franc and Michel [12] further established the theoretical foundations of cavitation dynamics and provided extensive experimental observations regarding cavity inception and development.

Besides improving numerical methodologies, considerable attention has been devoted to passive flow-control techniques aimed at mitigating cavitation and enhancing hydrodynamic performance. Various geometrical modifications, including leading-edge tubercles, dimples, grooves, and multi-element configurations, have shown promising capabilities for delaying flow separation, reducing cavity extent, and improving hydrodynamic efficiency. Young [13] demonstrated that fluid–structure interaction effects may significantly influence the hydrodynamic behavior and cavitation characteristics of marine lifting surfaces. Among passive flow-control techniques, surface modifications such as grooves and dimples have been investigated for their potential to alter local flow structures and hydrodynamic performance. Their effects depend on the geometry, location, and operating conditions. The performance of hydrofoils under ventilated and naturally cavitating conditions has also been investigated numerically [14]. In the present study, a shallow triangular groove is introduced on the suction surface of a NACA 4412 hydrofoil. Unlike a through-slot, this surface groove does not provide a passage between the pressure and suction sides.

Prabhakar et al. [15] numerically investigated the cavitating flow around a modified NACA 4412 hydrofoil incorporating a dimple and reported improvements in lift characteristics together with a reduction in drag. Unlike the dimpled NACA 4412 hydrofoil investigated in Ref. [15], the present study examines a triangular-slot configuration under the same operating conditions to assess the effect of the surface modification on hydrodynamic performance and cavitation behavior. The triangular-slot geometry is adopted from Biswas and Harish [16]. Therefore, the contribution of the present study lies in the comparative assessment of the triangular-slot and dimple configurations under the operating conditions considered, rather than in proposing a new slot geometry.

Therefore, the present study aims to numerically investigate the transient cavitating flow around conventional and triangular-slotted NACA 4412 hydrofoils using ANSYS CFX. The simulations are performed using the SST k–ω turbulence model coupled with the Rayleigh–Plesset cavitation model. Particular attention is devoted to evaluating the influence of slot implementation on hydrodynamic coefficients, pressure distribution, vapor volume fraction, and cavitation characteristics under intense cavitating conditions. The findings are expected to provide further insight into the effectiveness of passive flow-control strategies for improving hydrofoil performance in marine applications.

The remainder of this paper is organized as follows. Section 2 presents the governing equations and numerical methodology. Section 3 describes the computational domain and mesh generation. Section 4 presents the grid-independence study and validation procedure. Section 5 discusses the numerical results and hydrodynamic performance. Finally, Section 6 summarizes the main conclusions and future research directions.

Building on previous studies of cavitating flow around modified NACA 4412 hydrofoils [15,16], the present study compares the hydrodynamic performance and transient cavitation behavior of a baseline hydrofoil and a modified hydrofoil featuring a shallow triangular groove on the suction surface. The analysis examines the pressure coefficient distribution, vapor volume fraction, and hydrodynamic coefficients at a Reynolds number of approximately 7 10^5, an angle of attack of 8°, and a cavitation number of 0.8. The objective is to evaluate the influence of this surface modification under the selected operating conditions.

Table 1. Nomenclature.

σ	Cavitation number
α	Angle of attack,
α_v	Vapor volume fraction (dimensionless)
U	Free Stream Velocity, m/s
ρ_L	Density of Liquid, Kg/m^3
ρ_v	Density of Vapour, Kg/m^3
P_v	Vapor pressure of liquid, Pa
P	Local pressure, Pa
c	Chord length of hydrofoil,m
Re	Reynolds number based on chord length
A	Area of hydrofoil, m^2
F	body-force term per unit volume (N/m^3),
C_L	Lift coefficient
C_D	Drag coefficient
C_p	Pressure coefficient
μ	Molecular viscosity, Pa.s

2 Numerical setup

2.1 Governing Mathematical Equations

The governing equations for the present incompressible-flow formulation are based on the conservation of mass and momentum, which are expressed as partial differential equations (PDEs) as follows.

2.1.1 Conservation of Mass (Continuity Equation)

The continuity equation enforces the principle that mass cannot be created or destroyed within the control volume:

$$\partial\rho/\partial t + \nabla\cdot(\rho v) = 0 \qquad (1)$$

2.1.2 Conservation of Momentum (Navier-Stokes Equations)

The Navier-Stokes equations describe the evolution of the momentum field and are the centrepiece of every viscous flow simulation:

$$\partial(\rho v)/\partial t + \nabla\cdot(\rho_v v) = -\nabla p + \nabla\cdot[\mu(\nabla v + \nabla v^T)] + \rho g + F \qquad (2)$$

Where F represents an additional body-force term per unit volume (N/m³), if applicable.

2.2 Turbulence Modeling

The Shear-Stress Transport (SST) k-ω model is the industry-recommended choice for flows involving boundary-layer separation, adverse pressure gradients, and cavitation. It achieves this by blending the k-ω formulation in the near-wall region with the k-ε formulation in the free stream, avoiding the free-stream sensitivity of pure k-ω models.

Two transport equations are solved one for turbulent kinetic energy k and one for specific dissipation rate ω. The SST k–ω model has been widely applied to hydrofoil and turbomachinery flows and is suitable for simulations involving adverse pressure gradients and boundary-layer separation.

2.3 Multi phase Flow and Cavitation Modeling

2.3.1 Homogeneous Mixture Model

In the homogeneous mixture model, liquid and vapor phases are treated as sharing the same velocity and pressure field. The mixture density is computed from the vapor volume fraction α_v:

$$\rho_m = \alpha_v \cdot \rho_v + (1 - \alpha_v) \cdot \rho_L \quad (3)$$

This model is widely used for sheet and cloud cavitation simulations because it is computationally inexpensive while capturing the key physics of vapor generation and collapse.

2.3.2 Rayleigh-Plesset equation

The Rayleigh–Plesset equation describes the dynamics of a spherical vapor bubble in a liquid and provides the theoretical basis for modeling cavitation. In the ANSYS CFX framework, the Rayleigh–Plesset-based cavitation model is used to determine the interphase mass transfer rate associated with vaporization and condensation. The equation is expressed as follows:

$$R_B \cdot \frac{d^2 R_B}{dt^2} + \frac{3}{2} \cdot \left(\frac{dR_B}{dt}\right)^2 + \frac{2\sigma_s}{\rho_L R_B} + \frac{4\mu_L}{\rho_L R_B} \frac{dR_B}{dt} = \frac{P_v - P}{\rho_L} \quad (4)$$

where R_B is the bubble radius, P is the local liquid pressure, and σ_s is the liquid–vapor surface tension coefficient.

3 Computational Domain and Meshing

The computational domain and numerical setup were defined to investigate the transient cavitating flow around the baseline and modified NACA 4412 hydrofoils using ANSYS CFX. The hydrodynamic performance was evaluated in terms of the lift coefficient (C_L), drag coefficient (C_D), and lift-to-drag ratio (L/D).

The normalized NACA 4412 coordinates were imported into the ANSYS geometry editor and scaled to obtain a chord length of 0.1 m.

A spanwise thickness of 0.5 mm was used to construct a pseudo-three-dimensional computational domain while limiting computational cost. Symmetry boundary conditions were applied at the lateral boundaries to approximate two-dimensional flow behavior. The limitations associated with neglecting spanwise flow effects should be considered when interpreting the results.

The inlet and outlet boundary conditions were specified according to the prescribed flow conditions. The upper and lower boundaries were modeled as no-slip walls, while symmetry boundary conditions were applied to the lateral boundaries. The hydrofoil surface was also treated as a no-slip wall.

The computational domain is a rectangular channel of 3.2 m × 1.5 m. The hydrofoil leading edge is placed 1.2 m downstream from the inlet (12 chord lengths), and the outlet is located 2.0 m downstream of the leading edge (20 chord lengths). The upper and lower boundaries are treated as no-slip walls, replicating a confined water tunnel environment. This domain sizing ensures that inlet disturbances do not affect the near-foil flow field and that the wake is fully developed before reaching the outlet boundary.

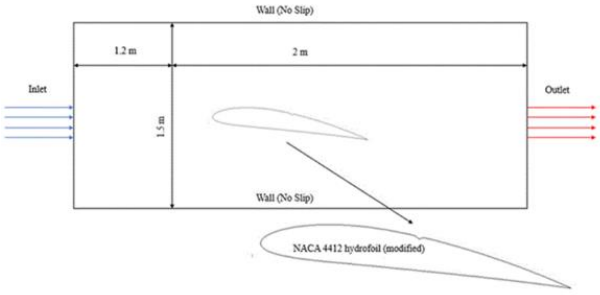


Fig. 1. Computational Domain and Boundary Conditions.

4 Grid Independence and Validation

A structured hexahedral mesh was generated for both the baseline and modified hydrofoil configurations. A mesh containing more than 500,000 cells was considered to resolve the boundary-layer velocity gradients and limit numerical diffusion in convection-dominated flow regions, which is important for simulating cavitating flows.

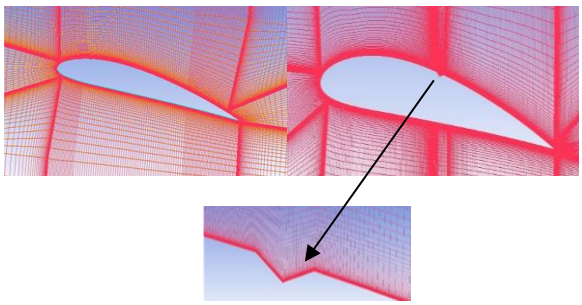


Fig. 2. Meshing around NACA 4412 baseline and slotted hydrofoil at α = 8º.

The near-wall mesh was designed to target y^+ values between 5 and 25, consistent with the intended near-wall resolution for the SST turbulence model.

To ensure solution independence from mesh resolution, a mesh sensitivity study was carried out using three successive refinement levels, as summarised in Table below:

Table 2. Time averaged lift coefficient vs Number of cells, NACA4412 hydrofoil without slot at α =8º and σ =1.

Case	Cells Number	Lift Coefficient(Cl) for NACA4412 (Base)
M1	200 000	0.70773
M2	500 000	0.87486
M3	800 000	0.87503

A mesh sensitivity study was performed using three grid resolutions. The time-averaged lift coefficients obtained with the medium and fine meshes were 0.87486 and 0.87503, respectively, corresponding to a relative difference of approximately 0.019%. This small difference indicates that the lift coefficient is relatively insensitive to further mesh refinement between these two grids under the tested conditions. The structured hexahedral mesh was used to resolve the flow field around the hydrofoil and the thin sheet cavity forming on the suction surface under cavitating conditions.

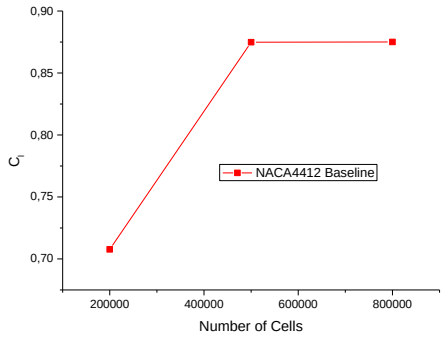


Fig. 3. Variation of Cl with number of cells for NACA4412 hydrofoil without slot at α =8º, σ =1.

The time-step sensitivity was examined using four time-step sizes: 10^{-2}, 5×10^{-3}, 10^{-3}, and 10^{-4} s. A time step of 10^{-3} s was selected for the transient simulations.

The numerical results for the NACA 4412 hydrofoil were compared with the experimental observations reported by Kermeen (1956) at a Reynolds number of approximately 7×10^5 and an angle of attack of 8°. Figure 4 presents a qualitative comparison of the vapor volume fraction contours at a cavitation number of σ = 1.87.

Figure 5 compares the time-averaged lift coefficient obtained in the present study with the reference results reported by Kermeen (1956) [8] and Prabhakar et al. [15] at a cavitation number of σ = 1.

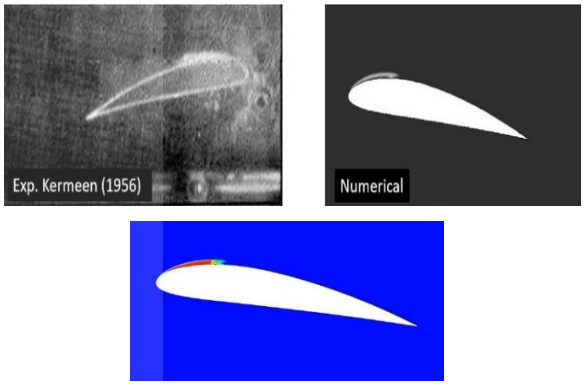


Fig. 4. Comparison of vapor volume fraction of present computational work and experimental work of (Kermeen, 1956) [8] at σ = 1.87 and α = 8º

As the angle of attack increases, the lift coefficient generally increases because the pressure difference between the pressure and suction sides becomes larger. However, this trend may change under cavitating conditions, depending on the flow regime.

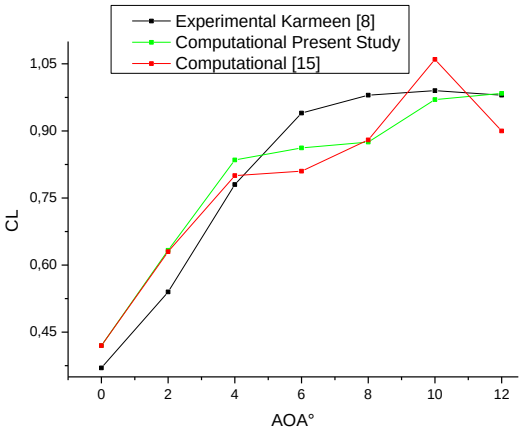


Fig. 5. Comparison of time averaged lift coefficient of present computational work with experimental work of Kermeen [8] and Prabhakar et al. [15]. Computational study at σ = 1.

5 Results and Discussion

All simulations were performed using ANSYS CFX with a pressure-based transient solver and the finite volume method (FVM). The inlet velocity was specified to obtain a Reynolds number of approximately 7×10^5, while the outlet pressure was set according to the prescribed cavitation number. No-slip boundary conditions were applied to the hydrofoil surface and the solid walls.

The cavitation number σ = 0.8 was selected to investigate the influence of the triangular slot on cavitation development and the hydrodynamic performance of the hydrofoil under severe cavitating conditions.

An angle of attack of 8° was selected to evaluate the influence of the triangular slot on the hydrodynamic performance and cavitation behavior of the hydrofoil.

The triangular slot was positioned at mid-chord (x/c = 0.5) to investigate its influence on the local flow field, pressure distribution, and cavitation development along the hydrofoil surface.

Turbulence was modelled using the shear stress transport (SST) k–ω model, which combines the near-wall formulation of the k–ω model with the free-stream behavior of the k–ε model. This model is suitable for hydrofoil flows involving adverse pressure gradients and boundary-layer separation.

The liquid–vapor phase change is governed by the Rayleigh–Plesset equation, which describes the inertia-driven growth and collapse of a spherical bubble in a surrounding liquid under a time-varying pressure field.

A time step of $\Delta t = 10^{-3}$ s was used. Time-averaged coefficients were calculated over the last 500 time steps after the flow reached a statistically periodic state.

5.1 Effect of Cavitation on Velocity Contours

Figure 6 presents the velocity contours around the baseline and modified hydrofoils. The velocity fields show spatial variations along the suction surface and in the downstream region for both configurations.

For the baseline hydrofoil, the contours show variations in velocity near the suction surface and downstream of the hydrofoil. These variations reflect the non-uniform flow field associated with the hydrofoil geometry and the cavitating flow conditions.

For the modified hydrofoil, the velocity distribution differs locally from that of the baseline configuration, particularly around the mid-chord region and downstream. These differences indicate that the triangular surface groove is associated with a modification of the local velocity field. However, the velocity contours alone do not establish a reduction in flow separation. Further flow-field analysis would be required to confirm this effect.

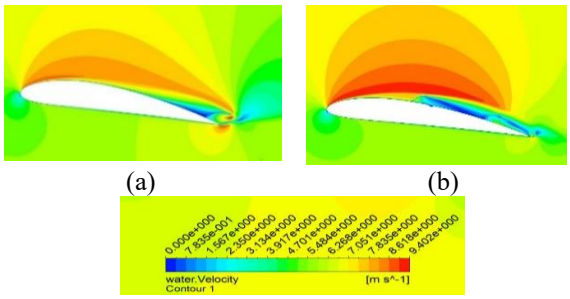


Fig. 6. Velocity contour for base and modified hydrofoil at σ = 0.8 and α = 8º

5.2 Temporal Evolution of Cavitation

Figure 7 presents the temporal evolution of the vapor volume fraction around the baseline and slotted hydrofoils at successive simulation times ranging from 0.25 s to 3 s. The contours provide a qualitative comparison of the transient cavitation patterns and their spatial distribution around the two configurations.

For the baseline hydrofoil, the vapor region develops near the leading edge and extends downstream along the suction surface. Its shape and extent change with time, indicating the unsteady nature of the cavitating flow. Vapor-rich regions are also observed farther downstream at several simulation times.

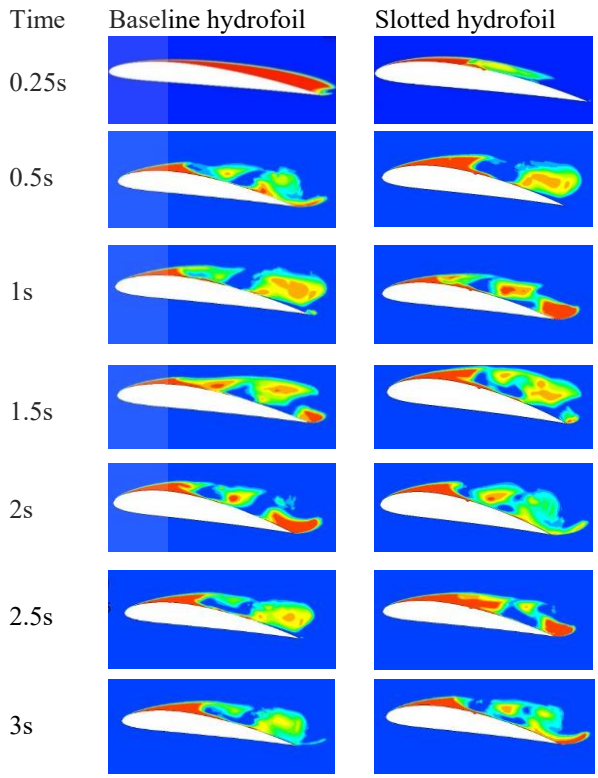


Fig. 7. Vapor volume fraction for base and modified hydrofoil at σ = 0.8 and α = 8º

For the slotted hydrofoil, the vapor distribution also evolves throughout the simulation, with noticeable changes in the shape, location, and continuity of the vapor-rich regions. Differences between the baseline and slotted configurations are visible at several time instants, suggesting that the surface modification is associated with changes in the transient cavitation pattern.

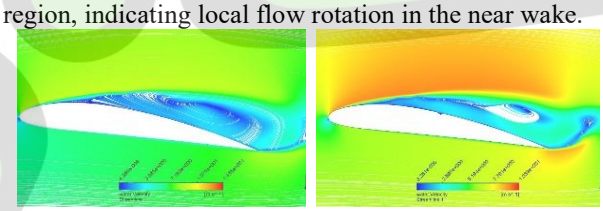
However, the contours alone do not establish a reduction in the total vapor volume or cavitation intensity. A quantitative comparison of the vapor volume fraction or cavity volume would be required to determine whether the observed differences correspond to an overall reduction in cavitation. The present results therefore demonstrate differences in the temporal and spatial distribution of cavitation between the two configurations under the investigated operating conditions.

5.3 Streamline Contours

Figure 8 presents the streamline patterns around the baseline and modified hydrofoils. These visualizations illustrate the flow organization near the hydrofoil surfaces and in the downstream region, allowing a qualitative comparison of the two configurations.

For the baseline hydrofoil, the streamlines follow the suction surface and exhibit curved patterns near the downstream portion of the hydrofoil. A recirculating

flow structure is also visible near the trailing-edge region, indicating local flow rotation in the near wake.



(a) (b)

Fig. 8. Streamline contours: a) baseline hydrofoil and b) modified hydrofoil

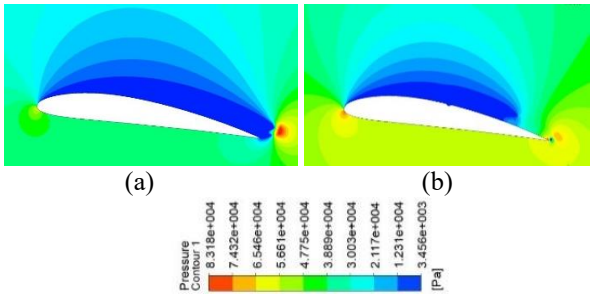
For the modified hydrofoil, the streamline patterns differ locally from those of the baseline configuration, particularly around the mid-chord region and downstream of the hydrofoil. These differences suggest that the triangular surface groove is associated with changes in the local flow organization. However, the present visualization alone does not establish whether the groove delays flow separation or reduces the intensity of the wake structures.

Overall, Figure 8 provides a qualitative comparison of the flow patterns around the two hydrofoils. Further quantitative analysis would be required to determine the effects of the surface modification on flow separation, vorticity, and wake development.

5.4 Pressure Contours

Figure 9 presents the static pressure distribution around the baseline and slotted hydrofoils under cavitating conditions. For both configurations, the pressure field varies along the hydrofoil surface, with a low-pressure region developing on the suction side. Differences in the pressure contours are visible between the two configurations, particularly in the distribution of pressure near the leading and trailing edges.

For the slotted hydrofoil, local variations in the pressure field are observed around the modified surface geometry and along the suction side. Since the triangular groove is confined to the suction surface, it does not provide a passage between the pressure and suction sides. These pressure variations may be associated with changes in the cavitation pattern, which are examined using the vapor volume fraction contours in Figure 7. However, the pressure contours alone do not establish a reduction in cavity extent or cavitation intensity.



(a) (b)

Fig. 9. Pressure distribution contours: a) baseline hydrofoil and b) modified hydrofoil

5.5 Global Hydrodynamic Performance (CL, CD, and Lift-to-Drag Ratio)

Table 3. Comparison of Hydrodynamic Coefficients and Performance Gains.

Parameter	Baseline Profile		Slotted Profile	
	C_L	C_D	C_L	C_D
Coefficient value	0.8708	0.1518	0.8735	0.1507
Lift-to-drag ratio (C_L/C_D)	5.736		5.796	
Performance Gains : Slotted vs Baseline				
Lift gain (ΔC_L)	+0.31 % (0.8708 → 0.8735)			
Drag reduction (ΔC_D)	−0.72 % (0.1518 → 0.1507)			
L/D ratio improvement (C_L/C_D)	+1.04 % (5.736 → 5.796)			

The analysis of this data highlights a measurable improvement in the overall performance of the hydrofoil after modification:

The comparison shows a modest improvement in hydrodynamic performance for the modified hydrofoil under the investigated conditions. The lift coefficient increases from 0.8708 to 0.8735, corresponding to a gain of 0.31%, while the drag coefficient decreases from 0.1518 to 0.1507, representing a reduction of 0.72%. Consequently, the lift-to-drag ratio increases from 5.736 to 5.796, an improvement of approximately 1.04%. These results indicate a small improvement in the overall hydrodynamic performance of the modified configuration at the considered operating condition. Further investigations are required to determine whether similar trends persist at other cavitation numbers and angles of attack.

5.6 Comparison of Numerical Results with Published CFD Data (AoA = 8°, σ = 0.8)

The present results are compared with the numerical results reported by Prabhakar et al. [15] for a NACA 4412 hydrofoil equipped with a hemispherical dimple. The lift and drag coefficients extracted approximately from their published curves are (CL ≈ 0.78) and (CD ≈ 0.11).

Table 4. Comparison of the Present Numerical Results with Published Hydrodynamic Coefficients at α = 8° and σ = 0.8.

α=8	σ = 0,8	Prabhakar et al. [15]		Present study	
		C_L	C_D	C_L	C_D
		0.78	0.11	0.87	0.15

The present study investigates a different passive flow-control configuration, namely a triangular surface slot, rather than a hemispherical dimple. Although both approaches aim to modify the flow around the hydrofoil,

their distinct geometries may lead to different hydrodynamic responses.

The present results yield a lift coefficient of 0.87 and a drag coefficient of 0.15. The relative difference in the lift coefficient is approximately 11.54% with respect to the value reported by Prabhakar et al. [15]. The comparison with published results should be interpreted cautiously because the reference coefficients were estimated from published plots, and the geometrical and numerical conditions may differ from those of the present study. Therefore, this comparison provides a general reference for the hydrodynamic coefficients but does not constitute a direct validation under identical conditions.

5.7 Analysis of the Pressure Coefficient (Cp) Distribution

Figure 10 presents the pressure coefficient (Cp) distribution along the non-dimensional chord (x/c) for both the baseline and the slotted NACA 4412 hydrofoils under cavitating conditions.

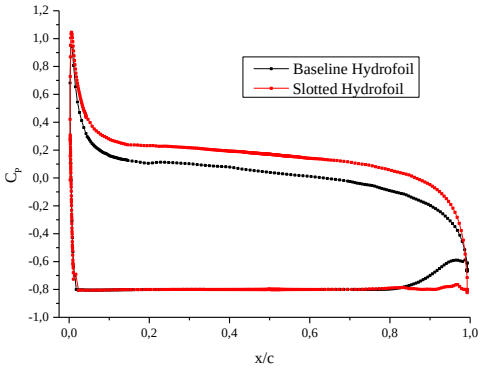


Fig. 10. Pressure coefficient distribution.

The upper curves correspond to the pressure side, whereas the lower curves represent the suction side.

On the pressure side, both hydrofoils exhibit a high positive pressure coefficient near the leading edge, followed by a rapid pressure decrease over the first portion of the chord as the flow accelerates around the hydrofoil. Downstream, the pressure recovery becomes gradual toward the trailing edge. Compared with the baseline hydrofoil, the slotted configuration maintains slightly higher pressure coefficient values over most of the pressure side, indicating that the slot modifies the pressure redistribution without introducing abrupt pressure variations.

On the suction side, both hydrofoils experience a strong pressure drop immediately downstream of the leading edge, where the local pressure reaches values close to the vapor pressure, promoting cavitation inception. For the baseline hydrofoil, the pressure coefficient gradually recovers near the trailing edge, suggesting the development of a stronger adverse pressure gradient associated with the cavity closure and wake formation.

On the suction side, the pressure coefficient distribution of the slotted hydrofoil is slightly higher (less negative) than that of the baseline hydrofoil over much of the chord. This difference indicates a modification of the surface pressure distribution associated with the groove. Near the trailing edge, the two curves approach each other, although some differences in pressure recovery remain visible. These variations are consistent with the small changes observed in the lift and drag coefficients. However, the pressure coefficient distribution alone is insufficient to establish whether the groove delays flow separation or reduces cavitation intensity. Further simulations at different cavitation numbers and angles of attack are required to determine whether these trends persist under other operating conditions.

6 Conclusions

This study investigated the effect of a triangular surface groove located at mid-chord (x/c = 0.5) on the cavitating flow around a NACA 4412 hydrofoil. Transient CFD simulations were performed using ANSYS CFX with the SST k–ω turbulence model and the Rayleigh–Plesset cavitation model. The simulations were conducted at a Reynolds number of approximately 7×10^5, an angle of attack of 8°, and a cavitation number of 0.8.

The results indicate that the triangular surface groove modifies the local pressure distribution and the cavitating flow around the hydrofoil. However, the present results do not establish a direct fluid jet from the pressure side to the suction side. The observed changes in the cavity distribution and downstream flow should therefore be interpreted in relation to the local effects of the groove geometry.

In terms of hydrodynamic performance, the modified hydrofoil achieved a lift coefficient increase of 0.31% and a drag coefficient reduction of 0.72%. Consequently, the lift-to-drag ratio increased by 1.04%, from 5.736 to 5.796. These results indicate a modest improvement in hydrodynamic performance for the investigated operating condition.

The present results suggest that the triangular surface groove can modify the pressure distribution and slightly improve the hydrodynamic performance of the NACA 4412 hydrofoil under the investigated cavitating condition. However, the extent of its influence on cavitation mitigation requires further assessment using additional operating conditions and more detailed flow-field analyses.

The present investigation is limited to a single cavitation number, one angle of attack, and a pseudo-three-dimensional computational model. Future studies should examine a wider range of operating conditions and employ fully three-dimensional simulations to investigate the influence of these parameters on the hydrodynamic performance and cavitation behavior of the hydrofoil.

Future work should investigate the influence of different cavitation numbers, angles of attack, and groove geometries on hydrofoil performance. Fully three-dimensional simulations could help clarify spanwise flow effects, while experimental measurements, such as PIV or LDV, would provide an independent assessment of the numerical predictions.

References

1. T. Kinsey, G. Dumas, Parametric study of an oscillating hydrofoil in a power-extraction regime. Renew. Energy 36, 131-142 (2011). https://doi.org/10.1016/j.renene.2010.06.011
2. C.E. Brennen, Cavitation and Bubble Dynamics (Oxford University Press, New York, 1995)
3. J.P. Franc, J.M. Michel, Attached cavitation and the boundary layer: experimental investigation and numerical treatment. J. Fluid Mech. 154, 63-90 (1985). https://doi.org/10.1017/S0022112085001453
4. A.K. Singhal, M.M. Athavale, H. Li, Y. Jiang, Mathematical basis and validation of the full cavitation model. J. Fluids Eng. 124, 617-624 (2002). https://doi.org/10.1115/1.1486223
5. P.J. Zwart, A.G. Gerber, T. Belamri, A two-phase flow model for predicting cavitation dynamics, in Proceedings of the Fifth International Conference on Multiphase Flow, Yokohama, Japan (2004)
6. G.H. Schnerr, J. Sauer, Physical and numerical modeling of unsteady cavitation dynamics, in Proceedings of the Fourth International Conference on Multiphase Flow, New Orleans, USA (2001)
7. F.R. Menter, Two-equation eddy-viscosity turbulence models for engineering applications. AIAA J. 32, 1598-1605 (1994). https://doi.org/10.2514/3.12149
8. R.W. Kermeen, Water tunnel tests of NACA 4412 and Walchner profile 7 hydrofoils in noncavitating and cavitating flows. California Institute of Technology Report 47-5 (1956)
9. B. Ji, X.W. Luo, R.E.A. Arndt, X.X. Peng, Large eddy simulation and theoretical investigations of the transient cavitating vortical flow structure around a NACA66 hydrofoil. Int. J. Multiphase Flow 51, 33-43 (2013). https://doi.org/10.1016/j.ijmultiphaseflow.2012.11.004
10. O. Coutier-Delgosha, R. Fortes-Patella, J.L. Reboud, Evaluation of the turbulence model influence on the numerical simulations of unsteady cavitation. J. Fluids Eng. 125, 38-45 (2003). https://doi.org/10.1115/1.1524584
11. R.E.A. Arndt, Cavitation in fluid machinery and hydraulic structures. Annu. Rev. Fluid Mech. 34, 143-175 (2002). https://doi.org/10.1146/annurev.fluid.34.082301.114920
12. J.P. Franc, J.M. Michel, Fundamentals of Cavitation (Kluwer Academic Publishers, Dordrecht, 2004)
13. Y.L. Young, Fluid-structure interaction analysis of flexible composite marine propellers. J. Fluids Struct. 24, 799-818 (2008). https://doi.org/10.1016/j.jfluidstructs.2007.10.010
14. B. Huang, Y.L. Young, Z. Liu, "Numerical investigation of ventilated and cavitating hydrofoil performance characteristics," *Ocean Engineering*, vol. 187, Article 106175, 2019. https://doi.org/10.1016/j.oceaneng.2019.106175
15. K. Prabhakar, S. Srijna, R.S. Rajesh, Assessment of unsteady cavitating flow around modified NACA4412 hydrofoil. Ocean Eng. 266, 113039 (2022). https://doi.org/10.1016/j.oceaneng.2022.113039
16. S. Biswas, R. Harish, Effect of unsteady cavitation on hydrodynamic performance of NACA 4412 hydrofoil with novel triangular slot. Heliyon 11, e42266 (2025). https://doi.org/10.1016/j.heliyon.2025.e42266

Effect of synthetic jet placement on the near- and post-stall aerodynamics of the NLF(1)-0416 airfoil

Baris Gungordu*

[1]Middle East Technical University, Northern Cyprus Campus, Kalkanlı, Güzelyurt via Mersin 10, 99738, Türkiye

Abstract. Synthetic jet actuation can improve near- and post-stall aerodynamic performance through periodic blowing and suction without net mass addition. This study examines actuator placement on the NLF(1)-0416 airfoil using two-dimensional unsteady Reynolds-averaged Navier–Stokes simulations with the generalised k–ω (GEKO) turbulence model and algebraic intermittency at $Re_c = 2 \times 10^6$. Baseline predictions are compared with experimental lift and drag measurements.

Actuation is imposed through a sinusoidal velocity boundary condition over a single 3 mm slot, approximately 0.49% of the 609 mm chord. Three locations, $x/c = 0.25$, 0.45, and 0.65, are evaluated at a fixed injection angle of 20° relative to the local surface tangent, with common amplitude and frequency. Twelve controlled cases covering $\alpha = 13°$–$16°$ are compared with their unactuated baselines.

Actuator placement produces a trade-off between lift enhancement and aerodynamic efficiency. Actuation at $x/c = 0.65$ yields the highest lift throughout the range, reaching $C_l = 2.0871$ at $\alpha = 16°$, a 67.0% increase over the baseline. The upstream location, $x/c = 0.25$, provides the lowest drag and the highest L/D at three of the four incidences. At $\alpha = 16°$, it reduces drag by 51.3% and increases L/D from 14.74 to 42.98, a 191.6% improvement. Conversely, actuation at $x/c = 0.45$ reduces L/D by 22.4% at $\alpha = 13°$ despite increasing lift.

These predictions demonstrate promising aerodynamic benefits from a single synthetic jet, with downstream placement favouring lift enhancement and upstream placement generally providing greater aerodynamic efficiency. For all three locations, lift continues to increase through the highest investigated angle of attack, $\alpha = 16°$.

1 Introduction

Maintaining lift and aerodynamic efficiency near stall is important for aircraft operating at elevated angles of attack, particularly during take-off and landing. Conventional high-lift devices improve aerodynamic performance but introduce additional mechanical complexity and weight. Active flow control offers an alternative means of modifying boundary-layer separation. Among these techniques, synthetic jet actuators (SJAs) transfer momentum through periodic blowing and suction without net mass addition over an actuation cycle, eliminating the

*e-mail: gbaris@metu.edu.tr

need for an external fluid supply [1]. Recent studies have demonstrated that synthetic jet actuators can achieve jet velocities of up to 100 and 150 m s^{-1} using single-crystal and bimorph piezoelectric diaphragms, respectively [2, 3], highlighting their potential for applications requiring substantial momentum input. Their interaction with the external flow can modify separation and improve aerodynamic performance [4]. Improving airfoil aerodynamic performance near and beyond stall has attracted recent experimental and computational research interest, particularly through active flow control methods [5].

The effectiveness of synthetic jet actuation depends on its location and operating parameters. In particular, actuator placement relative to the separation region determines where the imposed disturbances interact with the boundary layer and separated shear layer. This is relevant to natural-laminar-flow (NLF) airfoils, which are designed to maintain extended laminar regions for reduced drag [6, 7]. Evaluating their controlled performance near and beyond stall requires consideration of both lift and drag, since a configuration that increases lift may not provide the highest aerodynamic efficiency.

The present study numerically investigates the effect of synthetic jet placement on the NLF(1)-0416 airfoil at a chord-based Reynolds number of 2×10^6 and a freestream Mach number of 0.1. Three upper-surface locations, $x/c = 0.25$, 0.45, and 0.65, are examined at a fixed momentum coefficient of $C_\mu = 0.1$ and an injection angle of 20°. Each configuration is evaluated at angles of attack from 13° to 16°, yielding 12 controlled cases. The GEKO turbulence model coupled with an algebraic intermittency model is employed, and baseline predictions are validated against experimental measurements. Comparisons with the unactuated airfoil at corresponding angles of attack assess how actuator placement affects lift, drag, and lift-to-drag ratio. The objective is to identify placement-dependent benefits and trade-offs within the investigated near- and post-stall operating range.

2 Numerical Methodology

2.1 Governing equations and numerical approach

Two-dimensional unsteady Reynolds-averaged Navier–Stokes (URANS) simulations are performed using a commercial finite-volume solver [8]. The NLF(1)-0416 airfoil has a chord length of $c = 0.609$ m, consistent with the experimental configuration reported by Somers [9]. The freestream velocity is $U_\infty = 51$ m s^{-1}, corresponding to $M_\infty = 0.10$, and the present investigation considers a chord-based Reynolds number of $Re_c = 2 \times 10^6$. Density is assumed constant within each simulation.

The incompressible mass and momentum conservation equations are

$$\frac{\partial U_j}{\partial x_j} = 0, \tag{1}$$

$$\rho\left(\frac{\partial U_i}{\partial t} + U_j \frac{\partial U_i}{\partial x_j}\right) = -\frac{\partial p}{\partial x_i} + \frac{\partial}{\partial x_j}\left[2(\mu + \mu_t)S_{ij} - \frac{2}{3}\rho k \delta_{ij}\right], \tag{2}$$

where U_i and p denote the mean velocity and pressure, μ and μ_t are the molecular and turbulent dynamic viscosities, and

$$S_{ij} = \frac{1}{2}\left(\frac{\partial U_i}{\partial x_j} + \frac{\partial U_j}{\partial x_i}\right). \tag{3}$$

Repeated indices imply summation. Turbulence closure is provided by the generalised k–ω (GEKO) model coupled with an algebraic intermittency model. The turbulence transport equations are written in compact form as

$$\frac{\partial(\rho k)}{\partial t} + \frac{\partial(\rho U_j k)}{\partial x_j} = \frac{\partial}{\partial x_j}\left(\Gamma_k \frac{\partial k}{\partial x_j}\right) + \gamma P_k - Y_k, \tag{4}$$

$$\frac{\partial(\rho \omega)}{\partial t} + \frac{\partial(\rho U_j \omega)}{\partial x_j} = \frac{\partial}{\partial x_j}\left(\Gamma_\omega \frac{\partial \omega}{\partial x_j}\right) + P_\omega - Y_\omega + D_\omega. \tag{5}$$

Here, k is the turbulent kinetic energy, ω is the specific dissipation rate, and Γ_k and Γ_ω are effective diffusion coefficients. The terms P, Y, and D_ω represent production, destruction, and cross-diffusion, respectively, incorporating the GEKO closure functions. The algebraic intermittency γ modifies turbulent kinetic-energy production to account for boundary-layer transition.

Pressure–velocity coupling is achieved using the pressure-implicit with splitting of operators (PISO) algorithm. Time integration employs a second-order implicit scheme with a uniform time step of $\Delta t = 7.5 \times 10^{-4}$ s. Inner iterations at each time step use a residual convergence threshold of 10^{-3}. The initial 0.5 s of the solution is excluded from the subsequent averaging of aerodynamic quantities.

2.2 Computational Domain, Mesh and Turbulence and Transition Modelling

An unstructured mesh was generated within a C-type computational domain extending approximately $15c$ horizontally and $10c$ vertically. Local refinement was applied around the airfoil and trailing edge. Near-wall resolution of $y^+ < 1$ was achieved using a first-layer height of 2.6×10^{-6} m, with 45 inflation layers and a growth rate of 1.2. Following spatial and temporal sensitivity assessments, 450,000 elements and a time step of 7.5×10^{-4} s were used throughout the study.

Figure 1 shows the computational domain and its dimensions, the applied boundary conditions, and the mesh around the airfoil, including a close-up of the trailing-edge region.

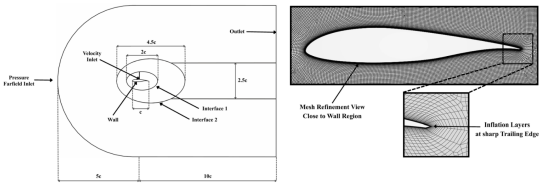


Figure 1: *Computational domain, dimensions, and boundary conditions (left); airfoil mesh with a detailed view of the trailing-edge refinement (right).*

The intermittency treatment accounts for laminar-to-turbulent transition, which is particularly relevant to the extended laminar-flow regions of the NLF(1)-0416 airfoil. Accounting for transition is particularly relevant to the NLF(1)-0416 airfoil, which is designed to maintain extended regions of laminar flow. A fully turbulent closure alone would not explicitly represent this behaviour.

2.3 Actuator Placement and Frequency Selection

The synthetic jet is modelled using a velocity-inlet boundary condition applied over a single upper-surface slot of width $h = 3$ mm. Three actuator locations, $x/c = 0.25$, 0.45, and 0.65,

were selected with reference to the separation locations observed in the unactuated high-incidence flows. The injection angle is fixed at 20° relative to the local downstream surface tangent, equivalent to 70° from the outward surface normal.

Preliminary simulations at $Re_c = 2 \times 10^6$ using surface-normal injection showed that post-stall lift enhancement could be accompanied by a drag penalty. In particular, actuation at $x/c = 0.25$ and 0.35 increased lift but also increased drag, whereas the drag reduction at $x/c = 0.55$ was accompanied by substantial lift loss. These observations motivated the investigation of inclined injection to improve the balance between lift enhancement and aerodynamic efficiency.

An injection angle of 20° relative to the local surface tangent was therefore selected for the present study. Compared with surface-normal injection, this orientation provides a larger downstream tangential velocity component during blowing, with the aim of enhancing near-wall momentum transfer while reducing the normal disturbance to the external flow. The injection angle was held constant to isolate the influence of actuator placement; determining the optimal angle remains outside the scope of the present study.

Following the convention shown in the actuator schematic, the present study uses an injection angle of 20° from the local downstream surface tangent, equivalent to 70° from the outward surface normal. Figure 2 illustrates the injection-angle convention of the synthetic jet injection angle.

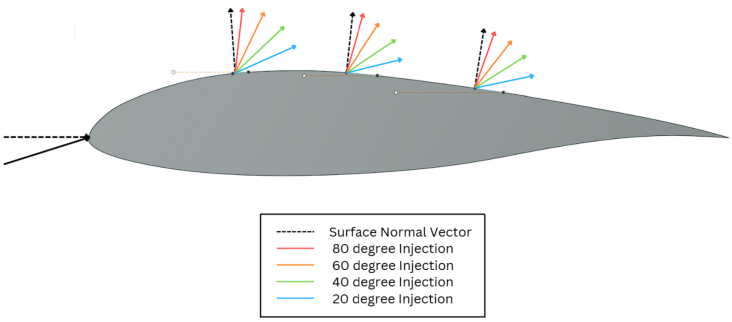


Figure 2: *Definition of synthetic jet injection angle*

The actuation frequency was selected through power spectral density (PSD) analysis of the baseline vertical velocity fluctuations. Probes were distributed within the separated-flow region, near the trailing edge, and in the near and far wake to characterise the dominant unsteady behaviour at high incidence. A dominant frequency of 16 Hz was identified and adopted for all controlled cases. The prescribed slot velocity therefore follows

$$\boldsymbol{u}_{\text{jet}}(t) = U_0 \sin(2\pi f_a t)\, \boldsymbol{e}_{\text{jet}}, \qquad f_a = 16 \text{ Hz}. \tag{6}$$

Where U_0 is the peak jet velocity, $\boldsymbol{e}_{\text{jet}}$ defines the injection direction. The present comparison isolates actuator placement by holding the injection angle, amplitude, and frequency constant.

The actuation strength is characterised by a peak-velocity-based momentum coefficient,

$$C_\mu = 2\frac{h}{c}\left(\frac{U_0}{U_\infty}\right)^2, \tag{7}$$

where c is the airfoil chord, and U_∞ is the freestream velocity. This definition uses the peak velocity rather than a cycle-averaged momentum flux. For $h = 0.003$ m, $c = 0.609$ m, and

$U_\infty = 34\ \mathrm{m\,s^{-1}}$, the prescribed $C_\mu = 0.1$ corresponds to $U_0 \approx 108.3\ \mathrm{m\,s^{-1}}$. The actuation amplitude and frequency are held constant across all actuator locations. For constant density, the sinusoidal boundary condition produces zero net mass flux over a complete actuation cycle.

The instantaneous lift and drag coefficients are defined as

$$C_l(t) = \frac{L'(t)}{\frac{1}{2}\rho U_\infty^2 c}, \qquad C_d(t) = \frac{D'(t)}{\frac{1}{2}\rho U_\infty^2 c}, \tag{8}$$

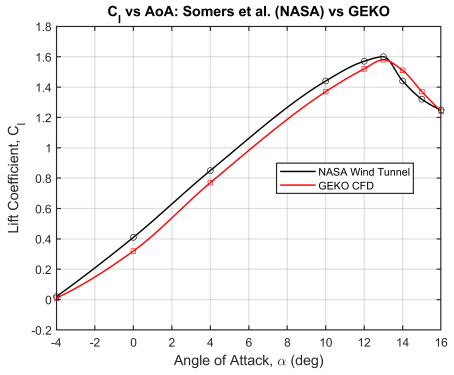
where L' and D' are the lift and drag forces per unit span, resolved perpendicular and parallel to the freestream, respectively. Aerodynamic performance is assessed using time-averaged coefficients after excluding the initial transient. The reported lift-to-drag ratio is calculated as

$$L/D = \frac{\overline{C_l}}{\overline{C_d}}, \tag{9}$$

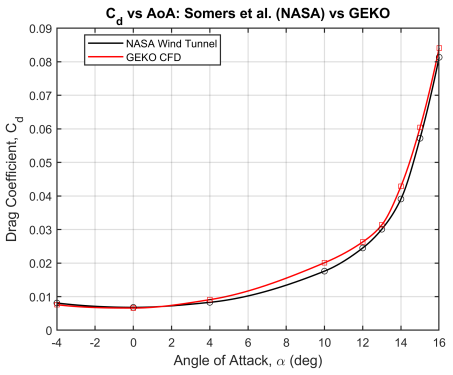
where the overbar denotes averaging over the retained sampling interval.

3 Validation of the Numerical Model

Figure 3 compares the baseline lift and drag predictions obtained using GEKO with algebraic intermittency against the experimental data of Somers [9] over $\alpha = -4°$–$16°$. The model captures the lift maximum near 13°, predicting $C_{l,\max} \approx 1.58$ compared with 1.60 experimentally. Lift is generally underpredicted before stall, with a more gradual initial post-stall decline. Drag agrees closely at low incidences and is moderately overpredicted at higher angles, while its post-stall increase is captured. These comparisons support comparative aerodynamic assessment, although baseline validation alone does not establish the accuracy of actuated-flow predictions.



(a) C_l validation



(b) C_d validation

Figure 3: *Comparison of aerodynamic coefficients with the results produced with the computational model at* $Re = 2 \times 10^6$ *with experimental data [9]*

4 Results and Discussion

The influence of synthetic jet placement on the near- and post-stall aerodynamic performance of the NLF(1)-0416 airfoil is examined at $Re_c = 2\times10^6$. Three actuator locations, $x/c = 0.25$, 0.45, and 0.65, are compared over $\alpha = 13°$–$16°$, with the injection angle fixed at 20° and the actuation amplitude and frequency held constant. This yields 12 actuated cases, each assessed against the corresponding unactuated baseline.

Performance is evaluated using the time-averaged lift and drag coefficients and their ratio, L/D. The discussion first examines the response at each actuator location, followed by a comparison of placement effects. Particular attention is given to maintaining lift beyond the baseline stall angle and to the accompanying changes in drag and aerodynamic efficiency.

4.1 Effect of Actuator Location

Figure 4 compares the aerodynamic performance of the three actuator locations at an injection angle of 20°. All locations increase lift throughout $\alpha = 13°$–$16°$, with $x/c = 0.65$ consistently producing the highest C_l. However, the greatest lift enhancement does not coincide with the highest aerodynamic efficiency. Actuation at $x/c = 0.25$ provides the lowest drag throughout the investigated range and the highest L/D except at $\alpha = 15°$, where $x/c = 0.45$ performs slightly better.

The influence of placement is particularly evident at $\alpha = 13°$. At $x/c = 0.25$ and 0.65, L/D increases by 17.3% and 10.0%, respectively. In contrast, actuation at $x/c = 0.45$ increases drag by approximately 31.0% while providing only a 1.7% lift improvement, reducing L/D by 22.4%. Thus, actuation does not necessarily improve efficiency near the baseline lift maximum.

Beyond the baseline stall angle, all three locations improve both lift and L/D, with the largest relative gains occurring at $\alpha = 16°$ (Table 1). The downstream location, $x/c = 0.65$, provides the greatest lift enhancement of 67.0%, whereas $x/c = 0.25$ achieves the largest drag reduction of 51.3% and L/D improvement of 191.6%. These results demonstrate a trade-off between maximising lift and aerodynamic efficiency when selecting the actuator location. Although lift increases through $\alpha = 16°$ for all controlled cases, the absence of a resolved lift maximum prevents quantification of the controlled stall angle.

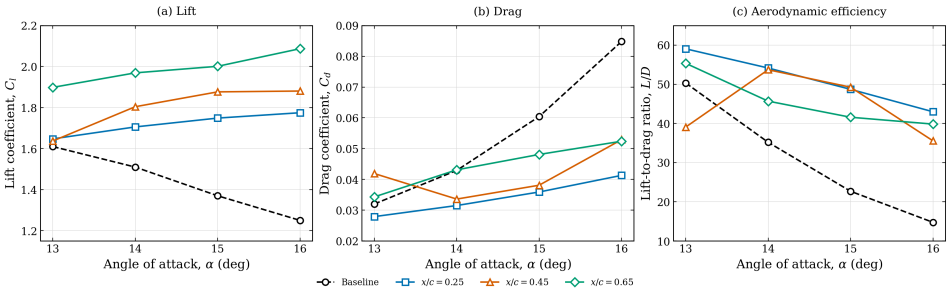


Figure 4: *Comparison of results for different actuator locations*

4.2 Instantaneous Aerodynamic Response

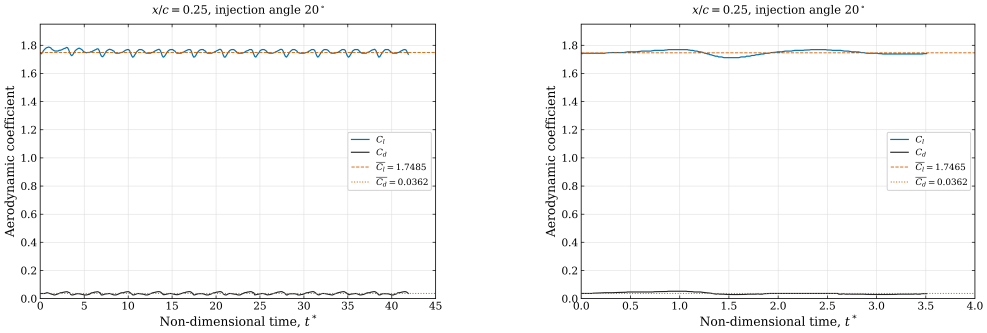
Figure 5 presents the time histories of the lift and drag coefficients for actuation at $x/c = 0.25$ with an injection angle of 20°. The time is nondimensionalized using $t^* = \frac{U_0 t}{c}$. Over the

Table 1: Percentage changes in aerodynamic performance at $\alpha = 16^\circ$ relative to the unactuated numerical baseline.

x/c	C_l increase	C_d reduction	L/D increase
0.25	42.0%	51.3%	191.6%
0.45	50.4%	37.6%	141.2%
0.65	67.0%	38.2%	170.2%

displayed interval, both coefficients exhibit bounded, recurring fluctuations around their mean values, with no evident sustained drift. The mean lift and drag coefficients are approximately 1.7485 and 0.0362, respectively.

The enlarged view reveals variations within the recurring oscillation pattern, indicating that the aerodynamic response is not purely sinusoidal despite the sinusoidal forcing. Lift remains elevated throughout the displayed record, showing that the mean lift enhancement is maintained in the presence of unsteady fluctuations. Although the drag oscillations appear small on the shared vertical scale, their magnitude should be assessed relative to the much smaller mean drag coefficient. These histories characterise the controlled response; a corresponding baseline comparison and spectral analysis would be required to establish whether actuation suppresses fluctuations or synchronises the flow with the forcing.



(a) extended time history

(b) enlarged view

Figure 5: *Instantaneous lift and drag coefficients for synthetic jet actuation at* $x/c = 0.25$ *with an injection angle of* 20°. *Dashed lines indicate time-averaged values.*

The contrasting lift and drag responses highlight the influence of actuator placement on aerodynamic performance. The lower drag at $x/c = 0.25$ is consistent with reduced separation-related losses, potentially because momentum is introduced earlier along the suction surface. Conversely, the higher lift at $x/c = 0.65$ suggests stronger modification of the aft loading. Its higher drag, however, shows that greater lift recovery does not necessarily imply reduced separation or a weaker wake deficit. Surface pressure, skin-friction distributions, and mean-flow fields are needed to establish these mechanisms.

The efficiency penalty at $x/c = 0.45$ and $\alpha = 13^\circ$ also demonstrates the dependence of control effectiveness on the baseline flow state: the modest lift benefit is outweighed by increased drag, whereas the same location becomes beneficial at higher incidences. The large relative improvements at $\alpha = 16^\circ$ partly reflect baseline deterioration; controlled L/D remains below its maximum at lower incidence. Thus, $x/c = 0.25$ generally favours aerody-

namic efficiency, whereas $x/c = 0.65$ favours lift augmentation under the tested conditions. Improvements in L/D do not establish a net energy benefit because actuator power consumption is not included.

These gains are achieved with a single 3 mm slot on a 609 mm-chord airfoil, corresponding to $h/c \approx 0.0049$ (0.49%), demonstrating the promise of localised actuation.

5 Conclusions

Two-dimensional URANS simulations using the GEKO turbulence model demonstrate promising aerodynamic improvements through synthetic jet actuation on the NLF(1)-0416 airfoil. Actuator placement produces a trade-off between lift enhancement and aerodynamic efficiency. At $\alpha = 16°$, actuation at $x/c = 0.65$ increases lift by 67.0%, while $x/c = 0.25$ provides the largest drag reduction of 51.3% and an L/D improvement of 191.6%. These gains are achieved with a single 3 mm slot, approximately 0.49% of the airfoil chord. The controlled stall angle remains undetermined within the investigated incidence range.

Future work should examine different injection angles, actuation amplitudes, and frequencies, and extend the angle-of-attack range to identify the controlled stall onset. Three-dimensional simulations should assess spanwise flow effects and finite-span actuator configurations, supported by experimental validation and evaluation of actuation power requirements.

Acknowledgements

This work was supported by Middle East Technical University, Northern Cyprus Campus, under project through the Scientific Research Project FEN-25-D-15.
The author thanks Felix J. Friese and Nigel J. Kerr for their contributions to the computational framework.

References

[1] A. Glezer, M. Amitay, Synthetic jets, Annual Review of Fluid Mechanics **34**, 503 (2002).

[2] B. Gungordu, M. Jabbal, A.A. Popov, Enhancing jet velocity and power conversion efficiency of piezoelectric synthetic jet actuators, AIAA Journal **61**, 4321 (2023).

[3] B. Gungordu, M. Jabbal, A.A. Popov, Experimental performance comparison of unimorph- and bimorph-driven synthetic jet actuators, AIAA Journal **00**, 1 (2026).

[4] D. You, P. Moin, Active control of flow separation over an airfoil using synthetic jets, Journal of Fluids and Structures **24**, 1349 (2008).

[5] Q. Sun, F. Bahri, M. Jabbal, W. Stryczniewicz, R. Jefferson-Loveday, B. Stefes, A. Büscher, Suppression of flow separation of a high-lift wing with active flow control, Aerospace Science and Technology **159**, 110017 (2025).

[6] R. Djeddi, K. Ekici, Natural laminar flow airfoil design via adjoint-based transition onset delay, Aerospace Science and Technology **145**, 108854 (2024).

[7] S. Wang, Z. Guo, Robust optimization of natural laminar flow airfoil based on random surface contamination, Applied Sciences **12**, 8757 (2022).

[8] ANSYS, Inc., Transition SST model (4-equation) theory guide, ANSYS, Inc. (2024), aNSYS Fluent Documentation, Release 2024 R2

[9] D.M. Somers, NASA Technical Paper 1861, NASA Langley Research Center, Hampton, VA (1981), https://ntrs.nasa.gov/citations/19810015487

Multiple flow states in a turbine tip-section cascade with supersonic inlet flow

Jindřich Hála[1,*], *Pavel* Psota[2], and *David* Šimurda[1]

[1]Institute of Thermomechanics, Czech Academy of Sciences, Prague, Czech Republic
[2]Faculty of Mechatronics, Informatics and Interdisciplinary Studies, Technical University of Liberec, Czech Republic

Abstract. Steady two-dimensional RANS computations of the TR-U-9 turbine tip-section cascade are performed using a coupled LU-SGS solver implemented in OpenFOAM. Opposing inlet-angle sweeps, initialised from unstarted and started fields, reveal hysteresis: the transitions occur at different prescribed angles, leaving an interval of history-dependent solutions. The off-design target inlet Mach number of approximately 1.4 is reached along the started branch but bypassed by the jump from the unstarted branch. The reverse sweep extends earlier observations of a discontinuous angle–Mach-number relation in a similar cascade. Complementary two-wavelength interferometry measurements show substantial inlet-shock motion, which has not been established as repeated switching between the computed states.

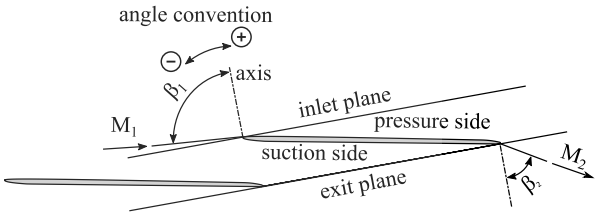
1 Introduction

The present investigation arose from difficulties in reproducing a measured flow regime in the TR-U-9 turbine tip-section cascade. An off-design condition with an inlet Mach number of approximately 1.4 was selected to test two-wavelength interferometry (TWI) in a flow containing multiple shock waves. Steady CFD computations were subsequently undertaken to complement the measurements. However, adjusting the prescribed inlet angle from an unstarted solution did not recover the target Mach number: the solution instead jumped to a substantially higher value.

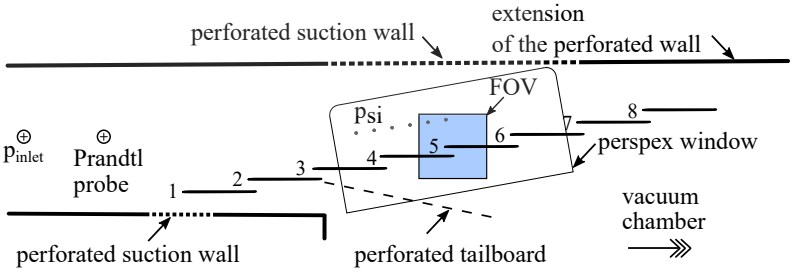
The target inlet Mach number was obtained numerically by starting from an established started solution and varying the angle in the reverse direction. This dependence on the initial field motivated a systematic study of both continuation histories. The resulting hysteresis, rather than the original application of TWI, is the main subject of this paper.

A subsequent review of earlier work identified a similar difficulty in the TR-U-8 cascade, a related nearly flat profile design. Musil et al. [2] reported a discontinuous angle–Mach-number relation and used $M_1 = 1.135$ against a nominal target of 1.2. Their published study did not identify reverse continuation from a started field as a means of reaching intermediate states. Together with earlier supersonic tip-section investigations [1] and cascade-starting studies [3], this provides context for the present results. The opposing TR-U-9 sweeps are examined alongside TWI observations of inlet-shock motion, without assuming that the experimental motion represents starting/unstarting cycles.

*e-mail: hala@it.cas.cz



(a) Profile and flow angles



(b) Measurement arrangement

Figure 1. TR-U-9 cascade geometry and measurement arrangement. Inlet and outlet flow angles are denoted by β_1 and β_2.

2 Cascade and operating conditions

The TR-U-9 cascade represents a nearly flat tip section of a steam-turbine rotor blade. Its chord is $c = 150$ mm, span 160 mm and pitch $s = 141$ mm ($s/c = 0.94$). The stagger angle is 78.8° and the design inlet flow angle is −79.92°. The design inlet Mach number is $M_1 = 0.8$, with design outlet Mach numbers of 1.6 or 1.8 depending on the application and available condenser vacuum. The present supersonic inlet regime, $M_1 \simeq 1.4$, was selected to provide a shock-rich flow field for testing TWI, rather than to reproduce a design operating point. The CFD outlet condition corresponds to $M_{2\mathrm{is}} = 1.6$.

Experiments use the intermittent in-draft wind tunnel at the Institute of Thermomechanics in Nový Knín. Its test section accommodates eight prismatic blades with small flow turning. Perforated upper and lower inlet-channel walls connect to a suction system for boundary-layer control. An adjustable perforated tailboard downstream of blade 2 allows the outlet flow to be adjusted. Figure 1 shows this arrangement and the optical field of view; the CFD model represents one periodic passage.

The prescribed inlet flow angle is denoted by β_1. In the experiment, the inlet Mach number is then evaluated using six pressure taps (p_{si}) at the sidewall and total pressure reading from the inlet Prandtl probe.

3 Numerical and experimental methods

3.1 Flow solver and boundary conditions

The computations solve the steady, two-dimensional compressible Reynolds-averaged Navier–Stokes equations with the coupled matrix-free LU-SGS solver implemented in OpenFOAM [6]. Turbulence and transition are represented by the SST model coupled with the

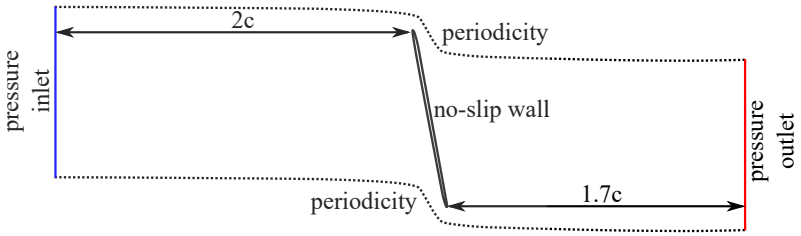


Figure 2. Periodic computational domain and boundary conditions. The inlet and outlet are located $2c$ upstream and $1.7c$ downstream, respectively.

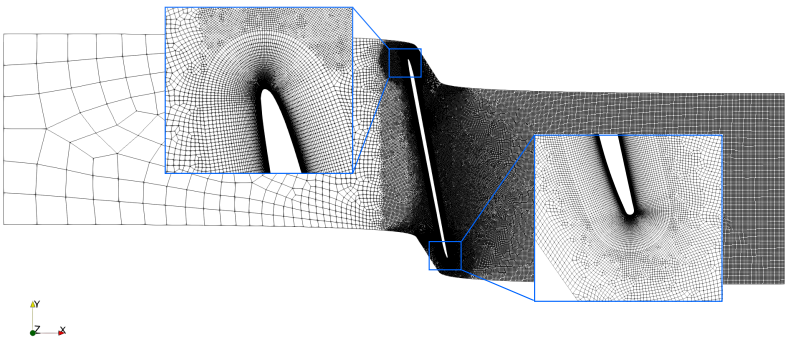


Figure 3. Computational mesh with leading- and trailing-edge details. The inlet region is coarsened, while near-wall refinement maintains $y^+ < 1$. The mesh contains approximately 130 000 cells.

γ–$Re_{\theta t}$ transition model [8]. The working fluid is a calorically perfect ideal gas with viscosity described by Sutherland's law. Spatial discretisation is nominally second order, using linear-upwind reconstruction with Venkatakrishnan-limited least-squares gradients for pressure, velocity and temperature.

The pressure inlet prescribes $p_0 = 10^5$ Pa, $T_0 = 288.15$ K and flow angle β_1. The prescribed turbulence intensity is 3%, decreasing to approximately 1.5% near the cascade inlet. The outlet imposes a mean static pressure corresponding to $M_{2\mathrm{is}} = 1.6$. Lateral boundaries are periodic and the blade surface is adiabatic and no-slip (Fig. 2).

The mesh was generated in Gmsh and contains approximately 130 000 cells. The near-wall region is refined to maintain $y^+ < 1$. The inlet is located $2c = 300$ mm upstream, and the outlet $1.7c = 255$ mm downstream. The mesh is deliberately coarsened towards the inlet to damp the upstream shock system numerically and reduce artificial shock reflections from the inlet boundary.

A two-dimensional periodic model was chosen as an initial approach to examine the dependence of the computed flow state on continuation history at a manageable computational cost. The experimental flow under supersonic inlet conditions is strongly three-dimensional, and the present model is therefore not intended to reproduce the measured flow field quantitatively.

3.2 Continuation procedure and convergence

Each angle run is initialised from the preceding solution. The unstarted seed is continued towards more negative angles, and the started seed towards less negative angles (Fig. 4). Both sweeps exhibit an abrupt Mach-number change.

The nominal angle increment is approximately 0.05°, reduced to approximately 0.01° near each transition.

Convergence is assessed from residuals and monitored flow quantities. Steady continuation is not a time-accurate calculation and does not establish dynamic stability.

3.3 Two-wavelength interferometry

A fibre-optic Mach–Zehnder arrangement records both wavelength channels simultaneously at 30 kHz (frame interval 33.3 μs), with distinct spatial carriers allowing Fourier separation. The processing follows the approach described by Psota et al. [4]; related applications to cascade flow are reported in Ref. [5]. The processing implementation is described in Ref. [7].

The laser sources operate at 550 and 660 nm, giving the synthetic wavelength $\Lambda = \lambda_1\lambda_2/|\lambda_2 - \lambda_1| = 3.3\ \mu$m. After spectral filtering and inverse transformation, the phases are referred to a no-flow reference. Their wrapped difference provides a synthetic phase with an extended unambiguous range. This information is used to determine the fringe order of the measurement-wavelength phase.

For a consistent object-minus-reference phase convention, the phase difference is related to density through

$$\Delta\phi_\lambda(x, y) = \frac{2\pi K_\lambda}{\lambda} \int_0^L [\rho(x, y, z) - \rho_{\mathrm{ref}}(x, y, z)]\, \mathrm{d}z, \tag{1}$$

where K_λ is the Gladstone–Dale coefficient and L is the optical path through the flow. The measurement is line-integrated; a local density interpretation assumes spanwise uniformity. Spectral filtering and fringe-order errors require attention near shocks.

4 Results and discussion

4.1 Hysteresis in the inlet-angle sweeps

Figure 4 shows the computed inlet Mach number as a function of prescribed inlet angle. The two continuation histories follow distinct branches over a finite angle interval. On the sweep initiated from the unstarted field, M_1 rises gradually as the angle becomes more negative, before jumping from approximately 1.08 to 1.90 near $\beta_1 = -80.29°$. The sweep initiated from the started field follows the upper branch towards less negative angles and reaches approximately $M_1 = 1.33$ before dropping to approximately 0.89 near $\beta_1 = -80.01°$.

The estimated hysteresis width is 0.28°. The gray band ($M_1 \simeq 1.08$–1.33) marks the gap between traced branches, without excluding other solutions. Lines connecting the branches link successive runs; they are not resolved transition trajectories.

Within the overlap interval, near −80.10°, the plotted branches give approximately $M_1 = 1.54$ and 0.93. The target $M_1 = 1.4$ lies on the upper branch near −80.04° but is bypassed by the lower-branch jump. Reaching it therefore depends on continuation history.

The started/unstarted classification must be established from passage-flow topology, not solely from upstream M_1: the lower branch extends slightly above unity before the jump.

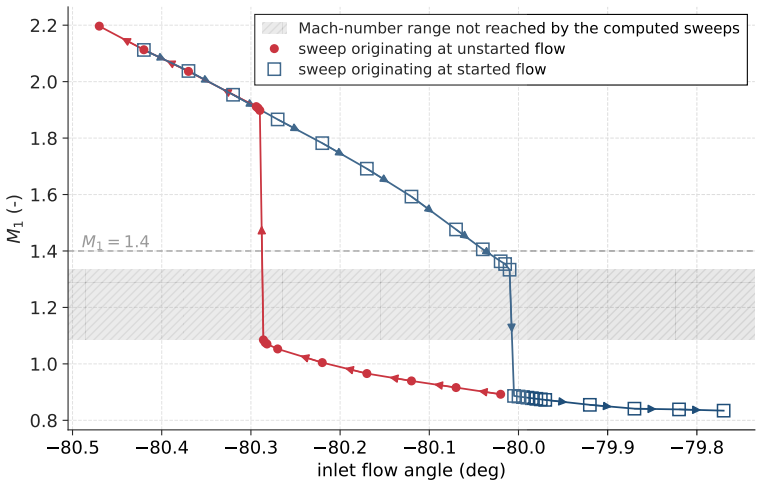
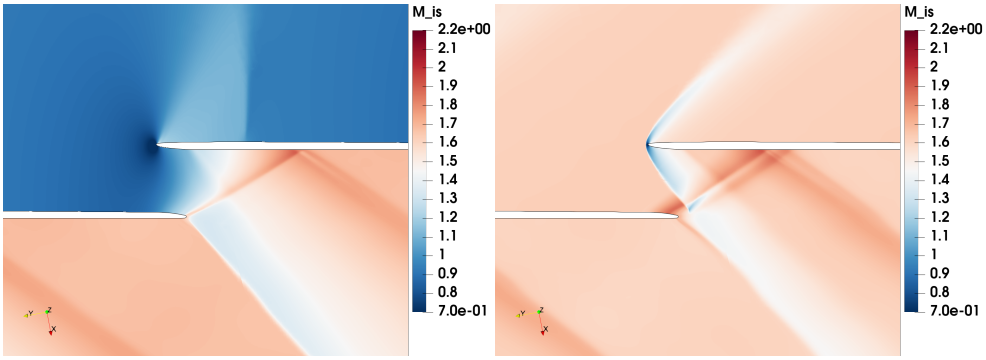


Figure 4. Inlet-angle sweeps initialised from unstarted (red filled symbols) and started (blue open symbols) flow. Arrows indicate continuation direction; colours identify sweep history, including after a transition. The horizontal gray band marks the approximate Mach-number gap not reached by either computed sweep. The dashed line marks $M_1 = 1.4$.



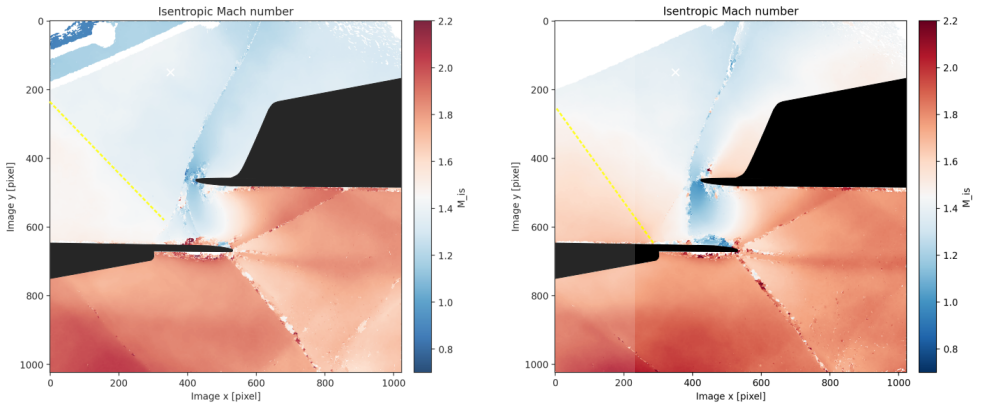
(a) Unstarted solution ($M_1 = 0.94$) (b) Started solution ($M_1 = 1.593$)

Figure 5. Isentropic Mach number contours showing configurations on the two branches at identical prescribed conditions $\beta_1 = -80.12°$.

4.2 Flow structures and relation to earlier computations

Figure 5 compares the flow fields obtained from the two continuation histories at identical prescribed boundary conditions within the overlap interval.

Figure 5(a) shows the unstarted regime, with subsonic inlet flow and supersonic outlet flow. A small supersonic region is present near the leading edge on the pressure side (the upper side in the figure). In contrast, Figure 5(b) shows the started regime, with supersonic inlet flow and a leading-edge shock whose inner branch extends well into the interblade passage.



(a) (b)

Figure 6. Isentropic Mach number distributions reconstructed from TWI measurements for two extreme positions of the inlet shock: (a) farther upstream and (b) farther into the interblade passage. The black regions mask the blades and their holders while the white regions represents invalid reconstruction regions. The yellow dashed line highlights the parasitic shock.

The reverse sweep extends the discontinuous relation reported for TR-U-8 [2] by retaining intermediate Mach numbers on the started branch. Different geometries, operating conditions and angle conventions preclude direct comparison of transition angles.

Endwall flow is not required for the computed loop, but may affect the experiment. Identifying the starting mechanism requires examination of shock topology and passage-flow constraints, alongside numerical sensitivity [3].

4.3 Experimental inlet-shock motion

The TWI measurements were processed to obtain isentropic Mach number distributions. Assuming spanwise uniformity, the phase–density relation in Eq. (1) gives

$$\rho(x,y) = \rho_* + \frac{\lambda}{2\pi K L}\left[\Delta\phi(x,y) - \Delta\phi(x_*,y_*)\right], \tag{2}$$

where ρ_* is the known static density at the reference point (x_*, y_*), λ is the wavelength used for the density reconstruction, K is the corresponding Gladstone–Dale constant, and L is the optical path length through the flow. Here, $\Delta\phi$ denotes the unwrapped flow-induced phase shift, with its sign defined consistently with Eq. (1).

Following the density-based reconstruction used in Ref. [7], the resulting density field is converted into an isentropic Mach number distribution using

$$M_{\mathrm{is}}(x,y) = \sqrt{\frac{2}{\gamma-1}\left[\left(\frac{\rho_0}{\rho(x,y)}\right)^{\gamma-1} - 1\right]}, \tag{3}$$

where γ is the specific heat ratio and $\rho_0 = p_0/(RT_0)$ is the inlet stagnation density, with R denoting the specific gas constant. The stagnation density ρ_0 is distinct from the reference static density ρ_*. Because this reconstruction uses the inlet stagnation state, M_{is} need not equal the local Mach number in regions affected by losses.

Because the experimental flow is three-dimensional, the reconstructed density represents an optical-path average. The resulting M_{is} is therefore an equivalent quantity derived from that averaged density, rather than a local midspan Mach number.

The reconstructed fields reveal substantial displacement of the inlet shock, although a correspondence between this motion and switching between the computed branches has not been established. Figure 6 shows two extreme configurations of the shock structure. A weak parasitic shock, marked by the yellow dashed line, most likely originates from the upper tunnel wall. In the recorded sequence, this shock interacts with the inlet shock, moving upstream and downstream and eventually merging with it.

The mechanism driving the observed motion requires further investigation. Oscillations of the parasitic shock may contribute to the inlet-shock displacement. If this interaction is driven by the tunnel wall, it cannot be reproduced directly in the idealised computational domain with periodic boundaries, which excludes the tunnel walls.

The numerical and experimental results address complementary aspects of the cascade flow. The two-dimensional computations demonstrate hysteresis under opposing inlet-angle sweeps, whereas TWI records substantial inlet-shock motion in the three-dimensional experimental flow. A direct correspondence between the computed branches and the observed configurations is therefore not claimed. In particular, the recorded shock motion does not by itself establish experimental hysteresis or repeated switching between the computed states. Three-dimensional simulations incorporating the relevant wind-tunnel geometry would be a natural next step towards investigating the connection between these observations.

5 Conclusions

Opposing inlet-angle sweeps reveal hysteresis in steady two-dimensional computations of the TR-U-9 turbine tip-section cascade. The target $M_1 \simeq 1.4$, bypassed when approaching from the unstarted branch, is accessible along the started branch. This extends earlier observations of a discontinuous angle–Mach-number relation. TWI shows substantial inlet-shock motion, but the present evidence does not establish experimental starting/unstarting cycles or dynamic stability of the computed branches. The computed branches coexist over an estimated inlet-angle interval of approximately 0.28°.

Acknowledgements

This work was supported by the Czech Science Foundation under Grant 24-11973S. Institutional support RVO 61388998 is also gratefully acknowledged.

References

[1] M. Luxa, J. Příhoda, D. Šimurda, P. Straka, J. Synáč, Investigation of the compressible flow through the tip-section turbine blade cascade with supersonic inlet. Journal of Thermal Science **25**, 138–144 (2016). https://doi.org/10.1007/s11630-016-0844-0

[2] J. Musil, J. Příhoda, J. Fürst, Numerical simulations of the 2D supersonic flow through the tip-section turbine blade cascade with a flat profile. Applied and Computational Mechanics **15**, 175–184 (2021). https://doi.org/10.24132/acm.2021.621

[3] N. Mushtaq, P. Gaetani, Understanding and modeling unstarting phenomena in a supersonic inlet cascade. Physics of Fluids **35**, 106101 (2023). https://doi.org/10.1063/5.0160706

[4] P. Psota, G. Çubreli, D. Šimurda, P. Šidlof, J. Kredba, M. Stašík, V. Lédl, Noise-resistant two-wavelength interferometry for single-shot measurement of high-gradient flows. Optics and Lasers in Engineering **164**, 107505 (2023). https://doi.org/10.1016/j.optlaseng.2023.107505

[5] D. Šimurda, P. Psota, P. Šidlof, R. Kielb, M. Luxa, J. Hála, J. Lepicovsky, Optical measurement and visualization of transonic airflow in a compressor blade cascade. Journal of Visualization **26**, 529–549 (2023). https://doi.org/10.1007/s12650-022-00901-3

[6] J. Fürst, Development of a coupled matrix-free LU-SGS solver for turbulent compressible flows. Computers & Fluids **172**, 332–339 (2018). https://doi.org/10.1016/j.compfluid.2018.04.020

[7] J. Hála, P. Psota, D. Šimurda, J. Lepicovsky, Experimental Visualization of Unsteady Flow in a Transonic Oscillating-Blade Compressor Cascade Using High-Speed Two-Wavelength Interferometry. Metrology **6**(2), 41 (2026). https://doi.org/10.3390/metrology6020041

[8] R. B. Langtry, F. R. Menter, Correlation-based transition modeling for unstructured parallelized computational fluid dynamics codes. AIAA Journal **47**, 2894–2906 (2009). https://doi.org/10.2514/1.42362

Mathematical models for forecasting photovoltaic power output

Jakub Hampejs[1], *Martin* Kozelka[1], *Václav* Beránek[1] and *Martin* Libra[1*]

[1]Department of Mathematics and Physics, Czech University of Life Sciences Prague, Kamýcká 129, 165 21 Prague 6, Czech Republic

Abstract. Adding meteorological forecasts to a neural prediction model reduced its average normalized mean absolute error (nMAE) from 11.26% to 6.31% across the forecast horizon of 24 hours. This comparison used operational records from a photovoltaic installation with a rated capacity of 1,293 kWp in Kunžak, Czech Republic. Hourly observations spanning 2020 to 2025 were supplemented with MeteoSource forecasts, calculated solar geometry and variables describing daily and seasonal cycles. Five modelling approaches were examined: historical averages, two physical formulations and two networks that combined convolutional processing with recurrent LSTM layers. An incidence angle correction improved the physical model, lowering its normalized error from 7.60% to 6.60%, compared with 12.48% for historical averages. Training used 80% of the dataset; the remaining 3,907 records formed the test set. Evaluation included only intervals with positive measured output. The network incorporating weather forecasts achieved a mean absolute error of 81.70 kW and an R^2 of 0.84. Its normalized error increased from 6.05% at hour one to 6.88% at hour 24. Feature attribution linked predictions primarily to global irradiance and previous output, with future weather inputs gaining influence over longer horizons. Rapid cloud changes remained challenging, suggesting that more accurate meteorological inputs could further improve predictions.

1 Introduction

Renewable energy sources (RES) are becoming an increasingly important component of energy systems, driven primarily by efforts to reduce CO_2 emissions and diversify energy supplies. According to the International Energy Agency's Renewables 2025 report, global renewable power capacity is projected to increase by almost 4 600 GW between 2025 and 2030, roughly double the deployment seen in 2019–2024. Solar photovoltaic (PV) technologies are expected to account for nearly 80 % of this growth, highlighting the rapid expansion of solar capacity worldwide [1]. The growing penetration of PV systems introduces significant challenges for power system operation. PV output is inherently variable and strongly dependent on weather conditions, complicating grid integration, energy trading, and operational planning. Accurate short-term forecasting of PV power production is therefore crucial [2].

Several AI-based methods for energy forecasting have been proposed [3–10]. However, methodologies to assess the actual energy performance of existing PV installations remain limited. In Central Europe, PV deployment is accelerating alongside rising energy prices. In the Czech Republic, approximately 150,000 small PV systems (≈10 kWp) were installed on residential buildings by early 2025, with a total of around 170,000 PV installations and an aggregated nominal output of 3,900 MWp. Agrovoltaic systems, enabling dual land use, are also gaining importance due to sustainability considerations [11, 12].

PV power plants offer advantages such as relatively simple installation, low maintenance, and minimal overhead. Their main drawbacks are low installed power density and variability of output, largely dependent on weather conditions. Rare events like solar eclipses can also significantly affect production [13]. Accurate forecasting, leveraging weather predictions, allows operators to optimize financial returns in markets where electricity prices are dynamic and updated every 15 minutes.

Short-term PV power forecasting has been addressed in several studies. Wang et al. [3, 4] examined one-day-ahead predictions. Sadowska et al. [5] validated a real-world PV energy model for a 1 MWp farm in Poland, with a production error of 15–16 %. Su et al. [6] applied neural networks for ultra-short-term predictions, achieving similar accuracy. Wang et al. [14] compared convolutional neural networks (CNN) and long short-term memory (LSTM) networks, demonstrating that a hybrid CNN–LSTM approach yielded the best predictive performance.

2 Problem formulation

The prediction model was created for a photovoltaic power plant located in the village of Kunžak in the Czech Republic (Fig. 1). It has a nominal output of 1,293

* Corresponding author: libra@tf.czu.cz

kWp. It consists of 5,625 photovoltaic panels. Each panel has a nominal output of 230 Wp with a permissible tolerance of ±5%. The panels had an initial efficiency of 14.1% at the time of installation (2010).

The dataset covers hourly measurements of aggregated PV power output and panel temperature from 2020 to 2025. It was subsequently extended with additional meteorological variables obtained from numerical weather models provided by MeteoSource. The MAE of global solar radiation for the study area is approximately 36 W/m². Further variables included atmospheric pressure, air humidity, wind speed and direction at 10 m, cloud cover, precipitation, dew point, ozone concentration, PM10, and ambient temperature. Additional features were computed using the pvlib library, including the sun's zenith, sun's azimuth and solar elevation. Temporal features capturing daily and seasonal cycles (sin_hour, cos_hour, sin_day_of_year, cos_day_of_year) were included, along with wind components (wind_u, wind_v) derived from wind speed and direction to represent east-west and north-south flow. Extensive preprocessing was performed, including correlation analysis, Yeo-Johnson transformation, standardization, and Min-Max scaling. Experiments confirmed that the combination of these features contributed most to model accuracy.

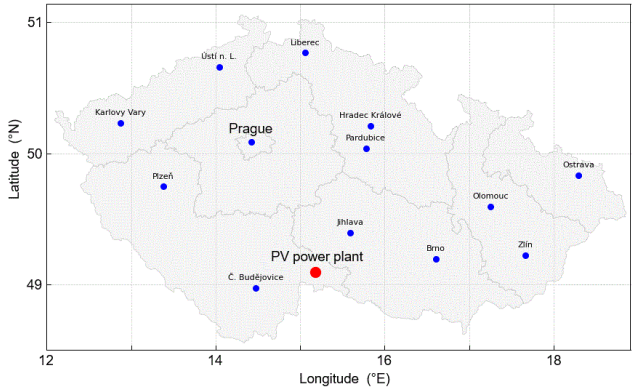


Fig. 1. Location of the PV power plant.

Fig. 2 shows the linear correlation of the resulting features used for the model that contribute most to the output power of the PV power plant.

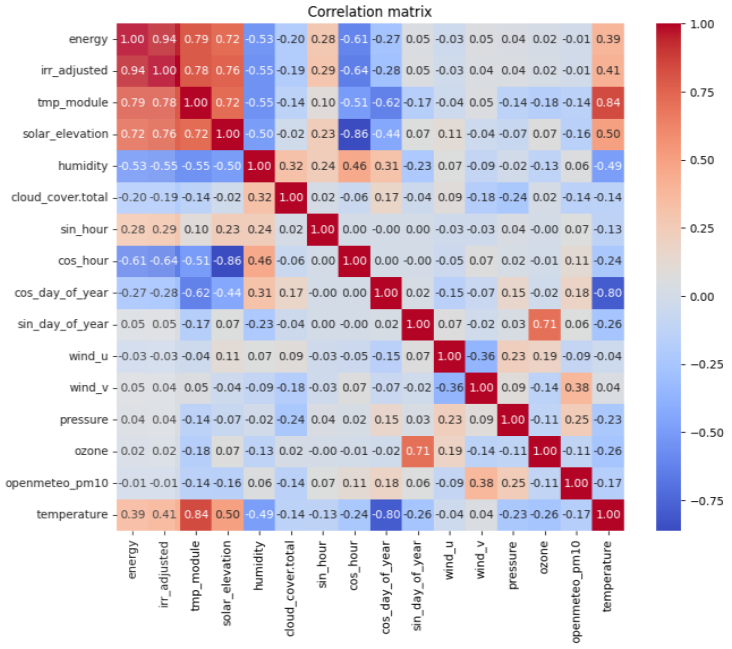


Fig. 2. Correlation matrix.

Subsequently, the dataset was split into a training set (80%) and a testing set (20%), with the testing set containing 3,907 records. All performance metrics were computed only for time steps with positive power output (y_true > 0).

2.1 Model based on historical averages of power for each hour and day of the year

The baseline model predicts the PV output power using historical averages for each specific hour and day of the year, without considering current meteorological conditions. This approach provides a basic level of prediction. The evaluation metrics of this model are summarized in Table 1.

The model shows relatively high errors: the normalized mean absolute error (nMAE) reaches 12.48 %, the mean absolute error (MAE) is 161.41 kW, and the mean bias error (MBE) is -9.65 kW, indicating a slight systematic underestimation. The coefficient of determination (R^2) is 0.51, reflecting a limited ability of the model to capture the variability of the actual PV power output. Finally, the mean absolute percentage error (MAPE) reaches 159 %. These results indicate that, while the baseline model provides a rough approximation, incorporating meteorological variables is necessary to improve prediction accuracy.

Table 1. Error metrics for the historical average prediction model.

Metrics	Value
nMAE [%]	12.48
MAE [kW]	161.41
MBE [kW]	-9.65
R^2 [-]	0.51
MAPE [%]	159

Fig. 3 compares the predicted and actual PV power output for the first 200 hours of the test data, illustrating the baseline model's limited ability to capture short-term fluctuations.

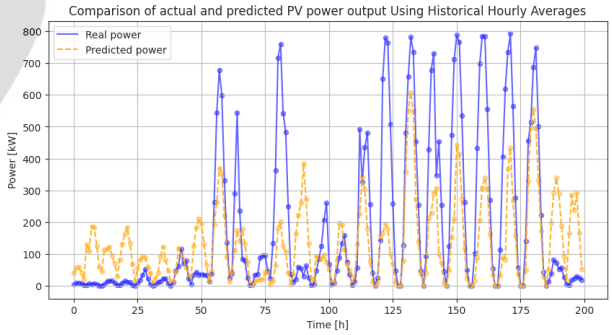


Fig. 3. Comparison of actual and predicted PV output Using Historical Hourly Averages.

2.2 Physical model using the basic formula for calculating the power of a PV panel

For the reference physical model, Eq. (1) was used to calculate the predicted output power of the PV power plant. Based on this equation, predicted power values for individual hours were determined. The panel inclination angle β was set to 35°, corresponding to the actual tilt of the PV panels.

$$P_{\text{theor}} = E_{\text{total}} \cdot \eta \cdot S \cdot \cos(\beta) \quad (1)$$

P_{theor} is the output power of the PV panel (W),
E_{total} is the total solar radiation (W/m²) perpendicularly on the earth's surface,
η is the efficiency of the PV panel (-),
S is the area of the PV panel (m²),
β is the angle of inclination of the PV panel to the horizon (°).

The evaluation metrics of this model are summarized in Table 2. The model shows a normalized mean absolute error (nMAE) of 7.60 %, a mean absolute error (MAE) of 98.35 kW, and a mean bias error (MBE) of -59.73 kW, indicating a systematic underestimation of output power. The coefficient of determination (R^2) is 0.80, showing that the model captures a significant portion of the variability of actual power, while the mean absolute percentage error (MAPE) is 77.30 %. Overall, this simple physical model provides a relatively accurate approximation of PV output compared to the model based on historical averages of power for each hour and day of the year.

Table 2. Error metrics for Physical model.

Metrics	Value
nMAE [%]	7.60
MAE [kW]	98.35
MBE [kW]	-59.73
R^2 [-]	0.80
MAPE [%]	77.30

Fig. 4 shows the comparison between the predicted and actual PV power output for the first 200 hours of the test dataset. The model captures general trends, but significant deviations remain, reflecting its simplified assumptions.

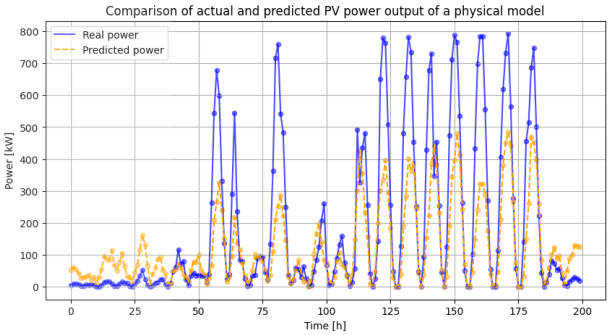


Fig. 4. Comparison of actual and Predicted PV power output of a physical model.

2.3 Physical model with IAM correction obtained using the pvlib library

The baseline physical model for PV power output was improved using the Incidence Angle Modifier (IAM) via the pvlib library to better account for actual solar radiation conditions. Unlike the previous model, which assumed a fixed panel tilt, the IAM correction considers the dynamic angle of incidence (AOI) between the panel surface normal and incoming solar radiation, calculated using the ASHRAE physical model along with the sun's azimuth and zenith angles. This approach captures variations in incident radiation and losses due to panel reflectivity, leading to more accurate power estimates. As shown in Table 3, the IAM-enhanced model demonstrates improved performance: the normalized mean absolute error (nMAE) is 6.6 %, MAE is 85.43 kW, MBE is -10.45 kW, R^2 is 0.85, and MAPE is 82.32 %. The model more closely tracks peak output, reducing systematic underestimation compared to the simpler physical model.

Table 3. Error metrics for the Physical model with IAM correction.

Metrics	Value
nMAE [%]	6.6
MAE [kW]	85.43
MBE [kW]	-10.45
R^2 [-]	0.85
MAPE [%]	82.32

Fig. 5 shows the comparison between the predicted and actual PV power output for the first 200 hours of the test dataset. Although the IAM correction improves the prediction, the model still fails to fully capture the peak values, which is partly due to unmodeled system losses and panel degradation.

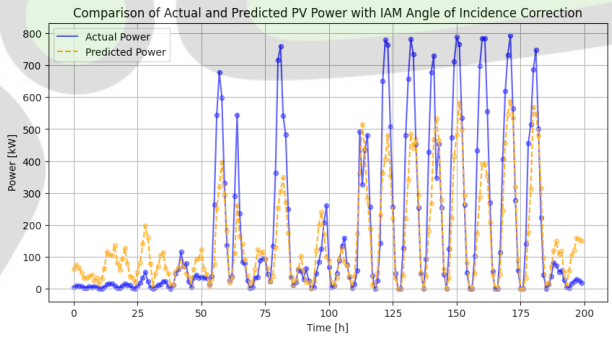


Fig. 5. Comparison of actual and predicted PV power with IAM correction.

2.4 Neural network-based model using only historical data

Many experiments were performed with different input features and model architectures. To ensure replicability, the same random seed was used for weight initialization in all experiments.

The most promising architecture combines a convolutional layer with an LSTM, capturing both short-term patterns and long-term dependencies. The convolutional layer extracts local correlations, while the LSTM layer models seasonal cycles.

The input tensor has dimensions of 24 time steps × 15 features, including historical PV power and meteorological measurements (global radiation, solar elevation, panel temperature, humidity, cloud cover, wind_u, wind_v, PM10, ozone, surface pressure), as well as time-related variables (sin and cos of the hour and day of the year). The architecture of this model is shown in Fig. 6.

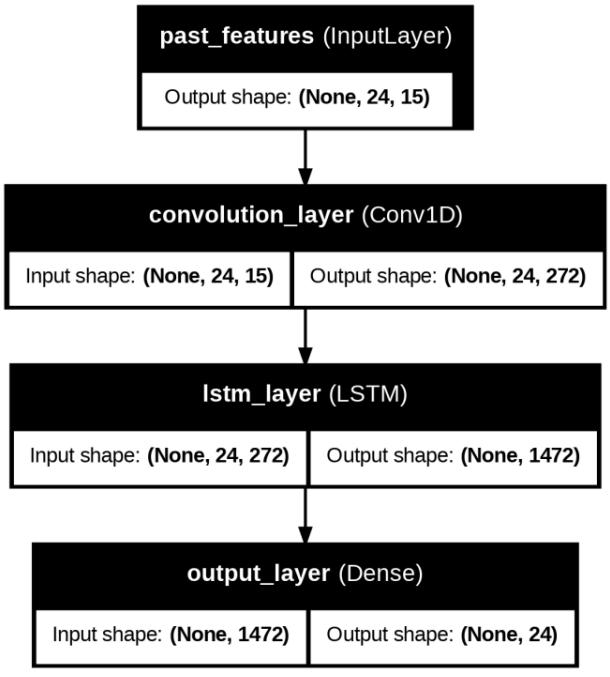


Fig. 6. Architecture of the neural network model using only historical data.

Keras Tuner with Bayesian optimization was used for hyperparameter selection. The optimized model includes a convolutional layer with 96 filters (kernel size 2, ReLU, same padding) and an LSTM layer with 2816 units and 10 % recurrent dropout. The Dense output layer predicts 24 hours ahead with a linear activation. The model was trained using the ADAM optimizer with MAE as the loss function, a learning rate of 0.0005, and a batch size of 64.

Fig. 7 shows the loss curves, where the validation curve gradually converges to the training curve, indicating that the model does not overfit. The fluctuations in the validation curve result from the use of a expanding window learning strategy.

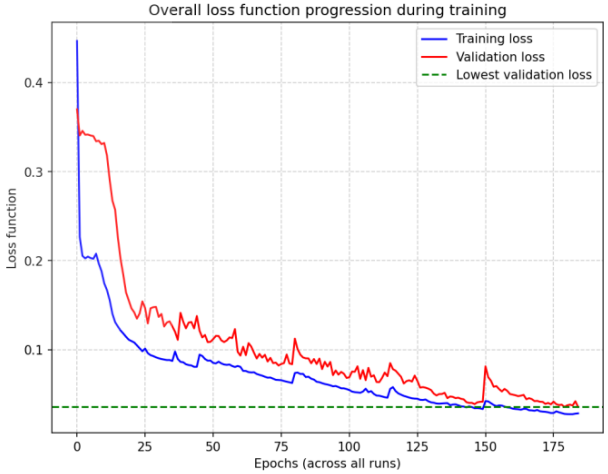


Fig. 7. Training and validation loss for the neural network model using only historical data.

The model achieves high accuracy, as summarized in Table 4. Normalized mean absolute error (nMAE) ranges from 7.11 % to 13.87 %, MAE from 92 kW to 179 kW, and the mean bias error (MBE) remains low, indicating minimal systematic deviation. The coefficient of determination R^2 decreases with forecast horizon but remains above 0.3, showing that the model captures a substantial portion of PV power variability. Compared to previous models, the neural network demonstrates substantially improved prediction performance, especially in capturing dynamic changes in output power.

Table 4. Error metrics for the Neural-based model using only historic data.

Hour	nMAE [%]	MAE [kW]	MBE [kW]	R^2 [-]	MAPE [%]
1.	7.11	92.00	14.35	0.80	55.29
6.	10.32	133.53	11.26	0.60	104.09
12.	11.14	144.01	4.54	0.56	119.70
18.	12.36	159.92	20.05	0.46	137.59
24.	13.87	179.32	68.17	0.32	148.45

Fig. 8 shows the predicted and actual PV power output for the first hour of the forecast horizon, while Fig. 9 shows the prediction for the last hour (24th) of the horizon. It is noticeable that the prediction error increases with the forecast horizon, as the model lacks information about future meteorological conditions.

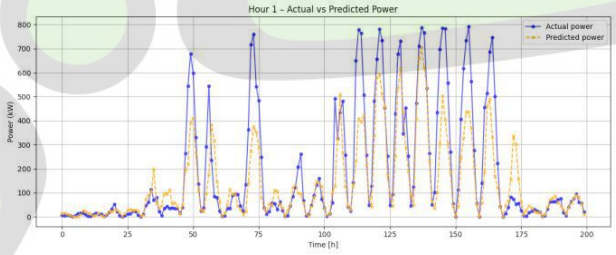


Fig. 8. Comparison of actual and predicted PV power for the first hour of the forecast horizon using the neural network model with historical data.

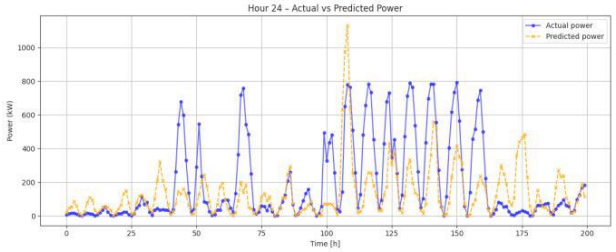


Fig. 9. Comparison of actual and predicted PV power for the last hour of the forecast horizon using the neural network model with historical data.

2.5 Model based on neural networks with the inclusion of weather forecasting

The final model incorporates both historical measurements and forecasted meteorological variables to improve short-term PV power predictions. A new branch was added to the model architecture to handle the predicted features, which expects a tensor of shape (24, 14) (see Fig. 10). This branch uses the same set of input features as the historical branch, with the exception of PV power, which is the target variable to be predicted.

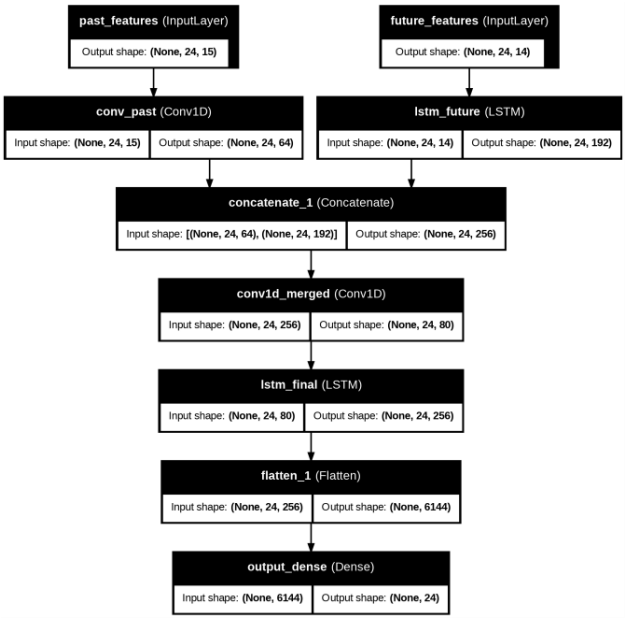


Fig. 10. Architecture of the neural network model using weather forecasting.

The validation loss curve again converges toward the training loss (Fig. 11), indicating that the model does not overfit.

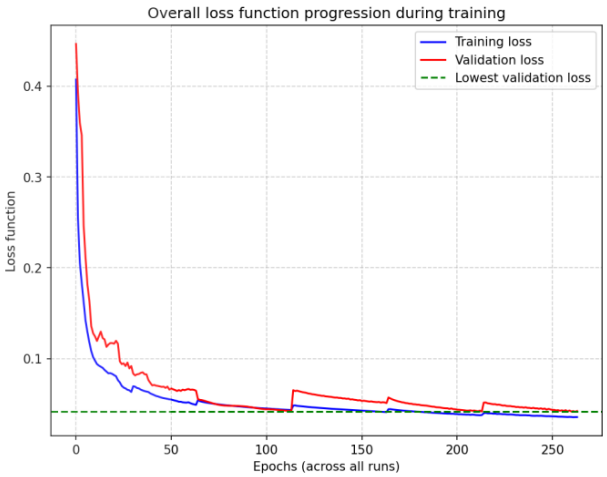


Fig. 11. Training and validation loss for the neural network model using weather forecasting.

The model achieves improved performance compared to the purely historical model, as summarized in Table 5. Prediction errors are lowest for the first hours of the forecast horizon (nMAE 6.05 %, MAE 78.25 kW, R^2 0.86 for hour 1) and slightly increase toward the 24th hour (nMAE 6.88 %, MAE 88.99 kW, R^2 0.82).

Table 5. Error metrics for the Neural-based model using weather forecasting.

Hour	nMAE [%]	MAE [kW]	MBE [kW]	R^2 [-]	MAPE [%]
1.	6.05	78.25	-3.00	0.86	47.31
6.	6.35	82.17	12.26	0.84	61.39
12.	6.30	81.58	-1.54	0.84	58.97
18.	6.27	81.07	1.81	0.84	59.50
24.	6.88	88.99	-4.2	0.82	61.61

Fig. 12 and Fig. 13 show the comparison between the predicted and actual PV power for the first and last hours of the forecast horizon. The largest inaccuracies occur on days with rapidly changing cloud cover, when the model struggles to capture sudden power fluctuations. Conversely, on clear-sky days, the model predictions align closely with actual measurements. Representative examples of an overcast day and a clear-sky day are shown in Fig. 14 and Fig. 15, respectively.

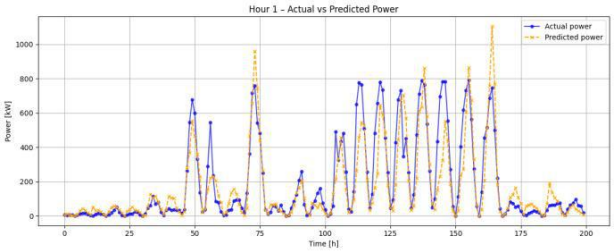


Fig. 12. Comparison of actual and predicted PV power for the first hour of the forecast horizon using the neural network model with weather forecasting.

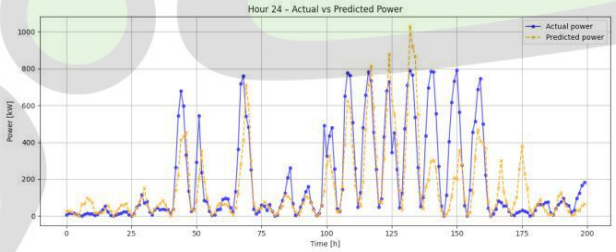


Fig. 13. Comparison of actual and predicted PV power for the last hour of the forecast horizon using the neural network model with weather forecasting.

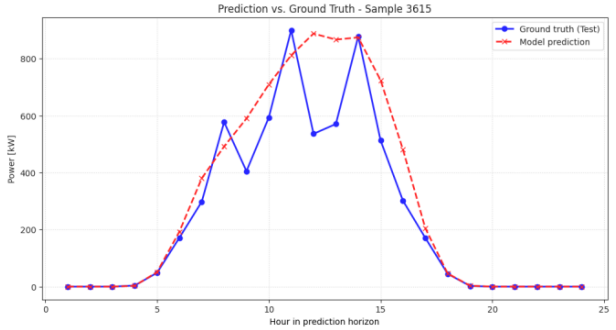


Fig. 14. Example of PV power prediction on a day with rapidly changing cloud cover, illustrating increased prediction errors caused by sudden irradiance fluctuations.

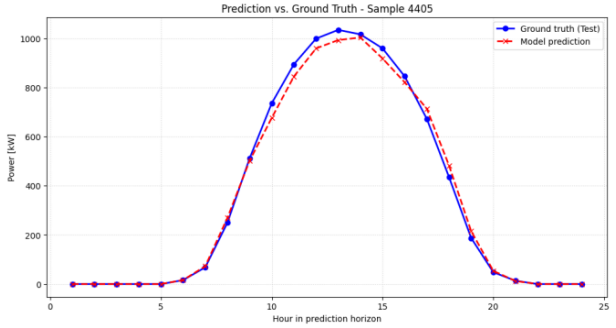


Fig. 15. Example of PV power prediction on a clear-sky day, showing close agreement between predicted and actual PV power output.

A SHAP analysis was performed on the first 100 input sequences to assess feature contributions to the model predictions. The analysis was carried out for the first forecasted hour (Fig. 16) and the last forecasted hour (24th hour) of the prediction horizon (Fig. 17). Historical input sequences (24 preceding time steps) are shown in blue, while forecasted meteorological sequences (24 predicted time steps) are shown in orange. The results show that global solar radiation and previous PV power values have the strongest influence on the predictions. With increasing forecast horizon, the importance of historical PV power decreases, whereas the contribution of forecasted meteorological variables—particularly global solar radiation—becomes more dominant, reflecting the growing dependence of the model on weather forecasts.

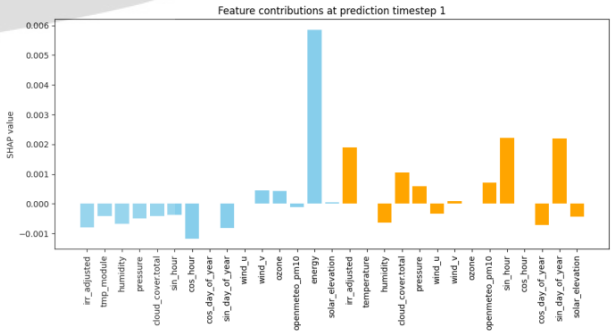


Fig. 16. SHAP feature importance for the first forecasted hour, showing contributions of historical (blue) and forecasted (orange) input features.

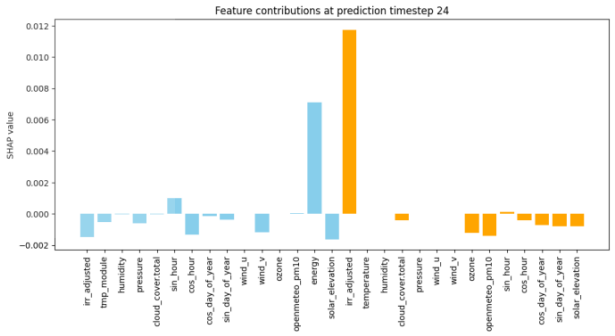


Fig. 17. SHAP feature importance for the 24th forecasted hour, highlighting the increasing influence of forecasted meteorological variables.

3 Problem solution

The performance of all developed models was evaluated using standard error metrics, summarized in Table 6. As expected, Model 1 (historical hourly averages) achieves the poorest results, with nMAE = 12.48 %, MAE = 161.41 kW, MBE = −9.7 kW, R^2 = 0.51, and MAPE = 159 %. This high error reflects the limited predictive power of purely climatological averages, which do not account for current meteorological conditions.

The physical model based on Eq. (1) (Model 2) improves prediction accuracy compared to historical averages; nMAE decreases to 7.60 %, MAE is 98.35 kW, MBE is −59.7 kW, and R^2 = 0.80. The notable negative bias indicates systematic underestimation of the output power.

Further improvement is achieved by the physical model incorporating the incidence angle modifier (IAM) (Model 3), which accounts for the actual angle of solar radiation incidence on the PV panels. This modification reduces systematic bias and improves overall accuracy, yielding nMAE = 6.60 %, MAE = 85.43 kW, MBE = −10.5 kW, R^2 = 0.85, and MAPE = 82.32 %.

Neural network–based models provide substantially better results. Model 4, trained solely on historical data (24-h horizon), achieves an average nMAE of 11.26 %, MAE of 145.61 kW, MBE of 9.0 kW, R^2 of 0.54, and MAPE of 116.95 % over the entire forecast horizon. The results indicate that, without forecasted meteorological inputs, the model's accuracy is limited for longer horizons.

The most accurate predictions are obtained with Model 5, which combines historical measurements with forecasted meteorological variables (24-h horizon), achieves an average nMAE of 6.31 %, MAE of 81.70 kW, MBE of 3.13 kW, R^2 of 0.84, and MAPE of 58.79 % over the entire forecast horizon, indicating a closer agreement between predicted and measured values.

Overall, these results confirm that neural networks, particularly when combined with weather forecasts, are the most suitable approach for short-term photovoltaic power prediction, while traditional methods, such as simple historical averages or basic physical models, exhibit significantly lower predictive performance.

Table 6. Overview of evaluation metrics for all models.

Model	Time horizon [h]	Avg. nMAE [%]	Avg. MAE [kW]	Avg. MBE [kW]	Avg. R^2 [-]	Avg. MAPE [%]
1.	-	12.48	161.41	-9.7	0.51	159
2.	1	7.60	98.35	-59.7	0.80	77.30
3.	1	6.60	85.43	-10.5	0.85	82.32
4.	24	11.26	145.61	9.0	0.54	116.95
5.	24	6.31	81.70	3.13	0.84	58.79

4 Conclusion

In this work, a mathematical model for short-term photovoltaic power prediction was developed and tested. The model combines convolutional (Conv1D) and LSTM layers, with the highest accuracy achieved by integrating forecasted meteorological variables. This model reaches an average nMAE of 6.31 %, MAE of 81.70 kW, and coefficient of determination $R^2 = 0.84$, demonstrating close agreement between predicted and actual values. The model was implemented in TensorFlow, trained in the Google Colaboratory environment.

Various approaches were compared, from simple historical averages through physical models to advanced neural networks with different input combinations. The results show that classical methods, which do not account for current meteorological conditions, perform significantly worse than machine learning–based models.

Further improvements could be achieved by using shorter prediction intervals (e.g., 15 minutes), combining physical and data-driven models in an ensemble approach, and employing more accurate meteorological inputs. Locally calibrated forecast data could also enhance performance, especially on days with rapidly changing cloud cover.

The obtained results have direct practical applications in operational planning and optimization of PV power plant output. High-quality short-term predictions also have economic implications, including more accurate estimation of spot electricity prices and improved planning of energy supplies to the distribution network.

Jakub Hampejs carried out all aspects of the research, including conceptualization, methodology, data collection, data analysis, model development, experiments, and manuscript preparation.
Martin Kozelka contributed to manuscript preparation, review, and editing, including revision of the abstract and adaptation of the manuscript to the conference template.
Martin Libra provided valuable advice and guidance throughout the research process.
Václav Beránek provided access to the photovoltaic power plant data used in the study.

References

1. IEA (2025). Renewables 2025: Analysis and forecasts to 2030. International Energy Agency. Available online: https://www.iea.org/reports/renewables-2025 (accessed on 18 December 2025).
2. M. Castillo-Cagigal, E. Matallanas, et al., Improving photovoltaics grid integration through short time forecasting and self-consumption. Appl. Energy **125**, 103-113 (2014). https://doi.org/10.1016/j.apenergy.2014.03.045
3. Y. Wang, W. Fu, J. Wang, Z. Zhen, F. Wang, Ultra-short-term distributed PV power forecasting for virtual power plant considering data-scarce scenarios. Appl. Energy **373**, 123890 (2024). https://doi.org/10.1016/j.apenergy.2024.123890
4. K. Wang, X. Qi, H. Liu, A comparison of day-ahead photovoltaic power forecasting models based on deep learning neural network. Appl. Energy **251**, 113315 (2019). https://doi.org/10.1016/j.apenergy.2019.113315
5. G. Sadowska, T. Cholewa, S. Nižetič, S. Papaefthimiou, K.A. Balaras, M. Arici, On real energy model of photovoltaic systems: Creation and validation. Energy Convers. Manag. **315**, 118810 (2024). https://doi.org/10.1016/j.enconman.2024.118810
6. Z. Su, S. Gu, J. Wang, P.D. Lund, Improving ultra-short-term photovoltaic power forecasting using advanced deep-learning approach. Measurement **239**, 115405 (2025). https://doi.org/10.1016/j.measurement.2024.115405
7. Y. Xie, J. Zheng, F. Mei, G. Taylor, A. Gao, An efficient approach for regional photovoltaic power forecasting optimization based on texture features from satellite images and transfer learning. Appl. Energy **385**, 125505 (2025). https://doi.org/10.1016/j.apenergy.2025.125505
8. L. Ilias, E. Sarmas, V. Marinakis, D. Askounis, H. Doukas, Unsupervised domain adaptation methods for photovoltaic power forecasting. Appl. Soft Comput. **149**, 110979 (2023). https://doi.org/10.1016/j.asoc.2023.110979

9. J. Tian, R. Ooka, Prediction of building-scale solar energy potential in urban environment based on parametric modelling and machine learning algorithms. Sustain. Cities Soc. **119**, 106057 (2025). https://doi.org/10.1016/j.scs.2024.106057
10. G. Mannino, G.M. Tina, M. Cacciato, L. Merlo, A.V. Cucuzza, F. Bizzarri, A. Canino, Photovoltaic Module Degradation Forecast Models for Onshore and Offshore Floating Systems. Energies **16**, 2117 (2023). https://doi.org/10.3390/en16052117
11. M. Libra, M. Kozelka, J. Šafránková, R. Belza, V. Poulek, V. Beránek, J. Sedláček, M. Zholobov, T. Šubrt, L. Severová, Agrivoltaics: dual usage of agricultural land for sustainable development. Int. Agrophys. **38**, 121-126 (2024). https://doi.org/10.31545/intagr/184133
12. V. Poulek, Z. Ales, T. Finsterle, M. Libra, V. Beránek, L. Severová, R. Belza, J. Mrázek, M. Kozelka, R. Svoboda, Reliability characteristics of first-tier photovoltaic panels for agrivoltaic systems - practical consequences. Int. Agrophys. **38**(4), 383-391 (2024). https://doi.org/10.31545/intagr/192173
13. M. Libra, V. Beránek, J. Sedláček, V. Poulek, I.I. Tyukhov, Roof photovoltaic power plant operation during the solar eclipse. Sol. Energy **140**, 109-112 (2016). https://doi.org/10.1016/j.solener.2016.10.040
14. K. Wang, X. Qi, H. Liu, A hybrid CNN–LSTM model for day-ahead photovoltaic power forecasting. Appl. Energy **255**, 113641 (2019). https://doi.org/10.1016/j.apenergy.2019.113641

Creative Commons Attribution License 4.0 (Attribution 4.0 International, CC BY 4.0) This article is published under the terms of the Creative Commons Attribution License 4.0 https://creativecommons.org/licenses/by/4.0/deed.en_US

A protocol for synchronized microclimate and air quality monitoring on a Prague metro platform

Jiří Haščyn[1*]

[1]Czech University of Life Sciences Prague, Prague, Czech Republic

Abstract. Environmental measurements on metro platforms should be interpreted alongside records of train movements, passenger activity and, where available, ventilation operation. This contribution proposes a monitoring and data evaluation protocol for a single platform in the Prague Metro. Core variables are air temperature, relative humidity and carbon dioxide concentration; particulate matter is included where suitable measurements are available. The protocol specifies sensor placement, clock synchronization, data quality checks and comparison of documented operating periods. Analysis around train arrivals and departures is designed to describe short-term variations while accounting for sensor response and temporal dependence. Station geometry and infrared images provide spatial context, with surface temperatures distinguished from air measurements. The methodological contribution is a reproducible procedure connecting environmental records with operational events and defining the limits of interpretation. The discussion considers the requirements for assessing ventilation energy use and associated CO_2 emissions. Winter use of warmer urban air and summer discharge of cooler underground air are framed as hypotheses requiring separate thermal, airflow and air quality assessment. Experimental validation and evaluation of these seasonal concepts are reserved for subsequent studies.

1 Introduction

Environmental conditions on a metro platform vary with train operation, passenger activity and air exchange. Measurements in the Barcelona subway showed that particulate concentrations and their response to tunnel ventilation depended on station configuration and sampling position [1]. A study on one Prague Metro platform also linked temporal variations in particulate matter to train operation [2]. These findings motivate a measurement design that records environmental conditions and operational events on a common time base.

The proposed platform monitoring protocol complements winter in-car research on Prague Metro line C [3]. The central question is how air temperature, relative humidity and CO_2 concentration vary between documented operating periods and measurement locations. Particulate measurements can extend the study where their method, timing and quality are documented.

The methodological output is a defined sequence from site documentation and synchronized acquisition to quality control and interpretable comparisons. Its application requires a bounded measurement campaign rather than a comparison of multiple stations or seasons. Station architecture provides context for this case; the protocol does not isolate a general architectural effect. Energy use and seasonal exchange between the metro and the city are addressed as subsequent assessment tasks.

2 Measurement framework

2.1 Case boundary and measurement locations

Two fixed locations are proposed: a central waiting area and a location influenced by train entry or passenger access. Their selection must respect operating restrictions and allow repeatable placement. A site record should identify position, sensor height, distance from the platform edge, nearby openings and the relationship to relevant ventilation paths. Photographs and a simple dimensioned plan should accompany the record.

Simultaneous measurements are preferred for comparing the two locations. If one instrument is moved sequentially, location and time become confounded; the resulting records must be treated as separate periods. Each sensor should be identified throughout the campaign so that changes in instrument, position or settings remain traceable. The campaign should cover repeated intervals with different documented train frequencies and passenger activity.

The study observes normal operation without changing fan direction or testing an urban cooling intervention. Ventilation changes require a separate experimental design.

* Corresponding author: hascyn@tf.czu.cz

Table 1. Proposed measurement records and contextual information.

Record	Core or conditional measurement	Required contextual information
Air temperature and humidity	Core: temperature [°C] and relative humidity [%]	Location, sensor height, sampling interval and response characteristics.
Carbon dioxide	Core: CO_2 concentration [ppm]	Instrument checks, occupancy record and any simultaneous outdoor reference.
Operational events	Core: train arrivals and departures; passenger activity	Common clock, track or direction where relevant, and observation method.
Particulate matter	Conditional: $PM_{2.5}$ and PM_{10} [$\mu g/m^3$]	Measurement principle, averaging time, calibration basis and valid coverage.
Ventilation and airflow	Conditional: documented fan state; local air velocity	Source of the operational record, measurement direction and instrument response.
Spatial and thermal context	Site plan, photographs and infrared images	Geometry and image acquisition conditions; surface and air temperatures distinguished.

2.2 Variables and interpretation

Table 1 separates the core records from measurements that depend on access to additional instruments or operating information. Air temperature, relative humidity and CO_2 should be recorded at the same location and linked to the operational log. Instrument model, measurement range, stated accuracy, response characteristics, calibration information and any field checks belong in the acquisition record. The sampling interval should be selected with the instrument response in mind.

CO_2 is interpreted jointly with passenger activity and ventilation context. ASHRAE cautions that CO_2 alone does not describe overall indoor air quality and that ventilation estimates depend on valid assumptions and accurate measurements [4]. In this protocol, changing occupancy and exchange with connected spaces prevent a simple conversion of platform CO_2 into an air change rate. Lower CO_2 also cannot establish lower particulate exposure.

For PM, the report must identify whether concentrations are derived from optical readings or another method, and state the basis of any conversion. Measurements with different principles or averaging times must remain distinguishable. Local velocity measurements, when available, describe conditions at the probe; they do not by themselves determine the volume flow through a ventilation shaft.

2.3 Synchronization and operational records

All instruments and the event log should use a common clock, checked before and after each session. Any residual offset or drift must be recorded. Raw timestamps are retained alongside corrected timestamps. A comparison interval is selected before interpreting the environmental changes, considering both logging frequency and sensor response. Rapid events that cannot be resolved reliably are assessed over longer operating periods.

The event log records train arrival, departure, track or direction where relevant, and a predefined measure of passenger activity. Counts or ordinal occupancy classes can be used, provided their definitions and observation intervals remain consistent. Ventilation states are entered only when supported by an operator record or direct observation of the relevant equipment. Unknown states remain unknown.

Higher and lower operating loads should be defined from the operational record, for example through train frequency and passenger activity, rather than from the measured pollutant concentration. The analysis should distinguish these two explanatory factors where the observations allow it. Maintenance, cleaning, instrument relocation and other documented disturbances are retained as annotations.

2.4 Data preparation and quality control

A data register should connect every channel to a sensor, location, unit and time interval. Checks address missing data, duplicate timestamps, unexpected units, clock inconsistencies and recorded instrument faults. Suspect readings receive a flag and a reason. An unusual value is not removed merely because it is extreme; operational events can also produce genuine short-term changes.

The analysis uses only the periods shared by the relevant records. Coverage is reported separately for each variable and location, with exclusions documented. Gaps spanning a train event are not filled to create an apparent response. Raw files, corrected files and the rules used for aggregation should remain separately identifiable so that the processing can be reproduced.

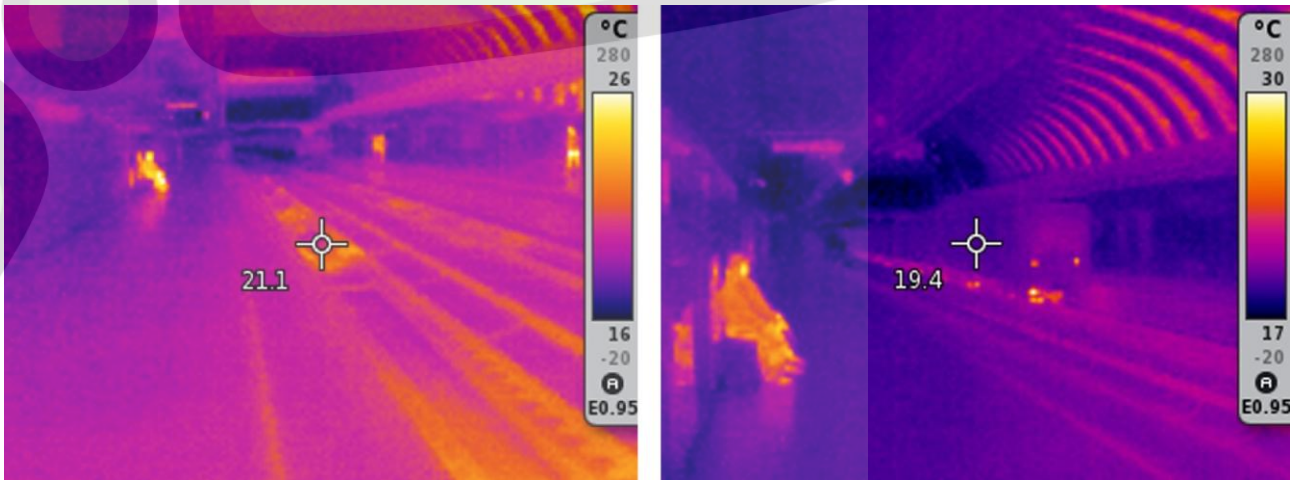


Fig. 1. Infrared images illustrate observed surfaces, not air temperatures. The images use different temperature scales and are not treated as a quantitative comparison.

3 Evaluation and supporting documentation

3.1 Spatial and thermal context

Figure 1 reproduces infrared images is supporting spatial documentation. Conventional thermal imaging concerns the apparent temperatures of observed surfaces rather than a direct measurement of air temperature [5]. Quantitative comparison additionally requires acquisition metadata, including emissivity settings, reflected temperature assumptions, viewing geometry and acquisition time. The displayed image scales differ, so matching colours cannot be interpreted as equal temperatures.

Within this protocol, the images help describe the site and identify surfaces that may merit additional investigation. They are not used to estimate ventilation flow, air pollutant concentrations or available cooling capacity. A diagram of a ventilation route likewise indicates a possible pathway, while its actual flow direction and magnitude require measurements or a documented operating state.

3.2 Comparisons between operating periods

The first output of a future application would be a coverage table stating the observation dates, valid duration and completeness of each record. Time profiles would then display environmental variables together with the train and occupancy log. Shared time axes help identify whether an apparent association persists across repeated periods or is driven by a single episode. Missing intervals and changes in operating information remain visible.

For each predefined operating period, the proposed summaries are the median, interquartile range and valid observation count. Simultaneous locations can be compared using paired differences over the same time windows. The report should retain the number of distinct sessions or operating periods separately from the number of sensor readings. Repeated readings within a period are not independent experimental replications.

Event-based analysis aligns records around train arrival or departure and compares a defined pre-event interval with the subsequent response. The observation window must account for instrument response and the time until the next train. Overlapping events should be flagged and analysed as overlapping operating conditions. A slow sensor may support a comparison of operating periods without resolving an individual train passage.

3.3 Interpretation and study limits

The proposed evaluation would describe the size and variability of observed differences, their timing and their relationship to the recorded context. Inferential analysis, if justified by the available replication, must respect temporal dependence and repeated observations at each location. The protocol does not prescribe a significance test before the structure of the eventual dataset is known.

An observational association with train frequency, occupancy or a documented fan state is not sufficient to isolate a causal ventilation effect. Simultaneous changes in these factors may be inseparable in a short campaign. Conclusions therefore apply to the observed platform, period and conditions. Assessing seasonal behaviour requires comparable campaigns in additional periods; extending the conclusions to station architecture requires a separate comparative design.

A compact empirical report can be built around three outputs: documented data coverage, synchronized environmental and operational profiles, and comparisons of clearly defined periods. Each output should state the observations it supports and the missing information that limits interpretation. Experimental validation of the protocol remains a subsequent step.

4 Sustainability and seasonal thermal exchange

The protocol can help identify operating conditions that warrant a more detailed ventilation assessment. Demonstrating an energy benefit requires an explicit baseline and measurements of the relevant energy use. Research in the Glasgow Subway has examined tunnel air as a heat source for heat pumps [6]. This supports investigating underground thermal resources, but does not establish the feasibility of either seasonal concept considered here.

4.1 Winter use of urban air

An urban heat island describes warmer urban conditions relative to surrounding areas [7]. This comparison does not establish that urban outdoor air is warmer than the metro. Winter intake from a warmer urban location could reduce ventilation heat loss relative to a colder intake, if a comparable alternative exists. Direct heating of an underground space requires supply air warmer than that space and an actual heating need. Assessment must include simultaneous temperatures, air quality, airflow and the existing operating regime.

4.2 Summer discharge of underground air

Reversing a suitable ventilation branch could be investigated for local cooling only when the discharged air is cooler than the receiving outdoor air and its quality is acceptable. The concept also depends on system compatibility, replacement air entering the metro, and effects on underground conditions. A temperature difference alone cannot quantify transferred heat without airflow. Demonstrating a benefit outdoors would require local reference measurements and assessment of mixing and weather. Cooling near an outlet would not establish a reduction of the city-scale heat island.

4.3 Energy and greenhouse gas accounting

A subsequent comparison should quantify the change in fan energy and any heating or cooling demand over equivalent operating periods. Added energy for air treatment or auxiliary equipment belongs within the same boundary. Associated emissions can then be assessed using documented energy consumption and appropriate emission factors; the GHG Protocol provides guidance for purchased electricity, heat and cooling [8]. Ambient CO_2 in ppm and operational emissions in mass units are different quantities. A reduction in measured CO_2 concentration does not demonstrate an emissions saving.

5 Conclusions

A focused protocol is proposed for linking platform microclimate and selected air quality variables to documented metro operation. Its practical contribution is the specification of measurement context, synchronization, quality control and comparisons that respect the limits of the records. The scope supports a bounded case study. Seasonal air exchange, urban cooling and quantified emissions reductions require additional evidence and remain separate research questions.

Data availability. No new time-series dataset is reported in this methodological contribution.

References

1. T. Moreno et al., Subway platform air quality: Assessing the influences of tunnel ventilation, train piston effect and station design. Atmos. Environ. **92**, 461–468 (2014). https://doi.org/10.1016/j.atmosenv.2014.04.043.
2. M. Cusack et al., Variability of aerosols and chemical composition of PM_{10}, $PM_{2.5}$ and PM_1 on a platform of the Prague underground metro. Atmos. Environ. **118**, 176–183 (2015). https://doi.org/10.1016/j.atmosenv.2015.08.013.
3. P. Kic, J. Hascyn, Winter In-Car Microclimate and Aerosol Variability on Prague Metro Line C: Passenger Load, Tunnel Ventilation, and Surface–Environment Coupling. Appl. Sci. **16**(14), 7161 (2026). https://doi.org/10.3390/app16147161.
4. ASHRAE, ASHRAE Position Document on Indoor Carbon Dioxide. Approved 12 February 2025. https://www.ashrae.org/file%20library/about/position%20documents/pd-on-indoor-carbon-dioxide-english.pdf.
5. FLIR, Do You Need a High Temp Range TIC? 13 October 2020. https://www.flir.com/discover/instruments/firefighting/high-temp-ranges-tics/.
6. K. Ninikas, N. Hytiris, R. Emmanuel, B. Aaen, P.L. Younger, Heat recovery from air in underground transport tunnels. Renew. Energy **96**, 843–849 (2016). https://doi.org/10.1016/j.renene.2016.05.015.
7. U.S. EPA, Learn About Heat Islands. Archived version, 19 January 2021. https://19january2021snapshot.epa.gov/heatislands/learn-about-heat-islands_.html.
8. WRI and WBCSD, GHG Protocol Scope 2 Guidance (2015). https://ghgprotocol.org/scope-2-guidance.

Measurement of coarse droplets in a steam turbine

Michal Hoznedl[1*], *Jakub* Vlasák[2], *Jindřich* Bém[1], *David* Hron[3] and *Matěj* Ranš[1]

[1]Doosan Škoda Power a.s., Experimental Research, Tylova 1/57, Plzeň, 30128, Czech Republic
[2]Doosan Škoda Power a.s., Material Engineering, Tylova 1/57, Plzeň, 30128, Czech Republic
[3]Doosan Škoda Power a.s., CFD and Thermal Loading, Tylova 1/57, Plzeň, 30128, Czech Republic

Abstract. Coarse droplets in steam turbines originate from disintegration of water films on nozzle trailing edges or from other surfaces. They flow to the last stage buckets (LSB) a suboptimal angle and cause leading edge erosion. The erosion damage is one of the limiting parameters of a steam turbine lifetime. Depth of erosion damage is predicted by so called erosion model. One of the most important inputs to the model is droplet size distribution. A novel method for measuring spectra of diameters, velocities, and angles of coarse droplets as well as measured results are described in the paper. Additionally static pressure and velocity distribution measurements were performed using pneumatic probe. The measurement itself was performed on a real-size 34 MW Waste-to-Energy steam turbine. It was realized behind the LSB and for nominal operation only. Measured results give a good reference material for numerical research of water films in steam turbines.

1 Introduction

One of the remaining problems in steam turbine design is water droplet erosion of last-stage blade caused by impact of coarse droplet. This is due to significant change in steam turbine operation in recent years. Formerly, steam turbines were designed as primary and stable sources working continuously at nominal output or close to it. This role has changed and now steam turbines are often used as a supplementary power source whereas renewables are main energy source. This is valid not only for small turbines with output up to 100 MW but also to coal and nuclear units. Nevertheless, steam turbines continue to play an important role in maintaining grid stability because of their large rotating inertia [1].

So-called low-load regimes (regimes with output less than 20 % of nominal regime) of steam turbines are becoming more common for the reasons mentioned above. This brings new problems and challenges for turbine designers. Among them LSB vibrations are investigated experimentally [2] and numerically [3]. The steam mass flow through the last stage, or even the one preceding it, is so small that they act as compressor. This behaviour is illustrated by measurements carried out on a 200 MW Doosan Škoda steam turbine, see Fig. 1. A simple but illustrative scheme is in Fig. 2. This picture shows pressure ratio over the LSB tip ($\Pi_t = p_{2tip} / p_{1tip}$) as a function of the LSB outlet axial velocity c_{2x} [4]. Here p_{1tip} and p_{2tip} are static pressures before and behind LSB tip, respectively. A critical vibration region with $p_{2tip} / p_{1tip} > 1$ for low c_{2x} is marked in this figure.

As a new phenomenon, a LSB flutter must be carefully examined [2, 3] as well.

Another issue associated with low-load regimes is overheating of the turbine end because the LSB does not generate work; it consumes it.

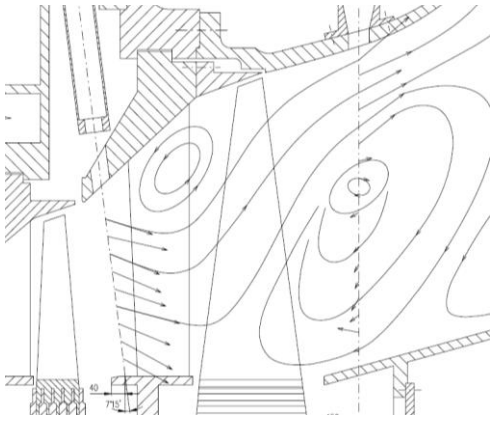


Fig. 1. Steam turbine low-load flow pattern

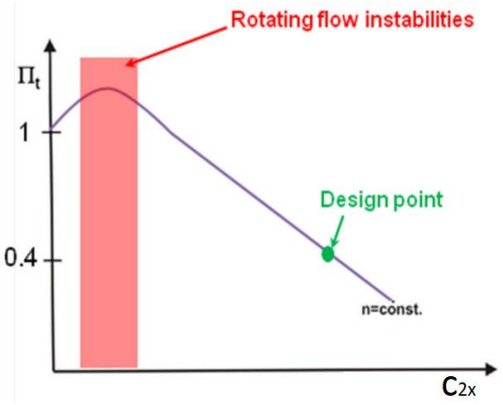


Fig. 2. Flow instabilities in the LSB space

* Corresponding author: michal.hoznedl@doosan.com

Turbine end overheating leads to excessive bearing housing vibration and to the overheating of following equipment, such as condenser or heat exchanger. Water nozzles with an appropriate amount of cooling water must be installed to the turbine exhaust casing and activated during low load. The amount of water as well as the direction of water droplets flow must be carefully examined to avoid LSB trailing edge erosion, especially close to the blade roots [5].
One of the most important factors limiting steam turbine lifespan and a gap between overhauls is LSB leading edge erosion, see Fig. 3.

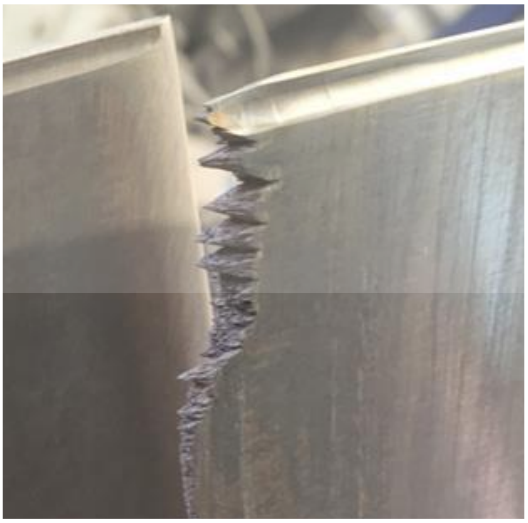


Fig. 3. LSB leading edge erosion example

Water droplets originate from the disintegration of water films at the upstream nozzle trailing edge or at a sharp edge in steam turbine flow path. Therefore, it is necessary to understand, simulate and experimentally validate water film formation, flow, and disintegration within the flow path area. It is one of the most challenging topics because of the lack of measured data needed to fully capture two-phase high-speed flow.

A lot of experimental work has been, and continues to be, conducted done in transonic nozzles operating with air and water intake through hollow blades [6, 7], whereas measurements in steam nozzles are rare and deal with primary condensation [8] and scarcely with water film presence [9].

High-quality time-resolved coarse droplet measurements on an experimental four-stage steam turbine have been described in [10, 11]. The coarse droplet flow field in both circumferential and radial directions was determined together with corresponding Weber numbers.

350 MW full-scale turbine coarse droplets measurement is described in [12]. The study provides not only measured results like velocities, flow directions, and coarse droplets sizes, but also briefly describes a method involving the implementation of hydrophobic surface to reduce droplet size.

Several empirical and numerical studies have been performed over the years [13, 14] including one paper prepared in cooperation between Doosan Škoda Power and Czech Technical University in Prague [15]. 2D code to calculate inertia, mass transfer, gravity, gas and wall frictions and other effects has been developed in [16]. This work builds upon classical literature [8].

The lack of experimental data is a common theme in most of the cited studies. The goal of present paper is to bring new information to the complicated and complex world of coarse droplets flow. Measured data seems to be useful to tune numerical models even though the probing was realized behind LSB. The knowledge of the coarse droplet field behind the blading will allow adjusting numerical and empirical models. These models then could be applied to model more important parts of the turbine, such as the gap between last stage nozzles and buckets.

2 Experiment description

2.1 Tested steam turbine

Measurements were carried out on a steam turbine with a maximum output of 34 MW. The rotational speed of the turbine is 5500 rpm. Last stage buckets are installed at a root diameter of 928 mm. The last stator blades have a shroud; tie-bosses are not used. The number of rotor blades is 64. The nominal pressure on the last stage outlet is 6100 Pa. The turbine outlet is axial, and the steam continues through a pipe to an air-cooled condenser.

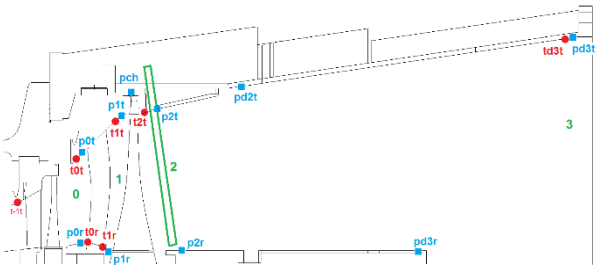


Fig. 4. Turbine cross-section and position of measuring locations

2.2 Pneumatic probe

The steam turbine last stage is equipped with devices for measuring pressures, temperatures, with access ports for probes and with a capability to monitor blade tip vibrations. The probe passage is behind the LSB only. The probe inclination in the axial direction relative to the turbine axis is 80°,and it is approximately parallel to the LSB trailing edge. In the circumferential direction, the probe passage is placed on the left side of the turbine; 45° above the dividing plane. The access port on the right side is prepared as well but it was not possible to insert the probe due to the presence of a steam pipe. The distance of the probe axis is 118 mm from the rotor blade tip and 140 mm from the rotor blade root. Position of the probe is schematically marked in Fig. 4 by a green rectangle.
For flow field probing, a 7-hole disc probe with a stem diameter of 30 mm and a head disc diameter of 20 mm was used. Four pressure taps are installed along the disc periphery to define the meridional angle of the steam flow ε. Two more taps were used to balance the probe in

the flow. The last pressure tap on the side of the probe was used to define the static pressure. Turning the probe in the circumferential direction made it possible to define flow angle α in any direction.

The traversing step was set to 50 mm. The measurement uncertainty of the probe radial position is 0.5 mm and the aerodynamic probe sensitivity to angle α is 0.5°. All seven pressure lines were continuously purged with atmospheric air. This reduced the possibility of pressure pipes being clogged by water droplets. The purging process causes a uniform systematic measurement error of 10 Pa across all pressure pipes.

A schematic of the pneumatic probe, including the abbreviation for the measured velocity components and angles, is presented in Fig. 5.

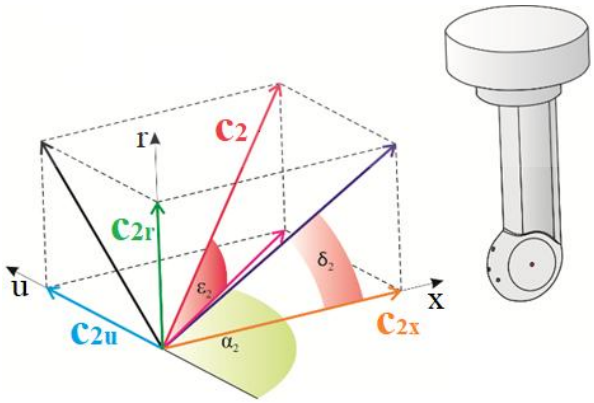


Fig. 5. Pneumatic probe head and measured velocity components

2.3 Videoprobe

Videoprobe is an optical probe for direct measurement of coarse droplet velocity, speed, and radial angle. Videoprobe scheme is shown schematically in Fig. 6.

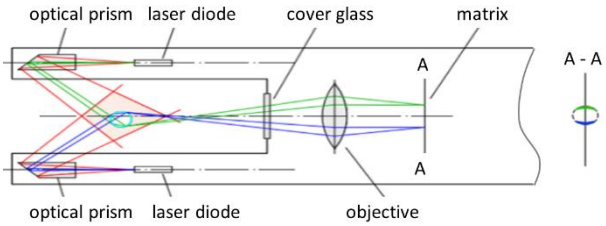


Fig. 6. Scheme of videoprobe

The videoprobe head is installed at the end of the same probe carrier as the pneumatic probe. The diameter of the videoprobe head is 25 mm. A printed circuit in the videoprobe head is connected to the external PC via a combined data and power supply cable. Electronics on the printed circuit provide the energy to the laser diodes. Frequency of laser diodes flashing is controlled by electronics and by control SW running on the laptop. Flashing light from two laser diodes is directed into the measuring space. Camera captures droplets through special optics as a line of dots. The distance between light points (L) is related to the droplet velocity (v), because the time between LED flashes (t) is known and v = L / t. The distance between double points is equal to the droplet diameter. The camera image of the videoprobe with one visible droplet is in Fig. 7. Three positions of the same droplet are marked on the same picture to make it easier to understand measuring and evaluation system.

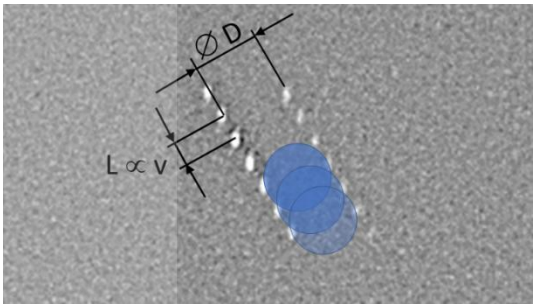


Fig. 7. A droplet with basic parameters as visible on the laptop screen

It should be noted that both cover glass and surroundings of optical prisms must be kept clean of condensing water by using filtered and dried air drawn from the surrounding atmosphere. The same air is used to cool the electronics inside of the probe. Base probe parameters are summarized in Table 1.

Table 1. Videoprobe parameters

Description	Value	Unit
Max. resolution	2592x1944	fps
Pulse duration	53/80/107	ns
Time between pulses	160 ÷ 6830	ns
Droplet diameter range	20 ÷ 600	µm
Droplet speed range	0.1 ÷ 300	m/s
Max. temp. inside probe	50	°C
Max. temp. outside probe	90	°C

Video data were recorded every 20 mm along the blade length. Data were captured for one minute in every radial position.

Insertion of the videoprobe into the machine is shown on the following Fig. 8.

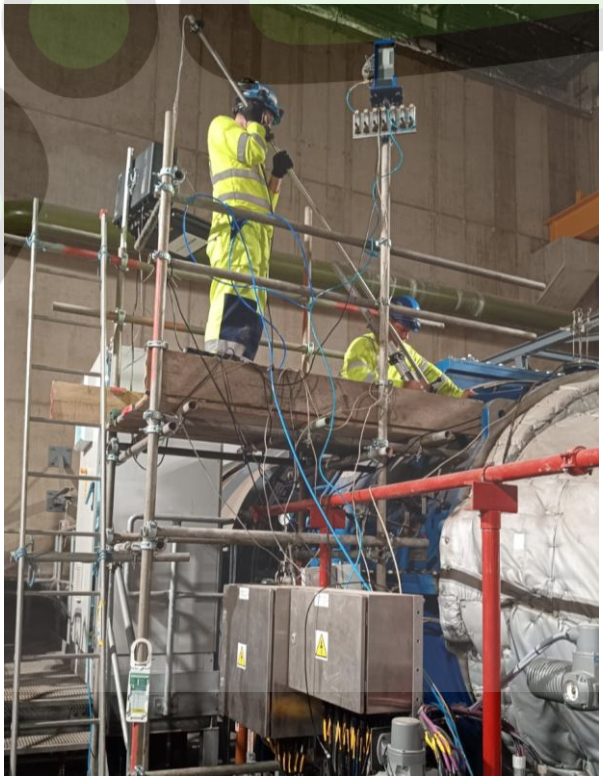


Fig. 8. Probe insertion into the turbine

3 Results and discussion

3.1 Pneumatic probe results

Steam velocity components in axial (c2x), circumferential (c2u) and radial (c2r) directions along the blade length are depicted in Fig. 9. Velocity vector c_2 is added to the picture as well.

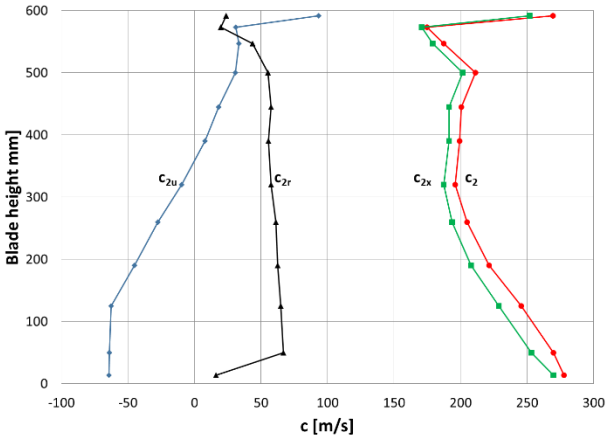


Fig. 9. Measured velocity components

It can be clearly seen that c_{2u} is around at the mid-span. This indicates that the outlet flow has an axial direction, and the turbine outlet operates close to the nominal conditions. This conclusion is confirmed by static pressure probe measurement, which shows a constant value around 6400 Pa over the blade length.

The measurements also reveal a velocity drop close to the blade tip caused by the presence of shroud as well as the sharp increase of the steam velocity due to radial clearance leakage.

3.2 Videoprobe results

Videoprobe results are marked by boxplots because at each probe position several dozen or even several hundred droplets were evaluated.

It is quite surprising that droplets exhibit bi-modal character from the point of view of their velocity. The first mode has average velocity around 60 m/s while the second mode´s velocity reaches up to 200 m/s. Velocity boxplot of both modes supplemented with the steam velocity profile c_2 is in Fig. 10. Small numbers around every measured position indicate the number of evaluated slow or fast droplets.

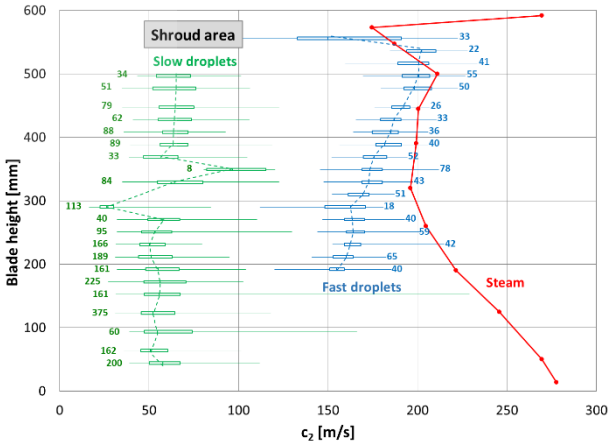


Fig. 10. Velocity of droplets and steam

It is evident that slow droplets are present from the root close to the tip but not in the area behind the LSB shroud. Fast droplets are in upper two thirds of the blade height. Their mean velocity approaches the steam velocity, especially close to the upper one third of blade height. Fast droplets follow the steam. They have sufficient time to be accelerated by steam flow.

The distribution of the angle for both droplets and steam provide another perspective on the measured data, as shown in Fig. 11.

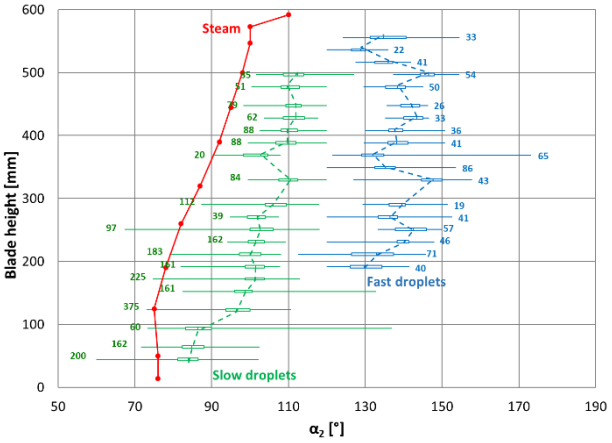


Fig. 11. Outlet angle of droplets and steam

Here, the angles of slow droplets are close to the steam angle. Fast droplets exhibit a strong swirl. The only plausible explanation for the bi-modal velocity and angle behaviour is the presence of two different sources of droplets in the flow path. Flow situation can be explained more simply by velocity triangles for steam together with the added velocities and angles for both slow and fast droplets. The steam velocity triangles are reconstructed based on the pneumatic probe measurement. The influence of the axial distance between the LSB trailing edge and the probe axis is negligible, up to 2°.

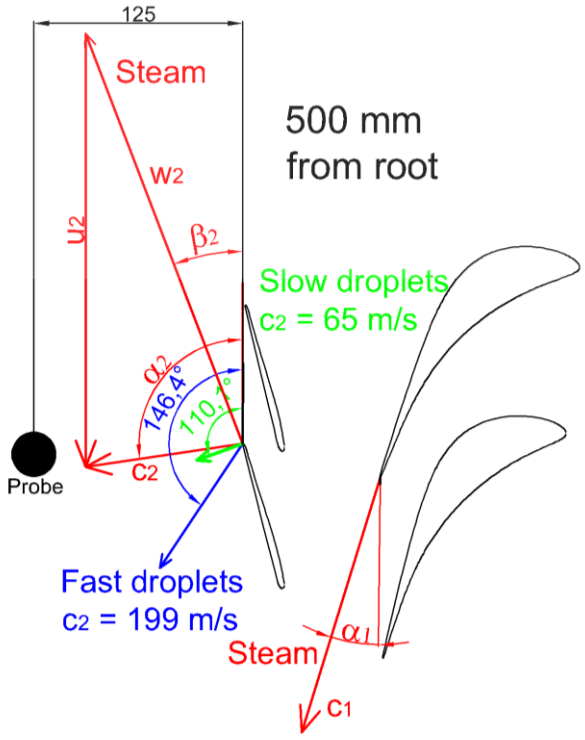


Fig. 11. Steam and droplets velocity triangles

Slow droplets follow the steam flow direction at the LSB outlet with only a small deviation. This suggests that the slow droplets originate at the LSB trailing edge, and do not have sufficient time to be accelerated to the steam velocity. Slow droplets were not captured behind the LSB shroud. It suggests that these droplets do not occur in the shroud region but at the blade sheet only.

Fast droplets have angle little bit larger than the steam angle α_1. Their velocity is around 70 % of steam velocity c_1. Fast droplets occurring at the last stage nozzles are decelerated while passing through the LSB and they are straightening up into the axial direction.

Droplets occur at both stator and rotor blade surfaces. That This is a very important observation useful for CFD modelling of water films.

The dimensionless Weber number must be defined for further consideration:

$$We = \frac{\rho_s \cdot c^2 \cdot D_{max}}{\sigma_w}. \qquad (1)$$

Here:

ρ_s density of steam (kg/m^3)
c velocity of steam (m/s)
D_{max} droplet with maximum diameter (m)
σ_w droplet surface tension (N/m)

In erosion model it is generally considered that $We = const.$ for steam turbine flow although some authors reported more complicated flow behaviour [17].

Situation for slow droplets is shown in Fig. 12. Absolute velocity c_1 is replaced by relative velocity w_2 in formula (1) because droplets occur at the LSB trailing edge and w_2 characterizes the flow conditions for droplet formation. The velocity w_2 was measured by pneumatic probe as well as static pressure profile. D_{max} was measured using the videoprobe, and it reaches 265 μm for slow droplets and 227 μm for fast droplets. The measured D_{min} was 14 μm. The measured w_2 profile and the profile w_2 calculated using the HBD method (heat balance calculation method) are in good agreement. To maintain $We = const.$ along the blade height, the velocity w_2 was adjusted. The profile of adjusted velocity $w_{2We=const.}$ is quite wavy. Its shape depends on the measured D_{max} which changes over the blade length. A longer measurement time will provide more measured droplets and increase the probability of detecting a larger droplet corresponding to $w_{2We=const.}$. Average value of wavy $w_{2We=const.}$ is denoted as w_{2move}. To obtain the correct D_{max} as a function of velocity, an empirical correction is required: $w_{2move} = 0.8 \cdot w_{2HBD}$. For slow droplets applies.

$$D_{maxslow} = \frac{\sigma_w \cdot We = const.}{\rho_s \cdot w_{2move}^2}. \qquad (2)$$

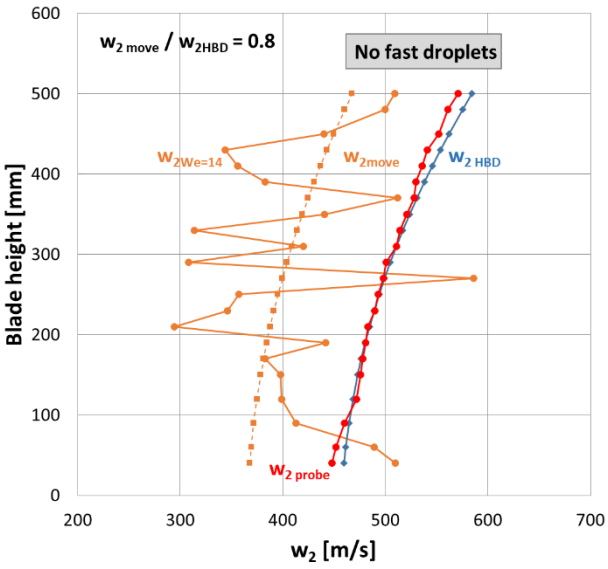


Fig. 12. Correction of w_2 velocity for slow droplets

A similar approach is used for fast droplets likely generated at the nozzle surfaces. Here, $c_{1move} = 0.7 \cdot c_{1HBD}$ and determination of the fast droplet maximum diameter is

$$D_{maxfast} = \frac{\sigma_w \cdot We = const.}{\rho_s \cdot c_{1move}^2}. \qquad (3)$$

Fig. 13 shows calculated trends for c_{1HBD} and c_{1move}, along with the fluctuating curve $c_{1We=const.}$ derived from D_{max} videoprobe measurement.

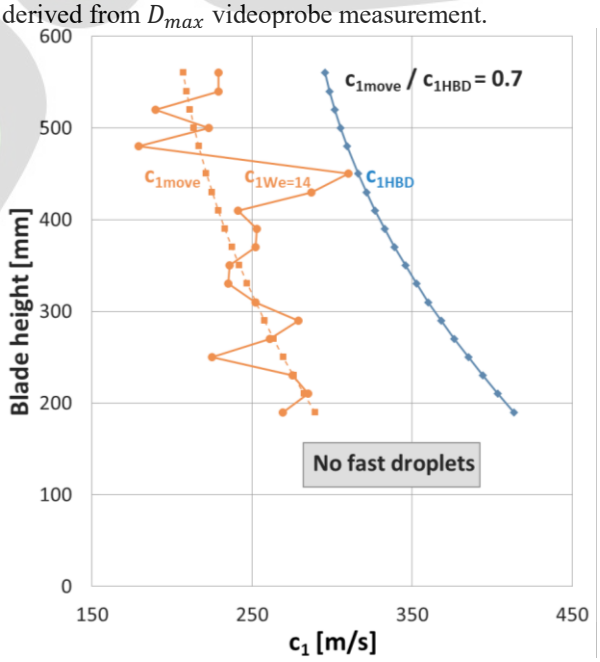


Fig. 13. Correction of c_1 velocity for fast droplets

Scaling the steam velocity by a factor of 0.7 or 0.8 respectively, has a physical meaning. c_1 or w_1 represent the steam velocity in the free interblade channel. Water films form on the blade surface and disintegrate at the trailing edge. The velocity around the trailing edge and in the downstream wake is much lower than free stream velocity. The corrected velocities w_{2move} a c_{1move} are therefore closer to the physical reality.

Coarse droplets count and volume distribution functions can be defined. To obtain number of droplets big enough for statistical evaluation, all droplets are summarized and evaluated in one graph, see Fig. 14. Count distribution function is defined by

$$f_n = \frac{n(\varnothing D)}{N} \cdot \frac{1}{\Delta \varnothing D} \qquad (4)$$

and volume distribution function,

$$f_v = \frac{v(\varnothing D)}{V} \cdot \frac{1}{\Delta \varnothing D} \qquad (5)$$

where:
n - number of intervals (n = 20),
$n(\varnothing D)$ - count of all droplets in an interval,
$v(\varnothing D)$ - volume of all droplets in an interval,
N - total number of droplets,
$\varnothing D$ - interval width.

The highest number of droplets is in the interval with a mean diameter 49 µm. The largest droplets affect the right side of volume distribution. It is important to point out, for example, that one droplet with diameter of 265 µm has the same volume as around 1200 droplets with a diameter of 50 µm. The measured volume distribution is in good agreement with accessible literature [18] except for its right-hand side. The difference can be explained by the presence of several very large droplets. Left-hand side of distribution has a Gaussian character.

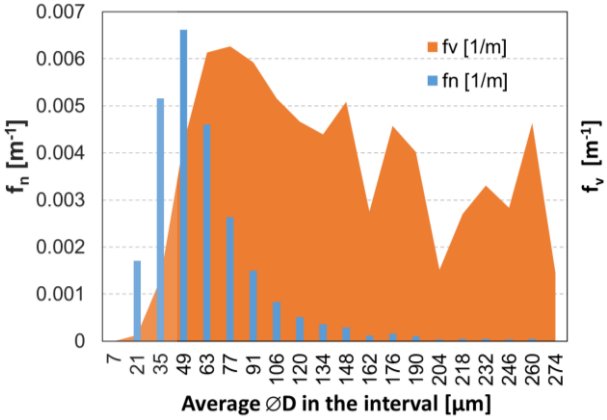


Fig. 14. Count and volume droplet spectra

Conclusions

Pneumatic and optical measurements were performed on a 35 MW steam turbine. The traversing line was located around 120 mm behind the LSB trailing edge and 45° above the horizontal joint. Only the nominal regime was measured.

Two modes of coarse droplets were identified based on their velocities and flow angles. Slow droplets have velocity of around 60 m/s and a flow angle approximately 100°, whereas fast droplets travel at around 180 m/s with a flow angle of 140°. Based on the velocity triangle analysis, it can be assumed that fast droplets occur at the last nozzle trailing edge, whereas slow droplets originate at the last bucket trailing edge. It suggests that at least two different sources of droplets are in the turbine in the exhaust hood space.

To accept the assumption that We = const. for all droplets, the steam velocities c_1 and w_2 must be reduced from their free flow values by factors of 0.7 ÷ 0.8, respectively, to obtain corrected velocities c_{1move} and w_{2move}, respectively. This correction is physically justified, because water films disintegrate at the blade trailing edges, where steam velocity is lower than the free flow velocity.

Together with the knowledge of the volume (or mass) distribution, the determination of the velocity used to calculate D_{max} is crucial for the development of a new version of water droplets erosion model.

Further measurement campaigns, especially in the axial gap between stator and rotor blades of the last stage and under a wider range of operating conditions, including low loads regimes, are strongly needed.

Authors thank for the financial contribution to the Technology Agency of the Czech Republic, program Théta 2, project number TS02020040.

References

1. N. Funahashi, Y. Takagi, 25 - Steam turbine roles and necessary technologies for stabilization of the electricity grid in the renewable energy era, (Woodhead Publishing Series in Energy, pp. 621-638, 2022). https://doi.org/10.1016/B978-0-12-824359-6.00003-2
2. A. Bessone et al., Aeromechanical Characterization of a Last Stage Steam Blade at Low Load Operation: Part 1 — Experimental Measurements and Data Processing. In ASME Turbo Expo (2020): https://doi.org/10.1115/GT2020-15450
3. L. Pinneli et al., Aeromechanical Characterization of a Last Stage Steam Blade at Low Load Operation: Part 2 — Computational Modelling and Comparison. In ASME Turbo Expo (2020): https://doi.org/10.1115/GT2020-15409
4. B. Megerle, I. McBean et al., Unsteady Aerodynamics of Low-Pressure Steam Turbines Operating Under Low Volume Flow, ASME. J. Turbomach (2014). https://doi.org/10.1115/1.4027373
5. M. Hoznedl et al., Cooling of Steam Turbine Exhaust Hood and Last Stage Blade, MATEC Web Conf. 383 00010 (2023), https://doi.org/10.1051/matecconf/202338300010
6. O. Bartoš, A. Huněk, P. Antoš, A Study of the coarse droplet formation from the liquid film in steam turbines, MATEC Web Conf. 383 00003 (2023), https://doi.org/10.1051/matecconf/202338300003
7. O. Bartoš, A. Huněk, P. Antoš, An Analysis of the Bi-modal Size Distribution of the Coarse Droplets in a Steam Turbine, MATEC Web Conf. 367 00003 (2022), https://doi.org/10.1051/matecconf/202236700003
8. F.G. Hammit, S. Krzeczkowski, J. Krzyżanowski, Liquid film and droplet stability consideration as applied to wet steam flow. Forsch Ing-Wes 47, 1–14 (1981). https://doi.org/10.1007/BF02560457
9. C. A. Moses, G. D. Stein, On the Growth of Steam Droplets Formed in a Laval Nozzle Using Both Static Pressure and Light Scattering Measurements, J. Fluids Eng. Sep 1978, 100(3): 311-322 (12 pages), https://doi.org/10.1115/1.3448672
10. I. Bosdas et al., Unsteady Flow Field and Coarse Droplet Measurements in the Last Stage of a Low-Pressure Steam Turbine With Supersonic Airfoils Near the Blade Tip, ASME. J. Eng. Gas Turbines Power (2017); 139(9): 091601. https://doi.org/10.1115/1.4036011
11. Y. Sasao et al., Coarse Droplet Measurement at the Last Stage Stator Exit of a Four-Stage Scaled Steam Turbine Using an Optical Backscatter Probe." Proceedings of the ASME Turbo Expo: (2023), https://doi.org/10.1115/GT2023-103378
12. X. Cai et al., Coarse water in low-pressure steam turbines, J. of Power and Energy, Volume 228, Issue 2 (2014), https://doi.org/10.1177/095765091351876
13. V. A. Tishchenko, V.A., R. A. Alekseev, Numerically Simulating the Formation and Motion of Water Films and Erosion-Hazardous Droplets in Flow-Through Parts of Steam Turbines. Therm. Eng. 66, 830–838 (2019). https://doi.org/10.1134/S0040601519110053
14. S. Schuster, D. Brillert, F. Benra, Condensation in Radial Turbines—Part I: Mathematical Modeling. ASME. J. Turbomach. (2018); 140(10): 101001. https://doi.org/10.1115/1.4040934
15. G. Jun et al., Modelling of Water Film and Secondary Droplet Formation in a Steam Turbine, Proc. of the ASME Turbo Expo (2025). https://doi.org/10.1115/GT2025-153115
16. A. Simon et al., A Model for Liquid Films in Steam Turbines and Preliminary Validations, Proc. of the ASME Turbo Expo (2016). https://doi.org/10.1115/GT2016-56148
17. Bartoš O., Huněk A., Antoš P., A study of the coarse droplet formation from the liquid film in steam turbines, EPJ Web of Conferences 299, 01001 (2024), https://doi.org/10.1051/epjconf/202429901001
18. Safiullah, V. McDonnel, S. Tabata, S. Senoo, Investigation of Liquid Film Atomization From the Trailing Edge of an Airfoil in a High-Speed Flow-Effect of Trailing Edge Thickness, Proc. of the ASME TurboExpo (2025), https://doi.org/10.1115/1.4069583

Influence of airfoil angle of attack on the size distribution of coarse droplets formed from a liquid film

Adam Huněk [1*], *Ondřej* Bartoš[1]

[1]CTU in Prague, Energy Department, Technická 4, Czechia

Abstract. Steam turbines remain an essential technology for energy conversion, particularly with the current resurgence of nuclear energy. Erosion of last-stage steam turbine blades caused by water droplet impacts is one of the key challenges affecting reliable and efficient turbine operation. Fine droplets generated by steam condensation accumulate on blade surfaces, where they form a liquid film that subsequently undergoes breakup, producing coarse droplets. The impact of these coarse droplets on the rotor blades of the last stages has a negative effect on turbine efficiency and reliability. The Laboratory of Energy Engineering at the Czech Technical University in Prague is equipped with a wind tunnel facility designed to investigate liquid-film breakup under controlled flow conditions. This study follows previous research primarily focused on the influence of pressure conditions and flow-field characteristics on coarse droplet formation. In the present work, the airfoil is positioned at three angles of attack (−5°, 0° and 5°), and the droplet size distributions are measured 40 mm downstream of the trailing edge by image analysis. The Sauter mean diameter increases by about 10% with increasing angle of attack, from 353 to 388 μm, while the Weber number based on the global flow conditions and D_{32} remains almost constant ($We_{32} \approx 34$). This increase is consistent with the decrease in dynamic pressure caused by the slightly higher pressure ratio at larger angles of attack, and it may also be related to the enlargement of the wake region behind the trailing edge, where droplets are exposed to lower aerodynamic forces and can accelerate towards the bulk flow velocity without reaching the conditions required for secondary breakup. The angle of attack also shifts the position of the droplet-laden flow, whereas the shape of the size distribution remains unchanged and follows the relation for a gamma distribution.

1 Introduction

The investigation of liquid film breakup under different operating conditions is essential for erosion models in applications such as steam turbines and compressors. In steam turbines, the liquid phase causes energy losses and erosion of turbine parts, especially rotor blades, which further reduces turbine efficiency and reliability. This is most relevant in the last stages, where the machine operates in the wet-steam region and the blade tip velocity is the highest. The need to operate turbines under off-design conditions makes the problem even more pressing. Understanding droplet formation is therefore essential, and reducing blade erosion would shorten turbine downtime and, through higher efficiency, lower the environmental impact of energy production.

Several studies have investigated coarse droplet dispersion directly in steam turbines [1, 2]. Measuring film breakup in a wind tunnel under laboratory conditions is a practical alternative to measuring coarse droplets in a turbine. A wind tunnel was developed at CTU in Prague, where droplet charging was studied [3]. The tunnel was later used to investigate the influence of velocity fluctuations and the velocity profile measured by hot-wire anemometry [4]. Tabata et al. [5] combined an Eulerian wall-film model with a Lagrangian droplet model including secondary breakup and validated it against earlier wind tunnel experiments on a NACA 0012 airfoil with a water film in airflow of up to 175 m/s. Murakami et al. [6] visualised a thin water film flowing down the wall of a 21 mm pipe and sheared by a central turbulent airflow, and measured the wavelength and speed of its ripple waves. Safiullah et al. [7] tested how the trailing edge thickness (0.5, 1.0 and 2.0 mm) of a NACA 0012 airfoil affects water film breakup at air velocities of 60, 100 and 175 m/s, using high-speed video to measure ligament length and liquid accumulation at the trailing edge, and microscopic imaging and laser diffraction to measure droplet sizes up to 70 mm downstream. A thicker trailing edge and a higher water flow rate increased liquid accumulation and ligament length and gave larger droplets near the edge. Once secondary atomisation was complete (about 70 mm downstream), however, the droplet size depended mainly on the air velocity.

Previous research [8] investigated the influence of the air pressure drop on the coarse droplet size (D_{32}) and found a Weber-number-like scaling for the specific experimental geometry and conditions. This paper presents preliminary results that continue this research, with the goal of further generalising the proposed

* Corresponding author: adam.hunek@fs.cvut.cz

model. In this study, three blade angles are investigated, representing different flow geometries, while the nominal pressure conditions are kept constant.

2 Experimental setup

This paper focuses on the investigation of water film breakup in a wind tunnel (Fig. 1). The flowing medium is compressed air supplied by a compressor equipped with an air tank. In this study, the compressor operates continuously and the pressure drop is determined by throttling the valve. The stagnation pressure p_c and stagnation temperature T_c are measured in the settling chamber. Static pressure is measured before the nozzle segment (p_{s0}) and after the nozzle segment (p_s). A NACA 0010 airfoil with a 50 mm chord length is placed behind the nozzle segment. A water dosing apparatus consisting of a pump and a flowmeter is used to dose water onto the airfoil through a 1 cm wide groove positioned in the centre. A water film is formed and breaks up at the trailing edge. The wind tunnel is equipped with optical mirrors to enable measurements with optical methods. This study uses droplet size evaluation by image analysis. The camera XIMEA MC050CG-SY with a CMOS digital image sensor Sony IMX250 LQR-C and a telecentric lens with 2× magnification is used. The sensor has 2464 × 2056 active pixels, with a pixel pitch of 3.45 µm. The method is based on taking images with a short exposure time, synchronised with a rapid flash from a diode, to sharply capture the entrained droplets. An in-house MATLAB script was developed to evaluate the droplet sizes using Otsu segmentation and gradient thresholding. The camera and the diode are placed on a common traversing system to enable radial investigation. The depth of field is adjusted to the centre of the wind tunnel (z axis).

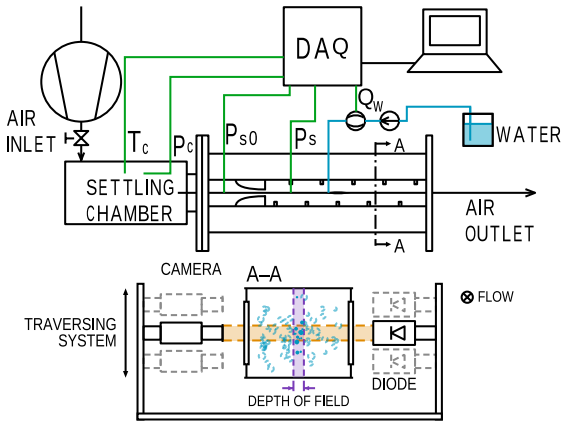


Fig. 1. The experimental setup.

The coordinate axes have their origin at the centre of the trailing edge for $\alpha = 0°$ (Fig. 2). The angle of inclination is defined according to Fig. 2. The air pressure drop (the difference between p_c and p_s) is set to approximately 3.5 kPa. First, the effect of the water flow rate Q_w set by the water pump is briefly investigated. The conditions of this investigation are shown in Table 1. Each measurement condition was measured once, with 1200 images. Subsequently, the influence of the angle of inclination of the airfoil is investigated (Table 2). In the investigation of the effect of α, the number of images taken per measurement is 600 and each position (varying x, y, α) is measured three times.

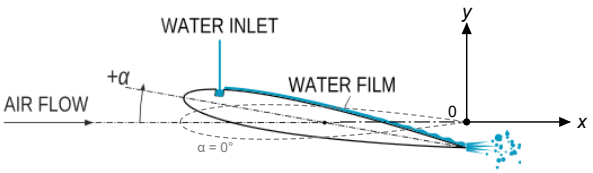


Fig. 2. The angled NACA 0010 airfoil.

Table 1. The conditions of the Q_w investigation.

Δp [kPa]	4
α [°]	0
Q_w [ml/min]	2, 5, 7, 10
y [mm]	0
x [mm]	40, 60
photos per measurement [#]	1200
measurements per position [#]	1

Table 2. The conditions of the α investigation.

Δp [kPa]	4
α [°]	−5, 0, 5
Q_w [ml/min]	5
y [mm]	−10, −5, 0, 5, 10
x [mm]	40
photos per measurement [#]	600
measurements per position [#]	3

3 Results

This section presents the results of the two investigations. The water flow rate investigation is conducted to demonstrate its influence on primary atomisation and to provide context for the subsequent investigation of the airfoil angle of inclination, which is performed at a single water flow rate because of the large number of measurement points. Furthermore, measurements at different distances downstream of the trailing edge (x = 40 and 60 mm) are included to demonstrate the effects of secondary atomisation and droplet transport. Section 3.2 then focuses on the main investigation, examining the influence of the airfoil angle of inclination on droplet atomisation.

Previous research has demonstrated the significant influence of airflow velocity, represented by the pressure drop (Δp), on droplet formation. Therefore, the present study focuses on investigating other influencing parameters while maintaining an approximately constant pressure drop.

An important aspect of this study is the distinction between the Weber number computed from the local velocity of the droplet (the local Weber number) and the Weber number related to the measured pressure drop in the wind tunnel (the global Weber number). The global Weber number is used here for a direct comparison of

the slightly different conditions between the runs. Because it is based on the bulk velocity upstream of the airfoil and not on the velocity deficit in the wake behind the airfoil, it takes higher values than the critical Weber number commonly used for local droplet velocities.

3.1 The water flow rate effect investigation

The influence of the water flow rate Q_w on droplet atomisation at y = 0 mm and x = 40 and 60 mm is presented in Table 3. The valve was set to a single position to ensure similar conditions ($\Delta p \approx 3.5$ kPa). The number of detected droplets increases approximately linearly with the water flow rate at both positions (Fig. 3). The increase is considerably steeper at x = 40 mm, where N rises from about 25 to about 120 droplets over the investigated range, than at x = 60 mm, where it rises only from about 20 to about 60 droplets. This indicates that the local droplet population does not increase uniformly downstream.

The Sauter mean diameter shows a large scatter and a non-monotonic dependence on the water flow rate (Fig. 4). The linear trend lines suggest a slight overall increase of D_{32} with Q_w at both positions, steeper at x = 40 mm. These differences indicate that the local droplet size distribution is influenced by downstream transport and possibly by secondary atomisation. However, the contribution of individual mechanisms cannot be distinguished from the present measurements alone. Since each condition was measured only once and the number of detected droplets is small, the trends are indicative only.

Based on the preliminary measurements, a water flow rate of 5 ml/min and a downstream measurement position of x = 40 mm are selected for the subsequent investigation of the airfoil angle of inclination. This represents an intermediate water flow rate at which a sufficient number of droplets is detected. These conditions are kept constant in the subsequent experiments to focus on the influence of the airfoil angle of inclination.

Table 3. The results of the Q_w investigation.

x [mm]	Q_w [ml/min]	N [#]	D_{32} [µm]
40	10	118	626.07
40	7	102	301.35
40	5	58	413.11
40	2	25	294.74
60	10	57	433.23
60	7	42	303.33
60	5	48	465.17
60	2	21	260.73

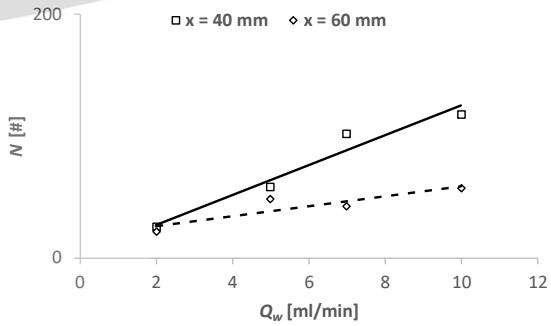


Fig. 3. Number of detected droplets at different water flow rates and downstream positions (y = 0 mm).

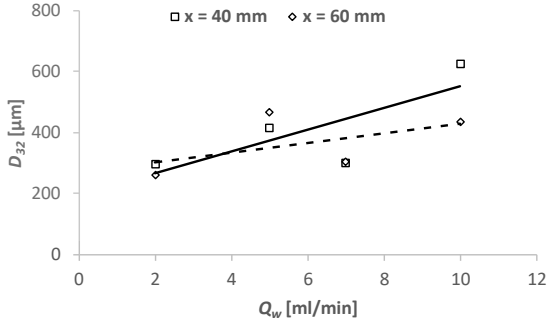


Fig. 4. Sauter mean diameter D_{32} at different water flow rates and downstream positions (y = 0 mm).

3.2 The airfoil angle effect investigation

Subsequently, the influence of the airfoil angle of inclination was investigated under the conditions defined in Table 4. The mean stagnation temperature T_0 and pressure p_0, together with their standard deviations, are presented to demonstrate the repeatability of the operating conditions between measurement runs performed on different days. The pressure ratio p_s/p_0 is also provided. The stagnation pressure p_0 increases from 102.2 kPa (α = −5°) to 103.2 kPa (α = 5°), and the pressure ratio from approximately 0.965 to 0.97. Because p_s/p_0 approaches unity, the corresponding Mach number decreases from about 0.23 to 0.21 and the dynamic pressure falls by roughly 13%. For a constant critical Weber number, where $d_{max} \sim \sigma/(\rho U^2)$, this corresponds to an increase of about 15% in the maximum droplet diameter introduced into the bulk flow. The differences in operating conditions must therefore be taken into account when interpreting the influence of α on droplet formation.

Table 4. The measurement conditions.

α [°]	T_0 [°C]	p_0 [kPa]	p_s/p_0 [–]
−5	21.4 ± 1.4	102.2 ± 0.1	0.96–0.97
0	20.7 ± 1.3	102.4 ± 0.4	0.96–0.97
5	18.7 ± 1.5	103.2 ± 0.2	0.97

The results are presented in Table 5 and Table 6. Table 5 lists the Sauter mean diameter D_{32} and the Weber number We_{32} at the individual positions y as the mean ± standard deviation of three measurement runs,

together with the total number of detected droplets Σ*N*. The Weber number was evaluated according to Eq. (1):

$$\mathrm{We}_{32} = \frac{2D_{32}p_0(1-p_s/p_0)}{\sigma} \quad (1)$$

Table 6 summarises the results for each inclination angle, obtained from all droplets detected at the individual positions. The same pooled approach was used for Fig. 5, where We_{32} was calculated as the d^2-weighted mean of the Weber numbers of all droplets at a given position, according to Eq. (2):

$$\mathrm{We}_{32} = \frac{\Sigma \mathrm{We}(d)d^2}{\Sigma d^2} \quad (2)$$

Since the number of droplets per run is small, pooling provides a larger statistical sample, so the values in Table 5 and Fig. 5 differ slightly, while the trends are consistent.

The overall results (Table 6) show that D_{32} increases with α from 353 µm ($\alpha = -5°$) through 369 µm ($\alpha = 0°$) to 388 µm ($\alpha = 5°$), by approximately 10%. This is consistent in direction and magnitude with the 15% increase in the maximum droplet diameter estimated from the decrease in dynamic pressure (Table 4). In contrast, We_{32} remains almost constant (33.6–35.1) because the increase in droplet size is compensated by the decrease in dynamic pressure. The large difference between D_{10} (≈100 µm) and D_{32} (350–390 µm) shows that the droplet size distribution is broad and that the volume is dominated by a small number of large droplets. The spatial distribution of We_{32} (Table 5, Fig. 5) shows that, for $\alpha = -5°$ and 0°, We_{32} is highest in the central part of the measured range ($y \approx -5$ to 5 mm, $We_{32} \approx 30$–38) and decreases towards the edges ($y = \pm 10$ mm, $We_{32} \approx 26$–28), where the fewest droplets were detected. For $\alpha = 5°$, no such systematic profile is observed.

Table 5. The results of individual measurements.

α [°]	y [mm]	n [#]	ΣN [#]	D_{32} [µm]	We_{32} [–]
−5	−10	3	39	242 ± 79	23.0 ± 7.6
	−5	3	109	278 ± 114	26.9 ± 11.3
	0	3	262	331 ± 58	31.8 ± 5.8
	5	3	222	407 ± 81	38.3 ± 8.6
	10	3	56	261 ± 85	24.2 ± 8.4
0	−10	3	84	296 ± 48	27.5 ± 2.3
	−5	3	278	381 ± 75	36.5 ± 6.8
	0	3	272	367 ± 37	34.6 ± 6.1
	5	3	169	378 ± 79	35.8 ± 8.5
	10	3	72	271 ± 57	26.3 ± 5.4
5	−10	3	63	409 ± 166	35.0 ± 13.5
	−5	3	101	288 ± 62	25.2 ± 5.6
	0	3	81	333 ± 162	30.4 ± 15.1
	5	3	49	263 ± 119	21.8 ± 8.3
	10	3	33	353 ± 155	31.2 ± 14.9

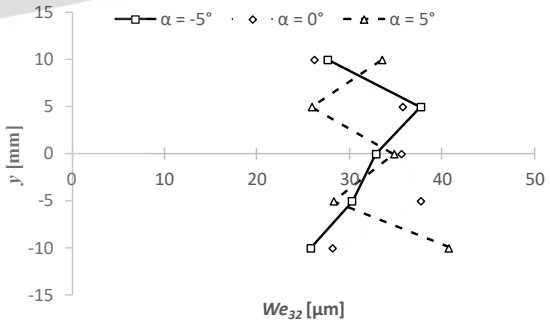


Fig. 5. The spatial distribution of We_{32}.

Table 6. The results for the different angles.

α [°]	N [#]	D_{32} [µm]	D_{10} [µm]	SD [µm]	We_{32} [–]
−5	688	353.35	100.47	114.96	33.56
0	875	368.90	97.20	114.63	35.05
5	327	388.03	101.70	118.77	33.61

The relative mass distribution of the droplets along y is shown in Fig. 6 for droplets with We ≤ 13 and in Fig. 7 for droplets with We > 13, with We calculated from the global conditions, not the local velocities. Droplets with global We > 13 would break up in the bulk flow field, but can survive in the wake behind the trailing edge. The relative mass m is the mass of droplets detected at a given position, expressed as a percentage of the total mass of droplets detected for the given α. Droplets with We > 13 carry the great majority of the mass (approx. 96–97%, Fig. 7), while droplets with We ≤ 13 account for only about 3–4% (Fig. 6). The spatial distribution depends clearly on the inclination angle. For $\alpha = -5°$, the mass is concentrated in the upper part of the measured range, with a maximum at $y = 5$ mm (approx. 40%) and a steep decrease towards negative y (approx. 3% at $y = -10$ mm). For $\alpha = 0°$, the distribution is broader and more symmetric, with its maximum at $y \approx 0$ mm (approx. 37%). For $\alpha = 5°$, the distribution is reversed: the highest share is found at $y = -10$ mm (approx. 38%), and it decreases towards positive y (approx. 9% at $y = 10$ mm).

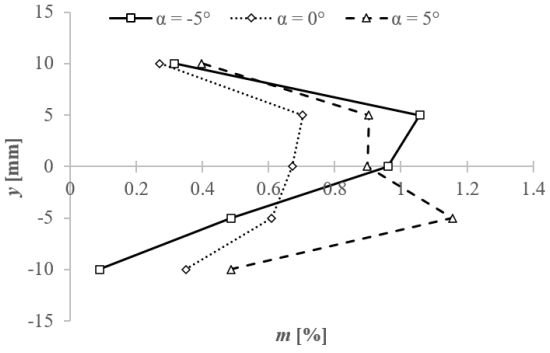


Fig. 6. The relative mass distribution for droplets with We ≤ 13.

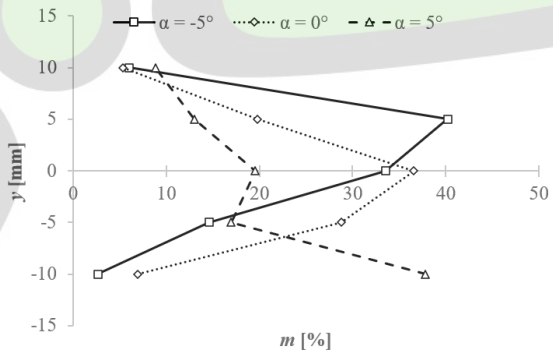


Fig. 7. The relative mass distribution for droplets with We_{32} > 13.

The droplet size distributions, obtained from all droplets detected at the individual positions, are shown in Fig. 8 (number-based) and Fig. 9 (volume-based). The number distribution is nearly identical for all three inclination angles. No droplets are detected below approximately 8 µm, which corresponds to the lower detection limit of the measurement. Owing to the small number of large droplets, the volume distribution is noisy at $d > 0.3$ mm.

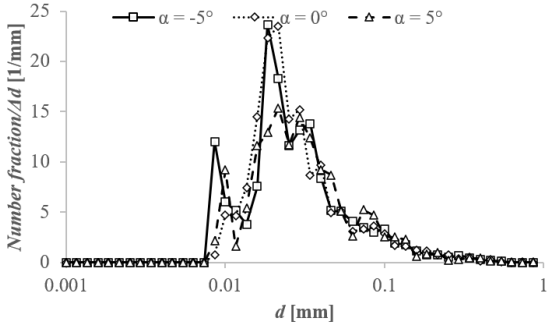


Fig. 8. The number-based distributions for different angles.

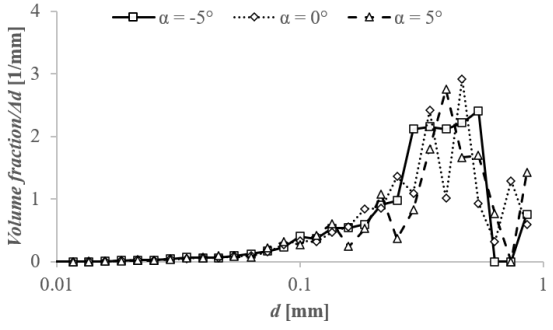


Fig. 9. The volume-based distributions for different angles.

The relationship between the characteristic diameters and the width of the droplet size distribution is shown in Fig. 10. For a distribution with mean D_{10}, standard deviation SD and skewness $\gamma = \mu_3/SD^3$, the ratio D_{32}/D_{10} depends only on the coefficient of variation CV = SD/D_{10} and on γ:

$$\frac{D_{32}}{D_{10}} = \frac{1+3CV^2+CV^3\gamma}{1+CV^2} \qquad (3)$$

For a lognormal distribution, this reduces to $D_{32}/D_{10} = (1 + CV^2)^2$, and for a gamma distribution ($\gamma = 2CV$) to $D_{32}/D_{10} = 1 + 2CV^2$. The approximate Sauter mean diameter can then be estimated according to Eq. (4).

$$D_{32} \approx D_{10} + 2\frac{SD^2}{D_{10}} \qquad (4)$$

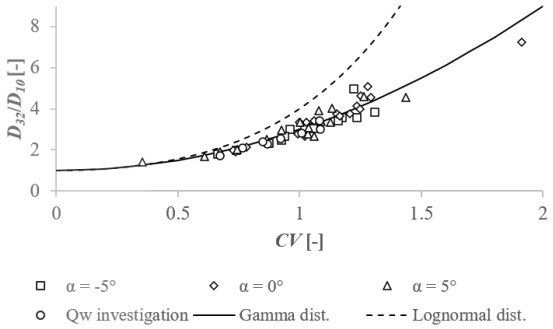


Fig. 10. Dependence of D_{32}/D_{10} on the coefficient of variation CV, compared with the gamma and lognormal distributions.

All measured data ($n = 58$, CV ≈ 0.35–1.9) collapse onto a single curve that follows the gamma relation ($R^2 = 0.89$, RMSE = 0.34), while the lognormal relation overestimates D_{32}/D_{10} for CV ≳ 0.8. This means that the shape of the size distribution is practically the same for all inclination angles, positions and operating conditions, and that these factors only shift the points along the curve through the width of the distribution. It should be noted that the agreement indicates consistency of the data with a gamma-type distribution, not proof of it.

4 Discussion

The overall Sauter mean diameter increased by about 10% with increasing angle of attack (Table 6), while the global Weber number We_{32} remained almost constant. This is consistent with the decrease of the dynamic pressure by about 13%, caused by the slightly higher pressure ratio at larger angles (Table 4), and with the Weber-number-like scaling found in [8]. The effect of the angle on D_{32} therefore cannot be separated from the effect of the changed operating point of the tunnel. The situation is made more sensitive by the steep dependence of D_{32} on the pressure ratio close to unity: a change of p_s/p_0 by 0.005, which is comparable to the uncertainty of the present measurement, changes the dynamic pressure by about 14%, i.e., by an amount comparable to the whole observed effect.

An important aspect of this study is the distinction between the Weber number computed from the local velocity of the droplet (local Weber number) and the global Weber number, related to the measured pressure drop in the wind tunnel and used here for a direct comparison between the slightly different conditions of the runs. Since the global Weber number is based on the bulk velocity upstream of the airfoil, it takes higher values than the critical Weber number commonly related to local droplet velocities. The values of We_{32} and the threshold We = 13 used in Figs. 6 and 7 should therefore be understood as a relative measure of droplet size normalised by the aerodynamic conditions, not as a breakup criterion.

The angle of attack also changes the local flow. The maximum of the mass distribution moved from y = 5 mm at $\alpha = -5°$ through $y \approx 0$ mm at $\alpha = 0°$ to y = −10 mm at $\alpha = 5°$.

Despite the changes in the spray position and in D_{32}, the number-based and volume-based size distributions show no clear differences between the angles, and the ratio D_{32}/D_{10} follows the gamma relation for all conditions (Fig. 10). The present data are limited by the small number of droplets (33–278 per position), a single downstream distance and a single water flow rate. The difference in D_{32} between the angles (about 10%) is of the same order as the scatter between positions, and its significance was not tested. To separate the effect of the angle from the effect of the pressure ratio, the model of [8] should be fitted separately for each angle using measurements over a wide range of pressure ratios. Phase Doppler anemometry would increase the number of detected droplets.

5 Conclusions

This paper follows the approach of previous research, in which the formation of coarse droplets is assumed to depend on global parameters, such as the pressure drop, and on local parameters, such as the wake structure. The previous semi-empirical model, which predicts the droplet size from the pressure ratio, was restricted to one experimental geometry. This paper presents preliminary data aimed at generalising the model by changing the experimental geometry. Three angles of inclination of the airfoil ($\alpha = -5°$, 0° and 5°) were investigated 40 mm downstream of the trailing edge, using image analysis, under similar pressure drop and water flow rate conditions. The results show clear differences in the spatial mass distribution between the angles, whereas the overall number-based and volume-based size distributions show no clear differences. Finally, the gamma distribution provided a useful approximation of the relation between D_{32}, D_{10} and SD.

Future work will focus on a broader range of inclination angles, air velocities, axial distances and water flow rates, combined with suitable wake parameters from CFD and experiments, in order to further generalise the proposed semi-empirical model.

The authors thank the Czech Technical University in Prague for the financial support provided by grant No. SGS24/127.

References

1. M. Kolovratnik, O. Bartoš, Experimental investigation of the steam wetness in a 1000 MW steam turbine, EPJ Web Conf. **114**, 02056 (2016). https://doi.org/10.1051/epjconf/201611402056
2. G.C. Jun, M. Hoznedl, M. Kolovratnik, Numerical simulations and experimental research into the genesis of the liquid phase of wet steam in the low-pressure part of a steam turbine, in Proceedings of the ASME Turbo Expo 2026, Milan, Italy, June 15–19, 2026, V006T20A016 (ASME, 2026). https://doi.org/10.1115/GT2026-178985
3. O. Bartoš, A. Huněk, An experimental analysis of droplet charging in a wind tunnel, EPJ Web Conf. **264**, 01002 (2022). https://doi.org/10.1051/epjconf/202226401002
4. O. Bartoš, A. Huněk, P. Antoš, A study of the coarse droplet formation from the liquid film in steam turbines, EPJ Web Conf. **299**, 01001 (2024). https://doi.org/10.1051/epjconf/202429901001
5. S. Tabata, S. Senoo, Safiullah, V. McDonell, Hybrid Eulerian-Lagrangian simulation of wall film and secondary droplet breakup in wet steam turbine stage, in Proceedings of the ASME Turbo Expo 2026, Milan, Italy, June 15–19, 2026, V006T20A013 (ASME, 2026). https://doi.org/10.1115/GT2026-178348
6. K. Murakami, Y. Kamada, Z. Wang, C. Inoue, Hot shear flows promote instabilities of liquid wall films, Int. J. Heat Mass Transf. **255**, 127783 (2026). https://doi.org/10.1016/j.ijheatmasstransfer.2025.127783
7. Safiullah, V. McDonell, S. Tabata, S. Senoo, Investigation of liquid film atomization from the trailing edge of an airfoil in a high-speed flow – effect of trailing edge thickness, J. Eng. Gas Turbines Power **148**, 1–18 (2025). https://doi.org/10.1115/1.4069583
8. A. Huněk, O. Bartoš, M. Hoznedl, Experimental study of coarse droplets formed from a liquid film under the conditions of the last stages of a steam turbine, in Proceedings of the ASME Turbo Expo 2026, Milan, Italy, June 15–19, 2026, V006T20A007 (ASME, 2026). https://doi.org/10.1115/GT2026-176747

Experimental investigation of a pyramid solar still enhanced with paraffin wax and natural sand for enhanced freshwater productivity

Tawfiq Chekifi [1*], *Reski Khelifi*[1], *Mebrouk Adouane*[2], *Ahmed Hamada*[1], *Khaled Touafek*[1]

[1] Unité de Recherche Appliqué en Energies Renouvelables, URAER, Centre de Développement des Energies Renouvelables, CDER, 47133, Ghardaïa, Algeria
[2] Renewable Energy and Energy Efficiency Program, Energy and Building Research Center, Kuwait Institute for Scientific Research, Safat, Kuwait

Abstract. This study evaluates the performance enhancement of a pyramid-type solar still using natural sand (sensible heat storage) and paraffin wax (PCM) in the hyper-arid climate of Ghardaïa, Algeria. Four configurations were tested: conventional pyramid solar still without insulation (CPSS-NoINS), with insulation (CPSS-INS), sand-assisted (PSS-S), and PCM-assisted (PSS-PCM). Results show that combining thermal insulation with heat storage significantly boosts performance. The PCM system performed best, maintaining basin water temperatures above 65 °C during peak hours and releasing latent heat at night, achieving a daily productivity of 10.4–13.2 L/m²·day (≈30% higher than the insulated conventional still) and thermal efficiency of 24–27%. The sand-assisted still also improved output to 7.2–10.0 L/m²·day through sensible heat storage.

1 Introduction

Various technologies have been developed to produce freshwater from non-conventional sources, even in geographically or chemically constrained environments. These include reverse osmosis, multi-stage flash desalination, electrodialysis, and other advanced separation processes. Among them, desalination has gained prominence as a rapidly expanding solution. In particular, solar distillation stands out as a sustainable, environmentally friendly, and cost-effective approach, especially suited for arid and remote regions. A solar still functions by harnessing solar energy to evaporate water, leaving behind impurities and salts, after which the vapor is condensed into potable freshwater. The overall efficiency of this process is governed by several key factors, including solar radiation intensity, basin water depth, evaporation and condensation rates, and thermal losses [1-3]. Researchers have investigated numerous enhancements to boost solar still performance, particularly through improved designs [4-7], auxiliary heating techniques [8-10] and heat storage materials [11-14]. These studies have focused on parameters such as water depth, solar irradiance, and the integration of components like fins, nanofluid [15-17] and phase change materials [8, 18, 19] to accelerate evaporation and condensation. Evaporation and condensation rates are directly affected by the available surface area. Pyramid solar stills offer a significantly larger condensation surface compared to conventional basin-type stills, resulting in markedly higher freshwater production [7]. Pyramid solar stills (PSS) are especially advantageous due to their expansive condensation area, ability to capture sunlight from multiple directions, and reduced shading effects. In their review of multi-slope solar stills with enhanced condensation surfaces. Patel and Modi [20] highlighted the square pyramid solar still (SqPSS) as a promising alternative to traditional designs. Its main strengths include a larger condensation surface, omnidirectional solar capture (eliminating the need for tracking), and minimal sidewall shading.

Several studies have explored various techniques to enhance the performance of pyramid solar stills. El-Sebaii and Khallaf [21] developed a fluid flow model for pyramid solar stills and validated it experimentally. Their results showed that increasing the condensing slope angle from 10° to 60° improved daily water productivity by approximately 0.2 L/m². Khelifi et al. [22] experimentally studied the performance enhancement of a pyramid solar still using natural gravel and volcanic pebbles as sensible thermal energy storage materials under the hyper-arid conditions of Ghardaïa, Algeria. The integration of thermal storage significantly improved freshwater productivity and thermal performance compared to the conventional system. Volcanic pebbles exhibited the best results, increasing distillate yield by 75% and achieving a thermal efficiency of 90% (versus 62% for gravel). Modi and Nay [23] examined a pyramid solar still enhanced with forced convection and phase change materials (PCM),

* Corresponding author: t.chekifi@cder.dz chekifi.tawfiq@gmail.com

achieving a significant 61.48% increase in distillate yield. In a follow-up study, In a recent experimental investigation, Patel et al. [24] evaluated the performance of a square pyramid solar still (SqPSS) using mono and hybrid nanofluids. Cu nanofluid outperformed Al_2O_3 in mono-nanofluid trials, delivering a total productivity of 1640 mL/m² and a diurnal efficiency of 17.00%. The best results were obtained with the Al_2O_3–Cu hybrid nanofluid at a 20:80 mixing ratio, yielding a maximum distillate output of 2644 mL/m² and a diurnal efficiency of 34.50%. This configuration provided a 27.41% improvement in efficiency and a 25.19% increase in water yield compared to conventional saline water. Taamneh and Kalpesh et al. [25] evaluated the performance of a triangular pyramid solar still enhanced with triangular cross-sectional aluminum hollow-fins and wool cloth wick-fins. For partially submerged fins, daily distillate output reached 2.5674 L/m² (12.36% increase) with hollow-fins and 2.5481 L/m² (11.51% increase) with wick-fins, compared to 2.2850 L/m² for the conventional still. With fully submerged fins, productivity was 2.2529 L/m² (9.00% increase) for hollow-fins and 2.3042 L/m² (11.49% increase) for wick-fins, relative to 2.0668 L/m² without fins. Efficiency improvements were 13.22% (hollow) and 15.70% (wick) for partially submerged fins, and 17.36% (hollow) and 29.34% (wick) for fully submerged fins, with wick-fins generally showing superior efficiency gains.

In this paper, a pyramid solar still (PSS) is experimentally investigated under the hyper arid climate of Ghardaïa, Algeria, a region characterized by extremely high solar irradiance, low relative humidity, and large diurnal temperature variations. These harsh conditions make Ghardaïa an ideal natural laboratory for testing solar desalination technologies, as water scarcity is a pressing challenge for both domestic and agricultural use. To enhance the performance of the PSS, two low cost and locally available materials (paraffin wax as a phase change material (PCM) and natural sand as a sensible heat storage medium) are integrated into the system. Comparative experiments are conducted on four configurations: Conventional Pyramid Solar Still CPSS-NoINS (without insulation), CPSS-INS (with insulation), PSS-S (with sand storage), and PSS-PCM (with paraffin wax PCM). The study aims to quantify improvements in distillate yield, basin water temperature stability, and overall thermal efficiency, while also evaluating the economic feasibility of these modifications for sustainable freshwater production in arid and semi arid regions.

2 Materials and methods

Identical pyramid solar stills (PSSs), each with a square base of 50 cm × 50 cm and a basin depth of 10 cm, were installed at the URAER research facility in Ghardaïa, Algeria. Each pyramid featured four transparent glass sides, 4 mm thick, inclined at approximately 48.7°, with a peak height of about 31.3 cm above the basin. The slant length of each glass side was roughly 39 cm, resulting in a condensation surface area of approximately 0.195 m² per side and a total effective condensation area of 0.78 m².

A black-coated aluminum basin is used to maximize solar absorption (Figure 1). To evaluate thermal performance, additional configurations were tested: PSS-INS (with insulation) and PSS-NoINS (without insulation). The modified stills incorporated 2 kg of thermal energy storage material, tested using either natural sand (PSS-S) or paraffin wax as phase change material (PSS-PCM). Temperatures were monitored using type-K thermocouples positioned in the basin water, on the basin plate, on the inner glass surfaces, and in the ambient air. Solar radiation intensity was recorded with a pyranometer, and the hourly freshwater output from each pyramid face was collected and measured using calibrated graduated cylinders.

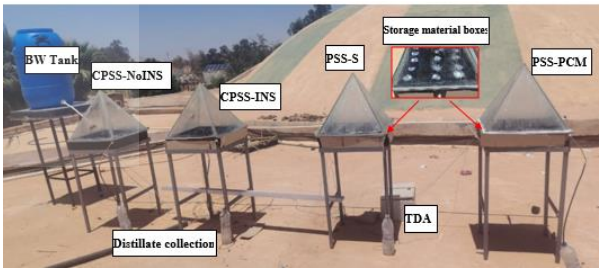


Fig. 1. Experimental setup with four pyramid solar stills: CPSS-NoINS, CPSS-INS, PSS-S, and PSS-PCM, connected to BW brackish water) Tank TDA (Thermocouple Data Acquisition).

The experimental setup included four pyramid solar stills with identical geometry: a 50 cm × 50 cm square base, 10 cm basin depth, peak height of 31.8 cm, and glass covers inclined at 48.7°. In PSS-S, the boxes were filled with natural sand (250 g per box, totaling 2 kg), providing sensible heat storage. In both PSS-S and PSS-PCM, the storage materials were enclosed in sealed aluminum containers placed inside the basin. Sand was used in PSS-S, whereas paraffin wax PCM was used in PSS-PCM. This setup maintained clear separation between the saline water and the storage media while enabling efficient heat transfer through the aluminum walls. All systems were oriented north–south to maximize solar exposure. The basins were made of black-coated aluminum to improve solar absorption, and 4 mm thick transparent glass covers served as condensation surfaces. Distillate was collected via channels along the lower edges of the glass.

3 The thermal efficiency

The thermal efficiency of a solar still indicates its effectiveness in converting solar energy into distilled water, a critical metric for evaluating its performance in water purification, especially in regions with scarce clean water resources. Improving thermal efficiency enables researchers and engineers to refine the still's design, boosting water output while reducing energy losses. The thermal efficiency (η) is calculated using the formula [26]

$$\eta_{d=}\frac{\sum \dot{m} \times h_{fg}}{A \times I \times t} \times 100 \qquad (1)$$

Where ṁ is the distillate production rate, h_fg is the latent heat of vaporization, A is the system area, and I is the solar radiation intensity and t is the total duration of operation (s). The latent heat of vaporization is given by:

$$h_{fg} = 2.501 \times 10^6 - 2.361 \times 10^3 T_w \qquad (2)$$

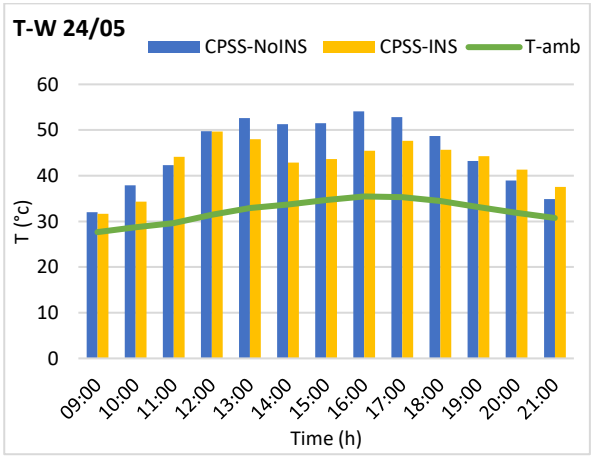
4 Results and discussion

4.1 Temperatures Evaluation

This section examines the thermal behavior of the pyramid solar stills under different configurations (CPSS-NoINS, CPSS-INS, PSS-S, and PSS-PCM). The evaluation focuses on the evolution of basin water temperature (T-W), basin plate temperature (T-B), and glass cover temperature (T-G) throughout the day. These parameters are critical for understanding evaporation–condensation dynamics and the influence of insulation and thermal storage materials on system performance.

4.1.1 Insulation effect

The comparison between CPSS-NoINS and CPSS-INS shows that insulation significantly reduces thermal losses. This improvement translates into higher evaporation rates and extended productivity, especially during windy conditions when uninsulated systems lose heat rapidly (figure 2).



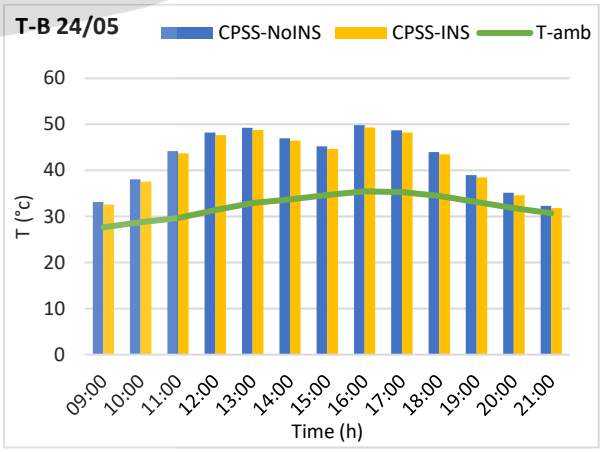
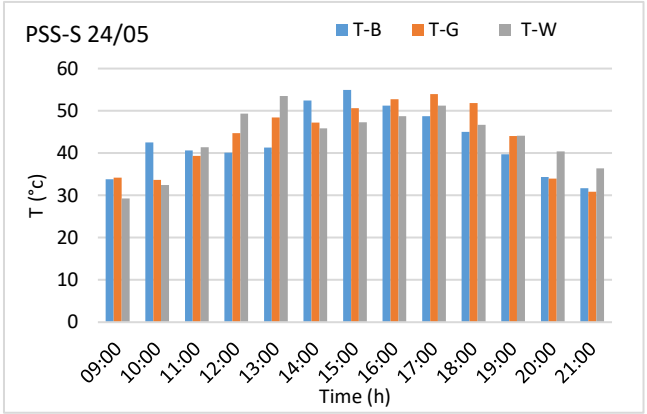


Fig. 2. Hourly evolution of basin water temperature (T-W) and basin plate temperature (T-B) for the conventional pyramid solar still without insulation (CPSS-NoINS) and with insulation (CPSS-INS), compared with ambient temperature (T-amb),

The comparison between the conventional pyramid solar still without insulation (CPSS-NoINS) and with insulation (CPSS-INS) shows that insulation consistently raised basin water temperatures by about **5–7 °C** throughout the day. For example, at midday (12:00), CPSS-INS reached **58–60 °C**, while CPSS-NoINS peaked at only **52–55 °C**. Basin plate temperatures followed the same trend, with CPSS-INS maintaining **~62 °C** compared to **~55 °C** in the non-insulated case. This improvement is due to reduced convective and conductive losses, resulting in higher evaporation rates and explaining the ~25% productivity gain observed in insulated systems. For that reason insulation has been considered for the three configuration (CPSS, PSS-S and PSS-PCM)

4.1.2 Pyramid solar still with sand

The sand-integrated system demonstrated smoother temperature profiles. Sand acted as a sensible heat medium, moderating fluctuations and stabilizing the thermal environment during peak solar hours (figure 3). However, after sunset, temperatures declined more quickly compared to PCM, limiting extended distillation.



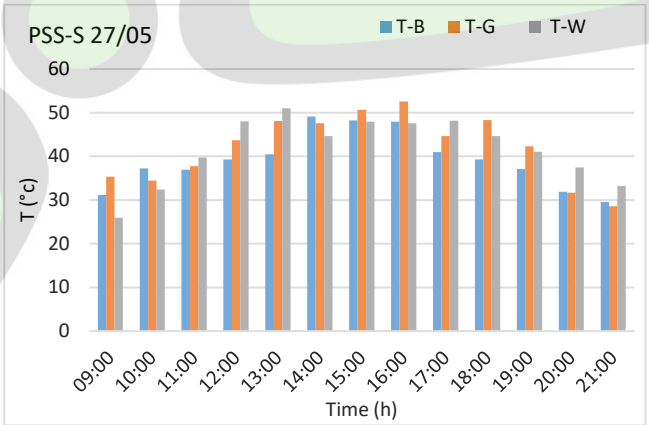


Fig. 3. Hourly basin water temperature (T-W) of PSS-S compared with the insulated conventional still (CPSS-INS) and ambient temperature (T-amb) on 24 May, and simultaneous evolution of basin plate temperature (T-B), inner glass cover temperature (T-G), and basin water temperature (T-W) for PSS-S.

The pyramid solar still with sand (PSS-S) exhibited smoother temperature profiles, with basin water temperatures peaking around 60–62 °C and basin plate temperatures reaching ~65 °C during peak solar hours (13:00–14:00). The sand acted as a sensible heat storage medium, absorbing heat during midday and releasing it gradually, which moderated fluctuations and stabilized the thermal environment. However, after sunset, temperatures declined more rapidly compared to PCM, dropping below 40 °C by 20:00, which limited extended distillation. This explains why PSS-S improved daytime stability but did not sustain productivity into the evening.

4.1.3 Pyramid solar still with PCM

The PCM-enhanced system exhibited superior heat retention. More importantly, PCM released latent heat during cooling periods, maintaining elevated temperatures into the evening (figure 4).

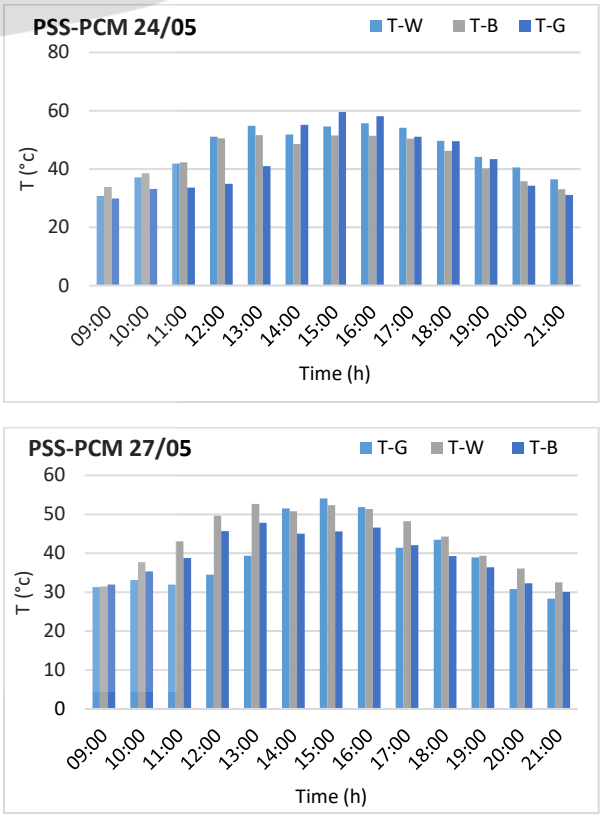
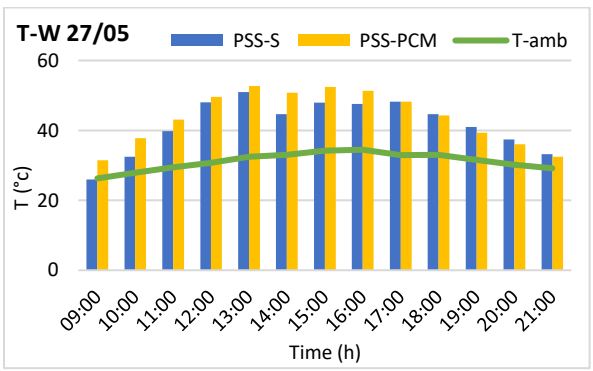


Fig. 4. Hourly basin water temperature (T-W) of PSS-PCM compared with the insulated conventional still (CPSS-INS) and ambient temperature (T-amb) on 24 May, and simultaneous evolution of basin plate temperature (T-B), inner glass cover temperature (T-G), and basin water temperature (T-W) for PSS- PCM.

The PCM-enhanced pyramid solar still (PSS-PCM) demonstrated superior heat retention, with basin water temperatures consistently exceeding 65 °C and basin plate temperatures reaching ~70 °C at midday. More importantly, PCM released latent heat during cooling, maintaining elevated temperatures of 50–55 °C even after 18:00, while other systems had already dropped below 45 °C. This extended the distillation process by 2–3 hours beyond sunset, resulting in cumulative yields up to 13 L/m²/day, about 30% higher than sand storage. The slower cooling curve confirms PCM's advantage in sustaining evaporation into nighttime hours.

4.1.4 PSS-S and PSS-PCM comparison



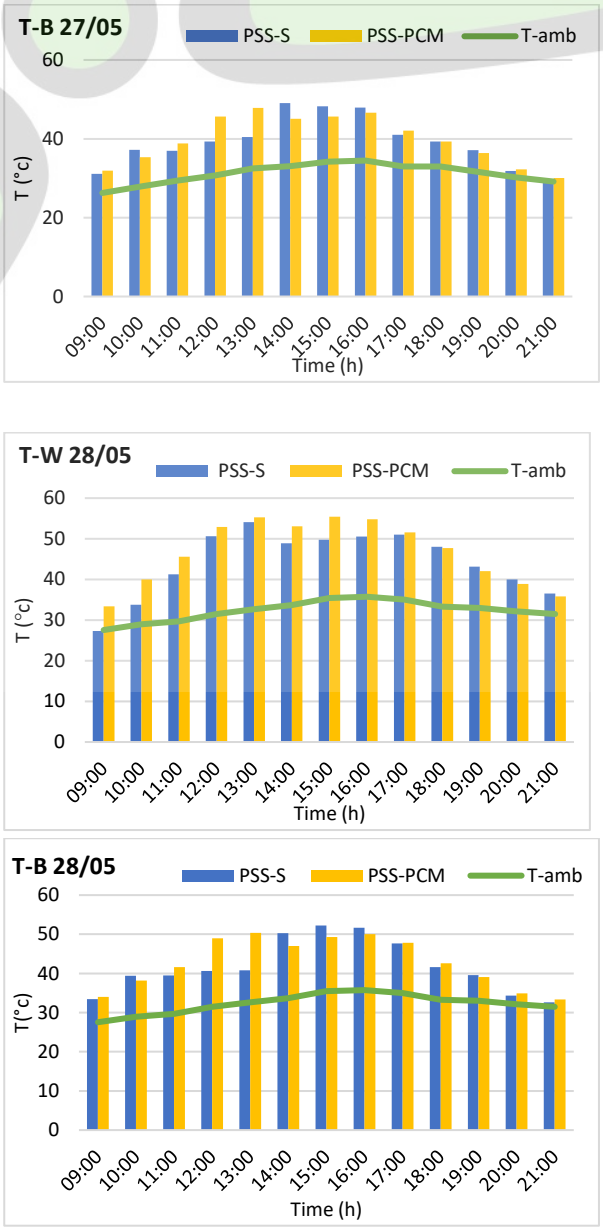


Fig. 5. Comparative hourly evolution of basin water temperature (T-W) and basin plate temperature (T-B) for the sand-assisted still (PSS-S) and the paraffin wax PCM-assisted still (PSS-PCM), alongside ambient temperature (T-amb), on three representative days: 27 and 28 May.

Figure 7 presents the hourly evolution of basin water temperature (T-W) and basin plate temperature (T-B) for the sand-assisted (PSS-S) and PCM-assisted (PSS-PCM) solar stills over three representative days (27, 28, and 30 May). During the morning, both systems showed similar heating behavior, with T-W rising from ~27–29 °C to 40–45 °C by 11:00, as the paraffin wax had not yet reached its melting point (57.3 °C). Divergence began near peak irradiance (>850 W/m²), where PSS-PCM exhibited a clear temperature plateau between 57–64 °C due to latent heat absorption during the solid-to-liquid phase transition. In contrast, PSS-S continued a steady temperature rise without any plateau. After 14:00, as solar irradiance decreased, cooling rates differed significantly. PSS-S cooled relatively quickly due to sensible heat release, while PSS-PCM maintained higher temperatures longer by releasing stored latent heat (≈351.6 kJ) during solidification. By 17:00, T-W in PSS-PCM was 4–6 °C higher than in PSS-S. After sunset (~18:00), the difference became more pronounced: PSS-PCM sustained T-W around 50–55 °C at 18:00 and ~50 °C at 20:00, compared to PSS-S dropping below 40 °C. This extended the productive distillation period by 2–3 hours, primarily explaining the ~30% higher productivity of the PCM-assisted system.

5 Distillation efficiency analysis

5.1 Productivity analysis

Productivity, measured as the volume of distilled freshwater produced. It is strongly influenced by climatic conditions and design parameters. In this study, four pyramid solar still configurations were tested: PSS-NoINS (no insulation), PSS-INS (with insulation), PSS-S (with sand storage), and PSS-PCM (with paraffin PCM storage). Daily freshwater yields were recorded over multiple consecutive days in the hyper-arid climate (figure 6).

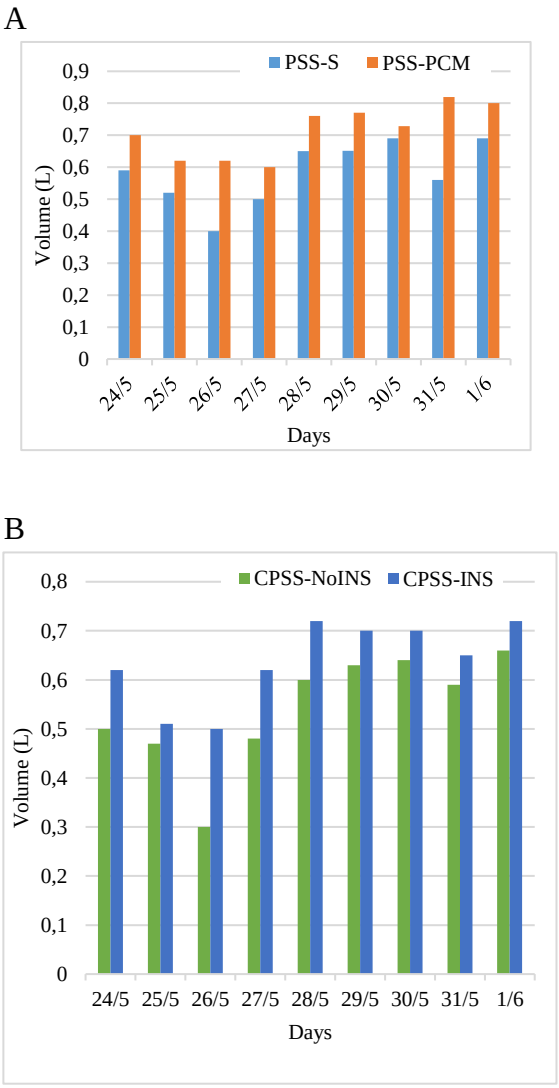


Fig. 6. Daily freshwater productivity of the pyramid solar stills: (A) comparison between PSS-S (sand storage) and PSS-

PCM (paraffin PCM storage); (B) comparison between PSS-NoINS (without insulation) and PSS-INS (with insulation).

The productivity results clearly demonstrate the benefits of both thermal storage and insulation in pyramid solar stills. Regarding thermal storage materials, the PSS-PCM consistently outperformed the PSS-S, achieving yields of 2.6–3.3 L/day compared to 1.8–2.5 L/day for the sand-based system (an improvement of approximately 30%). This superior performance is primarily due to the latent heat storage capacity of paraffin wax, which maintained basin water temperatures above 60–65 °C during peak hours, sustained distillation into the evening, and provided higher cumulative yields. In contrast, sand acted as a sensible heat storage medium, effectively moderating daytime temperature fluctuations and enhancing thermal stability, but its lower heat retention capacity limited productivity extension after sunset. Insulation also delivered significant gains. The PSS-INS produced 2.2–3.0 L/day, outperforming the non-insulated PSS-NoINS at 1.6–2.4 L/day, representing an average improvement of about 25%. This enhancement results from reduced thermal losses to the ambient environment, particularly noticeable under variable or windy conditions. The highest productivity was recorded in the PCM and insulated configurations, reaching up to 13 L/m²/day. These findings confirm that integrating latent heat storage (PCM) and insulation substantially boosts freshwater yield, offering an effective and sustainable solution for water production in arid regions. While PCM excels at extending operation beyond daylight hours, sand provides valuable daytime temperature regulation, highlighting their complementary roles.

5.2 Distillation performance

The daily efficiency of the Pyramid Solar Still (PSS) was calculated by comparing the total energy required for distillate production with the total solar energy incident on the basin area over the operating period from 09:00 to 21:00. Rather than using hourly values, the total solar input was determined using the daily average solar radiation multiplied by the basin area and the total operating time. This approach provides a single representative value for solar energy input, enabling a direct and comprehensive evaluation of the overall daily performance of both PSS-S and PSS-PCM configurations. It particularly highlights the contribution of sensible and latent heat storage in extending freshwater production beyond peak solar hours.

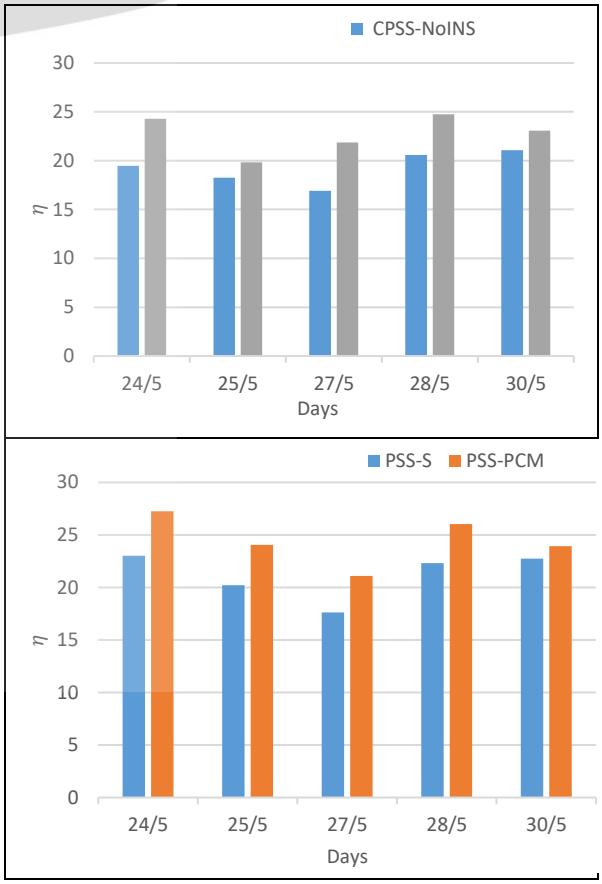


Fig. 7. Daily thermal efficiency of CPSS, PSS-S, and PSS-PCM over five days

Figure 7 presents the daily thermal efficiency of the four pyramid solar still designs: the conventional still without insulation (CPSS-NoINS), the insulated conventional still (CPSS-INS), the sand-assisted still (PSS-S), and the PCM-integrated still (PSS-PCM). The results clearly demonstrate the significant impact of insulation and thermal storage materials on overall system performance. The CPSS-NoINS configuration consistently exhibited the lowest efficiency, primarily because a large portion of the absorbed solar energy was lost through the uninsulated basin walls and bottom. Adding insulation in the CPSS-INS design effectively reduced conductive heat losses and improved energy utilization. However, without any thermal storage medium, its performance dropped noticeably after peak solar hours due to rapid cooling of the basin water. The incorporation of sand in the PSS-S configuration yielded a clear improvement over both conventional designs. Sand's favorable thermophysical properties (high density, moderate thermal conductivity, and reasonable specific heat capacity) enabled effective sensible heat storage during periods of high solar irradiance and gradual heat release as solar input decreased. This helped slow basin cooling, extend the evaporation phase, and maintain more uniform temperatures.

Nevertheless, sensible heat storage has inherent limitations compared to latent heat systems. The PSS-PCM configuration achieved the highest daily thermal efficiencies among all designs. This superior performance is due to the phase-change properties of the paraffin wax, which melts within the operating temperature range of the solar still (onset ≈57 °C, peak ≈62 °C). Excess thermal energy is stored as latent heat instead of causing excessive temperature spikes and is later released during solidification as solar radiation declines. Thanks to its high latent heat of fusion, the PCM maintained elevated basin water temperatures and a larger water–vapor temperature difference for longer periods, thereby prolonging evaporation and condensation well beyond peak sunshine hours. As a result, the PSS-PCM reached daily efficiencies of approximately 24–27%, substantially outperforming the sand-assisted and conventional systems.

5.3 Comparison with previous research

To contextualize the present study within the existing body of research, Table 3 compares the productivity and improvement rates of various solar still designs and modifications reported in prior literature. Researchers have investigated numerous enhancement techniques, such as nanofluid additives, basin modifications, external condensers, reflectors, and wicks. These approaches have produced notable gains in distillate output, with productivity improvements ranging from modest increases of around 6% to over 100% under optimal conditions. This variety of strategies reflects the continued efforts to address the limitations of conventional solar stills and boost freshwater production across different climatic settings.

Table 4. Comparison of the present work with previous studies on solar still designs, modifications, additives, productivity, and rate of improvement.

Design of SS	**Ref.**	**Modification/Additives**	**Productivity (Kg/m^2.day)**	**Rate increase (%)**
Tubular solar still	Kabeel et al. [29]	Wicks and v-corrugated basin	6.01	6.010
Single slope solar distiller	Elango et al. [30]	-0.1 wt% SnO_2 NF -0.1 wt% Al_2O_3 NF -0.1 wt% ZnO NF	0.805 0.935 0.750	18.62 29.95 12.67
Trays solar distiller	Abdullah et al. [31]	-Internal reflectors -Reflectors +CuOnano black paint -Reflectors +CuOnano black paint+CuOnano mixed PCM	3.45 4.10 5.00	57.00 70.70 108.0
Tubular solar still	Elshamy and El-said [32]	Hemi-circular v-corrugated basin	4.30	26.47
Single slope solar distiller	Johnstone Madhlopa [33]	External condenser	6.08	62.01
PSS-S PSS-PCM	Present work	- Local natural sand - Paraffin wax as a phase change material (PCM)	3.16 3.28	9.7 13.9

The table indicates that the present study's pyramid solar still configurations PSS-S and PSS-PCMachieved daily productivities of 3.16 and 3.28 kg/m²·day, corresponding to productivity increases of 9.7% and 13.9%, respectively. Although these values are lower than those obtained with advanced reflector-nanofluid hybrid systems, they remain significant given the use of simple, low-cost, and locally available materials. Nanofluid-based modifications (Elango et al. [30]) produced higher relative improvements, reaching nearly 30% with Al_2O_3. Reflector-based designs (Abdullah et al. [31]) delivered the most substantial gains, surpassing 100% when integrated with PCM. Similarly, geometric enhancements such as corrugated basins and external condensers yielded productivity increases ranging from 26% to 62%. By comparison, the sand- and PCM-enhanced pyramid solar stills provide more modest yet reliable gains. The sand-assisted system improved thermal stability through sensible heat storage, while the PCM-assisted system extended operational hours beyond sunset by releasing latent heat. Although the percentage improvements are smaller, the absolute productivity values (3.16–3.28 kg/m²·day) remain competitive with several more complex designs. Moreover, the simplicity of these modifications enhances reproducibility and scalability in hyper-arid environments. Overall, this analysis highlights that while high-tech solutions can achieve larger efficiency gains, integrating paraffin PCM and natural sand offers

a practical, affordable, and accessible pathway for freshwater production in regions where cost and material availability are key constraints.

6 Conclusion

An experimental investigation was carried out to assess the effects of thermal insulation, natural sand, and paraffin wax phase change material (PCM) on the performance of pyramid solar stills under the hyper-arid climatic conditions of Ghardaïa, Algeria. The main conclusions drawn from the results are as follows:

1. Thermal insulation substantially reduced heat losses from the basin, raising basin water temperatures by approximately 5–7 °C relative to the non-insulated configuration and yielding an average productivity increase of about 25%.
2. The addition of natural sand as a sensible heat storage medium enhanced thermal stability during daytime operation. The PSS-S configuration achieved freshwater yields of 1.8–2.5 L/day (7.2–10.0 L/m²·day), confirming the potential of low-cost, locally available materials for improving solar desalination performance.
3. The paraffin wax PCM demonstrated superior thermal storage performance through latent heat absorption and release. The PSS-PCM configuration maintained higher basin water temperatures during evening hours and extended the distillation process by approximately 2–3 hours beyond sunset.
4. Among the tested configurations, the PSS-PCM delivered the highest freshwater productivity, ranging from 2.6 to 3.3 L/day (10.4–13.2 L/m²·day), corresponding to an average improvement of approximately 30% over the conventional system.
5. The PCM-assisted configuration attained the highest daily thermal efficiency, reaching approximately 24–27%, due to more effective utilization of stored thermal energy and prolonged evaporation–condensation cycles.

In conclusion, the integration of thermal storage materials, particularly paraffin wax PCM, offers an effective approach for enhancing the productivity and operational stability of pyramid solar stills in arid environments.

References

[1] M. Edalatpour, K. Aryana, A. Kianifar, G. Tiwari, O. Mahian, and S. Wongwises, "Solar stills: A review of the latest developments in numerical simulations," *Solar Energy*, vol. 135, pp. 897-922, 2016.

[2] T. Chekifi, A. Benmoussa, and M. Boukraa, "Desalination Powered by Renewables: A Challenge and an AI Opportunity," *Water Resources Management*, pp. 1-43, 2024.

[3] T. Chekifi, A. Belaid, M. Boukraa, R. Khelifi, and M. Guermoui, "Solar still performance improvement: CFD insights and AI integration challenges," *International Journal of Energy and Water Resources*, pp. 1-26, 2025.

[4] S. V. Raj and A. M. Manokar, "Design and analysis of solar still," *Materials Today: Proceedings*, vol. 4, no. 8, pp. 9179-9185, 2017.

[5] K. Mukherjee and G. Tiwari, "Economic analyses of various designs of conventional solar stills," *Energy conversion and management*, vol. 26, no. 2, pp. 155-157, 1986.

[6] S. A. Mohiuddin, A. K. Kaviti, T. S. Rao, and V. S. Sikarwar, "Historic review and recent progress in internal design modification in solar stills," *Environmental Science and Pollution Research*, vol. 29, no. 26, pp. 38825-38878, 2022.

[7] P. V. Kumar, A. Kumar, O. Prakash, and A. K. Kaviti, "Solar stills system design: A review," *Renewable and sustainable energy reviews*, vol. 51, pp. 153-181, 2015.

[8] M. Al-harahsheh, M. Abu-Arabi, H. Mousa, and Z. Alzghoul, "Solar desalination using solar still enhanced by external solar collector and PCM," *Applied Thermal Engineering*, vol. 128, pp. 1030-1040, 2018.

[9] N. T. Alwan, S. E. Shcheklein, O. M. Ali, M. H. Majeed, and E. B. Agyekum, "Experimental and theoretical investigations of a modified single-slope solar still with an external solar water heater," *Sustainability*, vol. 13, no. 22, p. 12414, 2021.

[10] Z. Omara, A. Kabeel, and M. Younes, "Enhancing the stepped solar still performance using internal and external reflectors," *Energy conversion and management*, vol. 78, pp. 876-881, 2014.

[11] A. F. Abed, M. J. Alshukri, and D. M. Hachim, "Improving solar still performance via the integration of nanoparticle-enhanced phase change materials: a novel pyramid-shaped design with a numerical simulation approach," *Journal of Energy Storage*, vol. 97, p. 112980, 2024.

[12] R. Khelifi *et al.*, "Comparative performance analysis of hemispherical solar stills using date and olive kernels as heat storage material," *Scientific Reports*, vol. 15, no. 1, p. 7128, 2025.

[13] R. Khelifi, T. Chekifi, A. Zoukel, A. Belaid, M. Guermoui, and K. Touafek, "Experimental Study on Hemispherical Solar Still Performance Enhancement Using Aluminium and Galvanized Steel Floral Rings Inserts," *Journal of Renewable Energy and Environment*, 2025.

[14] R. Khelifi, T. Chekifi, E. R. di Schio, P. Valdiserri, and K. Touafek, "Experimental Evaluation of Hemispherical Solar Still Performance Using Aluminum and Galvanized Steel Floral Ring Inserts," in *2025 10th International Conference on*

Smart and Sustainable Technologies (SpliTech), 2025, pp. 1-6: IEEE.
[15] T. Chekifi and M. Boukraa, "Solar still productivity improvement using nanofluids: A comprehensive review," *International Journal of Ambient Energy*, no. just-accepted, pp. 1-103, 2023.
[16] S. Shoeibi, H. Kargarsharifabad, N. Rahbar, G. Ahmadi, and M. R. Safaei, "Performance evaluation of a solar still using hybrid nanofluid glass cooling-CFD simulation and environmental analysis," *Sustainable Energy Technologies and Assessments*, vol. 49, p. 101728, 2022.
[17] S. M. Parsa, A. Rahbar, M. Koleini, S. Aberoumand, M. Afrand, and M. Amidpour, "A renewable energy-driven thermoelectric-utilized solar still with external condenser loaded by silver/nanofluid for simultaneously water disinfection and desalination," *Desalination*, vol. 480, p. 114354, 2020.
[18] L. O. Afolabi *et al.*, "Experimental investigation of double slope solar still integrated with PCM nanoadditives microencapsulated thermal energy storage," *Desalination*, vol. 553, p. 116477, 2023.
[19] H. Ajdari and A. Ameri, "Performance assessment of an inclined stepped solar still integrated with PCM and CuO/GO nanocomposite as a nanofluid," *Journal of Building Engineering*, vol. 49, p. 104090, 2022.
[20] S. K. Patel and K. V. Modi, "Techniques to improve the performance of enhanced condensation area solar still: A critical review," *Journal of Cleaner Production*, vol. 268, p. 122260, 2020.
[21] A. El-Sebaii and A. E.-M. Khallaf, "Mathematical modeling and experimental validation for square pyramid solar still," *Environmental Science and Pollution Research*, vol. 27, no. 26, pp. 32283-32295, 2020.
[22] R. Khelifi *et al.*, "Experimental investigation of pyramid solar still performance enhanced by natural and volcanic pebbles-based thermal storage," *Environmental Progress & Sustainable Energy*, p. e70264, 2026.
[23] K. V. Modi and K. H. Nayi, "Efficacy of forced condensation and forced evaporation with thermal energy storage material on square pyramid solar still," *Renewable energy*, vol. 153, pp. 1307-1319, 2020.
[24] P. R. Patel, K. V. Modi, and S. K. Patel, "Experimental study of mono and hybrid nanofluids on square pyramid solar still," *Environmental Science and Pollution Research*, vol. 32, no. 2, pp. 693-724, 2025.
[25] K. V. Modi and A. R. Shah, "Effectiveness of partially and fully submerged triangular cross-sectional metal hollow-fins and wool cloth wick-fins on triangular pyramid solar still," *Environmental Science and Pollution Research*, vol. 29, no. 42, pp. 64040-64059, 2022.
[26] J. A. Duffie and W. A. Beckman, *Solar engineering of thermal processes*. John Wiley & Sons, 2013.
[27] M. Touil, N. Meftah, A. Achouri, R. Gheriani, and R. Benessedik, "MINERALOGICAL, PHYSICOCHEMICAL AND THERMAL INVESTIGATIONS OF TAIBET AND TENDLA SANDS MATERIAL FROM THE NORTHERN ALGERIAN SAHARA," *Acta Geodynamica et Geomaterialia*, vol. 20, no. 4, 2023.
[28] A. Luyt and I. Krupa, "Thermal behaviour of low and high molecular weight paraffin waxes used for designing phase change materials," *Thermochimica Acta*, vol. 467, no. 1-2, pp. 117-120, 2008.
[29] A. Kabeel, K. Harby, M. Abdelgaied, and A. Eisa, "Performance improvement of a tubular solar still using V-corrugated absorber with wick materials: Numerical and experimental investigations," *Solar Energy*, vol. 217, pp. 187-199, 2021.
[30] T. Elango, A. Kannan, and K. K. Murugavel, "Performance study on single basin single slope solar still with different water nanofluids," *Desalination*, vol. 360, pp. 45-51, 2015.
[31] A. Abdullah, F. Essa, H. B. Bacha, and Z. Omara, "Improving the trays solar still performance using reflectors and phase change material with nanoparticles," *Journal of Energy Storage*, vol. 31, p. 101744, 2020.
[32] S. M. Elshamy and E. M. El-Said, "Comparative study based on thermal, exergetic and economic analyses of a tubular solar still with semi-circular corrugated absorber," *Journal of cleaner production*, vol. 195, pp. 328-339, 2018.
[33] A. Madhlopa and C. Johnstone, "Numerical study of a passive solar still with separate condenser," *Renewable Energy*, vol. 34, no. 7, pp. 1668-1677, 2009.

Machine learning prediction of hourly urban NO_2 for air-quality management in decarbonising cities: A random forest approach with model-ladder evaluation

Michala Jakubcová[1,*]

[1]Institute of Thermomechanics of the Czech Academy of Sciences, Prague, Czech Republic

Abstract. Nitrogen dioxide (NO_2) is a key traffic- and combustion-derived pollutant, and its hourly prediction matters both for urban air-quality management and for verifying the effect of decarbonisation measures in cities. This study applies Random Forest (RF) regression to hourly NO_2 from 21 UK Automatic Urban and Rural Network (AURN) stations (January 2020–December 2025) covering rural background, urban industrial, and urban traffic sites. A four-step model ladder separates the sources of predictive skill: a persistence baseline; multiple linear regression (MLR); an RF that use only meteorological and temporal predictors; and an RF that additionally uses NO_2 lagged by 1 and 24 hours. The lagged RF reaches a mean test R^2 of 0.838 (range 0.701–0.928; RMSE 0.8–8.7 $\mu g\,m^{-3}$) and outperforms persistence (R^2 = 0.791) at all 21 stations, reducing the mean squared error by 21% on average. Without lags, the RF still explains 43% of the test variance (R^2 = 0.426) from meteorology and the emission time cycle alone. Permutation importances are physically consistent: hour of day dominates at traffic sites and the west–east wind component at rural sites. Because it separates weather-driven from emission-timing variability, the lag-free model is a candidate tool for attributing concentration changes to decarbonisation measures.

1 Introduction

Nitrogen dioxide (NO_2) is a regulated primary pollutant with direct health effects and a role in tropospheric ozone and secondary aerosol formation [1, 2]. In cities, road transport is the dominant source, while industrial facilities (steelworks, petrochemical plants, power generation) produce elevated concentrations at industrial sites. The UK Air Quality Strategy limits the annual mean to 40 $\mu g\,m^{-3}$ and allows 18 hourly exceedances of 200 $\mu g\,m^{-3}$ per year [3], so accurate short-term prediction has direct regulatory relevance. It also matters for decarbonisation: as transport electrifies and low-emission zones expand, robust tools are needed both to forecast episodes and to verify that interventions actually deliver cleaner air rather than merely shifting emissions in space or time [4, 5].

Traditional deterministic approaches such as Gaussian dispersion and photochemical transport models, grounded in boundary-layer meteorology [6], require detailed emission inventories and still exhibit substantial bias at individual receptor locations; the photochemical variants are also computationally expensive. Data-driven approaches, particularly tree-ensemble methods such as Random Forests (RF) [7], have emerged as competitive alternatives for station-level prediction because they can learn complex nonlinear interactions between meteorological drivers and source emissions without explicit mechanistic parameterisation [9, 10]. RF models have been applied successfully to $PM_{2.5}$, PM_{10}, O_3, and NO_2 prediction, achieving R^2 values of roughly 0.7–0.9 in hourly-resolution studies [9–11].

Machine-learning approaches to ambient NO_2 prediction span a wide range of complexity. Tree-ensemble methods trained on meteorological and temporal predictors are widely used for meteorological normalisation, i.e. for separating emission-driven from weather-driven variability [9, 11], while deep-learning architectures (convolutional, recurrent, and attention-based networks) are applied to multi-station forecasting and typically include lagged concentrations among their inputs [10]. A widely recognised limitation of such autoregressive models is the dominance of lag features: the previous-timestep observation captures the strong temporal autocorrelation of hourly concentrations, can account for most of the explained variance, and thereby masks the contribution of meteorological and source-related predictors [10, 11]. The reported skill is therefore rarely decomposed into the part attributable to meteorological or diurnal learning and the part inherited from autocorrelation.

This paper makes that decomposition explicit with a structured model-ladder evaluation across 21 AURN stations spanning three site typologies. I train four progressively more informed models, namely persistence, multiple linear regression (MLR), RF without lags, and RF with autoregressive lag terms, on the same chronological train/test split and compare them on identical held-out periods. This makes it possible to (a) quantify the skill attributable to meteorological and temporal features alone, (b) characterise

*e-mail: michala.jakubcova@it.cas.cz

how much the lag terms add on top, and (c) interpret feature importances from the lag-free RF without distortion from the persistence signal. The study covers January 2020 to December 2025, a period that includes the COVID-19 mobility restrictions of 2020–2021 and thus spans an unusually broad range of emission conditions [4, 5]. The decomposition also has a practical decarbonisation dimension: separating weather-driven variability from emission-timing variability is what is required to attribute concentration changes to genuine emission reductions (for example from vehicle electrification or low-emission zones) rather than to favourable dispersion.

2 Data and Study Sites

2.1 Monitoring Network

Hourly NO_2 measurements were downloaded from the UK Automatic Urban and Rural Network (AURN) with the `importAURN` function of the `openair` R package [12] for the period January 2020 to December 2025. The AURN is the UK's primary ambient air-quality monitoring network. Its data are quality-assured by the network operator: instruments are routinely calibrated, and the data are validated under the quality requirements of EU Directive 2008/50/EC, with values judged invalid released as missing. Twenty-one stations were selected (Fig. 1) to represent three site typologies defined in the Defra classification scheme [3]:

Rural background (n = 7) — sites not directly influenced by local emission sources, representative of background regional air quality: Bush Estate, Charlton Mackrell, Rochester Stoke, Narberth, Glazebury, Aston Hill, Yarner Wood.

Urban industrial (n = 7) — sites adjacent to or downwind of major industrial facilities: London Harlington, Port Talbot Margam (steel), Scunthorpe Town (steel), Grangemouth Moray and Grangemouth (petrochemical), Liverpool Speke, Billingham (chemical).

Urban traffic (n = 7) — roadside sites primarily influenced by road transport: Portsmouth Anglesea Road, Cardiff Newport Road, Coventry Binley Road, York Fishergate, Nottingham Western Boulevard, Belfast Stockman's Lane, Glasgow High Street.

Data completeness varied between 72% and 98% depending on station and year. Hours with missing NO_2, wind or temperature were removed, as were physically implausible values ($NO_2 < 0$ or $\geq 500\ \mu g\ m^{-3}$, wind speed ≥ 50 m s^{-1}). All timestamps are in UTC.

2.2 Meteorological Predictors

Concurrent hourly meteorological variables were taken from the same AURN data files: wind speed (m s^{-1}), wind direction, and air temperature (°C). These are not measured at the monitoring sites; they are modelled values for each site from the Weather Research and Forecasting (WRF) model operated by Ricardo Energy & Environment and distributed with the UK-AIR data [12]. Wind speed U and direction θ (the direction the wind blows from) were converted to the eastward and northward components

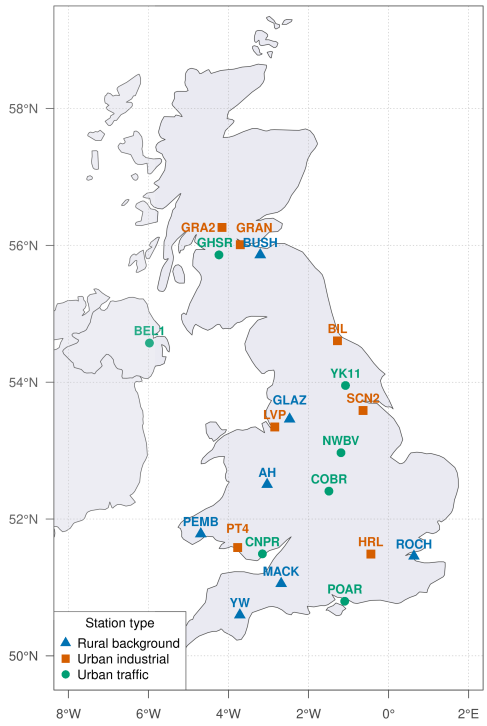


Figure 1. Monitoring stations used in this study (n = 21), coloured by site typology: rural background, urban industrial, urban traffic.

$u = -U \sin\theta$ and $v = -U \cos\theta$. Decomposition into u/v components preserves directional continuity (avoiding the 0°/360° discontinuity) and lets the RF learn directional source patterns without explicit sector encoding.

2.3 Feature Engineering

Temporal features were encoded cyclically to preserve circular continuity. Hour of day h (0–23) was encoded as $\sin(2\pi h/24)$ and $\cos(2\pi h/24)$; month of year m (January = 1, December = 12) as $\sin(2\pi m/12)$ and $\cos(2\pi m/12)$. Mapping each cyclic variable onto a sine/cosine pair avoids the artificial discontinuity of a raw integer scale (e.g., 23 h and 0 h, or December and January, being maximally distant numerically while being adjacent in reality). A binary weekend indicator (Saturday–Sunday = 1, Monday–Friday = 0) captures reduced road-traffic activity on non-work days.

Autoregressive features consist of NO_2 at lag 1 hour (`no2_lag1`) and lag 24 hours (`no2_lag24`). The lags are obtained by shifting each station's hourly record, in which missing hours are kept as missing values; a lag is therefore missing whenever the corresponding earlier hour is missing, and such rows are removed rather than bridged across data gaps. Because rows without valid lags are removed for all models, every model at a station is trained and tested on exactly the same hours. The final feature set therefore comprises nine met/temporal predictors (wind speed, u, v, temperature, hour sin/cos, month sin/cos, weekend) plus the two lags.

3 Exploratory Data Analysis

3.1 Temporal Trends and Seasonal Patterns

Figure 2 shows monthly-mean NO_2 concentrations by site group over the full study period. Urban traffic sites consistently show the highest concentrations (monthly means 15–35 $\mu g\,m^{-3}$), followed by urban industrial sites (8–23 $\mu g\,m^{-3}$) and rural background sites (3–10 $\mu g\,m^{-3}$). All site types exhibit a clear seasonal cycle with winter maxima and summer minima, consistent with increased domestic heating, shallower and more stable winter boundary layers [6], and reduced photolysis rates in winter. Spring 2020 traffic-site concentrations (about 15–16 $\mu g\,m^{-3}$) are among the lowest of the record, consistent with the COVID-19 lockdown (March–May 2020), when national road traffic fell by roughly 60–70% [4, 5]; however, similarly low spring values recur in 2025, so monthly means alone do not isolate the lockdown effect. Monthly-mean wind speed (dashed line) is also highest in winter, so at the monthly scale the seasonal cycles of wind and NO_2 co-vary rather than oppose each other. The expected dilution effect of wind acts on hourly to daily time scales and is resolved by the models (Section 5.4) rather than in monthly means.

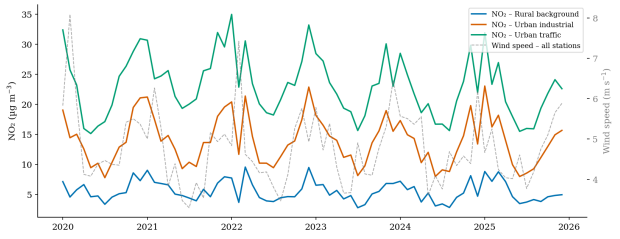


Figure 2. Monthly-mean NO_2 concentrations ($\mu g\,m^{-3}$) by site group (left axis) and mean wind speed across all stations (right axis, dashed).

3.2 Diurnal Profiles

Figure 3 presents mean diurnal NO_2 profiles by site group. Urban traffic sites exhibit a pronounced bimodal pattern with a morning peak at 07:00–08:00 UTC and a second, broader peak at 17:00–18:00 UTC, corresponding to the two commute periods; the night-time minimum (about 12 $\mu g\,m^{-3}$ at 02:00–03:00 UTC) remains well above rural levels. Urban industrial sites show the same bimodal timing, with a morning peak at 07:00 UTC (about 18 $\mu g\,m^{-3}$) of similar height to the evening maximum, but at a lower level and with a smaller day–night contrast, consistent with continuous industrial emissions superposed on traffic from nearby roads. Rural background sites show minimal diurnal variation (amplitude $\approx 2\ \mu g\,m^{-3}$), indicating that local primary emissions are negligible and that the observed variation reflects transported background NO_2. Because timestamps are in UTC, local commute peaks shift by one hour between winter (GMT) and summer (BST), which slightly broadens the mean peaks.

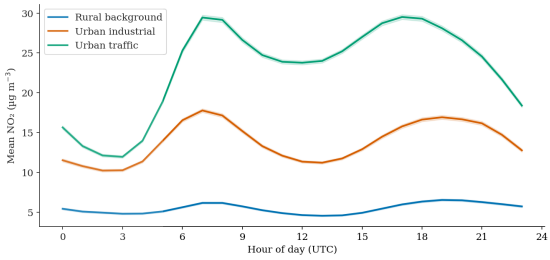


Figure 3. Mean diurnal NO_2 profiles by site group over the full study period.

4 Methods

4.1 Model Ladder Design

To disentangle the contributions of process information and temporal autocorrelation, I train four models at each station using an identical chronological 80/20 train/test split of that station's valid hourly records. Because the split is by record count, the test period starts between October and December 2024 depending on data completeness and runs to the end of 2025:

Persistence baseline: The simplest possible forecast: the predicted value for hour t equals the observation at hour $t-1$ (`no2_lag1`). No training is required. This establishes the lower bound of useful skill that any trained model must exceed.

Multiple Linear Regression (MLR, process features only): An ordinary least-squares linear regression on met/temporal features only (wind speed, u/v components, temperature, hour sin/cos, month sin/cos, weekend flag). Inputs are standardised. This establishes a linear process baseline with no autoregressive information.

Random Forest, process features only (RF_{nl}): An RF on the same lag-free feature set. This reveals the non-linear skill achievable from meteorological and temporal information alone — the "process" contribution of the model.

Random Forest with autoregressive lags (RF_{lag}): An RF on the full feature set including `no2_lag1` and `no2_lag24`. This is the best-performing station-specific model. The difference between RF_{lag} and RF_{nl} quantifies the marginal value of the autoregressive terms given the met/temporal features.

All models use modelled meteorology concurrent with the predicted hour. The set-up therefore corresponds to a one-hour-ahead nowcast with known weather; an operational forecast would use numerical weather prediction output, whose errors would lower the skill reported here.

4.2 Random Forest Configuration

All RF models use scikit-learn's `RandomForestRegressor` [14]. Hyperparameters (number of trees 100 or 200; maximum tree depth 10, 20, or unconstrained; minimum samples per leaf 2 or 5) are tuned by grid search with three-fold cross-validation within the training period (`GridSearchCV`, unshuffled folds, i.e.

three contiguous blocks of the training record), with RMSE as the scoring criterion; the selected configuration is then refitted on the whole training period. Negative predictions, which can only arise from the MLR, are clipped to zero. Feature importance is assessed by permutation importance on the test set (10 repeats, scored by R^2), which gives a model-agnostic estimate without the bias of the impurity-based metric. Because several predictors are correlated (hour sine/cosine, wind speed and u/v, month and temperature), permuting one of them leaves part of its information available through the others, so importances of correlated features should be read jointly rather than individually.

4.3 Pooled Models

Three pooled RF models are trained on the concatenated dataset from all 21 stations, using the same feature set as RF_{lag} and the same hyperparameter search. They are split at a fixed calendar date common to all stations: training on 2020–2023 and testing on 1 January 2024 to 31 December 2025. The variants progressively add categorical context: no categorical predictor, site group (one-hot), and station identity (one-hot). This tests whether station-specific emission characteristics can be absorbed by shared encodings.

4.4 Evaluation Metrics

Models are evaluated on the held-out test period using the coefficient of determination (R^2), root mean squared error (RMSE, $\mu g\,m^{-3}$), and mean absolute error (MAE, $\mu g\,m^{-3}$). To express the gain over persistence on a common scale, I also report the skill score

$$SS = 1 - \frac{MSE_{model}}{MSE_{pers}} = 1 - \frac{1 - R^2_{model}}{1 - R^2_{pers}}, \qquad (1)$$

where the second form holds because all models at a station are evaluated on the same test rows. For station-specific models, results are reported per station and aggregated as group means and all-station means with standard deviations.

4.5 Implementation and Data Availability

All processing is implemented in Python (`pandas`, `numpy`, `scikit-learn` [14]) with fixed random seeds, and was run on the MetaCentrum grid infrastructure (CESNET). The AURN NO_2 data and the modelled meteorology are openly available from Defra UK-AIR and were accessed via `openair` [12]. The trained models, all predictions, and cross-validation scores are stored for reproducibility and available from the author on request.

5 Results

5.1 Station-Specific Performance and the Model Ladder

Table 1 summarises test-set R^2 for all four models at each of the 21 stations, and Fig. 4 shows the corresponding ladder of all-station means. The persistence baseline achieves mean $R^2 = 0.791$ (range 0.596–0.925), reflecting the strong hourly autocorrelation of NO_2. It is strongest at rural background sites (mean 0.821), where concentrations vary smoothly, and weakest at urban industrial sites (mean 0.767), where episodes produce rapid step changes, with urban traffic intermediate (0.784).

MLR trained on met/temporal features alone achieves a mean R^2 of 0.336 (range 0.147–0.474). This is well below persistence, but the two numbers measure different things: MLR has no access to the autocorrelation that persistence exploits directly. RF_{nl} raises the mean R^2 to 0.426, but the non-linear gain is confined to the urban sites (industrial $0.298 \rightarrow 0.436$, traffic $0.395 \rightarrow 0.536$). At rural background sites RF_{nl} does not improve on MLR ($0.313 \rightarrow 0.306$) and is worse at three of the seven stations (Bush Estate, Aston Hill, Yarner Wood; e.g. Yarner Wood $0.407 \rightarrow 0.304$), which suggests that the weak, largely transported rural signal offers little non-linear structure and that the RF partly fits noise there.

RF_{lag} achieves a mean R^2 of 0.838 (range 0.701–0.928), with RMSE ranging from 0.83 to 8.68 $\mu g\,m^{-3}$. It outperforms persistence at all 21 stations. The mean gain in R^2 is modest (+0.047), but expressed as the skill score of Eq. (1), RF_{lag} reduces the persistence mean squared error by 21% on average (range 4–36%), most at urban traffic sites (28%), less at urban industrial (22%) and least at rural background sites (14%). Performance is broadly comparable across site types in terms of R^2 (rural background 0.849, urban industrial 0.820, urban traffic 0.844). The highest-concentration sites are not those with the best skill: performance is governed more by source predictability than by concentration level, which is why the smooth rural and commute-dominated traffic sites outperform the episodic industrial group.

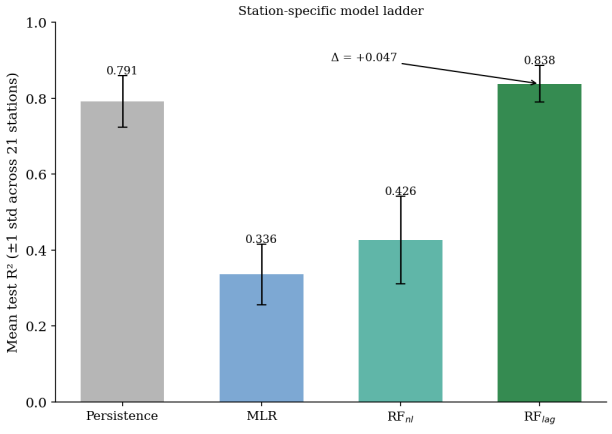


Figure 4. Station-specific model ladder: mean test $R^2 \pm 1$ standard deviation across all 21 stations for the four model variants (Persistence, MLR, RF_{nl}, RF_{lag}). The annotation gives the gain from persistence to RF_{lag}.

The bars of Fig. 4 should not be read as a ranking of model quality on a single scale: persistence and RF_{lag} benefit directly from the target's autocorrelation, whereas MLR and RF_{nl} have no access to it, so the gap between the two pairs reflects the information available rather than

Table 1. Station-specific test-set R^2 for the four model ladder steps. RB = Rural background, UI = Urban industrial, UT = Urban traffic. The Mean NO_2 column gives the observed mean concentration ($\mu g\,m^{-3}$) at each station over the full study period (January 2020–December 2025); group and all-station means are averages of the station means.

Code	Station	Type	Mean NO_2	Persist R^2	MLR R^2	RF_{nl} R^2	RF_{lag} R^2
BUSH	Bush Estate	Rural bg.	3.7	0.751	0.296	0.292	0.793
MACK	Charlton Mackrell	Rural bg.	4.6	0.820	0.279	0.299	0.849
ROCH	Rochester Stoke	Rural bg.	10.1	0.825	0.268	0.327	0.843
PEMB	Narberth	Rural bg.	2.8	0.710	0.312	0.322	0.771
GLAZ	Glazebury	Rural bg.	11.2	0.864	0.284	0.312	0.885
AH	Aston Hill	Rural bg.	2.9	0.925	0.348	0.287	0.928
YW	Yarner Wood	Rural bg.	3.0	0.853	0.407	0.304	0.871
HRL	London Harlington	Urban ind.	21.1	0.778	0.323	0.489	0.849
PT4	Port Talbot Margam	Urban ind.	11.4	0.596	0.147	0.298	0.701
SCN2	Scunthorpe Town	Urban ind.	12.5	0.808	0.393	0.551	0.847
GRA2	Grangemouth Moray	Urban ind.	11.8	0.805	0.331	0.425	0.837
LVP	Liverpool Speke	Urban ind.	13.7	0.820	0.312	0.457	0.852
BIL	Billingham	Urban ind.	12.7	0.765	0.382	0.514	0.824
GRAN	Grangemouth	Urban ind.	12.6	0.798	0.198	0.317	0.831
POAR	Portsmouth Anglesea Rd	Urban traffic	21.5	0.708	0.288	0.437	0.771
CNPR	Cardiff Newport Road	Urban traffic	19.6	0.815	0.399	0.552	0.863
COBR	Coventry Binley Road	Urban traffic	22.6	0.813	0.392	0.549	0.866
YK11	York Fishergate	Urban traffic	18.8	0.763	0.474	0.592	0.835
NWBV	Nottingham Western Blvd	Urban traffic	24.4	0.792	0.348	0.506	0.857
BEL1	Belfast Stockman's Lane	Urban traffic	34.7	0.744	0.453	0.609	0.837
GHSR	Glasgow High Street	Urban traffic	19.5	0.854	0.414	0.510	0.882
Group means							
	Rural background (n = 7)		5.5	0.821	0.313	0.306	0.849
	Urban industrial (n = 7)		13.7	0.767	0.298	0.436	0.820
	Urban traffic (n = 7)		23.0	0.784	0.395	0.536	0.844
	All stations (n = 21)		14.1	0.791	0.336	0.426	0.838

the learning algorithm. Because RF_{lag} skill is measured relative to each station's own persistence level, part of any group contrast in R^2 also flows through the baseline.

5.2 Predicted vs Observed

Figure 5 shows predicted versus observed NO_2 for all four models at one station of each site type. Persistence predictions cluster around the 1:1 line, but the fitted slope is below one by construction: regressing y_{t-1} on y_t gives a slope equal to the lag-1 autocorrelation, so high values are systematically under-predicted. MLR compresses its predictions into a narrow band and cannot reproduce the upper tail. RF_{nl} widens the predicted range and reduces scatter clearly at the traffic site (R^2 0.348 → 0.506), but not at the rural site (0.296 → 0.292). RF_{lag} lies closest to the 1:1 line over the full concentration range, although its slope also remains below one; the largest errors occur during the highest-concentration episodes, where conditions such as low-wind trapping, cold starts, or queuing traffic are difficult to predict from hourly modelled meteorology.

5.3 Temporal Tracking of the Best RF_{lag} Model per Site Type

Aggregate R^2 and point clouds average over timing errors, peak clipping, and sustained biases. Figure 6 therefore shows observed and predicted NO_2 as daily-mean time series over the test period for the station with the highest RF_{lag} R^2 in each site group. At Aston Hill (rural background, R^2 = 0.928) the model reproduces the individual multi-day episodes closely. At Liverpool Speke (urban industrial, R^2 = 0.852) episode timing is correct, but the highest peaks are attenuated, in line with the slope below one in Fig. 5. At Glasgow High Street (urban traffic, R^2 = 0.882) the model follows the higher, more variable winter concentrations and the quieter summer period. Because each hourly prediction uses the previous hour's observation, daily means of one-hour-ahead predictions follow the observations closely almost by construction; the panels show that RF_{lag} introduces no systematic bias or drift over more than a year of test data, rather than demonstrating independent predictive ability.

5.4 Feature Importance

Without access to the previous observation (Fig. 7a), the importance ranking differs clearly between site types. At urban traffic sites the diurnal cycle dominates: hour (cos) is the single most important feature (≈ 0.38), followed by wind speed (≈ 0.32) and hour (sin) (≈ 0.25), reflecting the commute peaks of Fig. 3. At rural background sites the west–east wind component u is by far the most important feature (≈ 0.34), ahead of wind speed (≈ 0.15) and temperature (≈ 0.10), while the hour terms matter little. A plausible interpretation is advection: westerly flow brings clean Atlantic air, whereas easterly flow carries NO_2 from UK conurbations and continental Europe. Urban industrial sites are intermediate, led by wind speed (≈ 0.25) with hour (cos), month (cos), temperature, u and hour (sin) all between 0.13 and 0.17. Wind speed, representing dilution and boundary-layer ventilation, is among the leading features everywhere. The weekend flag matters only at urban sites (≈ 0.06–0.07), consistent with reduced weekend traffic.

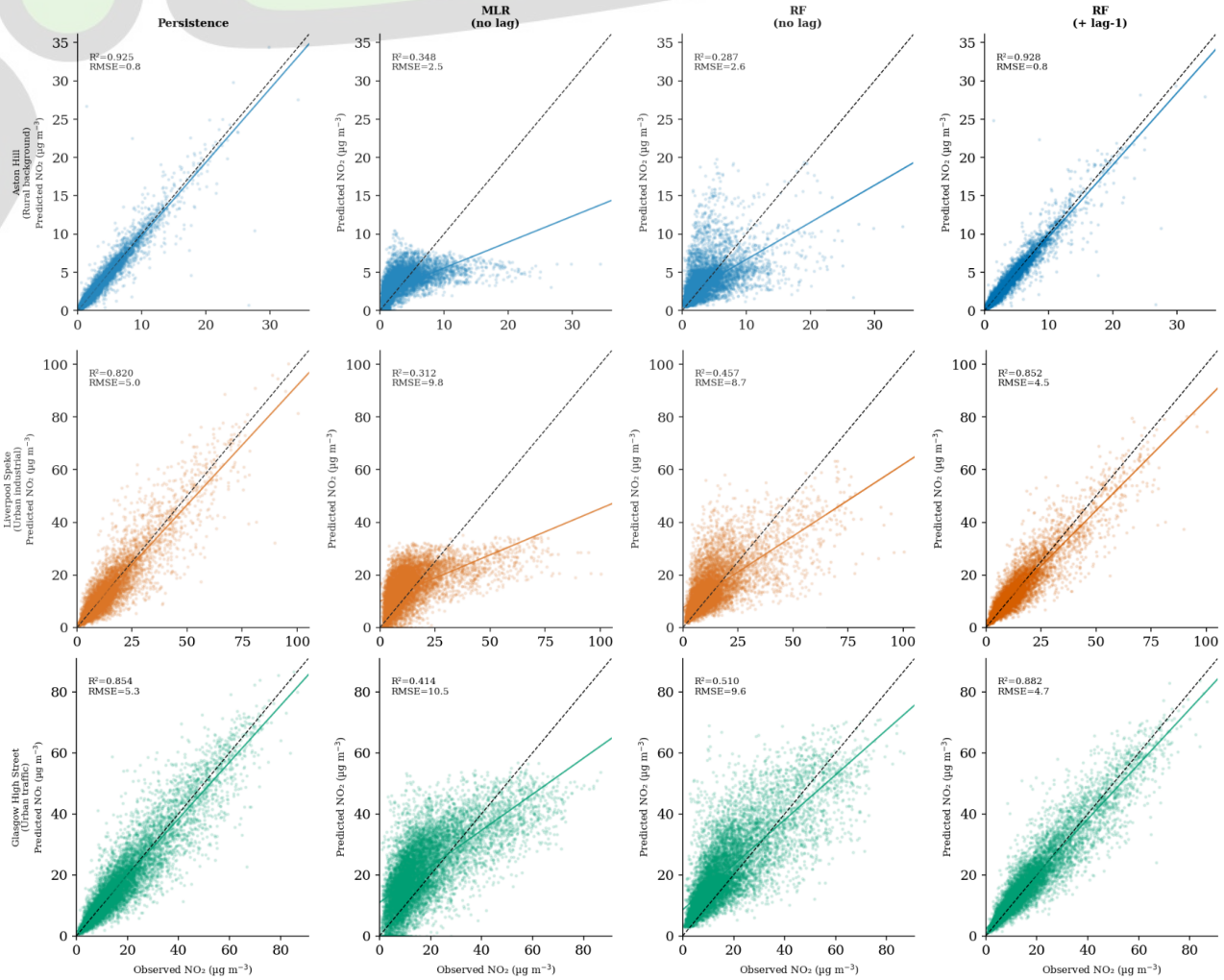


Figure 5. Predicted vs observed hourly NO_2 ($\mu g\,m^{-3}$) on the test period for the four model ladder steps (columns: persistence, MLR, RF_{nl}, RF_{lag}). Rows: Aston Hill (rural background, blue), Liverpool Speke (urban industrial, orange),Glasgow High Street (urban traffic, green). Dashed line: 1:1; solid line: least-squares fit.

When lags are available (Fig. 7b), lag-1 dominates with importances of 1.24–1.37. Values above one mean that permuting lag-1 drives the test R^2 below zero, i.e. the model then predicts worse than the mean, because it relies on lag-1 so strongly. All other features fall to ≤ 0.04; the diurnal terms keep the largest residual importance, particularly at traffic sites, whereas lag-24 adds almost nothing beyond lag-1 and the hour features. Once the previous observation is known, the met/temporal predictors serve mainly to correct the hour-to-hour change rather than the concentration level.

5.5 Pooled Model Results

Table 2 summarises pooled model performance on the 2024–2025 test period. The pooled RF without any categorical predictor reaches $R^2 = 0.880$. Adding site-group encoding gives a small improvement ($R^2 = 0.882$, $\Delta RMSE = -0.047\ \mu g\,m^{-3}$), and adding station identity improves it further to $R^2 = 0.885$ ($\Delta RMSE = -0.108\ \mu g\,m^{-3}$ versus no category). The marginal gains from categorical encoding are small relative to the overall performance, suggesting that the shared feature set captures most of the cross-station variance. Station identity may capture local emission characteristics, topographic shielding, or instrument-specific biases not represented in the modelled meteorology.

Table 2. Pooled RF (with lags) performance on the held-out test period 2024–2025 (N = 328,509 hourly observations across all 21 stations; training 2020–2023).

Model variant	R^2	RMSE ($\mu g\,m^{-3}$)	MAE ($\mu g\,m^{-3}$)
No category	0.880	4.763	2.794
+ site group	0.882	4.716	2.766
+ station ID	**0.885**	**4.655**	**2.734**

6 Discussion

6.1 Interpreting the Model Ladder

Most air-quality ML studies report only the final autoregressive model and note that lag features dominate the importances; without a lag-free baseline it is impossible

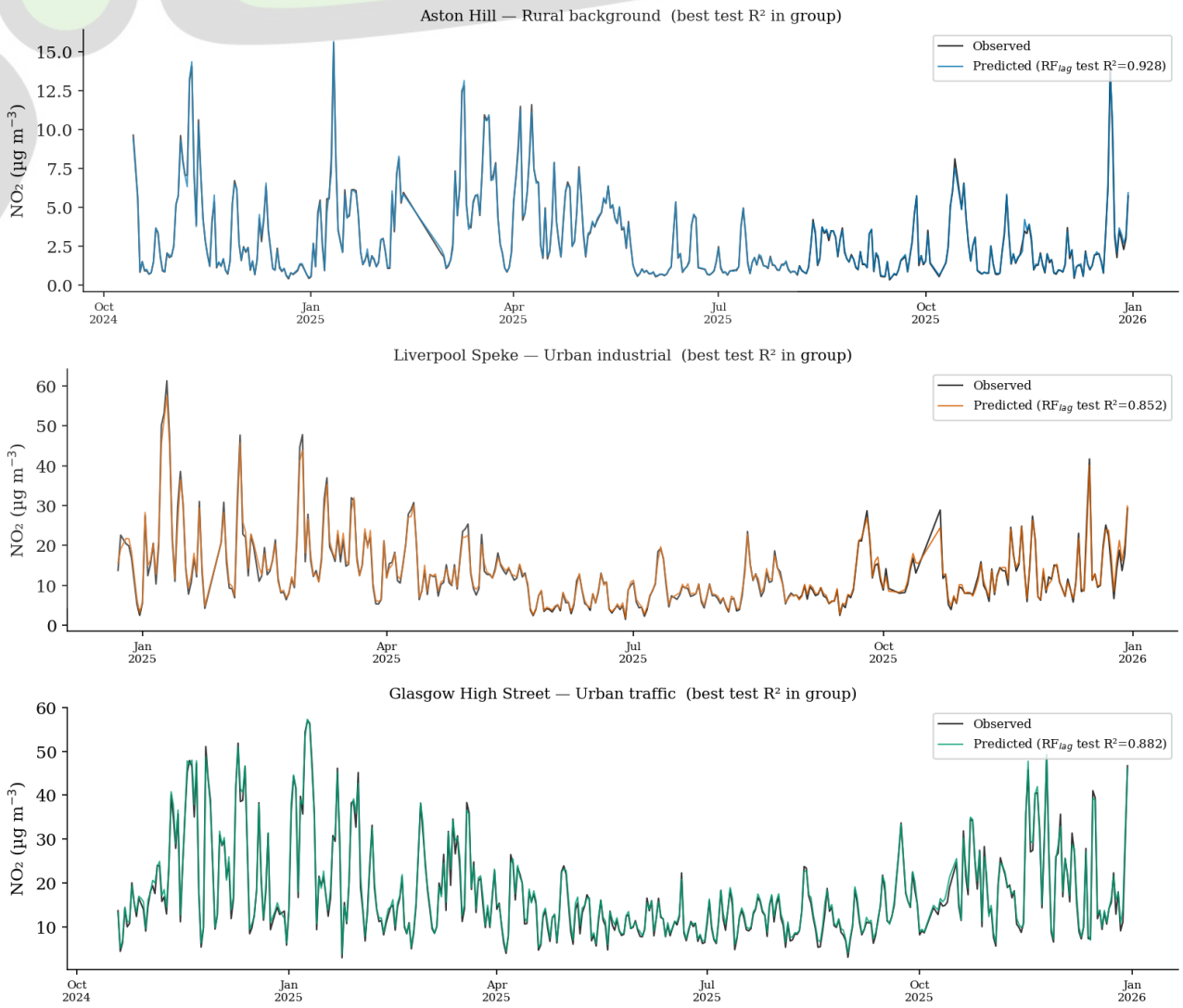


Figure 6. Observed versus predicted daily-mean NO_2 over the test period at the station with the highest RF_{lag} test R^2 in each site group. Top: Aston Hill (AH, rural background). Middle: Liverpool Speke (LVP, urban industrial). Bottom: Glasgow High Street (GHSR, urban traffic). Black curves: observed NO_2; coloured curves: RF_{lag} predictions. Each legend reports the station's hourly RF_{lag} test R^2.

to tell how much meteorological learning the model performs. Here, RF_{nl} explains 43% of the test variance from met/temporal features alone, and the lag terms add a further +0.412 in R^2 given those features. These two numbers are not an additive split of the variance, because the meteorological predictors are themselves autocorrelated and partly overlap with the information in lag-1. They do show, however, that the lag-free model learns physically consistent relationships and is not merely an artefact of autocorrelation.

The persistence baseline puts the headline R^2 in context: a naive one-hour forecast already explains nearly 80% of the variance. The additional skill of RF_{lag} (a 21% reduction in mean squared error) is the part that anticipates meteorologically driven changes that persistence cannot, which is the component relevant for short-horizon warning of exceedances. In this study that skill is obtained with concurrent modelled meteorology, so it is an upper bound for a genuine forecast driven by numerical weather prediction issued in advance.

The absolute skill levels are consistent with those reported elsewhere for hourly NO_2. Meteorological-normalisation studies using RF at UK roadside and background sites report comparable explained variance once meteorological drivers are accounted for [9, 11]; that technique, which uses a lag-free RF much like RF_{nl}, is the standard approach for quantifying the air-quality response to interventions, including the COVID-19 lockdowns [5, 11]. Deep-learning models for hourly forecasting typically include lagged concentrations among their inputs [10], i.e. they operate in the regime represented here by RF_{lag}. The contribution of the present comparison is therefore not a record R^2 but the attribution of that R^2 to its two sources, which guards against reading high lag-driven R^2 values as evidence of physical insight and provides a fair baseline for benchmarking new process models.

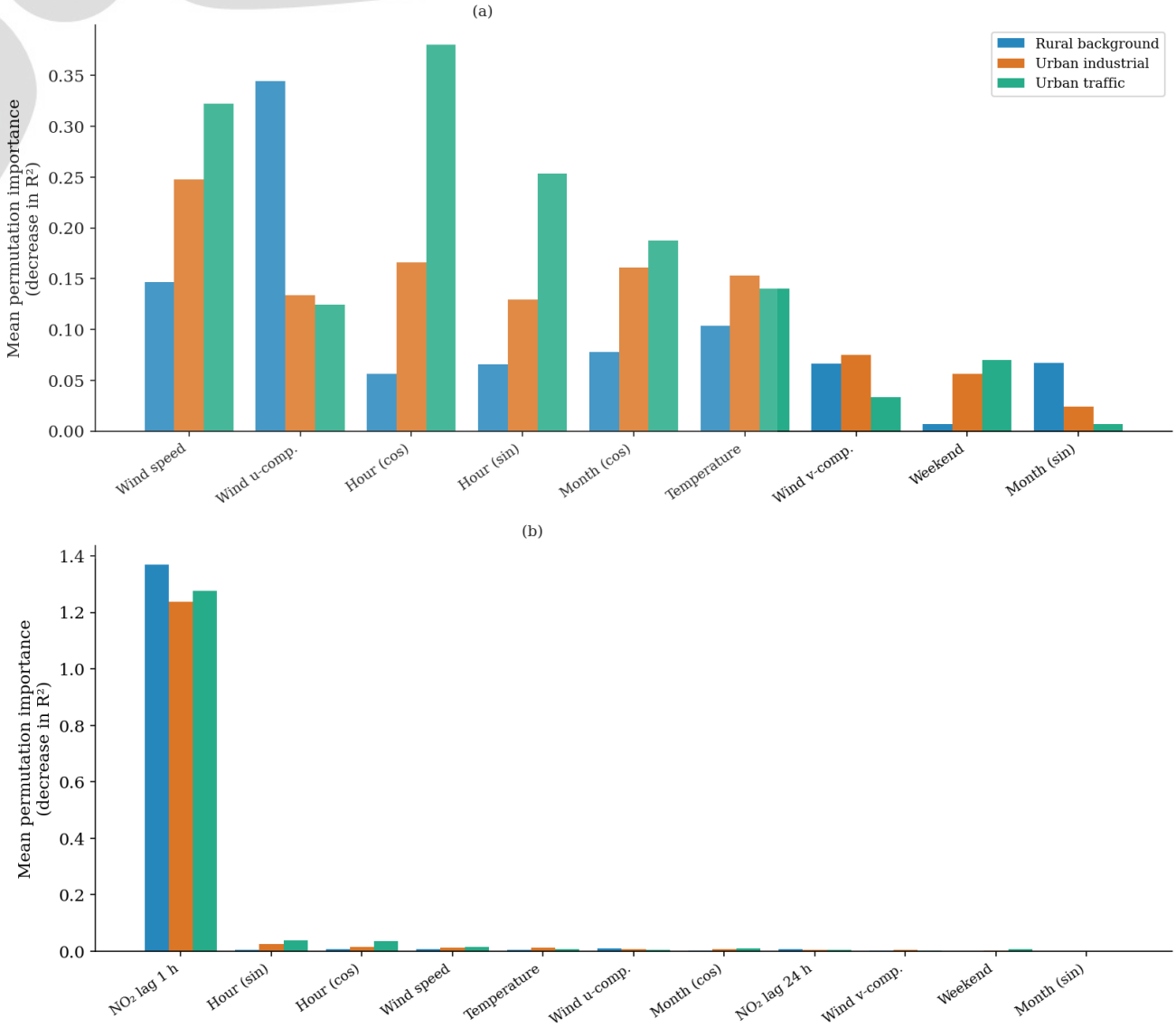


Figure 7. Mean permutation feature importances (decrease in test R^2 upon feature permutation) by site group. (a) RF_{nl}: contribution of meteorology and time of day. (b) RF_{lag}: lag-1 dominates and the remaining features contribute little.

6.2 Site-Type Differences

The diurnal profiles (Fig. 3) and the lag-free importances (Fig. 7a) distinguish the three site types in physically interpretable ways. At urban traffic sites the hour-of-day features lead, quantifying how strongly concentrations follow emission timing (commuting). At rural background sites the wind direction, expressed through the *u* component, leads, reflecting the dominance of regional transport over local emissions. Urban industrial sites combine both, consistent with continuous point-source emissions plus traffic on surrounding roads. The ubiquitous importance of wind speed, and the winter maximum of all site types, both point to near-surface ventilation as the common physical control: low wind speeds and shallow, stable boundary layers limit vertical and horizontal dilution of near-ground emissions [6].

The weak outlier, Port Talbot Margam (PT4, RF_{lag} R^2 = 0.701), is physically interpretable: the station sits downwind of the Tata Steel works, whose furnace and sinter cycles are poorly correlated with the modelled meteorology or time of day. Process scheduling, planned and unplanned releases, and plume-capture events produce spikes that look stochastic to the model — a limitation of any met-based statistical approach, not of RF specifically.

6.3 Pooled versus Station-Specific Models

The pooled models reach higher R^2 (0.880–0.885) than the station-specific mean (0.838), but the comparison is not like for like: pooled R^2 also rewards explaining the large between-site differences in mean concentration (Table 1), and the pooled models are tested on a different and longer period (2024–2025, with four instead of about 4.8 years

of training data). Much of the apparent advantage is therefore between-site variance, not better hourly prediction at any single site. For local use the station-specific models remain the relevant benchmark, whereas a pooled model is preferable when one deployable model must cover a whole network or sites with too little history to train on. The small gain from one-hot station encoding (R^2 0.880 $\rightarrow$ 0.885) indicates only minor residual site effects (local emission fingerprints, topographic sheltering, or instrument bias).

6.4 Limitations and Future Work

Several limitations should be acknowledged. First, the meteorological inputs are modelled (WRF) values used concurrently with the predicted hour; the reported skill is that of a nowcast with known weather, and the meteorology is not observed on site. Second, the modelled fields cannot resolve sub-grid effects such as street-canyon ventilation or local sea-breeze and valley-wind systems relevant to some stations. Third, the training period includes the COVID-19 lockdowns with anomalously low traffic emissions; this adds useful variability, but models trained on it may need recalibration for post-pandemic emission levels. Fourth, the chronological 80/20 split places roughly the last 13–15 months in the test set, and the hyperparameter search uses unshuffled K-fold blocks in which later training data can inform the validation of earlier blocks. Because emissions drift over time, a forward-chaining or purged cross-validation would give a complementary, more conservative estimate of generalisation. Fifth, RF has no explicit treatment of long-range transport or secondary NO_2 formation, both of which can raise rural concentrations independently of local conditions.

Future work could use numerical weather prediction inputs to test true forecasting skill, add local station meteorology or boundary-layer height as predictors, and apply transfer learning (pre-training on data-rich stations, fine-tuning on data-sparse ones). Extending the approach to NO_x partitioning (NO/NO_2) would link prediction more directly to source apportionment.

7 Conclusions

This study demonstrates a transparent, physically interpretable approach to hourly NO_2 prediction at 21 UK monitoring stations using a Random Forest model ladder. The principal conclusions are:

1. Station-specific RF models with autoregressive lags achieve mean $R^2 = 0.838$ (range 0.701–0.928) and outperform persistence at all 21 stations, reducing its mean squared error by 21% on average; the gain is largest at urban traffic sites (28%) and smallest at rural background sites (14%).

2. The persistence baseline ($R^2 = 0.791$) shows that hourly NO_2 is strongly autocorrelated; most of the R^2 of the lagged RF is inherited from lag-1.

3. Without lags, the RF still explains 43% of the test variance from meteorology and the emission time cycle. The non-linear gain over MLR is clear at urban sites but absent at rural background sites.

4. Lag-free permutation importances are physically consistent: hour of day dominates at urban traffic sites, the west–east wind component at rural background sites, and both contribute at urban industrial sites, with wind speed important everywhere.

5. Pooled RF models reach $R^2 = 0.880$–0.885 with only marginal gain from station-identity encoding; part of their higher R^2 reflects between-site differences rather than better hourly prediction.

These findings support the use of RF models for short-term NO_2 nowcasting at UK monitoring sites, with numerical weather prediction inputs required for genuine forecasting, and provide a methodological template (the model ladder with paired feature-importance analysis) that can be applied to other pollutants and networks. For decarbonising cities in particular, the lag-free process model is the more policy-relevant product: by isolating the meteorological and diurnal component of NO_2 variability, it offers a basis for attributing concentration changes to transport and industrial decarbonisation measures rather than to year-to-year weather variability.

Acknowledgment

The computational resources were provided by the e-INFRA CZ project (ID: 90254), supported by the Ministry of Education, Youth and Sports of the Czech Republic. This work was also supported by the research programme AI: Artificial Intelligence for Science and Society, which forms part of the Strategy AV21 of the Czech Academy of Sciences. I further appreciate the institutional support from the Institute of Thermomechanics of the Czech Academy of Sciences for its long-term conceptual development (RVO: 61388998). I thank the AURN station operators for maintaining data quality over the study period.

References

[1] J.H. Seinfeld, S.N. Pandis, Atmospheric Chemistry and Physics: From Air Pollution to Climate Change, 3rd edn. (John Wiley & Sons, Hoboken, NJ, 2016)

[2] World Health Organization, Tech. rep., World Health Organization, Geneva, Switzerland (2021)

[3] Department for Environment, Food and Rural Affairs (Defra), Tech. rep., Defra, London, UK (2007)

[4] Z.S. Venter, K. Aunan, S. Chowdhury, J. Lelieveld, Covid-19 lockdowns cause global air pollution declines, Proceedings of the National Academy of Sciences **117**, 18984 (2020). 10.1073/pnas.2006853117

[5] C. Jephcote, A.L. Hansell, K. Adams, J. Gulliver, Changes in air pollution during covid-19 'lockdown' in the united kingdom, Environmental Pollution **289**, 117588 (2021). 10.1016/j.envpol.2021.117588

[6] R.B. Stull, An Introduction to Boundary Layer Meteorology (Springer Netherlands, Dordrecht, 2012)

[7] L. Breiman, Random forests, Machine Learning **45**, 5 (2001). 10.1023/A:1010933404324

[8] C.M. Bishop, Pattern Recognition and Machine Learning, Information Science and Statistics (Springer, New York, NY, 2006)

[9] S.K. Grange, D.C. Carslaw, A.C. Lewis, E. Boleti, C. Hueglin, A new method for the meteorological normalisation of air quality data: Application to nitrogen dioxide and particulate matter concentrations at roadside sites, Atmospheric Environment **188**, 1 (2018). 10.1016/j.atmosenv.2018.06.011

[10] Q. Liao, M. Zhu, L. Wu, K.V. Panthi, F.H. Beni, Deep learning for air quality forecasts: a review, Current Pollution Reports **6**, 399 (2020). 10.1007/s40726-020-00159-z

[11] S.K. Grange, D.C. Carslaw, Using meteorological normalisation to detect interventions in air quality time series, Science of The Total Environment **653**, 578 (2019). 10.1016/j.scitotenv.2018.10.344

[12] D.C. Carslaw, K. Ropkins, openair — an r package for air quality data analysis, Environmental Modelling & Software **27–28**, 52 (2012). 10.1016/j.envsoft.2011.09.008

[13] H. Hersbach, B. Bell, P. Berrisford, S. Hirahara, A. Horányi, J. Muñoz-Sabater, J. Nicolas, C. Peubey, R. Radu, D. Schepers et al., The era5 global reanalysis, Quarterly Journal of the Royal Meteorological Society **146**, 1999 (2020). 10.1002/qj.3803

[14] F. Pedregosa, G. Varoquaux, A. Gramfort, V. Michel, B. Thirion, O. Grisel, M. Blondel, P. Prettenhofer, R. Weiss, V. Dubourg et al., Scikit-learn: Machine learning in python, Journal of Machine Learning Research **12**, 2825 (2011).

Experimental investigation of thin liquid films by the laser interferometry

Lukáš Jirásek*, *Ondřej* Bartoš and *Adam* Huněk

CTU in Prague, Energy Engineering Department, Technická 4, Prague 6, 166 07, Czechia

Abstract. Nowadays, steam turbines and other energy devices are widely discussed in relation to the erosive effects of the liquid phase. Because of the increasing use of renewable energy sources, steam power plants are forced to work in off-design regimes more than ever before. This places additional demands on their design conditions. Especially in steam turbines, more severe erosion of the last-stage stator blades may occur. This phenomenon motivated the new thorough research which is related to this article. This paper focuses on a new technique of measuring thin, dynamic liquid films. Understanding these films well is crucial for developing precise numerical models of steam turbine blade erosion. The proposed method using monochromatic interferometry may be used in various applications, including heat exchangers and experimental devices. The method was developed as a non-destructive and non-intrusive way of measurement for possible future use in a steam turbine environment. It may also be used for measuring shear-driven dynamic films in two-phase flow at specific points at a given moment. The article compares measured data obtained by the proposed interferometer with a model of gravity-driven film drainage on a vertical surface. The experimental setup is presented, and MATLAB was used for comparing the obtained experimental data and processing the images using Fourier transformation, which is presented and discussed further in this paper. Overall, the investigation demonstrated agreement between the film thicknesses predicted by the physical model and those measured experimentally using monochromatic interferometry.

1 Introduction

The initial motivation for the work in field of measuring techniques of thin liquid film is caused by the growing interest in steam turbine erosion. This phenomenon is furthermore enhanced by the growing use of renewable sources of energy, which is despite all their benefits leading to possible increasing the erosion of the last stage turbine blades. Because of the maximum usage of the renewable sources of energy, the fossil fuel powerplants are forced to work in off-design regimes more than ever before, which may cause more severe erosion. The erosion is caused by the secondary droplets forming by the breakup of the film on the stator blades. The parameters of the liquid film thickness play a crucial role in the whole erosion process. Although, there is not any measurement technique that can be use directly in turbines to determine the liquid film thickness.

The nowadays growing interest in research connected to the field of erosion caused by liquid phase in energy devices such as steam turbines, turbomachinery or heat exchangers is bringing new numerical models and simulative calculations. These novel simulations are mostly observing the two-phase flow. These studies [1-4] concentrating to the description of shear-driven liquid films powered by flowing gas phase are the most reliable for this article. For many of the papers listed above, it is crucial to have a precise input data or other experimental data for comparison and evaluating the new numerical methods. Furthermore, many of them are implicitly or explicitly calling for experimental evaluation and further for obtaining more experimental data.

A number of methods for measuring the thickness of thin liquid films have been developed [5]. A new method considering the ability of the whole measurement for further use of measuring shear-driven liquid films in the environment simulating turbomachinery conditions was developed following previous research [6] and built on previous work [7-9]. Commercially used electrical conductance and capacitance methods are robust, inexpensive, but they are intrusive and they often impact the flow. Spectral chromatic methods offer high accuracy, but their measurable thickness range is limited and as laser focus displacement methods, they usually require flat film surface without any turbulations, waves, which is not the case of the dynamic films in steam turbine like environment. Planar-laser induced fluorescence and other dye-based optical methods require a transparent liquid and dye directly in the flow. White light interferometry is despite its high accuracy limited by scattering and refraction in a wet steam environment. For a direct future use in steam turbine or other energy device is none of these methods suitable.

For these reasons a measurement method based on monochromatic interferometry was developed in our previous paper [6] and further investigated. The

monochromatic interference method is nonintrusive, non-destructive, it can measure unsteady dynamic films and thanks to the monochromatic light it is considered to be applicable in wet steam environment.

This paper focuses on further experimental testing of the previously developed method. As a validation step, the method is applied to gravity-driven film drainage on a vertical plate. This configuration was chosen for its simple description by Jeffreys model of gravitational drainage. This experimental study separates its own gas shear driven models and concentrates to different physical phenomenon for purposes of the method testing.

The goals of this paper are to obtain new experimental data on the temporal evolution of a thin water film thickness on a vertical plate using the developed interferometer. Then to compare measured data with the physical model of gravitational drainage. And further, to present a MATLAB-based procedure for evaluating experimental data using FFT-initialized cosine fitting. Nevertheless, this show different experimental use of the proposed monochromatic interference method.

The novelty of the present work lies in the application of the developed monochromatic interferometric system together with FFT-based image processing for automated evaluation of thin liquid film thickness. The capability of the method is demonstrated on a gravity-driven film drainage experiment and compared with the Jeffreys drainage model.

2 Measurement method

This paper brings new experimental data obtained by using monochromatic interferometry, which was thoroughly described in [6]. In the future it is considered that this method may be used in devices simulating conditions such as in steam turbines and in other experimental devices connected with energetics. Therefore, the chosen method was previously developed as a suitable one for use in such an environment. For the instance of the nowadays commercial used methods for measuring thin liquid films, the monochromatic interferometry is non-destructive and non-intrusive and can be used for measuring unsteady dynamic films. Thanks to the using of a monochromatic light, the possibility of measurement in wet steam environment is considered, in contrast to a white light interferometry, which may be furthermore more suitable for measuring even thinner films than the ones that may occur in steam turbine environment or generally by condensing of the vapour phase.

The method is generally considered as point measurement with easy ability to be further managed to grid-based measurement at discrete points. The principle of the proposed monochromatic interference measurement is corresponding to work of Ohyama [7] and related works [8], [9]. For the purpose of this paper, Eq. 1 is used. The liquid film thickness (δ) is expressed with variables that are easily measurable during the experiment, or with known material properties only, where (λ) is a wavelength of the incident light, (D) is a distance between the film and the place, where the interference fringes are observed, (n_a) is the refractive index of light in the air, (n_f) is the refractive index of light in the liquid film and (θ) is the angle of incidence.

$$\delta = \frac{\lambda D}{2y \tan\left(\arcsin\left(\frac{n_a}{n_f}\sin\theta\right)\right)\cos\theta} \tag{1}$$

The Eq. 1 is derived in the previous paper [6]. It is used to calculate the liquid film thickness (δ) using experimental data obtained by presented interferometer and further processed in MATLAB. The script reads the images, and it gives a mean value of the distance between the vertical axis of two interference fringes (y) for every photo.

3 Measurement setup

The presented measurement setup consists of interferometer and the device for mounting the plate at the certain place to have the position of the x coordinate fixed. Then a device for controlled drop of the beaker filled with a liquid was attached to the aluminium frame. At the start of one experimental set of measurement, the beaker sets up so the liquid in it is wetting the fixed plate up to predefined high, which matches with a value of x coordinate x = 0 mm for the whole measurement. The beginning of the x coordinate is the place, where the water is starting to wet the surface, therefore it is the border of the film formation after dropping the beaker. For the first series of experiments, the x coordinate indicated the measured location was set to x = 40 mm and during the second series to x = 60 mm.

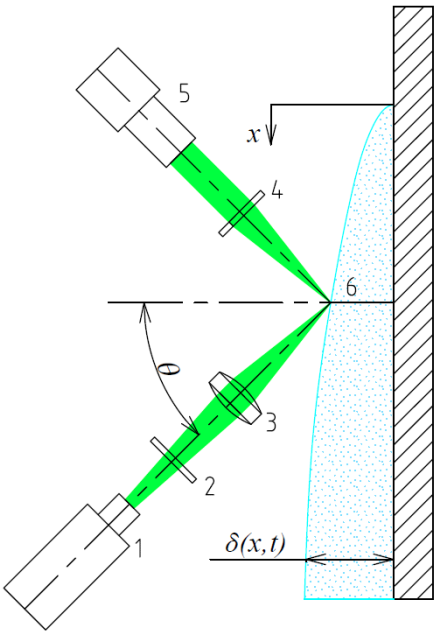


Fig. 1 Experimental setup layout

Whole measurement setup is depicted in Fig. 1, where (1) is laser with collimator, (2) polarizing filter, (3) an achromatic lens pair, (4) shade where the interference fringes can be observed, (5) telecentric objective with camera and (6) is the observed thin liquid film. The laser beam must be focused on the smallest area possible. Theoretically, this area is the only point, but due to the

aberration of the lens used, such accuracy cannot be achieved. An achromatic optical lens which is located on sliding table for its precise and very fine movement was used. The interferometer sets on the aluminium profiles allowing additional elements to be added if necessary and easy manipulation. It also prevents from unintended movements that would alter the geometry, to which the device is very sensitive, especially angles.

The shade with interference fringes can be placed in front of the camera in exact distance because of use of telecentric objective. This type of objective was chosen for its ability to not distort information about the size of the observed image depending on the distance between the camera and the shade, which is crucial for determination of the film thickness. The measurement may be performed without a shade with direct picture capture in exact place, where the camera is focused. This setup was chosen for the final measurement.

A UI-5240CP-M-GL camera equipped with an e2v EV76C560 1/1.8" CMOS monochrome chip was used for the experiment. In addition, a Melles Griot 05 LGR 025 helium-neon laser emitting green unpolarized light with a wavelength of 543.5 nm and a 55-278 achromatic lens with a focal length of 100 mm manufactured by Edmund Optics were used.

4 Image processing

The interference fringes obtained by the optical measurement are further processed using MATLAB. The purpose of the processing was to set the proper gauge between the vertical axis of the interference fringes and to judge its variability in chosen areas in the picture. The three areas were predefined (lines perpendicular to the interference fringes) and further automatically detected in every picture for the processing. That led to the processing the same parts of all the images, which were all considered as same sized for this purpose.

The greyscale intensity profile was generated along every prescribed line and further smoothened to filter any local fluctuation. The smoothening was done by mean value of perpendicular 5 pixels distance over and under the prescribed line. The greyscale profile was further smoothened and normalized linearly in the interval from 0 to 1.

During the processing there was clear that detecting the axis of the fringes by finding maximum of the brightness of every fringe is not acceptable because of the false detection caused by the irregularity and noise of the fringe's brightness level. For this reason, the approximation by cosine function was used to reconstruct a real grayscale intensity profile of the interference pattern. Every intensity profile was described by following Eq. 2.

$$I_{fit}(s) = b_0 + b_1 s + A\cos(2\pi f s + \varphi) \qquad (2)$$

where (s) is a distance from the beginning of the prescribed line, (b_0) is constant component of intensity, (b_1) is the coefficient of its linearity, (A) is the amplitude of the periodical component, (f) is the frequency and (φ) is the phase. Approximately constant gauge of the fringes along the prescribed observed lines was assumed by the model.

Initial estimate of the spatial frequency was obtained by fast Fourier transformation (FFT), which is detecting periodical changes along the defined line in the image. Even before counting an estimate of spatial frequency, the linear increase of light intensity was removed from the whole profile. The linear increase of light intensity was occurring in many pictures due to the lighting conditions, and it may influence the frequency calculation. The Hanning window was used to prevent causing any disturbance of the frequence fitting by the image edges.

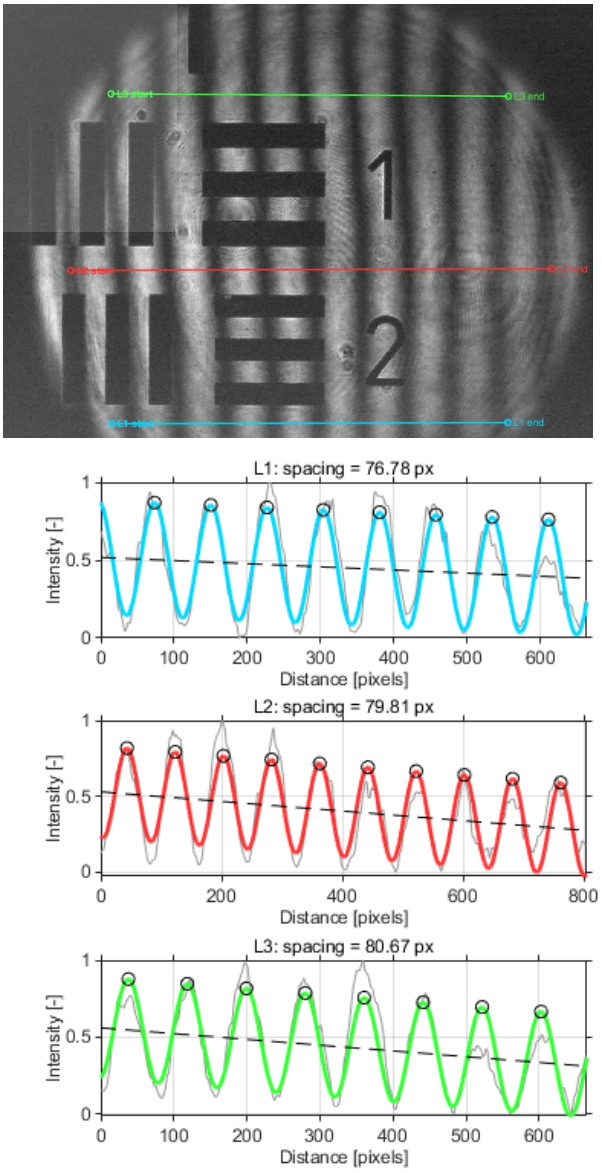


Fig. 2 Interference fringe pattern image with satisfactory lighting conditions for all; all cosine approximations are accepted. The linear light intensity decrease is clearly visible.

The frequence obtained by FFT was used as an initial estimate for the cosine approximation. Multiple frequences and amplitudes were tested in the predefined range. The matching with measured profile was inspected by the summation of squares between counted

and measured intensities. The most promising frequency were chosen and further being adjusted numerically to match the measured signal the most accurate way possible. This led to possible adjustment of cosine function and matching the measured signal more properly. The final gauge was determined as the reciprocal value of the spatial frequency.

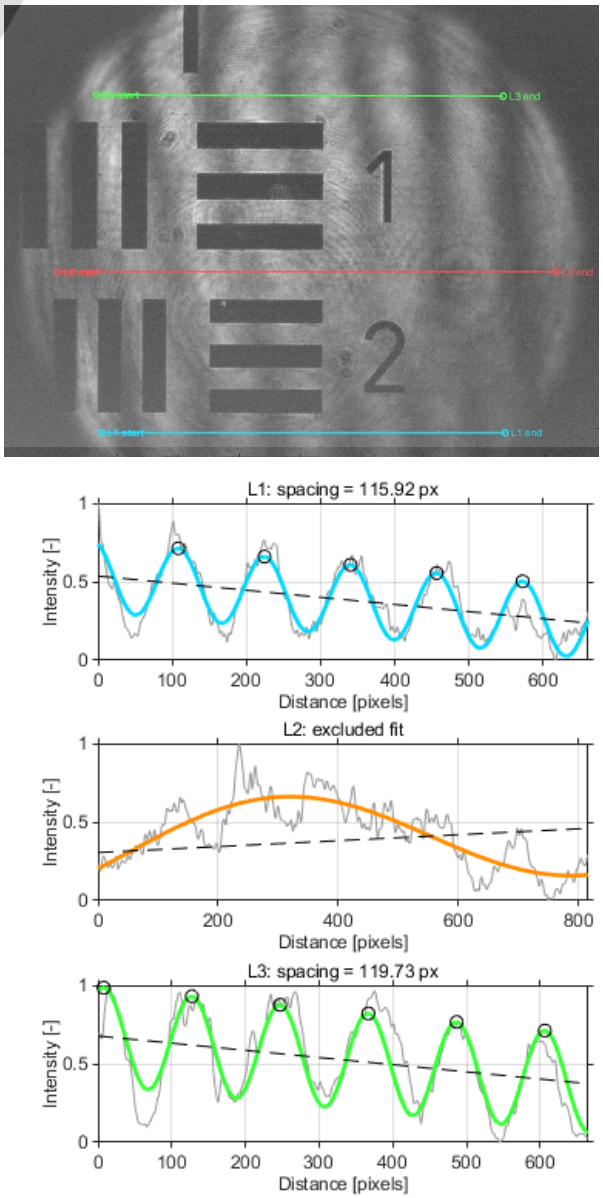


Fig. 3 Interference fringe pattern image with unsatisfactory lighting conditions for all predefined lines; the second cosine approximation is excluded.

Positions of the centres of the interference fringes were determined using maximums of cosine function. Therefore, there were not found as the peaks of brightness in the image because of the strong impact of the optical noise, not ideal lighting conditions on every image and irrelativity in intensity. Using the cosine fitting is ideal for the purpose described in this article because it assuming that the gauge is constant along the observed line.

Every approximation of the light profile was evaluated by the certain criteria to prevent misleading results. The cosine fitting was checked about its amplitude and periodicity matching with the light intensity profile. The maximal permissible gauge between two interference fringe axis was set as 400 pixels to prevent accounting the mismatched cosine profiles obtained by some pictures with bad lighting conditions.

The arithmetical mean pitch was counted from received profiled for every image. When at least two profiles were accepted, the sample standard deviation was counted, which characterised differences between evaluated areas in the image. If only one profile was accepted, there was no sample standard deviation to be counted, and the only profile's gauge was accepted. The images without any acceptable profile were excluded from the evaluation. The sample's standard deviation does not express uncertainty of the cosine approximation. The Fig. 2 shows the image processing in MATLAB while all cosine approximations are accepted, and Fig. 3 shows an image with excluded cosine approximation.

5 Comparison with the mathematical model

The Jeffreys model of gravitational flow down a vertical surface serves as a reference description of the temporal evolution of a liquid film thickness in this paper. The model assumes that the motion of thin layer of a Newtonian fluid is governed by the equilibrium between the gravity and the viscous force. It is assumed that there is zero velocity of the liquid film at the solid wall, and the shear stress is neglected. The model does not include the effect of inertia, capillary force and evaporation. Therefore, the model is used for the thin films in laminar flow condition, where the gravity and viscous mechanism dominates.

Let (x) to be the distance from the starting of the film formation – the highest point of submerging the plate to the liquid bath. The direction of the (x) coordinate is from top to the bottom. Therefore, we can write the Eq. 3 for the flux (q) as a function of (x) and time (t),

$$q(x,t)=\frac{\rho g \delta^3}{3\mu}(x,t) \tag{3}$$

where (ρ) is density of the liquid, (g) is gravitational acceleration and (μ) is dynamic viscosity. From the conservation law we can rewrite Eq. 4 using the Eq. 3 to the differential Eq. 5.

$$\frac{\partial \delta}{\partial t}+\frac{\partial q}{\partial x}=0 \tag{4}$$

$$\frac{\partial \delta}{\partial t}+\frac{\rho g}{\mu}\delta^2\frac{\partial \delta}{\partial x}=0 \tag{5}$$

The Eq. 5 can be rearranged by the separating the variables (x) and (t). In Jeffreys's work [10] it is shown, that the Eq. 5 has two solutions. The first solution

assumes a constant thickness along the coordinate $\delta \approx \delta_0$. That's generally the case, when the film thickness is converges to the solution according to Landau–Levich–Derjaguin model. The second solution Eq. 6 predicts parabolic profile which expresses a balance between gravitational and viscous forces and it is known as Jeffreys model of film thickness for gravitational drainage.

$$\delta(x,t) = \sqrt{\frac{\mu x}{\rho g t}} \tag{6}$$

For the purpose of the experiment, the surfactant was used to enhance the wettability of the liquid. The addition of surfactant drastically changes the film formation and its drainage. Therefore, the standard Nusselt flux formula must be expanded to include a clause that takes into account the effect of the surfactant This hypothesis requires further verification in subsequent research, where it will be considered to compare the experimental data with a numerical study taking into account the effect of the surfactant. The theoretical impact of the surfactant is shown in Fig. 4 and Fig. 5. For the purpose of this paper the upper range of the film thickness values is graphically represented by solid line, while the Jeffreys model thickness is represented by dotted line.

Therefore, the impact of the surfactant is presented by the limit estimate of total immobility of the liquid–air interface caused by Marangoni's stress. In the limit conditions the volume flux is given by Eq. 7.

$$q = \frac{\rho g h^3}{12\mu} \tag{7}$$

In Jeffreys's solution, this modification results in a film thickness twice that of a pure freely moving interface at the same position and time. The approximation is based on [11]. It represents the limit case, so these two cases of pure water and limit impact of surfactant give clear boundaries for the presented case with use of very small amount of surfactant, because its concentration was not measured precisely. On the other hand, there is no doubt that the impact of even very small amount of surfactant cannot be neglectable in future investigation and numerical modelling.

Therefore, the two models should be taken as a boundary limit for the film thickness and considered as maximum ranges for the film thickness variation. With the consideration, that the measured and processed data fit into defined boundaries, it is clear to assume the obtained data as reliable.

The acquisition time of each image was reconstructed from the recorded video using MATLAB. This procedure assigned corresponding precise time to each evaluated image allowing the the measured film thickness to be analysed precisely corresponding to the exact time the image was taken.

The comparison with the Jeffreys drainage model showed that the measured film thickness followed the expected decreasing trend over time, The differences from clean water and air interface prediction are consistent with qualitatively certain influence of the surfactant used to improve wettability. The two simple models provided reference limits for interpreting the measurement. However, since the surfactant concentration was not precisely determined, its effect requires further investigation under controlled experimental conditions. Therefore, the present comparison should be understood primarily as a validation of the measurement methodology rather than a detailed investigation of surfactant effects.

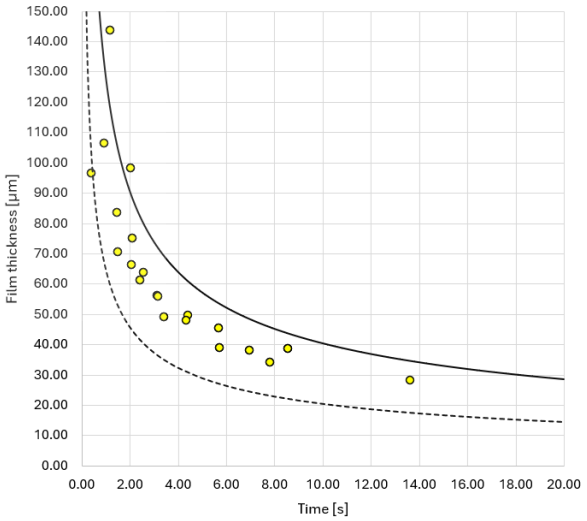


Fig. 4 Graphical representation of comparison measured values of the film thickness (dots) with Jeffreys model (dotted line) and limit impact of surfactant (solid line) boundaries for the distance x = 40 mm from the beginning of the film formation line.

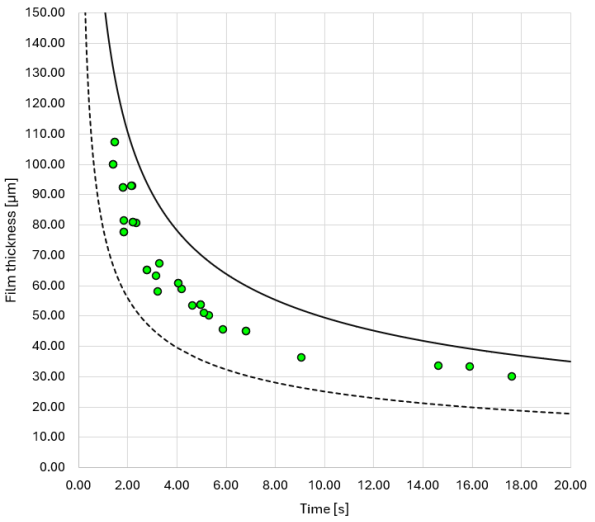


Fig. 5 Graphical representation of comparison measured values of the film thickness (dots) with Jeffreys model (dotted line) and limit impact of surfactant boundaries (solid line) for the distance x = 60 mm from the beginning of the film formation line.

6 Conclusion

Monochromatic laser interferometry was applied to investigate the temporal evolution of a gravity-driven

liquid film on a vertical plate. The experiments demonstrated the feasibility of the obtaining film thickness data from obtained interference patterns using the presented optical arrangement and image processing tools.

A key element of the evaluation was the determination of fringe spacing (the distance between the axis of interference fringes) using cosine fitting, initialized by the spatial frequency estimation by FFT. Comparing with direct detection of intensity maxima, this procedure reduced sensitivity of local brightness, irregularities and optical noise. Evaluating several intensity profile of each image also enabled comparison between different regions of the obtained interference pattern images. It also allowed to process the images and reject those images, where the fitting of cosine approximation was unsatisfactory.

Comparison with the Jeffreys model reproduced the temporal decrease in film thickness, while the differences highlighted the importance of the further inspection of interfacial boundary conditions. The surfactant was used to improve the wettability of the vertical plate, and its influence must be controlled and further investigated. For the impact of the surfactant, the simple approximation was used to demonstrate the both boundaries for the liquid film thickness.

Overall, the results show that the proposed interferometer provides film thickness measurement broadly consistent with the expected range represented by the considered drainage models. The proposed image-processing procedure combining FFT frequency estimation with cosine fitting proved to be a suitable method for evaluating large amount of the obtained interference patterns images.

Together, these findings support the feasibility of the measurement technique and proposed monochromatic light interferometer. The experiment provides reliable temporal data about film thickness at defined points on the vertical plate. Future work should focus on quantifying measurement uncertainty and controlling the influence of surfactants, followed by testing under shear driven condition relevant to steam turbine applications.

We gratefully acknowledge the support Grant Agency of the Czech Republic Grant No. 26-21364S and Grant of the Czech Technical University in Prague, Grant No. SGS24/127.

References

1. E. Nied, J. H. Ruesch, M. Schatz, B. Weigand. Direct numerical simulation of a thin shear-driven water film under turbomachinery relevant conditions. Online. *CEAS Aeronautical Journal*. 17, 2 (2025), 889–899. https://doi.org/10.1007/s13272-025-00890-7

2. D. Bohn, T. Uno, T. Yoshida, C. Betcher, J. Frohnheiser et al. Numerical and experimental study of droplet-film-interaction for low pressure steam turbine erosion protection applications. Online. *Journal of the Global Power and Propulsion Society*. 5 (2021), 90–103. https://doi.org/10.33737/jgpps/140173

3. J. H. Ruesch, P. J. Behn, E. Nied, M. Schatz, B. Weigand. Temporal and spatial experimental investigation on thin shear-driven fluid films under turbomachinery conditions. Online. *CEAS Aeronautical Journal*. 17, 3 (2025), 1025–1035. https://doi.org/10.1007/s13272-025-00904-4

4. A. Simon, M. Marcelet, J.-M. Hérard, J.-M. Dorey, M. Lance. A Model for Liquid Films in Steam Turbines and Preliminary Validations. Online. *Volume 8: Microturbines, Turbochargers and Small Turbomachines; Steam Turbines*. American Society of Mechanical Engineers (2016). https://doi.org/10.1115/GT2016-56148

5. S. Fan, J. Wan, H. Fan, Y. Liu, P. Hu et al. Water erosion experiments and protections for last-stage blades of steam turbine: A review. Online. *Energy Reports*. 15 (2026), 109095. https://doi.org/10.1016/j.egyr.2026.109095

6. L. Jirásek, O. Bartoš, A. Huněk. Study of methods for measuring thin water films for use in steam turbines. Online. *EPJ Web of Conferences*. 358 (2026), 01012. https://doi.org/10.1051/epjconf/202635801012

7. T. Ohyama, K. Endoh, A. Mikami, A. Mori, H. Yasuhiko. Optical interferometry for measuring instantaneous thickness of transparent solid and liquid films. Online. *Review of Scientific Instruments*. 59, 9 (1988). https://doi.org/10.1063/1.1140018

8. T. Nosoko, Y. H. Mori, T. Nagata. Improved interferometer for measuring unsteady film thickness. Online. *Review of Scientific Instruments*. 67 (1996). https://doi.org/10.1063/1.1147095

9. P. Kelly-Zion, W. Collins, D. Glawe. Application of Laser Interferometry for Transient Film Thickness Measurements. Online. *ASMEDC*. 1 (2004). https://doi.org/10.1115/HT-FED2004-56693

10. H. Jeffreys. The Draining of a Vertical Plate. Online. *Mathematical Proceedings of the Cambridge Philosophical Society*. 26, 2 (1930), 204–205. https://doi.org/10.1017/S0305004100015437

11. H. Manikantan, T. M. Squires. Surfactant dynamics: hidden variables controlling fluid flows. Online. *Journal of Fluid Mechanics*. 892 (2020). https://doi.org/10.1017/jfm.2020.170

Analysis of the uncertainty in determining heat flux and heat transfer coefficient during pool boiling

Robert Kaniowski[1,2*], *Robert* Pastuszko[1,2], *Karolina* Bębacz[1,2], *Julia* Sacharz[1,2], *Marta* Fryze[3]

[1]Kielce University of Technology, Al. 1000-lecia P. P. 7, PL-25-314 Kielce, Poland
[2]Central Office of Measures, Elektoralna 2, PL-00-139 Warsaw, Poland
[3]Institute OZE, Skrajna 41a, PL-25-650 Kielce, Poland

Abstract. This study analyzes the uncertainty in determining heat flux and heat transfer coefficient during pool boiling of water, ethanol, FC-72, and Novec-649 at atmospheric pressure. The experiments were conducted using a copper heating cylinder equipped with an internal electric heater and a thermocouple system for determining the temperature distribution. The measurement uncertainty was evaluated using the total differential method, taking into account, among others, the uncertainties associated with temperature measurement, the thermal conductivity of copper, and the geometrical parameters of the experimental setup. Over the heat flux range of 2.3 to 2188 kW/m^2, the relative uncertainty decreased from approximately 75% to 2.3%, whereas for the heat transfer coefficient, within the range of 5.8 to 400 kW/(m^2 K), it decreased from 74% to 4%. The results also demonstrated a significant influence of the boiling fluid on the accuracy of determining heat transfer quantities.

1 Introduction

The boiling process can be used to dissipate substantial heat fluxes while maintaining relatively small temperature differences between the heated surface and the cooling fluid. Owing to its high heat transfer efficiency, boiling is widely used in various industrial applications, including the cooling of electronic components, digital systems, power electronic devices, and high-power heat sources. Heat removal from devices generating high heat fluxes involves the transfer of thermal energy through a solid wall to a cooling fluid, in which phase change occurs. The efficiency of this process depends on both the thermophysical properties of the fluid and the geometry and characteristics of the heat transfer surface.

One of the effective methods for enhancing heat transfer during boiling is to increase the number of active nucleation sites and provide conditions that promote their continuous operation [1,2]. Metals, owing to their high thermal conductivity, are suitable materials for manufacturing extended and porous surfaces [3]. Surfaces incorporating metal foams [4,5] or metal meshes [6] offer considerable potential for achieving high heat transfer coefficients. Other solutions include microchannels, minichannels, and microfins [7,8], as well as channels with modified geometries, including inclined channels [9]. Such structures can be manufactured using machining, electrical discharge machining, or laser processing [10]. Their application makes it possible to modify the conditions governing vapor bubble nucleation and growth, as well as liquid and vapor transport in the immediate vicinity of the heated surface.

In experimental boiling studies, an important issue is not only the enhancement of heat transfer but also the accuracy of the methods used to determine the fundamental parameters describing this process. Heat flux density and the heat transfer coefficient are key quantities used to evaluate the thermal performance of surfaces and compare results obtained under different experimental conditions. The accuracy of their determination depends on the calculation method employed, the temperature measurement technique, the thermophysical properties of the specimen material, and the conditions governing heat transfer within the experimental setup. Particular importance should also be attached to determining the temperature difference between the heated surface and the fluid, as this quantity directly affects the calculated heat transfer coefficient.

The present study investigates the accuracy of the method used to determine heat flux density and heat transfer coefficients during the boiling of four fluids: water, ethanol, FC-72, and Novec 649, at atmospheric pressure. At a pressure of 1013 hPa, the boiling temperatures of the investigated fluids were 100 °C, 78.3 °C, 56.4 °C, and 49 °C, respectively. Copper specimens with parallel grooves machined by milling were used as heat transfer surfaces. Copper was selected because of its favorable thermal conductivity, while the surface geometry provided a defined configuration for investigating the boiling process.

Comparing the results obtained for four fluids with different thermophysical properties makes it possible to assess the applicability of the calculation method under

* Corresponding author: kaniowski@tu.kielce.pl

different boiling conditions. An analysis of the accuracy of the thermal parameter determination helps identify the limitations of the method and evaluate the extent to which the calculated values can be used for the quantitative characterization of heat transfer intensity. This issue is particularly important when comparing heat transfer coefficients for fluids with different saturation temperatures, since the correct interpretation of the observed differences depends on both the experimental conditions and the accuracy of the calculation procedure employed.

2 Experimental setup

Measurements related to the verification and calibration of temperature sensors were performed using an experimental setup designed to investigate heat transfer during phase change (Fig. 1). The main component of the setup was a copper heating cylinder equipped with thermocouples (Fig. 2). The apparatus enabled the measurement of the temperature difference between the fluid and the heated surface, the determination of heat flux, and the calculation of the heat transfer coefficient. These parameters are essential for constructing boiling curves.

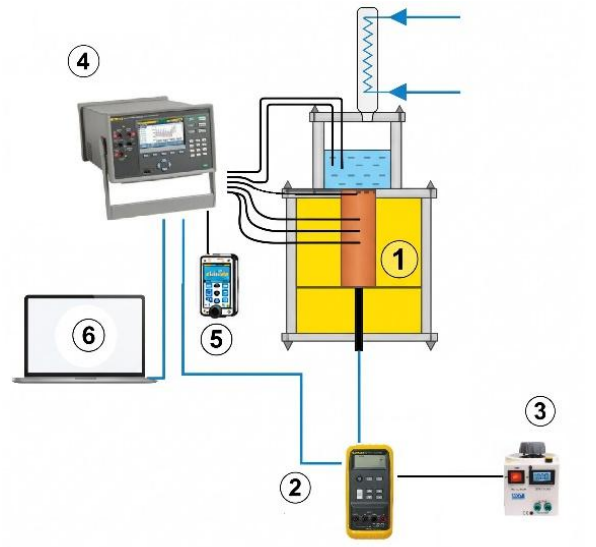


Fig. 1. Experimental setup: 1 – main unit, 2 – wattmeter, 3 – autotransformer, 4 – measurement data acquisition system, 5 – thermocouple calibrator, 6 – PC (personal computer).

An electric heating element rated at 1500 W, with a diameter of 16 mm and a length of 100 mm, was installed inside the copper rod. Temperature measurements were performed using Type K thermocouples. In the first series of experiments, measurements were conducted without prior calibration of the thermocouples. The thermocouples were subsequently calibrated using an Altek 422 calibrator, with a specified accuracy and resolution of 0.1 K. The calibration was performed using the comparison method, which involved comparing the temperature readings of the sensor under calibration with those of a reference thermometer. Calibration was carried out only after the temperature of the liquid and the calibration furnace containing the temperature sensors had stabilized. Temperature measurements were recorded using a FLUKE Hydra Series II data acquisition system.

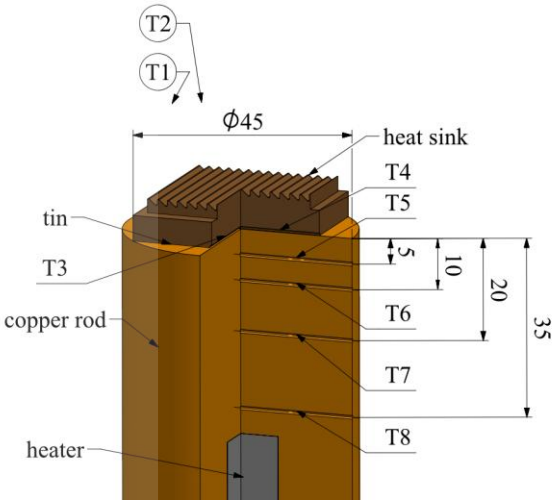
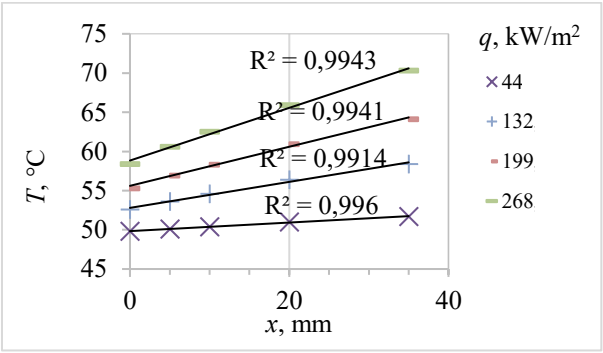


Fig. 2. Heating cylinder with the arrangement of temperature sensors.

3 Results

Temperature distributions within the heating cylinder obtained during the boiling of Novec 649 and FC-72, at heat flux values ranging from 8.3 to 196.2 kW/m², are presented in Fig. 3. Figure 4 shows the temperature distributions obtained during heat dissipation to boiling ethanol and water, at heat flux densities ranging from 30.4 to 1691.2 kW/m².

(a)



(b)

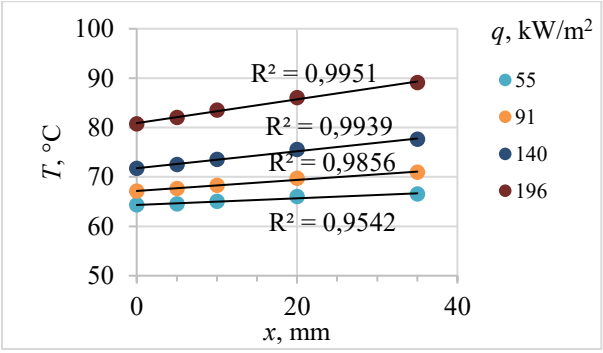
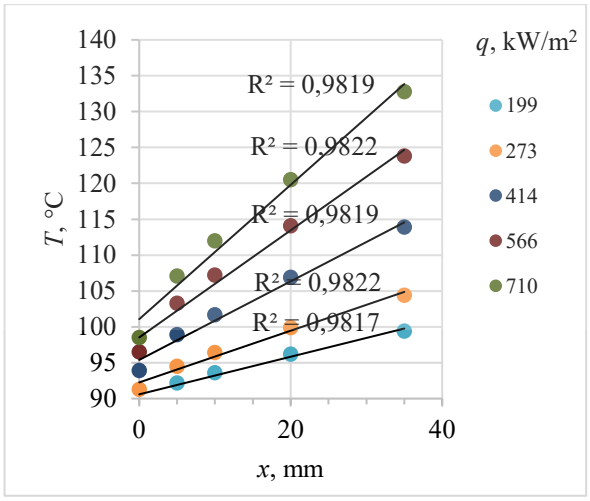


Fig. 3. Temperature distribution along the heating rod at different heat flux values: (a) Novec 649; (b) FC-72.

The linearity of the temperature variation between thermocouples T8 and T3 was examined, and the coefficients of determination, R^2, were calculated for different heat flux values. The obtained coefficients of determination, which were close to unity throughout the investigated range, confirm the strong linearity of the temperature distribution between thermocouples T8 and T3, indicating that one-dimensional heat conduction predominates in the upper part of the heating cylinder.

(a)



(b)

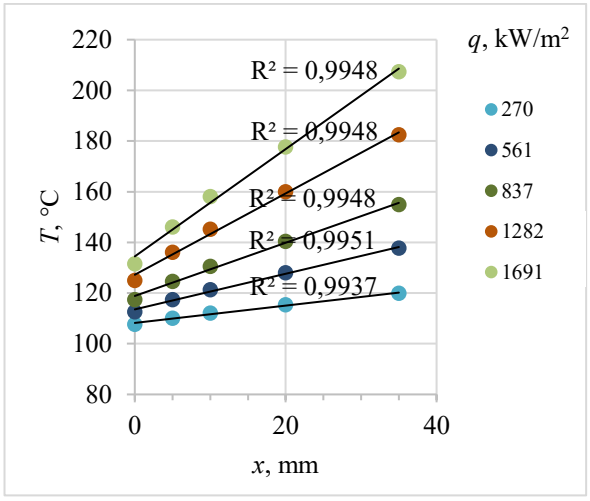


Fig. 4. Temperature distribution along the heating rod at different heat flux values: (a) ethanol; (b) water.

The heat transfer coefficient between the test surface and the fluid was determined using Newton's law of cooling :

$$HTC = \frac{q}{\Delta T} \tag{1}$$

The temperature difference was defined according to Fig. 2 as follows:

$$\Delta T = \frac{T_{T3}+T_{T4}}{2} - q\frac{\delta_s}{\lambda_{Cu}} - \frac{T_{T1}+T_{T2}}{2} \tag{2}$$

The heating cylinder was covered with a thick layer of thermal insulation to prevent lateral heat transfer. Therefore, the heat flux could be calculated assuming one-dimensional heat conduction, in accordance with Fourier's law:

$$q = \lambda_{Cu}\frac{T_{T8}-T_{T5}}{\delta_{T8-T5}}\frac{\pi d_{cyl}^2}{4l^2} \tag{3}$$

3.1 Thermal diffusivity of copper

The thermal diffusivity, a, of the material was determined using the laser flash analysis (LFA) method with a NETZSCH LFA 427 instrument, in accordance with [11] PN-EN ISO 22007-4. Disc-shaped specimens with a diameter of 12.7 mm and a thickness of approximately 3–4 mm were coated with a thin layer of graphite to optimize energy absorption and surface emissivity. The measurement involved heating the front surface of the specimen with a short neodymium-doped yttrium aluminum garnet (Nd:YAG) laser pulse while simultaneously recording the temperature rise on the rear surface using an infrared (IR) detector. The thermal diffusivity values were calculated using the Proteus software based on the half-rise time of the temperature response, taking into account mathematical models for heat loss correction and the finite duration of the laser pulse.

Measurement uncertainty

$$u_c(a) = a \cdot \sqrt{\left(\frac{u(a_{ref})}{a_{ref}}\right)^2 + u_{rep}^2} \tag{4}$$

where:

a– thermal diffusivity of the test specimen,

a_{ref}– thermal diffusivity of the reference material (graphite, stainless steel 310, Cu, or Pyroceram 9606).

Measurement repeatability uncertainty:

$$u_{\mathrm{rep}} = \frac{s(a)}{\overline{a_{rep}}\sqrt{n}} \tag{5}$$

where:

$s(a)$ – standard deviation of the mean of the thermal diffusivity results:

$$s(a) = \sqrt{\frac{1}{n-1}\sum_{i=1}^{n}\left(a_{rep_i} - \overline{a_{rep}}\right)^2} \tag{6}$$

a_{rep} – thermal diffusivity of the specimen material,

n – number of measurement repetitions.

The results of the thermal diffusivity measurements of copper are presented in Table 1.

Table 1. Thermal diffusivity of copper.

T ,°C	a ·10⁶ m²/s	U ·10⁶ m²/s
19.9	116.97	5.45
100.3	112.57	5.20
201.2	107.98	4.99
300.7	103.94	4.80
400.8	100.19	4.63
500.9	96.54	4.46

3.2 Specific heat capacity of copper

The specific heat capacity, c_p, of copper was determined over the temperature range of 100–450 °C using a NETZSCH DSC 214 Polyma differential scanning calorimeter. The measurements were performed in accordance with ISO 11357-4 [12], using sapphire (alpha-Al_2O_3) as the reference material. A copper specimen of known mass was placed in an aluminum crucible. The measurements were carried out under a nitrogen atmosphere at a flow rate of 60 mL/min, using a heating rate of 10 K/min. The temperature dependence of the specific heat capacity and baseline correction were determined using the dedicated NETZSCH Proteus Analysis software.
The measurement uncertainty was determined using the following relationship:

$$u_c(c_{p_s}) = c_{p_s}\sqrt{A^2 + \mathrm{B}^2 + \mathrm{C}^2 + D^2 + \mathrm{E}^2} \quad (7)$$

where:

$$A = \frac{u(c_{p_{ref}})}{c_{p_{ref}}};\ B = \frac{u(m_{ref})}{m_{ref}};\ C = \frac{u(m_s)}{m_s};$$

$$D = u_{rep_{ref}};\ E = u_{rep_s}.$$

The repeatability components were calculated as:

$$u_{\mathrm{rep_{ref}}} = \frac{s(q_{ref})}{\overline{q_{ref}}\sqrt{n}} \quad (8)$$

$$u_{\mathrm{rep_s}} = \frac{s(q_s)}{\overline{q_s}\sqrt{n}} \quad (9)$$

where:
$s(q)$– denotes the standard deviation of the mean heat-flow signal obtained from a series of measurements:

$$s(q_{ref}) = \sqrt{\frac{1}{n-1}\sum_{i=1}^{n}\left(q_{ref_i} - \overline{q_{ref}}\right)^2} \quad (10)$$

$$s(q_s) = \sqrt{\frac{1}{n-1}\sum_{i=1}^{n}\left(q_{s_i} - \overline{q_s}\right)^2} \quad (11)$$

where (n) is the number of measurement repetitions.
The reference material (sapphire), measured under laboratory conditions, exhibited a deviation of 2% from the tabulated specific heat capacity. Therefore, the relative uncertainty of the reference material's specific heat capacity was assumed to be 2% i. e., $u(c_{p_ref})/c_{p_ref} = 2$ %.

Mass measurement uncertainty

The combined standard uncertainty of mass measurement was calculated as:

$$u(m) = \sqrt{u_{rep}^2 + u_{cal}^2 + u_{exp}^2} \quad (12)$$

where the repeatability component was determined as:

$$u_{\mathrm{rep}} = \frac{s(m)}{\sqrt{n}} \quad (13)$$

$$s(m) = \sqrt{\frac{1}{n-1}\sum_{i=1}^{n}(m_i - \bar{m})^2} \quad (14)$$

$$u_{cal} = \frac{\mathrm{U}}{k} \quad (15)$$

where (U) is the expanded uncertainty of the mass measurement specified in the balance calibration certificate, and (k) is the coverage factor.
The resolution component was calculated assuming a rectangular probability distribution:

$$u_{exp} = \frac{d}{2\sqrt{3}} \quad (16)$$

where (d) is the balance scale interval.
The results of the specific heat capacity measurements of copper are presented in Table 2.

Table 2. Specific heat capacity of copper.

T ,°C	c_p, J/(kg K)	U, J/(kg K)
100	398	9
150	403	9
200	407	9
250	410	10
300	412	10
350	412	10
400	413	10
450	415	10

3.3 Coefficient of thermal expansion of copper

The coefficient of thermal expansion was measured in accordance with ASTM E228 [13], while the density and its variation with temperature were determined using a NETZSCH DIL 402 Expedis dilatometer equipped with the NanoEye optoelectronic sensor system. Measurements were performed in a helium atmosphere over the temperature range of 20–300°C at a constant heating rate of 3 K/min. The initial density of copper was determined using the Archimedes method with a Radwag XA 52.5Y laboratory balance ρ (T_{amb} = 20 °C) = 8961 kg/m^3. Changes in volume during the thermal cycle were calculated using NETZSCH Proteus software based on the recorded linear expansion. To eliminate the influence of the thermal expansion of the measurement system, each experimental curve was corrected using a baseline measurement performed with fused silica under an identical temperature profile.
Measurement uncertainty equation :

$$u_c(\alpha) = \alpha\sqrt{\left(\frac{u(\alpha_{ref})}{\alpha_{ref}}\right)^2 + \left(u_{rep}\right)^2} \quad (17)$$

α – linear coefficient of thermal expansion of the specimen,
α_{ref} – coefficient of thermal expansion of the reference material.
The repeatability uncertainty was calculated as follows:

$$u_{\text{rep}} = \frac{s(\alpha)}{\overline{\alpha_{rep}}\sqrt{n}} \quad (18)$$

where the standard deviation of the mean of the thermal expansion measurements was determined using the following equation:

$$s(\alpha) = \sqrt{\frac{1}{n-1}\sum_{i=1}^{n}\left(\alpha_{rep_i} - \overline{\alpha_{rep}}\right)^2} \quad (19)$$

α_{rep} – coefficient of thermal expansion of the specimen,
n– number of measurement repetitions.

Assuming isotropic thermal expansion of copper, its density can be calculated using the following equation:

$$\rho(T) = \frac{\rho_{20}}{[1+\alpha(T-20)]^3} \quad (20)$$

The thermal conductivity of copper, from which the copper rod and heat sink were manufactured, was determined using the following relationship:

$$\lambda = a \cdot c_p \cdot \rho \quad (21)$$

The results of the thermal expansion coefficient measurements for copper are presented in Table 3, while Table 4 summarizes the temperature-dependent density and thermal conductivity of copper.

Table 3. Coefficient of thermal expansion of copper.

T ,°C	α_s, 1/K	U, 1/K
125 - 450	$18.324 \cdot 10^{-6}$	$0.531 \cdot 10^{-6}$

Table 4. Density and thermal conductivity of copper.

T ,°C	ρ, kg/m^3	λ, W/(m K)
100	8 921,6	399,7
150	8 896,7	395,1
200	8 871,8	389,9
250	8 847,0	384,5
300	8 822,4	377,8

3.4 Heat flux

The uncertainty in heat flux determination was evaluated using the total differential method, accounting for uncertainties in the thermal conductivity coefficient $\Delta\lambda$ = 0.1 W/(m K), the temperature difference across the heating cylinder $\Delta(\Delta T_{cyl})$ = 0.2 K, the distance between temperature sensors, and the geometric dimensions, namely the diameter of the heating cylinder and the side length of the specimen. The uncertainties in the sensor spacing, cylinder diameter, and specimen side length were assumed to be, taking into account the thermal expansion of copper $\Delta\delta_{\text{T5–T8}} = \Delta d_{cyl} = \Delta l$ = 0.00025 m. The relationship was expressed as follows:

$$\Delta q = \sqrt{A^2 + B^2 + C^2 + D^2 + E^2} \quad (22)$$

where:

$$A = \frac{\partial q}{\partial \lambda}\Delta\lambda;\ B = \frac{\partial q}{\partial \Delta T_{T5-T8}}\Delta(\Delta T_{T5-T8});$$
$$C = \frac{\partial q}{\partial \Delta\delta_{T5-T8}}\Delta\delta_{T5-T8};\ D = \frac{\partial q}{\partial d_{cyl}}\Delta d_{cyl};\ E = \frac{\partial q}{\partial a}\Delta a.$$

For heat flux values ranging from 2.3 to 2188 kW/m^2, the relative uncertainty varied from 75% to 2.3% (Fig. 5).

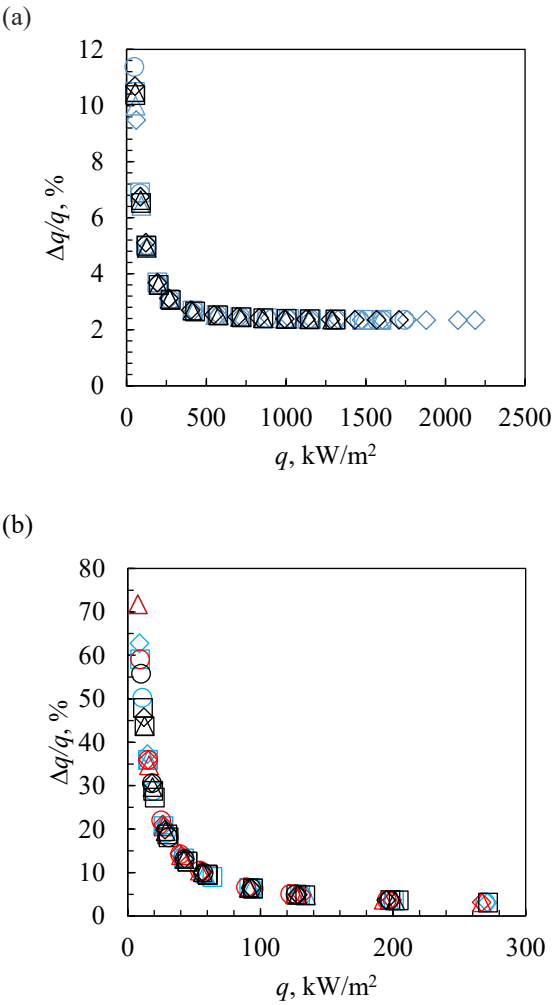


Fig. 5. Relative uncertainties in heat flux determination: (a) water; (b) FC-72.

3.5 Heat transfer coefficient

The uncertainty in the heat transfer coefficient, ΔHTC was determined using the following relationship:

$$\Delta HTC = \sqrt{\left(\frac{\partial HTC}{\partial q}\Delta q\right)^2 + \left(\frac{\partial HTC}{\partial \Delta T}\Delta(\Delta T)\right)^2} \quad (23)$$

The absolute uncertainty in the wall superheat was calculated as follows:

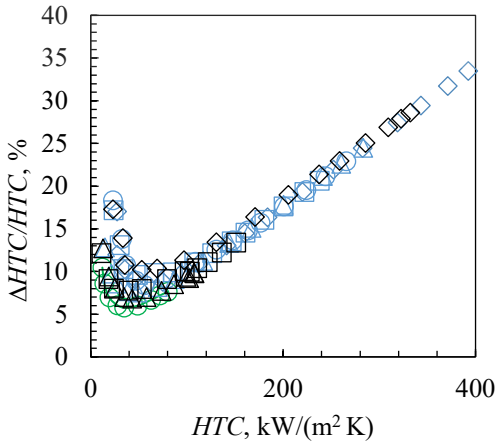
$$\Delta(\Delta T) = \sqrt{A^2 + B^2 + C^2 + D^2} \quad (24)$$

where:

$$A = \frac{\partial \Delta(\Delta T)}{\partial q}\Delta q;\ B = \frac{\partial \Delta(\Delta T)}{\partial \Delta T_{sat}}\Delta(\Delta T_{sat});$$
$$C = \frac{\partial \Delta(\Delta T)}{\partial \lambda}\Delta\lambda;\ D = \frac{\partial \Delta(\Delta T)}{\partial \delta_{bs}}\Delta\delta_{bs}.$$

The relative uncertainty in the heat transfer coefficient ranged from 74% to 4% over the heat transfer coefficient range of 5.8–400 kW/(m^2 K) (Fig. 6).

(a)



(b)

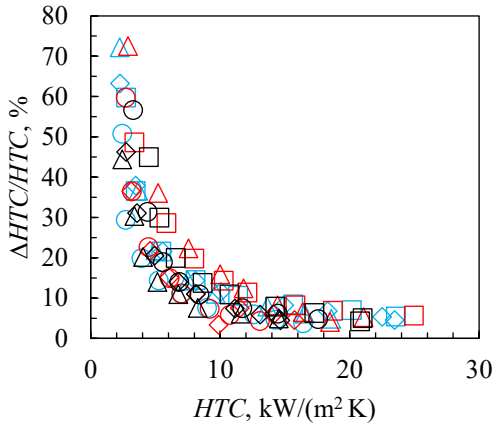


Fig. 6. Relative uncertainties in the determination of the heat transfer coefficient: (a) water; (b) FC-72.

4 Conclusion

Based on the measurements performed, the following conclusions can be drawn:

- The reduction in the relative uncertainty of heat flux determination depends on the properties of the boiling fluid:
- For water boiling, relative uncertainties below 3% are achieved at heat flux values exceeding 400 kW/m^2.
- For FC-72 boiling, relative uncertainties below 3% are achieved at heat flux values exceeding 270 kW/m^2.
- For both fluids, the relative uncertainty in heat flux, (q), decreases to below 5% at heat flux values exceeding 127 kW/m^2.

The variation in the relative uncertainty of the heat transfer coefficient is strongly dependent on the boiling fluid used:

- During water boiling, the lowest relative uncertainties (approximately 7%) are obtained for heat transfer coefficients in the range of 25–50 kW/(m^2 K).
- During FC-72 boiling, the lowest relative uncertainties (below 5%) are obtained for heat transfer coefficients exceeding 20 kW/(m^2 K).

Nomenclature

a	– thermal diffusivity, m^2/s
c_p	– specific heat capacity, J/(kg K)
d	– diameter, m or balance scale interval, kg
HTC	– heat transfer coefficient, kW/(m^{2}K)
l	– side length of the active surface, m
k	– coverage factor
m	– mass, kg
n	– number of measurement repetitions
q	– heat flux, kW/m^2
R	– coefficient of determination
s	– standard deviation
T	– temperature, K,
U	– expanded uncertainty
u	– standard uncertainty
x	– thermocouple distance from the cylinder surface, m

Greek symbols

α	– linear coefficient of thermal expansion, 1/K
δ	– thickness, mm,
λ	– thermal conductivity, W/(m K)
ρ	– density, kg/m^3

Subscripts

amb	– ambient
bs	– base
cal	– calibration
c	– combined
Cu	– copper
cyl	– cylinder
exp	– resolution
i	– measurement index
ref	– reference
rep	– repeatability
s	– specimen

sat – saturated
T1…T8 – thermocouple number

References

1. T.J. Chuang, Y.H. Chang, Y.M. Ferng, Investigating Effects of Heating Orientations on Nucleate Boiling Heat Transfer, Bubble Dynamics, and Wall Heat Flux Partition Boiling Model for Pool Boiling. Appl. Therm. Eng. **163**, 114358, (2019). https://doi:10.1016/j.applthermaleng.2019.114358
2. A. Surtaev, D. Kuznetsov, V. Serdyukov, A. Pavlenko, V. Kalita, D. Komlev, A. Ivanikov, A. Radyuk, Structured Capillary-Porous Coatings for Enhancement of Heat Transfer at Pool Boiling. Appl. Therm. Eng. **133**, 532–542 (2018). https://doi:10.1016/j.applthermaleng.2018.01.051
3. Z.G. Qu, Z.G. Xu, C.Y. Zhao, W.Q. Tao, Experimental Study of Pool Boiling Heat Transfer on Horizontal Metallic Foam Surface with Crossing and Single-Directional V-Shaped Groove in Saturated Water. Int. J. Multiph. Flow. **41**, 44–55 (2012). https://doi:10.1016/j.ijmultiphaseflow.2011.12.007
4. H. Hu; Y. Zhao, Z. Lai, C. Hu, Experimental Investigation on Nucleate Pool Boiling Heat Transfer Characteristics on Hydrophobic Metal Foam Covers. Appl. Therm. Eng. **179**, 115730 (2020). https://doi:10.1016/j.applthermaleng.2020.115730
5. H. Hu; Y. Zhao, Z. Lai, C. Hu, Influence of Surface Wettability on Pool Boiling Heat Transfer on Metal Foam Covers. Int. J. Therm. Sci. **168**, 107069 (2021). https://doi:10.1016/j.ijthermalsci.2021.107069
6. Z.G. Xu, C.Y. Zhao, Thickness Effect on Pool Boiling Heat Transfer of Trapezoid-Shaped Copper Foam Fins. Appl. Therm. Eng. **60**, 359–370 (2013). https://doi:10.1016/j.applthermaleng.2013.07.013
7. D. Cooke, S.G. Kadlikar, Effect of Open Microchannel Geometry on Pool Boiling Enhancement. Int. J. Heat Mass Transf. **55**, 1004–1013 (2012). https://doi:10.1016/j.ijheatmasstransfer.2011.10.010
8. R. Pastuszko, R. Kaniowski, Boiling visualization on vertical fins with tunnel-pore structures. EPJ Web Conf. **25**, 02019 (2012). https://doi.org/10.1051/epjconf/20122502019
9. R. Kaniowski, Pool boiling of Novec-649 on Inclined Microchannel. Energies. **16**, 2476 (2023). https://doi.org/10.3390/en16052476
10. Ł.J. Orman, N. Radek, A. Kapior, L. Dębska, Pool Boiling Heat Transfer Performance of the Surface Modified with Laser. MATEC Web Conf. **369**, 02003 (2022). https://doi:10.1051/matecconf/202236902003
11. PN-EN-ISO-22007-4 Plastics — Determination of thermal conductivity and thermal diffusivity — Part 4: Laser flash method.
12. ISO 11357-4 Plastics — Differential scanning calorimetry (DSC) — Part 4: Determination of specific heat capacity.
13. ASTM E228 Standard Test Method for Linear Thermal Expansion of Solid Materials with a Push-Rod Dilatometer.

Applicability of parallel compressor theory to centrifugal compressors with inlet total pressure distortion

David Koziel [1,2*]

[1]Brno University of Technology, Institute of Aerospace Engineering, 61600, Brno, Technická 2, Czechia
[2]PBS Velká Bíteš, Technical Development Division, 59501 Velká Bíteš, Vlkovská 279, Czechia

Abstract. Inlet flow nonuniformity is unavoidable in installed engine operation and degrades compressor performance, stability and service life. As the airframe is often unknown during engine development, manufacturers need computational tools feasible for evaluating many installations and missions. Parallel compressor theory (PCT) is a well-established reduced-order framework for total pressure distortion, developed mainly for axial compressors. A review of the centrifugal compressor distortion literature shows that the available data come mainly from turbocharger-type, low-pressure-ratio machines and rarely separate pressure distortion from swirl and intake losses. To the author's knowledge, PCT has not yet been applied to highly loaded jet engine centrifugal compressors directly exposed to distortion. A published turbocharger dataset with 90° and 180° distortion screens is compared with a parallel compressor model (PCM) using a constant-discharge-pressure boundary condition. The 180° case is consistent with the model, whereas the 90° case lies outside the bounds set by the uniform-screen results. The difference between the PCM and an equivalent uniform inlet loss is then evaluated across sector extent and distortion intensity. The comparison with the reported measurement uncertainty then indicates the conditions under which a test can distinguish between models. A combined CFD and experimental campaign is proposed to investigate sector coupling in high-pressure-ratio aerospace centrifugal compressors.

1 Introduction

Inlet total pressure distortion is characterized by a nonuniform total pressure distribution in a particular location upstream of an aerospace gas turbine (e. g. the aerodynamic interface plane). It is one of several types of flow nonuniformities that can occur during the field operation of an aerospace propulsion plant. The flow nonuniformity formation is governed by several factors.

Namely, it forms due to operating regimes characterized by relatively high angles of attack, ground operation, or use of other devices altering the gas properties near the engine inlet (e. g. use of weapons) during the in-flight operation. These effects are driven by the requirements for operability and manoeuvrability of the vehicle, and they are defined by the mission of the aircraft.

The other compound effect comes from the requirements on the design of the aircraft itself, particularly the integration of the engine into the airframe. The optimization target depends on the application requirements. In the field of small turbojet engines used in defence-related programmes, the aim is to reduce the overall volume and the radar footprint.

The occurrence of inlet nonuniformity affects the engine performance, stability, control, and life. This poses a challenge to designers who must not only predict the occurrence of distortion patterns, but also, they must predict the effects of these nonuniformities and create robust distortion-tolerant compression systems.

A single engine design may be integrated into multiple aircraft which may operate in diverse operating conditions. It is infeasible to evaluate the tolerance of a propulsion system to inlet flow distortion in the entire operating envelope for every potential installation experimentally. This creates a demand for a distortion-tolerant compressor design and reliable predictive low-fidelity reduced-order framework, such as Parallel Compressor Theory (PCT).

A critical review of the existing inlet distortion literature reveals that the existing research focuses predominantly on axial compressors or low-pressure-ratio centrifugal compressors (turbochargers and blowers). It also reveals that the aerodynamics-focused datasets frequently do not isolate the effects of total pressure distortion from flow angularity effects and intake pressure loss. Consequently, the predictive capability of the Parallel Compressor Model (PCM) framework and its core assumptions applied to highly loaded centrifugal compressors remain unresolved.

The aim of this paper is to determine whether existing centrifugal compressor data can support the current PCT-based approaches, whether the data are able to distinguish between the distortion-induced loss and uniform intake pressure loss, and whether it is possible to define conditions in which this can be resolved.

* Corresponding author: David.Koziel@vutbr.cz

This is supported by (1) the literature synthesis illustrating the insufficient extent of available data (2) the demonstration of a PCM on an existing turbocharger centrifugal compressor dataset that is unable to resolve the coupling and closure term question (3) the parametric study (over total pressure distortion intensity (δ) and circumferential extent (θ)) on a high-pressure-ratio centrifugal compressor predicting the gap between the distortion-induced and uniform losses driving the measurement equipment requirements, and (4) the outline of a combined test & CFD campaign.

2 Inlet Total Pressure Distortion Effects on Centrifugal Compressors

Despite its long history full of major discoveries, the field of total pressure distortion remains an active area of research. This section follows the approaches taken by researchers throughout history aimed to capture the effects of inlet flow nonuniformity on centrifugal compressor operation. This includes experiments, CFD, and application of reduced-order models.

2.1 Initial Experiments

The first notable paper published on inlet flow distortion effects on centrifugal compressors comes from Ariga et al. [1], who performed a study on a low-pressure-ratio centrifugal compressor for multiple operating points. They used upstream mounted honeycombs to quantify the effects of both the circumferential and the radial distortion on the stage performance and impeller flow field, indicating the detrimental effects of a change of impeller incidence angle.

A subsequent study by Ariga et al. [2] shifted focus on the nature of inducer stall under conditions of total pressure distortion. Their findings included qualitative differences in stall patterns and the absence of stall hysteresis documented under the uniform inlet conditions.

Both papers established the foundations of radial compressor inlet distortion research. However, a direct utility of the results in present aerospace applications is diminished due to the differences in the compressor design (particularly the low pressure ratio).

2.2 Intake Optimization

As the flow distortion induced by an upstream geometry was recognized to pose a problem for radial compressor operation, several papers by Kim et al. [3], Michelassi et al. [4], and Engeda et al. [5] were published in early 2000s to capture the nature of the flow through a bent pipe and optimize its geometry to minimize the adverse effect on the downstream compressor with vaned diffuser.

Their work described the presence of secondary flows introduced by the static pressure gradients in the bent pipe, which coexisted simultaneously with the total pressure distortion. The inlet pipe affected both pressure ratio and efficiency adversely. The authors also noted that the work of the compressor remained approximately constant for all cases.

Even though the papers captured the effects of upstream nonuniformity, the focus remained on understanding and eliminating adverse conditions posed on the compressor, rather than developing the robustness of the compressor itself. Moreover, the effects on the compressor performance did not isolate the loss of performance due to flow angularity, which makes the results not directly applicable to the case without any inlet swirl distortion.

2.3 Stress-Focused Research

The nature of the total pressure distortion interaction with compressor impeller blades is inherently unsteady. This became the subject of studies by Kammerer et al. [6; 7] and Zemp et al. [8], which focused on the time-dependent nature of the aerodynamic blade loading and its implications in terms of structural integrity and compressor life.

The aerodynamic response of the blades and its effects on performance were not the primary concern of these papers, limiting their usability in the performance-related field of research.

2.4 Inlet Geometry Influence

Further research focusing on the detrimental effects of upstream geometry includes steady and unsteady CFD studies performed by Vagnoli and Verstraete [9] with the focus on the rotating stall inception in the case of a bent inlet pipe. Conclusions describe no notable shift in surge margin, only in performance characteristics. This is attributed to the centrifugal effects dominating the compression process. Moreover, higher losses are observed to occur in higher mass flow regions. Unsteady calculations also show differing tip-vortex interactions with the leading-edge shock and the main flow.

In parallel, a significant portion of the effort is directed towards assessing the influence of different bent inlet pipes mounted in front of low-pressure turbocharger compressors with vaneless diffusers and outlet volutes. Wang et al. [10] and Yang et al. [11; 12] observed the influence of the inlet bend and the volute (the clocking effect) on compressor performance. They describe the frequency response changes in different inlet configurations and a profound detrimental effect on the compression ratio of the bend in high mass flows. Hou et al. [13] attribute the observed effects more to the swirl than to the total pressure distortion. Zhao et al. [14] also identify total pressure losses (distinct from the distortion losses) and bend-induced vortices as the main contributors to the losses in compressor efficiency. This agrees with the later findings of Zhang et al. [15].

When it comes to stability, the effects of inlet bent pipes are described as a secondary contributor to the surge margin losses compared to the effect of volute-induced distortion, as the inlet affects mainly the performance near choke [16].

Further headway was made by Galindo et al., who studied the impact of several axisymmetric inlet

geometries (and the induced radial distortion) with his primary focus being noise reduction through inlet geometry optimization [17; 18].

Even though the research progress presented in this section shows the importance of inlet geometry influence assessment (regarding to compressor performance and stability), the results come with an important drawback – the inlet pressure losses are not clearly isolated from the pressure distortion losses. Moreover, the total pressure distortion is accompanied by induced swirl, which introduces further complexity to the dataset. Hence, the individual effects of pressure distortion, swirl, and intake losses on performance and stability cannot be separated. The sole effect of total pressure distortion is, therefore, ambiguous, and these results should spark further research into the matter.

2.5 Distortion Screens Tests & CFD

Distortion screen tests are a standard way of testing the general susceptibility of compression systems to inlet flow nonuniformities prior to airframe-compressor integration.

A significant contribution to the centrifugal compressor dataset was provided by Sitaram et al. [19; 20]. His investigations focused on capturing the effects of multiple distortion patterns and their effects on the performance of a low-pressure centrifugal compressor. It has been shown that the compressor map shape is modified under the influence of total pressure distortion effects that had been isolated. The contribution also included the use of distortion descriptors for the purpose of correlating the distortion intensity with loss of performance that could be used comparatively. However, this approach is limited in cases of more complex cases of inlet distortion.

Another exhaustive experimental study was performed by Jaiswal et al. [21], who tested both uniform screen effects and distortion screen effects. It captures efficiency and pressure rise deterioration increasing with the distortion intensity (decreased screen porosity), especially towards higher mass flows.

A numerical approach to the problem is taken by Zhang et al. [22], who performed unsteady CFD focusing on inlet and outlet pressure distortion matching, capturing the effect of relative angular positions of spoiled regions on stage efficiency.

These papers represent a minority of datasets in which the influence of inlet nonuniformity is investigated independently of intake geometry, which makes them invaluable for the purposes of isolated total pressure distortion research activities.

2.6 Reduced Frequency Approach

Concept of reduced frequency was first used to describe compressor distortion-tolerant properties by Plourde et al. [23]. Cousins [24] proposed a physics-based explanation based on flow travel time to blade throat (and the blade's ability to respond to the changing conditions). In context of radial compressors, the reduced frequency was utilized by Grimaldi and Michelassi [25] who used a large experimental dataset for efficiency and pressure ratio loss based on the reduced frequency of the machine, with lower frequency yielding greater performance reductions.

The reduced frequency concept was then used to develop physical interpretation of the critical angle concept, first introduced by Reid [26].

The critical angle of distortion concept was tackled by Bond and Key [27], who used an alternative definition of the reduced frequency (the acoustic propagation reduced frequency introduced by Fatsis et al. [28], tracking the propagation of distortion through the impeller and using the reduced frequency to determine the critical angle extent.

Unlike empirical distortion descriptors, the information included in the reduced frequency approach can provide a physics-based foundation for reduced-order modelling of centrifugal compressor response to circumferential inlet distortion and therefore remains a concept that should be pursued further.

2.7 Reduced-Order Modelling

Even though there is an obvious overlap between axial compressor reduced order models (ROM) and radial compressor ROM, this section inspects only the mathematical models that have been applied to a radial compressor and published, regardless of application.

Models based on parallel compressor theory (PCT/PCM) are an obvious candidate for a ROM applied to a centrifugal compressor. Cousins and Davis evaluate the possibilities of extended parallel compressor models to assess complex flow distortion patterns [29]. The second part of the paper sees the model in its extended form to be applied to multiple complex distortion cases [30]. However, it is only the third paper that applies the PCM coupled with a 1D dynamic compressor model to a centrifugal compressor [31]. The centrifugal stage is located downstream of the multistage axial compressor. The dynamics of the whole system and the stabilizing influence of the centrifugal stage on pre-stall behaviour are described. However, the centrifugal stage is only exposed to relatively low distortion intensity due to the attenuation effect of upstream-mounted axial compressor. The paper also explores the effect of centrifugal compressor on axial compressor transient behaviour rather than exploring the effects of distortion propagation affecting the centrifugal machine.

A pure physics-based mathematical model for a turbocharger compressor is introduced by Song et al. [32]. The model assumes two parallel flows, similarly to a standard parallel compressor model. However, the mass flow distribution is determined by the Euler turbomachinery equation, instead of a uniform discharge pressure boundary condition. The formulation also does not use any compressor map, but it utilizes a meanline calculation approach to obtain the results. Consequently, the model does not incorporate any surge behaviour, nor predicts the surge boundary.

The work published in field of centrifugal compressors contrasts highly with the knowledge and predictive capabilities available in the axial compressor

inlet distortion research. Even though the axial compressor models can be, in its essence, utilized in the centrifugal compressor research field without significant modifications, the predictive capabilities remain to be demonstrated, especially in the case of high-pressure ratio systems.

Therefore, a generalized approach to inlet flow distortion effects on the stability and performance of centrifugal compressors is yet to be developed, identifying a clear path forward in this area.

3 Parallel Compressor Theory

3.1 Computational Methods Distinction

In general, the computational methods used to mathematically model the behaviour of the compression system under conditions of total pressure inlet distortion could be divided into the following groups (ordered from the least to the most computationally demanding):

- Meanline and Streamline Codes (MLC & SLCC)
- One-dimensional Dynamic Models (1DDM)
- Parallel Compressor Models (PCM)
- Two-dimensional Axisymmetric Models
- Three-dimensional Euler-based Models
- Three-dimensional Navier-Stokes-based Models

Meanline and streamline codes are usually used to predict stage/blade-row performance, 1D dynamic methods model the transient behaviour of the compression system, PCMs utilize the lower-fidelity approaches to describe the inlet nonuniformity response of compressors 3D codes can be used to model radial distortion, and the three-dimensional tools can tackle the complexity of the underlying flow field [33].

3.2 Theory Inception

Parallel compressor theory is a useful low-fidelity tool for inlet distortion sensitivity description if applied with sound assumptions.

PCT and its derivatives are a quasi-one-dimensional technique that could be used to describe a compression system that can be split into two or more distinct circumferential regions operating in different conditions (and consequently in different operating point).

Initial ideas about PCT can be traced to Pearson and McKenzie [34; 35] with further extensions being provided by Day [36]. Initially, the idea of PCM was used to model the in-stall performance of an axial compressor.

3.3 Application to Inlet Distortion

Later, the theory was used to predict compression system performance and stability in conditions of inlet total pressure distortion.

The assumption is that to simulate distorted flow effects, the compression system could be described by multiple separate compressors running in parallel. The approaches to instability determination, physics simplifications, and boundary condition implementation vary between different implementations. The simplest models use two parallel segments described by a steady-state compressor performance map (or MLC/SLCC) with constant discharge pressure boundary condition. PCT suffers from the same limitations as the models upon which they are based. Also, the results are limited by the simplifications and assumptions of the PCT itself, e.g., crossflow between segments and constant discharge pressure boundary condition [33].

Important improvement of its predictive capability in low-extent distortion cases was introduced by Reid [26], who described the concept of critical angle, stating that there is an angular extent of circumferential distortion under which the stability margin loss decreases with the decreasing extent of distortion.

Later, variable coupling factor was introduced, as shown in [37]. The coupling factor is said to be determined empirically and to be a function of compression operating regime.

Other notable examples of PCT extensions include the multiple-segment model developed by Mazzawy [38] that can be used for surge and performance predictions based on the compressor performance map. The model also allows for correction because of circumferential crossflow, rotor blade tip gap, unsteady flow, and viscosity effects.

Further research efforts included modification of a one-dimensional dynamic compression system code DYNTECC [39; 40] to incorporate inlet pressure and temperature distortion, also developing the circumferential crossflow effects.

The PCT is well documented by Davis in [41], and then later by Cousins and Davis [29]. They described the ways to extend the model using multiple circumferential and radial segments, introducing the swirl effects using multiple compressor maps for interpolation, illustrating the use on multiple distortion cases for axial compressors and fans in the second part of the same paper [30].

As most of the models aim to solve the response of the compression system to circumferential distortion, further modelling advancements focused on its combined effects with the inlet swirl. However, these models require (multiple) compressor maps that included swirl effects as input [42; 43].

The application of PCT to radial compressors is limited. Even though it is not explicitly stated that it cannot be used, only a fraction of authors documents the actual use of the model in radial compressor application [1; 31; 32].

3.4 Key Theory Details

The details of PCT have been discussed many times in existing literature (see e. g. [37; 38]). However, there are several features of the models that should be reiterated in the following paragraphs.

Every tool utilizing the PCT must also have a source of information about the performance of the compression system. The model then generally relies on MLC/SLCC or a stage map generated by a high-fidelity tool or experiment for an input. The limitations of the methods used to generate the data then become the limitation of the PCM as well.

PCT is based on the idea of multiple compressors operating in parallel. For a set of boundary conditions, a closure term is necessary. The classic PCT prescribes a constant discharge pressure boundary to the outlet. However, this is not true for tightly coupled machines experiencing a limited levelling of static pressures. The coupling factor is used to model the behaviour.

Another concept pertaining to the circumferential extent of the spoiled sector is the concept of blade aerodynamic response, which is related to the critical angle concept and rotor reduced frequency. This becomes a crucial consideration when assessing the effects of circumferential distortion of relatively low angular breadth, as the response of the blade to the spoiled region is no longer steady.

4 Application of PCM to Experimental Dataset

This section introduces the reader to key definitions and quantities used in the rest of the document. Then, a parallel theory approach is applied to a publicly available turbocharger dataset containing information suitable for both investigating the classical PCT approach and the experimental setup defining the possibilities of the measurements regarding uncertainty.

4.1 Key Definitions

4.1.1 Speedline Parameter (β)

To define the operating point location on a compressor speedline, a dimensionless parameter β that takes on a value between 0 (surge) and 1 (choke) is used. Therefore, any β value (except for β = 0) does not represent a particular physical condition and it is dependent on the dataset itself.

To utilize this in the model, a beta grid (uniformly discretized along the piecewise linear speedline curve) was constructed from the measured dataset and for the purposes of the calculation the data in-between the measured points are computed using linear interpolation.

The point of stage instability is determined (in accordance with the PCT) by the spoiled-sector operating point reaching the instability boundary (β = 0).

4.1.2 Coupling Factor (κ)

For the purposes of this paper, the definition of the coupling factor is given by Eqn. 1. It is based on the ratio of difference between the operating point location (β) with coupling ($\Delta\beta_{act}$) to difference between the operating point location without any coupling ($\Delta\beta_{\kappa=0}$).

$$\kappa = 1 - \Delta\beta_{act} / \Delta\beta_{\kappa=0} \quad (1)$$

A fully decoupled (κ = 0) PCM results in full equalization of sector outlet static pressures. A fully coupled computation (κ = 1) results in both compressor sectors operating at a single operating point.

4.1.3 Uniform Loss (UL)

The following sections work also with “equivalent uniform loss” (UL) representing the case in which the pressure loss introduced by a distortion screen would be redistributed uniformly without a mixing loss upstream of compressor inlet. This way, flow-distortion-induced response is isolated from the standard operation.

4.2 Source of Data & Reported Methods

The recent investigation of total pressure distortion effects on a turbocharger compressor was conducted by Jaiswal et al., who reported the data in a proceedings paper [21]. This dataset is deemed the most suitable (publicly available) set for the purposes of this paper.

The compressor was tested in clean inlet configuration, and the authors reported the results for five operating lines (80, 90, 100, 110, and 120 % of nominal speed). The compressor was also tested with two sets of uniform screens with 1 mm (S10) and 2.5 mm (S25) holes to test the isolated screen effects on performance for the 80, 100, and 120 % operating speeds. Using the S25 screen as a support mesh (undistorted sector) and S10 screen to create the distorted sector, a 90-degree and 180-degree distortion screen was created. This is illustrated in Fig. 1. The test data include the effect on performance at 80, 100, and 120 % operating speeds.

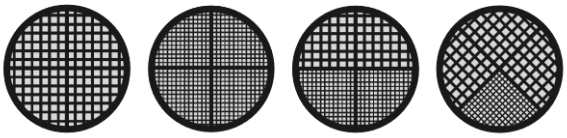


Fig. 1. S25, S10, 180°, and 90° Distortion Screen Illustration

The performance (static pressure ratio and isentropic efficiency) was evaluated between station 1 and 2. Both the temperature and the static pressure measurement were obtained upstream of distortion screen (station 1) and downstream of compressor volute (station 2). No measurement was performed in the section between screen and compressor inlet. The data are corrected to the nominal values based on the measurements taken at station 1.

The tabular data utilized in the presented analysis were obtained by digitizing the plots used to visualize the test results (see Fig. 2).

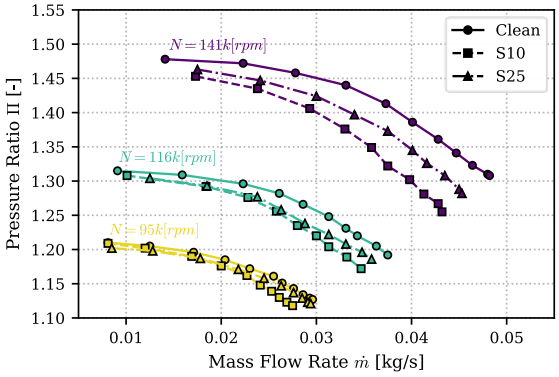


Fig. 2. Uniform Screen Test Results

The details on the measurement methods are presented in the original paper by Jaiswal et al. [21]. There, the authors [21] report the maximum pressure uncertainty to be 1.83 %, the isentropic efficiency to be 1.70 % and the mass flow to be 3.06 %. Based on the raster grid, additional digitization error is estimated to be 0.16 % for mass flow rate, 0.023 % for pressure ratio, and 0.037 % for efficiency.

The N120 speedline (120 % of nominal speed) is chosen for the PCM application. The screen losses provide more distinct results at higher speeds (at the N120 speedline, the difference in discharge pressure can exceed 10 kPa; at the N80 speedline, the difference extracted from the existing dataset does not exceed 2.5 kPa). Moreover, the losses of the S10 and S25 screens are virtually indistinguishable from each other in low-mass-flow part of the speedline in the 80 % and 100 % rotor speed cases, which provides unsuitable data for the PCM analysis.

In clean configuration the authors report the lowest losses, medium losses are present in the case of S25 screen, and the maximum-loss case is represented by the S10 screen test. This is consistent for the N120.

4.3 Model Application

The uniform screen mesh combinations are used to create distortion screens. Therefore, the results from the uniform screen tests can then be used in combination as a source for PCM.

Fully decoupled computations were performed. For a series of discharge pressures, mass-weighted averages were computed for both the configuration with 90-degree distortion screen (see Eqn. 2) and the 180-degree distortion screen (see Eqn. 3) to construct both distorted speedlines. As the test points are not captured at the same outlet static pressures, the mass flows are evaluated using linear interpolation at each outlet pressure value present in the distortion test dataset.

$$Q_{m,D90} = (90\ Q_{m,S10} + 270\ Q_{m,S25}) / 360 \quad (2)$$

$$Q_{m,D180} = (180\ Q_{m,S10} + 180\ Q_{m,S25}) / 360 \quad (3)$$

4.4 Model Results

The comparison of measured vs. computed speedlines is shown in Fig. 3.

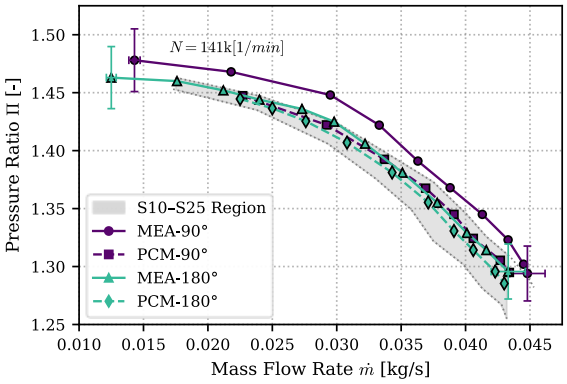


Fig. 3. Measured vs. Computed Effect on Performance

Every speedline represents the compressor performance (static-to-static pressure ratio vs. corrected mass flow) at 120 % of nominal speed under different inlet conditions, and/or obtained by different means (measurement / computation). The error bars account for the reported measurement uncertainty.

The uniform screen test results (used as an input to the PCM) are displayed by the dotted lines. The dark circles represent measured performance in 90-degree distortion case, dark squares represent computed performance in 90-degree distortion case, light triangles represent measured performance in case of 180-degree distortion, light diamonds denote the computed 180-degree distortion case.

4.5 Discussion

Based on the uniform-screen tests, it is expected that the screen featuring the combination of 90-degree spoiled segment (S10) and 270-degree clean segment (S25) will overperform the 180-degree spoiled segment combined with 180-degree clean segment. This is also supported by the measurement. However, the difference in pressure ratio delivered in both cases at a constant mass flow is higher than predicted by the PCM, with the 90-degree case being in some conditions order of a magnitude different.

The results obtained from the 180-degree distortion test behave consistently with the PCM prediction. Conversely, the following discrepancy arises when comparing the PCM data to the pressure ratio results in the 90-degree, showing the distorted-case pressure ratio being higher than the one with uniform inlet S25. As the static pressure at the outlet must be the same in both regions (the PCT prediction), the operating point cannot fall outside the greyed-out region of the performance map. There are various factors at play that can contribute to the quantitative discrepancy of the measured data compared with the simplified model.

- Combined screen loss may not exhibit the same loss characteristic as the uniform screen due to manufacturing differences and the different support frame geometry.
- Flow redistribution will modify the inlet conditions and mixing occurring prior to impeller inducer may increase the losses.
- Clocking effect (relative position of volute tongue to spoiled sector) is not discussed in the paper and it is known to affect the performance [22; 44].
- Total measurement error magnitude is comparable to the magnitude of the measured effect. Even though the measurement was performed on the same rig and the bias may cancel, it prevents us from drawing conclusive statements about the PCM applicability to this case.

Moreover, the Jaiswal dataset [21] does not provide any information for any intermediate flow path station. Without information on the flow redistribution and equalisation of static pressures it is merely a guess what is the rate of coupling that should be used to capture the performance and stability correctly.

This leads to a discussion concerning the closure term of any PCM applied to a radial machine. In the case of the presented analysis, the selection of station 2 to be

a constant discharge station is not supported by any dataset and it is driven by the availability of the data. As Sitaram shows [19], the distorted flow mixes and the pressure equalizes in the vaneless region. The distribution of pressures changes in the radial direction, supporting the notion that the closure term cannot be selected without sufficient consideration, and further data must be obtained in order to apply a PCM to a centrifugal compressor geometry in the future.

Therefore, due to the reported errors and stated discrepancies, the presented dataset is deemed inconclusive regarding the question of applicability of a PCT-based framework to a centrifugal compressor dataset.

It is also important to mention that the data used in the presented analysis come from a low-pressure-ratio machine subjected to a relatively mild distortion. This should motivate further investigation into the matter of highly loaded compressors under conditions of a severe inlet total pressure distortion, but also the parallel compressor approaches. Next section builds on this discussion and presents a PCM-focused analysis of high-pressure centrifugal compressor that serves as a basis for an experimental and CFD campaign aiming to capture the effects of distortion on compressor performance, as well as stability.

5 Parametric Sensitivity Study & Test Design Framework

This section utilizes the classical PCM formulation, which represents the most severe quasi-steady inlet total pressure distortion response (prior to inclusion of mixing losses), to construct a parametric study quantifying the response as a function of circumferential extent, intensity, and operating point of a high-pressure ratio centrifugal compressor.

Despite the unavailability of the distortion data, NASA HECC performance map is used for the analysis. This comes down to the availability of the geometric and measurement data, enhancing the possibility to validate the models and reproduce the results widely, and the comparativeness of the geometry to the aerospace centrifugal compressors.

The study is used to bound the region of detectability of the distortion-induced losses, formulating the design requirements for an experimental campaign designed to capture both first-order stability effects and second-order performance effects.

5.1 PCM Formulation

There are several ways a PCM can be implemented depending on the type of inputs, the depth of the knowledge of the system and the general need for quantitative accuracy. Based on the literature review, empirical constants for centrifugal compressors are unavailable and for the purposes of initial parametric study, it is beneficial to obtain qualitative results prior to improving the quantitative ability of the model.

The compressor is modelled as two compressors in parallel, each with a different boundary condition at the inlet. An available input for the model is a steady-state performance map featuring the total-to-total pressure ratio and total-to-total isentropic efficiency dependency on corrected air mass flow. No unsteady blade aerodynamic response effects are included (the impeller is assumed to respond immediately). This leads to both spoiled and clean sector operating points being on the compressor stage characteristics, with the spoiled sector being located closer to the instability boundary.

The outlet boundary condition (which is the closure term of a PCM) is modelled as a constant static pressure discharge (Eqn. 4), i. e. the static pressure in clean sector ($p_{s,cl}$) equals the static pressure in spoiled sector ($p_{s,sp}$). The static pressure at the outlet plane needs to be determined from the total temperature (T_t), total pressure (p_t), and mass flow (Q_m), and by the effective flow area at the outlet (Eqn. 5). For the purposes of the parametric study, the effective flow area (A_{ef}) is taken as the geometric area downstream at the exit guide vanes trailing edge times the cosine of the design swirl angle (see Table 1). The circumferential extent of the area in each sector is the same as the sector extent at the inlet.

$$p_{s,cl} = p_{s,sp} \tag{4}$$

$$p_s = f(T_t, p_t, Q_m, A_{ef}) \tag{5}$$

The model also assumes no crossflow to occur between the clean and spoiled sectors and no mixing losses when evaluating overall total-to-total pressure ratio and total-to-total isentropic efficiency.

To determine the overall operating point of the compression system, the mass-weighted-average (Eqn. 6) of sector total temperatures and total pressures is computed, determining the total-to-total stage pressure ratio (Π_{stg}, see Eqn. 7).

$$p_t = (Q_{m,cl}\, p_{t,cl} + Q_{m,sp}\, p_{t,sp}) / (Q_{m,cl} + Q_{m,sp}) \tag{6}$$

$$\Pi_{stg,t\text{-}t} = p_{t,out} / p_{t,in} \tag{7}$$

5.2 Source of Data

The centrifugal compressor used in this section is the High Efficiency Centrifugal Compressor (HECC) developed by NASA. It features an impeller, radial diffuser, exit guide vanes, and axial outlet.

Its design parameters can be found in Table 1. Final geometric parameters are given in Table 2.

Table 1. HECC Design Parameters [45]

Parameters	Units	Required Value
Design Rotor Speed	[min^{-1}]	21 789
Design Pressure Ratio	[-]	4.0 – 5.0
Polytropic Efficiency	[%]	> 88
D_{max} / D_2	[-]	< 1.45
Exit Swirl Angle	[°]	15

Table 2. HECC Geometric Parameters [45]

Parameters	Units	Value
Impeller Inlet Diameter	[mm]	81.0 / 215.4
Impeller Exit Diameter	[mm]	431.5
Diffuser Outlet Diameter	[mm]	602.9 / 625.1
Tip Clearance	[mm]	0.3
Number of Blade Pairs	[-]	15
Number of Diffuser Vane Pairs	[-]	20
Number of Exit Guide Vanes	[-]	60

Full description of geometry (including the areas necessary to formulate the PCM) and further resources featuring the HECC design and analysis are publicly available at NASA Technical Report Server [45]. The dataset also includes experimentally obtained data for several speedlines from choke to surge. This compressor map is utilized for the PCM analysis (see Fig. 4).

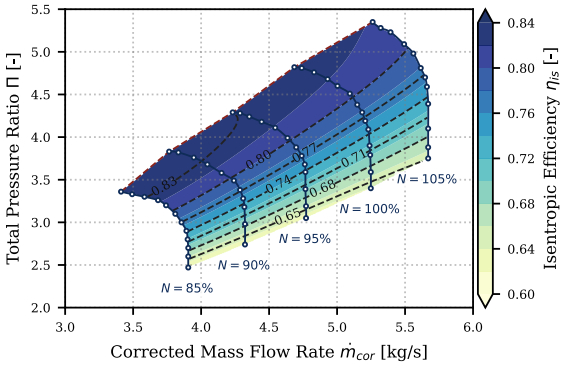


Fig. 4. Measured NASA HECC Pressure Ratio Map with Isentropic Efficiency Contours

5.3 Intensity and Extent Sweep Results

A parametric study of total pressure distortion intensity (δ, the pressure loss in the spoiled sector, in percents) and circumferential extent of the spoiled sector (θ, in degrees) is performed using the described PCM implementation on the HECC performance map in order to determine the compressor operating points most suitable for detecting of system-wide effects of total pressure distortion of performance and stability. The results are shown for the N100 speed (21 789 min^{-1}).

A clear pattern emerges when looking into the results of the sweep in Fig. 5, which depicts the stage pressure ratio in comparison to uniform-loss inlet conditions represented by the 0%-deficit line for β = 0.5. The adverse effect of inlet total pressure nonuniformity peaks in most cases between 90-degree distortion and 180-degree distortion cases. The behaviour is similar for other β values as well, with higher β values shifting the peak to lower distortion extents.

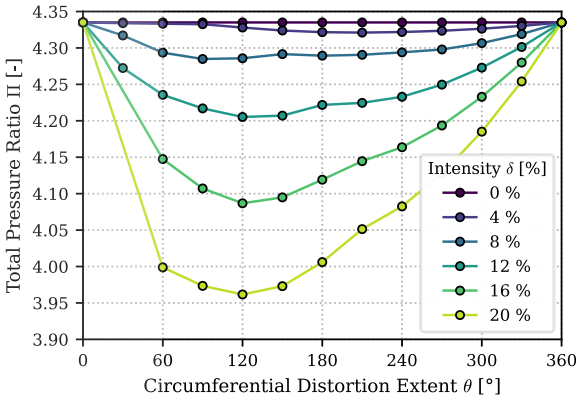


Fig. 5. θ and δ Sweep Effect on Π at β = 0.5

The dependence of the distorted vs. uniform loss on β is captured in Fig. 6 (the distortion extent is kept constant), illustrating the effect of operating point position on the performance map on the observability of the performance impact in both conditions.

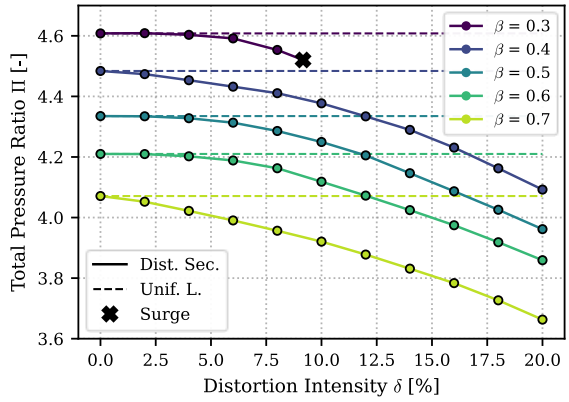


Fig. 6. β and δ Sweep Effect on Π at θ = 120°

5.4 Detectability Sweep

The detectability of the differences in performance is best captured in Fig. 7. Assessing the Figure the difference between the pressure ratios of the configurations ($\Delta\Pi_{loss}$) widens with the increase of β.

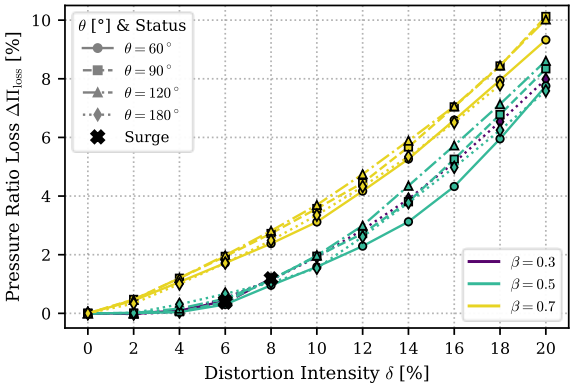


Fig. 7. β, θ, and δ Sweep Effect on $\Delta\Pi_{loss}$

A practical limit of 16-percent pressure loss is imposed for the distortion screen test to limit the pressure-gradient-induced secondary flows. The signal is defined at constant β as a gap between the two quantities – PCM and UL predictions of total pressure ratio Π (see Eqn. 8), which are themselves a ratio of two measured values (discharge pressure and ambient pressure).

$$\Delta\Pi_{loss} = |\Pi_{PCM} - \Pi_{UL}| / \Pi_{UL} \quad (8)$$

The ability to discern between the two models (UL representing uniform inlet conditions and PCM representing fully decoupled two sectors in parallel) is driven by the ratio of the predicted gap and the combined standard uncertainty of the measurements. The combined uncertainty includes outlet and reference pressures, repeatability, and speed and flow errors (map through a local characteristics slope). For independent pressure measurements the relative uncertainty of the pressure ratio is defined by the Eqn. 9. If the measurements in both configurations are carried out during the same testing session and on the same rig, systematic errors common to both configurations cancel in comparison, random errors do not, making the Eqn. 9 the upper-bound for the systematic part.

$$u_{\Pi} = u_p\sqrt{2} \quad (9)$$

The uncertainty required to resolve a coupling factor difference Δκ is defined by the Eqn. 10. This results in the upper bound on required uncertainty for the pressure measurement itself, assuming the pressure measurement dominates (Eqn. 11).

$$u_{\Pi,req} < \Delta\kappa\, \Delta\Pi_{loss} / k \quad (10)$$

$$u_{p,req} = u_{\Pi,req} / \sqrt{2} \quad (11)$$

The campaign shall require minimum Δκ = 0.5 to discern between the two models at a confidence of 95 % (coverage factor k = 2). The required pressure measurement uncertainty computed for the θ = 120° distortion screen in Table 3.

Table 3. Required measurement uncertainty $u_{p,req}$ [%]

δ [%] / β [-] (θ = 120°)	0.3	0.5	0.7
4	0.02	0.03	0.21
8	0.21	0.20	0.50
12	-	0.53	0.84
16	-	1.01	1.25
20	-	1.52	1.77

At the proposed δ = 16 % and $\theta > \theta_{crit}$, the gap $\Delta\Pi_{loss}$ reaches 5.7 % at β = 0.5 and 7.0 % at β = 0.7, which results in $u_{c,req}$ = 1.0 % and $u_{c,req}$ = 1.3 % respectively, depending on the regime and distortion intensity that will be achievable on the stand.

6 Campaign Proposal

The parametric study demonstrates the bounds of system-wide effects of total pressure distortion on a high-pressure ratio centrifugal compressor defined by the uniform inlet conditions and the uncoupled form of PCM. To validate PCM, establish the closure term for centrifugal machines, and investigate the coupling, a combined experimental and computational campaign is proposed.

The proposal is designed to investigate the effects on a high-pressure ratio machine representative of a highly loaded centrifugal compressors used in small turbojet engines.

6.1 Experimental Campaign

The experimental part of the campaign targets both stability and performance deviations. The test results aim to be used to validate the PCM and CFD predictions in suitable regions, additionally exploring the formulation of empirical coefficients.

It is proposed to investigate the effects at multiple operating speeds, as the high-pressure ratio compressors exhibit different behavior under increasing loading. The campaign also shall be run at $\theta > \theta_{crit}$ (the value is machine-specific) to ensure a quasi-static blade response. The paper proposes to increase the distortion intensity δ up to the practical limit of the rig (in the presented case δ = 16 %). Extra care should be taken with the inlet setup to minimize the secondary flow generation.

Stability-focused part of the testing effort should focus on the low-mass-flow regimes (β < 0.5). Performance drop should be measured in the near-choke regimes (β > 0.5), where the nonlinearity of the compressor characteristics drives the increase of difference between standard conditions and distortion performance.

Following the uncertainty formulation, this approach results in the requirements for measurement precision that would be able to distinguish the effects apart. An uncertainty of 1.0 % in pressure measurement is sufficient for δ ≥ 16 % and near-choke operating regimes (β > 0.5).

6.2 High-Fidelity Computational Campaign

Complementary CFD analysis, focusing on the flow field details affecting the quasi-steady assumptions of PCT and constant discharge pressure closure term, is proposed to enhance the predictive capability of PCT-class models applied to highly loaded centrifugal compressors. Specifically, the proposed analysis targets the unsteady response, sector flow redistribution, coupling evaluation, and closure term assessment.

To capture the inherent time-variant nature of the problem, a full-annulus URANS CFD should be used at minimum. To distinguish between the flow-directionality effects and pressure deficiency effects, it is proposed that the CFD is not run with realistic inlets but an inlet boundary condition representative of the

screen tests (both in distortion intensity and circumferential extent). A series of outlet conditions shall be investigated in order to determine the effect on the upstream sector coupling. This includes both the throttle outlet conditions and static discharge conditions.

6.3 PCM Validation

In the final stage of the campaign, data from the experimental stand and CFD will be used in combination to establish the coupling and closure suitable for a PCM applied to a high-pressure centrifugal compressor.

7 Conclusion

The literature synthesis yields a significant gap in the centrifugal compressor total pressure distortion response research. It follows the evolution of the research topics and machine types highlighting three conclusions:

1) the papers describing the effects of inlet geometry often conflate the total pressure distortion effects and flow angularity effects without the possibility to separate their individual contribution

2) the analysis is often performed on a low-pressure turbocharger-type centrifugal compressor that is not fully representative of an aerospace highly loaded machine characterized by significantly increased loading coefficients, reduced rotor-stator gaps, and axial diffuser discharge

3) public data and empirical correlations supporting the development of low-fidelity reduced-order models for application in inlet total pressure distortion problems featuring high-pressure-ratio centrifugal compressors are unavailable

Following the critical literature review, a PCT approach is taken to assess the existing total pressure distortion data available for a turbocharger-type compressor, highlighting the need for an enhanced measurement resolution needed to capture the performance effects.

A clean-inlet high pressure ratio centrifugal compressor dataset is used for a parametric study allowing for setting minimum measurement equipment requirements needed to capture the effects during a system-level test. The study also highlights the importance of operating point and distortion regime selection necessary to accomplish the campaign goals.

It is shown that existing centrifugal compressor distortion data cannot reliably discriminate between uniform inlet loss and distortion-induced loss due to reported uncertainties (over 1.8 % for pressure ratio measurement vs. data spread < 3 % of pressure ratio). On a high-pressure-ratio ($\Pi > 4$) compressor map, the author shows that the PCM departs from the uniform loss up to 10 % (of Π) at $\delta = 20$ %. This means that the difference is resolvable in a region bounded by operating point location, distortion extent, and distortion intensity. The proposed experimental and CFD analysis must therefore be designed around this region that would allow the researcher to investigate the difference between the distortion-induced losses and uniform losses and the details related to PCM coupling implementations.

References

1. I. Ariga, N. Kasai, S. Masuda, Y. Watanabe, I. Watanabe, The Effect of Inlet Distortion on the Performance Characteristics of a Centrifugal Compressor, in Proceedings of the ASME 1982 International Gas Turbine Conference and Exhibit. Volume 1: Turbomachinery, London, England, April 18–22 (1982). https://doi.org/10.1115/82-gt-92
2. I. Ariga, S. Masuda, A. Ookita, Inducer Stall in a Centrifugal Compressor With Inlet Distortion. J. Turbomach. **109**, 1, 27-35 (1987). https://doi.org/10.1115/1.3262066
3. Y. Kim, A. Engeda, R. Aungier, G. Direnzi, The influence of inlet flow distortion on the performance of a centrifugal compressor and the development of an improved inlet using numerical simulations, in P. I. Mech. Eng. A.-J. Pow. **215**, May 1 (2001), 323-338. https://doi.org/10.1243/0957650011538550
4. V. Michelassi, S. Pazzi, S. Echtner, P. Giangiacomo, F. Martelli, M. Giachi, Performances of Centrifugal Compressor Impellers in Steady and Unsteady Flow Regimes Under Inlet Flow Distortions, in Proceedings of the ASME Turbo Expo 2001: Power for Land, Sea, and Air. Volume 1: Aircraft Engine; Marine; Turbomachinery; Microturbines and Small Turbomachinery, New Orleans, Louisiana, USA, June 4–7 (2001). https://doi.org/10.1115/2001-gt-0325
5. A. Engeda, Y. Kim, R. Aungier, G. Direnzi, The Inlet Flow Structure of a Centrifugal Compressor Stage and Its Influence on the Compressor Performance. J. Fluid. Eng. **125**, 5, 779-785 (2003). https://doi.org/10.1115/1.1601255
6. A. Kammerer, R. S. Abhari, Experimental Study on Impeller Blade Vibration During Resonance—Part I: Blade Vibration Due to Inlet Flow Distortion. J. Eng. Gas. Turb. Power. **131**, 2 (2009). https://doi.org/10.1115/1.2968869
7. A. Kammerer, R. S. Abhari, Blade Forcing Function and Aerodynamic Work Measurements in a High Speed Centrifugal Compressor With Inlet Distortion. J. Eng. Gas. Turb. Power. **132**, 9 (2010). https://doi.org/10.1115/1.4000614
8. A. Zemp, A. Kammerer, R. S. Abhari, Unsteady Computational Fluid Dynamics Investigation on Inlet Distortion in a Centrifugal Compressor. J. Turbomach. **132**, 3 (2010). https://doi.org/10.1115/1.3147104
9. S. Vagnoli, T. Verstraete, URANS analysis of the effect of realistic inlet distortions on the stall inception of a centrifugal compressor. Comput.

Fluids **116**, 192-204 (2015). https://doi.org/10.1016/j.compfluid.2015.03.015

10. L. Wang, C. Yang, B. Zhao, D. Lao, C. Ma, D. Li, The change of the inlet geometry of a centrifugal compressor stage and its influence on the compressor performance. J. Therm. Sci. **22**, 197-208 (2013). https://doi.org/10.1007/s11630-013-0613-2
11. C. Yang, Y. Liu, L. Wang, D. Lao, C. Yang, Investigation on the Performance and Flow Structure of Centrifugal Compressor: Understand the Inlet Bent Duct Configurations, in Proceedings of the ASME Turbo Expo 2016: Turbomachinery Technical Conference and Exposition, Seoul, South Korea, June 13–17 (2016). https://doi.org/10.1115/gt2016-56169
12. C. Yang, B. Zhao, C. C. Ma, D. Lao, M. Zhou, Effect of Different Geometrical Inlet Pipes on a High Speed Centrifugal Compressor, in Proceedings of the ASME Turbo Expo 2013: Turbine Technical Conference and Exposition., San Antonio, Texas, USA, June 3–7 (2013). https://doi.org/10.1115/gt2013-94254
13. H. Hou, L. Wang, R. Wang, Y. Yang, Effects of bending-torsional duct-induced swirl distortion on aerodynamic performance of a centrifugal compressor. J. Therm. Sci. **26**, 97-106 (2017). https://doi.org/10.1007/s11630-017-0916-9
14. B. Zhao, H. Sun, L. Wang, M. Song, Impact of inlet distortion on turbocharger compressor stage performance. Appl. Therm. Eng. **124**, 393-402 (2017). https://doi.org/10.1016/j.applthermaleng.2017.05.181
15. H. Zhang, C. Yang, C. Yang, H. Zhang, L. Wang, J. Chen, Inlet bent torsional pipe effect on the performance and stability of a centrifugal compressor with volute. Aerosp. Sci. Technol. **93** (2019). https://doi.org/10.1016/j.ast.2019.105322
16. Z. Sun, B. Wang, X. Zheng, T. Kawakubo, H. Tamaki, R. Numakura, Effect of bent inlet pipe on the flow instability behavior of centrifugal compressors. Chinese. J. Aeronaut. **33**, 8, 2099-2109 (2020). https://doi.org/10.1016/j.cja.2020.02.013
17. J. Galindo, A. Tiseira, R. Navarro, D. Tarí, C. M. Meano, Effect of the inlet geometry on performance, surge margin and noise emission of an automotive turbocharger compressor. Appl. Therm. Eng. **110**, 875-882 (2017). https://doi.org/10.1016/j.applthermaleng.2016.08.099
18. J. Galindo, A. Gil, R. Navarro, D. Tarí, Analysis of the impact of the geometry on the performance of an automotive centrifugal compressor using CFD simulations. Appl. Therm. Eng. **148**, 1324-1333 (2019). https://doi.org/10.1016/j.applthermaleng.2018.12.018
19. N. Sitaram, M. Govardhan, K. V. Murali, Effects of Inlet Pressure Distortion on the Performance and Flow Field of a Centrifugal Compressor at Off-Design Conditions, in Proceedings of the ASME 2012 Gas Turbine India Conference, Mumbai, Maharashtra, India, December 1 (2012), 35-50. https://doi.org/10.1115/gtindia2012-9529
20. N. Sitaram, M. Govardhan, K. V. Murali, Effects of Inlet Pressure Distortion on the Performance and Flow Field of a Centrifugal Compressor at Design Condition. J. Aerosp. Sci. Technol. **64**, 4, 268-281 (2012). https://doi.org/10.61653/joast.v64i4.2012.471
21. S. K. Jaiswal, S. Bubanale, M. C. Keerthi, Inlet Distortion Studies on a Centrifugal Compressor, in Proceedings of the ASME 2023 Gas Turbine India Conference, Bangalore, India, December 7–8 (2023). https://doi.org/10.1115/gtindia2023-118322
22. M. Zhang, X. Zheng, Criteria for the matching of inlet and outlet distortions in centrifugal compressors. Appl. Therm. Eng. **131**, 933-946 (2018). https://doi.org/10.1016/j.applthermaleng.2017.11.140
23. G. Plourde, F. Roberts, F. Smakula, Insights into axial compressor response to distortion, in AIAA 4th Propulsion Joint Specialist Conference, Cleveland, Ohio, June 10-14 (1968). https://doi.org/10.2514/6.1968-565
24. W. Cousins, A theory for the prediction of compressor blade aerodynamic response, in 34th AIAA/ASME/SAE/ASEE Joint Propulsion Conference and Exhibit, Reston, VA, July (1998). https://doi.org/10.2514/6.1998-3308
25. A. Grimaldi, V. Michelassi, The Impact of Inlet Distortion and Reduced Frequency on the Performance of Centrifugal Compressors. J. Eng. Gas. Turb. Power. **141**, 2 (2019). https://doi.org/10.1115/1.4040907
26. C. Reid, The Response of Axial Flow Compressors to Intake Flow Distortion, in Proceedings of the ASME 1969 Gas Turbine Conference and Products Show, Cleveland, Ohio, USA, March 9–13 (1969). https://doi.org/10.1115/69-gt-29
27. E. H. Bond, N. L. Key, A Flow Physics Approach to Determining Critical Angle of Inlet Total Pressure Distortion for a Centrifugal Compressor. J. Eng. Gas. Turb. Power. **148**, 5 (2026). https://doi.org/10.1115/1.4070057
28. A. Fatsis, S. Pierret, R. Van den Braembussche, Three-Dimensional Unsteady Flow and Forces in Centrifugal Impellers With Circumferential Distortion of the Outlet Static Pressure. J. Turbomach. **119**, 1, 94–102 (1997). https://doi.org/10.1115/1.2841015
29. W. T. Cousins, M. W. Davis, Evaluating Complex Inlet Distortion With a Parallel Compressor Model: Part 1—Concepts, Theory, Extensions, and

Limitations, in Proceedings of the ASME 2011 Turbo Expo: Turbine Technical Conference and Exposition, Vancouver, British Columbia, Canada, June 6–10 (2011), 1-12. https://doi.org/10.1115/gt2011-45067

30. M. W. Davis, W. T. Cousins, Evaluating Complex Inlet Distortion With a Parallel Compressor Model: Part 2—Applications to Complex Patterns, in Proceedings of the ASME 2011 Turbo Expo: Turbine Technical Conference and Exposition, Vancouver, British Columbia, Canada, June 6–10 (2011), 13-23. https://doi.org/10.1115/gt2011-45068
31. W. T. Cousins, M. W. Davis, The Influence of the Characteristics of a Centrifugal Compressor on System Stability and Distortion Response, in Proceedings of the ASME Turbo Expo 2012: Turbine Technical Conference and Exposition, Copenhagen, Denmark, June 11–15 (2012), 37-49. https://doi.org/10.1115/GT2012-68214
32. K. Song, B. Zhao, H. Sun, W. Yi, A physics-based zero-dimensional model for the mass flow rate of a turbocharger compressor with uniform/distorted inlet condition. Int. J. Engine. Res. **20**, 6, 624-639 (2018). https://doi.org/10.1177/1468087418773673
33. S-16 Turbine Engine Inlet Flow Distortion Committee, Inlet Total-Pressure-Distortion Considerations for Gas-Turbine Engines. (2017). https://doi.org/10.4271/air1419c
34. H. Pearson, A. B. McKenzie, Wakes in Axial Compressors. J. R. Aeronaut. Soc. **63**, 583, 415-416 (1959). https://doi.org/10.1017/s0368393100071273
35. W. T. Cousins, History, Philosophy, Physics, and Future Directions of Aircraft Propulsion System/Inlet Integration, in Proceedings of the ASME Turbo Expo 2004: Power for Land, Sea, and Air, Vienna, Austria, June 14–17 (2004), 305-320. https://doi.org/10.1115/gt2004-54210
36. I. J. Day, E. M. Greitzer, N. A. Cumpsty, Prediction of Compressor Performance in Rotating Stall. J. Eng. P. **100**, 1, 1-12 (1978). https://doi.org/10.1115/1.3446318
37. J. Kurzke, Effects of Inlet Flow Distortion on the Performance of Aircraft Gas Turbines. J. Eng. Gas. Turb. Power. **130**, 4 (2008). https://doi.org/10.1115/1.2901190
38. R. S. Mazzawy, Multiple Segment Parallel Compressor Model for Circumferential Flow Distortion. J. Eng. P. **99**, 2, 288-296 (1977). https://doi.org/10.1115/1.3446288
39. A. Hale, M. Davis, DYNamic Turbine Engine Compressor Code (DYNTECC) - Theory and capabilities, in 28th Joint Propulsion Conference and Exhibit, Reston, Virigina, July (1992). https://doi.org/10.2514/6.1992-3190
40. K. Shahrokhi, M. Davis, Application of a modified dynamic compression system model to a low aspect ratio fan - Effects of inlet distortion, in 33rd Aerospace Sciences Meeting and Exhibit, Reno, NV, USA, January (1995). https://doi.org/10.2514/6.1995-301
41. M. Davis, Parametric investigation into the combined effects of pressure and temperature distortion on compression system stability, in 27th Joint Propulsion Conference, Sacramento, CA, USA, June (1991). https://doi.org/10.2514/6.1991-1895
42. M. Davis, A. Hale, A Parametric Study on the Effects of Inlet Swirl on Compression System Performance and Operability Using Numerical Simulations, in Proceedings of the ASME Turbo Expo 2007: Power for Land, Sea, and Air, Montreal, Canada (2007), 1-10. https://doi.org/10.1115/GT2007-27033
43. T. P. Hynes, E. M. Greitzer, A Method for Assessing Effects of Circumferential Flow Distortion on Compressor Stability. J. Turbomach. **109**, 3, 371-379 (1987). https://doi.org/10.1115/1.3262116
44. X. Wang, X. Yang, M. Yang, L. Jin, X. Li, X. Zheng, Coupled influence of flow distortion induced by inlet elbow and volute in a transonic centrifugal compressor with vaned diffuser. Aerosp. Sci. Technol. **168**, 110924 (2026). https://doi.org/10.1016/j.ast.2025.110924
45. G. Medic, O. P. Sharma, J. Jongwook, L. W. Hardin, D. C. McCormick, W. T. Cousins, E. A. Lurie, A. Shabbir, B. M. Holley, P. R. Van Slooten, High Efficiency Centrifugal Compressor for Rotorcraft Applications; NASA/CR—2014-218114/REV1, October (2017). https://ntrs.nasa.gov/citations/20180001471

Modernization of valve test rig and validation of measured results

Martin Miczan[1], *Jindrich* Bem[1], *Vaclav* Slama[1*]

[1]Doosan Skoda Power, Tylova 1/57, 30100 Pilsen, Czech Republic

Abstract. Experimental research plays an essential role in the development and validation of steam turbine control valves. Following the failure of the original compressor, the existing valve test rig required modernization to ensure its continued use for aerodynamic measurements. This paper presents the modernization of the experimental facility, including the integration of a new vacuum source based on the Campbell machine vessel, upgrades to the measurement instrumentation, and the development of an improved data acquisition system. The modified software enables high-speed, synchronized acquisition of pressure and temperature data, along with automated processing and export of the measured results. The performance of the modernized test rig was experimentally validated using a previously investigated valve model with well-established flow characteristics. The measured valve flow characteristics obtained on the upgraded facility were compared with older experimental data. The comparison showed excellent agreement over the entire operating range, confirming that the modernization did not affect the measurement accuracy. The upgraded test rig is therefore fully validated. It provides a reliable experimental platform for future investigations of steam turbine control valves, including studies of pressure losses, flow instabilities, and aerodynamic optimization.

1 Introduction

Valves are important parts of each turbomachinery device, including steam turbines. There are different types of valves according to the function for which they are used. The main requirements are that, for each valve type, there are many important requirements for operational reliability, low pressure losses, and higher competitiveness. In an effort to keep up with all the demands, the valves should be constantly improved. Therefore, before applying newly developed valve designs, their typical characteristics must be determined and checked.

Research on each valve assembly is primarily focused on two fundamental phenomena: pressure losses, the knowledge of which is essential for accurate prediction of the performance and efficiency of every turbine, and pressure fluctuations inside the valve, whose understanding is essential for assessing the potential risk of vibration of the valve cones.

Regarding the pressure losses, they can be clearly and fully described by so-called valve flow characteristics. They can be obtained using measurements or numerical simulations. Ideally, it is always good to have both numerical and measured results to compare them to find possible mistakes and validate the results. Regarding the pressure fluctuations within the valve, this phenomenon is so complex that numerical simulations require a specific methodology, which should be validated. This approach is not available at Doosan Skoda Power. Therefore, the measurement of pressure fluctuations is the only option right now.

To sum up, a reliable valve test rig is indispensable to achieve success in valve development competitions. For this reason, Doosan Skoda Power has had many different test rigs, one of which was an air-flow valve test rig for testing different valve models. The last extensive research performed using this test rig was connected with the study of the Coanda effect, which influences the pressure fluctuations connected to the stable and unstable flow detachment. This research is presented in detail in the dissertation [1]. Furthermore, other papers were published as well [2-4] using different numerical measurement methods, for example [5]. In addition, it also helped to understand the differences in the valve flow fields in different valve geometries [6]. For future experimental studies, for example, improving specific valve features, such as a muffler, the valve test rig needed to be modernized.

The objective of the present paper is to present the modernization of the valve test rig, including the new vacuum source, instrumentation, and data acquisition system, and to experimentally validate the upgraded facility using reliable valve flow characteristics measured on the former valve test rig.

2 Former valve test rig

The original valve test rig, shown in Fig. 1, consisted of an inlet pipeline, a valve model, a diffuser, an outlet

* Corresponding author: vaclav.slama@doosan.com

pipeline, a compressor, and the associated measuring instrumentation. The valve was connected to the suction side of the aerodynamic test rig. The experiments were performed in a vacuum-type configuration, in which ambient air was drawn through the test section into the compressor. The pressure downstream of the valve was controlled by adjusting the compressor speed, while the inlet pressure remained close to the ambient atmospheric pressure. The compressor was capable of generating pressure ratios corresponding to choked-flow conditions. Specifically, the achievable pressure ratio ranged from 0.3 to 1.0. Lower pressure ratios could not be reached because the compressor entered the surge regime.

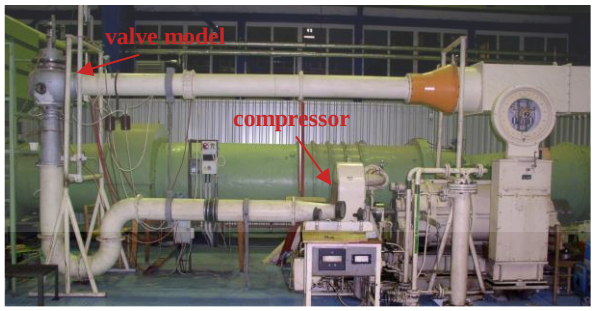


Fig. 1. Former valve test rig

Pressure measurements were performed using a pressure scanner controlled by a dedicated data acquisition system. The total pressure upstream of the valve, the static pressure downstream of the valve diffuser, the static pressures at the selected locations inside the valve, the differential pressure across the orifice plate, and the ambient barometric pressure were measured sequentially. Acquiring all pressure data for a single operating point, i.e., one valve cone lift and one pressure ratio, required more than 20 s. In addition to recording the measured pressures, the data acquisition software continuously calculated the corresponding pressure ratio, flow velocity, mass flow rate, and normalized mass flow rate.

Before each measurement, the compressor was switched off, and the valve cone lift was set to 0 mm. After the compressor was started, the required valve cone lift was adjusted, and the pressures were recorded. The operating point was then gradually changed by increasing the compressor speed, thereby decreasing the pressure ratio across the valve (i.e., increasing the pressure drop). Measurements were performed at discrete pressure-ratio intervals. At each operating point, the complete set of pressure data was recorded. When measurements at multiple valve cone lifts were required, the valve cone was adjusted to the next prescribed lift and the procedure was repeated. To improve measurement reliability, each pressure reading was acquired three consecutive times.

During one of the final experimental campaigns, the compressor suffered a mechanical failure. Owing to its age and the unavailability of spare parts, the original compressor could not be repaired. Consequently, the entire valve test rig used for valve measurements was modernized.

3 Modernized valve test rig

The modernization of the valve test rig primarily consisted of replacing the failed compressor. Instead of installing a new compressor, the valve test rig was connected to another experimental facility, namely the outer vessel of the Campbell machine, as shown in Fig. 2. A schematic diagram of the upgraded experimental arrangement is presented in Fig. 3.

The valve model was connected to the Campbell machine vessel through a DN200 pipeline equipped with a flexible expansion joint and a transition piece reducing the diameter from DN250 to DN150. To prevent vacuum loss from the Campbell machine vessel before the start of each experiment, a DN150 butterfly shut-off valve was installed in the connecting pipeline.

A vacuum inside the Campbell machine vessel was generated using three oil-sealed vacuum pumps. The measurement principle remained identical to that of the former valve test rig. Instead of drawing ambient air into a compressor, the air was now drawn from the atmosphere into the evacuated Campbell machine vessel. This modification preserved the original operating principle while eliminating the need for the obsolete compressor and providing a reliable source of sub-atmospheric pressure for the experiments.

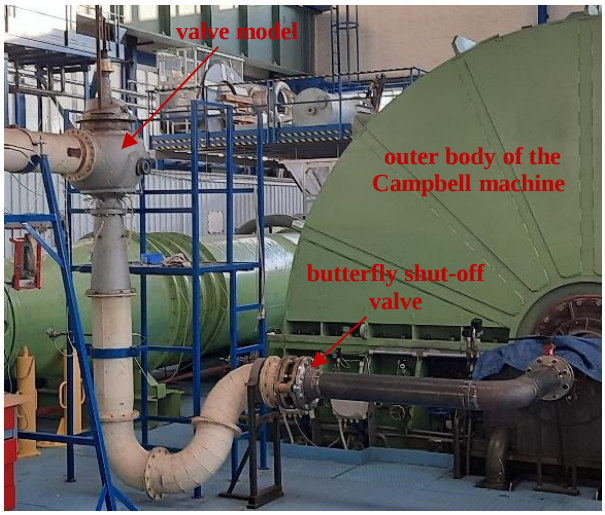


Fig. 2. Modernized valve test rig

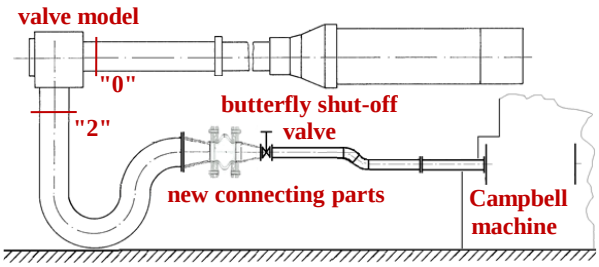


Fig. 3. Modernized valve test rig – scheme

3.1 . Instrumentation of the modernized test rig

The measurement system consisted of the following components: NetScanner 9116 pressure scanners for measuring the pressure distribution within the valve and the differential pressure across the flow nozzle. The total

pressure upstream of the valve was measured using a rake-type Pitot probe. The pressure taps installed on the valve provided circumferentially averaged static pressure values. VEGASCAN 693 units for measuring the air temperature upstream and downstream of the valve. VEGAMET unit for measuring the ambient barometric pressure.

The measured signals were transmitted digitally via an Ethernet network using the TCP/IP protocol and recorded by the data acquisition computer. The differential pressure measured across the flow nozzle was used to determine the valve mass flow rate, which represents the principal quantity for constructing the valve flow characteristics.

The mass flow rate was determined using a calibrated flow nozzle. During operation, the differential pressure across the nozzle was measured and converted into the corresponding mass flow rate. The flow nozzle had been calibrated before its installation and had been successfully used throughout the operational lifetime of the experimental facility. To prevent contamination of the measuring section, a fabric air filter was installed upstream of the test rig to capture solid particles. The mass flow rate through the nozzle was evaluated in accordance with EN ISO 5167-1–4 (2003) [7].

As part of the modernization, a new multi-hole orifice plate was also installed. The specification and sizing of the orifice plate were defined in cooperation with the Performance Testing Department. A MATTECH DN200 PN6 multi-hole orifice plate with corner pressure tappings and straight pipe sections of +2D/-2D was selected and integrated into the upgraded test rig.

3.2 . Data Acquisition Software

The data acquisition software was also upgraded as part of the modernization. The application was based on the software routinely used for performance measurements at power plants and developed in Microsoft Visual Studio NET using Visual Basic and C#. For the purposes of the experimental valve test rig, the software was extended with several additional functions that are not required for field measurements.

The most significant modifications included the implementation of communication with the NetScanner 9116 pressure scanners for pressure measurements and with the VEGASCAN and VEGAMET units used for temperature and barometric pressure measurements. The data acquisition routines were also adapted to enable high-speed time-resolved sampling required for laboratory experiments. Finally, the software was updated to ensure the correct conversion of the measured signals into physical quantities and to provide automatic export of the processed data for subsequent evaluation.

4 Validation of the Modernized Test Rig

To validate the upgraded experimental test rig and the newly developed data acquisition software, a series of verification measurements was carried out using a valve model that had been extensively investigated in previous studies and for which reliable flow characteristics were already available. The tested model was a steam turbine control valve with the valve seat angle $\alpha = 90°$ as shown in Fig. 4. The other important valve dimensions are the valve seat diameter D_s and the valve diffuser diameter D_1. The previously obtained experimental data served as a reference for assessing the accuracy and repeatability of the modernized test facility.

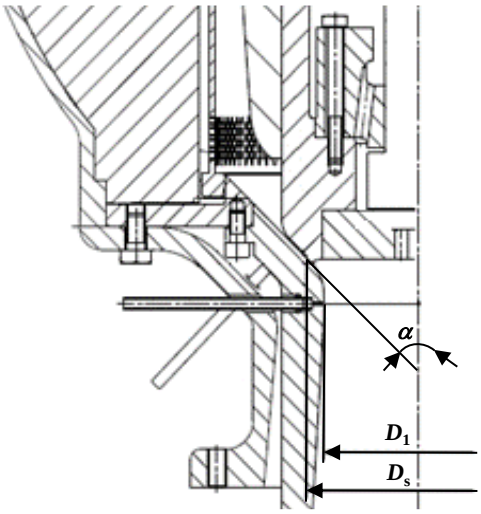


Fig. 4. Measured valve model

The measurement procedure was as follows. First, a vacuum was established inside the Campbell machine vessel using the vacuum pumps. After the required vacuum level had been reached, the data acquisition software was started, and the butterfly shut-off valve was opened, allowing ambient air to flow through the valve model into the evacuated vessel.

Unlike the original valve test rig, where the pressure ratio was adjusted stepwise by changing the compressor speed, the upgraded facility operated in a continuous mode. As the pressure inside the Campbell machine vessel gradually increased during the measurement, the pressure ratio across the valve continuously changed while the prescribed valve cone lift remained constant. The data acquisition software continuously recorded all measurement channels at a sampling frequency of approximately 25 Hz. The high-speed data acquisition and data export were successfully validated. The recorded data were subsequently processed and evaluated in Microsoft Excel using custom-developed macros.

The measured and calculated quantities were used to construct the valve flow characteristics, which represent the dependence of the mass flow ratio $q = m/m^*$ on the pressure ratio $\varepsilon_2 = p_2/p_{0t}$, for different relative valve cone lifts z/D_1 or directly the valve cone lift z. The critical mass flow m^* depends on the total pressure p_{t0} and enthalpy h_{t0} at the valve chamber inlet (position 0 in Fig. 3) and the cross-sectional area of the diffuser throat A_1 (position of D_1 in Fig. 4).

An example of the measured results for a valve cone lift of z = 14 mm is presented in Fig. 5. The same measurement procedure was repeated for other valve cone lifts. The resulting valve flow characteristics are

shown in Figs. 6 and 7, where the new results are depicted in different colours according to the valve cone lift, and the previously used results for validation are shown in black.

A comparison of the previously measured flow characteristics with those obtained using the modernized valve test rig reveals only negligible differences. The agreement between the two datasets confirms that the modernization of the experimental facility, including the new vacuum source, upgraded instrumentation, and redesigned data acquisition software, did not affect the measurement accuracy. The upgraded valve test rig can therefore be considered successfully validated and suitable for future experimental investigations of steam turbine control valves.

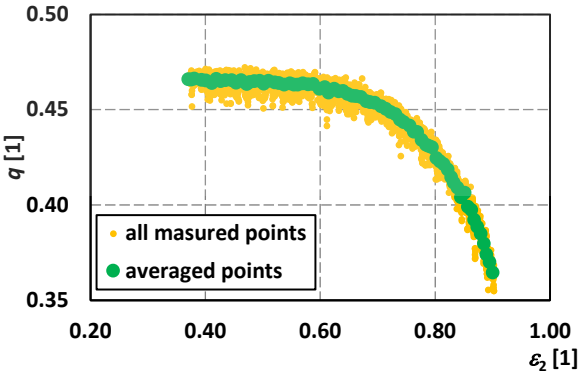


Fig. 5 Valve flow characteristic for z = 14 mm

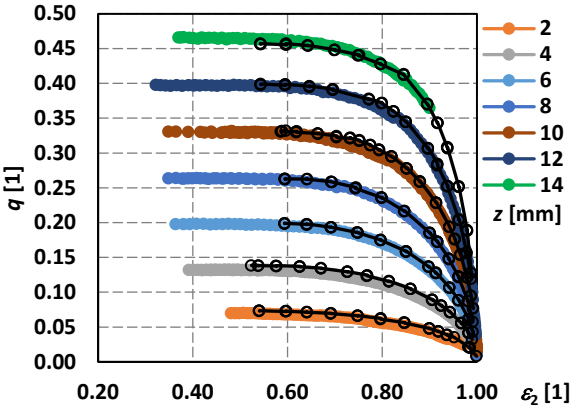


Fig. 6 Comparison of former and new valve flow characteristics results for chosen valve cone lifts 0 – 14 mm

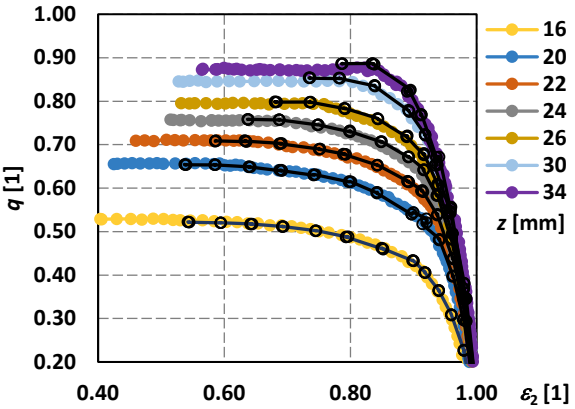


Fig. 7 Comparison of former and new valve flow characteristics results for chosen valve cone lifts 16 – 34 mm

5 Conclusion

The successful modernization provides a robust experimental platform for future investigations of pressure losses and fluctuations, flow instabilities, and the aerodynamic optimization of newly developed steam turbine control valves.

The modernization of the experimental valve test rig was completed in accordance with the proposed design and the planned implementation schedule. The upgraded facility was successfully commissioned, and the measurement methodology, data acquisition process, and valve flow characteristic determination were experimentally verified. The measured data were successfully exported and subsequently processed, confirming the correct operation of both the hardware and software components of the measurement system.

The comparison with previously obtained experimental data demonstrated excellent agreement, thereby validating the performance of the modernized valve test rig. The upgraded facility is therefore fully operational and ready for future experimental investigations. It will be used in accordance with the planned experimental program in the coming years.

The authors thank Doosan Skoda Power for permission to present the results of this study.

References

1. P. Kollross, Flow instability in turbine control valve, Ph.D. thesis, University of West Bohemia, Pilsen, Czech Republic, 2020. http://hdl.handle.net/11025/41318
2. P. Kollross, L. Tajc, An experimental research of the DSPW steam turbine control valve. AIP Conf. Proc. 2189, 020012 (2019). https://doi.org/10.1063/1.5138624
3. M. Panuška, L. Tajč, P. Kollross, The effect of a strainer in the control valve of the steam turbine. AIP Conf. Proc. 2047, 020015 (2018). https://doi.org/10.1063/1.5081648.
4. P. Kollross, Introduction to flow instability in turbine control valve. AIP Conf. Proc. 1889, 020022 (2017). https://doi.org/10.1063/1.5004356.
5. V. Slama, D. Simurda, P. Kollross, Valve seat angle influence on losses in valves for steam turbines. MATEC Web Conf. 383, 00019 (2023). https://doi.org/10.1051/matecconf/202338300019.
6. M. Luxa, R. Dvořák, D. Simurda, J. Vimmr, Pneumatic measurements downstream of a radial turbine nozzle cascade. J. Therm. Sci. 19(1), 42–46 (2010). https://doi.org/10.1007/s11630-010-0042-4.
7. ISO 5167-1–4, Measurement of fluid flow by means of pressure differential devices inserted in circular cross-section conduits running full, EN ISO Standard, 2003.

Fluid flow mixing efficiency in cylindrical and rectangular stirred tanks: an experimental comparison

Anna Młynarczykowska[1*], Klaudia Zwolińska-Glądys[1], Marek Jaszczur[2]

[1]AGH University of Krakow, Faculty of Civil Engineering and Resource Management, Mickiewicza 30, 30-059 Kraków, Poland
[2]AGH University of Krakow, Faculty of Energy and Fuels, Mickiewicza 30, 30-059 Kraków, Poland

Abstract. Mechanical mixing, common in industrial technologies, continues to be a subject of study and optimization. Although numerical modelling is a useful tool for assessing process efficiency in various impeller and vessel geometries, it requires experimental verification. The effectiveness of the mechanical mixing process depends on the tank design, the viscosity and density of the mixed phases, temperature, and above all, the impeller shape. The main objective of this study is to experimentally evaluate the effect of a new impeller geometry on fluid flow pattern and energy consumption during the mixing process in cylindrical and rectangular stirred tanks. Velocity vectors were determined using Particle Image Velocimetry (PIV) measurements, and energy consumption was measured with a precision torque meter. This paper presents and discusses a comparison of the new impeller efficiency for the two different tank geometries. The distribution of velocity vectors and power numbers was analyzed as a function of impeller rotational speed to determine the dimensionless numbers characterizing the fluid flow inside the tank. The optimal process conditions determined for each tank design were compared in terms of energy consumption and the operational efficiency of the tested impeller. It was demonstrated that the power number of the new impeller used in a cylindrical tank is, on average, eight times lower than that of the reference Rushton turbine, while maintaining high pumping efficiency and stable fluid flow characteristics. However, in the case of the rectangular tank, which is compact and often used in transport, its shape acts as baffles, reducing angular velocity, while intensifying the axial component of the fluid velocity. The results demonstrate that the proposed impeller can be used in both flat-bottomed cylindrical and rectangular tanks, provided that the appropriate geometric parameters are maintained. Because is generates a mixed (radial-axial) fluid motion in both tanks, the new impeller represents an interesting alternative to classic bladed impeller.

1 Introduction

Mechanical mixing is a fundamental unit operation across chemical engineering, wastewater treatment, biotechnology, pharmaceuticals, food production, and mineral processing. The quality of the mixing process directly governs product homogeneity, reaction kinetics, heat and mass transfer efficiency, and overall process yield. Consequently, optimizing the operating conditions and hydrodynamic effectiveness of mixing systems remains a significant engineering challenge [1]

The hydrodynamic behaviour of a medium within stirred tanks depends on interrelated factors, including fluid rheology, impeller geometry, rotational speed, and vessel configuration. Among these parameters, the impeller design and the geometry of the tank are the most critical variables influencing the global flow pattern and the energy requirements of the process.

Conventional cylindrical tanks, often equipped with Rushton-type turbines, remain the industry standard because they provide symmetrical circulation and predictable mixing characteristics. However, standard radial-flow turbines exhibit high power numbers (N_p) and tend to generate segregated, poorly mixed regions. To overcome these limitations, recent engineering efforts have focused on modifying impeller and internal vessel geometries to increase pumping capacity while simultaneously reducing energy consumption [2] demonstrated that self-similar impeller blades based on Hilbert curves break up large trailing vortices, reducing N_p by 34.6% to 51.9% and shortening mixing times compared to a conventional Rushton turbine. Similarly, Lugo-Hinojosa et al. [3,4] showed that replacing conventional flat baffles with tubular baffles increases impeller pumping efficiency by 13% to 20% and lowers power consumption, although it weakens axial circulation in the upper part of the tank. Furthermore, research by Jaszczur et al. [5, 6] and Młynarczykowaska et al.[7] revealed that bucket- and jet-type impellers generate a combined radial and axial discharge profile, providing substantially stronger circulation and

* Corresponding author: mindziu@agh.edu.pl

pumping effects at significantly lower power inputs than conventional disc turbines.

Beyond internal hardware, vessel geometry and feed location strongly influence homogenization. Ramírez-López [8] noted that in cylindrical vessels with curved bottoms, poor circulation near walls and bottom regions creates stagnant zones, making mixing time highly dependent on the tracer injection point. Conversely, investigations into non-cylindrical vessels have shown that asymmetric geometries promote chaotic advection. Li et al. [9,10] demonstrated that diameter-transformed (elliptical) stirred tanks induce a wall-squeezing effect that eliminates toroidal segregation zones, increasing spatial coverage from approximately 56% to 98% without additional power consumption. Similarly, Soares et al. [11] highlighted that optimizing baffle aspect ratios in turbulent stirred tanks is essential for equilibrating dead zones and minimizing tracer concentration variance. In eccentric unbaffled vessels, Plusa et al. [12] further confirmed that off-center impeller placement alters free-surface vortex dynamics and aeration mechanisms.

Rectangular and cubic tanks are increasingly adopted in industry for storage, transport, and point-of-delivery mixing due to their spatial and logistical advantages. Unlike cylindrical tanks, rectangular vessels feature sharp corners that disrupt symmetrical tangential flow and alter the internal velocity distribution. In these corner regions, localized recirculation and turbulence zones emerge, which can either enhance fluid dispersion or generate dead spots, fundamentally modifying mass transport throughout the entire fluid volume.

Despite growing industrial reliance on non-cylindrical vessels and advancements in high-efficiency agitators, direct empirical comparisons between cylindrical and rectangular tank geometries remain scarce. Specifically, there is a lack of systematic experimental data quantifying how the transition from a cylindrical to a rectangular cross-section alters the flow structures, pumping capacity, and energy demand of jet-type impellers relative to standard turbines.

Therefore, the aim of this study is to experimentally evaluate and compare the influence of tank geometry on fluid flow mixing efficiency and power characteristics for an innovative jet-type impeller (Jet-1) versus a standard Rushton turbine in cylindrical and rectangular tanks. Using Particle Image Velocimetry (PIV) and precision torque measurements across varying hydrodynamic regimes and fluid viscosities, this work determines the power number (N_p), normalized pumping capacity (K_c), and overall mixing efficiency (E). These three dimensionless parameters provide a rigorous basis for identifying optimal geometric and operating configurations that maximize homogenization while minimizing energy consumption.

2 Experimental set-up and methodology

The experiments were conducted in unbaffled vessels with smooth, transparent walls, featuring either cylindrical or rectangular (squire cross-section) geometries. The core component of the test rig was a mechanical agitator driven by an infinitely variable rotational speed motor, equipped with either a novel jet-type impeller (Jet-1) or a standard six bladed Rushton turbine (6-RT) serving as a reference benchmark (Figure 1). The Rushton turbine was used to validate the test setup and served as a reference impeller. The positioning of the impeller above the vessel bottom, along with its dimensions relative to the geometric parameters of the vessels under study, is summarized in Table 1. The vessels used in the experiments had smooth, transparent walls and without baffles. The cylindrical vessel was fabricated from Plexiglas with a wall thickness of 50 mm, while the rectangular vessel was constructed from optical-quality glass. In all configurations, the impeller off-bottom clearance was fixed at $h = 1/3 \cdot H$. As working fluids deionized water (ρ = 998.2 kg/m3, μ = 0.001004 kg/(m·s) at 20°C) and 100% glycerine (ρ=1261.1 kg/m^3, μ=1.4101 kg/(m·s) at 20°C) were used.

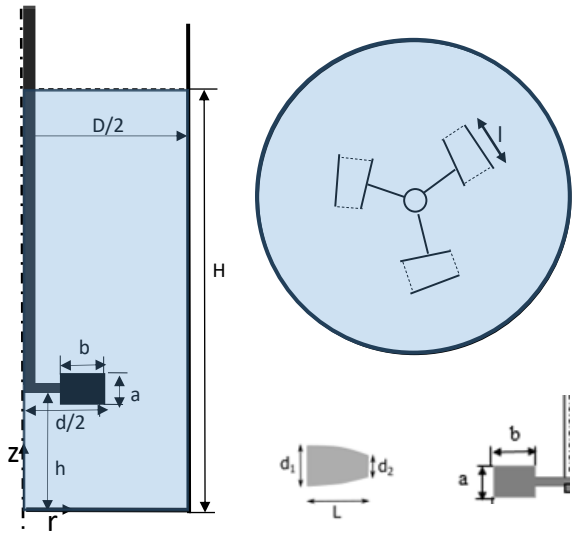


Fig. 1. Schematic diagram of experimental stirred tank configurations equipped with the used impellers

The Jet-1 impeller consisted of three tapered, bucket-shaped blades mounted symmetrically around the hub, capable of operating at three blade inclination angles: β= -15°, 0°, and +15°. The geometric dimensions of both vessels and impellers are summarized in Table 1.

Torque and power measurements. The impeller shaft was positioned coaxially at the center of the vessel, which was mounted directly onto an FSA-2 strain-gauge torque meter (AXIS; measurement range up to 2 Nm accuracy +/-0.001Nm, sampling frequency 1000 Hz. Measurements were recorded across rotational speeds ranging from N = 10 to 500 rpm to determine the mechanical power input required to overcome hydrodynamic drag.

Table 1. Dimensions of the tanks and impellers

Parameter	Symbol	Value, mm Cylindrical tank	Value, mm Rectangular tank
Tank height / Liquid height	H_c / H	300 / 170	500/300
Diameter of the tank	D	170	300
Diameter of the impeller	d	85/57	140
Impeller distance from tank bottom	h	57	100
Height, width for RT blades	a / b	12/15	--------
Length for Jet-1 bucket's	l	40	50
Diameter of the bucket's	d_1 / d_2	15 / 18	31.0/16.5
Geometric parameters relationships	H = D, d = 1/3D, h = 1/3D.		

Velocity field measurements (PIV and Stereo-PIV). Local instantaneous velocity fields were acquired in a vertical central plane (coinciding with the diagonal plane in the rectangular vessel). To eliminate optical refraction errors caused by wall curvature, the cylindrical vessel was enclosed within a square water-filled viewing jacket. Two-dimensional velocity fields in the cylindrical tank were recorded using a single LaVision CCD camera (2048x2048 pixels) illuminated by a dual-pulse Nd:YAG laser (30 mJ/pulse). For the rectangular vessel, three-component velocity fields were obtained via Stereo-PIV using two 12-bit LaVision Imager CX12 cameras (4080x2984 pixels) fitted with 50 mm f/1.8 lenses and a dual-pulse Nd:YAG laser (400 mJ/pulse). Each measurement series consisted of recording 200 image pairs at 15Hz and processed in DaVis 11.2 software using multi-pass cross-correlation with interrogation windows decreasing from 64x64 to 32x 32 (25% overlap) [13].

Evaluation of dimensionless performance parameters. Based on the experimental data, the impeller Reynolds number (Re), power number (N_p), normalized pumping capacity (K_c), and overall mixing efficiency (E) were calculated as follows:

$$Re = \frac{nd^2\rho}{\mu} \quad (1)$$

$$N_p = \frac{P}{\rho n^3 d^5} \quad (2)$$

where: ρ - density (kg/m^3), μ- viscosity (kg/m·s), n - agitator speed (1/s) , d - impeller rotor maximum diameter (m), P – power (W) required to rotate the impeller with the specified rotational speed. Power was calculated from torque measurement as follows:

$$P = 2\pi \cdot n \cdot \tau \quad (3)$$

where τ is the torque (N·m).

The last important parameters are mixing efficiency E and hydraulic efficiency, described by the equations:

$$E = \frac{K_c}{Np}, \quad (4)$$

$$\text{where, } K_c = \frac{Q_i}{nd^3} \quad (5)$$

where Q_i is pumping capacity dependents on the Reynolds number determined appropriately for the geometry of the impeller-tank system under analysis. Accordingly to definition, the flow rate of a fluid flowing through the cross-section of a tank is known as pumping capacity (Q_i).

For a cylindrical vessel, the flow of the working fluid was observed along a defined radius (r), while for a rectangular tank, changes were analyzed within a plane at a specific height (z).

The pumping capacity in the radial direction was determined for a radius of r = 35 mm (*Eq. 6*), whereas for flow through a horizontal plane, a height of z = 50 mm (midway between the tank bottom and the impeller) was used (*Eq. 7*).

This important parameter, which characterizes the operation of the impeller, was calculated by integrating the mean local values of the fluid's axial velocity components (respectively, u_r and u_z), using the following formulas:

$$Q_r = \int_{z_1}^{z_2} |u_r| dS \quad (6)$$

where the height is: z_1=0 and z_2=0.17 m

$$Q_z = \int_{r_1}^{r_2} |u_z| dS \quad (7)$$

where r_1 = 0 mm and r_2 = 70 mm are the horizontal radial integration limits corresponding to the tank axis and the impeller radius, respectively, u_r and u_z.

This parameter should be presented in a dimensionless form as the normalized pumping capacity (K_c), because these values can be compared directly for different impeller geometries in various flow conditions (*Eq.5)*

The overall flow characteristics for a given mixer geometry can be described using this parameter. Due to the absence of a single, universal criterion that could fully characterize mixing intensity across different mixing system geometries, researchers used to computational normalization of values such as energy demand or fluid flow intensity. The geometric dimensions of the impellers and/or the rotational speeds of the agitator are most commonly used as the basis for this normalization.

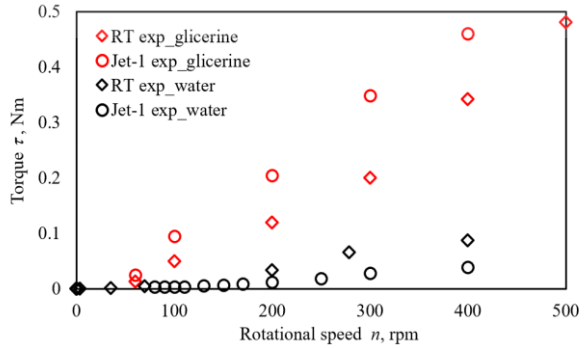
3 Results and discussion

3.1 Torque measurements and mixing process efficiency

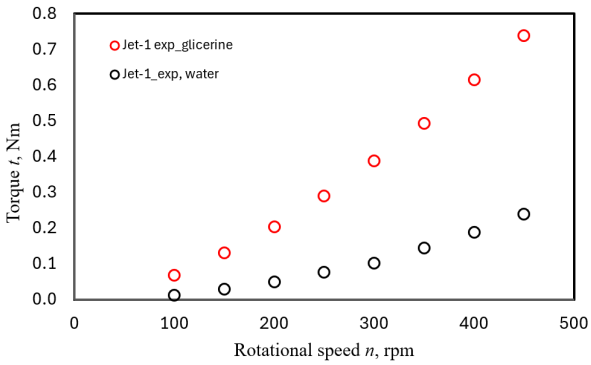
This chapter presents comparison of the hydrodynamic characteristics of an innovative jet agitator operating in cylindrical and rectangular tanks, based on experimental measurements supported by prior numerical analyses.

In accordance with the established measurement methodology, the first stage involved measuring the torque to assess fluid flow resistance during the operation of an agitator equipped with a Jet-1 impeller in various tank geometries without baffles. Figure 2 illustrates the variation in torque as a function of rotational speed, using water and glycerin as the working fluids in tested geometric tank.

The results obtained for Jet-1 in a cylindrical tank were compared with the data for the reference rotor in the form of a Ruhston turbine with six blades positioned perpendicular to the turbine disk (6-RT). The bucket blades of Jet-1 were set in position β=0 (Figure 2a). The high viscosity of glycerin, compared to water, leads to increased resistance during the operation of the agitator, which determine to higher torque values. This trend is particularly evident in the case of the Jet-1 impeller. The shape of the mixing elements (resembling buckets) significantly includes the nature of the fluid flow inside the buckets as well as on their outside.



(a)

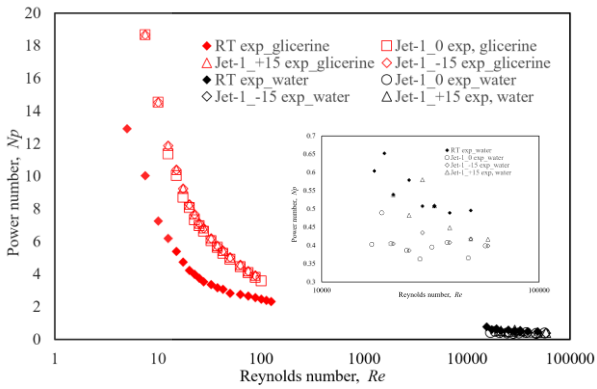


(b)

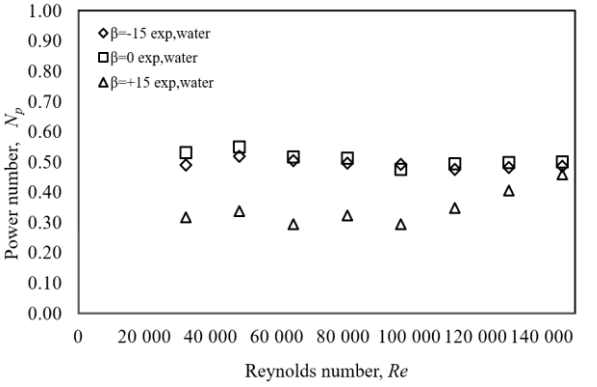
Fig. 2. Torque as a function of rotational speed for the Jet-1 impeller and the Rushton turbine (6-RT) in water and glycerine for the (*a*) cylindrical and (*b*) rectangular tanks.

In all tested configurations, torque increases monotonically with rotational speed, exhibiting a pronounced nonlinear rise above N = 200 rpm inertial effects intensify. Owing to its higher dynamic viscosity, glycerine generates substantially greater hydrodynamic drag than water across the entire speed range. In the cylindrical vessel, the streamlined, bucket-shaped geometry of the Jet-1 impeller reduces form drag compared to the flat, perpendicular blades of the 6-RT, resulting in lower torque requirements under equivalent operating conditions.

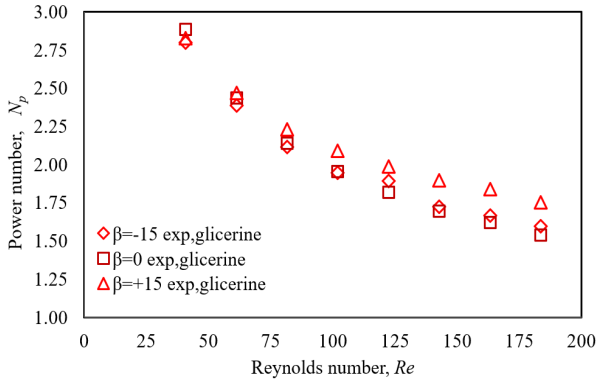
Based on the torque and PIV measurements, the dimensionless parameters pumping capacity *Kc*, power number *Np* and mixing efficiency were evaluated as a function of the Reynolds number. Figures 3-5 present these parameters as function of the Reynolds number for the tested impeller within various tank geometries.



(a)



(b)

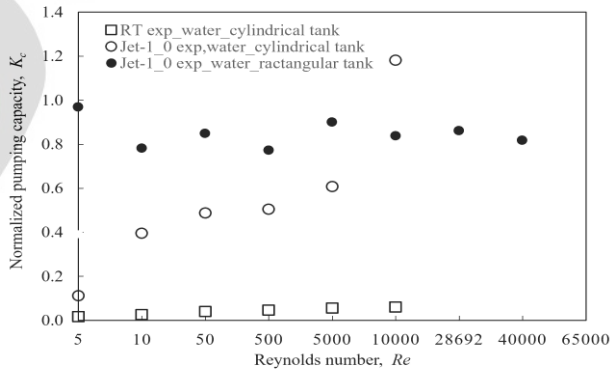


(c)

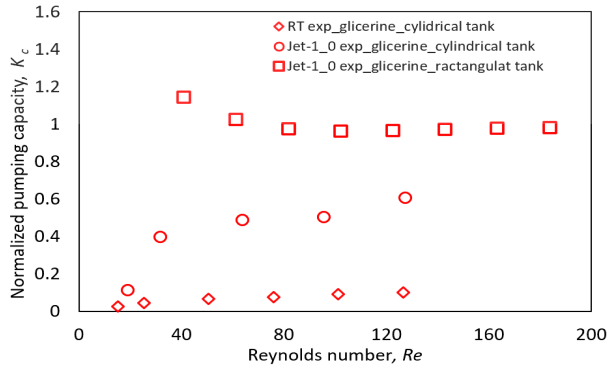
Fig.3. Power number N_p for a Jet-1 type impeller, operating across a wide range of viscosities in cylindrical (*a*) and rectangular *(b,c)* tanks

Preliminary tests examining the blade inclination angle (β=0, β =+15, β =-15) confirmed that the neutral configuration (β=0) and downward-inclined blades (β=+15) provide comparable hydrodynamic performance while maintaining low power

consumption; accordingly, the comparative analysis focuses primarily on the β=0 configuration.

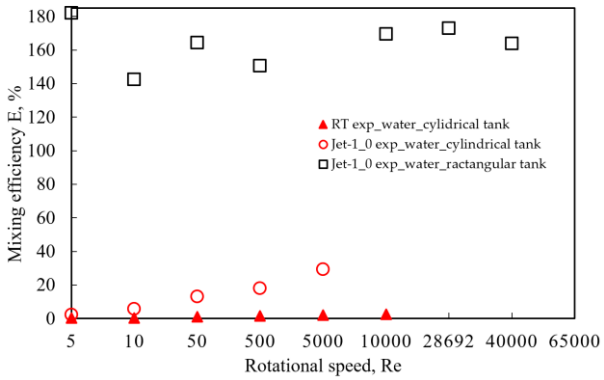


(a)

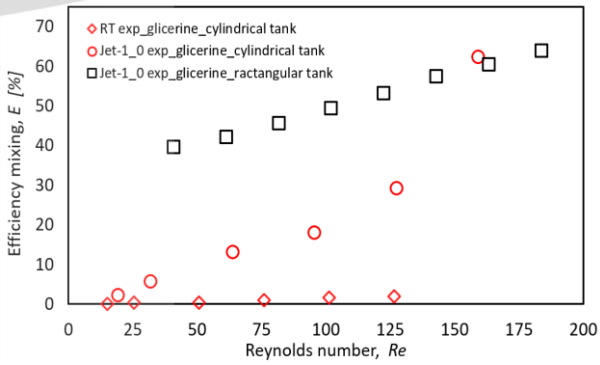


(b)

Fig. 4. Normalized pumping capacity K_c evaluated from experimental measurements as a function of the Reynolds number for analized impellers operating water (*a*) and glycerine (*b*)



(a)



(b)

Fig.5. The efficiency comparison analyzed impeller as a function of Reynolds number for different tank geometries operating in water (*a*) and glycerine (*b*)

Based on the provided plots (*Figures. 3–5*), a comparative analysis of the mixing process characteristics across the tested geometric configurations can be performed (see section 3.1). For a cylindrical tank, the innovative Jet-1 impeller exhibits a significantly lower energy demand compared to the classic Rushton turbine (RT). In the turbulent flow regime (water, Re > 10^4), the power number (*Np*) for the Jet-1 impeller falls within the range of 0.35–0.55, whereas for the RT, it is approximately 0.65 (Fig. 3a). At higher viscosities (glycerin) and low Reynolds numbers (Re), the *Np* values for the RT are slightly higher—reaching approximately 18.5 at Re~10) while for the Jet-1 impeller, they range from about 10 to 12.

In terms of pumping capacity (*Kc*), the Jet-1 impeller achieves significantly higher values and superior performance across a wide range of fluid viscosities compared to the reference impeller (*RT*). In a cylindrical tank, the Jet-1 impeller yields *Kc* values in the range of 0.4–0.6; in a rectangular tank, these values increase to 0.8–1.0 for water and 0.95–1.15 for glycerin. While the edges and corners of a rectangular tank can act as natural baffles preventing the entire fluid mass from rotating they do not necessarily induce forced circulation under all hydrodynamic conditions. Specifically, "dead zones" can form in the corners of the tank, as evidenced by flow velocity patterns obtained via PIV (Particle Image Velocimetry).

The Jet-1 impeller is incomparably more efficient than the RT impeller, as it combines lower energy consumption with high axial flow. It is worth noting that changing the geometry of the tank results in a significant increase in efficiency. In the case of glycerin, efficiency rises from approximately 5–30% (in a cylindrical tank) to 40–65% (in a rectangular tank). For water, the difference is even more pronounced: efficiency in a rectangular tank reaches 140–180%, compared to approximately 15–30% in a cylindrical tank.

The symmetric flow field is generated In a cylindrical tank, which dominated by radial-axial circulation. Liquid discharged from the impeller region moves toward the tank walls and subsequently recirculates both upward and downward, forming extensive circulation loops that encompass the entire volume of the fluid.

In contrast, in a rectangular tank, the trajectory of the discharged stream is altered. The flat walls dampen the global rotational motion and direct the liquid toward the corners of the tank. Consequently, a stronger axial circulation develops, accompanied by localized recirculation zones near the walls.

The observed behavior confirms that rectangular geometries function similarly to baffled cylindrical vessels, reducing the intensity of swirling and enhancing flow stabilization.

As a result, the flow structures within a rectangular tank become more stable, yet less symmetric, than those observed in a cylindrical vessel under analogous process conditions.

3.2 Analysis of patterns flow using PIV

The mean velocity vector fields acquired via PIV and Stereo-PIV in the vertical (r-z) plane for high-viscosity glycerol are presented in Figs. 7 and 8.

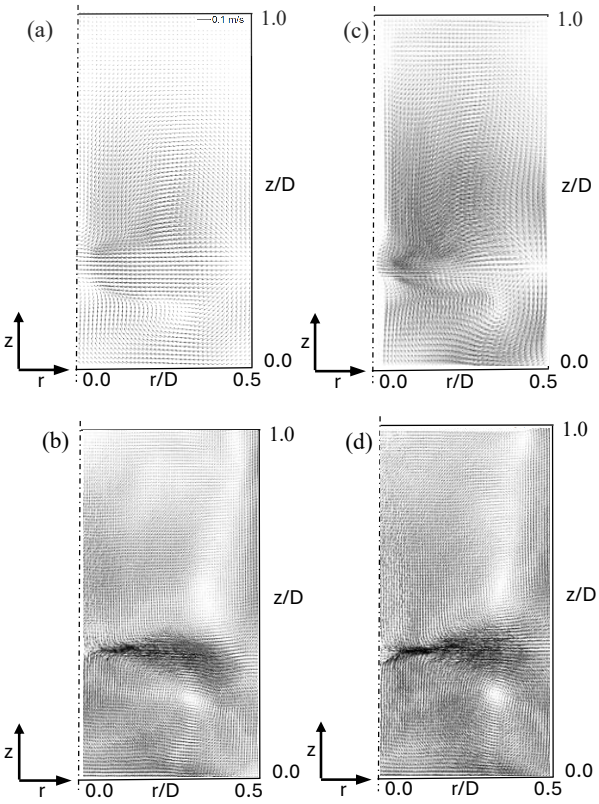
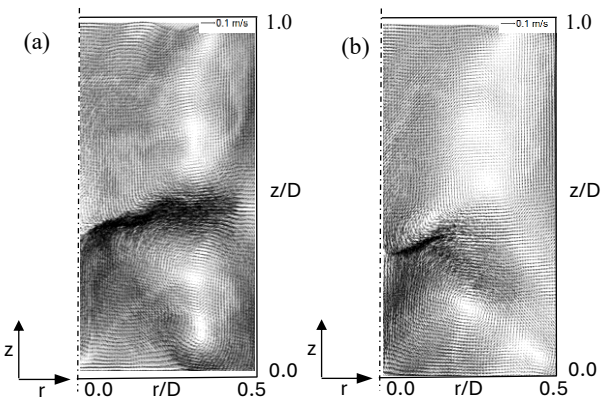


Fig. 6. Mean velocity field for Jet-1 impeller (β=0, h/H=1/3) for rotational speeds N=100 rpm (a,b), N=300 rpm (c, d) in cylicdrical (top) and ractangular (bottom) tank



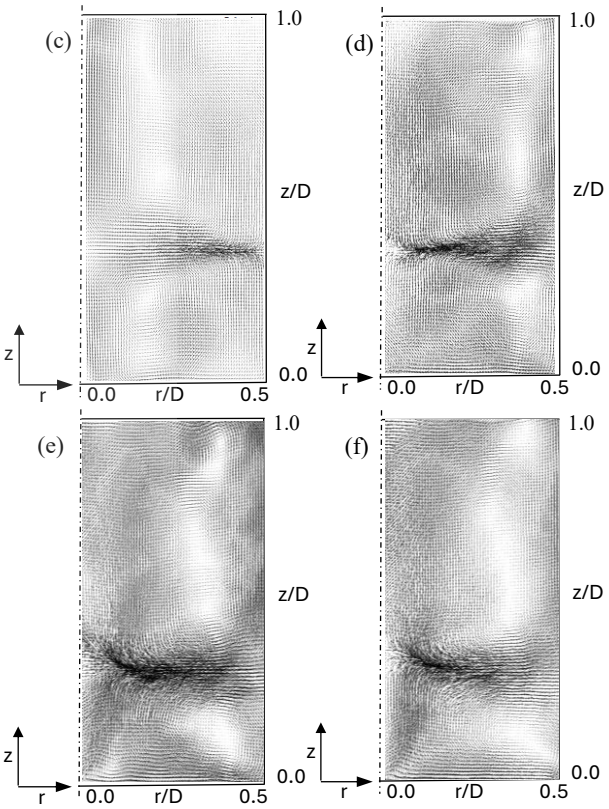


Fig. 7. Mean velocity field for Jet-1 impeller in rectangular tank (*h/H=1/3*) for rotational speeds N=50 rpm *(a, c, e*), N=150 rpm (*b, d, f)* in *β=-15* (top), *β=0* (middle) and *β=+15* (bottom) tank.

Based on the PIV velocity vector fields (Figures. 6 and 7), the fluid circulation structure around the Jet-1 impeller was analyzed. This impeller generates a strong, concentrated radial stream that flows horizontally from the blade region (at a height of h/H = 1/3) toward the side wall of the tank (r/D = 0.5).

Division of circulation into two loops: Upon striking the side wall, the fluid stream splits into two primary circulation patterns, or independent loops.

The upper circulation loop encompasses the space from the height of the impeller positioned above the tank bottom—up to the free surface of the liquid (z/D = 1.0). The fluid rises along the side wall and subsequently descends along the shaft axis (r/D = 0.0), returning to the suction zone of the rotating impeller.

The lower circulation loop covers the region near the bottom (z/D < 0.33). The fluid moves downward along the wall, turns back near the bottom, and is drawn upward into the impeller region.

Thus, a similar flow pattern can be identified for both tank geometries tested.

Figure 7(a)–(f) show the distribution of the average flow velocity field for the Jet-1 rotor, taking into account the change in the bucket position (change in the inclination angle) for the exemplary rotor rotational speeds in rectangular tank.

The influence of the bucket inclination angle is (β =-15°), which causes the discharge stream to be deflected slightly upward. This increases the fluid supply to the

upper circulation loop (as evidenced by the concentration of velocity vectors for z/D > 0.5 at N = 50 rpm), while simultaneously resulting in a weak flow below the impeller (Figure 7 a, b).
At (β=0°), the stream exits the impeller region horizontally, which ensures a more symmetrical and balanced distribution of the fluid's kinetic energy between the upper and lower circulation loops (Figures 7c,d).
In the case of β=+15, the discharge stream is directed distinctly downward. It penetrates the zone below the impeller (z/D < 0.33) very intensely and uniformly. An increase in rotational speed promotes the entrainment of fluid from the bottom of the tank.

4. Conclusion

The primary objective of this study was to experimentally analyze the influence of tank geometry (cylindrical versus rectangular) on the flow characteristics of liquids with varying viscosity, as well as on energy consumption and overall mixing efficiency. Mixing efficiency was evaluated based on local flow velocities determined using the Particle Image Velocimetry (PIV) and Stereo-PIV techniques, while power requirements were assessed through direct shaft torque measurements.
The results indicate that modified agitator designs, such as the Jet-1 impeller, with a specific tank geometry enables high pumping performance and mixing efficiency while simultaneously reducing energy consumption. Specifically, replacing a cylindrical vessel with a rectangular geometry suppresses global swirling and enhances axial circulation, elevating overall mixing efficiency (E) from 15–30% to 140–180%, in water and from approximately 5–30% to 40–65% in glycerol, while adjusting the bucket inclination angle (β) allows targeted control over bottom flow penetration. Consequently, the agitator configuration investigated here serves as an effective, low-energy alternative to baseline Rushton-turbine systems, particularly in processes involving a wide range of liquid viscosities.

Fundings. This work was partly funded by AGH University of Krakow, Faculty of Civil Engineering and Resource Management (No. 501.00-100302-10000) and Faculty of Energy and Fuels (No. 500.00-210000-10000). Research project was supported by the program "Excellence initiative – research university" for the AGH University of Krakow.
Data availability statement. Data will be made available on request
Author contribution statement. A. Młynarczykowska : Writing – review & editing, Writing – original draft, Visualization, Validation, Supervision, Software, Resources, Project administration, Methodology, Investigation, Funding acquisition, Formal analysis, Data curation, Conceptualization. K. Zwolińska-Glądys: Writing – review & editing, Software, Investigation, Data curation. M. Jaszczur : Writing – review & editing, Writing – original draft, Visualization, Software, Investigation, Formal analysis, Data curation, Supervision

References

1. Li, A., Yao, Y., Zhang, X., Wan, Y., Li, P., Wang, Y., Tao, C., & Liu, Z. (2024). Using CFD and machine learning to explore chaotic mixing in laminar diameter-transformed stirred tanks. Chemical Engineering Journal, 499, 156201. https://doi.org/10.1016/j.cej.2024.156201
2. Gu, D., Xu, H., Ye, M., Wen, L., 2022. Design of impeller blades for intensification on fluid mixing process in a stirred tank. Journal of the Taiwan Institute of Chemical Engineers 138, 104475. https://doi.org/10.1016/j.jtice.2022.104475
3. Lugo-Hinojosa, J.E., Martínez-Delgadillo, S.A., Yáñez-Varela, J.A., Garcia, A.A., 2025. Evaluation of flow patterns in a stirred tank equipped with tubular baffles using CFD numerical models and experimental PIV. Chemical Engineering and Processing - Process Intensification 216, 110466. https://doi.org/10.1016/j.cep.2025.110466
4. Lugo-Hinojosa, J. E., Martínez-Delgadillo, S. A., Yáñez-Varela, J. A., & Garcia, A. A. (2025). Evaluation of flow patterns in a stirred tank equipped with tubular baffles using CFD numerical models and experimental PIV. Chemical Engineering and Processing - Process Intensification, 216, 110466. https://doi.org/10.1016/j.cep.2025.110466
5. M. Jaszczur, A. Młynarczykowska, L. Demurtas, Effect of impeller design on power characteristics and Newtonian fluids mixing efficiency in a mechanically agitated vessel at low Reynolds numbers. Energies 13(3) 1-19, (2020). https://doi.org/10.3390/en13030640
6. M. Jaszczur, A. Młynarczykowska, L. Demurtas, An experimental and numerical analysis of the fluid flow in mechanical agitated vessel, ICCHMT, E3S Web of Conferences 128, 08002 (2019)
7. A. Młynarczykowska, S .Ferrari, L. Demurtas, M. Jaszczur, Impact of baffle geometry on the fluid motion in the stirred vessel, EPJ Web of Conferences, **269**, 01039, 1–6 (2022). https://doi.org/10.1051/epjconf/202226901039
8. Ramírez-López, A., 2024. Analysis of Mixing Efficiency in a Stirred Reactor Using Computational Fluid Dynamics. Symmetry 16(2), 237. https://doi.org/10.3390/sym16020237
9. Li, A., Yao, Y., Tang, X., Liu, P., Zhang, Q., Li, Q., Li, P., Zhang, F., Wang, Y., Tao, C., Liu, Z., 2024. Experimental and computational investigation of chaotic advection mixing in laminar rectangular stirred tanks. Chemical Engineering Journal 485, 149956. https://doi.org/10.1016/j.cej.2024.149956
10. Li, A., Yao, Y., Zhang, X., Wang, Y., Tao, C., Liu, Z., 2025. Asymmetric mixing in unbaffled stirred tank reactors: A mini-review. Chinese Journal of Chemical Engineering 87, 273–287. https://doi.org/10.1016/j.cjche.2025.04.020
11. Soares, L. L., Biserni, C., da Rosa Costa, R., Oliveira Júnior, J. A. A., dos Santos, E. D., &

Galarça, M. M. (2022). Numerical study and geometric investigation of the influence of rectangular baffles over the mixture of turbulent flows into stirred tanks. Applied Sciences, 12(10), 4827. https://doi.org/10.3390/app12104827

12. Płusa, T., Talaga, J., Duda, P., 2026. Experimental vs. numerical investigation of free surface formation in an unbaffled eccentric stirred tank. Chemical Engineering Science 331, 124041. https://doi.org/10.1016/j.ces.2026.124041
13. K., Zwolińska-Glądys, K., A., Młynarczykowska, M., Jaszczur, M., Borowski (2025). Mixing analysis in a stirred tank equipped with innovative impeller. 15th International Conference on Computational Heat & Mass Transfer : 19-22 May 2025, Antalya, Turkiye

Buoyant flows and pollutant dispersion in three-dimensional street canyons

Bayode Owolabi[1,*], *Stepan* Nosek[1,**], and *Vladimir* Fuka[2,***]

[1]Intitute of Thermomechanics of the Czech Academy of Sciences, Prague, Czechia
[2]Department of Atmospheric Physics, Charles University, Prague, Czechia

Abstract. Buoyancy generated by heated building surfaces can significantly alter airflow and pollutant dispersion in urban street canyons. While previous studies have demonstrated Reynolds number independence for isothermal canyon flows at Reynolds numbers above approximately 10,000, non-isothermal flows may not exhibit such independence. This study investigates buoyancy-driven flow and pollutant dispersion in a fully three-dimensional (3D) urban array comprising an 8×3 arrangement of buildings using large eddy simulations (LES) in OpenFOAM. The numerical model, based on a modified buoyantPimpleFoam solver with passive scalar transport, is validated against the 2D wind tunnel experiments of Marucci and Carpentieri (2019). Asymmetric heating is examined by heating the windward wall of the target canyon. At low Reynolds numbers, even relatively low Richardson numbers produce substantial flow restructuring, with the primary recirculation vortex shifting towards the upper canyon and strong upward motion developing along the heated wall. Consequently, pollutant concentrations increase near the windward wall, contrasting with the leeward-side accumulation observed in the isothermal case. However, the influence of buoyancy diminishes at higher Reynolds numbers. Finally, Reynolds number effects are systematically investigated at constant Richardson number to identify the conditions under which the flow and scalar fields become Reynolds number independent. The findings provide insight into buoyancy–inertia interactions and their implications for urban pollutant dispersion.

1 Introduction

Urban street canyons constitute important microenvironments in which building geometry, atmospheric turbulence and thermal effects interact to govern ventilation and pollutant dispersion. The restricted exchange of air between street canyons and the overlying atmosphere can promote pollutant accumulation, particularly under weak wind conditions (1; 2). Although wind-driven circulation is generally the dominant mechanism governing canyon ventilation, temperature differences between urban surfaces and the surrounding air can generate buoyancy forces that substantially modify the airflow and associated pollutant transport (3; 4). The influence of these thermal effects depends strongly on the location and intensity of surface heating. In particular, windward wall heating can modify or oppose the wind-driven circulation, producing secondary vortices and changing pollutant distribution within the canyon (5–7).

Considerable progress has been made in understanding thermally driven street-canyon flows through numerical simulations and wind tunnel experiments. Early investigations predominantly employed two-dimensional (2D) configurations to examine the effects of ground and wall heating (4; 5). However, real urban environments exhibit considerable three-dimensionality arising from finite building lengths, neighbouring structures and spanwise variations in the flow. Although three-dimensional (3D) investigations have subsequently examined thermal effects on urban airflow and pollutant dispersion (8; 9), the relationship between three-dimensional flow structures, buoyancy and pollutant transport remains insufficiently understood, particularly in arrays of buildings.

Another important consideration is the applicability of Reynolds number independence to non-isothermal street-canyon flows. For isothermal configurations, flow characteristics are generally considered independent of Reynolds number above a critical threshold, commonly taken as approximately 10,000. However, Chew *et al.* (10) demonstrated that this assumption may not hold when buoyancy opposes the wind-driven circulation. This distinction is particularly important when extrapolating reduced-scale experimental results to full-scale urban environments. More recently, Zhu and Chew (11) demonstrated that the critical Reynolds number for achieving Reynolds number independence in 3D isothermal street canyons depends on building geometry. Gong *et al.* (12) further investigated Reynolds number independence in wind- and buoyancy-driven street-canyon flows using computational fluid dynamics, highlighting the importance of Reynolds number effects in non-isothermal configurations. These findings raise an important question concerning the Reynolds number requirements for achieving Reynolds number independence in non-isothermal 3D urban flows.

The present study investigates the coupled effects of buoyancy and inertial forces on airflow and pollutant dis-

*e-mail: bayode@it.cas.cz
**e-mail: nosek@it.cas.cz
***e-mail: vladimir.fuka@mff.cuni.cz

persion in a 3D urban building array. Particular attention is given to how windward wall heating modifies the spatial organisation of the flow and pollutant concentration fields. Furthermore, a systematic Reynolds number analysis is performed at constant Richardson number to establish the critical Reynolds number above which the flow becomes independent of Reynolds number under non-isothermal conditions. By identifying this threshold, the study aims to provide a basis for assessing the applicability of Reynolds number independence in reduced-scale investigations of buoyancy-driven urban flows.

2 Numerical methodology and simulation settings

Large-eddy simulations (LES) were performed using the open-source computational fluid dynamics (CFD) software OpenFOAM to investigate flow dynamics and pollutant dispersion under both isothermal and non-isothermal conditions, the latter involving a heated windward wall. The simulations were conducted using the buoyantPimpleFoam solver, which solves the compressible Navier–Stokes equations coupled with an energy equation. This formulation accounts for density variations arising from temperature and pressure changes, thereby allowing buoyancy effects associated with thermal gradients to be captured. The solver was further modified to incorporate the transport of a passive scalar representing the pollutant concentration. Pollutant emissions were introduced through a line source, with the pollutant emission rate (Q) set to $1s^{-1}$. The scalar was treated as passive, meaning that its transport was governed by the resolved flow field without influencing the momentum or energy equations. This approach allows the dispersion characteristics to be investigated independently of any feedback of the pollutant on the flow. Figure 1 illustrates the computational configuration adopted in this study.

The subgrid-scale (SGS) stresses were modelled using the Wall-Adapting Local Eddy-viscosity (WALE) model. This model estimates the unresolved turbulent stresses through a spatially varying SGS eddy viscosity based on local velocity gradients. An important advantage of WALE is its ability to reproduce the appropriate near-wall scaling of the SGS eddy viscosity, which makes it particularly suitable for LES of wall-bounded turbulent flows. Furthermore, unlike some conventional SGS models, WALE does not require an explicit damping function to recover the correct near-wall behaviour.

To provide realistic turbulent inflow conditions, a synthetic turbulence generation method was employed at the inlet of the computational domain. This approach introduces artificial velocity fluctuations superimposed on the prescribed mean inlet velocity profile, allowing the incoming flow to contain turbulent structures rather than relying solely on the development of turbulence from an initially uniform or steady inflow. This is particularly important for ensuring a realistic representation of the incoming boundary layer and its interaction with the urban geometry.

For temporal discretisation, the Crank–Nicolson scheme with a blending coefficient of 0.8 was employed. This corresponds to an 80% Crank–Nicolson and 20% first-order Euler weighting, introducing a degree of numerical damping to improve the stability of the transient simulations while retaining the predominantly second-order temporal accuracy of the Crank–Nicolson scheme. The maximum Courant number was restricted to 0.5 to maintain adequate temporal resolution of the resolved flow structures and minimise numerical stability issues. Pressure–velocity coupling was handled using the PIMPLE algorithm, which combines features of the PISO and SIMPLE algorithms and is well suited to transient simulations.

Together, these modelling and numerical settings provide a framework for investigating the interaction between turbulent flow, thermal buoyancy and pollutant dispersion in the street canyon. The simulations under isothermal and heated-wall conditions enable the influence of thermal effects on the flow structure and pollutant transport to be examined under otherwise comparable conditions. The resulting flow and concentration fields were subsequently used to analyse the mechanisms governing pollutant dispersion and removal from the canyon. Figure 1 shows the computational domain used for the LES simulations

3 Results and Discussion

The numerical model was validated against the experimental measurements of Marucci and Carpentieri(7) for a two-dimensional (2D) street canyon with heated windward wall, at a Reynolds number Re of 5200 and a Richardson number Ri of -1.27. The Reynolds number is defined as

$$Re = \frac{U_{ref} H}{\nu}, \tag{1}$$

where U_{ref} is the reference velocity, H is the characteristic length (canyon height) and ν is the kinematic viscosity. The Richardson number, which characterises the relative importance of buoyancy and inertial effects, is defined as

$$Ri = \frac{g(\Theta_{2H} - \Theta_{Hot})H}{\Theta_{2H} U_{2\mathrm{H}}^2}, \tag{2}$$

where g is the gravitational acceleration, Θ_{Hot} and Θ_{2H} represent the temperature at the heated wall and at a reference height $2H$ respectively and U_{2H} is the velcity at the reference height $2H$

Figure 2 compares the LES predictions with the experimental measurements of the mean streamwise velocity U, turbulent kinetic energy TKE and temperature Θ profiles along the vertical mid-plane of the street canyon. Overall, the numerical results show very good agreement with the experimental data, reproducing the main features and distributions of the mean velocity, turbulent kinetic energy and temperature within the canyon. This agreement provides confidence in the ability of the numerical model to capture the coupled flow and thermal characteristics of the street-canyon configuration.

Figure 3 presents the mean velocity and pollutant concentration fields along the mid-plane of the isothermal three-dimensional (3D) street canyon for Reynolds numbers of $Re = 4860$ and $Re = 14582$. The results show

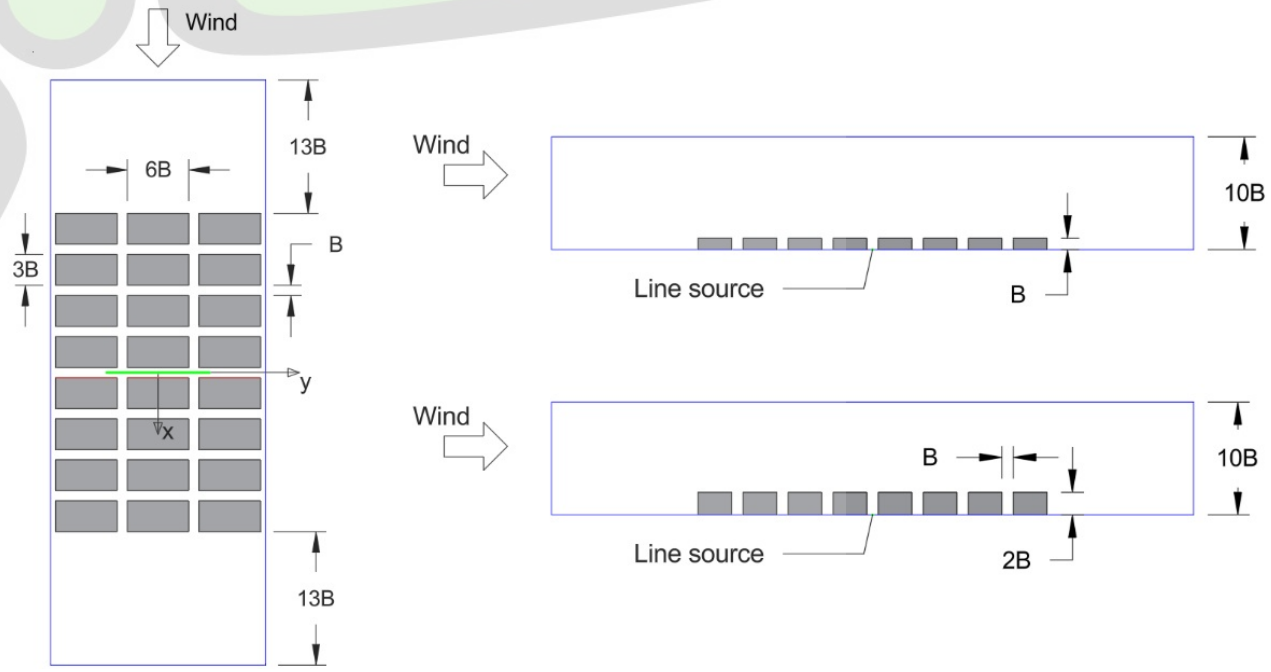


Figure 1. Computational domain

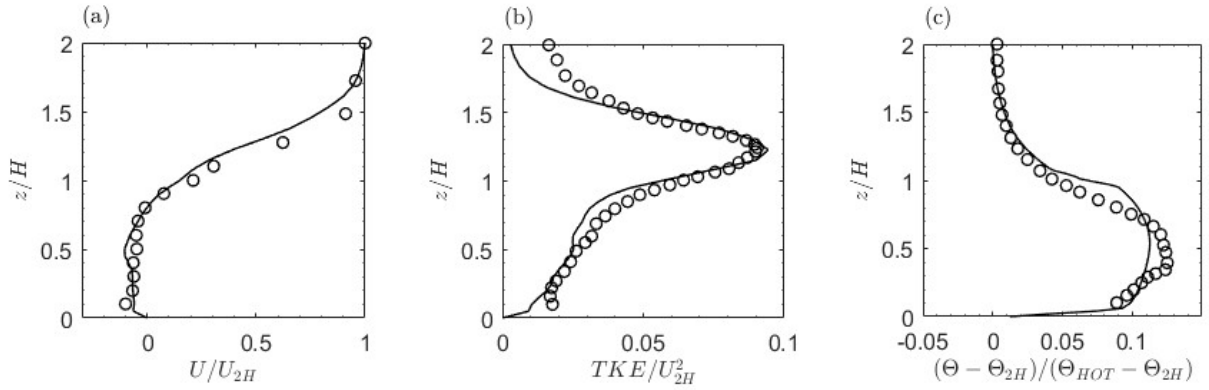


Figure 2. Validation of OpenFOAM code: (a) Mean streamwise velocity profile (b) Turbulent kinetic energy profile (c) Temperature profile. —-: Present LES; ∘: Marucci and Carpentieri (2019)

very similar flow and concentration distributions at both Reynolds numbers, indicating that Reynolds number independence has been achieved within the range investigated. The flow is characterised by a single dominant recirculation vortex within the canyon. This flow structure leads to an accumulation of pollutant near the leeward wall, where the recirculating flow transports the pollutant.

Figure 4 illustrates the evolution of the mean flow and pollutant concentration fields with increasing Reynolds number for the non-isothermal case, in which the windward wall of the canyon is heated. The Richardson number was maintained at $Ri = -0.202$ throughout the simulations. At Reynolds numbers below approximately 15,000, buoyancy has a pronounced influence on the flow, despite the relatively low magnitude of the Richardson number. The primary recirculation vortex is displaced towards the upper-right corner of the canyon, accompanied by an upward flow along the heated windward wall. This upward motion alters the pollutant distribution, resulting in higher concentrations near the windward wall, in contrast to the isothermal case, where pollutant accumulation occurs predominantly near the leeward wall.

With increasing Reynolds number, the influence of buoyancy on the flow structure progressively diminishes, and the flow approaches the pattern observed in the isothermal case. Correspondingly, the pollutant concentration becomes increasingly elevated near the leeward wall. At $Re = 131238$ and above, the flow and concentration fields exhibit very similar distributions, indicating that Reynolds number independence has been achieved. Notably, the Reynolds number required to attain this behaviour is considerably higher than that for the isother-

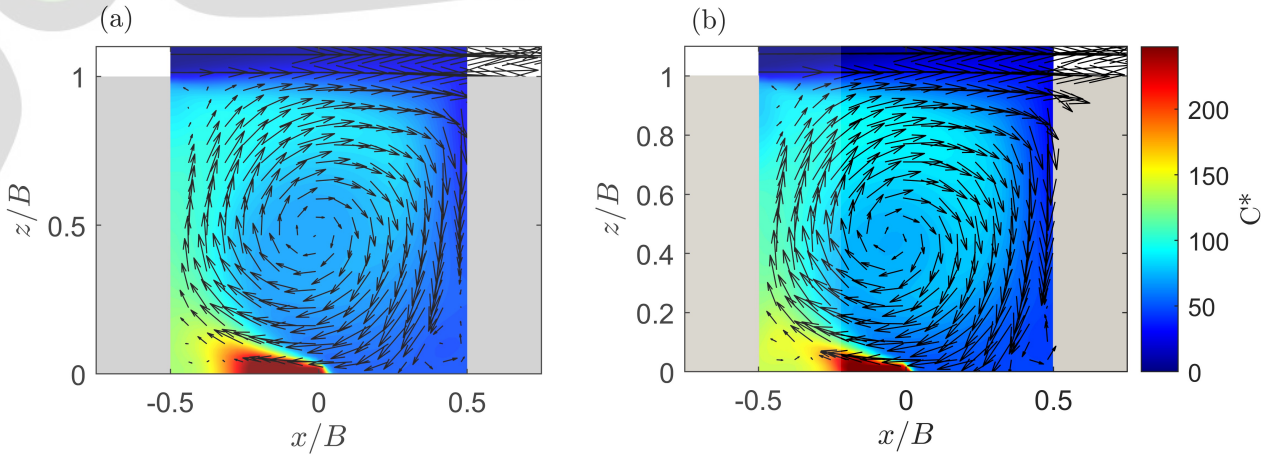


Figure 3. Mean velocity field and concentration across the canyon mid-plane for the isothermal case. (a) Re = 4860; (b) Re = 14582

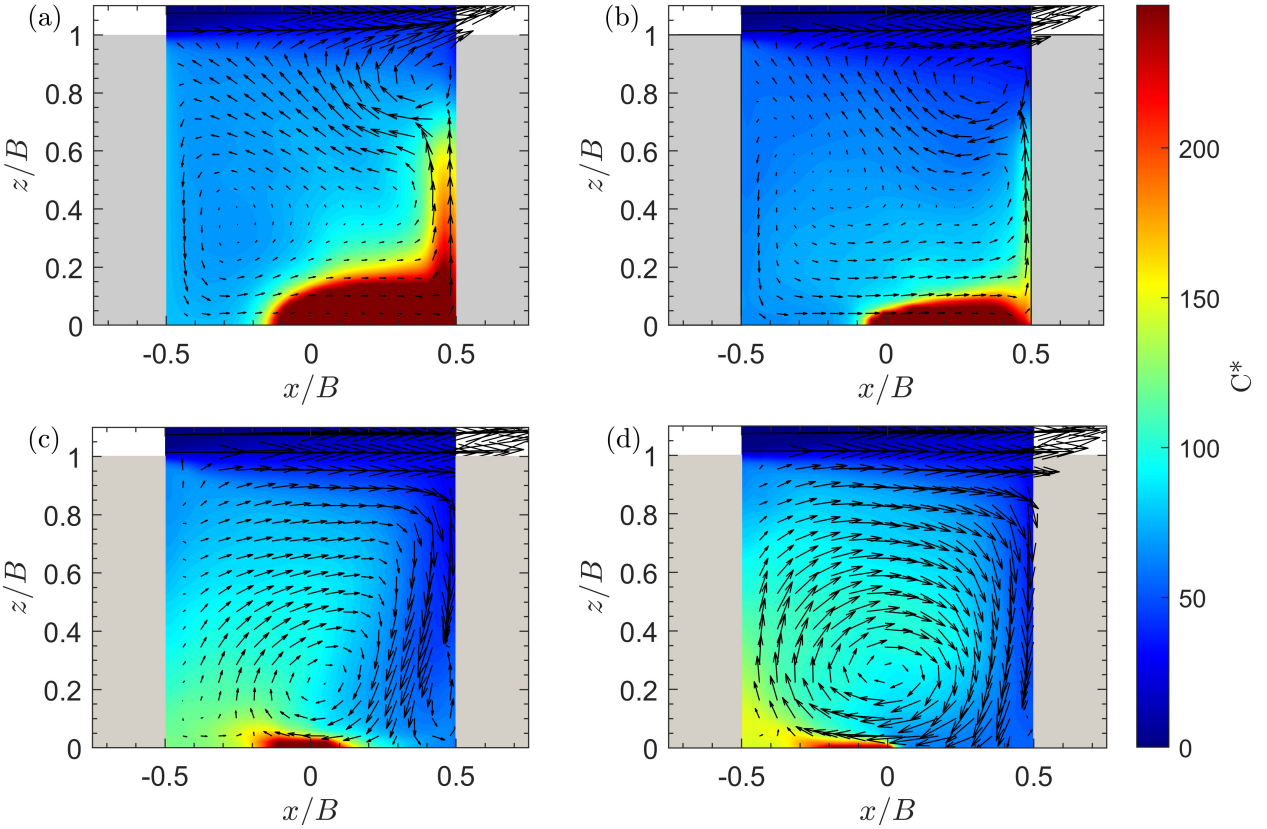


Figure 4. Mean velocity field and concentration across the canyon mid-plane for the case of Ri = −0.202. (a) Re = 4860; (b) Re = 14582; (c) Re = 43746; (d) Re = 131238

mal case. This suggests that the influence of thermal buoyancy persists over a wider range of Reynolds numbers, such that substantially stronger inertial effects are required before the flow becomes effectively independent of Reynolds number. These results highlight the importance of accounting for thermal effects when establishing Reynolds number independence in simulations of urban street-canyon flows.

4 Conclusions

Large-eddy simulations (LES) were performed using OpenFOAM to investigate the influence of Reynolds num-

ber on flow dynamics and pollutant dispersion in isothermal and non-isothermal three-dimensional street canyons. The numerical model was validated against the experimental measurements of Marucci and Carpentieri(7), showing good agreement in the mean velocity, turbulent kinetic energy and temperature profiles.

Under isothermal conditions, Reynolds number independence was achieved at relatively low Reynolds numbers, with the flow characterised by a single dominant recirculation vortex and higher pollutant concentrations near the leeward wall. In contrast, heating the windward wall introduced significant buoyancy effects, particularly at Reynolds numbers below 15,000, despite the relatively low Richardson number ($Ri = -0.202$). This modified the canyon flow structure, producing upward motion along the heated wall and increased pollutant concentrations in its vicinity. As Reynolds number increased, the influence of buoyancy diminished, and the flow and concentration fields approached those of the isothermal case.

An important finding is that Reynolds number independence in the non-isothermal case was achieved only at approximately $Re = 131238$, considerably higher than that required under isothermal conditions. This demonstrates that thermal buoyancy can substantially influence the Reynolds number dependence of street-canyon flows and highlights the importance of accounting for thermal effects when selecting Reynolds numbers for experimental and numerical investigations of urban pollutant dispersion.

References

[1] Oke, T.R., Street design and urban canopy layer climate. Energy and buildings **11(1-3)**, 103–113 (1988).

[2] Britter, R. E. and Hanna, S. R., Flow and dispersion in urban areas. Annual review of fluid mechanics **35(1)**, 469–496 (2003).

[3] Sini, J., Anquetin, S. and Mestayer, P. G., Pollutant dispersion and thermal effects in urban street canyons. Atmospheric environment **30(15)**, 2659–2677 (1996).

[4] Kim, J. and Baik, J., A numerical study of thermal effects on flow and pollutant dispersion in urban street canyons. Journal of applied meteorology **38(9)**, 1249–1261 (1999).

[5] Xie, X., Liu, C. and Leung, D.Y.C., Impact of building facades and ground heating on wind flow and pollutant transport in street canyons. Atmospheric Environment **41(39)**, 9030–9049 (2007).

[6] Li, X., Britter, R. E, Koh, T. Y., Norford, L. K., Liu, C., Entekhabi, D. and Leung, D.Y.C., Large-eddy simulation of flow and pollutant transport in urban street canyons with ground heating. Boundary-layer meteorology **137(2)**, 187–204 (2010).

[7] Marucci, D. and Carpentieri, M., Effect of local and upwind stratification on flow and dispersion inside and above a bi-dimensional street canyon. Building and Environment **156**, 74–88 (2019).

[8] Tsai, M., Chen, K. and Wu, C., Three-dimensional modeling of air flow and pollutant dispersion in an urban street canyon with thermal effects. Journal of the Air & Waste Management Association **55(8)**, 1178–1189 (2005).

[9] Allegrini, J, A wind tunnel study on three-dimensional buoyant flows in street canyons with different roof shapes and building lengths. Building and Environment **143**, 71–88 (2018).

[10] Chew, L. W., Glicksman, L. R. and Norford, L. K., Buoyant flows in street canyons: Comparison of RANS and LES at reduced and full scales. Building and Environment **146**, 77–87 (2018).

[11] Zhu, S. and Chew, L. W., Flows across 3D urban street canyons: Reynolds number independence revisited. In Building Simulation 2023 **18**, 2018–2025. IBPSA (2023).

[12] Gong, P., Tan, G. Y. A., Ng, S. T. T. and Zheng, X., A CFD Investigation of wind-and buoyancy-driven flows in urban street canyons: Assessment of wall-modelled LES and Reynolds number independence. Urban Climate **66**, 102854 (2026).

Determination of the temperature effectiveness of cross-flow and glycol run-around heat recovery systems

Robert Pastuszko[1,2*], *Robert* Kaniowski[1,2], and *Izabela* Cękiel[2]

[1]Kielce University of Technology, al. Tysiąclecia Państwa Polskiego 7, 25-314 Kielce, Poland
[2]Central Office of Measures (GUM), Elektoralna 2, 00-139 Warsaw, Poland

Abstract. Recuperators, which enable heat recovery, are increasingly used in the ventilation systems of buildings and means of transport, contributing to significant energy savings, reduced operating costs, and a lower carbon footprint. This study compares the temperature effectiveness of a cross-flow recuperator and a glycol run-around heat recovery system (RAHRS). The methodology for determining temperature effectiveness under conditions of equal supply and extract air mass flow rates is described, and the associated combined standard uncertainty is evaluated. The tests made it possible to identify the ranges of airflow and liquid flow rates at which the highest temperature effectiveness is achieved. Measurements were conducted over airflow rate ranges of 90 to 1100 m³/h for the cross-flow heat exchanger and 450 to 1350 m³/h for the run-around coil system. The calculated relative combined standard uncertainties associated with determining temperature effectiveness ranged from 2.5% to 5.4%. The cross-flow heat exchanger achieved a temperature effectiveness of 76% to 87% over the entire range of tested airflow rates, whereas the run-around coil system achieved maximum temperature effectiveness values of 50% to 60% at airflow rates below 900 m³/h. With a propylene glycol solution, the effectiveness remained close to 50% at liquid flow rates of at least 0.525 m³/h.

Keywords: heat recovery; cross-flow recuperator; run-around coil system; temperature effectiveness; measurement uncertainty

* Corresponding author: tmprp@tu.kielce.pl

1 Introduction

Heat recuperators transfer heat from extract air to supply air and are widely used in heating, ventilation and air-conditioning (HVAC) systems. By reducing the energy needed to heat or cool incoming air, they can lower operating costs and associated emissions.

Run-around heat recovery systems are particularly useful where the supply and extract airstreams must remain separate, including laboratories, healthcare facilities, and food and pharmaceutical production. They are also used in industrial ventilation and transport HVAC systems.

A run-around heat recovery system (RAHRS), also called a glycol recuperator, consists of two fin-and-tube coils connected by a closed liquid circuit and a circulating pump.

Mahmoud et al. [1] modelled the effects of airflow, coupling-liquid flow and glycol concentration on RAHRS performance and compared the predictions with experiments. Jouhara et al. [2] reviewed industrial waste-heat recovery technologies. Lu et al. [3] used field measurements and a power-law relationship to model RAHRS performance, while Wallin et al. [4] compared conventional liquid-coupled and heat-pump-assisted configurations. Vali et al. [5] developed a two-dimensional model of systems combining counter-flow and cross-flow coils. Haglund Stignor et al. [6] investigated liquid-side heat transfer and pressure drop in finned-tube coils. Balen et al. [7] analysed seasonal operating conditions, and Li et al. [8] proposed a thermo-economic assessment of RAHRS retrofits. Müller [9] discussed uncertainty in measuring heat recovery effectiveness and heat transfer rate.

Published analyses of measurement uncertainty for temperature effectiveness in ventilation heat recovery remain limited.

Because the airstreams do not mix, a liquid-coupled system can recover heat from contaminated extract air without directly contacting the fresh supply air. This separation is valuable in laboratories and healthcare and industrial settings.

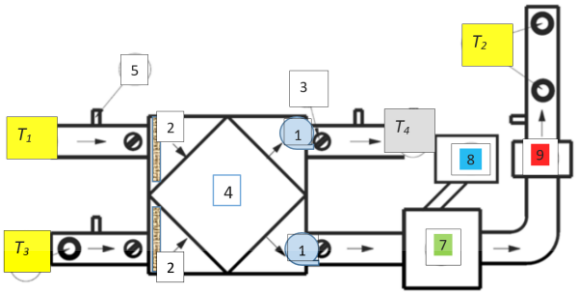
The purpose of this article is to compare the temperature effectiveness of two heat recovery systems at various ambient temperatures and airflow rates and to determine the ranges of airflow and liquid flow rates at which the highest effectiveness is achieved.

2 Experimental setups

Figures 1 and 2 show the cross-flow and glycol-based RAHRS test rigs, respectively. Temperature effectiveness was measured at different outdoor air temperatures and airflow rates. The experimental

procedure was based on the approach described by Mahmoud et al. [1], with reference to EN 308 [10].

In the first RAHRS test series, GLITHERM ET was used as the heat transfer fluid. It was a 30% aqueous solution of ethylene glycol with a nominal freezing point of approximately −15 °C. The closed glycol circuit transferred heat from the upper coil, located in the extract-air duct, to the lower coil, located in the supply-air duct (Fig. 2). Variable-speed fans were used to control the air volume flow rates. Air temperatures were monitored using the manufacturer's NTC 10 kΩ sensors and additional type-K thermocouples at positions T_1, T_2 and T_3. The stated absolute accuracy of the thermocouple readout was 0.3 K.



a)



b)

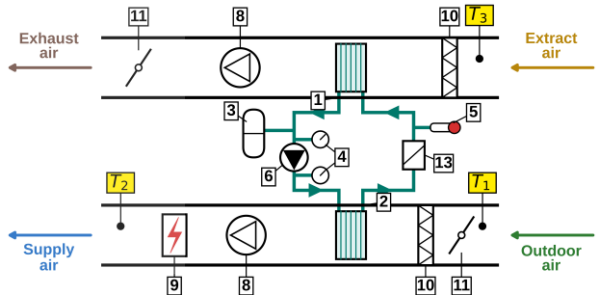
Fig. 1. RGS-2-H-P-W cross-flow recuperator (Juwent Szymański, Nowakowski Sp.j.). (a) Test-rig diagram with a heat pump and electric heater; (b) unit with the cover removed. T_1: outdoor-air inlet; T_2: supply-air outlet; T_3: extract-air inlet; T_4: exhaust-air outlet (temperatures in °C). 1: fan; 2: HEPA filters; 3: valve; 4: cross-flow exchanger; 5: resistance transducer; 6: bypass shutters; 7: heat-pump condenser; 8: heat-pump evaporator; 9: electric heater.

The thermocouples were connected to a Fluke Hydra 2625A logger. The differences between the recorded temperature readings did not exceed 0.1 K. For a conservative uncertainty assessment in the first test series, a temperature input uncertainty of 0.2 K per measurement channel was assumed.

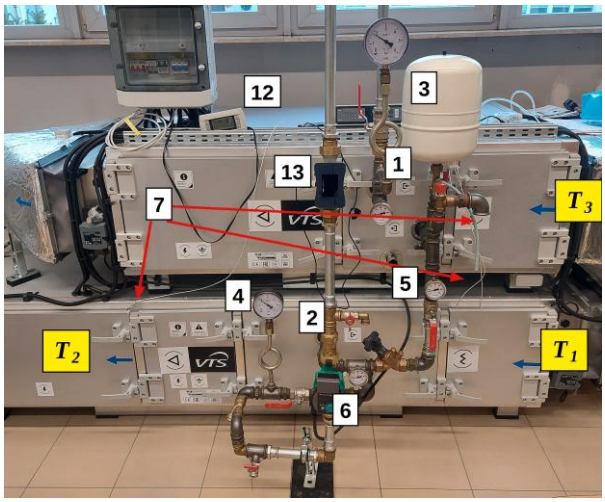
Both test rigs were equipped with filters and systems for heating the incoming outdoor air. Air volume flow rates were determined from differential pressure measurements across the fans:

- 90 to 400 m³/h: cross-flow recuperator with a HEPA filter;
- 450 to 1100 m³/h: cross-flow recuperator with a standard filter;
- 450 to 1350 m³/h: glycol RAHRS with a standard filter.

With an exhaust-duct cross-section of 821 × 313 mm², the glycol RAHRS airflow range corresponds to mean velocities of approximately 0.49 to 1.46 m/s.



a)



b)

Fig. 2. Glycol run-around heat recovery system (RAHRS) built from the VVS021-L-FGVH kit (VTS Polska Sp. z o.o.): (a) principle diagram; (b) view of the installed sections. T_1: outdoor-air inlet; T_2: supply-air outlet; T_3: extract-air inlet (temperatures in °C). 1 – glycol circuit connection to the upper (extract-air) coil; 2 – glycol circuit connection to the lower (supply-air) coil; 3 – expansion vessel; 4 – pressure gauge in the liquid circuit; 5 – liquid thermometer; 6 – pump; 7 – temperature sensors; 8 – fan; 9 –electric heater; 10 – HEPA/pocket filters; 11 – valve; 12 – control panel; 13 – ultrasonic flowmeter.

A centrifugal pump circulated the ethylene glycol solution through the coils (Fig. 2). Pressure gauges were installed on the suction and discharge sides; both control valves remained fully open during testing. The pressure drop in the liquid loop was approximately 100 kPa.

In the second test series, the liquid circuit was filled with Ergolid Eko -35 (approximately 52% propylene glycol by mass, with a nominal freezing point of -35 °C). The liquid flow rate was measured using a JUMO flowTRANS US W02 ultrasonic flowmeter (13), for

which the manufacturer specifies a maximum permissible error of ±1% of the reading. The flowmeter had not been calibrated for the glycol mixture used in the tests. Temperatures at measurement points T_1, T_2 and T_3 were measured using TP-361 sensors connected to channels 1, 2 and 3, respectively, of an EMT 200 thermometer equipped with a WRT-9-BOX multiplexer.

The thermometer and sensors were calibrated at the GUM Temperature Laboratory at -25, 0, 40 and 80 °C (certificate Z2-Z21.4180.17.2025.588.1). The indication errors at these points were -1.1, -1.0, -1.0 and -1.2 K for channel 1; -0.9, -0.8, -0.9 and -0.9 K for channel 2; and -1.7 K at each point for channel 3. The expanded calibration uncertainty was 0.1 K (k = 2). Since all recorded temperatures were within the range of 2.5–23.2 °C, the measured values were corrected using linearly interpolated calibration corrections based on the indication errors determined at 0 and 40 °C.

3 Measurement methodology

The cross-flow recuperator was tested under three outdoor-air temperature conditions, whereas the glycol-based RAHRS was tested under seven conditions.

The outdoor-air temperature T_1 ranged from 1.9 to 9.3 °C, relative humidity from 40% to 75%, and supply-air temperature T_2 from 9.5 to 15.5 °C. The extract-air flow rate was adjusted to minimise the risk of condensation on the heat exchanger surfaces.

Temperatures and flows were recorded after steady conditions had been reached. The measurement procedure was as follows:

- Position the temperature sensors and check the filters and enclosure for leaks.
- Open the supply- and extract-air dampers.
- Start the rig and check the controller for errors.
- Disconnect the electric heater and heat pump on the cross-flow rig.
- Start logging temperatures with the fans stopped; require agreement within 0.1 K.
- Start the fans at the lowest airflow setting.
- Start the glycol circulation pump (RAHRS only).
- Allow approximately 30 min for initial stabilisation.
- Record the initial measurements.
- Increase cross-flow airflow in steps of 50 to 100 m³/h. For the glycol system, increase airflow from 30% or 40% to 90% of the 1500 m³/h maximum (up to 1350 m³/h).
- After each change, wait approximately 15 min (5 min longer if needed), then record the readings when temperature changes are within ±0.1 K and airflow changes within ±25 m³/h. Use the same supply- and extract-fan settings for each first-series measurement.

4 Heat recovery effectiveness and uncertainty calculations

4.1 Temperature effectiveness

For equal supply- and extract-air mass flow rates, the enthalpy-based effectiveness of heat recovery, defined as the ratio of the enthalpy increase of the supply air to the enthalpy decrease of the extract air, can be expressed as follows [3]:

$$\eta = \frac{h_2 - h_1}{h_3 - h_1} \tag{1}$$

where:

h_1: specific enthalpy of the outdoor air, kJ/kg
h_2: specific enthalpy of the supply air, kJ/kg
h_3: specific enthalpy of the extract air, kJ/kg

For sensible heat transfer, the corresponding effectiveness can be expressed in terms of the heat capacity rates of the supply and extract air streams:

$$\eta = \frac{c_{p1-2}\rho_s Q_s (T_2 - T_1)}{c_{p1-3}\rho_e Q_e (T_3 - T_1)} \tag{2}$$

where:

c_{p1-2}: mean specific heat capacity of the supply air at constant pressure, kJ/(kg·K)
c_{p1-3}: mean specific heat capacity of the extract air at constant pressure, kJ/(kg·K)
ρ_s: mean density of the supply air, kg/m³
ρ_e: mean density of the extract air, kg/m³
Q_s: volume flow rate of the supply air, m³/s
Q_e: volume flow rate of the extract air, m³/s
T_1: outdoor air temperature, K
T_2: supply air temperature, K
T_3: extract air temperature, K

When the specific heat capacities, air densities and volume flow rates of the supply and extract air streams are approximately equal, Eq. (2) simplifies to the conventional temperature effectiveness:

$$\eta = \frac{T_2 - T_1}{T_3 - T_1} \tag{3}$$

The temperature effectiveness is influenced by the inlet and outlet air temperatures, air humidity, air volume flow rates and the pressure losses associated with the filters and heat exchanger. In a RAHRS, it is also affected by the glycol solution flow rate and concentration, as well as by the thermal properties of the heat transfer fluid.

4.2 Uncertainty of the temperature effectiveness

For the first-series readings, an assumed independent temperature input of ΔT = 0.2 K per channel was propagated by root-sum-square combination of the sensitivity coefficients $c_i = \partial\eta/\partial T_i$:

$$\Delta\eta = \Delta T\sqrt{c_1^2 + c_2^2 + c_3^2} \tag{4}$$

An alternative component-level budget includes the residual after thermocouple comparison, logger resolution and reading stability, treated as rectangular distributions with half-widths of 0.1, 0.05 and 0.1 K, respectively [11, 12]. If the 0.3 K absolute offset is fully common to all channels, it cancels in Eq. (3) because the sensitivity coefficients sum to zero. The three independent components give $u(T)$ = 0.087 K.

The sensitivity coefficients of Eq. (3) are c_1 = -(1 - η)/(T_3 - T_1), c_2 = 1/(T_3 - T_1) and c_3 = -η/(T_3 - T_1). Thus:

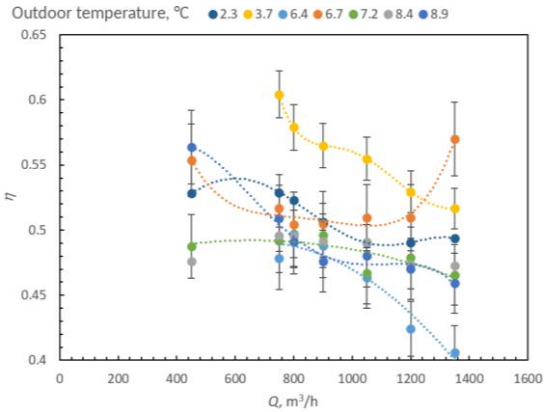
$$u(\eta) = \frac{u(T)\sqrt{(1-\eta)^2 + 1 + \eta^2}}{T_3 - T_1} \tag{5}$$

For $\eta \approx 0.5$ and $T_3 - T_1 = 16$ to 20 K, Eq. (5) gives u(η) = 0.0053 to 0.0067 and $U = 0.011$ to 0.013 ($k = 2$), or approximately 2.1% to 2.7% of η. A Monte Carlo simulation with 10^6 trials gave a coverage factor of 1.94 for a coverage probability of 95%, consistent with $k = 2$.

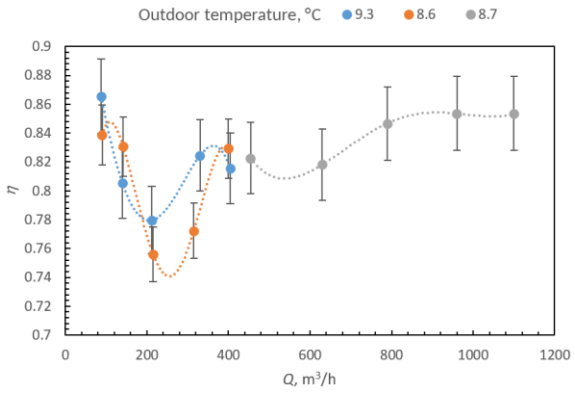
For the second series, each temperature reading was corrected for the indication error of its channel. The budget includes the calibration uncertainty from the certificate (standard uncertainty 0.05 K), a conservative residual of the interpolated correction (rectangular half-width 0.15 K), resolution (half-width 0.05 K) and stability (half-width 0.1 K). These give $u(T) \approx 0.12$ K. Channel errors were treated as uncorrelated; a common correlated component would partly cancel in Eq. (3). The resulting expanded uncertainty of η was 0.014 to 0.018 (k=2). These budgets include only temperature measurement effects. They exclude air-temperature non-uniformity across coil outlets, which would require cross-sectional traverses, and any bias from unequal air mass flow rates. The single-point measurements did not permit closure of the air-side energy balance.

5 Results

For the glycol RAHRS (Fig. 3a), the temperature effectiveness generally decreased as airflow increased from 450 to 1350 m³/h at outdoor temperatures of 2.3 to 8.9 °C. The highest observed value was 60% at 750 m³/h (mean T_1 = 3.7 °C). Across this airflow range, supply temperature T_2 fell by 1.3 to 2.4 K.



a)

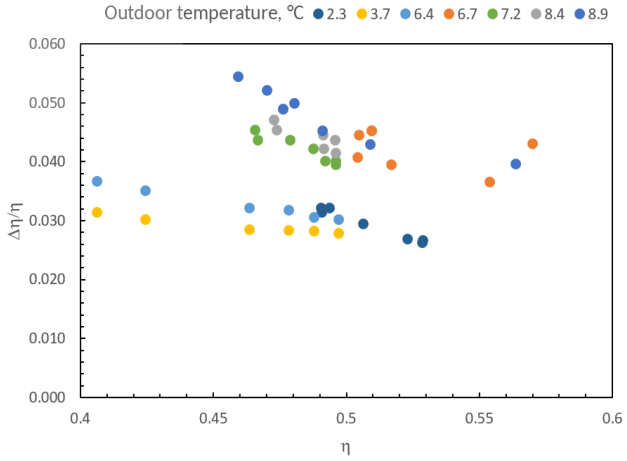


b)

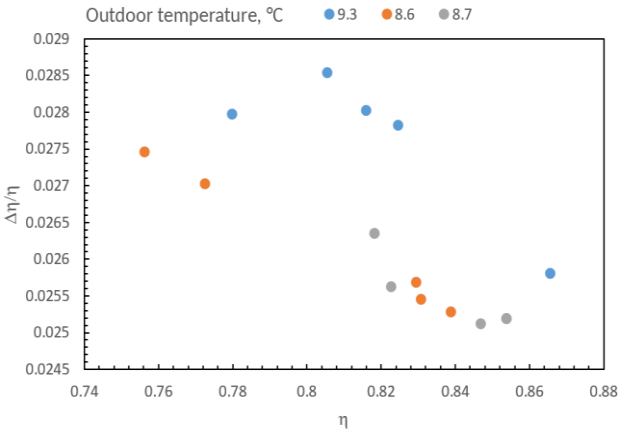
Fig. 3. Temperature effectiveness versus airflow rate at different outdoor-air temperatures: (a) glycol RAHRS; (b) cross-flow recuperator.

For the cross-flow recuperator (Fig. 3b), the 8.6 and 9.3 °C series were measured with HEPA filters at flows up to 400 m³/h, whereas the 8.7 °C series used a standard filter above 450 m³/h. The effectiveness peaked at about 87% near 90 m³/h, fell to approximately 76% near 200 m³/h, and then recovered to between 81% and 83% at higher HEPA-filter flows. With the standard filter, it increased gradually to about 85% at 1100 m³/h. The reported temperature change after installing HEPA filters was less than 1 K.

Figure 4 shows the relative combined standard uncertainty of the temperature effectiveness. For the cross-flow recuperator (Fig. 4b), it ranged from 2.5% to 2.9%. For the glycol RAHRS (Fig. 4a), it ranged from approximately 2.7% at $T_1 = 2.3$ °C to 5.4% at $T_1 = 8.9$ °C. The corresponding absolute combined standard uncertainties were 0.014 to 0.025.



a)



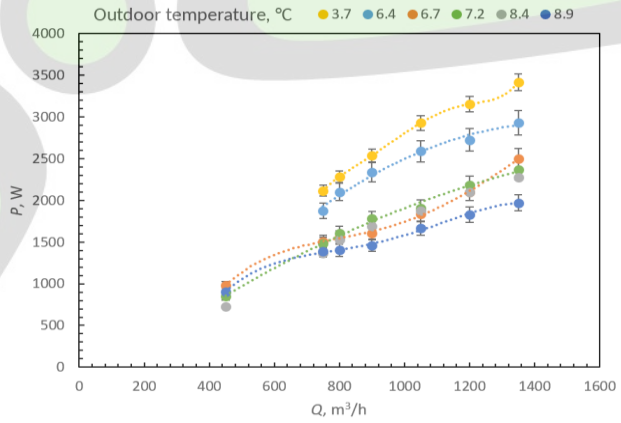
b)

Fig. 4. Relative combined standard uncertainty of the temperature effectiveness: (a) glycol RAHRS; (b) cross-flow recuperator.

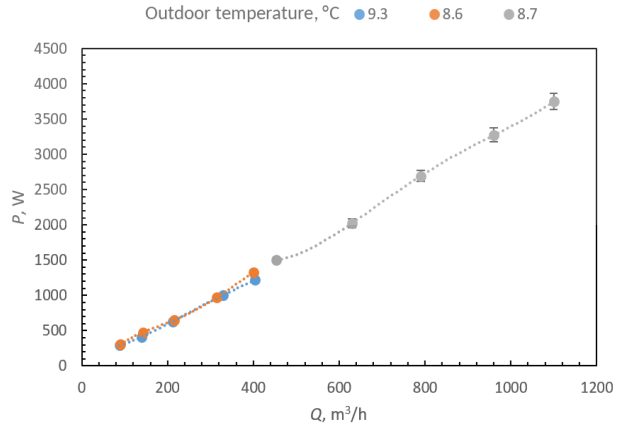
The heat transferred to the supply airstream (Fig. 5) was calculated as:

$$P = c_{p1-2}\rho_s Q_s (T_2 - T_1) \quad (6)$$

The heat transfer rate increased almost linearly with airflow in the cross-flow recuperator. In the glycol RAHRS, it was also higher at lower outdoor-air temperatures.



a)



b)

Fig. 5. Supply-air heat transfer rate versus airflow rate at different outdoor-air temperatures: (a) glycol RAHRS; (b) cross-flow recuperator.

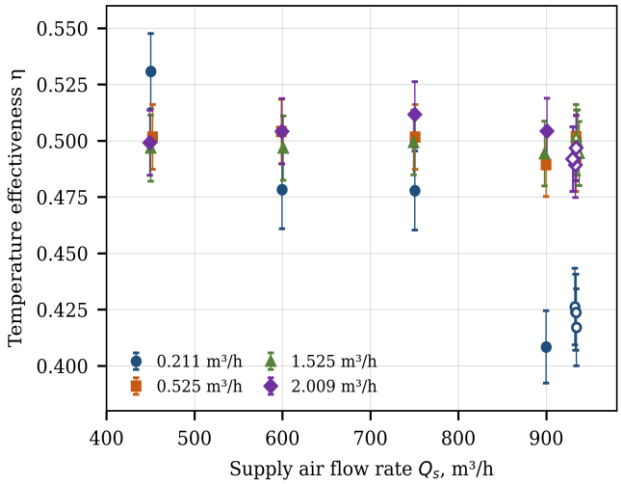


Fig. 6. Corrected temperature effectiveness in the second series versus supply airflow rate at four flow rates of the propylene glycol solution. Filled markers denote balanced airflows (fan settings 30% to 60%); open markers denote unbalanced airflows (70% to 100%). Error bars show expanded uncertainties (k = 2).

Figure 6 shows the corrected second-series temperature effectiveness at liquid flow rates of 0.211, 0.525, 1.525 and 2.009 m³/h and supply airflow rates of 449 to 938 m³/h. Values ranged from 0.408 to 0.531, with expanded uncertainties of 0.014 to 0.018. For liquid flows of at least 0.525 m³/h and balanced airflows (fan settings 30% to 60%), the effectiveness was 0.489 to 0.512 and changed little with airflow rate. At 0.211 m³/h, it fell from 0.531 at 450 m³/h to 0.408 at 901 m³/h as the air-side heat-capacity rate exceeded that of the liquid (212 W/K). At fan settings above 60%, extract airflow exceeded supply airflow by as much as 29% in three series; these points should therefore be interpreted as supply-air temperature ratios at unbalanced airflows rather than as balanced-flow effectiveness. Channel corrections lowered η by 0.027 on average, exceeding its expanded uncertainty.

6 Conclusions

The experimental investigation provided insights into the temperature effectiveness and heat transfer performance of a cross-flow recuperator and a glycol-based run-around heat recovery system (RAHRS), as well as the uncertainty associated with temperature measurements. The main findings can be summarised as follows:

- The cross-flow recuperator achieved high temperature effectiveness over the investigated airflow range. The effectiveness was approximately 87% at an airflow rate of 90 m³/h, decreased to about 76% at 200 m³/h, and subsequently increased to 81–83% at higher airflow rates with HEPA filters. With a standard filter, it reached approximately 85% at 1100 m³/h. The observed trends indicate that filter configuration and operating conditions should be considered when interpreting the results.
- The measured heat transfer rate in the glycol-based RAHRS ranged from approximately 730 W at an airflow rate of 450 m³/h under higher outdoor-air temperature conditions to 3417 W at 1350 m³/h and an outdoor-air temperature of approximately 4 °C.
- In the first test series, the glycol-based RAHRS achieved temperature effectiveness values of approximately 50–60% at airflow rates below 900 m³/h and 41–57% at 1350 m³/h. The effectiveness generally decreased with increasing airflow rate.
- The relative combined standard uncertainty of temperature effectiveness in the first test series ranged from approximately 2.5% to 5.4%, depending on the system and operating conditions. These values were determined using the conservative temperature measurement uncertainty assumption adopted for the first test series.
- In the second test series, correcting individual temperature-channel readings for their calibration errors reduced the calculated temperature effectiveness by an average of 0.027. This change exceeded the expanded uncertainty of the temperature effectiveness, demonstrating the importance of individual sensor calibration and correction in experimental assessments of heat recovery performance.
- For the propylene glycol-based RAHRS, the corrected temperature effectiveness ranged from 0.408 to 0.531, with expanded uncertainties of 0.014–0.018 (k = 2). Under balanced airflow conditions, the effectiveness remained relatively stable, at approximately 0.489–

0.512, for liquid flow rates of at least 0.525 m³/h. At the lowest investigated liquid flow rate of 0.211 m³/h, the effectiveness decreased with increasing airflow, indicating the influence of the liquid-side heat capacity rate on system performance.

References

1. M. Mahmoud, P. Filipsson, S. Brunninge, J.-O. Dalenbäck, Flow rate optimization in run-around heat recovery systems. Appl. Therm. Eng. **200**, 117599 (2022). https://doi.org/10.1016/j.applthermaleng.2021.117599
2. H. Jouhara, N. Khordehgah, S. Almahmoud, B. Delpech, A. Chauhan, S.A. Tassou, Waste heat recovery technologies and applications. Therm. Sci. Eng. Prog. **6**, 268-289 (2018). https://doi.org/10.1016/j.tsep.2018.04.017
3. T. Lu, X. Lü, C. Kibert, J. Puttonen, The application of linear regression and the power law relationship of air-side heat transfer with field measurements to model the performance of run-around heat recovery systems. Energy Build. **110**, 453-467 (2016). https://doi.org/10.1016/j.enbuild.2015.10.028
4. J. Wallin, H. Madani, J. Claesson, Run-around coil ventilation heat recovery system: A comparative study between different system configurations. Appl. Energy **90**, 258-265 (2012). https://doi.org/10.1016/j.apenergy.2011.05.012
5. A. Vali, C.J. Simonson, R.W. Besant, G. Mahmood, Numerical model and effectiveness correlations for a run-around heat recovery system with combined counter and cross flow exchangers. Int. J. Heat Mass Transf. **52**, 5827-5840 (2009). https://doi.org/10.1016/j.ijheatmasstransfer.2009.07.020
6. C. Haglund Stignor, B. Sundén, P. Fahlén, Liquid side heat transfer and pressure drop in finned-tube cooling-coils operated with secondary refrigerants. Int. J. Refrig. **30**, 1278-1289 (2007). https://doi.org/10.1016/j.ijrefrig.2007.02.007
7. I. Balen, P. Donjerković, I. Galaso, Analysis of the coil energy recovery loop system. Int. J. Energy Res. **27**, 363-376 (2003). https://doi.org/10.1002/er.881
8. W. Li, X. Li, Y. Gao, W. Shi, Thermo-economic evaluation for energy retrofitting building ventilation system based on run-around heat recovery system. Energy **260**, 125041 (2022). https://doi.org/10.1016/j.energy.2022.125041
9. J. Müller, Determining the uncertainty in testing the air conditioning systems [in Polish]. Tech. Trans. Environ. Eng., 4-Ś/2012, issue 28 (2012).
10. EN 308:2022, Heat exchangers. Test procedures for establishing performance of air-to-air heat recovery components (CEN, 2022).
11. European co-operation for Accreditation, EA-4/02 M:2022, Evaluation of the Uncertainty of Measurement in Calibration (2022).
12. JCGM 100:2008, Evaluation of Measurement Data. Guide to the Expression of Uncertainty in Measurement (BIPM, 2008). https://doi.org/10.59161/JCGM100-2008E

Effect of mass flow rate on the thermal behaviour of Thermasolv IM6 in a heated rectangular minichannel

Magdalena Piasecka[1*], *Mirosław* Grabowski[2], and *Artur* Piasecki[3]

[1] Faculty of Mechatronics and Mechanical Engineering, Kielce University of Technology, Al. 1000-lecia P.P. 7, 25-314 Kielce, Poland
[2] Faculty of Civil Engineering, Mechanics and Petrochemistry, Warsaw University of Technology, Łukasiewicza 17 Str., 09-400 Płock, Poland
[3] Faculty of Environmental Engineering, Geomatics and Renewable Energy, Kielce University of Technology, Al. 1000-lecia P.P. 7, 25-314 Kielce, Poland

Abstract. The thermal response of Thermasolv IM6 was investigated in a 1.5 mm × 4 mm × 180 mm rectangular minichannel heated through a copper block. Twelve representative quasi-steady points from the increasing-flow branches of two runs at approximately constant electrical powers of 14.77 and 16.31 W were analysed. Over the selected flow ranges, the fluid-temperature rise decreased from 7.6 to 1.9 K and from 7.0 to 3.0 K, respectively. The mean temperature recorded by three thermocouples embedded in the copper block varied by only approximately 0.2 and 0.1 K, respectively. A reduced energy-balance approach was applied to interpret the experimental results, taking into account the distinction between electrical power input and heat transferred to the fluid. The results showed that the fluid-temperature rise was considerably more sensitive to changes in mass flow rate than the mean temperature measured within the copper block.

1 Introduction

Heat transfer in minichannels is governed by fluid transport, conduction in the heated wall and the thermal boundary conditions of the test module. In a copper-block-heated configuration, the fluid temperature response also depends on energy redistribution in the solid. The influence of mass flow rate was therefore examined using fluid and copper-block temperatures measured under approximately constant electrical heating.

Previous experimental and numerical investigations provided a basis for the present study. Piasecki et al. [1] investigated single-phase heat transfer in a rectangular minichannel of 1 × 4 × 180 mm using HFE-73DE as the working fluid. A three-dimensional conjugate heat transfer model was also developed to analyse the thermal performance of selected HFE-73DE/ethyl acetate mixtures. The experimental module was based on a similar concept of asymmetrical heating in a narrow rectangular flow passage, although its geometry differed from that used in the present experiments.

Grabowski et al. [2] investigated heat transfer in an asymmetrically heated minichannel by combining infrared thermography with numerical modelling of temperature fields. Inverse heat conduction problems were solved to determine temperature distributions and local heat transfer conditions at the heater–fluid interface. Both studies demonstrated the importance of heat conduction in the heated solid for interpreting experimental temperature measurements. The related experimental configurations and modelling approaches provided a methodological background for the present investigation of Thermasolv IM6.

The selection and assessment of heat-transfer fluids were also addressed by Piasecki and Piasecka [3], who compared single-phase heat-transfer correlations for HFE/ethyl acetate mixtures using thermophysical-property data. In earlier investigations involving FC-72, Maciejewska et al. [4] compared Trefftz-based finite-element calculations with the ADINA software for determining local heat transfer coefficients. A subsequent time-dependent study [5] employed a Trefftz-type finite-element formulation to analyse heat transfer and flow instabilities during the onset of flow boiling. Unlike these numerical reconstruction approaches, the present study focuses on directly measured fluid and copper-block temperatures, supported by a reduced energy-balance interpretation. Related heat-transfer enhancement research has considered laser-structured surfaces under pool-boiling conditions [6] and hybrid water/Al2O3–SiO2 nanofluids in heat exchangers [7]. These studies concern different thermal configurations and are cited as methodological and application context, rather than as directly comparable IM6 data.

Thermasolv IM6 is a dielectric heat-transfer fluid with a normal boiling point of approximately 47 °C [8]. The combination of a relatively low boiling point, indirect heating through copper and a narrow flow passage made the thermal response to changes in flow rate of particular interest.

* Corresponding author: Magdalena Piasecka, tmpmj@tu.kielce.pl

The physical location of temperature sensors is important when discussing minichannel heat transfer. Piasecka et al. [9] analysed flow-boiling measurements with particular attention to temperature uncertainty and its effect on heat-transfer calculations. In a complementary experimental-numerical study, Pawińska et al. [10] examined flow boiling in a five-minichannel configuration using a combination of Trefftz functions and computational modelling. Such approaches can provide information on local thermal conditions, but require additional assumptions and boundary data. In contrast, the present work does not attempt to reconstruct the fluid-wall interface temperature or evaluate local heat transfer coefficients from temperatures measured inside the copper block.

Test-module design and thermal boundary conditions also affect the interpretation of results. Piasecki et al. [11] addressed the selection of geometric and operating features of compact minichannel heat exchangers using Quality Function Deployment. Although their objective differed from that of the present experiments, the analysis illustrates that the choice of channel arrangement, heating surface and operating conditions cannot be separated from the intended thermal performance. The copper-block-heated module used here provides a conductive and heat-storing solid structure, but its measured internal temperature is not equivalent to a prescribed uniform wall-temperature boundary condition.

The importance of documenting experimental context was further demonstrated by Piasecka and Piasecki [12], who integrated measurements from multiple rectangular-minichannel campaigns into a unified database and assessed the feasibility of group-aware machine learning. Their analysis highlighted differences between experimental configurations and the need to preserve information on fluid properties, heating conditions and measurement quality to ensure reliable interpretation and comparison of results.

Building on this experience, the authors are currently expanding the experimental database to include a wider range of working fluids, minichannel configurations and operating conditions. Particular attention is given to the consistency of experimental records and the comparability of thermal measurements across different test conditions. The resulting dataset is intended to support the development and validation of a generalised dimensionless heat-transfer correlation.

The present study investigates the effect of increasing mass flow rate on the fluid and copper-block temperatures at two approximately constant electrical-power levels. Twelve representative quasi-steady operating points are analysed, and a reduced energy-balance description is used to interpret the measured temperature trends.

The experimental data presented here were obtained at the Płock Branch of Warsaw University of Technology, Poland. These measurements constitute an additional contribution to the broader research programme, in which experimental results from the Płock facility and Kielce University of Technology are intended to be integrated into the developing database.

2 Experimental setup and data selection

The experiments were conducted at the Warsaw University of Technology in Płock, Poland, using a closed-loop experimental facility equipped with a circulation pump, flow-control devices, an electrically heated test section, and a data acquisition system. The experimental facility is presented in Fig. 1, while its schematic diagram is shown in Fig. 2. The measurement system enabled simultaneous recording of fluid temperatures, mass flow rate, pressure, and electrical parameters of the heating system. The operating conditions were controlled by adjusting the mass flow rate and the electrical power supplied to the heating section.

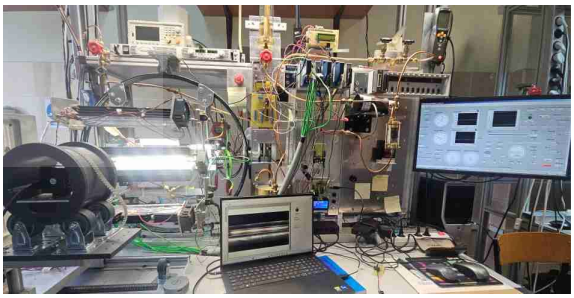


Fig. 1. Photo of the experimental setup.

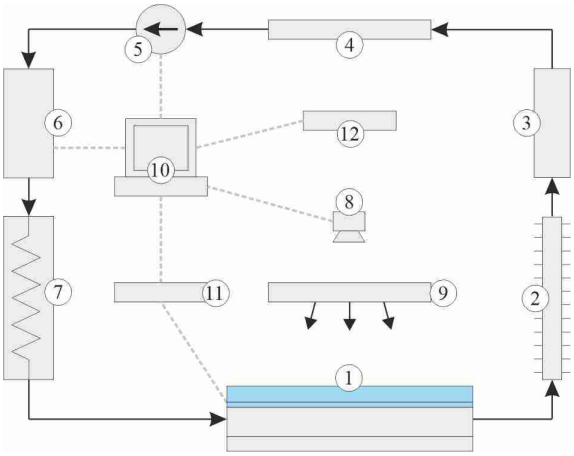


Fig. 2. Schematic diagram of the experimental test facility: 1 – measurement module with a minichannel; 2 – cooler; 3 – rotameter; 4 – filter; 5 – pump; 6 – Coriolis mass flow meter; 7 – preheater; 8 – high-speed camera; 9 – LED illuminator; 10 – computer with LabVIEW software; 11 – facility control unit; 12 – DC power supply.

The essential element of the experimental facility was the test module containing a rectangular minichannel with a depth of 1.5 mm, a width of 4 mm and a length of 180 mm. One of the channel walls was formed by a copper block, while the opposite wall was closed by a glass cover. The copper block was heated from the side opposite to the minichannel by four electrical resistance heaters arranged along the flow direction. Heat was transferred from the heaters through the copper block to the working fluid flowing through the minichannel. The construction of the test section and the arrangement of its main components are illustrated schematically in Fig. 3.

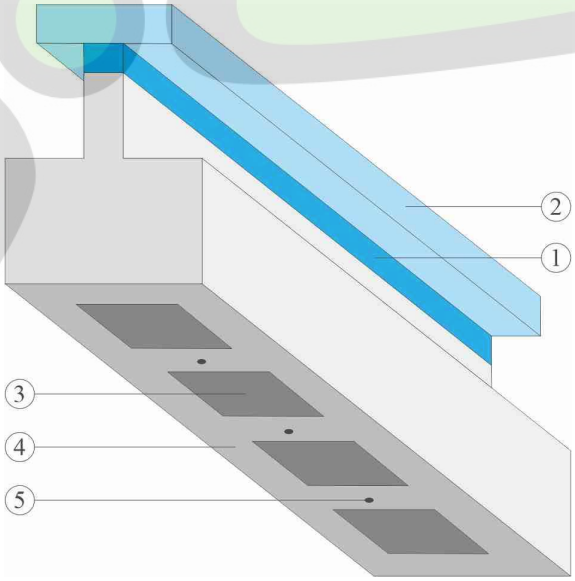


Fig. 3. Schematic view of the test section, 1 – minichannel, 2 – glass plate, 3 – resistance heater, 4 – copper block, 5 – thermocouple.

The temperature distribution within the copper block was monitored using three thermocouples embedded at different axial positions along the heated section. These measurements provided information about the thermal response of the copper block under varying flow conditions. The arithmetic mean of the three recorded temperatures was calculated and used to characterise the overall thermal behaviour of the heated block. Since the thermocouples were located inside the copper, their readings represented temperatures within the solid rather than the local temperature of the channel wall in direct contact with the fluid. Thermasolv IM6 (Inventec Performance Chemicals, France) was used as the working fluid. Fluid temperatures at the inlet and outlet, mass flow rate, pressure signals, electrical current and voltage were recorded. The mass flow rate was measured directly using a Coriolis flowmeter, while the corresponding volumetric flow rate was calculated using a reference density of 1600 kg m^{-3} at 20 °C, as specified in the manufacturer's data sheet [8].

The mass flow rate was successively increased while the electrical heating power was kept approximately constant. Two power levels, 14.77 and 16.31 W, were investigated.

For each flow setting, the median of the final 90 recordings was calculated. Twelve representative points, six at each power level, were selected from the increasing-flow branches on the basis of temperature and flow stability.

The selected mass-flow ranges were 37.4–68.6 g min^{-1} at 14.77 W and 45.7–74.0 g min^{-1} at 16.31 W. The inlet fluid temperature remained close to 31 °C. Differences in the flow and pressure conditions between the two power series were considered when interpreting the results.

The reported flow rates refer to the entire, single-minichannel test section. The twelve points were selected for comparison at approximately fixed electrical input, not to establish a complete flow-boiling characteristic or an operating-regime map. The final-record median reduces the influence of short isolated fluctuations, but does not itself prove that the thermal energy stored in the copper block remained constant throughout a measurement stage. Accordingly, the changes in the recorded copper temperatures are considered together with the inlet and outlet fluid temperatures, rather than being used as an independent measure of the heat flux at the copper–fluid interface.

3 Reduced calculation procedure

3.1 Geometry and measured quantities

Let a and b denote the channel depth and width, respectively. For the present rectangular cross-section, the flow area A_c and hydraulic diameter D_h are

$$A_c = ab = 6.00\times10^{-6}\ \mathrm{m}^2 \quad (1)$$

$$D_h = \frac{4A_c}{P_w} = \frac{2ab}{a+b} = 2.18\ \mathrm{mm} \quad (2)$$

where P_w is the full wetted perimeter. The hydraulic diameter in Eq. (2) is based on all four sides of the channel, irrespective of which wall is heated. The axial coordinate z is measured from the inlet of the heated section, whose length is $L = 0.180$ m.

The mass flow rate and mass flux are defined by

$$\dot{m} = \rho_{ref}\dot{V}, \qquad G = \frac{\dot{m}}{A_c} \quad (3)$$

Here $\dot{V}$ is the volumetric flow rate and ρ_{ref} is the reference density. The selected ranges corresponded to mass fluxes of approximately 104–191 and 127–206 kg m^{-2} s^{-1}, respectively. Mass flow rate was used as the independent variable in Figs. 4 and 5.

The electrical power P_{el} supplied to the heaters was calculated from the recorded voltage U and current I of the heater supply:

$$P_{el} = UI \quad (4)$$

Electrical power represented the energy supplied to the heaters and was distinguished from the thermal power transferred through the copper–fluid interface. The fluid temperature rise and the mean copper-block temperature were calculated as follows

$$\Delta T_f = T_{out} - T_{in} \quad (5)$$

$$T_{Cu,mean} = \frac{T_{Cu,1} + T_{Cu,2} + T_{Cu,3}}{3} \quad (6)$$

The three temperatures in Eq. (6) were recorded by thermocouples embedded at different axial positions. Their arithmetic mean characterised the response of the copper block.

3.2 Fluid and module energy balances

For a quasi-steady one-dimensional fluid description, neglecting axial conduction in the fluid and changes in kinetic and potential energy, the axial energy balance can be written as

$$\dot{m}\frac{dh_b}{dz} = q'_f(z) \quad (7)$$

The bulk specific enthalpy is denoted by h_b, and q'_f is the net heat supplied to the fluid per unit channel length, in W m^{-1}. This term represents the integral of the interfacial heat flux around the cross-section. It need not be uniform along the channel. Integration over the heated length gives

$$\dot{Q}_f = \int_0^L q'_f(z)\,dz \quad (8)$$

$$\dot{Q}_f = \dot{m}(h_{out} - h_{in}) \quad (9)$$

Integration of the fluid energy balance related the change in specific enthalpy to the net interfacial heat transfer, without prescribing its axial distribution.

If the inlet and outlet fluid can both be represented as liquid, pressure effects on liquid enthalpy are negligible and a representative specific heat c_p is applicable, Eq. (9) reduces to

$$\dot{Q}_f \simeq \dot{m} c_p \Delta T_f \quad (10)$$

It should be underlined that formula (10) was used as a liquid-only reference for interpreting the measured fluid temperature rise. Local subcooled boiling at the heated surface could not be ruled out, but its contribution to heat transfer was not quantified.

For the liquid-only reference balance, a specific heat of 1044 J kg^{-1} K^{-1} at 25 °C was taken from the manufacturer's data [8]. This approximation required the measured inlet and outlet temperatures to represent the corresponding bulk-fluid states.

For a control volume enclosing the heaters, copper block and fluid within the module, an approximate overall balance is

$$P_{el} = \dot{Q}_{adv} + \dot{Q}_{loss} + \frac{dE_{mod}}{dt} \quad (11)$$

Here, $\dot{Q}_{adv}$ represents the net enthalpy flow rate between the outlet and inlet of the test section, $\dot{Q}_{loss}$ denotes the heat losses through the external boundaries of the module, and $\frac{dE_{mod}}{dt}$ accounts for the rate of energy accumulation in both the solid components and the working fluid. Although the test module was thermally insulated, heat losses through its external boundaries, including supports and connections, were not determined experimentally. Therefore, these losses were retained as an unknown contribution to the overall energy balance. Changes in kinetic and potential energy, as well as other work interactions, were neglected.

Under quasi-steady fluid-flow conditions, the net enthalpy flow rate $\dot{Q}_f$ was approximately equal to the heat transferred to the fluid. The energy-storage term could be neglected only when the thermal state of the entire module was sufficiently stable.

3.3 Reference interpretation

Combining the liquid-only reduction with the quasi-steady fluid approximation gives the qualitative relation

$$\Delta T_f \simeq \frac{\dot{Q}_f}{\dot{m} c_p} \quad (12)$$

Under the reference assumption of constant heat transferred to the liquid and approximately constant specific heat, Eq. (12) predicted an inverse relationship between fluid-temperature rise and mass flow rate. This dependence was used to interpret the experimental trends. In the actual module, the heat received by the fluid could differ from the electrical input because of energy transfer through the external boundaries and transient energy storage.

As heat losses and energy accumulation were not independently quantified, the reference energy balance was applied solely as a qualitative basis for interpreting the measured temperature trends, rather than as a fitted temperature-prediction model.

This distinction is particularly relevant for a test module heated through a massive copper component. The electrical input, the energy entering the fluid and the thermal energy temporarily stored in the block are different quantities. Even when the imposed electrical power is nearly constant, the thermal conditions at the copper–fluid boundary may change with the coolant flow rate. The reference relation is therefore used as a comparison of expected temperature-rise trends under clearly stated assumptions, without assigning the observed discrepancy to a particular mechanism or quantifying unmeasured losses.

4 Results and discussion

4.1 Fluid temperature response

Fluid inlet and outlet temperatures were compared as functions of mass flow rate in Fig. 4. At 14.77 W, increasing the flow rate from 37.4 to 68.6 g min^{-1} reduced the outlet temperature from 38.8 to 33.1 °C. The corresponding fluid-temperature rise decreased from 7.6 to 1.9 K, or by approximately 75%, whereas the inlet temperature remained close to 31 °C.

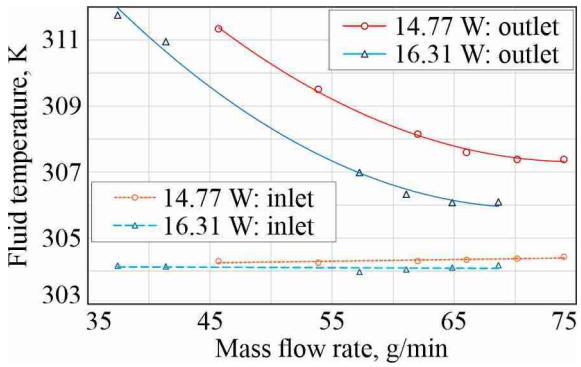


Fig. 4. Inlet and outlet temperatures of Thermasolv IM6 versus mass flow rate for two electrical-power settings.

At 16.31 W, increasing the flow rate from 45.7 to 74.0 g min^{-1} reduced the outlet temperature from 38.3 to 34.4 °C. The fluid-temperature rise decreased from 7.0 to 3.0 K, corresponding to approximately 57.1%. The inlet temperature varied within approximately 0.2 K throughout this series.

As shown in Fig. 4, the decrease in outlet temperature became less pronounced at the highest mass flow rates, approaching 33.1 °C and 34.4 °C for electrical powers of 14.77 and 16.31 W, respectively.

When analysing the results using Eq. (12), the reductions in temperature rise were greater than those

expected solely from the increase in mass flow rate under a constant liquid heat-input assumption. The measured decreases were approximately 75% and 57.1%, compared with corresponding reference reductions of about 45% and 38%. This difference indicated that the constant-fluid-heat-input assumption did not fully describe the measured thermal response.

Possible contributions included a change in the distribution of supplied energy, transient thermal behaviour of the module and the representation of the bulk fluid state by the measured temperatures. These factors were considered in the interpretation of the results.

4.2 Comparison of the electrical-power settings

The electrical power increased by approximately 10.4% between the two investigated series. In the overlapping flow-rate interval, the higher-power series generally produced higher outlet temperatures (Fig. 4). For example, at 61.1 and 62.0 g min^{-1}, the outlet temperatures were 33.3 and 35.2 °C, respectively, with temperature rises of 2.3 and 3.9 K.

The difference in outlet temperature was approximately 1.9 K, while the difference in temperature rise was 1.6 K. At these nearly matched flow rates, the higher-power series exhibited a greater fluid-temperature rise, although the flow rate, inlet temperature and pressure were not identical between the two series.

4.3 Copper-block temperatures and possible boiling

Figure 5 compares the mean temperatures measured by three thermocouples embedded in the copper block. The recorded mean temperatures ranged from 53.4 to 53.6 °C at 14.77 W and from 54.4 to 54.5 °C at 16.31 W, corresponding to variations of approximately 0.2 and 0.1 K, respectively.

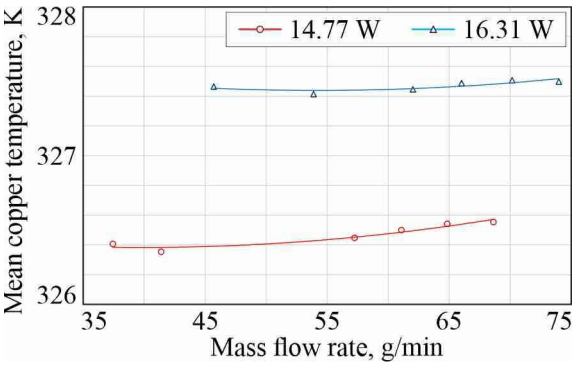


Fig. 5. Mean temperature recorded by three thermocouples embedded in the copper block versus mass flow rate.

When comparing the results at similar mass flow rates of approximately 61–62 g min^{-1}, the mean copper-block temperatures were 53.5 and 54.5 °C at the lower and higher electrical powers, respectively, indicating an increase of approximately 1 K. Within each series, the mean copper-block temperature varied considerably less than the outlet-fluid temperature. At 14.77 W, a slight increase in the mean copper-block temperature was observed over the selected mass flow rate range. However, these small temperature variations should be interpreted with caution, as a complete measurement-uncertainty assessment was not performed.

Conduction in the copper block and its thermal inertia may have moderated the measured temperature response to the changing flow conditions. The weak variation in the mean of the embedded thermocouple readings therefore described the behaviour of the block rather than a uniform wall-temperature boundary condition.

The two temperature responses should also be compared with regard to their measurement locations. The inlet and outlet thermocouples characterize the bulk fluid at the ends of the test section, whereas the copper thermocouples represent three selected positions within the heated solid. The latter values can therefore indicate the overall thermal behaviour of the block, but they cannot determine the axial distribution of the local surface temperature or identify the onset of boiling without additional evidence. The present comparison deliberately retains this distinction and avoids using the small differences in the mean copper temperature as a quantitative measure of thermal resistance.

The measured fluid temperatures remained below the normal boiling temperature of IM6, whereas the copper-block temperatures were higher. This separation suggested that local subcooled boiling might have been possible, depending on the actual wall temperature and saturation pressure within the channel.

5 Conclusions

The effect of mass flow rate on the thermal response of Thermasolv IM6 was investigated at two approximately constant electrical powers, 14.77 and 16.31 W. Increasing the mass flow rate reduced the fluid-temperature rise from 7.6 to 1.9 K and from 7.0 to 3.0 K, respectively. At the largest flow rates, the outlet-temperature response became less pronounced.

The mean temperature recorded in the copper block changed by approximately 0.2 and 0.1 K within the two series. A higher electrical-power input was accompanied by an approximately 1 K higher mean copper temperature, whereas the outlet-fluid temperature showed much greater sensitivity to changes in mass flow rate.

Comparison with the reduced liquid energy-balance relation showed that the observed temperature-rise reductions were greater than predicted for a constant heat input to the fluid. The results highlighted the importance of accounting for energy partition within a copper-block-heated minichannel and provided a basis for further quantitative thermal analysis.

In future joint work, experimental data from the Płock Branch of Warsaw University of Technology and from Kielce University of Technology will be combined to develop empirical heat transfer correlations for minichannels.

Nomenclature

a - channel depth (m)
A_c - flow area (m²),
b - channel width (m)
c_p - representative specific heat capacity (J kg⁻¹ K⁻¹)
D_h - hydraulic diameter (m)
E_{mod} - energy stored in the module (J)
G - mass flux (kg m⁻² s⁻¹)
h_b - bulk specific enthalpy (J kg⁻¹)
h_{in} - bulk inlet specific enthalpy (J kg⁻¹)
h_{out} - bulk outlet specific enthalpy (J kg⁻¹)
I - current supplied to the heater (A)
L - heated channel length (m)
$\dot{m}$ - mass flow rate (kg s⁻¹)
P_{el} - electrical heating power (W)
P_w - wetted perimeter (m),
Q_{adv} - net enthalpy flow rate between the outlet and inlet of the test section (W)
Q_f - net heat transferred to the fluid (W)
Q_{loss} - heat loss through the external boundaries of the module (W)
q'_f - heat supplied to fluid per unit channel length (W m⁻¹)
$T_{Cu,i}$ - copper thermocouple temperature (°C, K)
$T_{Cu,mean}$ - arithmetic mean of copper thermocouple temperature (°C, K)
T_{in} - fluid inlet temperature (°C, K)
T_{out} - fluid outlet temperature (°C, K)
U - voltage drop across the heater (V)
$\dot{V}$ - volumetric flow rate (m³ s⁻¹)
z - axial coordinate measured from the inlet of the heated section (m)
Greek
ΔT_f - fluid temperature difference (K)
ρ_{ref} - reference fluid density (kg m⁻³)

This research was partially funded by the National Science Centre, Poland, grant no. UMO-2025/57/B/ST8/00907.

For the purpose of Open Access, the authors have applied a CC BY public copyright licence to the Author Accepted Manuscript (AAM) version arising from this submission.

The experimental data supporting this study are stored in the PRACE-LAB data-storage environment at Kielce University of Technology and may be made available by the corresponding author upon reasonable request, subject to applicable institutional data-access policies.

During the preparation of this manuscript, the authors used ChatGPT (OpenAI, GPT-6) to assist with language editing, manuscript organisation and consistency checks. All scientific content, interpretations and conclusions were reviewed and approved by the authors, who take full responsibility for the final manuscript.

References

1. A. Piasecki, B. Maciejewska, M. Piasecka, M. Grabowski, P. Grabowski, Evaluation of HFE-73DE/Ethyl Acetate Mixtures for Use in Minichannel Heat Exchangers, Energies **19**, 110 (2026). https://doi.org/10.3390/en19010110
2. M. Grabowski, M.E. Poniewski, S. Hożejowska, A. Pawińska, Numerical Simulation of the Temperature Fields in a Single-Phase Flow in an Asymmetrically Heated Minichannel, J. Eng. Phys. Thermophys. **93**, 355–363 (2020). https://doi.org/10.1007/s10891-020-02128-1
3. A. Piasecki, M. Piasecka, Correlation-Based Single-Phase Heat Transfer Assessment of Binary HFE/Ethyl Acetate Mixtures in Minichannels, Energies **19**, 2291 (2026). https://doi.org/10.3390/en19102291
4. B. Maciejewska, P. Łabędzki, A. Piasecki, M. Piasecka, Comparison of FEM calculated heat transfer coefficient in a minichannel using two approaches: Trefftz base functions and ADINA software, EPJ Web Conf. **143**, 02070 (2017). https://doi.org/10.1051/epjconf/201714302070
5. B. Maciejewska, M. Piasecka, A. Piasecki, The heat transfer and instabilities results during the onset of flow boiling in minichannels, E3S Web Conf. **128**, 01016 (2019). https://doi.org/10.1051/e3sconf/201912801016
6. Ł. J. Orman, N. Radek, J. Pietraszek, J. Wojtkowiak, M. Szczepaniak, Laser Treatment of Surfaces for Pool Boiling Heat Transfer Enhancement, Materials **16**, 1365 (2023). https://doi.org/10.3390/ma16041365
7. S. Mukherjee, S. Wciślik, S. Ebrahim, P.C. Mishra, N. Ali, Enhancing Cooling Performance of a Heat Exchanger Driven by Water/Alumina-Silica Hybrid Nanofluid: Experimental Results, J. Enhanc. Heat Transf. **31**, 21–47 (2024). https://doi.org/10.1615/JEnhHeatTransf.2023048391
8. Inventec Performance Chemicals, THERMASOLV IM6, product data sheet, PDS2025-06v1. https://www.inventec.dehon.com/wp-content/uploads/2023/09/PDS-Thermasolv-IM6-EN-1.pdf (accessed 1 October 2026).
9. M. Piasecka, B. Maciejewska, D. Michalski, N. Dadas, A. Piasecki, Investigations of Flow Boiling in Mini-Channels: Heat Transfer Calculations with Temperature Uncertainty Analyses, Energies **17**, 791 (2024). https://doi.org/10.3390/en17040791.
10. A. Pawińska, A. Piasecki, N. Dadas, S. Hożejowska, M. Piasecka, Homotopy Perturbation Method with Trefftz Functions and Simcenter STAR-CCM+ Used for the Analysis of Flow Boiling Heat Transfer, Acta Mech. Autom. **18**, 233–243 (2024). https://doi.org/10.2478/ama-2024-0027.
11. A. Piasecki, S. Hożejowska, A. Masternak-Janus, M. Piasecka, Using Quality Function Deployment to Assess the Efficiency of Mini-Channel Heat Exchangers, Energies **17**, 2436 (2024). https://doi.org/10.3390/en17102436.
12. M. Piasecka, A. Piasecki, A Unified Experimental Database and Group-Aware Pilot Machine Learning for Flow Boiling in Rectangular Minichannels, Energies **19**, 4483 (2026). https://doi.org/10.3390/en19194483.

Proposed methodology for electrical and optical diagnostics of gas–liquid flows in pipes and minichannels

Magdalena Piasecka[1*] and *Artur* Piasecki[2]

[1]Faculty of Mechatronics and Mechanical Engineering, Kielce University of Technology, Al. 1000-lecia P.P. 7, 25-314 Kielce, Poland
[2]Faculty of Environmental Engineering, Geomatics and Renewable Energy, Kielce University of Technology, Al. 1000-lecia P.P. 7, 25-314 Kielce, Poland

Abstract. This paper proposes a methodological framework for electrical and optical diagnostics of gas–liquid flows in circular pipes and minichannels. The approach combines wire-mesh sensing, high-speed imaging and synchronised acquisition to compare phase-distribution indicators and flow-structure descriptors across channel scales. Particular attention is given to measurement resolution, sensor-induced disturbances and differences between electrical and optical observables. CFD and machine learning are proposed to support physical interpretation and descriptor analysis. The framework establishes a basis for future experimental investigations, including calibration, uncertainty assessment and validation of cross-scale descriptor transferability.

Keywords: two-phase flow; minichannels; wire-mesh sensors; optical diagnostics; cross-scale analysis; machine learning

1 Introduction

The investigation of gas–liquid flow structures requires information on phase distribution and its variation in time and along the channel. Wire-mesh sensors provide spatially resolved electrical signals associated with the distribution of the phases. Conductivity-based wire-mesh measurements were introduced by Prasser et al. [1], while da Silva et al. [2] developed a capacitance-based approach. These principles depend on different electrical properties of the fluids and require separate calibration procedures.

Channel dimensions also affect the interpretation of flow structures. Experiments in small channels have addressed bubble transport, slip and the influence of wall wetting [3]. In conventional pipes, spatially resolved gas-fraction measurements have been used to investigate axial flow development and bubble-size distributions [4]. These studies motivate a comparison of measurable characteristics across scales, but do not establish that similarly named flow patterns are physically equivalent.

Data-driven classification provides an additional means of analysing time-dependent measurements. Ambrosio et al. [5] classified flow patterns using wire-mesh void-fraction time series. Feng et al. [6] used microwave transmission through photonic crystals and deep learning to characterise multiphase flows, rather than wire-mesh measurements. Khandelwal et al. [7] developed neural-network-based flow-regime classifiers for narrow rectangular channels and a round pipe. These published studies provide methodological context but do not validate the proposed minichannel diagnostics or establish cross-scale transferability.

The aim of this paper is to establish a unified experimental and analytical framework for investigating gas–liquid flows at two channel scales. The proposed research is planned to be conducted at Kielce University of Technology. The methodological contribution focuses on defining comparable measurement observables, identifying measurement limitations, and establishing procedures for assessing the transferability of flow descriptors between the two scales. Since the minichannel sensor has not yet been constructed and the proposed framework has not been experimentally validated, the study is presented as a methodological proposal rather than a validated experimental approach.

2 Motivation for a multi-scale approach

Reducing the channel hydraulic diameter changes the relative importance of gravitational, inertial, viscous and surface-tension forces in gas-liquid flows. At the same time, the relative dimensions of sensing electrodes and the spatial sensitivity of electrical measurements may change. Consequently, differences observed between channel scales may result from changes in flow

* Corresponding author: Magdalena Piasecka, tmpmj@tu.kielce.pl

behaviour, measurement characteristics or their combined influence. Distinguishing between these effects is essential for a meaningful comparison.

The central scientific question is how channel scale, orientation relative to gravity and the presence of selected conductive elements influence gas–liquid flow structures and their dynamics, and to what extent these characteristics can be identified using electrical and optical measurements. The proposed methodology focuses on defining comparable phase-distribution indicators and temporal descriptors while accounting for the limitations of each measurement technique.

Figure 1 illustrates the proposed experimental and analytical framework for investigations at two channel scales, planned at Kielce University of Technology. The approach includes common measurement principles, scale-specific sensor configurations, data processing and comparative analysis. The transferability of selected descriptors between scales will be treated as a research question requiring experimental verification.

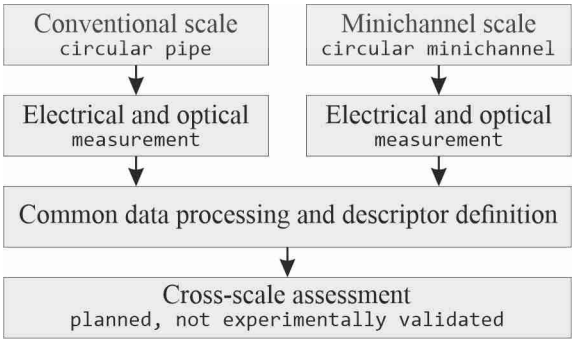


Fig. 1. Proposed experimental and analytical framework for gas–liquid flow investigations at two channel scales at Kielce University of Technology. The indicated relationships represent planned measurements, comparative analysis and transferability tests rather than experimentally validated results.

Where feasible, the same working fluid or gas–liquid system and comparable operating conditions should be used at both scales. Differences in channel orientation, inlet mixing, surface conditions, electrode geometry and measurement location must be documented. Where these factors cannot be matched, the results will represent a comparison of two experimental configurations rather than the isolated effect of channel diameter. Conventional-scale measurements may provide a comparative dataset, but they cannot be regarded as an absolute reference for minichannel measurements.

The proposed framework remains methodological. In particular, the minichannel sensor has not yet been constructed, and neither the complete measurement procedure nor cross-scale descriptor transferability has been experimentally validated.

3 Proposed experimental framework

3.1 Conventional-scale configuration

The conventional-scale investigations are planned to use a circular-pipe configuration to examine phase distribution and the temporal evolution of gas–liquid flow structures under selected operating conditions. Electrical measurements are proposed as the primary diagnostic method, supplemented by optical observations where suitable optical access can be provided.

Before establishing the common experimental matrix, the pipe geometry, measurement locations, electrical sensing principle, optical accessibility and data acquisition capabilities must be specified. The feasibility of implementing the proposed configuration using available laboratory infrastructure will also require assessment. No completed conventional-scale measurements or validated reference dataset are assumed in the present study.

The conventional-scale configuration is intended to provide comparative measurements for evaluating the corresponding descriptors obtained from the minichannel. Differences in spatial resolution, sensor sensitivity and flow conditions must be considered explicitly. The larger-scale measurements will therefore serve as a comparative basis rather than an absolute reference for the smaller-scale configuration.

3.2 Minichannel configuration

The minichannel configuration is intended for investigations of gas–liquid flow in a circular channel. A miniaturised wire-mesh sensor (WMS), combined with high-speed optical imaging, is envisaged for measuring phase distribution and analysing flow-structure dynamics. Additional axial measurement locations may be introduced to investigate the propagation and evolution of gas–liquid structures. Future extension to flow-boiling conditions would require a specified heating arrangement, pressure and temperature measurements, and validation of the electrical and optical diagnostics under phase-change conditions.

Figure 2 presents the proposed functional arrangement of the minichannel module, including the electrical measurement sections and the optical observation region. The term gas-liquid flow is used here in a broad sense, encompassing both externally introduced gas-liquid mixtures and liquid-vapour flows involving phase change, including flow boiling. The diagram does not specify the internal electrode geometry, number of wires, electrode spacing or electronic implementation. The final design of the minichannel sensor requires further technical assessment and experimental validation.

The ability to distinguish between the phases using electrical measurements must be verified for the selected working fluids. Conductance-based sensing relies primarily on differences in electrical conductivity, whereas capacitance-based sensing exploits differences in permittivity [1, 2]. Impedance measurements may involve both contributions. Consequently, calibration procedures developed for conductive water–gas systems cannot be directly transferred to electrically insulating liquids. When water is used, its conductivity and temperature must be measured under the relevant experimental conditions.

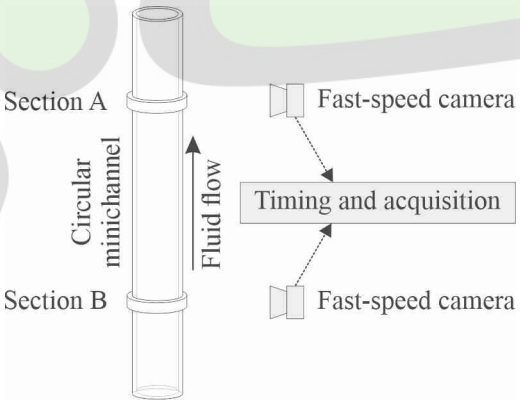


Fig. 2. Section B represents an optional additional measurement location. Electrical sensing sections, optical observation and synchronised acquisition are shown schematically.

Sensor miniaturisation also requires an assessment of possible disturbances introduced into the flow. Relevant geometric parameters include the ratios of wire diameter and electrode pitch to channel diameter, as well as the projected blockage of the flow cross-section.

Optical observations with and without the sensor should be compared under matched operating conditions. A removable sensor section would facilitate this assessment. Calibration alone cannot establish whether the sensor modifies bubble shape, movement or fragmentation. Previous investigations have examined the dependence of wire-mesh measurement accuracy on bubble size and liquid flow rate [8].

3.3 Existing experimental background and extension to flow boiling

Earlier experimental and design-oriented studies at Kielce University of Technology provide a relevant foundation for extending the present methodology to flow boiling. Piasecki et al. [9] applied Quality Function Deployment (QFD), supported by experimental heat-transfer data and numerical simulations, to identify key design and operating parameters affecting the thermal performance of compact minichannel heat exchangers, including channel geometry, heating-surface characteristics and flow conditions. Piasecka et al. [10] investigated flow boiling of HFE working fluids in rectangular minichannels, combining infrared thermography and thermocouple measurements with numerical heat-transfer calculations and detailed temperature uncertainty analyses. Piasecka, Piasecki and Maciejewska [11] directly compared liquid-crystal and infrared thermography during FC-72 flow boiling, demonstrating the value of carefully defined, complementary thermal observables. These studies were conducted using existing rectangular-minichannel facilities and do not establish the performance of the proposed circular wire-mesh sensor.

More recently, Piasecka and Piasecki [12] presented a harmonised database of rectangular-minichannel flow-boiling experiments covering six working fluids, varied heated surfaces, channel configurations and orientations, with source-file-grouped pilot machine-learning validation. Their work highlights the importance of data provenance and consistent reconstruction when combining measurement records. For future boiling-flow investigations, infrared heated-wall thermography and high-speed imaging could complement separately calibrated electrical phase-distribution indicators, provided that differences in observables and spatial sensitivity are respected. Such work would require a specified heating arrangement, local pressure and temperature measurements, and electrical-sensor calibration under relevant phase-change conditions.

3.4 Synchronisation and acquisition

For each experimental configuration, a common hardware timing signal is proposed to synchronise the electrical acquisition and high-speed camera system. Each measurement record should include timestamps, trigger identifiers, camera exposure time, electrical scan duration and relevant acquisition settings.

When electrodes are scanned sequentially, a complete electrical measurement map represents a finite time interval rather than an instantaneous observation. Comparison with optical images must therefore account for scan duration, exposure time and possible timing offsets between measurement channels.

The sampling frequency, camera exposure time and optical magnification should be selected according to the smallest flow structures and shortest characteristic time scales intended to be resolved. Motion during optical exposure and electrical scanning must be evaluated in relation to the effective spatial and temporal resolution.

A common hardware trigger does not automatically guarantee temporal coincidence between measurements. Acquisition delays, timing jitter and missing records must be identified and assessed. When electrical and optical measurement regions are located at different axial positions, the time required for structures to travel between these locations and their possible deformation must also be considered.

The proposed methodology will require experimental verification at both channel scales. Validation should include sensor calibration, electrical and optical measurement synchronisation, assessment of sensor-induced flow disturbances, and measurement uncertainty analysis. Repeated experiments under comparable operating conditions will be necessary to evaluate the reproducibility of selected descriptors and their transferability between scales. CFD and machine-learning methods may support subsequent analyses, provided that appropriate experimental data become available for their independent validation.

4 Cross-scale data analysis

4.1 Measured quantities and observability

The primary electrical record is a set of sensor responses. Conversion into local gas fraction requires a measurement model and calibration appropriate to the fluids and geometry. Until this conversion has been

verified, the output should be reported as a normalised electrical phase indicator. An area-averaged gas fraction may subsequently be estimated as

$$\bar{\alpha}(t) = \Sigma_i w_i \alpha_i(t), \ \Sigma_i w_i = 1, \quad (1)$$

where α_i is the calibrated local estimate and w_i is its representative area weight. Unequal boundary regions require appropriate weights. This discrete estimate is affected by the sensor sensitivity distribution and unresolved structures; the electrode crossings should not automatically be interpreted as independent point measurements.

Optical imaging is intended to provide projected contour dimensions, visible interface motion, event duration and evidence of deformation. A projected gas-area fraction differs from the gas fraction in a transverse cross-section. The two quantities will therefore be retained as separate descriptors. Direct comparison should concern shared observables, such as the passage time of an isolated structure, or a justified projection of a reconstructed or simulated distribution. Coalescence and breakup should only be labelled when the visible record supports the event; overlap in a single view is insufficient.

4.2 Normalisation and comparison

The proposed descriptor set includes mean phase indicators and their fluctuations, projected structure length, propagation velocity, event frequency and axial changes in these quantities. Let D denote the internal diameter, Q_k the local volumetric flow rate of phase k and A the channel cross-sectional area. The superficial velocities are $j_k = Q_k/A$, and the reference velocity is defined as $U = j_L + j_G$. Gas flow rates must be expressed at the local pressure and temperature. Candidate normalised descriptors are

$$L^* = L/D, \ u^* = u_s/U. \quad (2)$$

Here L is a stated optical or electrical structure-length estimate and u_s is the structure propagation velocity. The measurement basis of L must accompany every value. If no stable spectral peak or repeatable event sequence exists, a single characteristic frequency should not be forced onto the data.

The operating conditions can be described using liquid-reference Reynolds, Weber and Bond numbers, defined consistently as

$$Re_{L,U} = \rho_L U D/\mu_L, \ We_{L,U} = \rho_L U^2 D/\sigma, \quad (3)$$

$$Bo = (\rho_L - \rho_G) g D^2/\sigma. \quad (4)$$

The symbols ρ, μ, σ and g denote density, dynamic viscosity, surface tension and gravitational acceleration; subscripts L and G denote liquid and gas. These definitions use total superficial velocity and should not be confused with Reynolds or Weber numbers based on liquid superficial velocity alone. The gas-to-liquid flow-rate ratio, density and viscosity ratios, orientation and wetting conditions should also be retained. Equal values of one dimensionless group do not establish full dynamic similarity.

Propagation velocity between two sections can be estimated from $u_s = \Delta z/\tau_p$, where Δz is their separation and τ_p is the delay associated with an identifiable correlation peak. This estimate requires sufficiently persistent structures and a consistent timing reference. Multiple peaks, weak correlation or substantial deformation will be treated as reasons to withhold a velocity estimate. Structure velocity will not be identified with either phase mean velocity without additional evidence.

Resolution matching is required before comparing distributions. The ratios of effective spatial resolution to D and of sampling interval to D/U should be reported for both systems. Deliberate coarsening of the better-resolved dataset is proposed as a sensitivity test. Features that disappear under comparable spatial or temporal filtering cannot be interpreted as robust evidence of a scale effect.

5 CFD-supported interpretation

CFD is proposed for selected cases for which geometry, boundary conditions and diagnostic records are sufficiently characterised. Its role is to examine flow development between observation sections and to assist interpretation of measured phase distributions. The multiphase formulation and treatment of interfaces will be selected according to the flow structures and resolution required. No validated numerical model is assumed at this stage. Spatially resolved pipe-flow measurements such as those of Lucas et al. [4] illustrate the relevance of local data to this task.

Numerical verification should include spatial and temporal refinement and conservation checks. Experimental validation must subsequently compare like quantities: simulated phase fields should be averaged over the electrical sensitivity region or projected into the optical observation geometry, with compatible temporal averaging. Model parameters must not be tuned and evaluated on the same cases without an independent assessment. Separate computations with and without a representation of the sensor may be needed if experimental checks indicate appreciable disturbance.

The CFD results may assist in distinguishing advection from deformation and in interpreting scale-dependent differences. They will remain model-dependent predictions. Agreement of an integrated quantity alone will not establish accuracy of local interface evolution, and simulated samples will be identified separately from experimental records in all subsequent analyses.

6 Machine-learning-supported analysis

Machine learning is intended to assist physical interpretation through structure classification, feature extraction and the comparison of electrical and optical records. The initial analysis should use interpretable descriptors and simple reference classifiers before more complex representations are considered. Electrical-only, optical-only and combined models should be evaluated

using the same independent test cases. This comparison will determine whether data fusion adds useful information for a specified task; no improvement is assumed in advance.

The proposed analysis workflow is summarised in Fig. 3, showing the integration of electrical and optical measurements, CFD support, and evaluation of individual and combined models using independent test data before assessing cross-scale transferability.

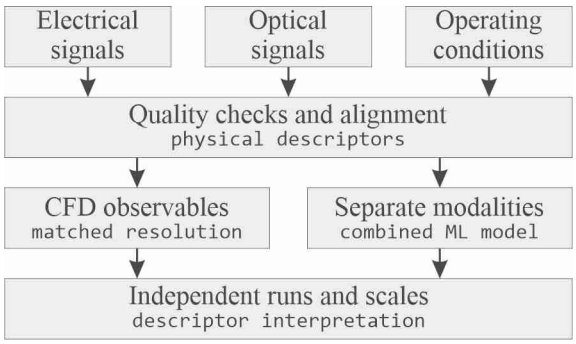


Fig. 3. Proposed workflow for electrical and optical data analysis, supported by CFD and machine learning.

Labels should follow a documented annotation protocol and distinguish clear structures from transitional or optically ambiguous cases. Agreement between annotators and the basis of each label should be retained. Windows from the same run, overlapping image sequences and records of the same structure at consecutive sections must remain in the same data partition. Preprocessing parameters and feature selection should be fitted using training data only. These requirements prevent correlated observations from producing an unduly favourable estimate of generalisation.

Performance should first be assessed on independent runs within each scale. A subsequent test should train on one scale and evaluate on the other, with the direction reversed where the data permit. Any adaptation using target-scale labels must be reported separately from transfer without adaptation. Class balance, class-specific errors and uncertainty should be evaluated using independent runs as the sampling units. A model may otherwise recognise the facility, image background or sensor resolution rather than the flow structure.

Transferable descriptors will be sought by examining their relationships with measured physical quantities and operating conditions, not only classification scores. A descriptor may remain informative while requiring a scale-dependent calibration. Conversely, failure of cross-scale prediction may indicate different physics, insufficient overlap of operating conditions or measurement bias. CFD-supported surrogate descriptions can be considered after the experimental and numerical datasets have been independently assessed.

7 Conclusions

A methodological framework has been formulated for the comparative investigation of gas–liquid flow structures in a conventional-scale circular pipe and a circular minichannel. Electrical phase-distribution measurements and optical imaging are considered complementary diagnostic techniques, with a clear distinction between cross-sectional phase-distribution estimates and quantities obtained from optical images.

The comparative approach relies on common flow descriptors, documented operating conditions and scale-dependent measurement resolution. Potential sensor-induced flow disturbances, acquisition synchronisation and the electrical properties of the working fluids are identified as essential factors affecting measurement interpretation. CFD and machine learning are envisaged as supporting analytical tools, subject to independent verification and validation.

This framework provides a basis for assessing the comparability of gas–liquid flow characteristics across channel scales. Its experimental feasibility, measurement uncertainty and the transferability of selected descriptors remain to be investigated.

Nomenclature

A - channel cross-sectional area (m²)
D - internal channel diameter (m)
f - characteristic event frequency (Hz)
g - gravitational acceleration (m s^{-2})
j_k - superficial velocity of phase k (m s^{-1})
L - projected structure length (m)
L^* - normalised structure length, L/D (-)
Q_k - local volumetric flow rate of phase k (m³ s^{-1})
t - time (s)
U - total superficial velocity used as reference (m s^{-1})
u_s - structure propagation velocity (m s^{-1})
u^* - normalised propagation velocity, u_s/U (-)
w_i - normalised area weight of cell i (-)
Δz - axial separation of measurement sections (m)
α_i - local gas-phase fraction in cell i (-)
$\bar{\alpha}$ - area-weighted mean gas-phase fraction (-)
μ_L - liquid dynamic viscosity (Pa s)
ρ_L, ρ_G - liquid and gas densities (kg m^{-3})
σ - interfacial tension (N m^{-1})
τ_p - time lag at the selected correlation peak (s)
Bo - Bond number (-)
$Re_{L,U}$ - liquid-reference Reynolds number (-)
$We_{L,U}$ - liquid-reference Weber number (-)

Subscripts and notation: G, gas; L, liquid; i, cell index; k, phase index; s, structure; p, correlation peak; *, normalised quantity; overbar, area-weighted mean.
Abbreviations: CFD, computational fluid dynamics; ML, machine learning; WMS, wire-mesh sensor.

This research was partially funded by the National Science Centre, Poland, grant no. UMO-2025/57/B/ST8/00907.

For the purpose of Open Access, the authors have applied a CC BY public copyright licence to the Author Accepted Manuscript (AAM) version arising from this submission.

Data availability is not applicable.

During the preparation of this manuscript, the authors used ChatGPT (OpenAI, GPT-6) to assist with language editing, manuscript organisation and consistency checks. All scientific content, interpretations and conclusions were reviewed and approved by the authors, who take full responsibility for the final manuscript.

References

1. H.-M. Prasser, A. Böttger, J. Zschau, A new electrode-mesh tomograph for gas–liquid flows. Flow Meas. Instrum. **9**, 111–119 (1998). https://doi.org/10.1016/S0955-5986(98)00015-6
2. M.J. da Silva, E. Schleicher, U. Hampel, Capacitance wire-mesh sensor for fast measurement of phase fraction distributions. Meas. Sci. Technol. **18**, 2245–2251 (2007). https://doi.org/10.1088/0957-0233/18/7/059
3. T. Cubaud, C.-M. Ho, Transport of bubbles in square microchannels. Phys. Fluids **16**, 4575–4585 (2004). https://doi.org/10.1063/1.1813871
4. D. Lucas, E. Krepper, H.-M. Prasser, Development of co-current air–water flow in a vertical pipe. Int. J. Multiphase Flow **31**, 1304–1328 (2005). https://doi.org/10.1016/j.ijmultiphaseflow.2005.07.004
5. J. dos Santos Ambrosio, A.E. Lazzaretti, D.R. Pipa, M.J. da Silva, Two-phase flow pattern classification based on void fraction time series and machine learning. Flow Meas. Instrum. **83**, 102084 (2022). https://doi.org/10.1016/j.flowmeasinst.2021.102084
6. L. Feng, S. Natu, V. Som de Cerff Edmonds, J.J. Valenza, Multiphase flow detection with photonic crystals and deep learning. Nat. Commun. **13**, 567 (2022). https://doi.org/10.1038/s41467-022-28174-2
7. A.K. Khandelwal, C.A. Tsoukalas, Y. Zhao, M. Ishii, Objective Neural Network-Based Flow Regime Classifiers with Application to Vertical, Narrow, Rectangular Channels and Round Pipe Geometry. J. Nucl. Eng. **7**, 15 (2026). https://doi.org/10.3390/jne7010015
8. S. Nuryadin, M. Ignaczak, D. Lucas, Deendarlianto, On the accuracy of wire-mesh sensors in dependence of bubble sizes and liquid flow rates. Exp. Therm. Fluid Sci. **65**, 73–81 (2015). https://doi.org/10.1016/j.expthermflusci.2015.02.022
9. A. Piasecki, S. Hożejowska, A. Masternak-Janus, M. Piasecka, Using Quality Function Deployment to Assess the Efficiency of Mini-Channel Heat Exchangers. Energies **17**, 2436 (2024). https://doi.org/10.3390/en17102436
10. M. Piasecka, B. Maciejewska, D. Michalski, N. Dadas, A. Piasecki, Investigations of Flow Boiling in Mini-Channels: Heat Transfer Calculations with Temperature Uncertainty Analyses. Energies **17**, 791 (2024). https://doi.org/10.3390/en17040791
11. M. Piasecka, A. Piasecki, B. Maciejewska, Liquid Crystal Thermography and Infrared Thermography Application in Heat Transfer Research on Flow Boiling in Minichannels. Energies **18**, 940 (2025). https://doi.org/10.3390/en18040940
12. M. Piasecka, A. Piasecki, A Unified Experimental Database and Group-Aware Pilot Machine Learning for Flow Boiling in Rectangular Minichannels. Energies **19**, 4483 (2026). https://doi.org/10.3390/en19194483

A modular acquisition and data architecture for wire-mesh sensors in multiphase flow diagnostics

Artur Piasecki[1*], *Przemysław* Kłys[2], and *Magdalena* Piasecka[3]

[1]Faculty of Environmental Engineering, Geomatics and Renewable Energy, Kielce University of Technology, Al. 1000-lecia P.P. 7, 25-314 Kielce, Poland
[2]Faculty of Electrical Engineering, Automatic Control and Computer Science, Kielce University of Technology, Al. 1000-lecia P.P. 7, 25-314 Kielce, Poland
[3]Faculty of Mechatronics and Mechanical Engineering, Kielce University of Technology, Al. 1000-lecia P.P. 7, 25-314 Kielce, Poland

Abstract. This work proposes an architecture for wire-mesh sensor (WMS) electronics, synchronised acquisition and data organisation in multiphase flow diagnostics. Each raw record is linked to its acquisition time, hardware configuration and processing history. Versioned calibration records and quality flags allow electrical and diagnostic quantities to be recalculated from retained ADC samples. A timing model distinguishes the sampling rate within a channel window from the rate at which complete scans can be assembled. For two illustrative serial schedules with identical step duration and zero scan overhead, increasing the number of channels from 32 to 128 reduces the scan rate from 3125 to 781.25 Hz while the retained sample-data rate remains 1.00 MB/s. A parallel readout example shows how the same number of crossing responses can be acquired in fewer steps. All performance figures are calculated from the assumed schedules. Prototype testing remains necessary.

Keywords: wire-mesh sensor; data acquisition; synchronisation; calibration; data provenance

1 Introduction

Wire-mesh sensors (WMS) acquire spatially distributed electrical responses for multiphase flow diagnostics. Conductance-based measurements were established by Prasser et al. [1], while da Silva et al. [2] developed a capacitance-based method. These approaches require acquisition electronics and calibration procedures matched to the electrical properties of the measured system. Dias et al. [3] showed that front-end gain selection affects the response of capacitance WMS in conductive fluids. Thus, the acquisition configuration forms part of the measurement definition and should accompany the recorded values.

Processing architecture is also relevant. Sahovic and Quinten [4] reported a hybrid system combining a field-programmable gate array (FPGA), a central processing unit (CPU) and a graphics processing unit (GPU) for real-time WMS data processing. Such implementations demonstrate the importance of allocating acquisition and computation to suitable hardware. The present work addresses a complementary methodological problem: how to preserve timing, configuration and calibration provenance when acquisition modules or processing procedures are changed. It does not propose a new electrode arrangement or claim an improvement in hardware performance.

The proposed record structure links each digitised signal to its acquisition window, the configuration in use at the time of measurement and its calibration history. These links identify which observations belong to the same scan while preserving the timing of individual channel measurements within that scan. The same raw samples can then be reprocessed with an updated calibration applicable to the recorded conditions, and the resulting values can be compared with those obtained using the original calibration. Illustrative acquisition schedules are used to assess how sequential readout affects scan duration and data rate. Prototype performance remains to be established experimentally.

2 Requirements for modular WMS acquisition

Each acquisition node must associate digitised values with the active excitation, analogue settings and channel schedule. Excitation waveform, frequency, amplitude convention and phase reference are required, together with gain, filter response, analogue-to-digital converter (ADC) encoding, sampling rate and acquisition-window duration. Channel identifiers are logical labels resolved through a versioned mapping; they do not prescribe electrode topology. Table 1 summarises the principal functional requirements.

* Corresponding author: Artur Piasecki, apiasecki@tu.kielce.pl

Table 1. Functional requirements and associated records.

Module	Required function	Stored metadata	Failure mode
Excitation	Defined stimulus	Waveform, frequency, amplitude, phase	Wrong stimulus
Analog front end	Condition and protect	Gain, filter, mode, hardware ID	Clipping; settling error
Selection and ADC	Execute acquisition schedule	Channel map, sample rate, encoding, window	Wrong channel; lost sample
Timing and node	Assign hardware time; buffer	Clock, trigger, scan and sequence IDs	Drift; trigger loss
Storage and processing	Preserve source and history	Configuration, calibration, processing IDs	Overwrite; version mismatch

A configuration becomes immutable once acquisition starts. A setting change creates a new configuration identifier with an explicit effective record boundary. The record sequence must expose missing samples, repeated packets and incomplete scans. Quality status is recorded independently of the measured value, so that a failed acquisition cannot be mistaken for a zero response.

3 Proposed acquisition architecture

Figure 1 separates the sensor interface, acquisition node and host-side processing. Excitation is delivered to the electrical interface; the measured response passes through analogue conditioning, channel selection and an ADC. Their physical ordering may depend on circuit implementation. The front end may include amplification, filtering, impedance matching, protection and demodulation. The documented transfer function and settling behaviour must correspond to the selected operating mode. WMS implementation requires defined potentials on inactive transmitters and suitable receiver terminations, with crosstalk and loading assessed for the selected switching arrangement.

A microcontroller-based or FPGA-assisted node executes the acquisition schedule, assigns sequence identifiers and buffers data. Hardware choice follows the required timing and throughput. Multiple nodes use a common time reference, while retaining station identity and the configuration of each local acquisition path. Host reception time is stored separately from measurement time.

The proposed raw-data boundary is the ADC output. Digitised samples are retained before digital averaging, calibration or demodulation, including any such processing within the acquisition node. If analogue demodulation precedes the ADC, the original carrier waveform cannot be recovered; this limitation must be stated in the mode description.

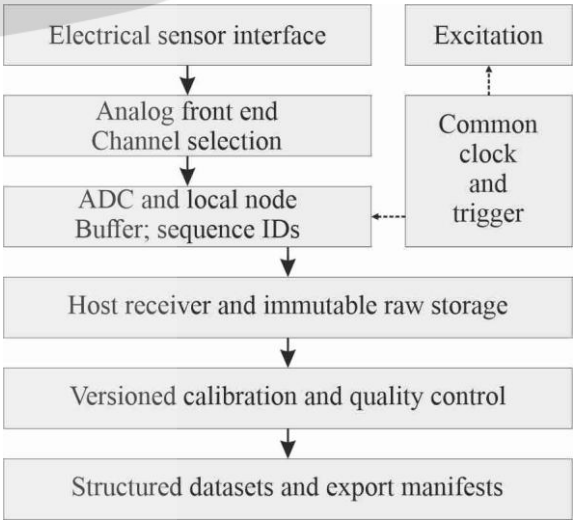


Fig. 1. Proposed WMS acquisition architecture. Dashed connections show timing distribution. The acquisition node can be replicated at multiple stations.

Storing only averaged or demodulated digital values similarly restricts future reprocessing and cannot be described as preservation of all ADC samples. Sequence checks and block checksums detect transport or storage faults, while local buffering accommodates temporary host delays.

4 Timing and synchronisation

A sample is one digitised observation. A channel acquisition window may contain several samples used to estimate one electrical response. A scan is a scheduled traversal of the required logical channels. An electrical frame is the assembled set of responses associated with that scan. A trigger requests or marks an acquisition event; a timestamp specifies the time of a defined event or sample within a stated clock domain. These terms must not be used interchangeably.

Figure 2 illustrates why a common trigger does not establish simultaneous measurements. Trigger distribution, channel settling, acquisition-window duration and filter delay contribute different timing offsets. Each frame should retain its start and end times, channel offsets and completeness status. A representative frame timestamp is acceptable only when its convention is recorded and the scan interval remains available. An optional optical frame requires its own exposure interval and trigger association.

For a local clock counter c_i, a segment-wise mapping to reference time can be written as

$$t_i = a_s\, c_i + b_s + \delta_i \qquad (1)$$

where a_s is the counter-to-time scale, b_s is the offset for that station and timing segment and δ_i represents a residual timing error characterised by an uncertainty or bound. Clock epoch, counter rollover, synchronisation interval and estimates of offset and drift must be recorded. For each station, the index s identifies an interval over which the same clock mapping applies. A missed trigger is flagged in the event sequence. A new timing segment is required when a reset or a change in clock behaviour invalidates the existing mapping.

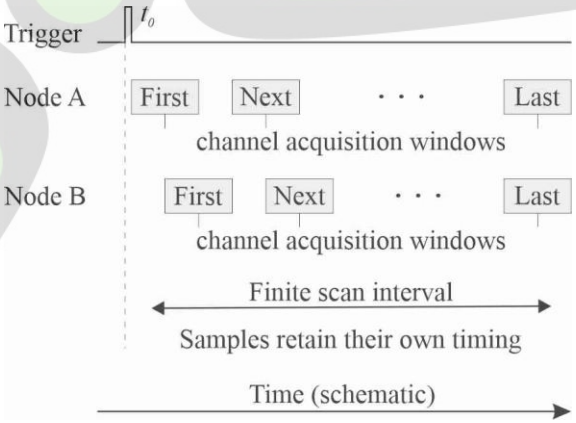


Fig. 2. Timing hierarchy for two illustrative nodes. Offsets and window widths are schematic. Tick marks indicate representative sample times; an assembled frame spans a finite interval.

Relative alignment should be checked using a common electrical test event at the acquisition inputs and verified across the intended recording duration. Permissible timing error follows from the shortest interval to be resolved; no achieved jitter is assumed here.

5 Calibration and data provenance

Calibration is associated with a specific hardware and acquisition configuration. Electrical reference loads establish the response of the acquisition chain, while single-phase fluid states provide application-specific references. Zero/span adjustment is suitable only where the selected transfer model supports it. Reference values, repeat measurements, temperature, fitting method, coefficients and their uncertainty should be retained. Temperature compensation is particularly relevant to conductivity-based measurements, as examined by Wiedemann et al. [5].

A calibration record includes its creation date, applicability interval, operating range and linked configuration. Replacement of hardware, changes in gain or excitation, and evidence of drift require a new applicability assessment and, where necessary, recalibration. Historical data may be reprocessed only with a calibration model applicable to their recorded conditions. A newly fitted model cannot compensate for unrecorded changes or information already discarded.

Figure 3 represents processing as a sequence of versioned derivations. The separation of data entities and processing activities follows the provenance concepts formalised in PROV-DM [6]. Each execution records its input ranges, calibration version, software version, parameters and output identifiers. Raw data are never overwritten by calibrated values; repeated processing creates new derived records. This preserves data provenance. Metrological traceability additionally requires a calibration chain linked to appropriate references, with associated measurement uncertainties [7]; metadata alone do not establish it.

Quality flags cover ADC saturation, missing data, incomplete scan, synchronisation error, trigger loss, calibration out of range, excessive noise, configuration mismatch and manual exclusion. Multiple conditions may coexist. “Valid” means that all required checks were performed and passed under a specified rule version; “not assessed” is distinct from valid. Noise limits and acceptance thresholds require experimental determination. Manual decisions retain author, time and reason. Flags affect dataset selection without deleting or silently replacing the original observations.

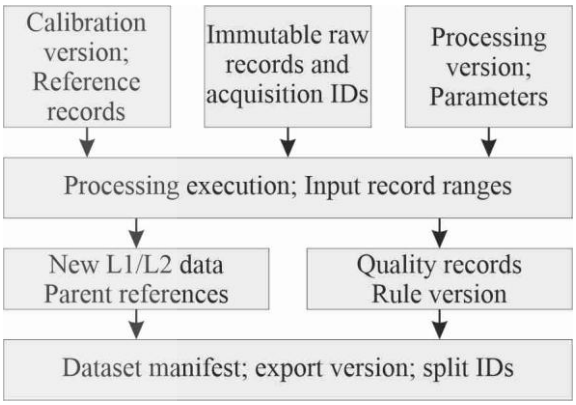


Fig. 3. Provenance relationships. Reprocessing creates a new execution and new outputs from the same retained raw records. Quality assessments remain separately identifiable and versioned. The L1/L2 block summarises successive transformations with retained parent links.

6 Data organisation for CFD and ML

Table 2 distinguishes the three data levels. Conductance G or capacitance C is stored only when identifiable from the measurement mode and calibration. A single amplitude response is not generally sufficient to determine both. Unsupported quantities are marked unavailable. Conversion to phase fraction requires a separately validated electrical-to-physical model; otherwise the output remains a normalised response or phase indicator.

Table 2. Proposed data hierarchy and required provenance.

Level	Stored content	Essential links
L0	Raw ADC samples; sample index and acquisition time	Run, station, channel, scan, trigger, configuration
L1	Calibrated electrical response; units; G or C when supported	L0 input range; calibration and processing versions
L2	Physical or diagnostic quantity; position; quality status	L1 parents; transformation version; geometry mapping

The logical schema separates MeasurementRecord, AcquisitionConfig, CalibrationRecord, ExperimentMetadata, ProcessingRecord and QualityRecord. A MeasurementRecord has a unique record ID and links to run, station, channel, scan, trigger and configuration IDs, together with timestamp, sample index and raw value. Shared timing or configuration fields may be stored once per block, provided that their relationship to every sample is unambiguous. AcquisitionConfig contains excitation and digitisation settings, channel-map version and firmware identity.

ExperimentMetadata links the run to geometry version, coordinate system, sensor position, fluids, temperature, pressure, flow rates and orientation.

CalibrationRecord describes the reference conditions and model. ProcessingRecord identifies each execution and its parent records, while QualityRecord identifies the assessed object, check version and flags. Keys are explicit, and units and missing-value conventions form part of the schema. Bulk arrays may be stored separately from the relational catalogue using stable identifiers and checksums. Geometry mappings can remain access-controlled while public records use opaque channel identifiers. For example, suppose that the five ADC samples from one acquisition window are converted to an electrical response using calibration v1. If calibration v2 is subsequently found applicable to that window, a second processing record links the same five L0 samples to a new L1 result. The original L1 result and its calibration identifier remain available for comparison.

For computational fluid dynamics (CFD), an export should contain measurement positions, spatial support, time intervals, operating conditions and applicable uncertainty information. Numerical fields must be converted to observables with compatible spatial and temporal averaging. The architecture prepares data for that comparison; it does not define a direct solver input or a validated CFD model.

For machine learning (ML), each sample retains links to its run, acquisition configuration, calibration, processing version and raw input interval. Dataset manifests record these links and the partition assignments. Runs, overlapping windows and shared events are grouped before splitting, with related records from different stations kept together. Learned preprocessing and feature selection use training data only. These requirements address the leakage mechanisms discussed by Kapoor and Narayanan [8]. Retaining provenance permits an audit of a split but does not by itself guarantee independence.

In transient FC-72 experiments, changes in heater temperature, pressure and mass flow rate were recorded at the onset of boiling in minichannels [9]. A separate study used liquid crystal and infrared thermography simultaneously to measure heated-wall temperatures [10]. A future experiment could pair wall thermography with a WMS downstream of the heated region. Recording the axial separation, thermal acquisition times and crossing-specific time offsets within each scan would allow a downstream electrical response to be compared with a thermal event with sequential readout accounted for and transport delays assessed independently.

7 Parametric acquisition requirements

For a characteristic observation duration τ_c and a required count N_p of observations during that duration, a design criterion is

$$f_{req} \geq N_p / \tau_c \tag{2}$$

If a length L_c passes the observation region at speed u_s, the kinematic estimate is $\tau_c = L_c/u_s$. Equation (2) specifies temporal sampling density; it is not an anti-aliasing criterion or a guarantee of sufficient analogue bandwidth. For repeated channel observations, the relevant revisit rate is the scan rate rather than the within-window ADC rate.

Consider one non-overlapping, serial acquisition path with N_c logical channels, each allocated switching, settling and acquisition times. With scan-level overhead T_0,

$$T_{scan} = N_c(T_{sw} + T_{set} + T_{win}) + T_0 \tag{3}$$

$$f_{scan} = 1/T_{scan} \tag{4}$$

Here T_{win} includes all conversions and integration required for one channel response. Overlapping conversion, simultaneous channels or multiple parallel paths require a different scheduling model. For continuous sampling within each window, the retained sample count is approximately $M = f_{\mathrm{ADC}}T_{\mathrm{win}}$, subject to the actual integer acquisition schedule. Settling and switching samples are excluded in this model. The assumed times require verification against the front-end bandwidth, demodulator response and ADC acquisition and conversion timing. A 1 MSample/s rate is compatible only with an appropriately band-limited ADC input or a separately justified sampling scheme.

$$R_{raw} = N_c\, f_{scan}\, M\, B_{ADC} \tag{5}$$

$$R_{total} = R_{raw} + f_{scan} B_{meta} \tag{6}$$

The storage width B_{ADC} is measured in bytes per retained ADC sample and need not equal the nominal converter bit depth divided by eight. B_{meta} is the effective metadata allocation per scan. Equation (6) excludes packet framing, retransmission and storage-system overhead. Simultaneous modes or additional stations require summation of their respective rates. Where one stored value per channel is sufficient, $M\,B_{\mathrm{ADC}}$ can be replaced by the appropriate record width, but the resulting data may no longer preserve the full digitised waveform.

Table 3 contains deliberately hypothetical design cases, unrelated to any proposed electrode layout. All cases assume $T_{\mathrm{sw}}=2$ µs, $T_{\mathrm{set}}=3$ µs, $T_0=0$, $f_{\mathrm{ADC}}=1$ MSample/s, $B_{\mathrm{ADC}}=2$ bytes and $B_{\mathrm{meta}}=64$ bytes/scan. The metadata allocation represents compact shared headers with a deterministic channel schedule, not a complete set of individually stored timestamps. Values are calculated without compression; MB denotes 10^6 bytes.

Increasing the channel count from A to B reduces scan frequency by a factor of four while leaving the retained ADC-data rate unchanged. Under the stated serial schedule and zero scan overhead, the product N_c f_{scan} is constant. The metadata rate decreases because fewer scans are completed per second. Case C increases the acquisition-window duration, further reducing scan frequency while increasing the raw-data rate through a larger acquisition duty fraction. Consequently, higher recorded throughput does not necessarily indicate better temporal resolution.

Table 3. Illustrative serial-acquisition cases; calculated values, not measured performance.

Quantity	A	B	C
N_c	32	128	128
T_{win} (µs)	5	5	15
M (samples/channel)	5	5	15
T_{scan} (ms)	0.32	1.28	2.56
f_{scan} (Hz)	3125.00	781.25	390.63
R_{raw} (MB/s)	1.00	1.00	1.50
R_{total} (MB/s)	1.200	1.050	1.525

Applying Eq. (2) with four observations per 1 ms event gives a 4 kHz revisit-rate criterion, giving a scan budget of 250 µs. With the 10 µs step duration of cases A and B and zero scan overhead, at most 25 sequential steps fit within that budget. None of the three serial schedules in Table 3 meets this requirement. This criterion assumes uniform revisits and negligible timing error relative to the event duration.

The number of sequential steps depends on the readout topology. An 8 × 16 mesh yields 128 crossing responses per frame in either mode. For hypothetical serial digitisation, each of the eight transmitters is selected in turn and its sixteen crossings are read sequentially. At 10 µs per crossing and zero scan overhead, the 128 readout steps take 1.28 ms (781.25 scans/s, case B). With sixteen simultaneous receiver paths, one transmitter step yields sixteen responses. Eight steps then take 80 µs (12,500 scans/s). This calculation assumes the same 10 µs step, including switching, settling and acquisition, and sufficient bandwidth on all paths. At five retained two-byte samples per crossing, the parallel schedule would produce 16.00 MB/s of raw ADC data. The 1 MSample/s rate applies to each parallel receiver path during its acquisition window. Serial multiplexing must preserve the required electrical termination of all receiver wires.

Buffer sizing also follows from the data model. For a host interruption of duration T_{pause} with no data drainage, an average-rate lower bound on available payload capacity is $S_{buf} \geq R_{total}T_{pause}$, before implementation overhead and margin. For a 0.1 s interruption, case B gives 0.105 MB by this average-rate estimate. With whole-scan blocks of 1344 bytes and arbitrary pause phase, capacity for 79 blocks (0.106176 MB) is required for new arrivals, plus any existing backlog and implementation margin. If the sustained output rate remains below the input rate, finite buffering cannot prevent eventual data loss. Bench verification must therefore measure scan timing, settling, clock alignment, saturation, buffer overflow and recovery, followed by replay of the same raw data through versioned calibration procedures.

8 Conclusions

A modular acquisition and data architecture has been formulated for WMS diagnostics. The proposed separation of raw, calibrated and derived records preserves the acquisition context and supports reproducible reprocessing. Explicit timing conventions and versioned configuration, calibration and quality records define the information that must accompany a measurement.

For the illustrative 1 ms event, the required revisit rate limits a serial schedule to 25 steps of 10 µs each. Parallel readout changes the number of sequential steps needed to assemble a frame, while each crossing still contributes data to storage. Bench tests are needed to establish whether the assumed settling time, clock alignment and sustained transfer rate can be achieved together.

The proposed architecture is intended to support future WMS-based investigations of multiphase flows at Kielce University of Technology, including potential applications to flow boiling in minichannels. In particular, synchronised electrical measurements and wall thermography could provide complementary information on vapour structures and thermal behaviour. The acquisition and data-management procedures developed here would support the integration, comparison and subsequent analysis of these measurements. Their applicability will require experimental verification after implementation of the measurement system.

Nomenclature

B_{ADC}, bytes per ADC sample; B_{meta}, metadata bytes per scan; f_{ADC}, ADC sampling rate; f_{req}, required observation rate; f_{scan}, scan rate; L_c, characteristic length; M, retained samples per channel per scan; N_c, logical channel responses per scan; N_p, required observations; R, data rate; S_{buf}, available buffer payload capacity; T_0, scan overhead; T_{sw}, switching time; T_{set}, settling time; T_{win}, acquisition window; T_{scan}, scan duration; T_{pause}, host interruption; u_s, passage speed; τ_c, characteristic duration. In Eq. (1), c_i is a counter value, a_s its time scale, b_s the offset for a station and timing segment, δ_i the residual timing error and t_i the reference time. G, conductance (S); C, capacitance (F); R_{raw} and R_{total}, raw-sample and total retained-data rates (bytes/s); i, sample index; s, clock-mapping segment index for a given station.

This research was partially funded by the National Science Centre, Poland, grant no. UMO-2025/57/B/ST8/00907.

For the purpose of Open Access, the authors have applied a CC BY public copyright licence to the Author Accepted Manuscript (AAM) version arising from this submission.

Data availability. No experimental dataset was generated. The values in Table 3 and the serial and parallel scan examples can be reproduced from the acquisition schedules and assumptions in Section 7.

During the preparation of this manuscript, the authors used ChatGPT (OpenAI, GPT-6) to assist with language editing, manuscript organisation and consistency checks. All scientific content, interpretations and conclusions were reviewed and approved by the authors, who take full responsibility for the final manuscript.

References

1. H.-M. Prasser, A. Böttger, J. Zschau, A new electrode-mesh tomograph for gas–liquid flows. Flow Meas. Instrum. **9**, 111–119 (1998). https://doi.org/10.1016/S0955-5986(98)00015-6
2. M.J. da Silva, E. Schleicher, U. Hampel, Capacitance wire-mesh sensor for fast measurement of phase fraction distributions. Meas. Sci. Technol. **18**, 2245–2251 (2007). https://doi.org/10.1088/0957-0233/18/7/059
3. F. d. A. Dias, P. Wiedemann, M.J. da Silva, E. Schleicher, U. Hampel, Tuning capacitance wire-mesh sensor gains for measurement of conductive fluids. tm – Technisches Messen **88**, s107–s113 (2021). https://doi.org/10.1515/teme-2021-0055
4. B. Sahovic, M. Quinten, Hybrid FPGA-CPU-GPU system for real-time multiphase flow monitoring using wire-mesh sensors. Results Eng. **27**, 106188 (2025). https://doi.org/10.1016/j.rineng.2025.106188
5. P. Wiedemann, F. de Assis Dias, E. Schleicher, U. Hampel, Temperature compensation for conductivity-based phase fraction measurements with wire-mesh sensors in gas-liquid flows of dilute aqueous solutions. Sensors **20**, 7114 (2020). https://doi.org/10.3390/s20247114
6. L. Moreau, P. Missier (eds.), PROV-DM: The PROV Data Model. W3C Recommendation (2013). https://www.w3.org/TR/2013/REC-prov-dm-20130430/
7. JCGM, International vocabulary of metrology – Basic and general concepts and associated terms (VIM), 3rd ed., JCGM 200:2012, §2.41. https://jcgm.bipm.org/vim/en/2.41.html
8. S. Kapoor, A. Narayanan, Leakage and the reproducibility crisis in machine-learning-based science. Patterns **4**, 100804 (2023). https://doi.org/10.1016/j.patter.2023.100804
9. B. Maciejewska, M. Piasecka, A. Piasecki, The study of the onset of flow boiling in minichannels: Time-dependent heat transfer results. Heat Transf. Eng. **43**, 223–237 (2022). https://doi.org/10.1080/01457632.2021.1874181
10. M. Piasecka, A. Piasecki, B. Maciejewska, Liquid crystal thermography and infrared thermography application in heat transfer research on flow boiling in minichannels. Energies **18**, 940 (2025). https://doi.org/10.3390/en18040940

Experimental investigation of flow-field topology in a hybrid wind tunnel test section for aeroelastic studies of steam turbine blades under low-load conditions

Pavel Procházka [1*], *Vladislav* Skála[1], and *Pavel* Antoš[1]

[1]Institute of Thermomechanics of the Czech Academy of Sciences, 18200, Praha 8, Czech Republic

Abstract. Aeroelastic stability remains a significant challenge in the design and operation of turbomachines, particularly for long, slender turbine blades operating under off-design conditions. In modern thermal and nuclear power plants, low-load operation can substantially alter the flow conditions within steam turbines, potentially affecting blade vibration and aeroelastic stability. This is particularly relevant to boiling water reactors (BWRs), in which steam generated directly within the reactor core is supplied to the turbine. To investigate the flow conditions associated with low-load operation, a hybrid wind tunnel test section was developed to study the aerodynamic and aeroelastic behavior of a turbine blade cascade. The facility incorporates a secondary bypass tunnel that generates a strong radial cross-flow and promotes flow recirculation, reproducing selected flow features characteristic of low-load steam turbine operation. In the present study, Particle Image Velocimetry (PIV) was employed to characterize the flow field topology under different combinations of the primary and bypass flow rates. The analysis focuses on velocity distributions and increments, turbulence intensity, and the size and structure of the recirculation region. The influence of the flow-rate ratio on these parameters is evaluated to characterize the resulting flow structures and assess their potential implications for the aerodynamic loading and aeroelastic response of the blade cascade. The results provide insight into the flow phenomena generated by the hybrid test section and support its application in experimental investigations of steam turbine blade aeroelasticity under low-load conditions.

* Corresponding author: prochap@it.cas.cz

1 Introduction

Aeroelasticity addresses the coupled response of deformable solid structures and surrounding fluid flows, with the resulting dynamics governed by the interaction of inertial, elastic and aerodynamic forces. Among the most critical phenomenon of dynamic aeroelasticity is flutter, an instability in which unsteady aerodynamic loading supplies sufficient energy to sustain or amplify structural oscillations. In turbomachinery, the stability of a blade vibration mode depends strongly on the aerodynamic damping associated with its motion. A negative aerodynamic damping contribution may overcome the available structural damping and lead to growing vibration amplitudes, potentially resulting in high-cycle fatigue or blade failure. Accurate characterization of the flow conditions in the vicinity of the blades is therefore essential for reliable aeroelastic assessment [1]. Although substantial progress has been achieved in theoretical and numerical modelling, the prediction of cascade flutter remains challenging, particularly when the incoming flow is strongly non-uniform or separated.

Aeroelastic instability is relevant to aircraft wings and various civil-engineering structures, but it is especially important in turbomachinery (compressors and turbines), where adjacent blades interact aerodynamically through a confined and often three-dimensional flow field. The analysis of a complete bladed rotor is complicated by the number of interacting blades, the annular geometry, the inter-blade-phase angle, and the coexistence of multiple structural modes. Consequently, simplified linear cascades installed in rectangular wind tunnel test sections are widely used to investigate fundamental unsteady aerodynamic mechanisms under controlled conditions. The blades may be allowed to respond freely to the flow, the self-induced vibration happens [2], or selected blades may be excited externally. In kinematic excitation, the imposed blade displacement typically follows a prescribed harmonic motion. In force excitation, the applied periodic forcing is controlled, while the actual blade motion is determined by the coupled structural and aerodynamic response. The latter approach provides flexibility in the selection of excitation frequency and forcing amplitude but requires careful measurement of the resulting motion and dynamic loading. Previous experimental studies of oscillating cascades have demonstrated the sensitivity of aerodynamic damping to flow regime, excitation frequency, incidence and blade configuration [3]. Accordingly, a controlled experimental environment is necessary for isolating the contribution of individual flow coherence structure to aeroelastic behaviour.

An important limitation of many conventional cascade experiments is the assumption of a nearly uniform, two-dimensional inlet flow. This approximation does not adequately represent some operating conditions encountered in the final stages of low-pressure (LP) steam turbines, particularly when the turbine operates substantially below its design load. There is a need for more flexible operation of thermal power plants to compensate fluctuations in electricity generation from renewable sources, such conditions are more relevant for actual study: At reduced steam input, the flow pattern may change considerably: backflow regions and large-scale vortical structures can occur, the effective flow passage becomes restricted, and the remaining through-flow may be redistributed towards the blade tip region [4, 5]. Numerical investigations have additionally associated low-load operation with complex three-dimensional flow instabilities and pronounced radial transport [6]. These changes may modify blade incidence angle and local aerodynamic loading can lead to flutter risk. The present work therefore investigates a hybrid wind tunnel test section designed to reproduce selected features of such low-load flow fields in a controllable test section. Rather than attempting complete similarity with a real steam turbine, the experiment focuses on the generation and systematic characterization of spanwise flow deflection, velocity non-uniformity and recirculation. The objective is to establish the response of the flow field topology to the bypass flow setting and to assess the suitability of the facility for future aeroelastic tests involving a blade cascade.

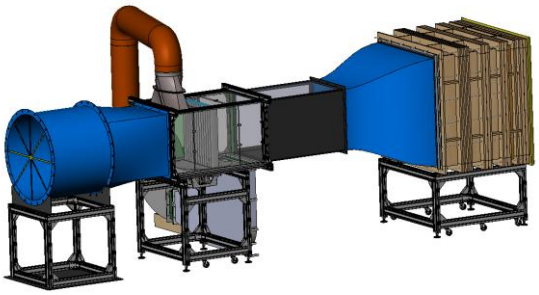


Fig. 1. The design of the Eiffel tunnel and the bypass tunnel with circular pipes for the suction part and a rectangular pipe for the blowing; the test section is between both orifices.

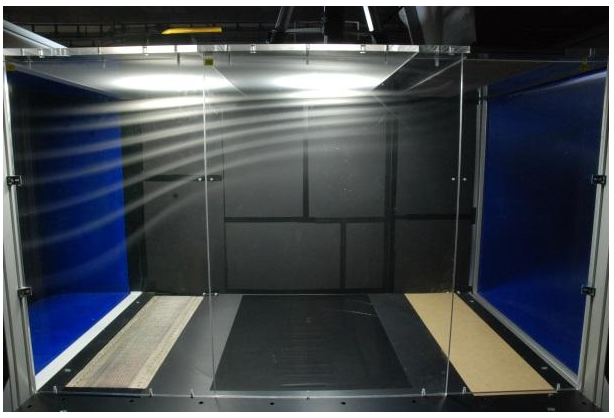


Fig. 2. Smoke lines to visualize the effect of bypass cross-flow, blowing orifice at left down corner.

2 Experimental setup

Several approaches can be considered for introducing a substantial spanwise velocity component into the predominantly axial flow of a rectangular wind tunnel. One possibility is a passive shear-flow generator

composed of a suitably shaped fine mesh screen, such as an S-shaped [7] arrangement based on the principle of an Elder-type generator. Although such a device can modify the velocity profile, its effect is essentially fixed by the geometry and is accompanied by an additional pressure loss. Alternatively, the cross-sectional geometry of the test section can be modified, for example by using curved upper and lower walls or stationary guide vanes to deflect the incoming flow. A diverging cross section could also generate a non-uniform flow. However, these solutions offer limited independent control over the resulting radial component and introduce geometric constraints that are undesirable for subsequent installation of an oscillating blade cascade.

Active flow control is highly desired to set various flow regimes. The blowing air [8] jet or suction effect [9] can be preferable however their effect will not be sufficient to affect and to introduce strong radial flow component across the entire test section. To obtain a controllable cross flow, an auxiliary bypass wind tunnel was designed using CFD tools and integrated with the existing Eiffel-type facility (Fig. 1). The principle is based on simultaneous injection of air through an orifice in the upstream portion of the bottom wall and suction through the second orifice in the downstream portion of the upper wall. The resulting "bypass" flow is superimposed on the axial flow produced by the main tunnel fan and generates an oblique mean-flow direction, as illustrated qualitatively by the smoke visualization in Fig. 2. Compared with a local blowing jet or isolated suction slot, the coupled arrangement is intended to influence a substantial fraction of the test section height. The rectangular test section is 1200 mm long and has a cross section of 700 × 700 mm. The blowing orifice measures 650 × 100 mm, extends across most of the tunnel width and contains a fine mesh screen to improve the uniformity of the delivered air. The suction orifice has the same dimensions and is installed in the upper wall downstream of the blowing opening. The axial centre-to-centre spacing of the orifices is 855 mm. The openings are connected externally to form a closed-loop wind tunnel, whose mass flow is driven by a powerful radial fan. When the main tunnel is switched off, or operated at a sufficiently low rate, the bypass produces a pronounced diagonal flow through the common test section.

The bypass suction pipeline has a nominal circular diameter of DN 300. Downstream of the radial fan, the flow is conveyed through a rectangular duct of varying cross section towards the lower blowing orifice. Owing to laboratory space limitations, the circuit contains several elbows and the available straight lengths are insufficient for complete natural recovery of a uniform velocity profile. Guide vanes were therefore installed to reduce the non-uniformity introduced by the bends, and the exit screen provides additional flow conditioning. The maximum volumetric flow rate of the bypass circuit is approximately 5 000 $m^3\ h^{-1}$, corresponding to a blowing slot velocity of the order of 20 $m\ s^{-1}$. For comparison, the main wind tunnel fan can deliver up to approximately 44 000 $m^3\ h^{-1}$. These capacities permit independent adjustment of the main and bypass flow rate over a useful range of operating conditions.

The quality of the blowing and suction flows was assessed experimentally using Particle Image Velocimetry (PIV) and Hot-Wire (HW) anemometry. Both measurement systems were supplied by Dantec Dynamics. The PIV arrangement employed a V611 high-speed camera with a nominal resolution of approximately 1 Mpx, internal memory of 8 GB and a maximum acquisition rate of up to 6 kHz. Illumination was provided by a dual-head DMX 30 laser emitting at 527 nm; the stated pulse energy is 30 mJ at 1 kHz, and the maximum repetition rate is 10 kHz. The flow was seeded with tracer particles suitable for optical velocimetry. Complementary pointwise measurements were carried out using a single hot-wire probe operated with a StreamLine anemometry system. Because a single wire measures the cooling response associated with the velocity component normal to the wire, the interpretation of the resulting velocity profiles is restricted to the probe orientation used during calibration and traversing.

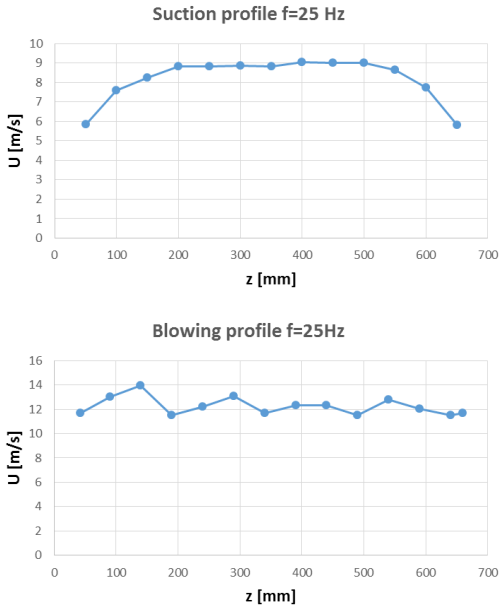


Fig. 3. Spanwise velocity profiles measured by hot-wire anemometry approximately 20 mm from the suction (up) and blowing (down) orifices.

Figure 3 presents the HW velocity profiles measured approximately 20 mm from the suction and blowing orifices. The probe was traversed across the 650 mm spanwise extent of each slot. The suction profile is approximately symmetric and exhibits an extended central region of nearly constant velocity, with lower velocities close to the two lateral edges. The blowing profile shows small but noticeable variations across the width. These variations are consistent with residual non-uniformities produced by upstream bends and their associated guide vanes, which are not fully removed by the fine mesh screen. Nevertheless, the measured turbulence intensity remains below approximately 5% over the main part of the blowing orifice. The profiles therefore indicate an acceptably

uniform supply for the intended generation of a large-scale controlled cross flow, while identifying departures from ideal uniformity that should be considered in subsequent measurements.

Additional PIV measurements were performed in a plane aligned with the main tunnel axis and spanning the 100 mm dimension of the blowing orifice. The extracted velocity profiles, located 20 mm above the bottom wall, are compared in Fig. 4. With the axial tunnel inactive, the jet exhibits an approximately symmetric profile with slightly elevated velocities near its edges. When the main tunnel flow is activated, the blowing jet becomes progressively deflected in the downstream direction, and the profile is modified by its interaction with the cross flow. The values expressed in hertz in Fig. 4 denote the frequency settings of the fan drives (e.g. 25Hz is half power, 50Hz is full power). The following section describes how the same interaction develops across the complete test section domain.

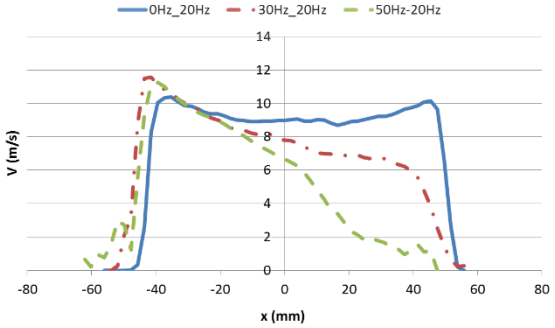


Fig. 4. PIV-derived velocity profiles of the blowing jet, extracted 20 mm above the bottom wall for different operating conditions of the main and bypass tunnel. The fan-drive frequency settings are indicated in the legend.

3 Results

Mapping the velocity field across the full hybrid test section by PIV presented several experimental difficulties. The investigated area was substantially larger than the region that could be illuminated effectively by the available laser sheet in a single acquisition, with an illuminated extent of approximately 300 mm. In addition, joints between transparent wall panels and scratches in the optical windows locally reduced image quality and introduced regions susceptible to systematic vector-evaluation errors. Maintaining a sufficiently homogeneous concentration of tracer particles was particularly challenging in the strongly recirculating bypass flow cases. For these reasons, the overall field of view (FoV) was assembled from nine individual measurement regions. Some boundaries between adjacent regions exhibit visible discontinuities or reduced spatial coverage, primarily owing to local limitations of illumination and seeding. To maintain transparency regarding the raw experimental information, the presented PIV maps were not subjected to additional cosmetic filtering. The comparisons of pointwise quantities were instead performed along a line in the central portion of the section, where the velocity evaluation was judged sufficiently reliable. Consequently, discontinuities in the composite maps should not automatically be interpreted as physical flow structures. In addition, the plotted turbulent kinetic energy should be considered an estimate derived from the velocity fluctuations resolved by the PIV measurement, rather than necessarily a complete three-component description of turbulent motion.

Three operating regimes were selected to demonstrate the effect of increasing bypass flow while maintaining main tunnel velocity of 10 m s^{-1}. The reference regime, denoted 10_0, corresponds to operation of the main wind tunnel without the bypass flow. The second regime, 10_10, combines a nominal main tunnel velocity of 10 m s^{-1} with a blowing slot velocity of approximately 10 m s^{-1}. Although these characteristic velocities are equal, the corresponding volumetric flow rates are substantially different because the cross-sectional area of the bypass slot is approximately 7.5 times smaller than that of the main tunnel. The strongest investigated regime, 10_20, retains the same main tunnel setting but increases the characteristic blowing slot velocity to 20 m s^{-1}. These labels specify nominal operating velocities, not measured mass flow ratios. The three cases therefore provide a controlled qualitative comparison of the evolution from nearly axial flow to increasingly pronounced diagonal transport and recirculation.

In the reference case, the velocity magnitude distribution is comparatively uniform, with values close to the nominal main tunnel velocity of 10 m s^{-1} throughout most of the accessible section (Fig. 5a). The corresponding velocity vectors and streamlines are nearly horizontal, indicating that the mean spanwise component is small in comparison with the axial component (Fig. 5c,d). The fluctuation energy distribution is also relatively weak, apart from localized regions influenced by the test section geometry and measurement limitations (Fig. 5b). This operating point thus represents the conventional approximately two-dimensional inlet condition commonly adopted in simplified linear-cascade studies. It also provides a useful baseline against which the effects induced by the bypass flow can be evaluated.

Activating the bypass at the moderate flow rate, corresponding to regime 10_10, produces a marked change in the flow topology (Fig. 6). The blowing air penetrates the axial stream immediately downstream of the blowing orifice and is progressively redirected towards the suction orifice in the upper downstream part of the section. The combined action of blowing and suction generates a diagonal region of relatively high mean velocity. In contrast, a broad region of low velocity and reversed axial flow develops near the bottom wall, occupying approximately the lower one-fifth of the test section height. The recirculation boundary is indicated in the corresponding figure (solid black line), and the mean streamlines reveal a coherent large-scale recirculating motion that extends downstream. The strongest fluctuation energy areas are not concentrated at the centre of the injection slot;

instead, they occur predominantly along the shear layer separating the bypass-dominated through-flow from

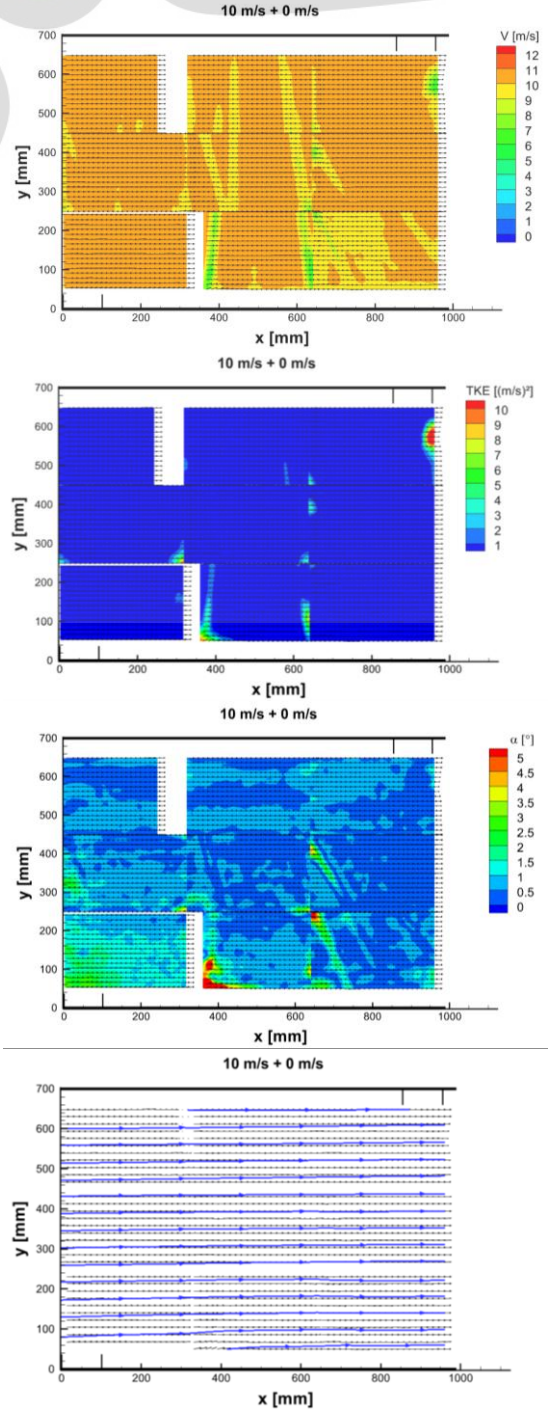


Fig. 5. The distribution of a) velocity magnitude b) turbulent kinetic energy c) the angle of radial flow component and d) velocity vector lines evaluated from time-averaged snapshots in the whole hybrid test section for reference case 10_0 (main tunnel set to 10 m/s, no bypass flow).

the recirculating region and locally near the suction orifice. This distribution is consistent with the strong velocity gradients that develop at the interface between the two flow regions. The mean flow direction in the through-flow region departs from the nominal axial direction by an angle of the order of 10°, demonstrating that a measurable spanwise component can be introduced over a substantial part of the section. A moderate increase in velocity is also observed towards the upper region corresponding to the blade tip. The coexistence of recirculation, flow deflection and spanwise redistribution makes this regime promising for reproducing selected qualitative features reported for LP steam turbines at reduced load [4-6].

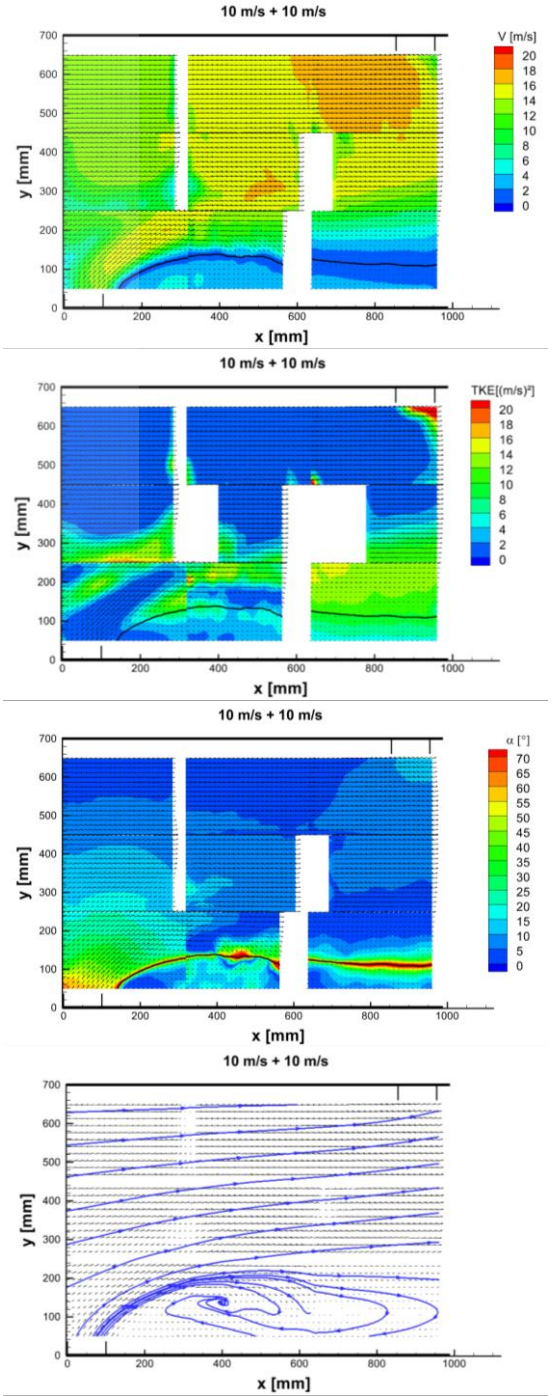
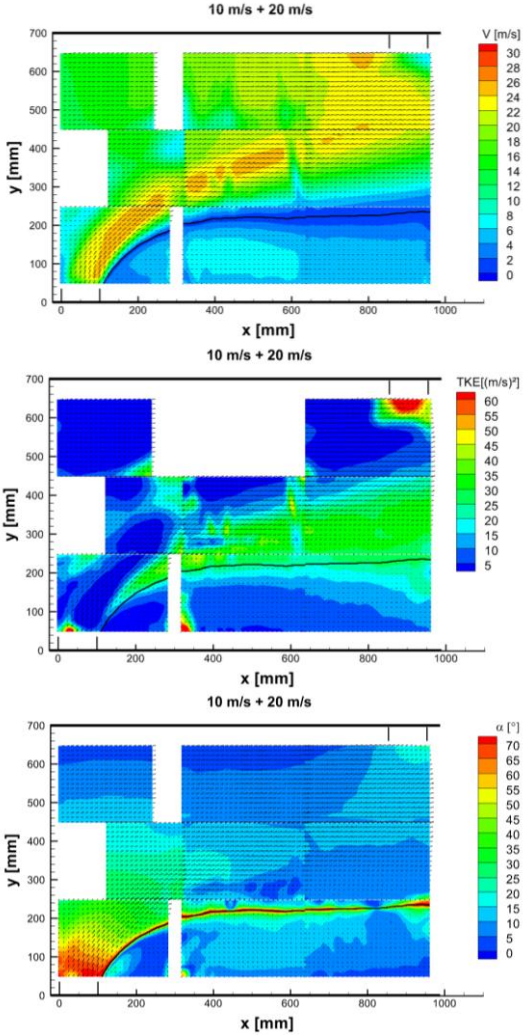


Fig. 6. The distribution of a) velocity magnitude b) turbulent kinetic energy c) the angle of radial flow component and d) velocity vector lines evaluated from time-averaged snapshots in the whole hybrid test section for reference case 10_10 (main tunnel set to 10 m/s, bypass to 10 m/s).

Further increasing the bypass slot velocity to about 20 m s^{-1} while keeping the nominal axial velocity at 10 m s^{-1} produces the strongly distorted flow illustrated in Fig. 7. The low velocity and backflow region expands to approximately one-third of the test section height, and its downstream extent becomes sufficiently large that the full recirculation structure is not entirely

contained within the observed field of view and is probably spread up to the area of axial ventilator. At the same time, the bypass-dominated flow occupies a larger fraction of the diagonal passage between the two orifices and produces pronounced velocity overspeed in the upper portion of the section. Local velocities in this region can exceed twice the nominal reference case velocity, indicating strong spanwise redistribution of momentum. The regions of higher fluctuation energy remain broadly associated with the boundary of the recirculation zone and the vicinity of the suction orifice. Their peak or representative levels are substantially higher than in the moderate bypass regime, with an increase of approximately a factor of three inferred from the reported distributions. The mean flow inclination also increases, reaching values of the order of 13° in the middle of the test section. Such a flow configuration qualitatively resembles more severe low-input conditions, for which extensive backflow zones and enhanced three-dimensional instability have been observed or predicted in LP turbine stages.



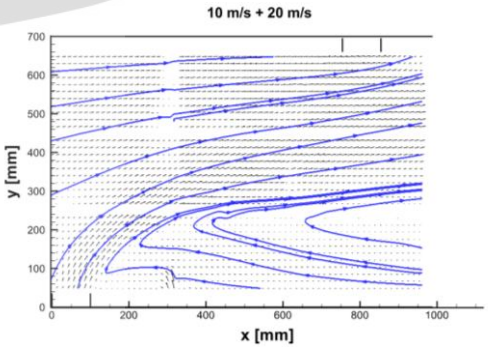
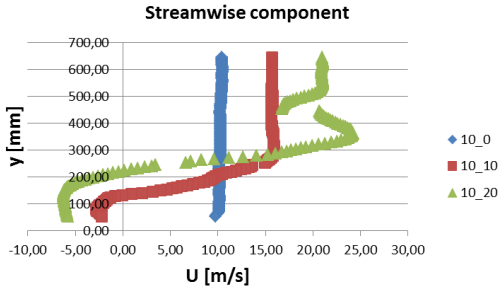
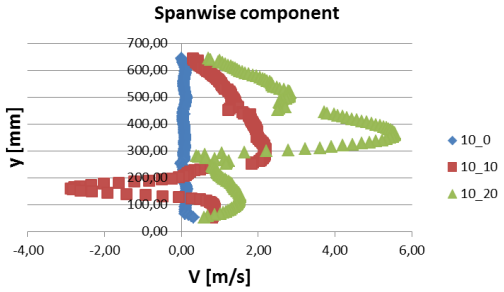


Fig. 7. The distribution of a) velocity magnitude b) turbulent kinetic energy c) the angle of radial flow component and d) velocity vector lines evaluated from time-averaged snapshots in the whole hybrid test section for reference case 10_20 (main tunnel set to 10 m/s, bypass to 20 m/s).

To compare the three regimes, profiles of axial and spanwise velocity, fluctuation energy and local flow inclination were extracted at x = 500 mm (Fig. 8). In the reference case, axial velocity is nearly uniform, while spanwise component and mean flow inclination remain small. The bypass flow introduces strong profile non-uniformity, including reduced or reversed axial velocity near the lower wall, increased spanwise flow and enhanced fluctuation activity. These effects are most pronounced in the 10_20 regime, which exhibits the broadest recirculation region and the greatest overspeed towards the upper wall. The profiles confirm that independent adjustment of these two regimes provides useful and reproducible operating settings for subsequent experiments on blade cascades exposed to off-design flow.





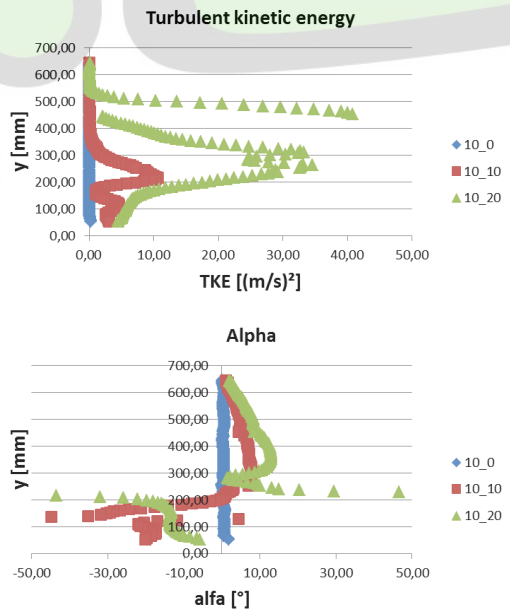


Fig. 8. Profiles extracted at x = 500 mm for regimes 10_0, 10_10 and 10_20: axial (streamwise) velocity component, spanwise velocity component, turbulent kinetic energy estimate and local flow inclination angle.

4 Conclusion

A hybrid wind tunnel test section combining a conventional axial flow wind tunnel with an independently driven bypass tunnel (suction and blowing) has been investigated experimentally by PIV and by hot-wire anemometry. The objective was to assess whether this arrangement can generate, in a controlled environment, the substantial spanwise flow deflection (radial component) and large-scale recirculation modelling selected low-load LP steam turbine flow patterns. Three representative operating regimes were compared at a fixed nominal main tunnel velocity of 10 m s^{-1}. The measurements demonstrate that the relative strength of the bypass flow governs the topology of the mean flow, the distribution of velocity magnitude and the location and intensity of fluctuating regions.

With the bypass inactive (10_0), the test section exhibits a predominantly uniform, approximately two-dimensional flow: the mean streamlines remain nearly horizontal, the span velocity component is small and the fluctuation activity is comparatively weak. At the moderate bypass setting (10_10), a distinct recirculation region develops along the lower wall and occupies approximately one-fifth of the section height. The principal through-flow is redirected diagonally towards the upper suction orifice, with a characteristic mean flow inclination of approximately 10°. A moderate local overspeed appears in the upper, blade tip region, while elevated fluctuation levels are concentrated mainly along the shear layer bordering the recirculation zone. This combination represents a promising laboratory approximation of several qualitative flow features expected in an LP turbine operating under reduced load conditions.

At the highest investigated bypass regime (10_20), the recirculation region expands to approximately one-third of the test section height and becomes extensive in the axial direction. The characteristic mean flow deflection increases to approximately 13°, while the fluctuation energy becomes markedly higher, by roughly a factor of three relative to the moderate regime. The overspeed velocities near the upper wall, in some regions exceeding twice the reference case velocity, indicate a substantial redistribution of flow towards the tip region. These features are consistent with a more severe low-input flow state, although this situation is not very likely on a real-world scale.

The results establish that the proposed bypass concept offers a practical means of continuously adjusting inlet-flow non-uniformity without changing the geometry of the main test section. In particular, the moderate regime appears suitable as an initial operating point for subsequent aeroelastic investigations, while the stronger regime provides a demanding limit case for studying the influence of extensive separation and high velocity gradients. Nevertheless, the present experiments characterize the empty test section flow only; they do not establish the aerodynamic damping or flutter threshold of a blade cascade. Future work should therefore include measurements with an installed, externally excited cascade, evaluation of unsteady blade loading and vibration response, and more detailed assessment of three-dimensionality, repeatability and measurement uncertainty. Such investigations will clarify how the observed recirculation and spanwise transport affect aeroelastic stability under off-design conditions.

Table . Summary of the experimentally investigated operating regimes, their characteristic flow-field features and implications for subsequent aeroelastic investigations.

Element	Style
Reference case (10_0)	Nearly uniform, predominantly two-dimensional flow with horizontal streamlines, negligible spanwise velocity and low fluctuation activity. Represents conventional flow conditions for linear blade-cascade experiments.
Moderate bypass flow (10_10)	A recirculation region occupies **20% of the test-section height**, accompanied by a flow deflection of approximately **10°**. Moderate velocity amplification occurs near the upper wall, with enhanced fluctuations concentrated along the recirculation shear layer. This regime provides a promising approximation of selected low-load steam turbine flow characteristics.

Strong bypass flow (10_20)	The recirculation region expands to approximately **33% of the test-section height**, while the characteristic flow inclination reaches **13°**. Fluctuation energy levels increase approximately threefold relative to the moderate regime, and local upper wall velocities exceed twice the reference velocity. This regime qualitatively represents more severe low-throughput conditions.
Overall experimental findings	The hybrid test section enables controlled generation of non-uniform flow fields featuring substantial spanwise transport, recirculation and adjustable velocity gradients. Independent bypass flow regulation provides flexibility for reproducing selected off-design flow characteristics.
Implications and future research	The moderate regime is a suitable starting point for subsequent blade cascade investigations, while the strong bypass regime provides a more demanding condition. Future experiments should investigate unsteady aerodynamic loading, blade vibrations and aerodynamic damping to establish the relationship between the observed flow structures and aeroelastic stability.

The Acknowledgements
This research was supported by the project of Czech Science Foundation No. 24-12144S "Investigation of 3D flow structures and their effects on aeroelastic stability of turbine-blade cascades using experiment and deep learning approach" and by institutional support RVO61388998.

References

Journal articles and proceedings

1. H. Försching, "Aeroelastic stability of cascades in turbomachinery," Progress in Aerospace Sciences, vol. 30, no. 3, pp. 213–266, 1994. https://doi.org/10.1016/0376-0421(94)90004-3.
2. P. Procházka, V. Vlček, P. Šidlof, "Preliminary evaluation of interferometry measurements of the flow field in the vicinity of a self-excited single profile", : EPJ Web Conf., EDP Sci. (2022) 01049. https://doi.org/10.1051/epjconf/202226901049
3. P. Procházka, S. Chindada, P. Šnábl, V. Uruba, C. S. Prasad, L. Pešek et al., "The broad study of blade cascade under controlled torsional flutter: Dynamics of the flow and stability analysis," European Journal of Mechanics – B/Fluids, vol. 109, pp. 66–79, 2025. https://doi.org/10.1016/j.euromechflu.2024.08.006
4. R. Sigg, C. Heinz, M. V. Casey and N. Sürken, "Numerical and experimental investigation of a low-pressure steam turbine during windage," Proceedings of the Institution of Mechanical Engineers, Part A: Journal of Power and Energy, vol. 223, no. 6, pp. 697–708, 2009. https://doi.org/10.1243/09576509JPE826
5. A. Mambro, F. Congiu, E. Galloni and L. Canale, "Experimental study and modelling of the ventilation power and maximum temperature of low-pressure steam turbine last stages at low load," Applied Energy, vol. 241, pp. 59–72, 2019. https://doi.org/10.1016/j.apenergy.2019.03.003
6. P. Hu, T. Lin, R. Yang, X. Zhu and Z. Du, "Numerical investigation on flow instabilities in low-pressure steam turbine last stage under different low-load conditions," Proceedings of the Institution of Mechanical Engineers, Part A: Journal of Power and Energy, vol. 235, no. 6, pp. 1544–1562, 2021. https://doi.org/10.1177/0957650921997199
7. P. Antoš, "Development of Temperature Fluctuation in a 2D Shear Turbulent Flow", 32. stretnutie katedier mechaniky tekutín a termomechaniky, 2014, Conference proceeding pp. 1-4
8. J. Wang, Ch. Jiang, X. Zhou, J. Kang, S. Yu and G. Bai, "Experimental Study on Flow Characteristics of Jet Ventilation in Crossflow in Confined Mine Spaces", Scientific Reports, Vol. 14, No. 8022, 2024. https://doi.org/10.1038/s41598-024-58267-5
9. X. He, D. R. Williams and S.T.M. Dawson, "Transverse gust generation in a wind tunnel: a suction-driven approach", Experiments in Fluids, Vol. 63, No. 125, 2022. https://doi.org/10.1007/s00348-022-03484-9

Comparison of correlations for liquid density of aqueous binary mixtures with selected salts

Rajkumar Sarma[1,*], *Monika* Součková[1], *Olga* Prokopová[1], *Miroslav* Černský[1], *Aleš* Blahut[1], and *Václav* Vinš[1,**]

[1]Institute of Thermomechanics of the CAS, Dolejškova 1402/5, 182 00 Prague 8, Czech Republic

Abstract. A comprehensive analysis of the liquid density of binary aqueous solutions with NaCl, $CaCl_2$, KCl, and $(NH_4)_2SO_4$ is performed using established density correlations by Novotný and Söhnel (1988), Laliberté and Cooper (2004), Mao and Duan (2008), and Clegg and Wexler (2011). Model predictions are compared with experimental data from the literature as well as own measurements carried out in this study using the vibrating tube densimeter and a single-sinker buoyancy method. The extrapolation behavior of the density correlations is studied from 100 °C down to the subzero temperature region of −20 °C. Overall, the results show good agreement between the predicted densities and the experimental values within the established ranges of the correlations. However, the differences between individual models become pronounced at subzero temperatures and higher concentrations. Further experimental measurements at subzero temperatures are therefore necessary to improve model parameterization and density predictions.

1 Introduction

The density of liquid electrolytes is a fundamental thermophysical property relevant to both science and engineering, including physical chemistry, environmental science, chemical engineering, and electrochemical energy storage systems. For such systems, density can vary with temperature, concentration, and pressure of the solution. Depending on the solute-solvent interaction (i.e., the interplay between dissolved ions and solvent molecules), the variation of this thermodynamic quantity can be different for different electrolyte systems [1, 2]. Measurement of density, therefore, yields valuable information about the hydration of dissolved ions and the structural changes induced in the solvent [3]. Since water exhibits an unusual temperature dependence of density (with a maximum at approximately 4 °C under atmospheric pressure), its effect is also expected in aqueous solutions, particularly in the low-temperature region of dilute solutions. This, together with the possibility of phase change, thus demands special attention to the investigation of solution density at subzero temperatures. Such investigations are relevant to cold-environment applications and are also valuable for developing predictive density models.

Over the years, a number of correlations have been reported in the literature for estimating the density of single- and multicomponent electrolyte systems. Of these, the Pitzer model [4], developed in the 1970s, is the most extensively used density correlation. This equation is derived from the Debye-Hückel model and can accurately estimate the density of multielectrolyte solutions up to saturation concentration. A number of modifications to the Pitzer model have also been proposed. This includes the work of Archer [5], Pérez-Villaseñor et al. [6], and Rard and Wijesinghe [7]. More recently, Mao and Duan [8] extended the Pitzer correlation to include pressure as a model parameter, whereas Clegg and Wexler [9] presented a modification to estimate density at subzero temperatures. A few empirical correlations are also available to predict the density of electrolyte solutions. Notably, this includes the models of Novotný and Söhnel [10] and Laliberté and Cooper [11]. Although these empirical correlations lack thermodynamic modelling, they are often much simpler, omitting the Debye-Hückel term, and remain accurate over a wide range of temperatures and concentrations.

In this study, we analyze the density variation of aqueous NaCl, $(NH_4)_2SO_4$, $CaCl_2$, and KCl solutions following a combined theoretical and experimental approach. The above mentioned salts are widely encountered in seawater, industrial processes, fertilizers, electrochemical systems and in case of $(NH_4)_2SO_4$ also in atmospheric research. For these salt solutions, we compare the density predicted by the available correlations with the experimental data sets and study their extrapolation behavior down to the subzero temperatures. It will be shown that this kind of comparative analysis can serve as a basis for evaluating the limitations of existing models and identifying the areas where additional experiments are required.

2 Models for density of aqueous electrolytes

We primarily focus on the density models pertinent to the salts of our interest, namely aqueous solutions of sodium chloride – NaCl, ammonium sulfate – $(NH_4)_2SO_4$, calcium chloride – $CaCl_2$, and potassium chloride – KCl.

*e-mail: sarma@it.cas.cz
**e-mail: vins@it.cas.cz

Among the models reviewed, the Novotný and Söhnel [10] and Laliberté and Cooper [11] models are the only ones capable of describing density variations across all selected electrolyte solutions. On the other hand, the Mao and Duan [8] model predicts the density of NaCl, $CaCl_2$, and KCl solutions, whereas the Clegg and Wexler [9] correlation estimates for NaCl and $(NH_4)_2SO_4$ solutions. Below, we briefly discuss the selected density models.

2.1 Novotný and Söhnel (1988)

Novotný and Söhnel [10] introduced a model in 1988 (hereafter abbreviated as the N&S model) that describes the density of a broad spectrum of binary aqueous mixtures as a function of temperature t (in °C) and solute concentration c (in mol/dm^3). Denoting the mixture density by ρ_{mix} (in kg/m^3) and pure water density by ρ_{w} (in kg/m^3), the correlation reads

$$\rho_{\text{mix}} = \rho_{\text{w}} + Ac + Bct + Cct^2 + Dc^{3/2} + Ec^{3/2}t + Fc^{3/2}t^2 \,, \quad (1)$$

where A to F are fitted model parameters. For the salt solutions under considerations, the N&S model holds good within 0 – 100 °C and up to the saturation concentration, i.e. the conditions under which the salt begins to crystallize in a liquid solution. In the original work [10], the water density at 0.1 MPa was obtained from a simple empirical correlation. However, with the aim of extrapolating the results to subzero temperatures, we use the IAPWS-95 [12] equation of state to compute the pure water density in the current work for all selected electrolyte solutions.

2.2 Laliberté and Cooper (2004)

Laliberté and Cooper [11] developed an empirical model (abbreviated afterwards as the L&C model) for predicting the density of aqueous solutions containing chloride and sulphate salts of a broad range of common metal cations. The model calculates the mixture density ρ_{mix} in terms of the specific volume of the electrolyte $\overline{V}_{\text{app}}$ (in m^3/kg), through the relationship $\rho_{\text{mix}} = 1/(\text{wt}_{\text{w}}\overline{V}_{\text{w}} + \text{wt}\overline{V}_{\text{app}})$, where wt_{w} and wt stand for the weight fractions of water and solute, respectively, and $\overline{V}_{\text{w}}$ (in m^3/kg) denotes the specific volume of water. For calculating the water density $\rho_{\text{w}}(= 1/\overline{V}_{\text{w}})$, L&C used the temperature correlation by Kell [13], which is consistent with the IAPWS-95 equation considered in this work. $\overline{V}_{\text{app}}$ is defined by the following empirical correlation

$$\overline{V}_{\text{app}}(t, \text{wt}) = \frac{\text{wt} + c_2 + c_3 t}{(c_0\text{wt} + c_1)\, \text{e}^{10^{-6}(t+c_4)^2}} \,, \quad (2)$$

with c_0 to c_4 as the empirical constants.

In terms of its applicability, the L&C model can predict the mixture density within the temperature range 0 – 100 °C up to the saturation concentration. We analyze the extrapolation behavior of the model to subzero temperatures employing the IAPWS-95 correlation. An important distinction between the N&S and the L&C model is that, while the N&S model is derived on mole-based concentration unit (molarity), the L&C model uses mass-based unit (weight fraction), a more practical unit for engineers.

2.3 Mao and Duan (2008)

Both N&S and L&C models estimate the density of salt solutions at atmospheric pressure (sea level). In 2008, Mao and Duan [8] proposed a model (abbreviated as the M&D model afterwards) that overcomes this limitation and predicts ρ_{mix} as a function of pressure P (in MPa), temperature T (in K) and concentration m (in molality) over a broad range of binary aqueous chloride solutions. This semi-empirical model is structurally similar to the Rogers and Pitzer model [14] and predicts density using 23 fitted parameters. It expresses density through the apparent molar volume of the solute V_ϕ (in cm^3/mol) in a pure aqueous solution, defined by

$$V_\phi = V_\phi^o + \nu|z_+z_-|A_V h(I) + 2\nu_+\nu_- mRT(B_V + \nu_+ Z_+ mC_V). \quad (3)$$

In Eq. (3), V_ϕ^o is the apparent molar volume of the solution at infinite dilution, m is the molality, ν_+ and ν_- are the number of cations and anions per formula unit of dissolved salts, $\nu = \nu_+ + \nu_-$, and z_+, z_- are the charges of cations and anions, respectively. Furthermore, $h(I) = \log(1 + b\sqrt{I})/2b$ where I is the molal ionic strength, $b = 1.2(\text{kg/mol})^{0.5}$, and $R = 8.314472\,\text{cm}^3 \cdot \text{MPa}/(\text{mol} \cdot \text{K}) = 8.314472\,\text{J}/(\text{mol} \cdot \text{K})$ is the universal gas constant. A_V stands for molal Debye-Hückel constant. B_V and C_V are the second and third virial coefficients, respectively, and are functions of temperature. V_ϕ is related to ρ_{mix} by the equation

$$\rho_{\text{mix}} = \frac{(1000 + mM_s)\,\rho_{\text{w}}}{1000 + mV_\phi\,\rho_{\text{w}}} \,, \quad (4)$$

where M_s is the molar mass (in g/mol) of the electrolyte, and ρ_{w} (in g/cm^3) is the density of water. In their work, Mao and Duan calculated the water density considering the IAPWS-97 model [15], which was developed from the scientific equation of state IAPWS-95 [12]. For an aqueous NaCl solution, the M&D model is applicable within the temperature range (273 – 573) K and pressure range (0.1 – 100) MPa for concentrations up to 6.0 molality. On the other hand, for KCl and $CaCl_2$ solutions, the relevant T, P, m ranges are ((273 – 543) K, (0.1 – 50) MPa, and (0 – 4.5) molality) and ((273 – 523) K, (0.1 – 60) MPa, and (0 – 6.0) molality), respectively.

2.4 Clegg and Wexler (2011)

More recently, in 2011, Clegg and Wexler [9] (abbreviated hereafter as the C&W model) proposed a model to estimate the density of a few atmospherically important electrolyte solutions, including aqueous NaCl and $(NH_4)_2SO_4$ solutions. While the models discussed before are derived only for $t > 0$ °C and concentrations up to the saturation point, the C&W model aims to overcome this barrier by predicting the solution density at subzero

temperatures and concentrations up to pure-liquid electrolytes (i.e., melt). This is achieved by defining separate correlations on the basis of temperature and concentration of the solution, namely (a) subsaturated aqueous solutions above 0 °C, (b) aqueous solutions below 0 °C, (c) solution at a reference concentration (for aqueous NaCl and $(NH_4)_2SO_4$ solution, this reference concentration is the saturation concentration), and (d) concentrated solutions (i.e., solutions above reference concentration). Since our primary focus is on subsaturated electrolyte solutions, we discuss here density correlations only for the first two regimes.

(a) *Subsaturated solutions above* 0 °C

In this regime, the C&W model is analogous to the M&D model with V_ϕ defined by

$$V_\phi = V_\phi^o + \nu|z_+z_-|A_V h(I) + \mathrm{wt}^{0.5}C_1(T) + \mathrm{wt}^{0.75}C_2(T) + \mathrm{wt}\,C_3(T) + \mathrm{wt}^{1.5}C_4(T) + \mathrm{wt}^2C_5(T) + \mathrm{wt}^{2.5}C_6(T) + \mathrm{wt}^3C_7(T) + \mathrm{wt}^{3.5}C_8(T)\,, \quad (5)$$

where C_1 to C_8 are fitted parameters. V_ϕ is substituted in Eq. (4) to compute ρ_{mix} in the same way as in the M&D model.

(b) *Solutions below* 0 °C

For $T \leq 273.15$ K and concentrations lower than the reference concentration, V_ϕ is given by

$$V_\phi = V_\phi(extr., m, T) + Y_{\mathrm{N}}(m)[V_\phi(extr., m^*, T, \rho^*) - V_\phi(extr., m^*, T)], \quad (6)$$

where $V_\phi(extr., m, T)$ is the extrapolated apparent molar volume and m^* is the reference concentration. We note that the extrapolated correlation for V_ϕ defined in [9] appears to be inaccurate. The appropriate form of the correlation is (neglecting the higher order terms)

$$V_\phi(extr., m, T) = V_\phi\big|_{(m,T_r)} + \left.\frac{dV_\phi}{dT}\right|_{(m,T_r)}(T - T_r) + \frac{1}{2!}\left.\frac{d^2V_\phi}{dT^2}\right|_{(m,T_r)}(T - T_r)^2\,, \quad (7)$$

where $T_r = 298.15$ K. In Eq. (6), $Y_{\mathrm{N}}(m) = Y_m/Y_{m^*}$, with $Y_m = E_1 + E_2(m/m^*) + E_3(m/m^*)^{1.5} + E_4(m/m^*)^2 + E_5(m/m^*)^{0.5} + E_6(m/m^*)^{2.5} + E_7(m/m^*)^3 + E_8(m/m^*)^{3.5} + E_9(m/m^*)^4$. While $V_\phi(extr., m^*, T)$ can be directly calculated from Eq. (7), $V_\phi(extr., m^*, T, \rho^*)$ is estimated using Eq. (7) with V_ϕ and its derivatives calculated from $\rho^* = D_0 + D_1T + D_2T^{1.5} + D_3T^2 + D_4T^{2.5} + D_5T^{2.75} + D_6T^3$, where D_1 to D_6 are fitted coefficients defined in [9].

In their original work, Clegg and Wexler employed the Kell correlation [13] to calculate the density of water. In the present study, however, we stick to the IAPWS-95 formulation to estimate water density, as mentioned above.

3 Own experimental data of liquid density

3.1 Vibrating tube densimeter

A commercial vibrating tube densimeter (VTD) Anton Paar DMA 5000 M [16] was used to collected the density data at 0.1 MPa for binary aqueous mixtures with NaCl and $(NH_4)_2SO_4$ in the temperature range from 0 to 90 °C. The instrument calibrated using accurate measurements with dry air and ultrapure water achieves the expanded uncertainty (with $k = 2$) of the liquid density better than 0.072 kg/m^3 in case of NaCl and 0.061 kg/m^3 in case of $(NH_4)_2SO_4$ mixtures. Own calibration technique was used for the data evaluation [17].

3.2 Comparative buoyancy measurement

In addition, comparative experiments based on the single-sinker buoyancy technique were carried out with densimeter Krüss K100Mk2. The measuring principle is based on an accurate weighing of a single-crystal silicon in air and entirely submerged in the liquid sample. The experiments should be considered only as comparative due to rather high expanded uncertainty of around 0.8 kg/m^3 [18]. The buoyancy measurements are approximately ten times less accurate than the VTD. The density data were collected from 0 °C to 66 °C and to 30 °C in case NaCl and $(NH_4)_2SO_4$, respectively.

4 Comparison of liquid density

In this section, we investigate the density variations of aqueous NaCl, $(NH_4)_2SO_4$, $CaCl_2$, and KCl solutions using the models discussed above.

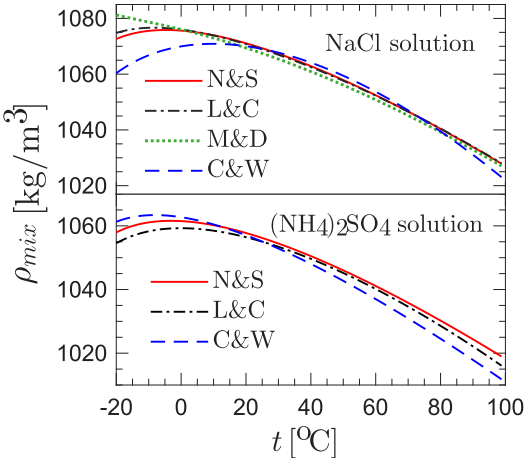


Figure 1. Density variation of aqueous NaCl (top panel) and $(NH_4)_2SO_4$ (bottom panel) solution with temperature. Results are computed for salt concentration of 10 wt % and extrapolated to subzero temperatures utilizing Novotný & Söhnel (1988), Laliberté & Cooper (2004), Mao & Duan (2008), and Clegg & Wexler (2011) models. All densities are estimated at 0.1 MPa pressure.

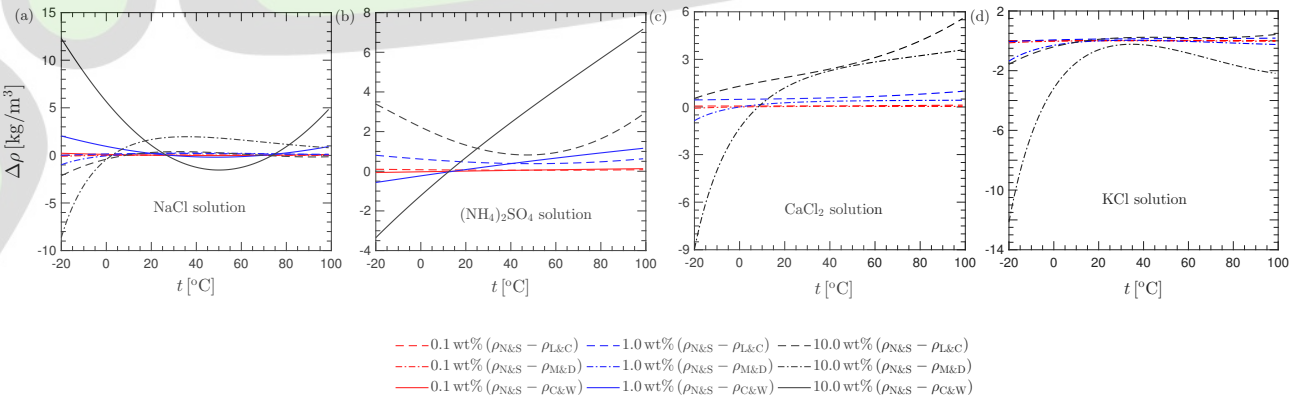


Figure 2. Deviation of density predicted by L&C, M&D and C&W models from the N&S model across a range of temperatures. Comparison is made for aqueous solutions of (a) NaCl, (b) $(NH_4)_2SO_4$, (c) $CaCl_2$, and (d) KCl at concentrations 0.1 wt %, 1.0 wt % and 10.0 wt %. All comparisons are made at 0.1 MPa.

Figure 1 illustrate the density variation as a function of temperature for 10 wt % concentrated solutions of NaCl and $(NH_4)_2SO_4$, respectively. Note that, while all four models predict the density of NaCl solution, the M&D model does not include the salt $(NH_4)_2SO_4$. Both subplots further demonstrate the model performance at subzero temperatures down to $t = -20\,^{\circ}C$. The top panel of Fig. 1 shows that, for the NaCl solution, there is fair agreement among the models for $t > 20\,^{\circ}C$. However, as one moves towards the low-temperature region, this agreement fades. At subzero temperatures, the C&W model underpredicts the density, whereas the M&D model slightly overpredicts it. Consequently, the density maximum predicted by these two models differs from that of the N&S and L&C models. On the other hand, for the $(NH_4)_2SO_4$ solution, the bottom panel of Fig. 1 shows that the C&W model overpredicts the density at subzero temperatures but underpredicts it at higher temperatures compared to the predictions of N&S and L&C models.

To better analyze the differences in density predictions among individual models, Fig. 2 presents the temperature dependence of $\Delta\rho$ for each electrolyte solution at three different concentration levels (viz., 0.1 wt %, 1 wt %, and 10 wt %). Here we have considered the N&S model as the reference, and $\Delta\rho$ is the difference in density estimation between this model and the others. We found that for the N&S model [10], the fitted coefficients reported for $CaCl_2$ are inaccurate. The parameters are therefore refitted using experimental data [19–27], yielding $A = 98.19952672$, $B = -0.08741106$, $C = 0.001424866$, $D = -8.426282971$, $E = 0.01046492$, and $F = -0.000374113$. Figures 2(a-d) demonstrate that at lower concentrations of each solution, the differences among the individual models remain relatively small, indicating a good agreement between their predictions. However, as one moves towards the regime of higher concentration, $\Delta\rho$ become more pronounced, in particular, in the subzero temperature regime. It is important to note that, with the exception of the C&W model, which employs an extrapolation method to estimate solution density at subzero temperatures, the other models are originally developed for temperatures above $0\,^{\circ}C$. These observations highlight the need for further refinement of the model parameters using experimental density data at subzero temperatures to improve the accuracy of density predictions.

Figure 3 depicts the density difference between the prediction of the N&S model and the experimental data as a function of salt concentration for each solution. For this purpose, we use the density data reported in the literature as well as our own measurement data with methodology detailed in Sec. 3. Each plot also shows the difference in density estimated by the N&S and the other models at varying concentrations. All estimations are made at $t = 25\,^{\circ}C$.

Of all the electrolytes we are analyzing, the aqueous NaCl solution is the most well-studied system experimentally. A large number of studies have been reported in the literature [23, 28–42] across a wide range of pressures, temperatures and concentrations for this system. However, here we select only the studies [23, 29–35, 42] for which the density models remain applicable at the reference temperature of $25\,^{\circ}C$. For the NaCl solution, it is found that, except for the data sets [30, 31, 33, 42], the other data points remain consistent with each other over the chosen concentration range. Therefore, all but [30, 31, 33, 42] are included for our comparison. Results plotted in Fig. 3(a) demonstrate that, except for the M&D model, which slightly underpredicts density at higher concentrations, the predictions of remaining models agree well with the reported experimental data as well as with our own measurements.

For the aqueous $(NH_4)_2SO_4$ solution, relevant experimental studies within the temperature and concentration ranges of our interest include the work of Goldsack and Franchetto [43], Albright et al. [44], Semmler et al. [45], Hervello and Sanchez [46] and Wang et al. [47]. Among these, the data points from [47] aside, the remaining datasets show good mutual consistency. The compari-

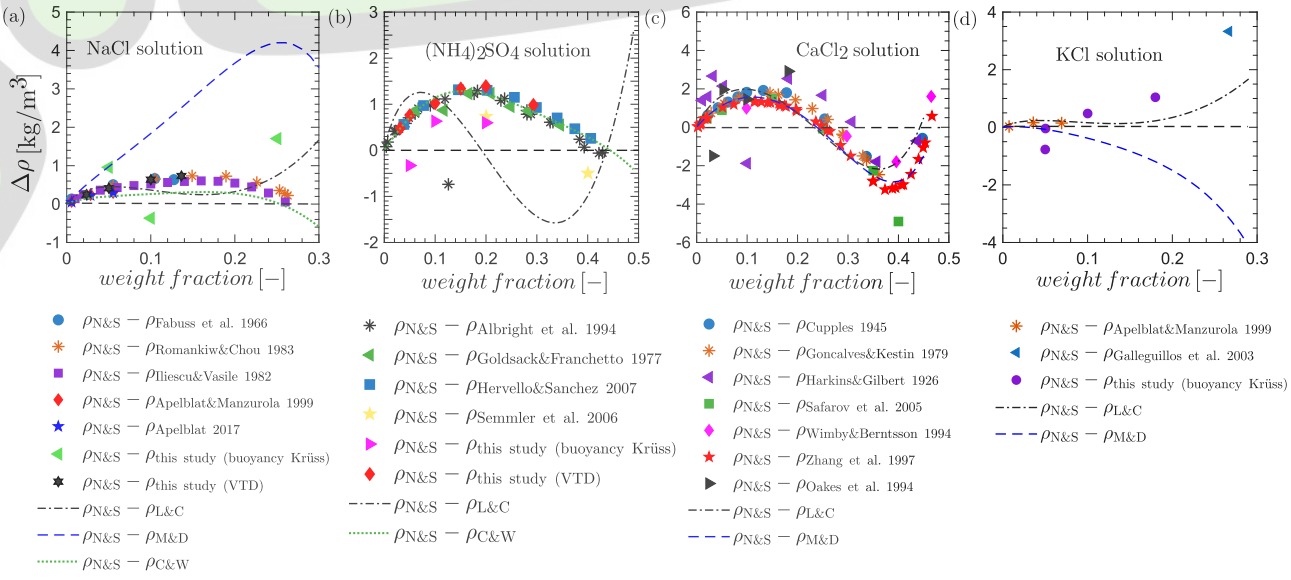


Figure 3. Comparison of the density deviations predicted by the N&S model from experimental data for aqueous solutions of (a) NaCl, (b) $(NH_4)_2SO_4$, (c) $CaCl_2$, and (d) KCl at 25 °C. For each electrolyte, the N&S model is further compared with other density models over a range of concentrations. All calculations are made at 0.1 MPa. The reference model N&S was introduced in 1988, well before the measurements of a few experimental datasets included for comparison.

son made in Fig. 3(b) shows that the N&S and C&W models exhibit close agreement with the experimental measurements. In contrast, the L&C model shows a relatively larger deviations from the experimental data, indicating poor agreement with other models over the considered concentration range.

A considerable number of experimental studies have also been reported in the literature on the density of aqueous $CaCl_2$ solutions [19–21, 23–26, 48]. With the exception of the data reported in [23], the available datasets are, in general, consistent with one another. As illustrated in Fig. 3(c), the L&C and M&D models predict density values that closely agree with the experimental measurements. However, the predictions of the N&S model exhibit noticeable deviations from the experimental data over the concentration range considered.

Compared with the electrolyte solutions discussed so far in this study, experimental density data for aqueous KCl solutions are relatively scarce. Among the available studies [34, 42, 49], all datasets, except those reported in [42], show good consistency with one another. The comparison plot in Fig. 3(d) reveals that the predictions of all models agree reasonably well with the experimental measurements in the low-concentration regime. However, the experimental data in the high concentration regime are limited, making it difficult to assess the model performance in this region conclusively. Within the available data points in the high-concentration range, the L&C model tends to underpredict density, whereas the M&D model generally overpredicts the values.

5 Conclusions

We compared the performance of existing density models for aqueous solutions of NaCl, $(NH_4)_2SO_4$, $CaCl_2$, and KCl over a broad range of concentrations and temperatures. Using the IAPWS-95 formulation to calculate water density and, where needed, implementing model corrections, the density prediction is extrapolated to subzero temperatures. For the electrolyte solutions considered, the model predictions are, in general, consistent with the experimental data reported in the literature and our own measurements. However, the agreement deteriorates under subzero temperatures, in particular, at higher electrolyte concentrations. This disagreement may be due to the fact that, with the exception of C&W model, the parameters of other models were originally fitted using experimental data above 0 °C. This can lead to larger deviations when extrapolated to subzero temperatures, especially at elevated concentrations. These findings highlight the need for further refitting of the model parameters using experimental data obtained at subzero temperatures to improve the accuracy of density predictions.

Acknowledgements

The study was supported by the Czech Science Foundation grant no. GF24-10191K and the institutional support RVO:61388998.

References

[1] A. Anderko, P. Wang, M. Rafal, Electrolyte solutions: from thermodynamic and transport prop-

erty models to the simulation of industrial processes, Fluid Phase Equilibria **194-197**, 123 (2002). 10.1016/s0378-3812(01)00645-8

[2] Y. Marcus, The standard partial molar volumes of ions in solution. part 4. ionic volumes in water at 0-100 °C, The Journal of Physical Chemistry B **113**, 10285 (2009). 10.1021/jp9027244

[3] O.R. Daspit, M.A. Grabill, A.E. Baker, A.E. Jipping, A. Stonehouse, L. Imanzi, E.D. Mensah, R.S. Tatko, N.K. Addo, A. Halteman et al., Solvation ion volumes from solution densities, Inorganic Chemistry **65**, 7773 (2026). 10.1021/acs.inorgchem.5c05999

[4] K.S. Pitzer, Thermodynamics of electrolytes. i. theoretical basis and general equations, The Journal of Physical Chemistry **77**, 268 (1973). 10.1021/j100621a026

[5] D.G. Archer, Thermodynamic properties of the NaCl+H2O system II thermodynamic properties of NaCl(aq), NaCl·2H2O(cr), and phase equilibria, Journal of Physical and Chemical Reference Data **21**, 793 (1992). 10.1063/1.555915

[6] F. Pérez-Villaseñor, M.L. Bedolla-Hernández, G.A. Iglesias-Silva, Osmotic and activity coefficients of 1:1, 1:3, 1:4, 2:1, 2:2, 3:1, 3:2 and 4:1 strong electrolytes at 298.15 k using a modified pitzer equation, Industrial & Engineering Chemistry Research **46**, 6366 (2007). 10.1021/ie070228w

[7] J.A. Rard, A.M. Wijesinghe, Conversion of parameters between different variants of pitzer's ion-interaction model, both with and without ionic strength dependent higher-order terms, The Journal of Chemical Thermodynamics **35**, 439 (2003). 10.1016/s0021-9614(02)00377-4

[8] S. Mao, Z. Duan, The P,V,T,x properties of binary aqueous chloride solutions up to T = 573 K and 100 MPa, J. Chem. Thermodynamics **40**, 1046 (2008).

[9] S.L. Clegg, A.S. Wexler, Densities and apparent molar volumes of atmospherically important electrolyte solutions. 1. The solutes H_2SO_4, HNO_3, HCl, Na_2SO_4, $NaNO_3$, NaCl, $(NH_4)_2SO_4$, NH_4NO_3, and NH_4Cl from 0 to 50 °C, including extrapolations to very low temperature and to the pure liquid state, and $NaHSO_4$, NaOH, and NH_3 at 25 °C, J. Phys. Chem. A **115**, 3393 (2011).

[10] P. Novotný, O. Söhnel, Densities of binary aqueous solutions of 306 inorganic substances, J. Chem. Eng. Data **33**, 49 (1988).

[11] M. Laliberté, W.E. Cooper, Model for calculating the density of aqueous electrolyte solutions, J. Chem. Eng. Data **49**, 1141 (2004).

[12] W. Wagner, A. Pruss, The IAPWS formulation 1995 for the thermodynamic propertiesof ordinary water substance for general and scientific use, J. Phys. Chem. Ref. Data **31**, 387 (2002).

[13] G.S. Kell, Thermal expansitivity, and compressibilityof liquid water from 0 to 150 °C: Correlations and tables for atmospheric pressure and saturation reviewed and expressed on 1968 temperature scale, J. Chem. Eng. Data **20**, 97 (1975).

[14] P.S.Z. Rogers, K.S. Pitzer, Volumetric properties of aqueous sodium chloride solutions, Journal of Physical and Chemical Reference Data **11**, 15 (1982). 10.1063/1.555660

[15] W. Wagner, J.R. Cooper, A. Dittmann, J. Kijima, H.J. Kretzschmar, A. Kruse, R. Mareš, K. Oguchi, H. Sato, I. Sto¨cker et al., The iapws industrial formulation 1997 for the thermodynamic properties of water and steam, Journal of Engineering for Gas Turbines and Power **122**, 150 (2000). 10.1115/1.483186

[16] Anton Paar GmbH, Reference Guide DMA 4100 M, DMA 4500 M, DMA 5000 M, document no. XDLIB016EN-E, Graz, Austria (2018)

[17] O. Prokopová, A. Blahut, M. Čenský, M. Součková, V. Vinš, Comments on temperature calibration and uncertainty estimate of the vibrating tube densimeter operated at atmospheric pressure, J. Chem. Thermodyn. **173**, 106855 (2022).

[18] V. Vinš, M. Součková, O. Prokopová, M. Čenský, J. Hrubý, A. Blahut, Density and surface tension of water + ethylene glycol mixtures as key components of heat transfer liquids, Int. J. Refrig. **171**, 191 (2025).

[19] H.L. Cupples, The surface tensions of calcium chloride solutions at 25 ° measured by their maximum bubble pressures, Journal of the American Chemical Society **67**, 987 (1945). 10.1021/ja01222a030

[20] F.A. Gonçalves, J. Kestin, The viscosity of $cacl_2$ solutions in the range 20 – 50 °C, Berichte der Bunsengesellschaft für physikalische Chemie **83**, 24 (1979). 10.1002/bbpc.19790830105

[21] W.D. Harkins, E.C. Gilbert, The structure of films of water on salt solutions. ii. the surface tension of calcium chloride solutions at 25 °, Journal of the American Chemical Society **48**, 604 (1926). 10.1021/ja01414a008

[22] W.R. Harrison, E.P. Perman, Vapour pressure and heat of dilution of aqueous solutions, Transactions of the Faraday Society **23**, 1 (1927). 10.1039/tf9272300001

[23] L.A. Romankiw, I.M. Chou, Densities of aqueous sodium chloride, potassium chloride, magnesium chloride, and calcium chloride binary solutions in the concentration range 0.5 – 6.1 m at 25, 30, 35, 40, and 45 °C, Journal of Chemical & Engineering Data **28**, 300 (1983). 10.1021/je00033a005

[24] J.M. Wimby, T.S. Berntsson, Viscosity and density of aqueous solutions of lithium bromide, lithium chloride, zinc bromide, calcium chloride and lithium nitrate. 1. single salt solutions, Journal of Chemical & Engineering Data **39**, 68 (1994). 10.1021/je00013a019

[25] H.L. Zhang, G.H. Chen, S.J. Han, Viscosity and density of h_2o + nacl + $cacl_2$ and h_2o + kcl + $cacl_2$ at 298.15 k, Journal of Chemical & Engineering Data **42**, 526 (1997). 10.1021/je9602733

[26] C.S. Oakes, R.J. Bodnar, J.M. Simonson, K.S. Pitzer, Critical and supercritical properties for 0.3 to 3.0 mol · kg^{-1} $CaCl_2$(aq), Geochimica et Cosmochimica Acta **58**, 2421 (1994). 10.1016/0016-7037(94)90021-3

[27] E.P. Perman, W.D. Urry, The compressibility of aqueous solutions, Proceedings of the Royal Society of London. Series A **126**, 44 (1929). 10.1098/rspa.1929.0204

[28] L.M. Connaughton, J.P. Hershey, F.J. Millero, Pvt properties of concentrated aqueous electrolytes: V. densities and apparent molal volumes of the four major sea salts from dilute solution to saturation and from 0 to 100 °C, Journal of Solution Chemistry **15**, 989 (1986). 10.1007/bf00645194

[29] B.M. Fabuss, A. Korosi, A.K.M.S. Huq, Densities of binary and ternary aqueous solutions of nacl, na_2so_4 and $mgso_4$ of sea waters, and sea water concentrates, Journal of Chemical & Engineering Data **11**, 325 (1966). 10.1021/je60030a010

[30] J.A. Gates, R.H. Wood, Densities of aqueous solutions of sodium chloride, magnesium chloride, potassium chloride, sodium bromide, lithium chloride, and calcium chloride from 0.05 to 5.0 mol · kg^{-1} and 0.1013 to 40 MPa at 298.15 K, Journal of Chemical & Engineering Data **30**, 44 (1985). 10.1021/je00039a015

[31] C.T.A. Chen, J.H. Chen, F.J. Millero, Densities of sodium chloride, magnesium chloride, sodium sulfate, and magnesium sulfate aqueous solutions at 1 atm from 0 to 50.degree.c and from 0.001 to 1.5 m, Journal of Chemical & Engineering Data **25**, 307 (1980). 10.1021/je60087a013

[32] G.M. Iliescu, C. Vasile, Caracteristici termofizice ale produselor alimentare (Romania, 1982)

[33] A.L. Surdo, E.M. Alzola, F.J. Millero, The (p, v, t) properties of concentrated aqueous electrolytes i. densities and apparent molar volumes of NaCl, Na_2SO_4, $MgCl_2$, and $MgSO_4$ solutions from 0.1 mol· kg^{-1} to saturation and from 273.15 to 323.15 K, The Journal of Chemical Thermodynamics **14**, 649 (1982). 10.1016/0021-9614(82)90080-5

[34] A. Apelblat, E. Manzurola, Volumetric properties of water, and solutions of sodium chloride and potassium chloride at temperatures from t = 277.15 K to t = 343.15 K at molalities of (0.1, 0.5, and 1.0) mol · kg^{-1}, The Journal of Chemical Thermodynamics **31**, 869 (1999). 10.1006/jcht.1999.0487

[35] A. Apelblat, Effect of temperature on compressibility properties of 0.1, 0.5 and 1.0 molal solutions of alkali metal halides. part 1. aqueous solutions of sodium chloride, sodium bromide, sodium iodide, potassium chloride, potassium bromide, potassium iodide, rubidium chloride and rubidium iodide in the 278.15 k to 353.15 k temperature range, Journal of Molecular Liquids **242**, 1263 (2017). 10.1016/j.molliq.2017.07.110

[36] E.V. Chulkova, A.M. Emelyanenko, K.A. Emelyanenko, L.B. Boinovich, Parameters of supercooled droplets of water and aqueous solutions of chlorides of alkali metals in the temperature range of +25 to −19 °C, Russian Journal of Physical Chemistry A **94**, 564 (2020). 10.1134/s0036024420030061

[37] V. Majer, J.A. Gates, A. Inglese, R.H. Wood, Volumetric properties of aqueous NaCl solutions from 0.0025 to 5.0 mol · kg^{-1}, 323 to 600 K, and 0.1 to 40 MPa, The Journal of Chemical Thermodynamics **20**, 949 (1988). 10.1016/0021-9614(88)90224-8

[38] G. Carvalho, F. Chenlo, R. Moreira, J. Telis-Romero, Physicothermal properties of aqueous sodium chloride solutions, Journal of Food Process Engineering **38**, 234 (2014). 10.1111/jfpe.12160

[39] W.D. Harkins, H.M. McLaughlin, The structure of films of water on salt solutions i. surface tension and adsorption for aqueous solutions of sodium chloride, Journal of the American Chemical Society **47**, 2083 (1925). 10.1021/ja01685a002

[40] M.V. Mironenko, G.E. Boitnott, S.A. Grant, R.S. Sletten, xperimental determination of the volumetric properties of NaCl solutions to 253 K, J. Phys. Chem. B **105**, 9909 (2001).

[41] T. Teng, J. Sangster, F. Lenzi, Additivity rules for the prediction of the density of aqueous solutions containing mixed-type solutes, The Canadian Journal of Chemical Engineering **54**, 600 (1976). 10.1002/cjce.5450540621

[42] A.u.H.A. Shah, K. Ali, S. Bilal, Surface tension, surface excess concentration, enthalpy and entropy of surface formation of aqueous salt solutions, Colloids and Surfaces A: Physicochemical and Engineering Aspects **417**, 183 (2013). 10.1016/j.colsurfa.2012.10.054

[43] D.E. Goldsack, A.A. Franchetto, The viscosity of concentrated electrolyte solutions iii. a mixture law, Electrochimica Acta **22**, 1287 (1977). 10.1016/0013-4686(77)87012-6

[44] J.G. Albright, J.P. Mitchell, D.G. Miller, Interdiffusion coefficients, densities, and refractive indices of ammonium chloride + water and ammonium sulfate + water at 25 °C, Journal of Chemical & Engineering Data **39**, 195 (1994). 10.1021/je00013a055

[45] M. Semmler, B. Ping Luo, T. Koop, Densities of liquid $H^+/NH_4^+/SO_4^{2-}/NO_3^-/H_2O$ solutions at tropospheric temperatures, Atmospheric Environment **40**, 467 (2006). 10.1016/j.atmosenv.2005.09.056

[46] M.F. Hervello, A. Sánchez, Densities of univalent cation sulfates in ethanol + water solutions, Journal of Chemical & Engineering Data **52**, 752 (2007). 10.1021/je060335h

[47] J. Wang, H. Zhao, Y. Ren, Measurement of physical properties and correlation of the solubility of calcium carbonate in ammonium sulfate aqueous solution at t = (298.15, 323.15, and 348.15) k in the process of preparing calcium carbonate products by the desulfurization of gypsum, Journal of Chemical & Engineering Data **61**, 3827 (2016). 10.1021/acs.jced.6b00454

[48] J.T. Safarov, G.N. Najafov, A.N. Shahverdiyev, E. Hassel, (p, ρ, t) and (p_s, ρ_s, t_s) properties, and

apparent molar volumes v_ϕ of $CaCl_2$(aq) at t = 298.15 to 398.15 K and at pressures up to p = 60 MPa, Journal of Molecular Liquids **116**, 165 (2005). 10.1016/j.molliq.2004.07.083

[49] H.R. Galleguillos, M.E. Taboada, T.A. Graber, S. Bolado, Compositions, densities, and refractive indices of potassium chloride + ethanol + water and sodium chloride + ethanol + water solutions at (298.15 and 313.15) k, Journal of Chemical & Engineering Data **48**, 405 (2003). 10.1021/je020173z

Numerical simulation of cylindrical rotating cavity noise

Matěj Ranš[1,2,*], *Richard* Matas[2], *Michal* Hoznedl[1], and *Josef* Voldřich[2]

[1]Doosan Škoda Power, Pilsen, Czech Republic
[2]University of West Bohemia, Pilsen, Czech Republic

Abstract. Turbine couplings contain many cavities that have the potential to act as acoustic resonators. Under certain conditions, the shear-layer vortex shedding excites resonance, leading to a significant increase in acoustic pressure levels. For deep cylindrical cavities, the dominant mechanism is the quarter-wavelength ($\lambda/4$) resonance, where the depth of the cavity is equal to 1/4 of the standing wave's wavelength. While this has been described thoroughly for non-rotating cavities, experiments conducted at the Doosan Škoda Power laboratory revealed that the $\lambda/4$ signal on a rotating disc is modulated by the frequency of rotation. This work focuses on numerical simulations to describe the principles of rotating cavity noise. Unsteady Large Eddy Simulation and the Ffowcs Williams-Hawkings analogy were used to model the sound generation and the influence of rotation on the acoustic signature captured by a stationary observer. Lastly, the numerical simulation results were compared with experimental data and theoretical predictions for non-rotating cavities, thereby isolating the core resonant tone from the rotational modulation.

1 Introduction

The noise generated by turbine couplings can easily surpass the 85 dB occupational health and safety limit. On-site diagnostic testing using acoustic cameras has revealed that deep cylindrical cavities located on the rotating coupling flanges are the primary source of this noise. While flow past cavities on non-rotating objects is a well-described aeroacoustic phenomenon, the effects of rotation are absent from the researched cavity noise literature, such as the foundational reviews by Rockwell and Naudascher [1] or the Von Karman Institute lecture series by Gloerfelt [2] and, more recently, the comprehensive review in a journal paper by Hanna and Mohany [3].

To address this challenge, an experimental campaign was conducted to analyze the acoustic behavior of these cavities across multiple geometric variations and rotational speeds. Although this campaign was successful in suggesting practical design measures to reduce noise, it also revealed a highly complex, comb-like acoustic frequency signature that could not be fully explained through empirical data alone. Unsteady computational fluid dynamics simulations (CFD) were performed to investigate the underlying physical mechanisms. This paper builds on previous work that compares experimental data with numerical simulations [4], while adding a new perspective that came with more research, experiments, and simulations.

The sound generated by cavities is fundamentally aerodynamic. Based on the framework used by Gloerfelt [2], the acoustic behavior of cavities is based on two principles and their interaction (visualized in Figure 1):

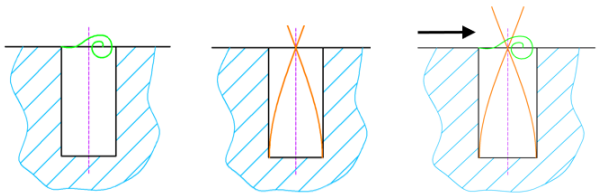


Figure 1: Cavity noise mechanisms (left: vortex shedding, middle: resonator, right: aeroacoustic lock-in)

- **Shear layer vortex shedding** occurs during grazing flow over a cavity and is influenced by a feedback mechanism between the leading and trailing edge, frequently described by Rossiter's frequency f_R.
- **Acoustic resonator** — in this case, a deep cylindrical cavity acting as an open-closed pipe (quarter-wavelength resonator where the depth is equal to one quarter of the resonant mode's wavelength).
- **Aeroacoustic lock-in** is a phenomenon that occurs when vortex shedding frequency f_R approaches the frequency of the resonator $f_{\lambda/4}$ and excites a standing wave, which leads to increased levels of acoustic pressure emission.

To model how these mechanisms interact to produce their specific acoustic signatures, the governing formulations for both hydrodynamic feedback and passive acoustic resonance must be established.

The shear layer feedback loop is a self-sustained chain of events between the upstream and downstream edges of the cavity that governs vortex shedding. The simplified

*e-mail: matej.rans@gmail.com

explanation of the shear layer feedback loop is based on Gloerfelt's framework [2], which includes four phases.

1. Acoustic pressure waves generated at the downstream edge travel upstream. They reach the separating shear layer at the upstream edge, which is the region most sensitive to acoustic disturbances.

2. These pressure waves trigger small flow instabilities within the shear layer as it separates from the rigid boundary.

3. As these instabilities travel downstream, they rapidly amplify into vortices that continue to grow.

4. When these vortices arrive at the downstream edge (impingement), they deform and generate new acoustic pressure waves, which travel back upstream, closing and restarting the loop.

Rossiter [5] formulated a semi-empirical model to predict the frequency of vortex shedding:

$$f_{R,m} = \frac{U_\infty}{L} \frac{m - \gamma}{M + \frac{1}{\kappa}}, \tag{1}$$

where L is the cavity impingement length, U_∞ is the freestream velocity, and M is the freestream Mach number. The integer $m = 1, 2, 3, \ldots$ represents the shear layer mode number, which corresponds to the number of coherent vortices simultaneously spanning the cavity opening at any given instant. Furthermore, γ is an empirical phase delay constant accounting for the time lag between vortex impingement and acoustic wave generation, and $\kappa = U_c/U_\infty$ denotes the ratio of the average vortex convection velocity (U_c) to the freestream velocity.

Under specific conditions, deep cylindrical cavities act as quarter-wavelength ($\lambda/4$) acoustic resonators. The characteristics of their standing waves are defined by the cavity geometry (most importantly, the depth) and the local speed of sound [1], [6]. The studied cavities are associated with open-closed pipe modes, with the fundamental wavelength equal to four times the cavity depth and the first overtone wavelength equal to four-thirds of the cavity depth. At the rigid bottom of the cavity, the acoustic pressure amplitude reaches its maximum (pressure antinode) while the acoustic particle velocity approaches zero (velocity node). The situation is reversed at the cavity opening, which acts as a pressure node (minimal pressure fluctuations) and a velocity antinode. For an ideal resonator, the fundamental frequency is given by

$$f = \frac{c_0}{4h}. \tag{2}$$

However, an accurate representation must account for acoustic radiation impedance at the cavity opening. Rayleigh [7] derived an end correction factor of $\alpha \approx 0.85$ for flanged cylindrical pipes. Incorporating this boundary correction alongside the higher-order overtones yields

$$f_{\lambda/4,n} = \frac{(2n-1)c_0}{4\left(h + \alpha\frac{d}{2}\right)}, \tag{3}$$

where $n = 1$ denotes the fundamental acoustic mode, and $n = 2, 3, 4, \ldots$ represent the subsequent overtones.

Rossiter frequency rises proportionally with rising freestream velocity. The shear layer vortex shedding acts independently until it approaches the constant $\lambda/4$ frequency. During this time, the cavity's acoustic resonance, which can emit much more acoustic energy, takes over and dictates the vortex shedding. This phase is called aeroacoustic lock-in. Increasing the freestream velocity further leads to either de-synchronization, where shear layer vortex shedding takes over without influence of the resonator, or mode-swapping, where a higher overtone of the resonator is excited, resulting in another aeroacoustic lock-in [2],[6]. The relation of aeroacoustic lock-in is depicted in Figure 2 in the relative and absolute frequency - velocity diagram.

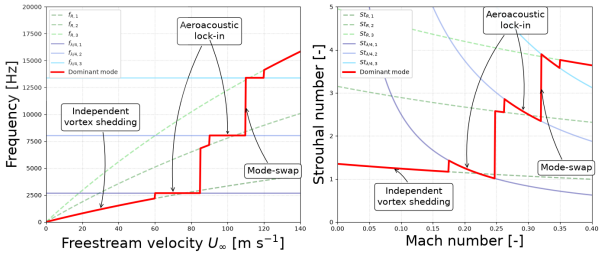


Figure 2: Example of dominant mode in specific (left) and relative (right) velocity frequency diagrams

2 Experimental results

Before the simulations, the acoustic pressure from the rotating disc with radial cavities was measured in the experimental laboratory at Doosan Škoda Power. These measurements were the initial motivation to study cavity noise further using CFD. A Brüel & Kjær 2270 sound level meter was positioned exactly 1.0 m horizontally from the disc. The measuring device itself handled the signal capture and the FFT processing. The full experimental campaign included two discs with varying numbers and depths of cavities. This allowed the acoustic measurement of 32 different configurations. A detailed analysis of all these variations is beyond the scope of this work. However, the specific variant replicated during the numerical simulations is shown in Figure 3. This 155 mm diameter flange features 16 evenly spaced, 18 mm deep radial cavities. It was spun at rotational speeds up to 12000 RPM.

The naming convention used to reference the specific configurations is explained with the example 8xM6x18. 8 represents the number of unsealed cavities, M6 represents the metric thread size of the cavity, and 18 represents the depth in mm. Results from other variations, gathered by changing the number of open cavities and their depth, are described in the work by Sýkora [8] and in the author's previous work [4]. These studies note several important observations:

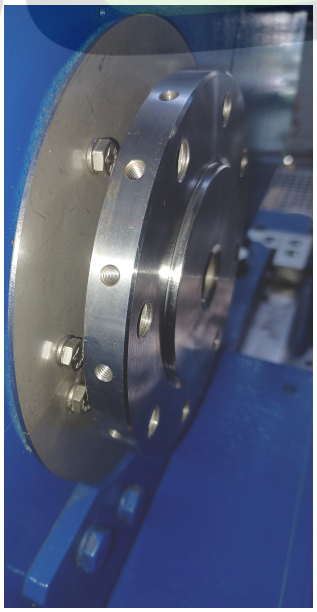


Figure 3: Photo of the 155 mm flange.

- Cavities with aspect ratios (depth/diameter) above 1.25 appear to create strong resonance. Ratios below 1.25 mostly produce broadband noise.
- Making the cavity deeper or adding cavities generally raises the acoustic pressure levels.
- A sudden sharp increase in OASPL usually occurs when the circumferential velocity reaches a certain limit. This limit occurred around 70 m/s for the measured configurations (see Figure 4).
- This increase slows down, and for some configurations even drops below the peak value.
- The acoustic signature in the frequency domain for cavities with high aspect ratio and high velocities is characterized by a band of evenly spaced tonal peaks (see Figure 5).
- The frequency spacing Δf between sidebands matches the shaft's rotational frequency (f_{RPM}). This pattern suggests signal modulation of the sound generated by the cavity, caused by the physical rotation of the disc.
- The resonant peaks stay in a frequency band. The lower and upper frequency bounds of the band are not always easily definable.
- As velocity increases, the frequency band broadens asymmetrically. This can be seen in Figure 6, a frequency-velocity diagram with the corresponding rotational speed and a color-bar based on sound pressure levels.

3 Numerical simulation setup

The experiments were inconclusive in explaining the principles of observed acoustic phenomena. Numerical simulation enabled inspection of the aeroacoustic mechanisms

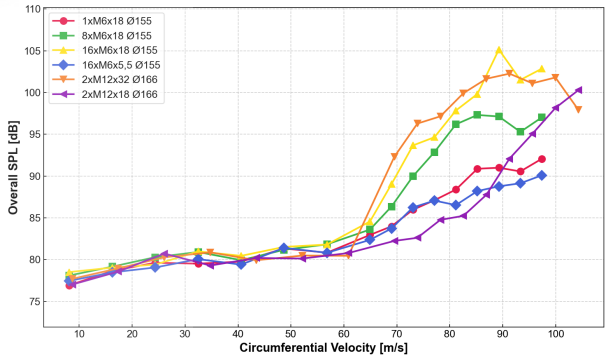


Figure 4: Overall Sound Pressure Level (OASPL) comparison across varying circumferential velocities and geometries, illustrating the sudden noise amplification at critical velocities.

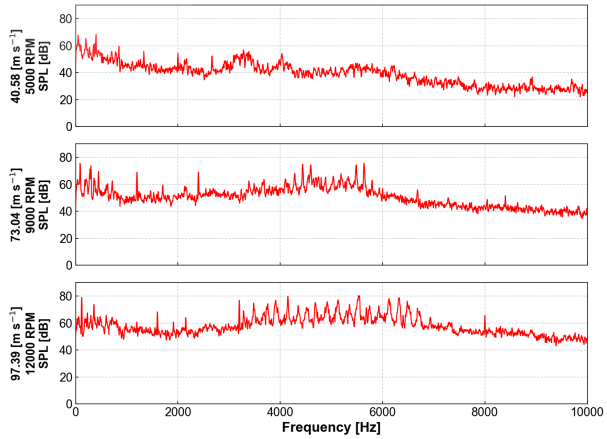


Figure 5: FFT comparison of sound pressure levels for three rotational speeds of the 155 mm disc with 8 radial cavities ($d = 6$ mm, $h = 18$ mm).

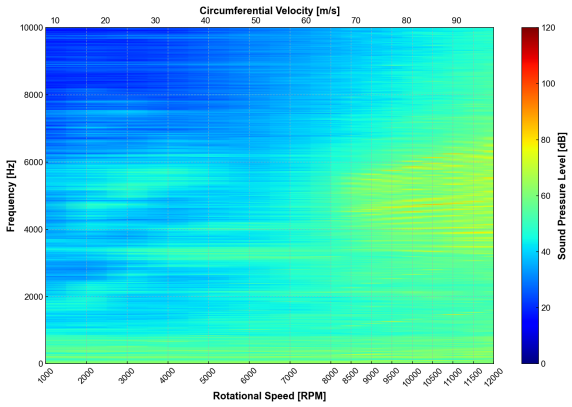


Figure 6: Spectrogram of sound pressure levels for different rotational speeds of the 155 mm disc with 8 radial cavities ($d = 6$ mm, $h = 18$ mm).

causing cavity noise in greater detail. There were two parts of the problem that needed to be tackled:

1. The aerodynamic principles of sound generation in a spinning cylindrical cavity (dominant frequencies and angular velocities that mark the lock-in region)

2. The principles of sound propagation between a rotating sound source and a static observer located in the plane of rotation

Ansys Fluent was used for its integrated Ffowcs Williams-Hawkings acoustic model. The FW-H model enables hybrid acoustic modeling, which separates aerodynamic sound generation from its propagation. This allows computing sound propagation in the far field without the need for a fine mesh across the entire computational domain. The aeroacoustic source is encapsulated by a surface that stores the relevant parameters for each time step during the calculation of the flow. After the flow simulation finishes, the resulting pressure oscillations propagate from the source surface to the far-field acoustic receivers (virtual microphones defined by coordinates that store raw acoustic pressure over time). The acoustic receivers were strategically positioned to analyze the effects of rotation. The first receiver was placed 1 m from the disc within its rotational plane. The second receiver was positioned on the axis of rotation to maintain a constant distance between the rotating cavity (the source) and the observer, thereby eliminating distance-based amplitude variations. A third receiver was intended for the cavity opening, but the FW-H implementation does not support rotating receivers. As an alternative, static pressure monitors can be placed along the cavity depth to find the shape and dominant frequency of the standing wave, as previously demonstrated by Ranš for the 2xM12x32 geometry [4]. Setting the minimum time step Δt and the maximum cell size Δx depends on the highest frequency of interest, f_{max} , the local speed of sound, c_0, and on points-per-wavelength parameter, PPW. The Nyquist-Shannon theorem requires at least two samples per cycle, but the literature suggests a higher value (PPW $>$ 25 for error $\beta < 1\%$) [6]. The equations are defined as follows:

$$\Delta t = \frac{1}{\mathrm{PPW} \cdot f_{\max}}, \tag{4}$$

$$\Delta x = \frac{c_0}{\mathrm{PPW} \cdot f_{\max}}. \tag{5}$$

The limitation lies in the computational power and in the one-dimensional acoustic Courant–Friedrichs–Lewy (CFL) condition, which dictates that a propagating wave should ideally not cross more than one cell per time step, accounting for both the sound speed and the local convective velocity. The condition is described by the equation

$$\mathrm{CFL} = \frac{(c_0 + |U_\infty|) \cdot \Delta t}{\Delta x} \leq 1.0, \tag{6}$$

where $|U_\infty|$ represents the local flow velocity. Since the literature on rotating cylindrical cavities as sound sources is limited compared with grazing flow over non-rotating cavities, the baseline validation was performed for the stationary cavity configuration.

After comparing the results from the non-rotating cavity model with available literature, a rotating disc model was developed and simulated. The domain dimensions are visualized in Figure 7 and summarized in Table 1.

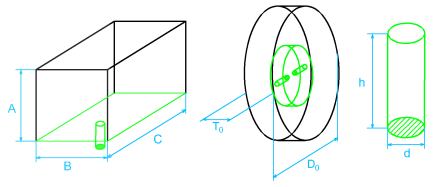


Figure 7: Computational domain dimensions. Green lines represent wall edges; black lines represent fluid region edges. Left: Stationary geometry $A \times B \times C$; Middle: Rotating disc $T_0 \times D_0$; Right: Cylindrical cavity geometry with diameter d and depth h.

Table 1: Overview of computational domain dimensions and mesh quality (orthogonal quality, aspect ratio). All models use a poly-hexcore volume mesh.

Geometry	Size [mm]	Cells	Min. O.Q.	Max. AR
Stationary				
1xM6x18	70x20x200	276k	0.4	73
Rotating				
8xM6x18	20xø180	933k	0.2	112

Large Eddy Simulation (LES), which is highly suitable for modeling shear-layer instabilities, was selected to accurately predict the aeroacoustic sources. The other computational parameters are shown in Table 2.

Table 2: Summary of the numerical setup and solver settings.

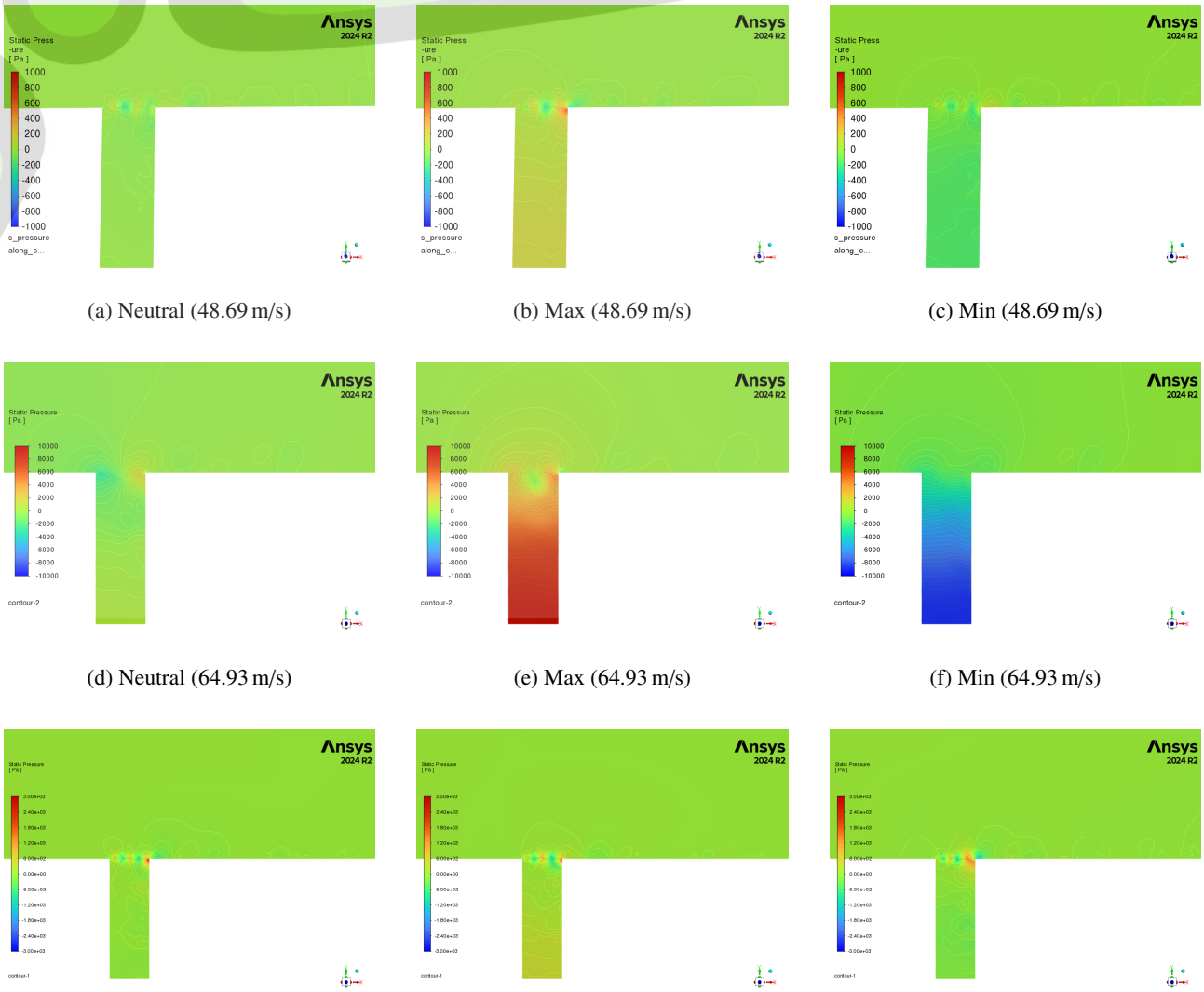
Parameter	Value
Simulation	LES
Subgrid-scale model	WALE
Volume mesh	Poly-hexcore
Pressure-velocity coupling	PISO
Momentum disc.	Bounded Central Diff.
Density disc.	Second-Order Upwind

Post-processing inside Ansys Fluent was abandoned when more in-depth analysis was deemed to be necessary. The raw acoustic receiver signals were processed in Python using the `scipy.fft` module for spectral analysis. The frequency resolution was given by the duration of the acoustic signal, T.

$$\Delta f_{res} = \frac{1}{T}. \tag{7}$$

4 Numerical simulation results

The results chapter focuses on the sound pressure levels and frequencies evaluated based on unsteady simulations.



(a) Neutral (48.69 m/s) (b) Max (48.69 m/s) (c) Min (48.69 m/s)

(d) Neutral (64.93 m/s) (e) Max (64.93 m/s) (f) Min (64.93 m/s)

(g) Neutral (97.39 m/s) (h) Max (97.39 m/s) (i) Min (97.39 m/s)

Figure 8: Static pressure contours [Pa] for the 1xM6x18 cavity at neutral, maximum, and minimum bottom pressure states.

The analysis is divided into two main parts. First, the near-field is examined, which involves analyzing the vortex shedding and pressure fluctuations inside the cavity. Second, the far-field acoustic propagation is evaluated. By combining the near-field flow data with the far-field frequency spectra, the mechanisms that generated the noise during the physical experiments can be identified.

4.1 Stationary cavity campaign

Figure 8 depicts static pressure contours for the same static geometry with one cavity exposed to a grazing flow of variable velocities (each row representing a different inlet velocity condition). The pressure oscillations moving across the cavity opening represent the shear layer vortex shedding. The columns represent the limit values for the pressure oscillations inside the cavity. During the 48.69 m/s and 97.39 m/s runs, the shear layer vortex shedding and impingement on the downstream edge contribute the most to the overall SPL. On the other hand, the 64.93 m/s run reaches peak static pressure amplitudes of circa 10 kPa at the bottom of the cavity, tenfold the pressure amplitude during the 48.69 m/s run. This effect can be explained by the excitation of the $\lambda/4$ resonance by the shear-layer vortices. In Figure 8(e), it is visible that the shear-layer feedback loop is overwhelmed by resonance, and no vortex is present.

When comparing the signals from the far-field acoustic receiver in the frequency domain, a change in overall sound pressure levels is evident (see the top right corner of the sub-figures in Figure 9). The OASPL grows with increasing velocity. It reaches a maximum of 99.7 dB at 81.16 m/s before dropping significantly at the highest velocity of 97.39 m/s. The first and most dominant acoustic peak occurs between 4000 and 4500 Hz increasing with velocity.

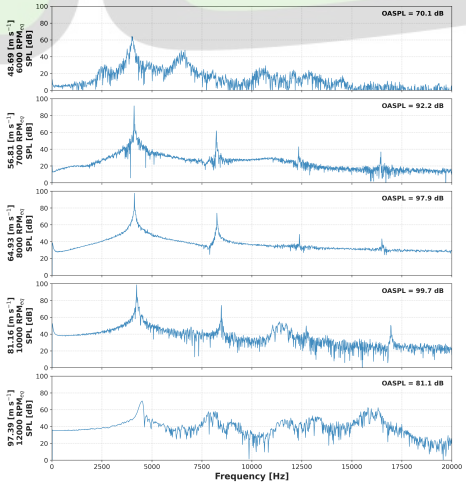


Figure 9: Sound Pressure Level (SPL) frequency spectra captured by the acoustic receiver located 1 m above the stationary cavity across varying freestream velocities.

The experimental validation of the numerical results for the stationary run was unavailable. Therefore, the comparison relied on fitting the numerical data with the published semi-empirical formulas. The aforementioned formulas were used for mode frequencies (Equations 1 and 3). While the recommended value of the end correction factor varies across articles, the most often used value for flanged cavities is $\alpha = 0.85$ [7]. The stationary runs found the best fit for $\alpha = 0.82$. For the frequency of vortex shedding, Rossiter himself suggested values of $\kappa = 0.57$–0.66 and $\gamma = 0.25$ [5]. Later literature that includes cylindrical deep cavities expands the interval down to $\kappa = 0.5$, which was used for the dashed lines in Figure 10. Finding good agreement between the numerical results and the established literature allowed setting up the rotating geometry simulation with more confidence in the simulation settings.

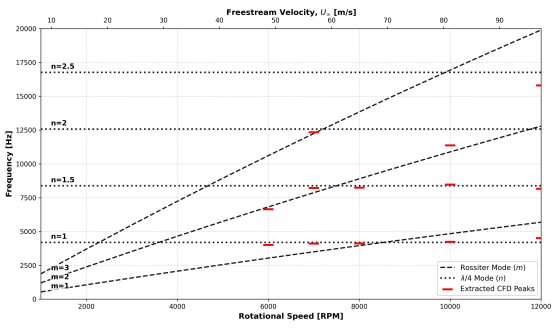


Figure 10: Comparison of theoretical results with CFD runs for the 1xM6x18 geometry using the constants $\alpha = 0.82, \kappa = 0.5, \gamma = 0.25$. The CFD FFT peaks represent the highest SPL values for each run, measured 1 m above the cavity opening.

4.2 Rotating disc campaign

For the rotating scenario, the centrifugal force acting on the cylinder resulted in a static pressure drop closer to the axis of rotation. For the 155 mm disc, the analytical pressure drop (Δp) across the 18 mm cavity depth is 1060 Pa at 8000 RPM, 1656 Pa at 10000 RPM, and 2385 Pa at 12000 RPM. These values assume a standard air density of 1.225 kg/m^3.

This centrifugal gradient changes the mean static pressure field in the simulation. Figure 11 shows the pressure distribution inside one M6x18 cavity during its neutral, maximum, and minimum pressure states. The pressure gradient is clearly visible in the neutral phase (Figure 11(a)). The pressure steadily decreases from cavity opening inwards. During the maximum (Figure 11(b)) and minimum (Figure 11(c)) states, the unsteady acoustic oscillations superimpose on the pressure gradient. Although the mean pressure is shifted, the main resonance is still driven by the shear layer feedback loop and the $\lambda/4$ mode. The centrifugal force does not stop the standing wave from forming.

Figure 12 shows the static pressure field around the whole 8xM6x18 rotating disc. No apparent logical phase locking was observed between the cavities in the simulation results. The cavities most likely act as independent sound sources that are distributed around the perimeter. This creates a very complex sound signal in the far field where the acoustic receivers are located.

These virtual receivers were used to record the time-domain pressure signals. Receiver R1 is placed 1.0 m from the disc in the plane of rotation. This matches the microphone position from the experiments. Receiver R3 is also 1.0 m away, but it lies directly on the axis of rotation (Z-axis). The placement of R3 allows for maintaining a constant distance from all cavities, thereby eliminating the effects of varying propagation distances.

The time-domain signals from the on-axis receiver R3 (Figure 13) show that the cavity flow does not reach a completely steady resonance. Instead, the waveforms indicate some mode switching and instability [2]. At 8000 RPM and 12000 RPM, the R3 signal appears as a sine wave with a slowly varying amplitude. The sound grows and shrinks over time. At 10000 RPM, the signal becomes chaotic. The clear sine wave breaks down. At the same time, the off-axis signal at R1 is heavily modulated because the cavities are moving relative to the microphone. A fast Fourier transform algorithm was applied in order to analyze the present frequencies.

Figure 14 shows the SPL frequency spectra calculated from the most stable parts of the signals. Looking at the on-axis receiver R3, there is a dominant peak at 8000 RPM and 12000 RPM. This peak matches the resonant frequency of the cavities. It shows that even when the cavities oscillate out of phase, they still emit the same core tone. The frequency of this peak goes up slightly with rotational speed. This agrees with the stationary results discussed earlier.

At 10000 RPM, however, the R3 spectrum has three peaks around the expected main frequency. This peak splitting might be caused by amplitude modulation at the source, in which energy from the main tone is split into two sidebands. The exact mechanism underlying this in-



(a) Neutral pressure state (b) Maximum pressure state (c) Minimum pressure state

Figure 11: Local static pressure contours [Pa] cross-section of a single M6x18 cavity on the rotating disc (D = 155 mm) during neutral, maximum, and minimum internal pressure phases.

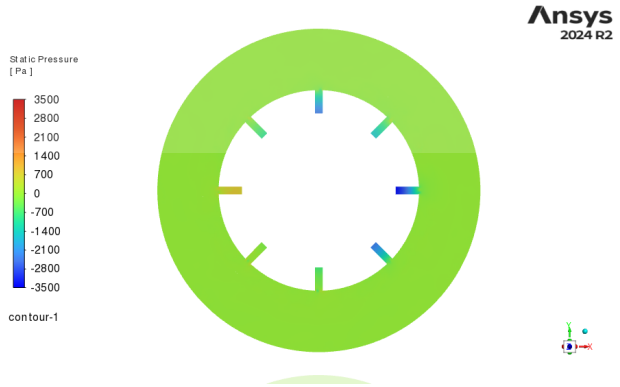


Figure 12: Global static pressure distribution [Pa] in the fluid domain surrounding the rotating 8xM6x18 disc (D = 155 mm).

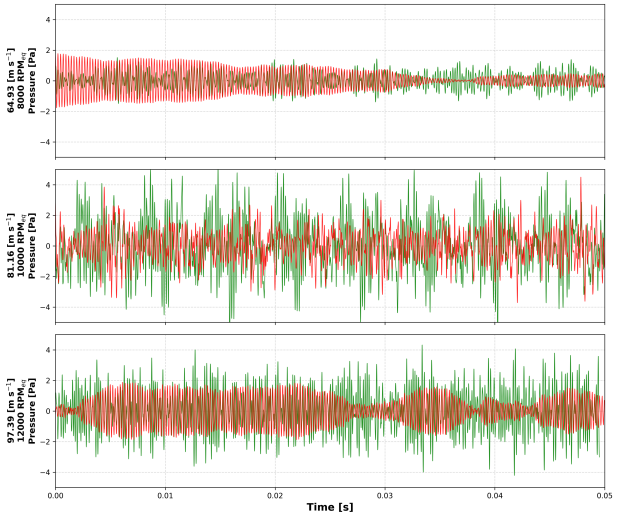


Figure 13: Time-domain acoustic signals for the rotating 8xM6x18. Green (R1): modulated off-axis microphone. Red (R3): unmodulated on-axis receiver.

ternal modulation remains unclear and warrants further research.

On the other hand, the spectra from the off-axis receiver R1 show a wide, comb-like structure at all speeds. These multiple peaks are caused by changes in the dis-

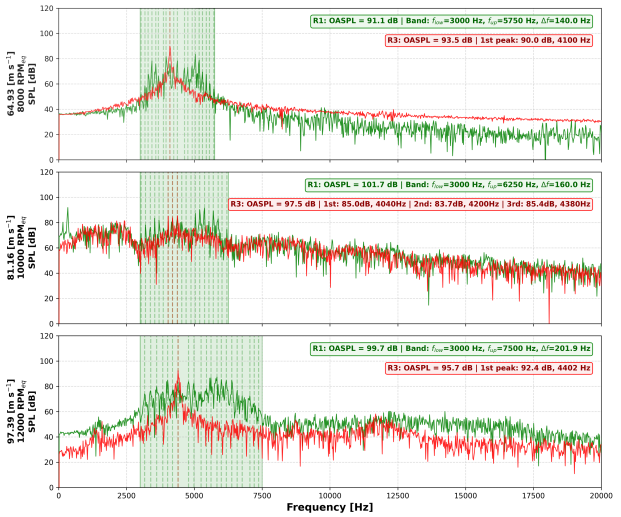


Figure 14: Sound Pressure Level (SPL) frequency spectra for the rotating 8xM6x18 configuration. Green (R1) is the off-axis receiver; red (R3) is the on-axis receiver.

tance and directionality between the rotating cavities and the static acoustic receiver. Defining the exact lower and upper bounds of this modulated region is difficult, but it can be stated that the bands widen as the RPM increases. Even though some peaks are damped and the frequency resolution is somewhat coarse, the spacing between the peaks (Δf) matches the rotational frequency of the shaft in all runs.

To verify the numerical model, the CFD results were compared directly with the experimental measurements. Figure 15 presents this validation. The diagram plots the frequency spectra from the physical laboratory microphone alongside the simulation data (receivers R1 and R3) and theoretical models (Rossiter equations and $\lambda/4$ resonance). The experimental data show a broad region of elevated noise beginning around the 8000 RPM threshold, which most likely marks the onset of acoustic lock-in.

At this speed, the theoretical Rossiter shear-layer mode $m = 1$ (4175 Hz) is close to the fundamental quarter-wavelength resonance mode $f_{\lambda/4}$ (4191 Hz). The unmodulated CFD signal from the on-axis receiver R3 (red markers) tracks this horizontal $n = 1$ quarter-wavelength reso-

nance across all three simulated speeds. The off-axis receiver R1 (green markers) captures the kinematic modulation around these core tones. The vertical spread of the green markers corresponds to the sidebands observed in the experimental campaign, with the frequency spacing Δf increasing as rotational speed increases.

The numerical simulation captures this main frequency band quite well. The lower and upper frequency limits of the comb-like structure in the CFD match the acoustic signature seen in the experiment. The experiment contains background noise from the electric motor and bearings. Further analysis and comparison with background noise (rotating disc with no open cavities) are detailed in previous work [4].

Evaluation of Overall Sound Pressure Level (OASPL) captures the overall behavioral trend across different speeds but overpredicts the noise levels (experimental OASPLs were 83.7 dB, 96.2 dB, and 97.0 dB for the 8000, 10000, and 12000 RPM runs, respectively). As shown in the top-right corners of Figure 14 for the simulated results (R1 and R3), the maximum simulated OASPL (101.7 dB) is reached during the 10000 RPM run on the off-axis receiver R1. This means higher rotational speed does not always result in higher noise levels, which is true for both simulation and experiment (see Figure 4). Instead, the maximum SPL depends on how strong and stable the aeroacoustic lock-in is. Interestingly, the difference between on-axis and off-axis receivers changes with increasing velocity. This remains unexplained, but it is clearly visible when comparing different RPM runs in Figure 14. For example, during the 8000 RPM, run the SPL captured by the on-axis receiver outside of the highlighted modulated region is higher than the off-axis one. In contrast, during the 12000 RPM, run the situation is reversed. This might be caused by the change in directionality for different modes.

5 Conclusion

High noise levels in modern steam turbine-generator installations can be caused by open rotating cavities, for example, on turbine rotor couplings. Empty balancing and bolt cavities along the coupling flanges were identified as the primary acoustic generators. This article investigates the physical mechanisms behind this noise using unsteady Large Eddy Simulation (LES) and the Ffowcs Williams-Hawkings (FW-H) acoustic analogy.

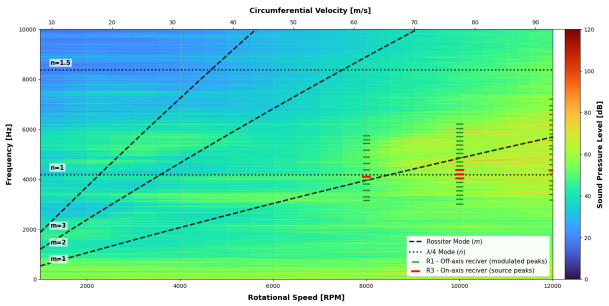


Figure 15: Comparison of the acoustic frequency spectra between the laboratory experiment and the CFD numerical simulation for the 8xM6x18 rotating disc.

As grazing flow passes over a cavity opening, instabilities in the separated shear layer develop into vortices described by Rossiter modes. When their shedding frequency aligns with the natural acoustic frequency of the cavity, an acoustic lock-in occurs.

Simulations of a rotating disc introduced additional aerodynamic effects. However, rotating cavities can still behave as quarter-wavelength resonators despite centrifugal forces. Their geometric depth remains the main parameter defining the resonance mode, suggesting that theories for stationary cavities also apply to rotating configurations. The CFD simulations reproduced the acoustic signature observed in the experiments.

Although CFD successfully predicted the frequency spectra, several limitations remain. The main one is the disagreement between predicted and measured absolute Overall Sound Pressure Levels (OASPL). Future work should describe the velocity lock-in range, validate absolute SPL predictions, compare measurements using an on-axis microphone and investigate the effects of chamfers and other modified cavity geometries.

The results were developed within specific research (UWB SGS-2025-013). The authors thank Doosan Škoda Power a.s. for the courtesy of publishing research based on their documentation and measurement data.

References

[1] D. Rockwell, E. Naudascher, Review—Self-Sustaining Oscillations of Flow Past Cavities, Journal of Fluids Engineering **100**, 152 (1978). https://doi.org/10.1115/1.3448624

[2] X. Gloerfelt, C. Bogey, C. Bailly, Cavity noise, Lecture notes (2007)

[3] M. Hanna, A. Mohany, Aeroacoustics and shear layer characteristics of confined cavities subject to low Mach number flow, Journal of Fluids and Structures **121**, 103949 (2023). https://doi.org/10.1016/j.jfluidstructs.2023.103949

[4] M. Ranš, Unsteady CFD simulation of noise around turbine coupling, Master's thesis, University of West Bohemia, Pilsen (2026)

[5] J. Rossiter, Wind-tunnel experiments on the flow over rectangular cavities at subsonic and transonic speeds, Reports And Memoranda (1964).

[6] E. Gjoni, Numerical study on acoustic phenomena in cavities for aero-engine applications, Master's thesis, KTH Royal Institute of Technology, Stockholm, Sweden (2023)

[7] J.W.S.B. Rayleigh, The Theory Of Sound, Vol. 2 (Macmillan, 1896)

[8] J. Sýkora, Noise of turbine couplings, Bachelor's thesis, University of West Bohemia, Pilsen (2024)

Experimental validation of the properties of a hybrid low-voltage cable

Jan Sedláček[1*] and *Richard* Matas[1]

[1]New Technologies – Research Centre, University of West Bohemia in Pilsen, Univerzitní 8, 301 00 Plzeň, Czech Republic

Abstract. This paper presents experiments conducted to verify the thermal properties of a functional sample of a hybrid low-voltage power cable. This innovative cable is designed to simultaneously utilize heat from the ground and Joule losses from the conductors by means of a heat pump. The development of the cable was carried out as part of the TA ČR Theta project. The cable was designed and virtually validated using CFD (Computational Fluid Dynamics) analyses, after which a functional sample was manufactured. Given the challenges associated with verifying its performance in real installation conditions, an alternative laboratory-based testing method was employed. The measurement results were then compared with the results obtained from corresponding CFD analyses.

1 Introduction

Energy losses are an inherent part of technological processes and represent a major challenge for improving energy efficiency and reducing greenhouse gas emissions. A significant share of the energy supplied to industrial systems, power generation facilities, and urban infrastructure is ultimately dissipated into the environment as waste heat. Although these losses are often unavoidable from a thermodynamic perspective, a substantial portion of waste heat can be recovered and reused, thereby reducing primary energy consumption and environmental impacts.

The global potential of waste heat utilization is considerable. Forman et al. [1] estimated that large amounts of thermal energy are continuously rejected from industrial, commercial, and transportation systems, creating significant opportunities for improved energy efficiency. Similarly, Bianchi et al. [2] demonstrated that the industrial sector in the European Union contains substantial technically recoverable waste heat resources, which could contribute significantly to energy savings and decarbonization efforts.

In addition to medium- and high-potential waste heat, which can be directly utilized, a large amount of low-potential heat is also generated. Currently, the amount of this heat continues to rise due to the rapid development of AI data centres. Its utilization depends on the use of other technologies, such as heat pumps. Wegner et al. [3] demonstrated the benefits of recovering heat from electrical cable tunnels, where cooling requirements can be combined with useful heat production for urban energy systems. Furthermore, Lam et al. [4] highlighted the potential of utilizing geothermal mine water as a low-temperature heat source for district heating networks.

This paper focuses on an unconventional method of combined utilization of waste heat - Joule losses in low-voltage power cables and ground heat. Joule losses in electrical equipment and cables are not typically utilized further. In the case of cables, in special situations, such as fast chargers for electric vehicles or welding cables and other cables with high current loads, only cooling measures are applied without any further use of the waste heat. In our case, in collaboration with the lead partner of a joint project under the Theta program of the Technology Agency of the Czech Republic PRAKAB Pražská Kabelovna s.r.o., a hybrid low-voltage power cable was developed that utilizes both Joule losses and ground heat. The heat acquired can then be effectively used in heat pumps to heat connected residential and industrial buildings.

The project included the design of the cable structure, theoretical verification using CFD analyses, optimization of the design in terms of heat gains and manufacturing technology, and the production of functional samples of one of the proposed hybrid cable designs. To optimize and evaluate the cable characteristics, 2D and 3D CFD analyses were used during the development phase on shorter model lengths, as well as proprietary 1D software for analysing real cable sections lengths. After completing the functional sample of the hybrid cable, it was necessary to experimentally verify its predicted parameters. It was not feasible, either from a technical or a measurement perspective, to carry out the measurements under real-world conditions where the cable is laid in a trench.

For this reason, two alternative methods were proposed that could be carried out under laboratory conditions while ensuring defined and sufficiently stable measurement conditions. The objective of this paper is

* Corresponding author: sedlacek@ntc.zcu.cz

to describe the measurements performed on the functional sample of the hybrid cable and to compare the measurement results with the corresponding CFD analyses.

2 Experimental test

2.1 Functional sample of the hybrid cable

The hybrid cable was developed in two basic variants. In both variants, HDPE pipes for the collection and transport of heat by a flowing working fluid were incorporated into an AYKY 3x240+120 mm² low-voltage cable. The cable thus consists of four aluminium conductors with a cross-sectional area of 240 mm² and one aluminium conductor with a cross-sectional area of 120 mm². The individual conductors and the entire cable are insulated with PVC. For network configurations where looping is possible, a cable was designed with a single 32x3 mm HDPE pipe located in the centre of the cable; for radial networks or short sections, a cable was designed with two 25x2.5 mm HDPE pipes between the cable cores - Fig. 1. A functional sample was produced for the first variant with a single pipe. The sample was manufactured to a length of several tens of meters; 6-meter-long sample were prepared for testing, which were subsequently shortened and adapted for both electrical and hydraulic connections.

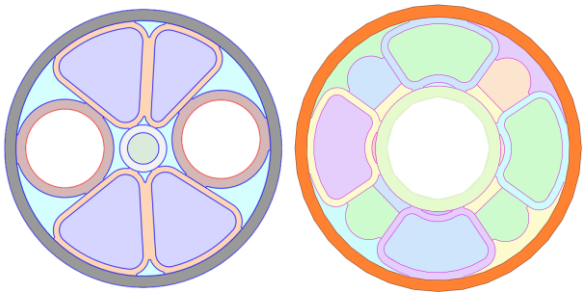


Fig. 1. Hybrid cable models with two and one HDPE pipes.

Due to the technological complexity of the manufacturing process, the planned dimensional accuracy of the cores was not achieved in the first samples, and at the same time, the polypropylene inserts between the cores became deformed – Fig. 2.



Fig. 2. Functional sample section (without sheath).

To coat the functional sample, an alternative method was used involving a heat-shrinkable insulating sleeve that was thinner than the standard PVC coating applied by extrusion.

2.2 Experimental setup

Under real-world conditions, the cable is placed in the surrounding soil, which has varying thermal properties depending on its type and moisture content. Depending on the operating conditions, heat is transferred between the cable and the ground. Determining and ensuring consistent soil properties during measurements is very difficult or impossible.

For this reason, soil was replaced with water during the measurement, as the thermal properties of water are very well known. Given the technical limitations on the size of the experimental model and the high heat capacity of water, the cable was placed inside a PVC pipe with an inner diameter of 190 mm - KG DN200. The KG pipe was fitted with eight thermocouples (four at the top and four at the bottom). The pipe was insulated with 100 mm thick mineral wool.

To limit temperature stratification in the KG pipe caused by natural convection, continuous circulation was ensured by a GRUNDFOS Alpha2 15-40 circulation pump (approximately 10–11 l/min between the upper edge of one flange and the bottom of the pipe near the other flange). The pumps power consumption during the measurement was approximately 19 W.

The HDPE pipe of the hybrid cable was connected to an external, electrically heated water loop with regulated flow rate and water temperature. Along the length of the sample, the loop was supplemented with a bypass to stabilize the parameters prior to the main period of the measurement.

The aluminium cores of the cable were connected in series (in the functional sample made, they had a uniform cross-sectional area of 240 mm²) and connected to a regulated current source (up to 1000 A).

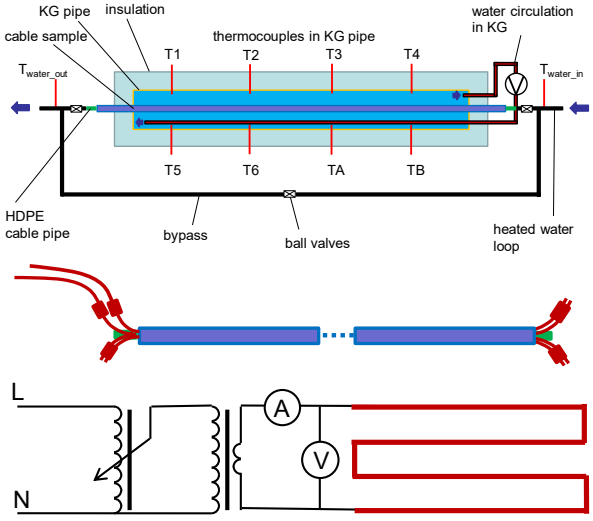


Fig. 3. Experimental setup diagram – hydraulic connection, temperature measurement and electrical connection.

The measurements were performed using NI DAQ system and Agilent 34970A unit. Temperatures were measured in the liquid loop (boiler, HDPE inlet, HDPE

outlet - T-type thermocouples) and the KG pipe (eight K-type thermocouples). The flow rate through the heated water loop was measured by KROHNE inductive flowmeter, and the environmental conditions during the test (room temperature, atmospheric pressure, and humidity) were measured with COMET sensor. The thermocouples in the KG pipe were submerged in water to a depth of approximately 2.5 cm. Using the Agilent unit, the voltage at the input terminals of the sample cores and the output voltage from the FLUKE 3000 A current probe were measured.

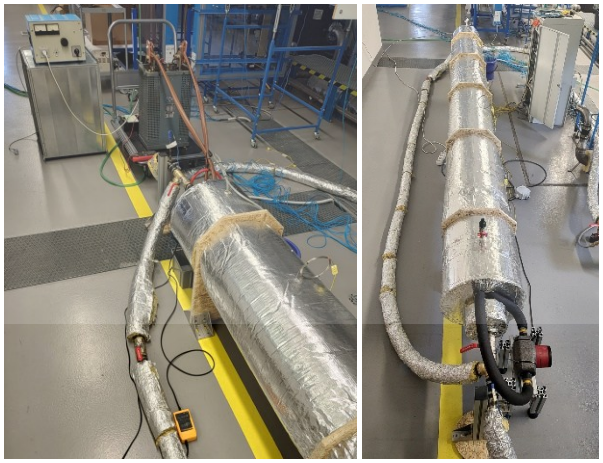


Fig. 4. Experimental setup in the laboratory.

2.3 Test 1

The first measurement was focused on verifying the overall thermal conductivity of the cable structure. On the prepared test stand was monitored the heat transfer from the central HDPE pipe (through which heated water flowed) to the water circulating in the outer insulated KG pipe (DN200). For practical reasons and to ensure the highest possible measurement accuracy, the temperature gradient was defined in the opposite direction from the intended use of the cable. To shorten the duration of the experiment, the gradient 30 K was set, that is higher than under normal conditions in the ground. The actual gradient at the start of the measurement was 51.8 °C in the HDPE pipe to 21.8 °C in the KG pipe.

First, water circulation was initiated in the KG pipe to equalize the water temperature. Due to the higher ambient air temperature and losses from the circulation pump, the average water temperature rose slowly. Subsequently, the circulation and heating of the water in heated loop were also initiated. After switching the heating water bypass to the HDPE pipe, measurements of the water temperature rise in the KG pipe began. The measurement period lasted three hours.

The measured temperature courses in Fig. 5 and Fig. 6 show a uniform increase in water temperature in the KG pipe. The measurements capture only the initial phase of the exponential heating curve of the cable and water. Given the high heat capacity of water, the time constant is quite large. Nevertheless, the information on the heating dynamics is sufficient for comparison with theoretical CFD analyses and for validating the cables thermal properties.

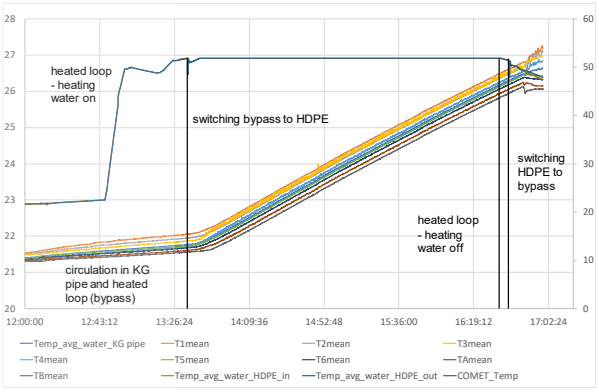


Fig. 5. Test 1 – Measured temperatures - measurement sequence.

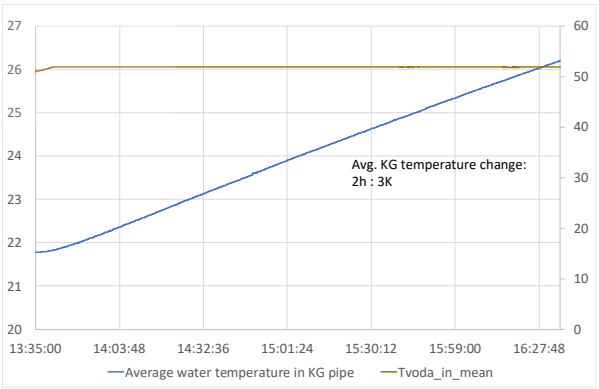


Fig. 6. Test 1 – Measured heating water temperature and aggregated average water temperature in the KG pipe - change over control time range.

2.3.1 Comparison with CFD

A computational model corresponding to the planned experimental setup was developed (the CFD simulation was performed prior to the measurement to determine the rate and uniformity of water heating in the KG tube and thus to confirm the feasibility and duration of the experiment).

The model was partially simplified: it does not include spacers to secure the cable position or the precise routing of the circulation hose. Furthermore, it does not account for the twisting of the cable cores along their axis, but assumes straight cores. Given the high flow rate of hot water through the HDPE pipe, the condition defining the external heat source was specified as a constant temperature on the inner wall of the HDPE pipe.

First, a steady-state calculation was performed assuming only water circulation in the KG pipe and a constant assembly temperature of 20 °C, followed by a transient preliminary calculation under the same conditions. Subsequently, the main transient calculation was performed to investigate heat transfer from the HDPE pipe through the cable to the external environment (water in the KG pipe), with the specified condition of a constant temperature of 50 °C on the inner wall of the HDPE pipe surrounding the cable already

applied. The calculation was performed over a period of 8,000 seconds with a time step of 0.1 s for the first 1,200 s and subsequently with a time step of 0.2 s. During the calculation, the average temperatures in individual sections of the cable and the water in the KG pipe were monitored. After the calculation was completed, the heat fluxes from the HDPE pipe and through the cable sheath into the water in the KG pipe, as well as the average temperatures at the locations of the thermocouples, were evaluated.

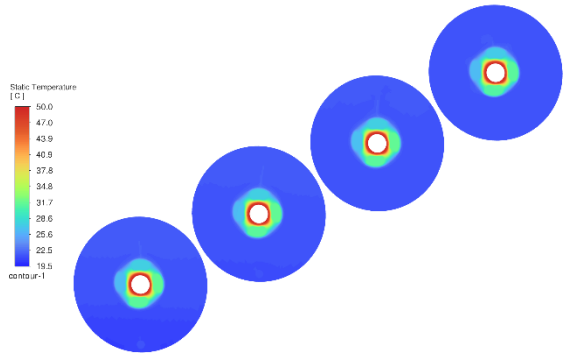


Fig. 7. Test 1 – CFD predicted temperature contours in cross-sections of the model – time 3600 s.

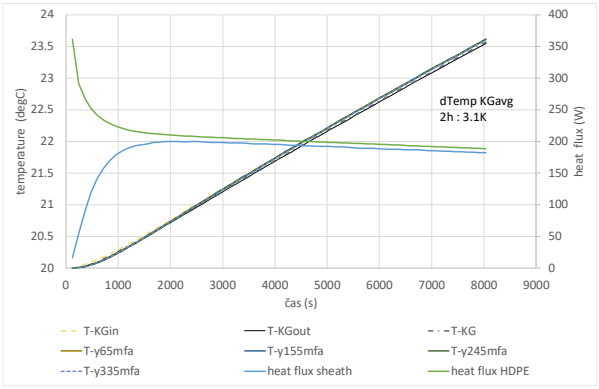


Fig. 8. Test 1 – CFD evaluation of water temperature rise in the KG pipe and heat fluxes through the HDPE pipe and from the cable into the surrounding water in KG.

When comparing the average measured and calculated water temperature rise in the KG pipe over the same time interval, the difference is 0.1 K, which is approximately 3 % of the temperature rise. This value is also within the range of expected measurement errors and CFD model errors.

2.4 Test 2

The second measurement more closely simulated the typical use of the cable. The measurement focused on heat transfer from the cable cores, heated by an electric current, to the water flowing through the HDPE pipe and, simultaneously, to the water circulating in the insulated KG pipe. The temperature gradient was induced by the electric current flowing through all the cable cores. To shorten the measurement time, the current greater than the rated current was applied (approximately 470 A / 527 W when recalculated for the measured length of the cable). Water flow through the inner HDPE pipe was reduced to low flow rate (5 l/min) to achieve a measurable temperature gradient between the inlet and outlet of the cable sample.

First, the measurement was started, and water circulation was initiated in both the KG pipe and the water loop (HDPE pipe) to equalize the temperature of the measured system (both the water and the cable). Due to the higher ambient air temperature and pump losses, the average water temperature rose slowly.

Circulation without electric heating was maintained for approximately 30 minutes; subsequently, the power source was connected and the current set to 480 A. After the temperature of the conductors rose, the current dropped fairly quickly (while the voltage, conversely, increased). The current was then further regulated to achieve a constant total power of approximately 650 W (the entire cable, including the external connections between the conductors). The measurement period with heating lasted 75 minutes. After the heating was turned off, the measurement continued for another 20 minutes.

The evaluation was performed at 50 minutes interval, during which the water heating in both pipes was almost uniform (after the initial transient phenomenon caused by the cable mass warming up had subsided).

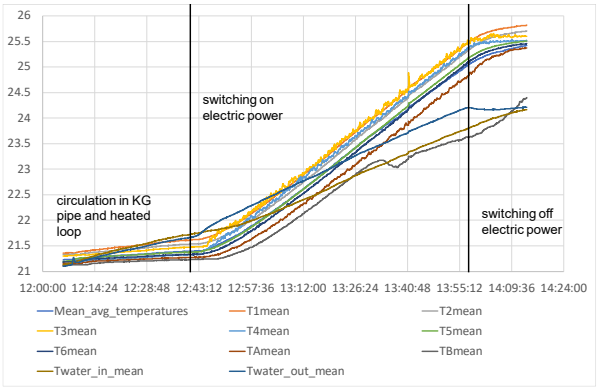


Fig. 9. Test 2 - Measured temperatures – measurement sequence.

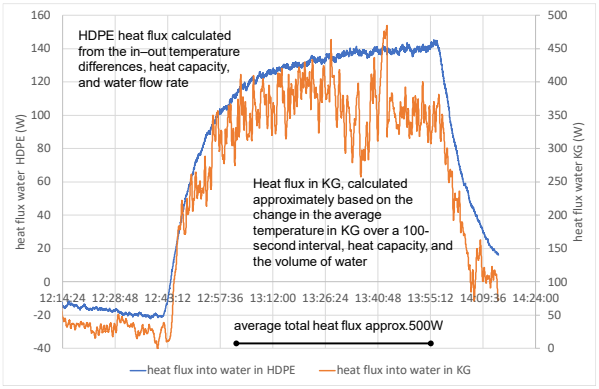


Fig. 10. Test 2 – Heat fluxes from the cable to the water in KG and HDPE pipes, calculated from measured temperature changes.

2.4.1 Comparison with CFD

A computational model corresponding to the experimental setup was developed. The model was based on the configuration used for Test 1; in this case, the volume of water in the HDPE pipe was added, and

the flow rate, initial water temperature, and Joule losses were defined.

The calculation was performed after the experiment, allowing the measurement parameters (flow rate, initial temperatures, inlet water temperature into the HDPE pipe, and Joule losses) to be entered in close alignment with the measurements.

First, a steady-state calculation was performed with only water circulation in both the KG and HDPE pipes and a constant assembly temperature of 21.4 °C, followed by a transient calculation under the same conditions. Subsequently, the main transient calculation was performed to investigate the heat transfer from the cable cores to the water in the HDPE and KG pipes. Constant Joule losses in the cores (526 W) were applied and the temperature of the water entering the HDPE pipe was defined using a user-defined function as a function of time based on measurement results.

The calculation was performed over a total period of 4,500 seconds, with a time step of 0.1 s for the first 1,200 seconds and a time step of 0.2 s thereafter. During the calculation, the average temperatures in individual sections of the cable and the water in both the KG and HDPE pipes together with the heat fluxes into the water in both the KG and HDPE pipes were monitored.

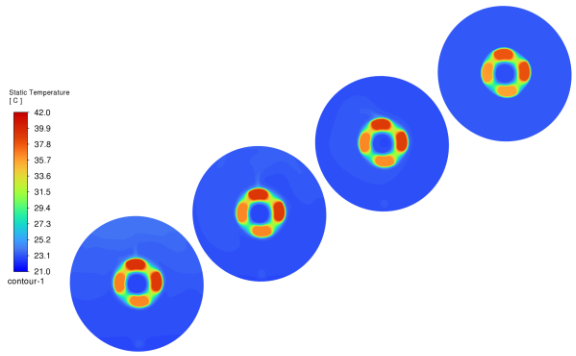


Fig. 11. Test 2 – CFD computed temperature contours in cross-sections of the model – time 2400 s.

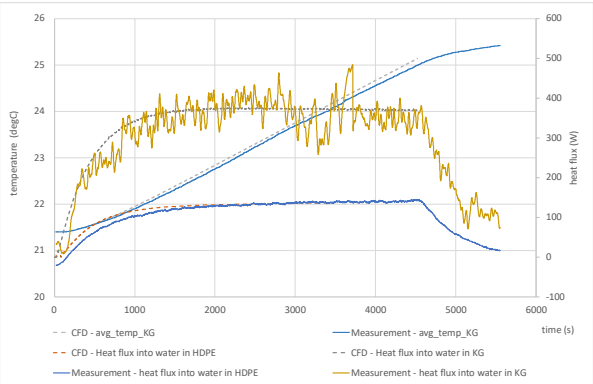


Fig. 12. Test 2 – Comparison of measured and calculated temperatures and heat fluxes.

A comparison of selected measured and calculated temperatures and heat fluxes in Fig. 12 shows very good agreement between the measurements and the calculations.

3 Conclusions

The comparison of the measurement results and the performed CFD analyses shows good agreement, despite the partial simplification of the CFD model and measurement uncertainties.

The measurements thus confirmed that the CFD computational model, including the specified material properties, corresponds to the real cable sample.

It can therefore be assumed that other CFD analyses performed on this cable sample, as well as on other geometric and operational variants of the cable, will also well predict heat transfer to the surrounding environment under various conditions.

The development of the cable functional sample and theoretical and experimental analysis were co-financed from the state budget by the Technology agency of the Czech Republic under the Theta Programme.
We would like to thank our colleagues at PRAKAB for their excellent cooperation and for their consent to the publication of selected analyses and results.

References

1. C. Forman, I. K. Muritala, R. Pardemann, B. Meyer, Estimating the global waste heat potential. Renewable and Sustainable Energy Reviews. **57**, 1568-1579 (2016). https://doi.org/10.1016/j.rser.2015.12.192
2. G. Bianchi, G. P. Panayiotou, L. Aresti et al., Estimating the waste heat recovery in the European Union Industry. Energ. Ecol. Environ. **4**, 211–221 (2019). https://doi.org/10.1007/s40974-019-00132-7
3. M. Wegner, H. Turnell, G. Davies, A. Revesz, G. Maidment, Combined benefits of cooling with heat recovery for electrical cable tunnels in cities, Sustainable Cities and Society. **73**, (2021). https://doi.org/10.1016/j.scs.2021.103100
4. F. Lam, W. Warner, T. Gökpinar, T. Heinze, Technical lessons learned from the usage of geothermal mine water for heat supply and economic scenarios to predict feasibility. Energy Conversion and Management. **349**, (2026). https://doi.org/10.1016/j.enconman.2025.120809

A comparative RANS-EDC study of HEFA (hydroprocessed esters and fatty acids) and Jet A-1 combustion in the Sandia Flame D configuration

Huzaifa Amir Syed[1], and *Kemal* Masera[1*]

[1]Mechanical Engineering, Middle East Technical University, Northern Cyprus Campus, Guzelyurt via Mersin 10, 99738 Kalkanli, Türkiye

Abstract. Aviation sector has been a significant contributor towards carbon emissions and greenhouse gases: with contribution of 2% total energy-related carbon emissions in the world in 2022. Efforts have been made in developing drop-in liquid sustainable aviation fuels (SAF) that do not compromise the energy density requirement of the fuel and the emission limit of GHG. SAF has multiple fuel solutions for achieving net-zero aviation, of which the most prominent is HEFA (Hydroprocessed Esters and Fatty Acids). SAF combustion studies involve complex geometry and spray effects, where fuel's intrinsic behaviour is difficult to isolate Sandia Flame D is a simple, controlled and non-premixed framework that isolates turbulent-chemistry interaction, providing clean comparison, where fuel is the only variable. This study applies these advantages to investigating SAF combustion in Sandia Flame D configuration (specifically HEFA and Jet A-1), which hardly any study in the literature has performed. Turbulence is modelled with Reynolds Stress Model with Eddy Dissipation Concept (EDC) as the combustion model. GRI-Mech 3.0 is used as chemical mechanism to simulate combustion behaviour. Numerical results are validated with TNF workshop data with an error of approximately 9%, which is under standard reported error of 10% for EDC simulations for Sandia Flame D.To obtain a converged solution, the HEFA case was run with a 400 K jet and an equivalence ratio of about 2.8. Both fuels show closely similar flame behaviour: peak centreline temperatures of 2189 K for Jet A-1 and 2227 K for HEFA, with the difference arising mainly from the hotter HEFA jet, nearly identical fuel consumption, and peak CO_2 within 2%. HEFA produces about 20% lower peak NO, consistent in direction with experimental observations. The results suggest that HEFA behaves similarly to Jet A-1 at flame level, supporting its suitability as a drop-in fuel.

1 Introduction

The aviation sector has significantly contributed to carbon emissions and greenhouse gases. A study found that civil aviation accounted for 2% of total energy-related carbon emissions worldwide in 2022 [1]. The rate increased faster than any other mode of transport [1]. These concerns have driven major efforts to decarbonize the civil aviation sector.

Aircraft rely on high-density fuels that provide the maximum energy per unit weight due to take-off and landing weight restrictions. Electric batteries have lower energy per unit weight than conventional jet fuels. Therefore, electrifying the aircraft power plant is inefficient [2]. Since decarbonization and electrification are difficult for civil aircraft, researchers have developed drop-in liquid sustainable aviation fuels that do not compromise fuel energy density or GHG emission limits. Studies on developing SAF primarily focus on maximizing net-zero carbon reduction. SAF is the most practical pathway for achieving net-zero aviation in the short-to-medium term (2025–2050). A life-cycle CO_2 reduction of 70% to 85% can be achieved, and the fuel is drop-in compatible with existing aircraft, enabling immediate implementation without engine modification [2].

SAF offers multiple fuel solutions for achieving net-zero aviation, the most prominent of which is HEFA (Hydroprocessed Esters and Fatty Acids). An LCA review (2024) reports that HEFA remains one of the most well-researched, mature, and commercially viable fuels to process. HEFA is certified as a drop-in fuel up to 50% by ASTM D7566 [3].

Researchers have made rigorous efforts to test HEFA. Xu et al. conducted a combustion experiment with HEFA, injecting it into a heavy-fuel aircraft piston engine. They reviewed combustion and emission characteristics by measuring gaseous and particulate emissions [4]. Raji et al. (2026) burned different blends of HEFA and Jet A-1 in a NexGen burner, where the CO_2 and NOx emissions were recorded and studied. It reported that higher HEFA content in the blend increased the NOx and CO_2 emissions, whereas HEFA as a standalone fuel had lower NOx and CO emissions [5].

However, experimentation costs time and resources. Rigs are manufactured to test fuels, which limits the study

* Corresponding author: kmasera@metu.edu.tr

of fuel characteristics outside the rig's limitations. Therefore, Computational Fluid Dynamics (CFD) of SAF can further extend the research domain. Numerous CFD studies on SAF have been conducted in recent years. RANS (Reynolds-Averaged Navier-Stokes) and LES (Large Eddy Simulation) are among the most used methods for turbulence modelling in SAF CFD, with LES applied to aero-engine spray combustion [6]. Detailed chemistry mechanisms require high computational power and time. Therefore, CFD of aviation fuels has been performed with skeletal mechanisms that reduce computational power and time while preserving the essential combustion characteristics [6,7]. CFD of SAF combustion enables examination from a broader perspective, without the limitations of a testing rig; however, the methodology must be validated. A validated methodology for SAF combustion CFD ensures that the output produced is meaningful and agrees with reality within an acceptable error margin. Researchers have used multiple configurations to perform CFD of SAF combustion: swirl spray combustor, bluff-body/Cambridge burner, and swirl-stabilized model flame [6,7,8,9]. A reliable validation benchmark requires exhaustive experimental characterization, so that simulation results can be checked against experimental data from the literature. The Sandia Flame D is one of the most exhaustively measured turbulent combustion benchmarks, with detailed velocity, temperature, and species data (Barlow & Frank) [10], making it a standard reference for validating turbulent-combustion models. While turbulent combustion in Sandia Flame D has been extensively validated for methane, its simple, well-characterized geometry and extensive dataset make it an ideal yet, to the author's knowledge, unexplored configuration for studying aviation fuel combustion. This study leverages these advantages to investigate SAF combustion in the Sandia Flame D configuration (specifically HEFA and Jet A-1).

2 Methodology

2.1 Setup

This study was carried out on the methane-air pilot flame model, which was developed by Sandia National Laboratory [10]. The model is non-premixed, turbulent flame with three inlets: jet, pilot and co-flow. Numerical study was performed on ANSYS Fluent, where setup used was two-dimensional axisymmetric domain. The computational domain extends 20D radially and 139D axially, where D represents jet diameter (7.2 mm). The inter-stream walls separating jet, pilot, and co-flow were set to 2 mm. The domain was discretized into 69,376 quadrilateral cells, with refinement near nozzle and reaction zone.

2.2 Boundary Conditions

The jet is the mainstream that transports the fuel mixture. Pilot is the stream of hot-burnt gases that stabilizes flame by preventing flame extinction. The co-flow provides cold air that act as the oxidizer.

Jet, pilot and co-flow were modelled as velocity inlets, where each was defined by velocity, temperature, species and hydraulic diameter. Table 2 mentions exact inlet settings for the 3 main inlets [10].

Table 2. Boundary conditions for the velocity inlets.

Inlet	Velocity (m/s)	Hydraulic Diameter (mm)	Temp. (K)
Jet	49.6	7.2	294
Pilot	11.4	10.5	1880
Co-flow	0.9	270	291

Species transport model with volumetric reactions was used with chemistry defined by imported mechanism files containing reaction set and thermodynamic data. For the validation, mechanism used is GRI-Mech 3.0 [11], most extensively used mechanism for validating Sandia Flame D, contains 53 species and 325 reactions.

Jet A-1 is simulated by mechanism from Stanford HyChem library, HyChem Jet A2 [12]: a skeletal mechanism with 41 species that is most suitable for simulating Jet A-1 (POSF10325), skeletal mechanism makes combustion tractable while retaining essential combustion characteristics. The skeletal HEFA-SPK mechanism by Liang and Wang [13] is used to simulate HEFA in Sandia Flame D domain. It consists of 66 species, where HEFA is simulated as mixture of n-dodecane and iso-dodecane by weight of 73/27.

For a fair fuel comparison, all the configuration conditions are set as same, where only difference is the mechanism file that simulates the fuel. Different fuel requires different amounts of air to burn. For fair analysis instead of keeping mass same, the equivalence ratio at jet is kept the same. This ensures the study is based on same fuel-air stoichiometry.

$$\varphi = \frac{\left(\frac{A}{F}\right)_{stoich}}{\left(\frac{A}{F}\right)_{actual}} \quad (1)$$

The equivalence ratio for Sandia Flame D is **φ = 3.18.** This controlled-approach for fuel comparison (Operating point kept same and configuration are kept unchanged, and only fuel is varied) follows well-established practice for comparing alternative-fuels in identical domain such as Sandia Flame D. Therefore, pilot and co-flow species are kept identical, whereas jet species are varied as per the equivalence ratio. Table 2 presents species used for Pilot and co-flow followed by table 3 that presents mass fractions of Jet for all three cases (Methane, Jet A-1, HEFA).

Table 3. Pilot and co-flow inlet species mass fractions.

Inlet	Species	Mass fraction
Pilot	N_2	0.734
	CO_2	0.110
	H_2O	0.098
	O_2	0.056
	OH	0.002
Co-flow	N_2	0.767
	O_2	0.233

Table 4. Jet inlet species mass fractions for the three fuel cases.

Fuel	Species	Mass fraction
Methane	N_2	0.647
	O_2	0.197
	CH_4	0.156
Jet A-1	N_2	0.630
	O_2	0.192
	POSF10325	0.178
HEFA	N_2	0.632
	O_2	0.192
	n-$C_{12}H_{26}$	0.128
	iso-$C_{12}H_{26}$	0.047

2.3 Governing Equations

The turbulent reacting flow of Sandia Flame D is governed by Reynolds-averaged conservation of mass, energy, momentum conservation,together with the transport equation.

The equations:

Continuity, where ρ is the density, u the velocity vector, and t the time:

$$\partial\rho/\partial t + \nabla\cdot(\rho\mathbf{u}) = 0 \quad (2)$$

Momentum, where p is the static pressure, τ the viscous stress tensor, and R the Reynolds-stress tensor arising from turbulence closure; ρ and u retain their earlier definitions:

$$\partial(\rho\mathbf{u})/\partial t + \nabla\cdot(\rho\mathbf{u}\mathbf{u}) = -\nabla p + \nabla\cdot\boldsymbol{\tau} + \nabla\cdot\mathbf{R} \quad (3)$$

Energy, where E is the total energy, k_{eff} the effective thermal conductivity, T the temperature, and S_h the energy source term accounting for the heat release from the chemical reactions; ρ and u retain their earlier definitions:

$$\partial(\rho E)/\partial t + \nabla\cdot(\rho\mathbf{u}E) = \nabla\cdot(k_{\text{eff}}\,\nabla T) + S_{\text{h}} \quad (4)$$

Species Transport, where Y_s is the mass fraction of species s, D_s its mass diffusion coefficient, and $\dot{\omega}_s$ its net rate of production from the reaction mechanism; ρ and u retain their earlier definitions

$$\partial(\rho Y_s)/\partial t + \nabla\cdot(\rho\mathbf{u}Y_s) = \nabla\cdot(\rho D_s\,\nabla Y_s) + \dot{\omega}_s \quad (5)$$

2.4 Turbulence and combustion setup

Turbulence is modelled by RANS (Reynolds-Averaged-Navier-Stokes Equations) with the Reynolds Stress Model (RSM) using a linear pressure-strain formulation [16]. Unlike the k-ϵ, which overpredicts spreading rate of round jet [17,18], RSM solves transport equations for individual stress components, capturing turbulence anisotropy. As Sandia Flame D is a round jet, RSM is selected to mitigate the round-jet anomaly [18].

The turbulence-chemistry interaction is modelled with Eddy Dissipation Concept (EDC) [19] with volumetric reactions. It computes reactions in fine turbulent structures, which are on the order of Kolmogorov scale, coupling turbulence with finite-rate chemistry, where chemistry is defined by fuel-specific mechanisms.

Radiation is modelled with Discrete Ordinates (DO) [20], with weighted-sum-of-grey-gases model (WSGGM) [21] for the absorption coefficient.

2.5 Validation

The methodology was validated against Sandia Flame D experimental data from TNF workshop (Barlow & Frank) [10]. The temperature plots at centreline and mass-fraction of CH_4 were compared with the experimental data.

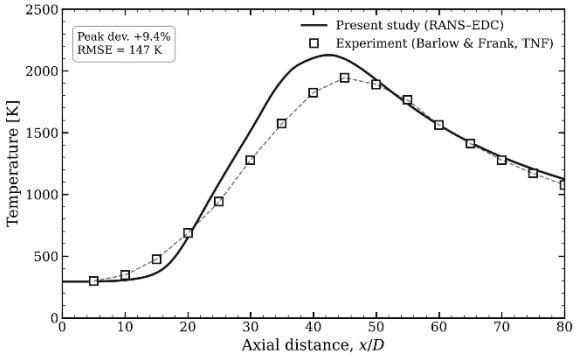


Fig. 1. Centreline temperature for Sandia Flame D: present RANS–EDC prediction and experimental data (Barlow & Frank, TNF) [10].

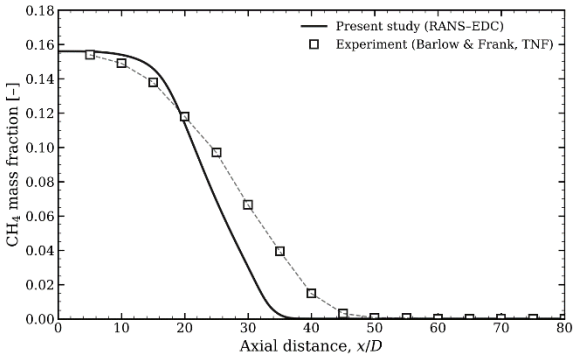


Fig. 2. Centreline CH_4 mass fraction for Sandia Flame D: present RANS–EDC prediction and experimental data (Barlow & Frank, TNF) [10].

It is observed from figure 2 that the peak temperature was 2128K, which is deviated by 9% from the experimental data with a RSME (Root Mean Square Error) of 143K. The over-prediction is confined towards middle. The error is within the reported ~10% deviation typically reported for EDC based simulations of Sandia

Flame D [18,22]. The validation case used the GRI-Mech 3.0 mechanism.

The validation confirms turbulence and combustion modelling reproduces the Sandia Flame D thermal field. Since the framework is fuel-agnostic, Jet A-1 and HEFA are compared by only changing the inlet mass composition of jet and the mechanism file, while keeping the validated configuration unchanged.

3 Results and discussion

After having a validated case, fuel species were changed from the species transport for the respective fuel run: HyChem A2 for Jet A-1 and HEFA surrogate mechanism by Wang for HEFA.

Since HEFA surrogate has a dew point of 380K (higher then 294K), the inlet temperature was set as 400K to avoid condensation and have HEFA as vaporized. The case where inlet temperature was 294K and equivalence ratio was 3.18 for HEFA was diverged, a reduced equivalence ratio of 2.8 was used to get a converged field. The difference is likely associated with stiffer chemical mechanism as compared with Jet A-1. HEFA surrogate has 66 species and Jet A-1 skeletal mechanism has 41 species. Therefore, Jet A-1 was converged with same equivalence ratio as Sandia D, whereas HEFA was converged with lower equivalence ratio. A higher equivalence ratio has richer fuel that becomes stiffer and becomes real challenge for EDC to resolve.

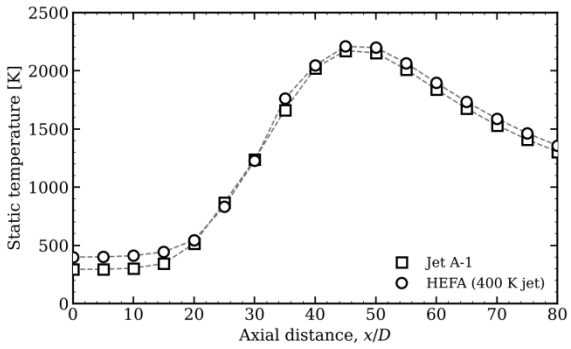


Fig. 3. Centreline temperature for Jet A-1 and HEFA (HEFA jet at 400 K).

Figure 3 shows that the temperature near nozzle region (x/D = 0 to 15) is about same as inlet temperature. From x/D = 15 to 30, the inlet difference disappears at x/D = 20, and from x/D = 25 to 30 HEFA is observed numerically slightly cooler than Jet A-1. At peak, both fuels reach almost their maximum temperature reported in their respective mechanism file: 95.7% of maximum temperature at equilibrium flame temperature (calculated from each mechanism thermodynamic data) for Jet A-1 and 96.3% for HEFA. At the downstream, HEFA is hotter than Jet A-1 is consistent with extra heat associated with higher inlet temperature.

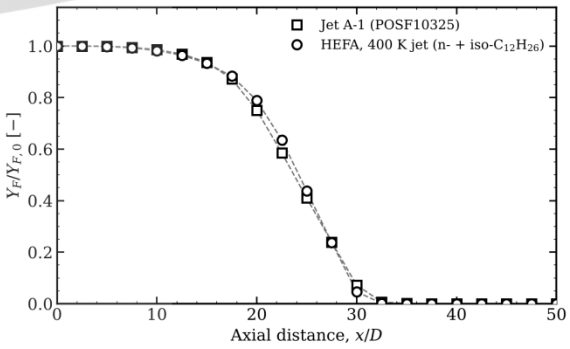


Fig. 4. Normalised centreline fuel mass fraction for Jet A-1 and HEFA (HEFA jet at 400 K).

According to figure 4, mass fraction plot along the axis, both fuels are consumed over similar distribution. Almost half the fuel is consumed at x/D = 23.8 for Jet A-1 and at x/D = 24.3 for HEFA. both fuels are consumed before temperature peaks that signals complete breakdown of fuel molecules that result in release of heat energy. The fuel disappears before temperature peaks in both case as the large molecules break into fragments that further break into smaller fragments, where those smaller fragments burn and release most of the heat. Despite the inlet temperature and equivalence ratio difference, both fuels essentially follow close path. In this flame, the fuel has little effect on where and how quickly the fuel ends.

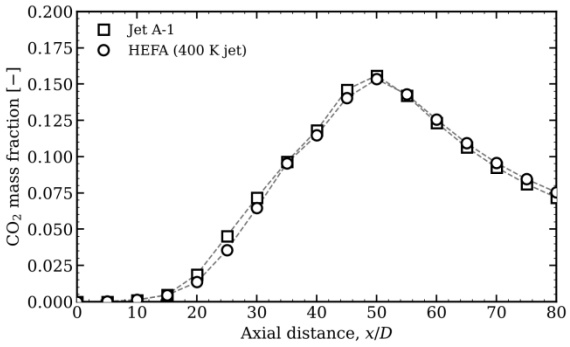


Fig. 5. Centreline CO_2 mass fraction for Jet A-1 and HEFA (HEFA jet at 400 K).

Figure 5 illustrates that the region near nozzle (x/D = 0 to 15) has almost no CO_2 as the fuel has not burnt yet. CO_2 starts to build up from x/D = 15 to 30 as the fuel starts to burn up. Both peaks at x/D = 49 (are just after temperature peaks), which is the expected consequence, products accumulate once the heat has been released. The peaks differ by only 2% (0.157 for Jet A-1 and 0.153 for HEFA). Lower CO_2 values for HEFA appear only in life-cycle assessment of HEFA, because carbon released was absorbed during feedstock growth and fuel synthesis [2]. Hence, HEFA benefit of lower CO_2 emission is invisible at flame level. CO_2 for HEFA is 10-28% lower than Jet A-1 from x/D = 20 to x/D = 30 and 5-9% higher at downstream, alongside the higher temperature at the same region.

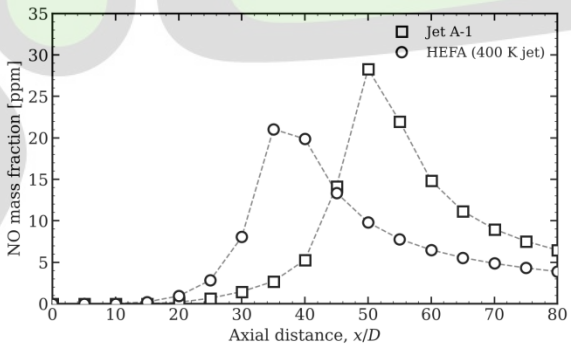


Fig. 6. Centreline NO mass fraction for Jet A-1 and HEFA (HEFA jet at 400 K).

NO was computed on frozen flame after convergence, using thermal and prompt routes with identical settings for both fuels. Absolute values are under-predicted, therefore NOx profile over axial distance is compared with each other rather than absolute emission comparison. As illustrated in figure 6, near the nozzle (x/D = 0 to 20) neither fuel forms NO as jet core is still cold. Jet A-1 NOx rises slower compared with HEFA, where HEFA peaks at x/D = 36.9, where it is 22.7 ppm, and NO due to Jet A-1 peaks at x/D = 50.4, where it is 28.4 ppm. Such behaviour is the expected signature of thermal NOx in the case of Jet A-1, which forms where the temperature is the highest. However, for HEFA the NO peaks 10 diameters before its temperature peak. Downstream, both fuels show decline in NO content, NO due to HEFA leaves the domain at 1.8 ppm, about 28% less, whereas Jet A-1 leaves at 2.5 ppm. HEFA peak NO is 20% lower than Jet A-1, and such a trend is consistent in the direction with Raji et al. [5], where NO_x due to pure HEFA is lower than Jet A-1. Lower trend of NO emission in the case of HEFA is notable, since the jet was hotter and equivalence ratio was lower for HEFA, the emission was expected to be higher. However, lower NO cannot be attributed to the fuel alone as jet temperature was hotter for HEFA.

4 Conclusion

A RANS–EDC framework using the Reynolds Stress Model was validated against Sandia Flame D measurements (peak temperature deviation ≈ 9%, RMSE 143 K) and, to the author's knowledge, applied for the first time to compare HEFA and Jet A-1 in this configuration. The two fuels showed closely similar flame behaviour. Peak temperatures were 2189 K for Jet A-1 and 2227 K for HEFA, the difference arising mainly from the hotter HEFA jet. Both fuels were consumed along the same axial path (complete by x/D ≈ 31–32), and their peak CO_2 differed by only 2%, showing that HEFA's life-cycle CO_2 benefit is not visible at flame level. HEFA produced about 20% lower peak NO than Jet A-1, a trend consistent in direction with experimental observations.

These results suggest that HEFA behaves much like Jet A-1 at the flame level, supporting its use as a drop-in fuel. However, the HEFA case required a higher jet temperature (400 K) and a lower equivalence ratio (φ ≈ 2.8) to converge, both fuels were treated as pre-vaporised, and absolute NO was under-predicted. The NO result should therefore be read as a trend. Future work should compare the fuels at matched inlet conditions, include spray injection and detailed NO chemistry, and extend the study to HEFA–Jet A-1 blends and soot formation.

5 Acknowledgement

This research project is funded by Middle East Technical University, Northern Cyprus Campus, Scientific Research Projects under the code of FEN-26-D-5

References

1. International Energy Agency, Aviation (tracking report, IEA, Paris, 2023), accessed [date]
2. M.N. Uddin, F. Wang, Energies **18**, 5510 (2025)
3. E. Borrill, S.C.L. Koh, R. Yuan, Front. Fuels **2**, 1397962 (2024)
4. Z. Xu et al., Environ. Pollut. **368**, 125661 (2025)
5. M. Raji, M.B.A. Manescau, K. Chetehouna, L. Lamoot, in Joint Meeting of the Italian and Spanish Sections of the Combustion Institute (Piano di Sorrento, 2026)
6. A. Åkerblom, M. Passad, A. Ercole, N. Zettervall, E.J.K. Nilsson, C. Fureby, Aerospace **11**, 31 (2024)
7. K. Ajmani, J.P. Moder, in 13th U.S. National Combustion Meeting (College Station, 2023)
8. A. Åkerblom, C. Fureby, Combust. Flame **272**, 113895 (2025)
9. P. Vauquelin et al., in AIAA SciTech Forum 2025, AIAA 2025-0163 (2025)
10. R.S. Barlow, J.H. Frank, Proc. Combust. Inst. **27**, 1087–1095 (1998)
11. G.P. Smith, D.M. Golden, M. Frenklach, N.W. Moriarty, B. Eiteneer, M. Goldenberg, C.T. Bowman, R.K. Hanson, S. Song, W.C. Gardiner Jr., V.V. Lissianski, Z. Qin, GRI-Mech 3.0 (1999), http://combustion.berkeley.edu/gri-mech/
12. R. Xu, K. Wang, S. Banerjee, J. Shao, T. Parise, Y. Zhu, S. Wang, A. Movaghar, D.J. Lee, R. Zhao, X. Han, Y. Gao, T. Lu, K. Brezinsky, F.N. Egolfopoulos, D.F. Davidson, R.K. Hanson, C.T. Bowman, H. Wang, Combust. Flame **193**, 520-537 (2018)
13. Y. Liang, J. Wang, Combust. Flame **280**, 114366 (2025)
14. K. Bayramoglu, A. Bahlekeh, K. Masera, Int. J. Hydrogen Energy **48**, 39586-39598 (2023)
15. ANSYS Inc., ANSYS Fluent Theory Guide (ANSYS Inc., Canonsburg, PA)
16. B.E. Launder, G.J. Reece, W. Rodi, J. Fluid Mech. **68**, 537-566 (1975)
17. S.B. Pope, AIAA J. **16**, 279-281 (1978)
18. D. He, Y. Yu, Y. Kuang, C. Wang, Appl. Sci. **11**, 4107 (2021)

19. B.F. Magnussen, in 19th AIAA Aerospace Sciences Meeting (St. Louis, 1981)
20. G.D. Raithby, E.H. Chui, J. Heat Transfer **112**, 415-423 (1990)
21. T.F. Smith, Z.F. Shen, J.N. Friedman, J. Heat Transfer **104**, 602-608 (1982)
22. D. He, Y. Yu, H. Ma, H. Liang, C. Wang, Appl. Sci. **12**, 9162 (2022)

Experimental evaluation of THF-promoted CO_2 hydrate formation for seasonal energy storage and Power-to-X applications

František Veselý[1], *Adam* Huněk[1], *Ondřej* Bartoš[1*], *Václav* Vinš[2]

[1]Czech Technical University in Prague, Faculty of Mechanical Engineering, Department of Energy Engineering, Technická 4, 166 07 Prague 6, Czech Republic
[2]Institute of Thermomechanics AS CR, v. v. i., Dolejškova 1402/5, 182 00 Prague 8, Czech Republic

Abstract. The contribution presents a project focused on the possible energy accumulation of seasonal uneven electricity production. The proposed technology uses waste CO_2 from flue gas, which is at first stored as a hydrate for a short time and, in times of excess electricity, transformed into synthetic fuels using hydrogen, i.e. with Power-to-X technology. The use of gas hydrates appears to be a promising way of separating and storing CO_2 from flue gas. The project addresses the issue of CO_2 hydrate production efficiency. This can be supported by using additives (promoters) that can favourably influence the kinetics of gas hydrate formation or shift the onset of formation to the regions with technically more convenient pressures and temperatures. The objective of the project is an experimental evaluation of the best approach of CO_2 separation and utilization.

1 Introduction

Carbon dioxide (CO_2) is the dominant anthropogenic greenhouse gas, with its atmospheric concentration rising from pre-industrial ~280 ppm to over 420 ppm today [1]. Post-combustion flue gases from fossil-fuel power plants typically contain 10–15 vol% CO_2, the balance being largely N_2. Current industrial-scale capture relies on amine absorption, which is energy-intensive: regeneration of the amine solvent consumes 3.5–4 MJ per kg of CO_2 captured [2]. Novel separation technologies with lower energy penalties are therefore actively sought.

Hydrate-based gas separation (HBGS) exploits the selective inclusion of CO_2 over N_2 in clathrate hydrate lattices [3, 4]. Clathrate hydrates are ice-like crystalline solids that form under elevated pressure and low temperature when gas molecules are encaged in a hydrogen-bonded water framework. CO_2 preferentially occupies structure I (sI) hydrate cages, while N_2 requires considerably higher pressures for stable hydrate formation. This thermodynamic selectivity is the basis for CO_2/N_2 HBGS [5].

Laboratory-scale HBGS studies have demonstrated CO_2 separation degrees of 35–60% in single-stage operation at 25–30 bar and 2–5°C [5, 9]. A key challenge is the high operating pressure, which drives compression costs. Thermodynamic promoters – additives that stabilise the hydrate structure at milder conditions – address this. Tetrahydrofuran (THF) at the stoichiometric 5.56 mol% forms sII hydrate with water. At the sub-stoichiometric 1 mol%, it still significantly shifts the equilibrium while leaving the majority of cages available for CO_2 [6, 7]. Combined with mechanical agitation, which overcomes the mass-transfer limitation of quiescent hydrate formation [8], THF enables high separation at substantially reduced pressures.

Most published HBGS experiments use batch reactors in the 0.3–2 L range [3, 5, 9]. Continuous isobaric systems, which more closely represent industrial conditions, are rarer. This work presents results from a large-volume (14,190 mL) continuous isobaric reactor commissioned at the Czech Technical University in Prague (CTU in Prague). Ten experiments characterised reactor kinetics with pure CO_2 and evaluated CO_2/N_2 separation performance with and without THF and mechanical mixing. A thermodynamic computational model, implemented in Python, was developed and validated against all experimental runs.

2 Theoretical background

2.1 Clathrate hydrate thermodynamics

Hydrate formation is governed by phase equilibrium between gas, liquid, and solid phases. The Clausius–Clapeyron equation can estimate the slope of equilibrium curves, while the van der Waals–Platteeuw (vdWP) statistical thermodynamic model provides a rigorous prediction of hydrate stability. CO_2 hydrate equilibrium (sI) in the binary CO_2+H_2O system lies at

* Corresponding author: ondrej.bartos@cvut.cz

approximately 25 bar at 2°C and drops to ~6 bar at 0°C, making low-temperature operation attractive [4].

With THF as a co-former, the system transitions from sI to sII hydrate, where large cages are occupied by THF and small cages can accommodate CO_2. The equilibrium pressure is substantially reduced: at 6.7°C, CO_2+THF hydrate forms at approximately 5–6 bar, compared to ~12 bar for pure CO_2 hydrate at that temperature [6].

2.2 Mass transfer and kinetics

The overall CO_2 uptake rate in a bubble column or stirred reactor is controlled by gas–liquid mass transfer. The volumetric mass transfer coefficient k_La characterises this transport and depends primarily on the gas superficial velocity or volumetric flow rate Q:

$$k_La = C \cdot Q^n \qquad (1)$$

where C is a system-specific constant and n is an empirical power-law exponent typically between 0.5 and 2. Higher mixing speeds and smaller bubble sizes increase k_La and thereby accelerate hydrate formation.

2.3 CO_2 separation metrics

The separation performance is quantified by the CO_2 separation degree S:

$$S = \frac{m_{CO_2,hyd}}{m_{CO_2,feed}} \times 100\% \qquad (2)$$

where $m_{CO2,hyd}$ is the mass of CO_2 captured in hydrates and $m_{CO2,feed}$ is the total CO_2 supplied. The gas uptake (mol CO_2/mol H_2O) and the split fraction are additional metrics.

3 Experimental setup

The experimental apparatus consists of a stainless-steel autoclave reactor (8,100 mL internal volume) connected in series to a buffer vessel (6,090 mL), giving a total working volume of 14,190 mL (Fig. 1). The system is designed for continuous isobaric operation: a pneumatically actuated back-pressure regulator (BPR) maintains constant pressure while CO_2 is continuously supplied to compensate for consumption by hydrate formation.

Pressure was measured by two Keller PA-21S transducers (range 0–25 bar, accuracy ±0.01 bar). Temperature was monitored at eight locations using PT100 sensors (accuracy ±0.1°C). Gas composition in the vapour phase was tracked using equations of state (CoolProp library) from measured T and P, with the initial composition known from the gas supply.

For the gas mixture experiments, premixed CO_2/N_2 cylinders were used: 77/23 mol% and 70/30 mol% compositions. Experiment 10 used 73/27 mol% CO_2/N_2 with 1 mol% THF dissolved in water. Mechanical mixing was provided by a propeller stirrer at 200 rpm in selected experiments.

3.1 Experimental protocol

Before each experiment, the reactor was filled with distilled water (or 1 mol% THF solution for Exp. 10) and pressurised with CO_2 (or CO_2/N_2 mixture) to the target pressure. The system was then cooled to the target temperature using a thermostat bath. Hydrate formation was indicated by a temperature spike (exothermic crystallisation) and was confirmed by the sustained pressure draw-down by the BPR.

After the primary hydrate formation phase, a secondary phase with mechanical mixing (propeller stirrer, 200 rpm) was initiated for selected experiments. This allowed direct comparison of quiescent and agitated conditions in the same run. The experiment was terminated when the pressure draw-down rate fell below a threshold indicating saturation of hydrate formation sites.

Temperature profiles at eight points in the reactor and buffer vessel were used to detect the spatial progress of hydrate formation. The onset temperature of hydrate formation (T_{nuc}) and the equilibrium temperature at the experimental pressure (T_{eq}) were combined to calculate the subcooling $\Delta T = T_{eq} - T_{nuc}$. Greater subcooling drives faster nucleation and growth.

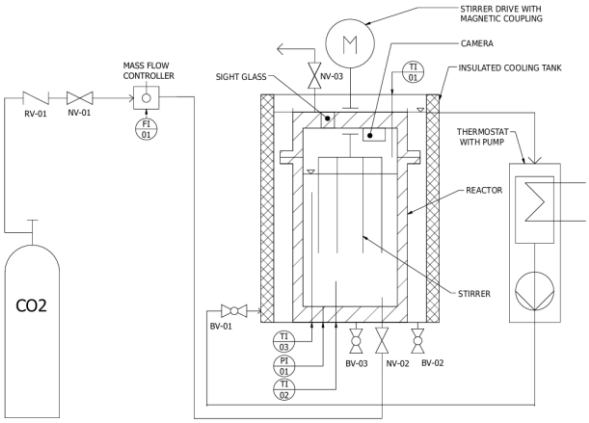


Fig. 1. Schematic P&ID diagram of the experimental apparatus. CO_2 is supplied from a cylinder through a mass flow controller (MFC) and needle valves (NV) into the insulated autoclave reactor (REACTOR) equipped with a magnetic-drive stirrer (M). A thermostat bath (THERMOSTAT) maintains the temperature. Pressure and temperature are monitored at multiple points.

4 Results and discussion

4.1 Kinetics with pure CO_2 (Exp. 1–7)

Seven experiments with pure CO_2 and water were performed at pressures of 20–30 bar and temperatures of 2–8°C. Induction times (time to onset of hydrate formation) ranged from 3 to 47 hours depending on subcooling $\Delta T = T_{eq} - T_{exp}$. Greater subcooling consistently reduced induction times.

The volumetric mass transfer coefficient was determined from the CO_2 uptake rate in the linear growth phase:

$$k_La = 1.0 \times 10^{-4} \cdot Q^{1.57} \qquad (3)$$

with Q in standard mL/min and k_La in s^{-1}. This power-law exponent of 1.57 is consistent with correlations reported for bubble column reactors with gas-to-liquid mass transfer [8].

Table 1. Selected results of the pure CO_2 experiments.

P [bar]	T [°C]	ΔT [°C]	CO_2 hyd. [g]	Induction [h]
24.2	2.0	3.5	72.4	3.2
28.7	3.5	4.1	89.1	1.8
22.5	1.5	2.9	61.3	6.4
30.1	4.0	4.8	95.7	1.1

Induction times showed a strong dependence on subcooling. At $\Delta T < 2.5$°C, induction times exceeded 20 h, whereas at $\Delta T > 4$°C they fell below 2 h. This follows classical nucleation theory, according to which the nucleation rate scales as $\exp(-\Delta G^*/kT)$ with $\Delta G^* \sim 1/\Delta T^2$. The memoryless character of nucleation was confirmed by the high variability in induction times across runs at nominally identical conditions.

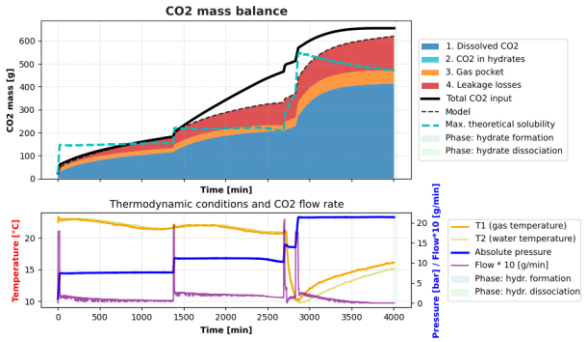


Fig. 2. Representative CO_2 mass balance time evolution for a pure CO_2 experiment. Upper panel: stacked area chart showing dissolved CO_2, CO_2 in hydrates, gas-phase CO_2, and leakage losses. Lower panel: temperature and pressure profile with hydrate formation and dissociation phases highlighted.

4.2 Thermodynamic model validation

A thermodynamic computational model was implemented in Python using the CoolProp equation-of-state library for fluid properties, together with Pandas for data handling and NumPy for numerical computations. The model integrates the measured pressure–time profile with the known reactor geometry and the CO_2 equation of state to compute the cumulative CO_2 transferred from the gas phase into hydrate.

At each time step, the model calculates the moles of CO_2 remaining in the gas phase from the real-gas equation of state at measured T and P. The difference between consecutive steps, after accounting for dissolved CO_2 in liquid water (Henry's law), gives the incremental CO_2 incorporated into hydrate. Summed over the experiment, this yields the total hydrate-bound CO_2 in grams, which is compared to the gravimetrically determined hydrate mass after melting.

Validation against all seven pure CO_2 experiments yielded a mean absolute error (MAE) below 10 g (Table 1 values). The maximum single-experiment error was 14.2 g (Exp. 6, $\Delta T = 2.9$°C), where slow dynamics introduced larger integration uncertainty. The model is therefore suitable for estimating CO_2 conversion under conditions representative of the mixture separation experiments.

4.3 CO_2/N_2 separation experiments (Exp. 8–10)

Three experiments were conducted with CO_2/N_2 mixtures to evaluate HBGS performance. Table 2 summarises the conditions and key results. Firstly, 77 mol% CO_2 without mixing was used as a baseline. Then the effect of mechanical mixing at similar conditions was investigated. Finally, THF was added as a promoter.

Table 2. Summary of the CO_2/N_2 separation experiments.

Exp.	Composition	P [bar]	T [°C]	CO_2 hyd. [g]	Sep. [%]
baseline	77/23 mol%	26.15	2.0	48.9	40.2
mixing	70/30 mol%	25.44	2.5	63.1	54.1
mixing+ THF	73/27 mol%+ THF	17.21	6.7	48.3	67.2

Baseline experiment (no mixing, no promoter) achieved 40.2% separation. Introducing mechanical mixing in subsequent experiment raised the separation to 54.1%, confirming that mass transfer is the limiting step under quiescent conditions. Gas uptake increased from approximately 0.7 to 1.1 mol CO_2/kg H_2O.

Subsequent experiment demonstrated the combined effect of THF promoter and mixing. Despite operating at only 17.21 bar (vs ~25 bar in Exp. 8–9), the separation rate reached 67.2%, the highest observed. THF effectively stabilises the CO_2 hydrate at milder T–P conditions, reducing energy requirements for compression. The induction time was also shorter (approximately 2 h), suggesting THF aids nucleation.

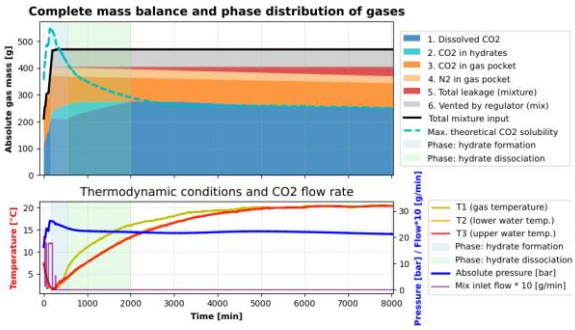


Fig. 3. Mass balance and phase distribution for the CO_2/N_2 separation experiment (Exp. 10, 1 mol% THF, mixing). Upper panel: gas mass in each phase versus time. Lower panel: temperature at three reactor locations and absolute pressure. The hydrate formation and dissociation phases are shaded.

4.4 Energy and efficiency considerations

The reduction in operating pressure from 25 bar to 17.2 bar achieved by THF corresponds to a significant reduction in compression work. Assuming isothermal compression of CO_2/N_2 from 1 bar, the compression work scales as

$$W \sim \ln(P_{out}/P_{in}) \qquad (4)$$

Hence, the compression energy ratio is $\ln(17.2)/\ln(25) \approx 0.84$, meaning an approximately 16% reduction in compression work. This estimate does not include energy for mixing or THF regeneration, which must be evaluated in a full process analysis.

The trade-off is that THF occupies large hydrate cages, reducing the available volume for CO_2 uptake. The gas uptake in experiment with THF (0.9 mol CO_2/kg H_2O) was lower than in the experiment with no THF (1.1 mol/kg). Optimising THF concentration and temperature presents a clear goal for future work.

4.5 Comparison with literature

Table 3 contextualises the present results against selected published HBGS studies. Linga et al. [3] reported 40–46% CO_2 separation from 16.9 mol% CO_2/N_2 mixtures in a 0.6 L stirred reactor at 7.5–8.5 MPa, without a promoter. Kumar et al. [5] achieved 55% separation using a 2 L unstirred reactor at 7 MPa with 1 mol% THF. Babu et al. [9] reported 68% separation at 4 MPa with 1 mol% THF and agitation from a silica gel bed.

Table 3. HBGS literature comparison (single-stage, CO_2/N_2).

Source	*P* [Mpa]	*T* [°C]	Sep. [%]	Conditions
Linga [3]	7.5–8.5	2–4	40–46	No promoter, stirred
Kumar [5]	7.0	2.5	55	1 mol% THF, unstirred
Babu [9]	4.0	2.5	68	1 mol% THF+SiO_2 bed
This work	1.72	6.7	67.2	1 mol% THF, stirred

The present results are comparable with literature values while operating at substantially lower pressure (1.72 vs. 4.0–8.5 MPa). The use of mechanical mixing (propeller at 200 rpm) is more practically scalable than the fixed silica gel bed used by Babu et al. [9]. The larger reactor volume (14,190 mL vs. ≤2,000 mL in cited studies) also provides a more representative dataset for engineering scale-up calculations, particularly for the k_La correlation, which depends on reactor geometry and gas distribution.

4.6 Scale-up outlook

The results obtained with the 14,190 mL reactor at CTU in Prague provide an engineering foundation for scale-up design. The k_La correlation given by Eq. (3) and derived at this scale can be used to dimension gas distributors and agitation systems for pilot-scale units. However, the correlation was derived under specific gas flow conditions (10–50 standard mL/min) and should be validated at higher flow rates typical of industrial applications.

Multi-stage HBGS can further improve separation efficiency. In a two-stage configuration, the hydrate phase from the first stage is melted and the released gas, enriched with CO_2, is fed back to a second hydrate formation stage. Modelling studies suggest that two-stage HBGS with 1 mol% THF could achieve over 90% CO_2 purity from a feed of 15–20 vol% CO_2 [10]. The thermodynamic model developed in this work is directly applicable to such multi-stage optimisation.

A key practical challenge for THF-assisted HBGS is THF recovery during hydrate dissociation. Since THF has a higher boiling point (66°C) than CO_2 (sublimes at −78.5°C at 1 bar), flash separation after hydrate melting can separate the gas product from the THF–water liquid phase, which is recycled. The energy demand for THF heating and cooling must be included in a full life-cycle assessment. Preliminary estimates suggest that the compression energy saving of ~16% from reduced operating pressure outweighs THF cycle energy costs at the scale evaluated here.

5 Conclusions

A continuous isobaric HBGS reactor was successfully designed, built, and commissioned at CTU Prague. The key conclusions from ten experimental runs are:

1. The mass transfer coefficient k_La scales with the gas volumetric flow rate as $k_La = 1.0 \times 10^{-4} \cdot Q^{1.57}$, consistent with bubble column correlations.
2. The CO_2/N_2 separation rate without mixing is 40.2%; mechanical mixing at 200 rpm increases this to 54.1%, confirming that the process is mass-transfer limited.
3. The THF promoter (1 mol%) reduces the required formation pressure by ~8 bar (from ~25 to 17.2 bar), enabling operation at 6.7°C.
4. The combination of THF and mechanical mixing achieves the highest separation degree of 67.2%, with reduced energy consumption for compression.
5. A Python thermodynamic model predicts CO_2 uptake with an MAE below 10 g for all experiments.
6. Future work should optimise THF concentration, investigate multi-stage HBGS, and perform a full energy analysis including THF recovery.
7. The k_La correlation and thermodynamic model are directly transferable to pilot-scale design and multi-stage configuration modelling.
8. THF recovery by flash separation at ambient pressure is thermodynamically favourable, and the associated energy cost is estimated to be offset by the ~16% compression work saving from reduced operating pressure.

The study was supported by the Technology Agency of the Czech Republic project no. TS01030115 within the Théta 2 Programme, the Czech Technical University in Prague, grant no. SGS24/127 and the institutional support of IT CAS RVO: 61388998.

Nomenclature

C empirical mass-transfer constant [s^{-1} $(mL/min)^{-n}$]
k_La volumetric mass transfer coefficient [s^{-1}]
MAE mean absolute error [g]
m mass [g]
n power-law exponent [–]
P pressure [bar]

Q volumetric gas flow rate [mL/min]
S CO_2 separation degree [%]
T temperature [°C]
ΔT subcooling = $T_{eq} - T_{exp}$ [°C]
V volume [mL]
α gas-to-liquid mass-transfer area per unit volume [m^{-1}]
ΔG^* activation energy of nucleation [J]
μ dynamic viscosity [Pa·s]
ρ density [kg/m^3]
τ induction time [h]
φ fugacity coefficient [–]

Subscripts: eq – equilibrium; exp – experimental; feed – feed gas; hyd – hydrate phase; in – inlet; nuc – nucleation; out – outlet.

References

1. IPCC, Climate Change 2023: Synthesis Report. Contribution of Working Groups I, II and III to the Sixth Assessment Report of the Intergovernmental Panel on Climate Change (IPCC, Geneva, 2023)
2. P. Linga, R. Kumar, P. Englezos, Chem. Eng. J. **149**, 33 (2009)
3. B. Castellani, S. Savelli, F. Rossi, Energy Procedia **45**, 617 (2014)
4. E.D. Sloan, C.A. Koh, Clathrate Hydrates of Natural Gases, 3rd edn. (CRC Press, Boca Raton, 2007)
5. R. Kumar, P. Linga, J.A. Ripmeester, P. Englezos, J. Environ. Eng. **135**, 411 (2009)
6. P. Babu, A. Nambiar, T. He, I.A. Karimi, J.D. Lee, P. Englezos, P. Linga, ACS Sustainable Chem. Eng. **6**, 8 (2018)
7. A. Babu, M. Linga, R. Kumar, P. Englezos, Energy Fuels **29**, 4 (2015)
8. R. Kumar, H.J. Lee, M. Song, J.-D. Park, Energy Fuels **22**, 3312 (2008)
9. P. Babu, C.-Y. Ho, R. Kumar, P. Englezos, Energy **78**, 517 (2014)
10. T. Zhong, Q. Cao, C. Liu, Chem. Eng. Sci. **233**, 116366 (2021)
11. M. Yang, Y. Song, L. Jiang, Y. Zhao, X. Liu, Chem. Eng. J. **225**, 342 (2013)
12. R. Raj, N.K. Gaikwad, P.D. Ghosh, Int. J. Heat Mass Transf. **94**, 63 (2016)
13. Z. Long, Y. Sun, X. Wang, J. Zheng, P. Li, Fluid Phase Equilib. **427**, 248 (2016)
14. J. Cai, Y. Liu, W. Guo, B. Shi, J. Gong, Chem. Eng. Sci. **174**, 81 (2017)
15. P. Di Profio, S. Arca, F. Rossi, G. Filipponi, Int. J. Hydrogen Energy **32**, 3860 (2007)
16. N. Nair, R. Bhattacharjee, V. Eswaran, Sep. Purif. Technol. **175**, 391 (2017)
17. F. Veselý, CO_2 Hydrate-Based Gas Separation: Design, Commissioning and Experimental Characterisation of an Isobaric Reactor System, MSc thesis, Czech Technical University in Prague (2026)
18. A. Eslamimanesh, A.H. Mohammadi, D. Richon, P. Naidoo, D. Ramjugernath, J. Chem. Thermodyn. **46**, 62 (2012)
19. S. Fan, X. Li, Y. Wang, X. Lang, Y. Liang, K. Meng, Energy Convers. Manag. **51**, 2611 (2010)
20. A. Chapoy, C. Coquelet, D. Richon, Fluid Phase Equilib. **214**, 101 (2003)
21. B. Tohidi, A. Chapoy, J. Yang, in Proceedings of the 7th International Conference on Gas Hydrates, Edinburgh, UK (2011)
22. Y. Wang, X. Lang, S. Fan, J. Nat. Gas Chem. **22**, 39 (2013)

Influence of electrode geometry on airflow characteristics in a needle-to-cylinder EHD fan: an experimental study

Klaudia Zwolińska-Glądys[1*], *Jean Paul Cardona* Murillo[2], *Marek* Borowski[1] and *Marek* Jaszczur[2]

[1]AGH University of Krakow, Faculty of Civil Engineering and Resource Management, A. Mickiewicza 30, 30-059 Kraków, Poland
[2]AGH University of Krakow, Faculty of Energy and Fuels, A. Mickiewicza 30, 30-059 Kraków, Poland

Abstract. Electrohydrodynamic (EHD) fans generate airflow without moving parts through corona discharge and ion–neutral momentum transfer, offering a solid-state, vibration-free and compact alternative to rotary fans for electronics cooling. Their performance depends strongly on electrode geometry, yet systematic experimental data on individual geometric parameters remain limited. This work presents a parametric experimental study of the airflow generated by a needle-to-cylinder EHD fan. A modular test rig allows independent variation of the collector diameter, active collector length and inter-electrode spacing; the total flow-straightening length is kept constant by extending the shorter collector with a 3D-printed dielectric tube, so that the active electrode length is isolated from the length of the downstream duct. A positive DC high voltage is applied to the needle, with the collector grounded, and is increased stepwise from the corona onset voltage to spark breakdown. The time-averaged outlet velocity is measured along the device axis by hot-wire anemometry while the discharge current is recorded simultaneously, yielding the current–voltage, velocity–voltage and velocity–current characteristics of eight configurations. The inter-electrode spacing is the dominant parameter: moving the needle from the collector inlet ($S = 0$) to $S = D/2$ increases the maximum mean outlet velocity by a factor of 2.2–3.5, reaching up to 3.5 m/s. The active collector length has no significant effect at $S = D/2$, whereas at $S = 0$ the 30 mm collector yields a 37–68% higher maximum velocity than the 5 mm one. With the 30 mm collector, the smaller diameter reaches a peak velocity comparable to that of the larger one at about a quarter of the electrical power.

1 Introduction

The continuous miniaturization of electronic components, driven by decreasing transistor dimensions alongside increasing clock frequencies and power densities, has made localized heat flux dissipation a primary thermal management bottleneck [1]. Conventional cooling architectures rely on heat sinks and heat pipes coupled with forced convection, which is typically supplied by rotary blade fans [2, 3]. However, mechanical fans impose strict packaging constraints, generate acoustic noise, and suffer from mechanical wear due to moving parts. Electrohydrodynamic (EHD) gas pumps, often termed ionic wind blowers or EHD fans, provide solid-state alternative capable of inducing airflow without mechanical transmission [4, 5].

An EHD fan operates via a corona discharge established between two or more electrodes subjected to a high potential difference. A sharp high-voltage emitter electrode generates an intense localized electric field that ionizes surrounding air molecules [6]. Driven by Coulombic forces, the resulting unipolar ions drift toward a grounded collector electrode, colliding with neutral gas molecules along their trajectory. This momentum transfer induces a macroscopic, unidirectional bulk airflow [4]. Because EHD devices contain no moving components, they operate silently, experience negligible mechanical degradation and offer high geometric adaptability. A wide range of electrode topologies has been explored, pairing needle, wire or sharp-plate emitters with wire, mesh, ring, plate, or cylindrical collectors [3, 7–9]. Investigations of needle-to-ring-net configurations demonstrated that peak electric field strengths concentrate around the needle tip and ring edges, whereas the ring electrode itself does not induce significant local space-charge accumulation. In such systems, airflow velocity and energy conversion efficiency increase monotonically with applied voltage, reaching a maximum value of 4.26% under specific geometric parameters [10].

To overcome the static pressure and flow rate limitations inherent to single-stage units, multi-stage and cascaded architectures have been developed [11]. Integrating secondary collecting ring electrodes enables successive acceleration of charged particles, increasing ionic wind velocity by 32% to 52% compared to single-stage blowers and broadening the downstream velocity profile once initial localized vortices near the collectors subside [12]. Evaluations of multi-stage EHD pumps with varying emitter pin counts (8, 24, 56 pins) showed that sparser emitter arrays achieve higher maximum velocities, larger volumetric flow rates, and higher energy efficiency by limiting excessive corona current at a given voltage, whereas flush-mounted wall emitters produce inverted parabolic velocity profiles [13].

Among the available topologies, coaxial needle-to-cylinder and wire-to-cylinder arrangements are

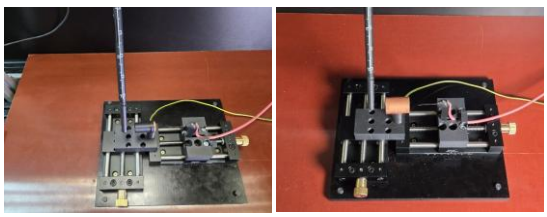
particularly suited for ducted cooling systems due to their radial symmetry and compact geometry [7, 8, 14, 15]. Although previous investigations have examined the effects of inter-electrode gap and grounded electrode dimensions in gas pumps [16], systematic studies isolating the influence of collector geometry remain limited. Notably, Primas et al. [17] varied the length of a 70 mm diameter grounded cylindrical collector (40–100 mm) housed inside a dielectric outer tube across inter-electrode gaps of 0–40 mm. They reported that the longest collector yielded the highest mean axial velocity (approximately 2.0 m/s) prior to spark breakdown at 16 kV. However, when a metallic collector is embedded within an insulating outer duct of fixed total length, altering the collector length simultaneously changes the length of the downstream dielectric section, which acts as a flow-straightening channel.

Consequently, a distinct research gap exists regarding the decoupled effects of electrode geometry on the aerodynamic and electrical performance of needle-to-cylinder EHD fans. In particular, the effect of the active collector length, isolated from that of the downstream flow-straightening duct, and its interaction with the emitter-to-collector spacing and the cylinder diameter have not been systematically quantified. Such data are a necessary step toward geometric design guidelines for ducted EHD blowers. The objective of this experimental investigation is to quantify the influence of electrode geometry on the airflow characteristics and discharge behaviour of a positive-DC needle-to-cylinder EHD fan by independently varying the active collector length at a constant flow-straightening duct length, together with the collector diameter and the emitter-to-collector spacing.

2 Experimental setup and methodology

2.1 Test rig and configurations

The EHD fan consists of a high-voltage needle emitter and a grounded cylindrical collector (Fig. 1). The emitter is a steel needle with a radius of $r = 0.5$ mm. The cylindrical collectors are fabricated from copper, with outer diameters of $D = 22$ mm and $D = 16$ mm and a wall thickness of 1 mm. The electrodes are mounted in 3D-printed matte black polylactic acid (PLA) holders and the entire assembly is attached to Bakelite plates for electrical insulation. Two linear translation stages allow precise adjustment of the inter-electrode spacing and coaxial alignment of the needle electrode [18].



(a) (b)

Fig. 1. Test rig with the needle emitter and the cylindrical collector mounted on linear translation stages: (a) spacing $S = 0$; (b) spacing $S = D/2$.

Two inter-electrode distances S, measured axially between the needle tip and the collector inlet, were evaluated: $S = 0$ (with the needle tip aligned with the collector inlet) and $S = D/2$. For each combination of collector diameter and spacing, two active collector lengths (L_c) were tested: 30 mm and 5 mm. To isolate the effect of the active electrode length, the 5 mm collector was extended to a total length of 30 mm using a 3D-printed dielectric PLA extension tube of the same inner and outer diameters (variant L5+ext, Fig. 2). These combinations yielded eight distinct geometric configurations in total.



(a) (b)

Fig. 2. Collector electrodes, $D = 22$ mm (left) and $D = 16$ mm (right) in each panel: (a) bare copper collectors, L30 (top) and L5 (bottom) length; (b) the same collectors with the dielectric PLA extension fitted to the 5 mm variant (L5+ext).

This experimental matrix enables a direct comparison: the extended 5 mm collector (L5+ext) with the 30 mm collector (L30) isolates the effect of the active electrode length at a constant total flow-straightening length ($L_{tot} = 30$ mm). The two collector length variants are summarized in Table 1.

Table 1. Collector length variants. Each variant was tested for $D = 22$ mm and $D = 16$ mm, and for $S = 0$ and $S = D/2$, giving eight configurations.

Variant	L_c (mm)	L_{ext} (mm)	L_{tot} (mm)
L30	30	0	30
L5+ext	5	25	30

2.2 Measurements

A positive DC high voltage was applied to the needle emitter using a Genvolt 74060P power supply (0–40 kV, 1.5 mA, 60 W), while the collector was grounded. The discharge current I was determined from the voltage drop V_R measured across a precision resistor ($R_1 = 99.1$ kΩ), connected in series with the ground return line, using a digital multimeter (UNI-T UT803),

$$I = V_R / R_1 \quad (1)$$

The centerline axial airflow velocity was measured at a distance of $1D$ downstream of the duct exit (corresponding to the collector outlet for L30 and the dielectric extension outlet for L5+ext) using a hot-wire anemometer. Velocity data were sampled at 1 Hz over a 60 s interval, yielding 60 samples per voltage step,

following the protocol established in prior work [18]. Ambient temperature and relative humidity were recorded using a Benetech GM1361+ thermo-hygrometer prior to each experimental run to monitor environmental conditions, as ambient humidity affects corona discharge behaviour and ionic wind velocity [18].

2.3 Procedure and data processing

For each configuration, the applied voltage was first increased to identify the corona onset voltage V_0, defined as the lowest potential yielding a measurable discharge current. After recording the initial data point at V_0, subsequent measurements were taken at integer kilovolt values, starting from the nearest integer above V_0, in increments of $\Delta V = 1$ kV until spark breakdown or unstable streamer discharge occurred.

At each voltage step, the airflow velocity is reported as the arithmetic mean of the 60 recorded samples, with error bars representing one standard deviation. Experimental results are presented as current–voltage (I–V) and velocity–voltage (U–V) characteristics for each configuration, where U denotes the mean axial airflow velocity and V the applied voltage.

3 Results

3.1 Current–voltage characteristics

EHD fans operate in the stable corona discharge regime, in which the discharge current follows the Townsend relation $I = CV(V - V_0)$, where C is a geometry-dependent constants. To verify this, the current drawn by the device was plotted against the applied voltage.

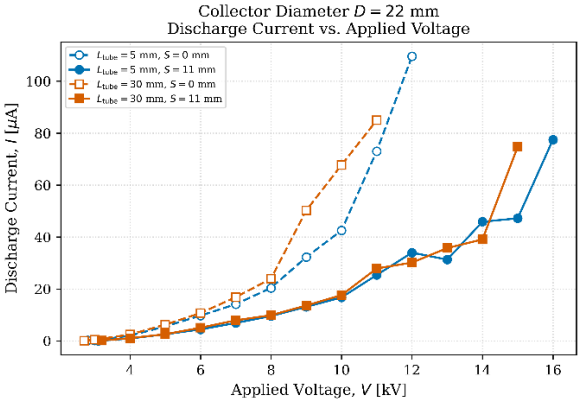


Fig. 3. Discharge current versus applied voltage for D=22 mm.

For the 22 mm collectors at $S = D/2$, the trend follows the expected quadratic behaviour up to approximately 10 kV; above this threshold the current becomes intermittently unstable (for L5+ext, decreasing from 34 to 31 μA between 12 and 13 kV), which indicates the onset of transient pre-breakdown discharges. These instabilities grow with the applied voltage until sparks breakdown occurs. For the shorter spacing $S = 0$, similar behaviour is observed, with a lower instability threshold at 8 kV. Across both spacings the longer collector (L30) exhibited a lower breakdown voltage. At $S = 0$ the 30 mm collector also draws a markedly higher current above 8 kV (approximately 50 μA versus 32 μA at 9 kV), consistent with its larger ion-collecting surface.

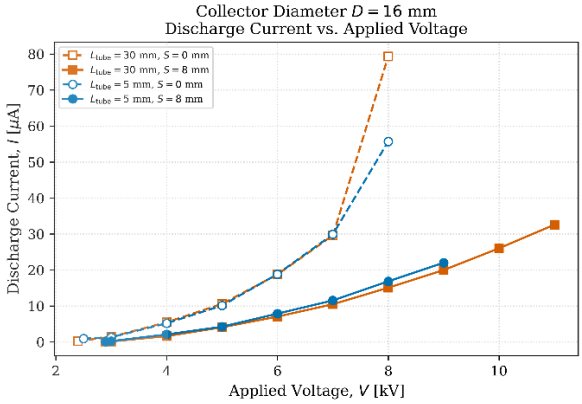


Fig. 4. Discharge current versus applied voltage for D=16 mm.

For the 16 mm collector diameter at $S = D/2$, no unstable regime was observed: the current increased smoothly up to the final stable voltage step prior to spark breakdown. At $S = 0$, by contrast, the current rose abruptly between 7 and 8 kV (from 30 to 80 μA for L30 and from 30 to 56 μA for L5+ext) before breakdown. At spacing $S = 0$, breakdown occurred at the same voltage for both collector lengths, whereas at $S = D/2$ the longer collector (L30) exhibited a wider working operating range, extending up to 11 kV. For L5+ext , stable operation ended at 9 kV and 22 μA, without the steep current rise that preceded breakdown at $S = 0$.

Across all tested configurations, an operating range exists in which the current increases smoothly and follows the quadratic Townsend relation, confirming stable corona discharge operation.

3.2 Velocity–voltage and velocity–current characteristics

The mean axial velocity measured at a distance of 1D downstream of the outlet is plotted against the applied voltage for each collector diameter in Figs. 5 and 6.

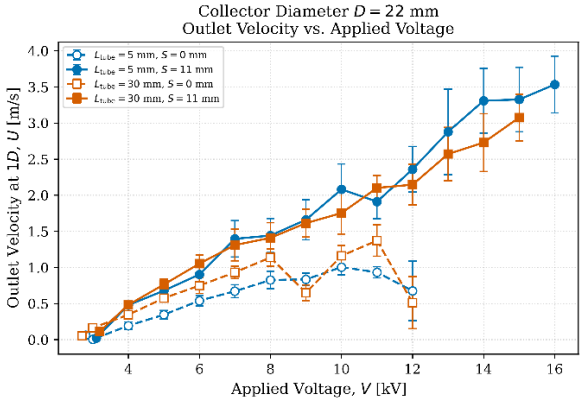


Fig. 5. Outlet velocity versus applied voltage for D = 22 mm.

For D = 22 mm at $S = D/2$ (Fig. 5) both collector lengths yield comparable velocities: although the shorter collector (L5+ext) generates slightly higher mean values

at most voltage steps above 9 kV, these differences remain within one standard deviation. At S = 0, in contrast, the longer collector (L30) generated substantially higher velocities over most of the voltage range, reaching a maximum of 1.37 m/s compared with 1.00 m/s for L5+ext. At this spacing, the velocity is also non-monotonic, decreasing at 9 kV for L30 and at 12 kV for both collectors, accompanied by a sharp increase in the standard deviation; these drops coincide with the current instabilities observed in Fig. 3.

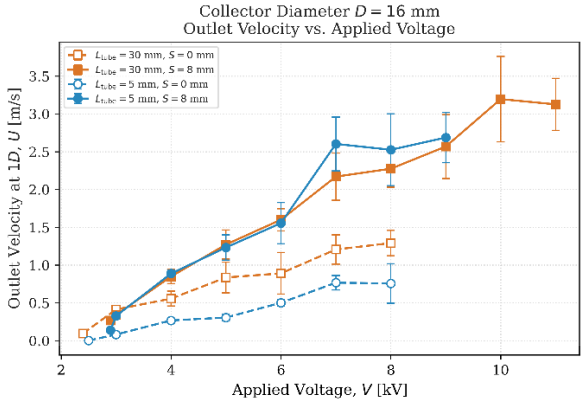


Fig. 6. Outlet velocity versus applied voltage for D = 16 mm.

Fig. 6 shows a similar trend for the smaller diameter: at S = D/2 the shorter collector yields slightly higher velocities between 7 and 9 kV (2.60 versus 2.17 m/s at 7 kV), although the error bars overlap; above 9 kV only the longer collector (L30) could be operated, reaching a peak velocity of 3.20 m/s at 10 kV. Conversely, at S = 0 the longer collector again generates a consistently higher velocity across the entire operating range (1.29 versus 0.77 m/s at the maximum).

This behaviour can also be related to the discharge current. Because the electrohydrodynamic body force is proportional to the current density, higher velocities are expected at higher currents; in simplified one-dimensional models the velocity scales approximately with the square root of the current.

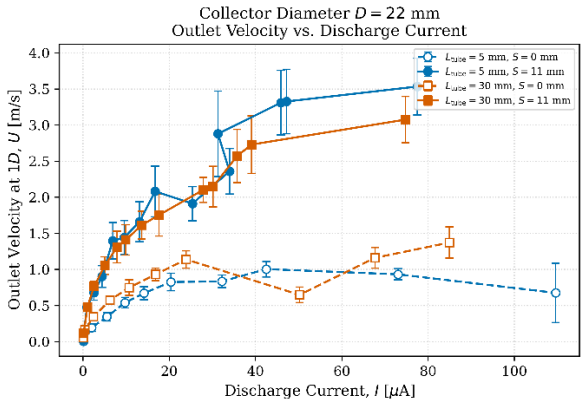


Fig. 7. Outlet velocity versus discharge current for D=22 mm.

For the 22 mm diameter (Fig. 7) this relationship holds at low currents; as the current increases and instabilities appear, the trend becomes less clear and the velocity at a given current is less predictable.

In contrast, for the smaller D = 16 mm collector at S = D/2 the current–voltage characteristic was smooth over the entire operating range.

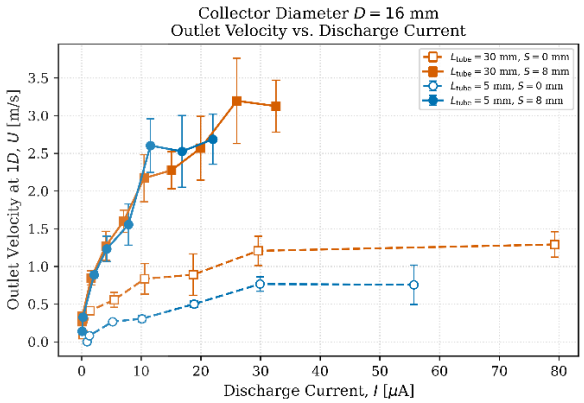


Fig. 8. Outlet velocity versus discharge current for D=16 mm.

Fig. 8 shows that at S = D/2 the velocity increases steadily with the current for both collector lengths and the two curves near coincidence, indicating that collector length does not alter the relation between current and velocity. At S = 0, in contrast, the velocity saturates: a two- to threefold increase in current (from approximately 30 μA to 56 μA for L5+ext and to 80 μA for L30) raises the velocity by less than 0.1 m/s. At a current of approximately 10 μA the velocity at S = D/2 (2.2–2.6 m/s) is three to eight times higher than at S = 0 (0.3–0.8 m/s).

The effect of collector length mirrors that observed in the velocity-voltage curves: at S = D/2 collector length has no systematic effect on the velocity at a given current (yielding shortly higher or lower velocities depending on the current level), whereas at S = 0 the longer collector achieves consistently higher velocities.

The main parameter for the peak velocity is therefore the inter-electrode spacing: the effect of the collector length depends on the spacing, whereas S = D/2 consistently yields higher velocities, as summarized in Table 2.

This phenomena can be attributed to differences in the dominant direction of ion drift. At S = D/2 the ions are accelerated predominantly axially in the gap between the needle tip and the collector inlet, so most of the momentum is transferred upstream of the collector inlet, and whether the duct wall downstream of the inlet is conducting or dielectric has little influence. At S = 0 the needle tip lies in the inlet plane and the ions drift largely radially towards the collector wall. A longer grounded collector allows the field lines, and hence the ion trajectories, to terminate further downstream, adding an axial component to the drift; with the 5 mm collector the ions must reach a narrow copper band, and positive charge deposited on the dielectric extension may deflect them further. This interpretation is supported by configurations with similar tip-to-collector distances: for D = 22 mm at S = 0 and for D = 16 mm at S = D/2 the distance from the needle tip to the inner edge of the collector inlet is approximately 10 mm and 10.6 mm, the onset voltages are similar (2.7–2.8 kV and 2.9 kV), and so are the currents at 8 kV (approximately 20–24 μA and 15–17 μA respectively), yet the velocity at 8 kV is two

to three times higher in the latter case (2.3–2.5 m/s versus 0.8–1.1 m/s). Numerical simulations of the coupled electric field and space-charge transport are required to confirm this mechanism.

Table 2. Maximum mean outlet velocity U_{max} (one standard deviation over the 60 s sampling) at the two inter-electrode spacings; $S = D/2$ corresponds to 11 mm for $D = 22$ mm and 8 mm for $D = 16$ mm.

D (mm)	L_c	U_{max} (m/s) $S = 0$	U_{max} (m/s) $S = D/2$	Ratio
22	L30	1.37 ± 0.22	3.08 ± 0.32	2.2
22	L5+ext	1.00 ± 0.11	3.53 ± 0.39	3.5
16	L30	1.29 ± 0.17	3.20 ± 0.57	2.5
16	L5+ext	0.77 ± 0.10	2.69 ± 0.33	3.5

3.3 Effect of collector diameter

The effect of the collector diameter is less evident than that of the inter-electrode distance, but there are still marked effects, summarized in Table 3.

Table 3. Effect of the collector diameter: corona onset voltage V_0, and the applied voltage, maximum mean outlet velocity and discharge current at the maximum.

L_c (mm)	S	Onset V_0 (kV)		V at U_{max} (kV)		U_{max} (m/s)		I at U_{max} (μA)	
D (mm)		22	16	22	16	22	16	22	16
30	0	2.7	2.4	11	8	1.37	1.29	85.0	79.3
30	$D/2$	3.2	2.9	15	10	3.08	3.20	74.8	26.0
5+25	0	2.8	2.5	10	7	1.00	0.77	42.5	29.9
5+25	$D/2$	3.1	2.9	16	9	3.53	2.69	77.5	22.0

The effect of the diameter is presented first in the onset voltage: as smaller collectors correspond to a shorter net distance between the electrodes, the voltage required to achieve a flow of ions is decreased. From this it also follows that the peak velocity occurs at a consistently lower voltage and current than for the larger diameter. For the 30 mm collector the peak velocities of the two diameters are similar (3.20 and 3.08 m/s at $S = D/2$), so the smaller diameter attains them at a much lower electrical power (about 0.26 W versus 1.12 W). With the 5 mm collector, however, the smaller diameter reaches a lower peak velocity (2.69 versus 3.53 m/s at $S = D/2$). An upper-bound estimate of the electromechanical conversion efficiency, $\eta = \rho A U^3/(2VI)$, with the centreline velocity applied over the whole inner cross-section A, gives about 1.2% for $D = 16$ mm and 0.5% for $D = 22$ mm with L30 (0.9% and 0.7% with L5+ext), all at $S = D/2$, and only 0.02–0.05% at $S = 0$, where the velocity saturates while the current keeps rising. Because S scales with D, the diameter and the absolute tip-to-collector distance change together in the present test matrix, so their effects cannot be fully separated.

4 Conclusions

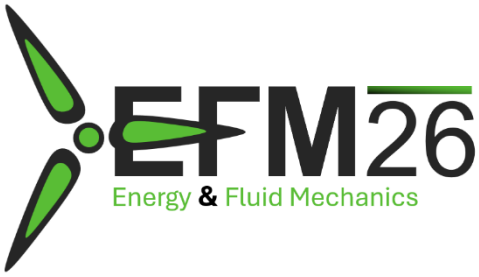
The discharge current and centerline axial outlet velocity of a needle-to-cylinder EHD fan were experimentally investigated across two collector diameters (22 and 16 mm), two inter-electrode spacings ($S = 0$ and $S = D/2$) and two active collector lengths (30 mm, and 5 mm extended to a total length of 30 mm with a dielectric tube), up to spark breakdown. Inter-electrode spacing is the dominant geometric parameter: increasing spacing to $S = D/2$ increases the maximum mean velocity by a factor of 2.2 to 3.5, up to 3.5 m/s, and widens the operating voltage range prior to breakdown. At a constant total flow-straightening length, the influence of active collector length depends strongly on inter-electrode spacing: at $S = D/2$ it has no statistical significant effect on either outlet velocity or on the current–velocity relationship, whereas at $S = 0$ the longer collector gives a 37–68% higher maximum velocity, which is tentatively attributed to an axial component of the ion drift toward the longer grounded wall. Reducing the collector diameter lowers the onset voltage; with the 30 mm collector it reaches a peak velocity comparable to that of the larger diameter at approximately one-quarter of the electrical input power. At $S = 0$ the estimated conversion efficiency is more than an order of magnitude lower than at $S = D/2$ because outlet velocity saturates despite continued discharge current growth. These findings contrast with thoset of Primas et al. [17], who reported the highest velocity for the longest collector; in the present work this holds only at $S = 0$, which suggests that part of the length effect reported there may stem from the simultaneous change in the length of the dielectric section, or from differences in geometry (a 70 mm collector inside a dielectric tube, longer collectors and larger gaps). Because each configuration was evaluated over a single monotonically increasing voltage sweep, the observed trends should be regarded as indicative; repeated runs hysteresis checks, and intermediate spacings and collector lengths remain for future work. Spatially resolved velocity profile measurements and coupled numerical modelling of the electric field and space-charge transport are planned to verify the proposed ion-drift mechanism.

Fundings. This work was partly funded by AGH University of Krakow, Faculty of Civil Engineering and Resource Management (No. 501.00-100302-10000) and Faculty of Energy and Fuels (No. 500.00-210000-10000). Research project was supported by the program "Excellence initiative – research university" for the AGH University of Krakow.

Data availability statement. Data will be made available on request

References

1. S. Cheng, J. Leong, F. Lai, EHD gas pump as a cooling device for electronic components in a horizontal channel. J. Electrost. **129**, 103935 (2024). https://doi.org/10.1016/j.elstat.2024.103935
2. D. Go, R.A. Maturana, T.S. Fisher, S.V. Garimella, Enhancement of external forced convection by ionic wind. Int. J. Heat Mass Transf. **51**, 6047–6053 (2008). https://doi.org/10.1016/j.ijheatmasstransfer.2008.05.012
3. M. Cogollo, P.M. Balsalobre, A. Díaz Lantada, H. Puago, Design and experimental evaluation of innovative wire-to-plane fins' configuration for atmosphere corona-discharge cooling devices. Appl. Sci. **10**, 1010 (2020). https://doi.org/10.3390/app10031010
4. J. Wang et al., Review on the recent development of corona wind and its application in heat transfer enhancement. Int. J. Heat Mass Transf. **152**, 119545 (2020). https://doi.org/10.1016/j.ijheatmasstransfer.2020.119545
5. Y. Peng et al., A review on electrohydrodynamic (EHD) pump. Micromachines **14**, 321 (2023). https://doi.org/10.3390/mi14020321
6. Y.P. Raizer, *Gas Discharge Physics* (Springer, Berlin, 1991). https://doi.org/10.1007/978-3-642-61247-3
7. H. Li et al., Effect of cylinder electrode arrangement on the ionic wind properties of needle–cylinder electrodes. J. Electrost. **86**, 59–68 (2017). https://doi.org/10.1016/j.elstat.2017.01.013
8. E. Moreau et al., Electrohydrodynamic force produced by a corona discharge between a wire active electrode and several cylinder electrodes – application to electric propulsion. J. Electrost. **76**, 194–200 (2015). https://doi.org/10.1016/j.elstat.2015.05.025
9. Y. Zhang et al., Characteristics of ionic wind in needle-to-ring corona discharge. J. Electrost. **74**, 15–20 (2015). https://doi.org/10.1016/j.elstat.2014.12.008
10. R.-X. Cai, W. Chen, F. Zhang, W.-C. Yan, A systematic investigation on flow characteristics of needle-ring-net electrohydrodynamic gas pump. Phys. Fluids **35**, 047108 (2023). https://doi.org/10.1063/5.0140445
11. B. Xu, J. Zhong, Z. Mao, J. Shintake, L. Song, J. Ohgi, J. Zhang, Toward intelligent fluidic systems: a roadmap for electrohydrodynamic pumping. Cyborg Bionic Syst. **7**, 0648 (2026). https://doi.org/10.34133/cbsystems.0648
12. J. Wang, Y.-J. Liu, T. Zhu, Y.-Q. Chen, R.-J. Cai, G.-K. Liu, Flow distribution and cooling performance of needle-to-ring ionic wind blowers with multiple electrodes. Int. J. Heat Mass Transf. **193**, 122971 (2022). https://doi.org/10.1016/j.ijheatmasstransfer.2022.122971
13. A.K.M.M.H. Mazumder, G.S. Trombley, B.G. Cousino, Number of emitting electrodes effect on a two stage electrohydrodynamic gas pump performance. J. Electrost. **140**, 104274 (2026). https://doi.org/10.1016/j.elstat.2026.104274
14. M. Toptaş, M. Yılmaz, Investigating the effects of Lorentz forces on electrohydrodynamic flow generated by corona discharge in a multi needle-to-cylinder configuration. Therm. Sci. Eng. Prog. **61**, 103543 (2025). https://doi.org/10.1016/j.tsep.2025.103543
15. J. Lee et al., Analysis and optimization of the electrohydrodynamic (EHD) flow with a wire-to-two-cylinder configuration for convective heat transfer. Int. J. Heat Mass Transf. **182**, 121959 (2021). https://doi.org/10.1016/j.ijheatmasstransfer.2021.121959
16. A.K.M.M.H. Mazumder, F. Lai, Effect of grounded electrode size on a single-stage EHD gas pump performance in a square channel. J. Electrost. **99**, 49–58 (2019). https://doi.org/10.1016/j.elstat.2019.05.001
17. J. Primas et al., Detailed analysis of airflow generated by high voltage on a point-tube electrode geometry. Fluids **8**, 115 (2023). https://doi.org/10.3390/fluids8040115
18. K. Zwolińska-Glądys, J.P. Cardona Murillo, M. Jaszczur, Impact of relative humidity and PIV seeding on the electro-aerodynamic performance of needle-to-ring ionic fans. Exp. Fluids **67**, 168 (2026). https://doi.org/10.1007/s00348-026-04322-y



Edited by: Jaroslav Pulec

First edition